

# ***SOILS and ROCKS***

An International Journal of Geotechnical and Geoenvironmental Engineering

## **Editor**

Renato Pinto da Cunha  
University of Brasília, Brazil

## **Co-editor**

Ana Vieira  
National Laboratory for Civil Engineering, Portugal

## **Associate Editors**

António Alberto S. Correia  
*University of Coimbra, Portugal*

Cristiana Ferreira  
*University of Porto, Portugal*

Fernando Feitosa Monteiro  
*Unichristus, Brazil*

Gilson de F. N. Gitirana Jr.  
*Federal University of Goiás, Brazil*

José A. Schiavon  
*Aeronautics Institute of Technology, Brazil*

Juliane Marques  
*Federal University of Alagoas / AGM, Brazil*

Karina C. Arruda Dourado  
*Federal Institute of Pernambuco, Brazil*

Leandro Neves Duarte  
*Federal University of São João del-Rei, Brazil*

Luciano Soares da Cunha  
*University of Brasília, Brazil*

Luis Araújo Santos  
*Polytechnic Institute of Coimbra, Portugal*

Marcio Leão  
*Federal University of Viçosa / IBMEC-BH, Brazil*

Margarida Pinho Lopes  
*University of Aveiro, Portugal*

Neusa M. B. Mota  
*University Center of Brasília, Brazil*

Nuno Cristelo  
*University of Trás-os-Montes and Alto Douro, Portugal*

Paulo J. R. Albuquerque  
*Campinas State University, Brazil*

Rui Carrilho Gomes  
*Technical University of Lisbon, Portugal*

Sara Rios  
*University of Porto, Portugal*

Silvrano Adonias Dantas Neto  
*Federal University of Ceará, Brazil*

Teresa M. Bodas Freitas  
*Technical University of Lisbon, Portugal*

## **Advisory Panel**

Alejo O. Sfriso  
*University of Buenos Aires, Argentina*

Harry Poulos  
*University of Sidney, Australia*

Luis A. Vallejo  
*Complutense University of Madrid, Spain*

Emanuel Maranhã das Neves  
*Technical University of Lisbon, Portugal*

Michele Jamiolkowski  
*Studio Geotecnico Italiano, Italy*

Roger Frank  
*École des Ponts ParisTech, France*

Willy Lacerda  
*Federal University of Rio de Janeiro, Brazil*

## **Editorial Board**

Abdelmalek Bouazza  
*Monash University, Australia*

Alessandro Mandolini  
*University of Naples Federico II, Italy*

Alessio Ferrari  
*École Polytechnique Fédérale de Lausanne, Switzerland*

Antônio Roque  
*National Laboratory for Civil Engineering, Portugal*

Antônio Viana da Fonseca  
*University of Porto, Portugal*

Armando Antão  
*NOVA University Lisbon, Portugal*

Beatrice Baudet  
*University College of London, UK*

Catherine O'Sullivan  
*Imperial College London, UK*

Cristhian Mendoza  
*National University of Colombia, Colombia*

Cristina Tsuha  
*University of São Paulo at São Carlos, Brazil*

Daniel Dias  
*Antea Group / Grenoble-Alpes University, France*

Debasis Roy  
*Indian Institute of Technology Kharagpur, India*

Denis Kalumba  
*Cape Town University, South Africa*

Fangwei Yu  
*Inst. Mt. Haz. Env. Chinese Acad. of Sci. China*

Ian Schumann M. Martins  
*Federal University of Rio de Janeiro, Brazil*

Jean Rodrigo Garcia  
*Federal University of Uberlândia, Brazil*

José Muralha  
*National Laboratory for Civil Engineering, Portugal*

Kátia Vanessa Bicalho  
*Federal University of Espírito Santo, Brazil*

Krishna R. Reddy  
*University of Illinois at Chicago, USA*

Limin Zhang  
*The Hong Kong Univ. of Science Technology, China*

Márcio de Souza Soares de Almeida  
*Federal University of Rio de Janeiro, Brazil*

Marcelo Javier Sanchez Castilla  
*Texas A&M University College Station, USA*

Marco Barla  
*Politecnico di Torino, Italy*

Marcos Arroyo  
*Polytechnic University of Catalonia, Spain*

Marcos Massao Futai  
*University of São Paulo, Brazil*

Maria de Lurdes Lopes  
*University of Porto, Portugal*

Maurício Martines Sales  
*Federal University of Goiás, Brazil*

Nilo Cesar Consoli  
*Federal University of Rio Grande do Sul, Brazil*

Olavo Francisco dos Santos Júnior  
*Federal University of Rio Grande do Norte, Brazil*

Orianne Jenck  
*Grenoble-Alpes University, France*

Paulo Venda Oliveira  
*University of Coimbra, Portugal*

Pijush Samui  
*National Institute of Technology Patna, India*

Rafaela Cardoso  
*Technical University of Lisbon, Portugal*

Roberto Quental Coutinho  
*Federal University of Pernambuco, Brazil*

Sai K. Vanapalli  
*University of Ottawa, Canada*

Samir Maghous  
*Federal University of Rio Grande do Sul, Brazil*

Satoshi Nishimura  
*Hokkaido University, Japan*

Siang Huat Goh  
*National University of Singapore, Singapore*

Tácio Mauro Campos  
*Pontifical Catholic University of Rio de Janeiro, Brazil*

Tiago Miranda  
*University of Minho, Portugal*

Zhen-Yu Yin  
*Hong Kong Polytechnic University, China*

Zhongxuan Yang  
*Zhejiang University, China*

## **Honorary Members**

André Pacheco de Assis  
Clovis Ribeiro de M. Leme (in memoriam)  
Delfino L. G. Gambetti  
Eduardo Soares de Macedo  
Ennio Marques Palmeira  
Eraldo Luporini Pastore  
Francisco de Rezende Lopes  
Francisco Nogueira de Jorge  
Jaime de Oliveira Campos  
João Augusto M. Pimenta

José Carlos A. Cintra  
José Carlos Virgili  
José Couto Marques  
José Jorge Nader  
José Maria de Camargo Barros  
Manuel Matos Fernandes  
Maurício Abramento  
Maurício Erlich  
Newton Moreira de Souza  
Orencio Monje Villar

Osni José Pejon  
Paulo Eduardo Lima de Santa Maria  
Paulo Scarano Hemi  
Ricardo Oliveira  
Ronaldo Rocha  
Rui Taiji Mori (in memoriam)  
Sussumu Niyama  
Vera Cristina Rocha da Silva  
Waldemar Coelho Hachich  
Willy Lacerda

Soils and Rocks publishes papers in English in the broad fields of Geotechnical Engineering, Engineering Geology, and Geoenvironmental Engineering. The Journal is published quarterly in March, June, September and December. The first issue was released in 1978, under the name *Solos e Rochas*, being originally published by the Graduate School of Engineering of the Federal University of Rio de Janeiro. In 1980, the Brazilian Association for Soil Mechanics and Geotechnical Engineering took over the editorial and publishing responsibilities of *Solos e Rochas*, increasing its reach. In 2007, the journal was renamed Soils and Rocks and acquired the status of an international journal, being published jointly by the Brazilian Association for Soil Mechanics and Geotechnical Engineering, by the Portuguese Geotechnical Society, and until 2010 by the Brazilian Association for Engineering Geology and the Environment.

***Soils and Rocks***

1978,	1 (1, 2)
1979,	1 (3), 2 (1,2)
1980-1983,	3-6 (1, 2, 3)
1984,	7 (single number)
1985-1987,	8-10 (1, 2, 3)
1988-1990,	11-13 (single number)
1991-1992,	14-15 (1, 2)
1993,	16 (1, 2, 3, 4)
1994-2010,	17-33 (1, 2, 3)
2011,	34 (1, 2, 3, 4)
2012-2019,	35-42 (1, 2, 3)
2020,	43 (1, 2, 3, 4)
2021,	44 (1, 2, 3, 4)
2022,	45 (1, 2, 3,

ISSN 1980-9743  
ISSN-e 2675-5475

CDU 624.131.1



# ***Soils and Rocks***

An International Journal of Geotechnical and Geoenvironmental Engineering  
ISSN 1980-9743 ISSN-e 2675-5475

## **Publication of**

ABMS - Brazilian Association for Soil Mechanics and Geotechnical Engineering  
SPG - Portuguese Geotechnical Society  
Volume 45, N. 3, July-September 2022

## **Table of Contents**

### **ERRATUM**

*ERRATUM: Contaminant transport model in transient and unsaturated conditions applied to laboratory column test with tailings*

Eliu James Carbajal, Mariana dos Santos Diniz, Roberto Lorenzo Rodriguez-Pacheco,  
André Luís Brasil Cavalcante

### **LECTURE**

*Displacement of piles from pressuremeter test results - a summary of French research and practice*  
Roger Frank

### **ARTICLES**

*Geotechnical characterization of the estuarine deltaic deposits in the Guayaquil city through in situ and laboratory tests*

Bosco Intriago Álvarez, Hernán Bazurto Palma, Davide Besenzon, Xavier Vera-Grunauer, Sara Amoroso

*Vacuum preloading and PVDs in soft soils beneath embankments: 3D coupled analysis incorporating overall stability study*

José Leitão Borges

*A case study of bearing capacity of piles partially embedded in rock*

Marília Dantas da Silva, Roberto Quental Coutinho, Bernadete Ragoni Danziger

*An evaluation of reinforcement mechanical damages in geosynthetic reinforced piled embankments*

Ennio Marques Palmeira, José Melchior Filho, Ewerton Clayton Alves Fonseca

*Soil-water characteristic curve of polypropylene fibrereinforced sandy soil*

Cíntia Lopes de Castro, Anderson Borghetti Soares, Marcos Fábio Porto de Aguiar

*Prediction of soil water retention curve based on physical characterization parameters using machine learning*

Enzo Aldo Cunha Albuquerque, Lucas Parreira de Faria Borges, André Luís Brasil Cavalcante,  
Sandro Lemos Machado

*Lining forces in tunnel interaction problems*

António M. G. Pedro, José C. D. Grazina, Jorge N. V. Almeida e Sousa

*Estimative of shaft and tip bearing capacities of single piles using multilayer perceptrons*

Luciana Barbosa Amâncio, Silvrano Adonias Dantas Neto, Renato Pinto da Cunha

*Simplified model for dam rockfill creep and influence of constructive delay of concrete face*

Renato Santos Paulinelli Raposo, Yasletty Zamora Hernández, André Pacheco de Assis

*Contribution for a root pile installation control approach using a digital odometer*

José Melchior Filho, Alfran Sampaio Moura, Fernando Feitosa Monteiro

*Effect of steel slag on the mechanical behavior of surficial yellow marl of Tabriz*

Hossein Soltani-Jigheh, Hamed Golmohammadi, Manouchehr Tajrostami

*Use of low-cost accelerometers for landslides monitoring: results from a flume experiment*

Malena D'Elia Otero, Ana Elisa Silva de Abreu, Amin Askarinejad, Marcela Penha Pereira Guimarães,  
Eduardo Soares de Macedo, Alessandra Cristina Corsi, Rynaldo Zanotele Hemerly de Almeida

*Methodology for risk management in dams from the event tree and FMEA analysis*

Rafaela Baldi Fernandes, Ana Cristina Castro Fontenla Sieira, Armando Prestes Menezes Filho



## ***ERRATUM***

***Soils and Rocks***  
**v. 45, n. 3**



## ERRATUM: Contaminant transport model in transient and unsaturated conditions applied to laboratory column test with tailings

Erratum

The article entitled “Contaminant transport model in transient and unsaturated conditions applied to laboratory column test with tailings” (DOI <https://doi.org/10.28927/SR.2022.076021>), from Soils and Rocks 45(2):e2022076021 (2022), was published with a typo that caused misspelling of the first author’s name.

On page 1, where it reads:

Eliu James Carbaja<sup>1</sup> 

It should read:

Eliu James Carbajal<sup>1</sup> 

On pages 1-15, where the text reads:

Carbaja et al.

It should read:

Carbajal et al.

The publisher apologizes for the errors.

<https://doi.org/10.28927/SR.2022.076021err1>



This is an Open Access article distributed under the terms of the Creative Commons Attribution License, which permits unrestricted use, distribution, and reproduction in any medium, provided the original work is properly cited.



# ***LECTURE***

***Soils and Rocks***  
**v. 45, n. 3**





## Displacement of piles from pressuremeter test results – a summary of French research and practice

(5<sup>th</sup> Victor de Mello Goa Lecture)

Roger Frank<sup>1#</sup> 

Lecture

### Keywords

Pile  
Displacement  
Settlement  
Lateral behaviour  
Ménard pre-borehole pressuremeter  
Self-boring pressuremeter  
Barrette.

### Abstract

This paper presents the ‘load-transfer functions’  $t$ - $z$  and  $p$ - $y$  methods for determining the axial and lateral displacements of single piles. They are based on the results of pressuremeter tests. The methods from the results of the Ménard pre-borehole pressuremeter tests (MPM) and the self-boring pressuremeter tests (PAF, for *Pressiomètre AutoForeur* in French) are described. Especially, the  $t$ - $z$  and  $p$ - $y$  methods derived from the MPM test results are commonly used in the French practice. For both  $t$ - $z$  and  $p$ - $y$  curves, some theoretical background (usually FEM calculations in linear elasticity) is given. The results of the  $t$ - $z$  and  $p$ - $y$  analyses are compared to the measurements from loading tests on full scale piles. A proposal concerning *barrettes* is also presented.

## 1. Introduction

It is widely accepted that pile foundations should be designed not only with regard to their bearing capacity, but also with regard to their vertical and horizontal displacements. This comes, in particular, from the need to check the deformation of the structures which they carry, under serviceability conditions, as recommended in most of the recent codes, such as Eurocode 7 (CEN, 2004). In other words, the traditional way of mastering pile movements by applying relatively large factors of safety to the bearing capacity does not appear to be anymore the ‘good’ solution. Piles movements are to be assessed directly.

This paper describes how the approaches using the ‘load-transfer functions’  $t$ - $z$  and  $p$ - $y$  were developed in France for determining, respectively, axial (vertical) and lateral (horizontal) displacements of single piles from the results of pressuremeter tests. The behaviour of *barrettes* is also mentioned.

The results of two different types of pressuremeter tests are used: the results of pre-borehole Ménard pressuremeter tests (MPM) and the results of self-boring pressuremeter tests (PAF, for ‘Pressiomètre AutoForeur’ in French). The advantage of pressuremeter tests is that they allow to measure in situ deformation properties of the ground (as the expansion curve represents a full shear curve measured in situ). Furthermore, because of the pre-borehole, the MPM can be performed in all kinds of ground from soft soils to very stiff or very dense soils and soft rocks. The advantage

of the PAF is that it measures in situ nearly ‘intact’ elastic shear moduli  $G$  of the ground. In the case of the MPM, the (Ménard) pressuremeter moduli  $E_M$  are used in an empirical manner. This is due to the pre-borehole which does not allow to control and/or ‘measure’ accurately the disturbance of the ground. In the case of the PAF, the moduli  $G$  (or the whole expansion curve), can be used in ‘theoretical’ solutions obtained for an elastic continuum.

Figure 1 compares typical expansion curves. It clearly shows that the PAF curve is stiffer than the MPM curve. From the PAF expansion curve different shear moduli are defined  $G_{p0}$ ,  $G_{p2}$ ,  $G_{p5}$ , etc. corresponding to an expansion  $\Delta V/V_0$ , respectively equal to 0% (tangent initial), 2%, 5%, etc. For the MPM, a single modulus is defined, i.e.  $G_M$  between  $p_{0M}$  (initial at rest pressure for the MPM) and  $p_p$  the ‘creep pressure’. With the assumption that Poisson’s ratio  $\nu = 0.33$ , the conventional (Ménard) pressuremeter modulus is obtained from  $G_M$ :

$$E_M = 2.66 G_M \quad (1)$$

Table 1 gives some mean values of the ratios  $G_{p0}/G_{p2}$ ,  $G_{p2}/G_{p5}$ ,  $G_{p2}/G_M$ ,  $G_{p5}/G_M$  and  $G_{p0}/G_M$  for clays and sands.

At working levels, the mean strain in the ground around a pile under axial loads is of the order of  $\varepsilon \approx 10^{-3}$ , while it is of the order of  $\varepsilon \approx 10^{-2}$  in the top layers around a pile under lateral loads. The initial stiffnesses of the  $t$ - $z$  and  $p$ - $y$  models

<sup>#</sup>Corresponding author. E-mail address: roger.frank@enpc.fr

<sup>1</sup>École des Ponts ParisTech, Civil Engineering Department, Laboratoire Navier, Geotechnical team-CERMES, Paris, Marne-la-Vallée, France.

Submitted on July 10, 2022; Final Acceptance on August 5, 2022; Discussion open until Invited Lecture. No discussions.

<https://doi.org/10.28927/SR.2022.006822>



This is an Open Access article distributed under the terms of the Creative Commons Attribution License, which permits unrestricted use, distribution, and reproduction in any medium, provided the original work is properly cited.

established from MPM and PAF test results for single piles are consistent with these orders of magnitude (see, e.g., Hoang et al., 2018, for the  $t$ - $z$  model from MPM test results).

Finally, the models for single piles described in this paper, are meant to be inserted into the so-called ‘hybrid’ approach for assessing the displacements of group of piles (O’Neill et al., 1977; Estephan et al., 2003, 2006; Perlo et al., 2005).

## 2. Axial displacements (settlements)

The determination of the load-settlement curve of a single pile under axial loading is based on the concept of shaft friction mobilisation curves, also known as  $t$ - $z$  curves (‘load-transfer functions’ for the axial direction).

### 2.1 $t$ - $z$ curves from MPM results

The first work on the settlements of piles from MPM results was the work carried out by Gambin (1963). The ‘Fascicule 62-V’ French Code (France, 1993) and more recent French Standard (AFNOR, 2012) suggest, in case a settlement estimate must be made, to use the  $\tau$ - $s$  curves (unit shaft friction-local displacement curves) and  $q$ - $s_p$  curve (mean base pressure-base displacement curve) proposed by Frank & Zhao (1982) and Frank (1984). These curves are shown on Figure 2, with  $k_t$  and  $k_q$  (Equations 2 and 3) given as functions of the pressuremeter modulus  $E_M$  and the diameter ( $2r_0$ ) of the pile:

$$k_t = 2.0 \frac{E_M}{(2r_0)} \text{ and } k_q = 11.0 \frac{E_M}{(2r_0)} \quad (2)$$

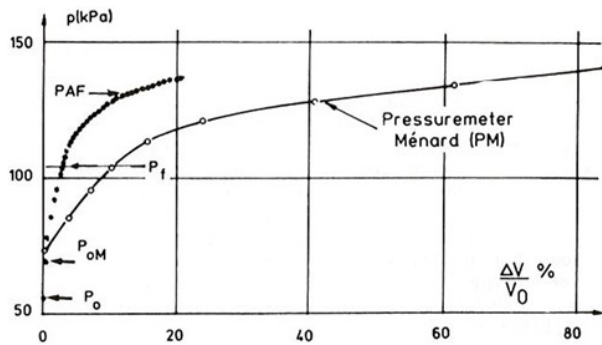


**Figure 1.** Typical pressuremeter MPM and PAF expansion curves (Baguelin et al., 1978).

for granular soils:

$$k_t = 0.8 \frac{E_M}{(2r_0)} \text{ and } k_q = 4.8 \frac{E_M}{(2r_0)} \quad (3)$$

These curves were originally proposed for bored piles in cohesive soils. They were extended to granular soils by using correlations such as those shown in Table 1 and using theoretical results for linear isotropic elastic media (see next section). They are proposed for bored piles and driven piles.

The limit values of unit shaft friction  $q_s$  and base pressure  $q_b$  are estimated from any well accepted method of calculation of the bearing capacity of piles, e.g., from MPM or PAF tests.

Examples of the use of this MPM method for predicting load-settlement curves of piles are given by Frank (1984), Bustamante et al. (1989) and Bustamante & Frank (1999). More recent developments about the Frank & Zhao curves are given by Abchir et al. (2016) and by Bohn et al. (2017). Figures 3 and 4 show such examples of the use of the Frank

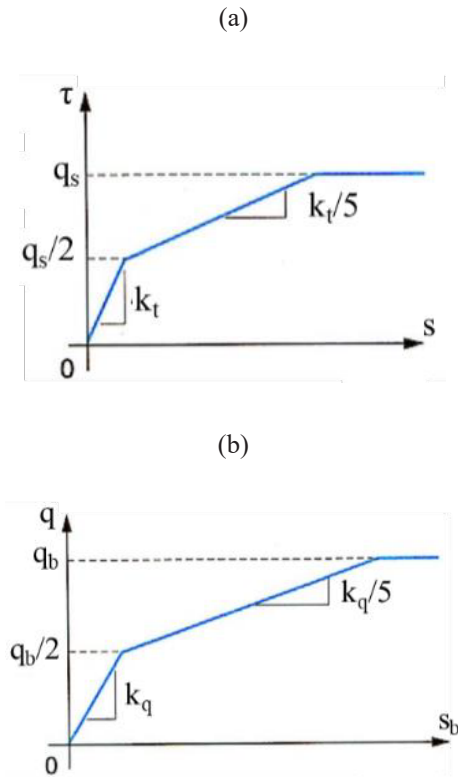


**Figure 2.** MPM (a)  $\tau$ - $s$  ( $= t$ - $z$ ) and (b)  $q$ - $s_b$  ( $= q$ - $z_b$ ) curves (Frank & Zhao, 1982).

**Table 1.** Correlations between PAF and MPM moduli (Jézéquel & Le Méhauté, 1979).

	$G_{p0}/G_{p2}$	$G_{p2}/G_{p5}$	$G_{p2}/G_M$	$G_{p5}/G_M$	$G_{p0}/G_M$
Clays	2.09	1.72	5.42	3.03	11.3
Sands	1.19	1.29	3.47	2.53	4.1

& Zhao (1982) MPM method for the analysis of full-scale static load tests. The Koekelare pile of Figure 3 is a cased screw pile  $B = 350\text{mm}/650\text{mm}$  constructed in an Ypresian clay. It can be seen that the prediction of the load-settlement curve is excellent.

Figure 4 shows all the results of the prediction exercise which was organized for the International Symposium ISP5-PRESSIO 2005, taking place at the occasion of the '50 years of pressuremeters' (Reiffsteck, 2006). The pile is a CFA (continuous flight auger bored pile) with a diameter  $B = 0.5\text{ m}$  and a length  $D = 12\text{ m}$ . The pile is embedded

in a 9.6 m thick clay layer, below a 2.4 m thick silt layer. The water-table is located 1.8 m below ground level. It is interesting to note the predictions made by Robas & Kuder (2006) and by Said et al. (2006) are the closest predictions to the whole initial part of the measured load-settlement curve, both used the Frank-Zhao MPM method, and were established completely independently.

## 2.2 $t$ - $z$ curves from PAF results

### 2.2.1 Theoretical background

The finite element method (FEM) was used to study the mechanism of shaft friction in isotropic linear elastic media (Frank, 1974). The mechanism was confirmed for linear cross-anisotropic elastic media of vertical axis, also using the FEM (Orsi, 1978). The FEM mesh used for the study is shown on Figure 5. No soil-pile interface elements are inserted. The soil and pile are bound together.

The analyses carried out allowed to establish the predominant mode of deformation near the pile shaft: it is a pure shearing of vertical concentric annuli, as shown on Figure 6.

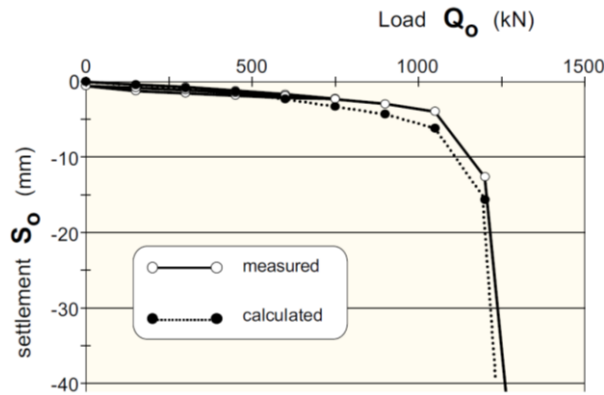


**Figure 3.** Comparison of measured and calculated load-settlement curves for the Koekelare pile (Bustamante & Frank, 1999).

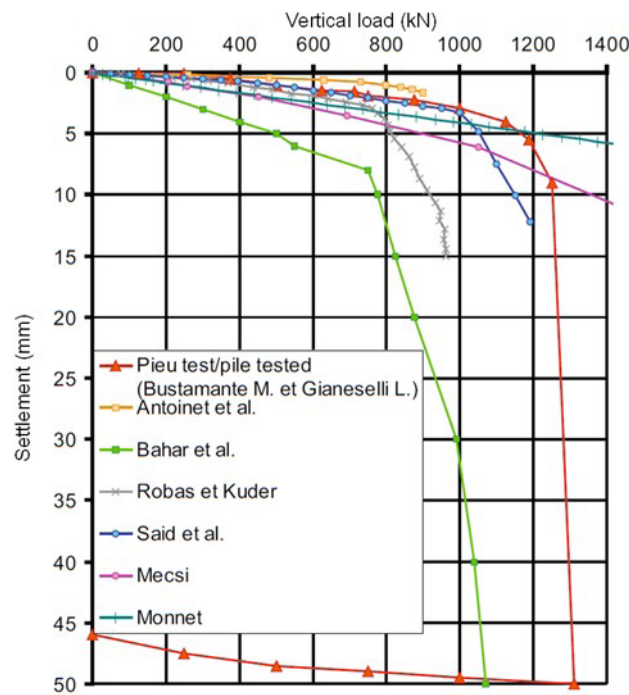


**Figure 4.** Comparison of the experimental curve with the participants' predictions (Reiffsteck, 2006).

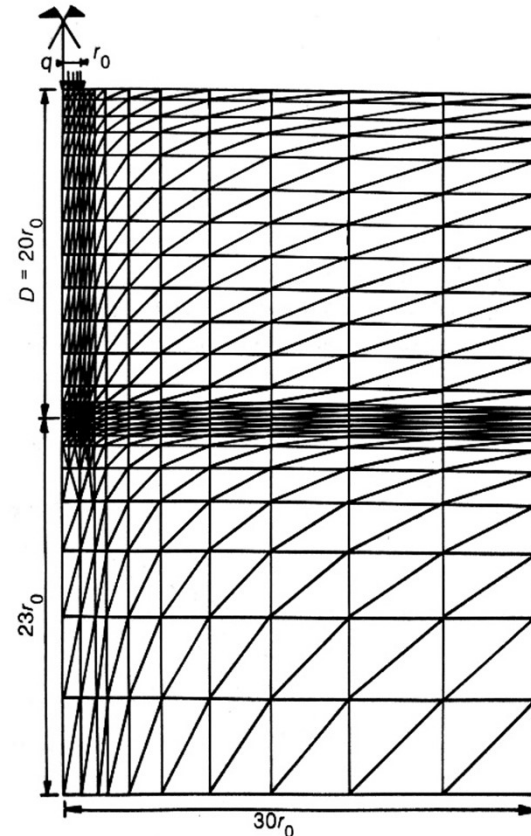


**Figure 5.** FEM mesh for the study of the mechanism of shaft friction of piles in isotropic linear elastic media (Frank, 1974).

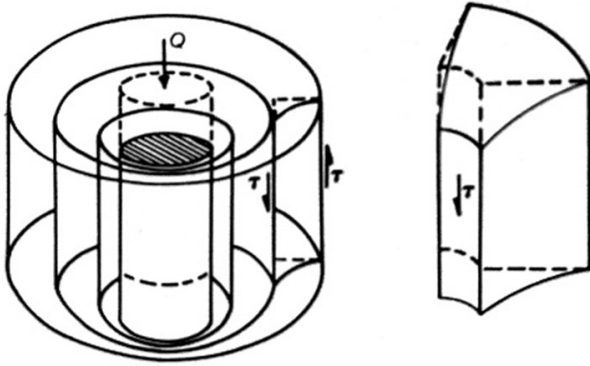


**Figure 6.** Sketch of the mechanism of pure shearing of vertical concentric annuli (Frank, 1974).

The main outcome of the studies is that the initial stiffness of the  $t$ - $z$  curve is related to the elastic shear modulus  $G_0$  of the ground through the relation:

$$t/z = \frac{G_0}{kr_0} \quad (4)$$

where the dimensionless parameter  $k$  is a function of the slenderness ratio of the pile  $D/2r_0$  ( $D$  is the embedded length of the pile and  $r_0$  is the diameter of the pile) and of Poisson's ratio  $\nu$  of the ground. Figure 7 shows the values of  $k$  obtained from Poulos & Davis (1968) and by Randolph (1977) and Orsi (1978). The modulus  $G_0$  can be obtained from undisturbed samples or from the results of PAF tests. In the case of the PAF tests, it is to be noted that the (tangent) initial modulus from the expansion curve  $G_{p0}$  usually corresponds to an expansion  $\Delta V/V_0$  around 0.2%.

The model was further extended to non-linear media. Figure 8 is a typical example showing the influence of the non-linear terms of the shear curve of the ground ( $\tau, \gamma$ ) on the friction curve ( $t_0, w_0/r_0$ ). As seen, the non-linearity of the ground behaviour has a very limited influence on the  $t$ - $z$  curve until the mobilization of the limit shaft friction  $q_s$ . Thus, a bi-linear curve (initial mobilization followed by a plateau at  $t = q_s$ ) is quite acceptable for all practical purposes. For more details, see e.g. Baguelin & Frank (1980) and Baguelin et al. (1982).

The procedure to establish the bi-linear  $t$ - $z$  curve from the results of PAF test is the following:

- make an estimate of the elastic shear modulus  $G_0$  of the ground (e.g.  $G_{p0}$ , from the tangent initial stiffness of the PAF expansion curve);
- apply the parameter  $k$  (Figure 7) in order to derive the stiffness of the  $t$ - $z$  curve:  $k_t = G_0/kr_0$ ;
- make an estimate of the limit shaft friction  $q_s$  (as in the case of the MPM method).

With regard to the base of the pile, a simple tri-linear curve  $q$ - $z_p$  is also proposed. The initial slope is derived from the Boussinesq settlement of a shallow foundation:

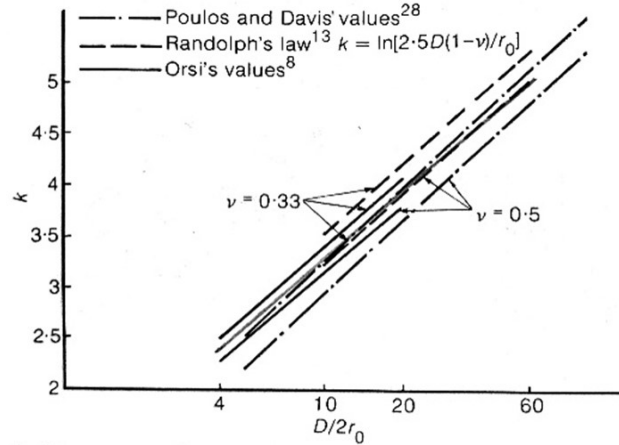


**Figure 7.** Parameter  $k$  as a function of  $D/2r_0$  and  $\nu$  (in isotropic elasticity) (Baguelin & Frank, 1980).

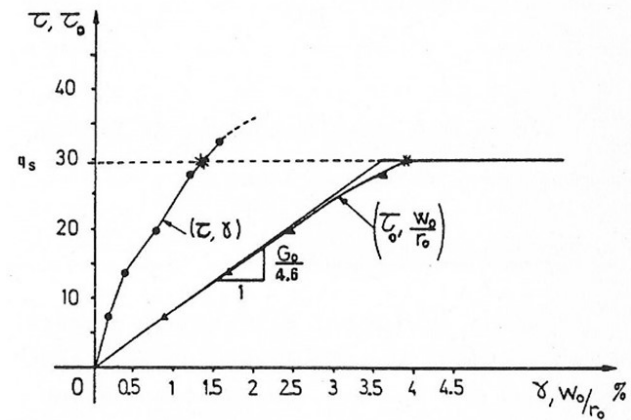


**Figure 8.** Shear curve ( $\tau, \gamma$ ) derived from a PAF expansion test and corresponding shaft friction curve ( $t_0, w_0/r_0$ ) at 3 m depth for the Plancoët pile (Baguelin et al., 1982).

$$k_b = \frac{q}{z_b} = \frac{4G_0}{\pi(1-\nu)r_0I} \quad (5)$$

where  $I$  is around 0.85 to 1 (Randolph & Wroth, 1978; Frank, 1984). The mean base pressure  $q$  is then limited by the limit base pressure  $q_b$  (as in the case of the MPM method).

## 2.2.2 Examples

The PAF method was applied, in particular, to analyse full scale pull-out tests of two close-ended steel pipe piles driven in marine soils at Cran and Plancoët (Baguelin et al., 1982). Both piles are 27.3 cm in diameter and 6.3 mm thick. The load-displacements curves obtained are compared to the measured (experimental) ones shown on Figures 9 and 10. Results from FEM analyses are also shown. They include interface elements which allow limiting the shear stress to the



limit shaft friction  $q_s$ . The Cran pile is 17 m long. The soils at Cran are soft plastic clays underlain by plastic, slightly organic silt. The Plancoët one is 13 m long. The soils at Plancoët are sandy silts, underlain by loose sands and silty clays.

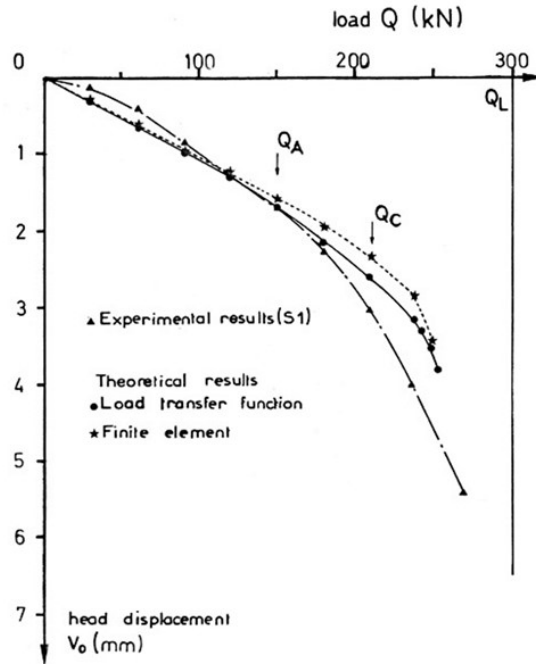


**Figure 9.** Comparison of measured and calculated load-settlement curves for the pull-out test at Cran.

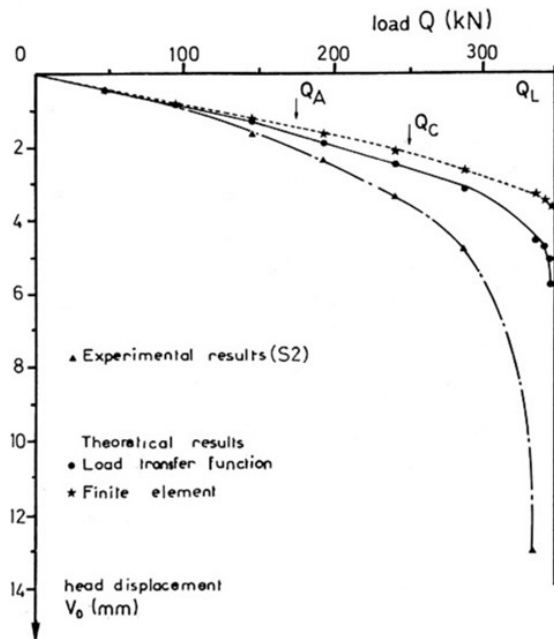


**Figure 10.** Comparison of measured and calculated load-settlement curves for the pull-out test at Plancoët.

In the case of Cran, the  $t$ - $z$  load transfer function analysis matches quite well the experimental results, especially near the working load of the pile (around 150 kN).

In the case of Plancoët, the  $t$ - $z$  analysis underestimates the displacement in the vicinity of the working load by a factor of about 0.7 to 0.75, which seems quite acceptable.

### 3. Lateral displacements

The methods using the subgrade reaction modulus (or  $p$ - $y$  reaction curves,  $p$  – reaction pressure,  $y$  – horizontal displacement) are now well known for the design of piles under lateral loads.

In the following some features of the research carried out by the French Bridges and Highways Laboratories (LPCs) are given. They concerned not only overturning loads at the head, but also lateral thrusts when the soft soil pushes directly on the pile, due to lateral soil movements (at the toe of an embankment, for instance). In this latter case, the pile soil movement  $y$  is replaced by the relative displacement  $\Delta = y - g$ , where  $g$  is the displacement of the soil in absence of the pile.

#### 3.1 P-y curves from MPM results

The basic method from MPM results (Ménard, 1962) is also detailed by Baguelin et al (1978). From the results of the test at the considered depth ( $E_M$ , Ménard pressuremeter modulus;  $p_c$ , creep pressure and  $p_p$ , limit pressure), the reaction curve ( $p$ ,  $y$ ) of a single pile at a given depth, is established, for long duration loadings, as shown on Figure 11.

The subgrade reaction modulus  $k_s = p/y$  of part OA is the one originally proposed by Ménard (1962). When multiplying by the frontal width (or diameter of the foundation)  $B$ , the Ménard (horizontal) reaction modulus  $E_{sM} = k_s B$  is obtained:

$$E_{sM} = E_M \frac{18\rho}{4(2,65\rho)^\alpha + 3\alpha\rho} \text{ with } \rho = \max\left(\frac{B}{B_0}; 1\right) \quad (6)$$

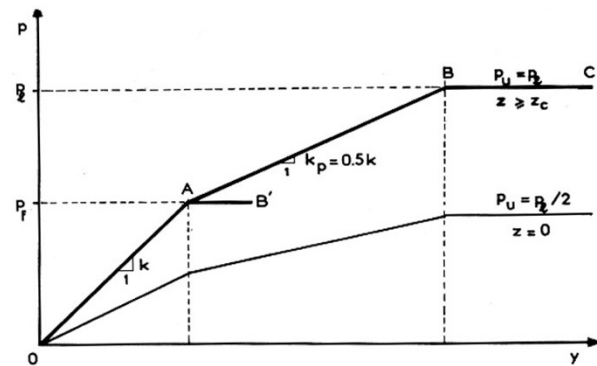


**Figure 11.**  $p$ - $y$  reaction curve from MPM results for long duration loadings (Baguelin et al., 1978).

$E_M$  is the pressuremeter modulus measured at the level under consideration,  $\alpha$  is a ‘rheological factor’ depending on the nature of the ground and  $B_0$  is a reference width (or diameter) equal to 0.6 m.

Table 2 gives the values of  $E_{sM}/E_M$  for  $B \leq 0.6$  m and for  $B = 1.2$  m for the various values of  $\alpha$ . Note that  $E_{sM}/E_M$  ranges between 1.33 and 4 (even 5, or so, for larger piles).

Above the creep pressure  $p_f$  ( $p_f = p/2$  can be used as an estimate), the non-linear effect is taken into account by reducing the tangent reaction modulus by one half (segment AB on Figure 11). Finally, the ultimate pressure on the pile  $p_u$  is taken as being equal to the limit pressure  $p_l$  measured with the MPM (segment BC). However, in current practice, the creep pressure should normally not be exceeded, and the displacements and moments should be determined using the law OAB’, which is on the safe side in the case of loads at the head of the pile (it might be the contrary when the pile is submitted to lateral thrusts from the soil – see below).

The p-y curve is, in principle, modified for depth values  $z$  lower than a critical depth  $z_c$ , due to surface effect. For  $z = 0$ , the pressures are divided by 2 for the same displacement  $\Delta y$  (or  $y - g$ ) and are then linearly interpolated until  $z = z_c$ . For cohesive soils  $z_c$  is taken equal to  $2B$  ( $B$  is the diameter of the pile) and for granular soils it is taken equal to  $4B$ .

The design of piles subjected to lateral soil thrusts, created by nearby slopes for instance, is based on the ‘free soil displacement’ concept. It is assumed that the lateral reaction curve now links the lateral reaction pressure  $p$  to the ‘relative’ displacement  $\Delta = y - g$ , where  $y$  is the equilibrium soil-pile lateral displacement sought, and  $g$  is the free lateral soil displacement (or displacement in absence of the pile) – see e.g., Bigot et al. (1982) and Frank (1984). The ‘Fascicule 62-V’ French Code (France, 1993) and more recent French standard (AFNOR, 2012) suggest a method for predicting  $g(z)$ , as a function of depth  $z$ , of the characteristics of the slope, of the characteristics of the underlying soft soil and of the location of the pile (see also Frank et al., 2018).

It must be admitted that there are not many cases of comparison of the prediction of the Ménard MPM method with full-scale test results for piles under lateral loadings. However, a certain number of such comparisons are available, in particular some experiments carried out by the LPCs (see Baguelin et al., 1978).

**Table 2.** Ratio  $E_{sM}/E_M$  for estimating the Ménard horizontal reaction modulus  $E_{sM}$  from the pressuremeter modulus  $E_M$  (Baguelin et al., 1978).

		$B < 0.6$ m	$B = 1.2$ m
Peat	$\alpha = 1$	1.33	1.33
Clay	$\alpha = 2/3$	1.9	2.25
Silt	$\alpha = 1/2$	2.3	3
Sand	$\alpha = 1/3$	2.8	4
Sand and Gravel			

As for those with the determination of the reaction curves along the shaft, the experiment on Provins site (which will be briefly reported below) and different research projects at Plancoët on isolated piles, on a group of two piles and on a group of six piles must be mentioned. Also, the measurements taken during 16 years on a steel pipe driven through an unstable slope at Sallèles (Puy-de-Dôme) are very valuable (Frank & Pouget, 2008). For the group of two piles at Plancoët it is interesting to note that the reaction measured on the trailing pile is found to be reduced by a factor of 0.4 to 0.5 relatively to the leading (front) pile, the distance between the 2 axes being 3 times the frontal width.

From the various experimental evaluations, Baguelin et al. (1978) conclude that the standard MPM method (Figure 11) is, in general, pessimistic for quick monotonic loadings. It tends to overestimate the head displacements and maximum bending moments of piles submitted to loads at their head, and thus is conservative. In reality foundations must often sustain cyclic and/or long duration loads, and the soil can be severely damaged by the installation of the piles, all being parameters very difficult to quantify in everyday practice.

These different facts allow one to think that the method is quite acceptable.

The experiment on the site of Provins in 1974 is interesting because the behaviour of a full scale instrumented pile was examined under head loading, and also when being submitted to lateral thrusts due to the construction of an embankment. The pile is a steel instrumented pipe, of OD =  $B = 0.926$  m and thickness  $e = 0.015$  m. Furthermore, the 4 stages of the experiment (initial head loading to 120 kN, then embankment construction to a height of 3.8 m, to a height of 6.8 m and after 3 months of consolidation under this final height) were analyzed in detail by using different pressuremeter prediction methods (Bigot et al., 1982).

Figure 12 compares the measured values  $M$  of bending moments (left) and displacements (right) ( $M$ ) for the last level of applied load at the head (120 kN shear load at 0.2 m from ground level) to the results of 3 prediction methods:

- method A, with MPM reaction curves (Figure 11);
- method B uses p-y curves built in the same manner as MPM reaction curves but using appropriate moduli obtained with the PAF. For brevity method B is not discussed in the present paper;
- method C1, with p-y reaction curves constructed on the basis of PAF tests results (see next section).

In the surface layer (silt and clay), the governing one for head loadings, the use of the MPM method of Figure 11 yields a mean soil reaction modulus:

$$E_{sM} = k_s B = 2900 \text{ kPa (method A)} \quad (7)$$

It is clear from Figure 12 that the MPM method (method A) is on the safe side for short duration head loadings: the maximum bending moment is slightly overestimated and

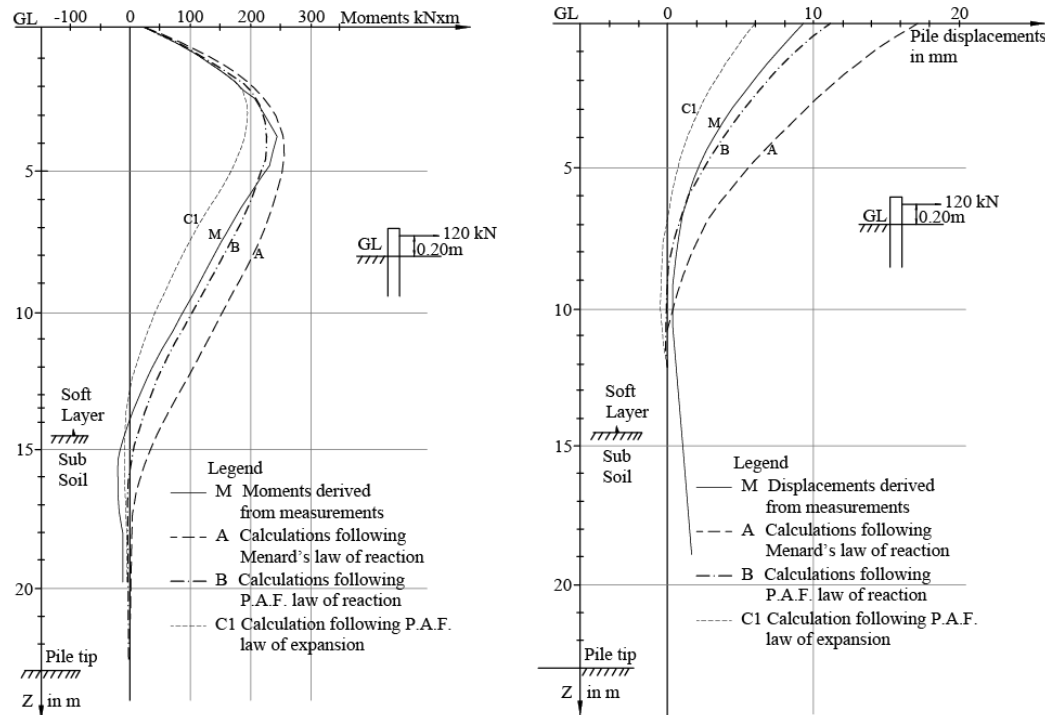


Figure 12. Provins pile: comparison of measured and calculated bending moments and displacements for head loading (Bigot et al., 1982).

the displacements are overestimated by a factor of 2. This is consistent with the conclusions of Baguelin et al. (1978). This also shows that for long duration loadings at the head, the MPM method is quite acceptable, given all the uncertainties.

Figure 13 compares the measured values  $M$  of bending moments (left) and displacements (right) ( $M$ ) after 3 months of consolidation under the final height of the embankment to the results of 3 prediction methods (A, B and C2). Here, the difficulty is the prediction of the bending moments, as it is a 'displacement-imposed' problem. The measured bending moment (curve  $M$ ) in the upper part is well predicted by the MPM method (curve A). In the lower part the method overestimates the bending moment by a factor of around 1.8, which is largely on the safe side.

The full scale experiment of Sallèdes (steel pipe pile installed through an unstable slope), where the measurements were taken during 16 years, confirmed the great difficulty in predicting accurately the long duration behaviour of piles undergoing lateral thrusts from a moving ground; it is clear that the MPM method overestimates the bending moments of such piles (see Frank & Pouget, 2008, for the extensive analysis of this unique experiment).

### 3.2 $P$ - $y$ curves from PAF results

#### 3.2.1 Theoretical background

Several theoretical and numerical studies were carried out in order to investigate the behaviour of piles under lateral loads. Bi-dimensional (2D) as well as three-dimensional (3D)

FEM were used, in isotropic linear elasticity. No soil-pile interface elements are used. The pile section (in 2D) or pile (3D) is bound to the soil. Plasticity effects around a pile section were also studied in 2D (Said, 1977; Baguelin et al., 1977). For the 3D analyses, because of the axi-symmetrical geometry of the problem (in the case of circular piles), the method consisting in expressing the loads and displacements in Fourier series is used. Only one single Fourier harmonic is needed here (Carayannacou-Trézos, 1977; Baguelin et al., 1979). For more details, see Baguelin & Frank (1980).

The effects of the shape of the horizontal cross-section of the pile ( $L/B$ ) were assessed by a 2D study, where  $L$  is the length in the horizontal plane and  $B$  is the frontal width (the dimension perpendicular to the lateral load). The  $L/B$  ratio ranged from 1/5 to 5. Figure 14 shows the mesh used for  $L/B = 2$ .

For studying the behaviour of *barrettes* under horizontal loads, the soil reaction  $P$  is split into its frontal reaction  $P^{FRONT}$  (in front and on the back of the pile or "barrette") and its tangential reaction  $P^{TANG}$  (on the sides of the pile or "barrette") – see next section, where  $P$  is the total soil reaction per unit length of the pile ( $P = -dT/dz$ , with  $T$  the shear load; note that  $P = pB$ ,  $p$  being defined as the soil lateral 'reaction pressure').

Figures 15 and 16 show the influence of  $L/B$  on  $P^{FRONT}$  and  $P^{TANG}$  in the case of a homogeneous (intact) linear elastic medium (with  $E$ , Young's modulus and  $\nu$ , Poisson's ratio). The influence of various degrees of remoulding was also studied.

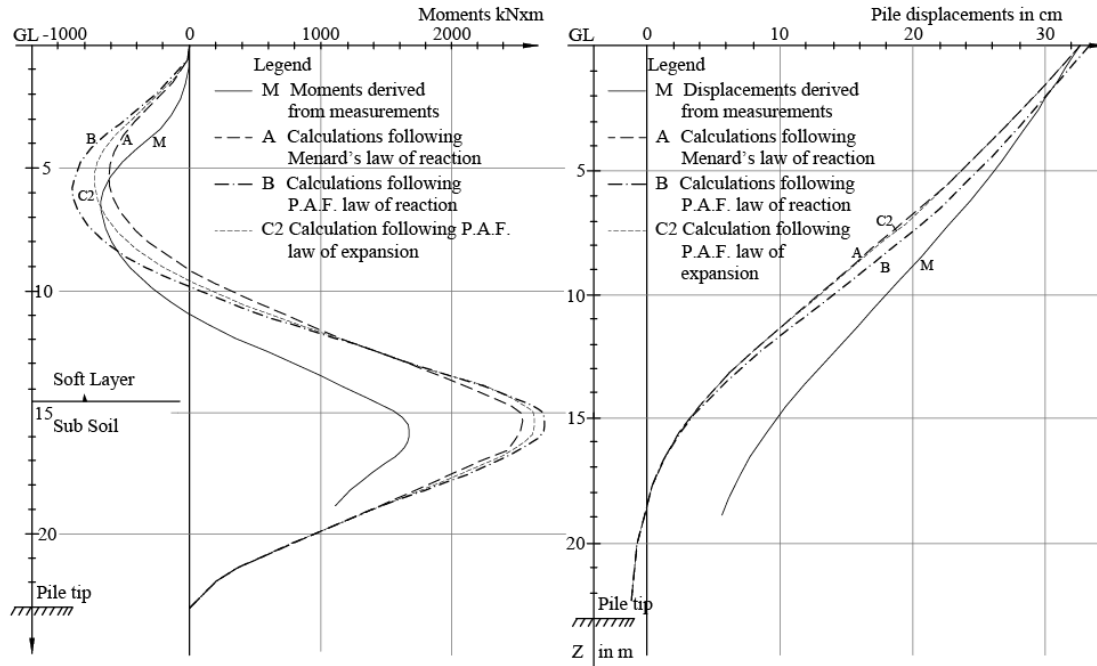


**Figure 13.** Provins pile: comparison of measured and calculated bending moments and displacements after 3 months of consolidation under final height of embankment (Bigot et al., 1982).

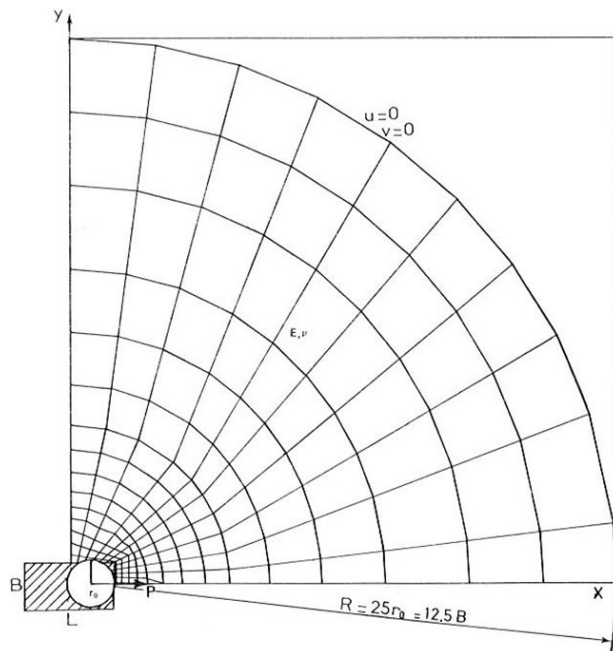


**Figure 14.** Bi-dimensional FEM mesh in isotropic linear elastic media for a cross-section  $L/B = 2$  (Baguelin et al., 1979).

The charts of Figures 15 and 16 allow assessing the corresponding horizontal reaction moduli  $E_s^{FRONT}$  and  $E_s^{TANG}$  for the frontal and tangential reaction curves, respectively, which are needed for the calculation of the displacements of *barrettes*.

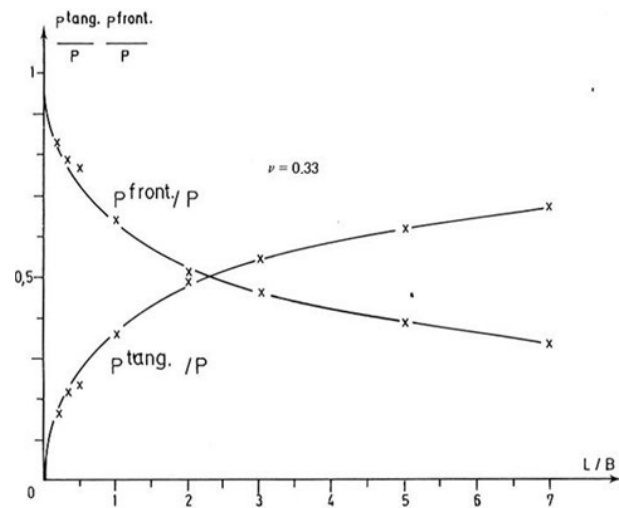


**Figure 15.**  $P^{FRONT}$  and  $P^{TANG}$  for  $\nu = 0.33$  from 2D finite element calculations.

The effects of the relative pile-soil stiffness, of the slenderness ratio of the pile  $D/2r_0$  and of the type of head loading (horizontal force  $H$  or bending moment  $M$ ) are studied in 3D conditions. Two slenderness ratio values are used:  $D/2r_0 = 10$  and  $D/2r_0 = 25$ . The mesh for  $D/2r_0 = 10$  is shown on Figure 17.

The soil is represented by a homogeneous (intact) linear elastic medium with Young's modulus  $E$  and Poisson's ratio  $\nu = 0.33$  (Poisson's ratio has nearly no influence).  $E_p$  is the modulus of the pile.



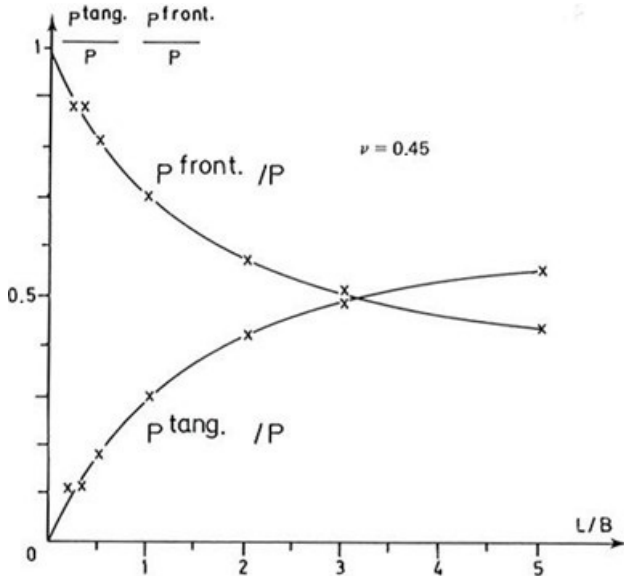


Figure 16:  $P_{FRONT}$  and  $P_{TANG}$  for  $\nu = 0.45$  from 2D finite element calculations.

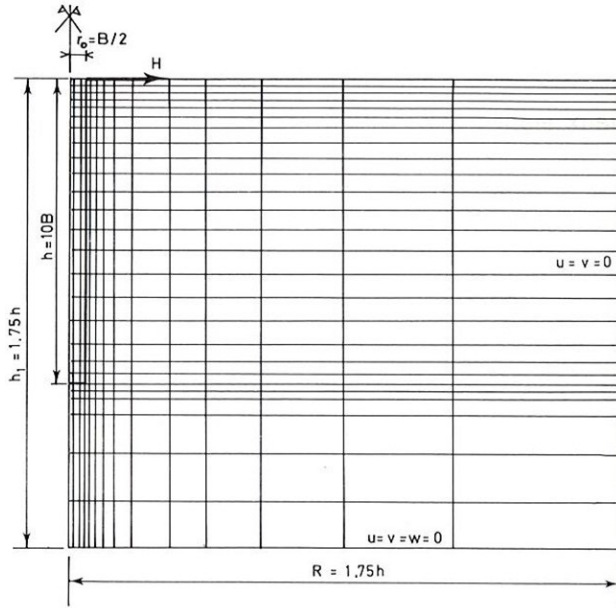


Figure 17. FEM mesh in isotropic linear elastic media for 3D study of laterally loaded piles for piles with  $D/2r_0 = 10$ .

The study aimed at determining a single ‘equivalent’ reaction modulus  $E_{s(u)}$  which would yield the same head horizontal displacement as the FEM calculation. The main findings are reported on Figure 18 for the two slenderness ratios, for the force and moment loadings and for a large range of the relative pile-soil stiffness  $E_p/E$  (Frank, 1984).

The main conclusion of this 3D study is that, for all practical purposes,  $s = E/E_{s(u)} \sim 0.6-0.7$ . Thus the following approximate relation is obtained for the (horizontal) reaction modulus:

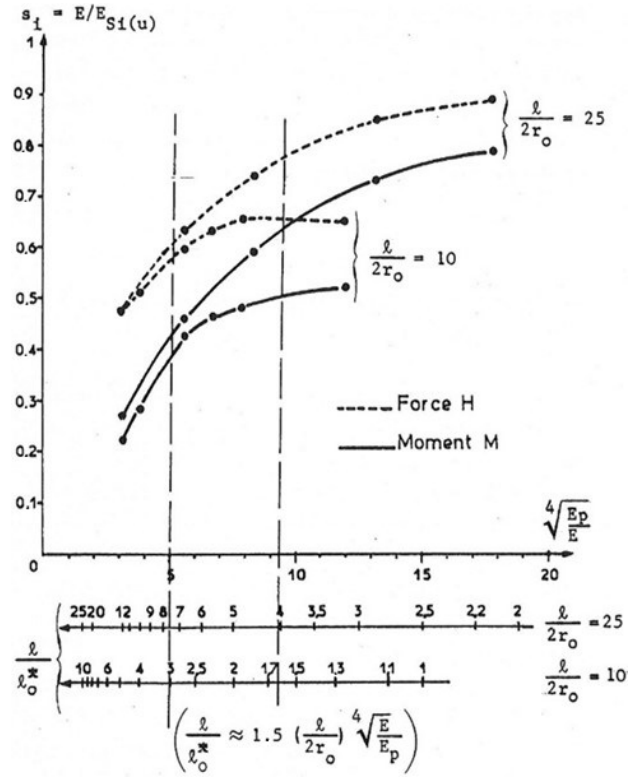


Figure 18. Equivalent horizontal reaction modulus in an intact soil  $E_{s(u)}$  as a function of the slenderness ratio  $l/2r_0$  ( $= D/2r_0$ ), of the relative pile-soil stiffness  $E_p/E$  and of the head loading (H or M).

$$E_s = 4G \quad (8)$$

where  $G$  is the shear modulus of the elastic soil.

The way of applying PAF test results is then shown on Figure 19 (Amar et al., 1981a, b). For quick monotonic lateral loading the  $p$ - $y$  corresponds to the PAF expansion curve itself. The reaction pressure  $p$  on the pile is the net pressure  $p^* = p - p_0$  of the PAF test and the relative horizontal displacement  $y/r_0$  of the pile is then the radial strain  $\Delta r/r_0$ , which is approximately half the expansion  $\Delta V/V_0$  of the PAF probe [ $\Delta r/r_0 \sim (\Delta V/V_0)/2$ ]. The ultimate pressure on the pile  $p_u$  is equal to the net pressure  $p_{20}^*$  at 20% of expansion of the PAF probe. For repeated or permanent (long duration) lateral loadings, such as lateral thrusts on piles, the displacement  $y$  (or  $y - g$ ) is multiplied by 2 for the same reaction pressure  $p$ . Furthermore,  $p$  is respectively limited to  $pu = 0.75p_{20}^*$  for sandy soils and to  $p_u = 0.5p_{20}^*$  for clayey or silty soils.

Given the fact that the slope of the curve [ $p^*$ ,  $(\Delta V/V_0)/2$ ] is  $2G_0$  for an isotropic linear elastic medium (Lamé’s solution for the thick cylinder), the use of the PAF expansion curve itself as a  $p$ - $y/r_0$  comes to assume that the (horizontal) modulus of reaction is

$$E_s = \frac{pB}{y} = \frac{p2r_0}{y} = 4G_p \quad (9)$$

( $G_p$  is  $G_{p0}$ ,  $G_{p2}$  or  $G_{p5}$  from the PAF expansion curve).

It thus can be said that the use of the PAF expansion curve as the  $p$ - $y/r_0$  curve for quick monotonic loadings matches the theoretical findings for an isotropic linear elastic medium (given in Figure 18).

In the case of repeated or permanent loading:

$$E_s = 2G_p \quad (10)$$

Furthermore, the non-linearity of the reaction curve (until  $p_u$  is reached) is assumed to be same as for the pressuremeter expansion curve.

Table 2 indicates that  $E_{sM}/E_M$  ranges between 1.33 and 4, or, in other words, that  $E_{sM}/G_M$  ranges between 3.5 and 10.6 which is consistent with the fact that  $G_M < G_p$ . (Table 1).

### 3.2.2 Examples

The PAF method indicated on Figure 19 was applied to the Provins pile (Figures 12 and 13).

Figure 12 compares the measured values  $M$  of bending moments (left) and displacements (right) for the last level of applied load at the head (120 kN horizontal load at 0.20 m

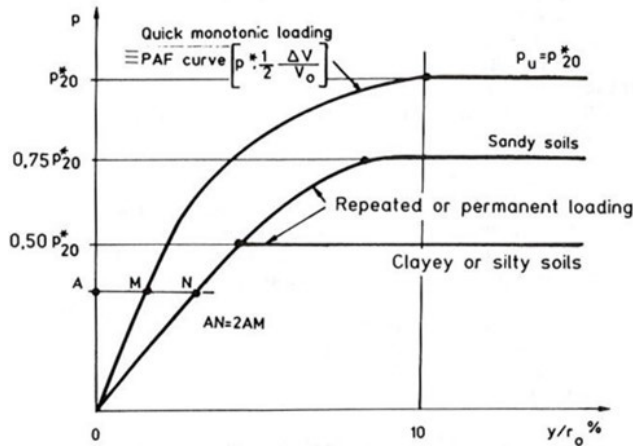


Figure 19.  $p$ - $y$  curves derived from PAF expansion curves (Amar et al., 1981a, b).

from ground level) to the calculations with the  $p$ - $y$  reaction curves for quick monotonic loadings constructed on the basis of PAF tests results, as shown on Figure 19 (method C1).

In the surface layer (silt and clay), the governing one for head loadings, the use of the PAF expansion curve yields:

$$E_s = 4G_{p2} = 11700 \text{ kPa (method C1)} \quad (11)$$

which is 4 times larger than the Ménard reaction modulus  $E_{sM}$ . Indeed, this leads to underestimating both the displacements along the pile, as well as the maximum bending moment.

Figure 13 compares the measured values  $M$  of bending moments (left) and displacements (right) after 3 months of consolidation under the final height of the embankment to the calculations with  $p$ - $y$  reaction curves for permanent (long duration) loadings constructed on the basis of PAF tests results, as shown on Figure 19 (method C2). For this stage of the experiment, the prediction using the PAF expansion curve with the factor 2 on the  $y$  axis is quite satisfactory.

In the case of the experiment of Sallèdes (steel pipe pile installed through an unstable slope), where the measurements were taken during 16 years, the PAF method also overestimates largely the bending moments, as reported above for the MPM method (Frank & Pouget, 2008). It confirms the great difficulty in predicting accurately the long duration behaviour of piles undergoing lateral thrusts from a moving ground.

## 4. Behaviour of barrettes

*Barrettes* are bored deep foundations of large dimensions in the horizontal plane. They are cast in place with the help of slurry. Usually:  $L/B > 2$ , where  $B$  is the frontal width, perpendicular to the lateral loading (Figure 20).

For axial displacements, the MPM  $t$ - $z$  and  $q$ - $z_p$  curves of Figure 2 can be used, as well as the PAF method described in section 1.

As these methods are meant for circular piles, some geometrical conversion should be made. The 'equivalent' diameter  $B = 2r_0$  can be obtained from:

$$A = \frac{\pi B^2}{4} \quad (12)$$

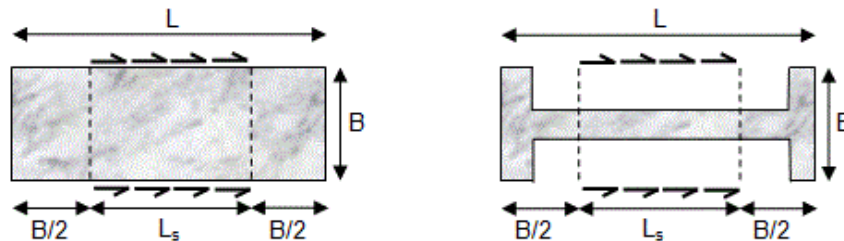


Figure 20. Design lengths for the reaction curves of *barrettes* (France, 1993; AFNOR, 2012).

where  $A$  is the area of the ‘full’ horizontal cross-section of the “barrette”  $A = BL$ .

The limit values of the unit shaft friction  $q_s$  and of the base pressure  $q_u$ , can be determined from the bearing capacity rules for bored piles with slurry, together with the real area of the shaft and base, respectively. Nevertheless, in the case of *barrettes*, special attention should be paid to the estimate of the equivalent limit pressure  $p_l^*$  at the base and equivalent embedment depth for the determination of  $q_u$ , as their slenderness ratio  $B/D$  may lead to consider them as semi-deep foundations.

The method for assessing behaviour of *barrettes* under lateral loadings is described on Figure 21 (Baguelin et al., 1979).

The principle of the method is to split the total reaction force  $P$  (soil reaction per unit length of the pile, in kN/m or MN/m) at a given level into a frontal reaction  $P^{FRONT.}$  (on the front and on the back) and a tangential reaction  $P^{TANG.}$  (on the sides) for the same horizontal displacement  $U$ :

$$P(U) = P^{front.}(U) + P^{tang.}(U) \quad (13)$$

On Figure 21, the lateral reaction forces  $P$ ,  $P^{FRONT.}$  and  $P^{TANG.}$  are drawn as functions of the horizontal displacement  $U$ . The slopes  $E_s$  are thus reaction moduli (in kPa or MPa).

The two reactions  $P^{FRONT.}$  and  $P^{TANG.}$  correspond, respectively, to the soil reaction (Figure 20):

- on the front and the back and taking into account  $B/2$  on each side of the “barrette”;
- on the sides, taking into account  $L_s = L - B$  on each side of the “barrette”.

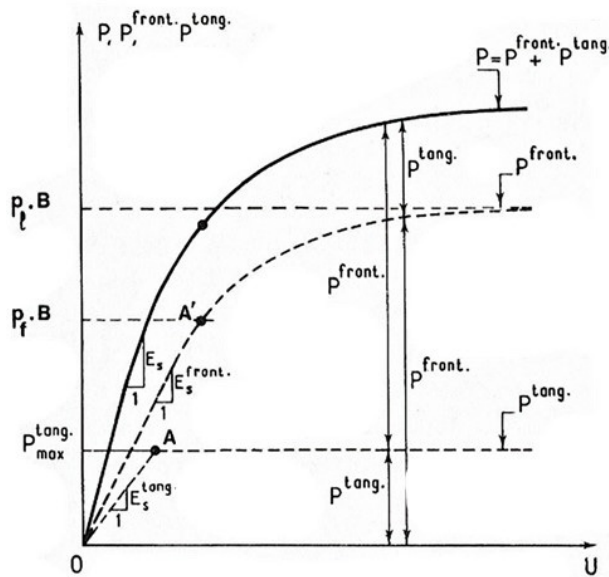


Figure 21. Lateral reaction curves for the design of *barrettes*.

The determination of the reaction curves is the following:

- for  $P^{FRONT.}(U)$ , the same curve is used as for a pile of diameter  $B$  (see previous section);
- for  $P^{TANG.}(U)$ , the initial slope  $E_s^{TANG.}$  up to  $P = P_{max}^{TANG.}$  is assessed from the results of the 2D FEM analyses described in the previous section (Figures 15 and 16). These results allow to determine the ratio  $E_s^{TANG.}/E_s^{FRONT.}$ . The ultimate reaction  $P_{max}^{TANG.}$  is equal to:

$$P_{max.}^{tang.} = 2q_{sh}L_s \quad (14)$$

where the horizontal unit shaft friction  $q_{sh}$  can be taken as equal to the (axial) limit shaft friction  $q_s$  for bored piles with slurry.

## 5. Conclusion

This paper presented the main results concerning the determination of displacements of single piles from pressuremeter test results. The methods for constructing the ‘load-transfer functions’  $t-z$  and  $p-y$  are described. The great advantage of pressuremeter tests is that they provide for deformation parameters measured in situ.

In the case of the Ménard pressuremeter tests (MPM), the pressuremeter modulus  $E_M$  is used for deriving such load transfer curves which, in turn, allow to assess the axial (vertical) and lateral displacements of the piles. The transfer curves are mainly empirical. Both the  $t-z$  and  $p-y$  models derived from the MPM parameters ( $E_M$  and  $p_l$ ) are commonly used in practical design in France.

These types of models, obtained for “simple” problems, are also used for calibrating and validating the choice of moduli of deformation when it comes to solving more complicated problems by numerical methods, such as the finite element method (see, e.g., Bourgeois et al., 2018).

The corresponding curves from the self-boring pressuremeter (PAF) are mainly based on theoretical studies carried out for elastic media. These studies assume that ‘intact’ shear moduli are used. They are taken from the PAF expansion curves.

In all cases, the limit values of shaft friction and end-bearing (for  $t-z$  and  $q-z_p$  curves) can easily be obtained from any well accepted method for assessing the (vertical) bearing capacity of piles. The (horizontal) ultimate pressures (for  $p-y$  curves) are derived from limit pressures measured with the pressuremeter.

The proposed  $t-z$  and  $p-y$  curves are meant to be inserted into methods for assessing the displacements of group of piles, such as the ‘hybrid’ approach method.

Their validity was exclusively checked on the basis of the results of loading tests on full scale piles. Clearly more well documented full scale test results would help develop them further. But this also means that the influence on the ground of the insertion or of the casting of piles is better known and quantified.

## Acknowledgements

It is a great honour for me to be the recipient of the 5<sup>th</sup> Victor de Mello Goa Lecture. I warmly thank the Goa Chapter of the Indian Geotechnical Society for the nomination.

Dr. Victor de Mello was not only an extraordinary expert in all fields of geotechnical engineering, but also a great example to follow for the younger ones, like me, who had the chance to meet him. It was each time an immense pleasure to have the privilege to discuss with him. He would devote his time and patience to pass on to us his unique vision and love for our profession.

Victor was, of course, always extremely interested in others' work and I must confess that I was very proud when he asked me to send him papers from my research on piles, while he was preparing his book.

For the 5<sup>th</sup> Victor de Mello Goa Lecture, delivered on the 31<sup>st</sup> of May 2022, I chose to speak about the prediction of pile displacements from pressuremeter results, which is a subject we often talked about Victor and myself. It happens that I have recently written a synthetic paper about this subject, but never had the chance to present its full content during a lecture\*.

Indeed, the paper which follows was originally published as a contribution to the special issue of the Geotechnical Engineering Journal of the SEAGS & AGSSEA, honouring Prof. Harry G Poulos. Its reference is:

FRANK R. (2020). "Displacement of piles from pressuremeter test results – A summary of French research and practice". Geotechnical Engineering Journal of the SEAGS & AGSSEA Vol. 51 No. 2 June 2020 ISSN 0046-5828, 73-82.

I am grateful to the Journal of the SEAGS & AGSSEA and to the Soils and Rocks Journal for the permission to reproduce this synthetic paper.

Paris, 19<sup>th</sup> April 2022

Roger Frank

\*Roger Frank's presentation is available at Victor de Mello's website: <https://victorfbdemello.com.br/>

## Declaration of interest

The author has no conflicts of interest to declare.

## References

- Abchir, Z., Burlon, S., Frank, R., Habert, J., & Legrand, S. (2016). T-z curves for piles from pressuremeter test results. *Geotechnique*, 66(2), 137-148. <http://dx.doi.org/10.1680/jgeot.15.P097>.
- AFNOR P 94-262. (2012). *Justification des ouvrages géotechniques. Normes d'application nationale de l'Eurocode 7 - Fondations profondes*. Association Française de Normalization, Paris (in French).
- Amar, S., Baguelin, F., Frank, R., & Jézéquel, J.F. (1981a). L'autoforage. *Travaux*, 552, 63-76. (in French).
- Amar, S., Baguelin, F., Frank, R., & Jézéquel, J.F. (1981b). L'autoforage (Erratum et addendum). *Travaux*, 553, 91. (in French).
- Baguelin, F., & Frank, R. (1980). Theoretical studies of piles using the finite element method. In *Proceedings of the International Conference on Numerical Methods in Offshore Piling* (pp. 83-91), London. Institution of Civil Engineers.
- Baguelin, F., Carayannacou-Trézos, S., & Frank, R. (1979). *Réaction latérale des pieux: effets de forme et effets tridimensionnels* (Bulletin de Liaison des Laboratoires des Ponts et Chaussées, No. 104). Paris: Laboratoire Central des Ponts et Chaussées (in French).
- Baguelin, F., Frank, R., & Jézéquel, J.-F. (1982). Parameters for friction piles in marine soils. In *Proceedings of the 2nd International Conference of Numerical Methods in Offshore Piling* (pp. 197-214), Austin. University of Texas at Austin.
- Baguelin, F., Frank, R., & Said, Y.H. (1977). Theoretical study of lateral reaction mechanism of piles. *Geotechnique*, 27(3), 405-434. <http://dx.doi.org/10.1680/geot.1977.27.3.405>.
- Baguelin, F., Jézéquel, J.F., & Shields, D.H. (1978). *The pressuremeter and foundation engineering* (617 p.). Clausthal-Zellerfeld: Trans Tech Publications.
- Bigot, G., Bourges, F., & Frank, R. (1982). Etude expérimentale d'un pieu soumis aux poussées latérales du sol. *Revue Française de Géotechnique*, 18(18), 29-47. (in French). <http://dx.doi.org/10.1051/geotech/1982018029>.
- Bohn, C., Lopes dos Santos, A., & Frank, R. (2017). Development of axial pile load transfer curves based on instrumented load tests. *Journal of Geotechnical and Geoenvironmental Engineering*, 143(1), 04016081. [http://dx.doi.org/10.1061/\(ASCE\)GT.1943-5606.0001579](http://dx.doi.org/10.1061/(ASCE)GT.1943-5606.0001579).
- Bourgeois E., Burlon S. & Cuira F. (2018). Modélisation numérique des ouvrages géotechniques. *Techniques de l'Ingénieur*, 258, 1-33. <https://doi.org/10.51257/a-v1-c258>.
- Bustamante, M., & Frank, R. (1999). *Current French design practice for axially loaded piles* (Ground Engineering, pp. 38-44). London: Transport Research Laboratory.
- Bustamante, M., Frank, R., & Gianceselli, L. (1989). Prévision de la courbe de chargement des fondations profondes isolées. In *Proceedings of the 12th International Conference on Soil Mechanics and Foundation Engineering* (Vol. 2, pp. 1125-1126), Rio de Janeiro. Taylor & Francis (in French).
- Carayannacou-Trézos, S. (1977). *Comportement des pieux sollicités horizontalement* [Doctoral thesis]. Université Pierre et Marie Curie (Paris VI) (in French).
- Estéphan, R., Frank, R., Degny, E., & Perlo, S. (2006). *GOUPEG: application de la méthode « hybride » pour le calcul du comportement des groupes et des réseaux élémentaires de micropieux* (Bulletin de Liaison des Laboratoires des Ponts et Chaussées, No. 260). Paris: Laboratoire Central des Ponts et Chaussées (in French).

- Estephan, R., Frank, R., & Degny, E. (2003). Effet d'inclinaison des micropieux dans un groupe: Approche par une méthode hybride. In *Proceedings of the European Conference on Soil Mechanics and Geotechnical Engineering* (pp. 541-546), Prague.
- European Committee for Standardization – CEN. (2004). *Eurocode 7: geotechnical design - part 1: general rules, EN 1997-1:2004 (E), (F) and (G)*. Brussels.
- France. Ministère de l'Équipement, du logement et des transports – MELT. (1993). Règles Techniques de Conception et de Calcul des Fondations des Ouvrages de Génie Civil. Cahier des clauses techniques générales applicables aux marchés publics de travaux. *Journaux Officiels* (Fascicule No. 62, Titre V, Textes Officiels N° 93-3 T.O). (in French).
- Frank, R. (1974). *Etude théorique du comportement des pieux sous charge verticale: introduction de la dilatance* [Doctoral thesis] Université P. et M. Curie (Paris VI) (in French).
- Frank, R. (1984). *Contributions à l'étude des fondations profondes et des essais en place par autoforage* [Thèse de Doctorat d'état ès Sciences Physiques]. Université P. et M. Curie (Paris VI) (in French).
- Frank, R., & Pouget, P. (2008). Experimental pile subjected to long duration thrusts owing to a moving slope. *Geotechnique*, 58(8), 645-658. <http://dx.doi.org/10.1680/geot.2008.58.8.645>.
- Frank, R., & Zhao, S.R. (1982). *Estimation par les paramètres pressiométriques de l'enfoncement sous charge axiale de pieux forés dans des sols fins* (Bulletin de Liaison des Laboratoires des Ponts et Chaussées, No. 119). Paris: Laboratoire Central des Ponts et Chaussées. (in French).
- Frank, R., Cuira, F., & Burlon, S. (2018). *Calcul des fondations superficielles et profondes*. Paris: Presses des Ponts. (in French).
- Gambin, M. (1963). Calcul d'une fondation profonde en fonction des résultats pressiométriques. *Sols-soils*, 7, 11-31. (in French).
- Hoang, M.T., Fahd, C., Dias, D., & Miraillet, P. (2018). Estimation du rapport E/EM: application aux radiers de grandes dimensions. *Journées Nationales de Géotechnique et de Géologie de l'Ingénieur*, 2018, 13-15. (in French).
- Jézéquel, J.F., & Le Méhauté, A. (1979). *Rapport de F.A.E.R.* Paris: Laboratoire Régional des Ponts et Chaussées de St Brieuc. (in French).
- Ménard, L. (1962). Comportement d'une fondation profonde soumise à des efforts de renversement. *Sols-soils*, 3, 9-27. (in French).
- O'Neill, M.W., Ghazzaly, O.I., & Ha, H.B. (1977). Analysis of three dimensional pile groups with non-linear soil response and pile-soil-pile interaction. In *Proceedings of the 9th Offshore Technology Conference* (pp. 245-256), Houston.
- Orsi, J.P. (1978). *L'autoforage et le frottement latéral des pieux: étude théorique de l'essai à la sonde frottante* [Doctoral thesis]. Ecole Nationale des Ponts et Chaussées (in French).
- Perlo, S., Frank, R., Degny, E., & Estephan, R. (2005). Analyse de groupes de micropieux sous charge transversale par une méthode hybride. In *Proceedings of the 16th International Conference on Soil Mechanics and Geotechnical Engineering* (pp. 2031-2034). Osaka: IOS Press. (in French). Retrieved in July 10, 2022, from <https://ebooks.iospress.nl/publication/43780>
- Poulos, H.G., & Davis, E.H. (1968). The settlement behaviour of single axially loaded incompressible piles and piers. *Geotechnique*, 18(3), 351-371. <http://dx.doi.org/10.1680/geot.1968.18.3.351>.
- Randolph, M.F. (1977). *A theoretical study of the performance of piles* [Doctoral thesis, University of Cambridge]. University of Cambridge's repository. Retrieved in July 10, 2022, from <https://www.repository.cam.ac.uk/handle/1810/250739>
- Randolph, M.F., & Wroth, C.P. (1978). Analysis of deformation of vertically loaded piles. *Journal of the Geotechnical Engineering Division*, 104(12), 1465-1488. <http://dx.doi.org/10.1061/AJGEB6.0000729>.
- Reiffsteck, P. (2006). Portance et tassements d'une fondation profonde - Présentation des résultats du concours de prévision. In *Proceedings of the International Symposium 50 years of Pressuremeters (ISP 5-Pressio 2005)* (pp. 521-535), Marne-la-Vallée. Presses des Ponts (in French).
- Robas, A., & Kuder, S. (2006). Bearing capacity and settlement, prediction of a bored pile. In *Proceedings of the International Symposium 50 years of Pressuremeters (ISP 5-Pressio 2005)* (pp. 609-611), Marne-la-Vallée. Presse des Ponts.
- Said, I., Frank, R., & De Gennaro, V. (2006). Capacité portante et tassements d'un pieu foré à la tarière continue (prévision pour ISP –Pressio 5). In *Proceedings of the International Symposium 50 years of Pressuremeters (ISP 5-Pressio 2005)* (pp. 613-617), Marne-la-Vallée. Presse des Ponts.
- Said, Y.H. (1977). *Etude théorique des pieux sollicités horizontalement* [Doctoral thesis]. Université Pierre et Marie Curie (Paris VI).








## ***ARTICLES***

***Soils and Rocks***  
v. 45, n. 3





## Geotechnical characterization of the estuarine deltaic deposits in the Guayaquil city through in situ and laboratory tests

Bosco Intriago Álvarez<sup>1</sup> , Hernán Bazurto Palma<sup>1</sup> , Davide Besenon<sup>1#</sup> ,  
Xavier Vera-Grunauer<sup>2</sup> , Sara Amoroso<sup>3,4</sup> 

Article

### Keywords

Seismic dilatometer test  
Piezocone test  
Soft clays  
Diatoms  
Estuarine deltaic deposits  
Geotechnical characterization

### Abstract

According to previously available research and seismic microzonation studies a large area of the Guayaquil (Ecuador, South America) sits on estuarine deltaic deposits which consist of weak and highly compressible clays with diatoms. The nature of these fine-grained deposits may determine difficulties in a proper estimation of the soil properties. In this respect, the paper provides a detailed geotechnical and geophysical characterization of these soft clays, carried out in the estuarine complex of the Ecuadorean city. Borehole logs, standard penetration tests (SPT), piezocone tests (CPTu), a seismic dilatometer test (SDMT), a non-invasive geophysical survey, and laboratory tests were performed and then compared to analyze the static and dynamic geotechnical parameters of these deposits. The interpretation of the results highlighted the higher reliability of CPTu and SDMT rather than SPT and characterization lab testing to estimate soil shear strength, compressibility and stress history due to the soft nature of these clays, underlining also a certain sensitivity to the presence of the diatoms.

## 1. Introduction

Guayaquil is located on the West margin of the Guayas River along the Pacific coast of South America. Its soil deposits have been widely studied in the last decades due to the increasing urbanization this Ecuadorian city has experienced. Nevertheless, limited information is available in the literature on estimating geotechnical parameters related to this area.

The estuarine zone of the Guayas River deposits is highly heterogeneous. The soil stratigraphy consists of very soft, weak, and highly compressible sediment over hard rocks of Piñon and Cayo Formation (Vera-Grunauer, 2014). These soils present in their clayey matrix clay minerals including diatoms that result abundant in the upper 15-20 m depth of the Guayaquil deposits (Vera-Grunauer, 2014; Torres et al., 2018). The chemical composition of diatoms and their porous microstructure affect clay behavior, since the diatom skeletons or frustules contain a large number of voids or open pores, approximately between 60 and 70% according to Losic et al. (2007). These spaces allow great absorption of water, leading to a possible alteration of the soil properties.

Caicedo et al. (2018) established that for Bogota soils, diatoms increase the plasticity index ( $I_p$ ), compromising the use of the Unified Soil Classification System (USCS)

(ASTM, 2017). Similarly, Shiwakoti et al. (2002) concluded that the Atterberg limits increase significantly due to the presence of diatoms. Besides, as long as the concentration of diatoms increases, the coefficients of compressibility and permeability also increase. Due to the minerals' rough surface and interlocking shape, the effective friction angle and shear strength rise too (Díaz-Rodríguez & González-Rodríguez, 2013).

For the above considerations it assumes relevance to study the soil behavior of these Ecuadorean soft soils, evaluating also that most methods or geotechnical correlations are calibrated on datasets that do not consider the diatom content in soft clays. A proper characterization of soil parameters requires an integrated approach whereby the geophysical method, in situ, and laboratory tests are used. However, data from geotechnical tests depend on many factors, including stress history, grain size, minerals, composition and packing of the particles. Consequently, a generalized correlation, consistent for some soil types, does not necessarily fit well for other geomaterials (Mayne, 2006).

In Ecuador, the standard penetration test (SPT) is overused for geotechnical design, considering the limited cost of execution during the cores, the usual availability of the SPT equipment, and its easy implementation. However,

<sup>#</sup>Corresponding author: E-mail address: besenon@espo.edu.ec

<sup>1</sup>Escuela Superior Politécnica del Litoral, Facultad de Ingeniería en Ciencias de la Tierra, Guayaquil, Ecuador.

<sup>2</sup>Geostudios S.A., Guayaquil, Ecuador.

<sup>3</sup>University of Chieti-Pescara, Department of Engineering and Geology, Pescara, Italy.

<sup>4</sup>Istituto Nazionale di Geofisica e Vulcanologia, L'Aquila, Italia.

Submitted on August 5, 2021; Final Acceptance on June 3, 2022. Discussion open until November 30, 2022.

<https://doi.org/10.28927/SR.2022.074021>



This is an Open Access article distributed under the terms of the Creative Commons Attribution License, which permits unrestricted use, distribution, and reproduction in any medium, provided the original work is properly cited.

its use should not be generalized to all soils, especially to soft clays (Stroud, 1988). Besides, the samples obtained are highly altered, and therefore not representative of the in-situ conditions (Mayne et al., 2009). In this respect, it is advisable, as recommended by Mayne et al. (2009), to use direct push in situ tests, such as the piezocone test (CPTu) and the seismic dilatometer test (SDMT), fast and very convenient for routine site investigations, to better capture the undrained and drained behavior of cohesive and incoherent soils, respectively. This paper aims to provide a scientific contribution to the limited subsoil information available in the literature for the Ecuadorian city of Guayaquil, supplying a detailed geotechnical and geophysical characterization of the estuarine deposits, composed by soft clays with diatoms. The results of the in situ and laboratory tests are presented and compared to verify the use of the different geotechnical tests and correlations for these diatom rich fine-grained sediments.

## 2. Site investigation

### 2.1 Geological settings

Ecuador is considered a country with high seismic risk due to its location on an active subduction tectonic margin with direction N80°E (Benítez, 1995; Benítez et al., 2005; Egüez et al., 2003), where the Nazca plate collides

and subducts with the Continental segment formed by the Northern Andean block and the Southern American plate (Chunga et al., 2019).

The study area of Guayaquil city, in the Kennedy Norte sector, is located in the Ecuadorian coastal region with an average ground surface level of 3.3 m above mean sea level (Figure 1). This area presents different geological formations, where the three main representative geological units are known as Guayaquil, Cayo, and Piñon formations. Guayaquil Formation is mainly constituted by siliceous shales, Piñon Formation is associated with siliceous sediments and Cayo Formation is characterized by intra-oceanic volcanic arc sequences (Benítez, 1990; Benítez et al., 2005; Salocchi et al., 2020). These geomorphological features of Guayaquil support the convergence of three macro-geological domains: alluvial plain of the Daule and Babahoyo rivers; Chongón-Colonche Cordillera hills and the estuarine deltaic complex of the Guayas River. This latter complex (later defined also as lithological unit D3) results composed by very soft and highly compressible deposits that, once analyzed microscopically, show in their clayey matrix minerals of heterogeneous composition.

Diatoms are one of these components and, as reported by Vera-Grunauer (2014), in the Kennedy Norte area their content fluctuates between 5.6 million per gram of soil to 1.4 million per gram in the upper 15-20 m, being less at greater

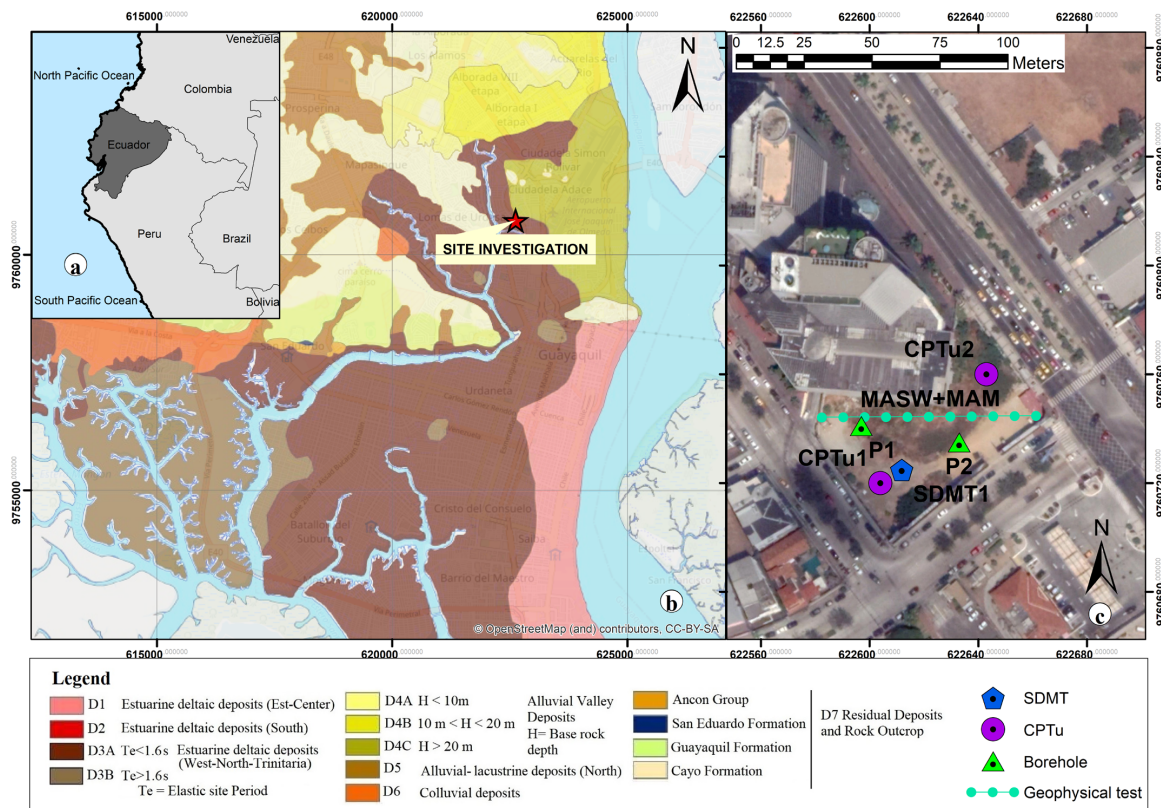


**Figure 1.** (a) location of the test site (a); (b) geological map of the study area; (c) location of the investigations at the Murano site.

depth. The diatom species with the highest abundance are *Thalassiosira*, *Actinocyclus*, *Stephanopyxis*, *Chaetoceros*, *Cyclotella*, *Coscinodiscus*, *Actinopterychus*, *Rhaphoneis*, *Cocconeis*, and *Diploneis* spp., that correspond mostly to centric diatoms (Vera-Grunauer, 2014). The abundance of diatoms could be related to the extremely high number of volcanoes of the Ecuadorian region (Vera-Grunauer, 2014). Figure 2 shows the microstructure identified in the estuarine deltaic deposit of Guayaquil.

A seismic microzonation study is also available for Guayaquil, classifying the city into seven lithological units (Figure 1b; Vera-Grunauer, 2014). The study area of this research is Murano, located in the Kennedy Norte sector (North-East of the city), along two estuarine branches of the Guayas River, and characterized by soft sediments with a relevant diatom content in the upper 15-20 m depth (Vera-Grunauer, 2014; Torres et al., 2018). According to the microzonation map the Murano site corresponds to the lithological unit D3, defined as Holocene estuarine deltaic deposits.

## 2.2 Description of the site campaign

Multiple geotechnical and geophysical surveys were carried out to reconstruct a more accurate subsoil characterization at the Murano site (Figure 1c, Table 1). The investigation included two boreholes, with SPTs and retrieval of disturbed samples for soil classification, two piezocones, one seismic dilatometer including dissipation

tests and one multichannel analysis of surface waves (MASW) survey with one microtremor array measurement (MAM). The undisturbed samples were not herein considered since, according to Lunne et al. (1997) criterion, the quality of these samples was in general classified as poor to very poor.

## 2.3 Direct and intermediate measurements

Figure 3 summarizes the results of the direct and intermediate measurements obtained from the in situ geotechnical and geophysical investigations: for SPT, the SPT blows counts ( $N_{SPT}$ ); for CPTu, the corrected cone resistance ( $q_t$ ), sleeve friction ( $f_s$ ), and pore water pressure ( $u_2$ ); for the SDMT, the two corrected pressure readings, namely  $p_0$  (1<sup>st</sup> reading) and  $p_1$  (2<sup>nd</sup> reading), the horizontal stress index ( $K_D$ ) and the shear wave velocity ( $V_s$ ). The low  $N_{SPT}$  and  $q_t$  measurements and the high  $f_s$  and  $u_2$  values in the upper 30 m of depth, together with the proximity of  $p_0$  and  $p_1$  pressures depth by depth, agree to identify the profile of a soft and clayey soil preliminarily. As shown in Figure 3, CPTu and DMT direct parameters increase quite gradually with depth, while the  $N_{SPT}$  profile show clearly a layer change at about 10 m depth. Moreover, for DMT, one measurement for the 3<sup>rd</sup> corrected pressure reading ( $p_3$ ) is available and equal to 135 kPa in a thin sandy layer located at 17 m of depth. According to Marchetti et al. (2001),  $p_2$  values are generally used to estimate the hydrostatic pore water pressure ( $u_0$ ) in incoherent deposits. Therefore, the ground water level (GWT) can be estimated at 3.24 m of depth at the

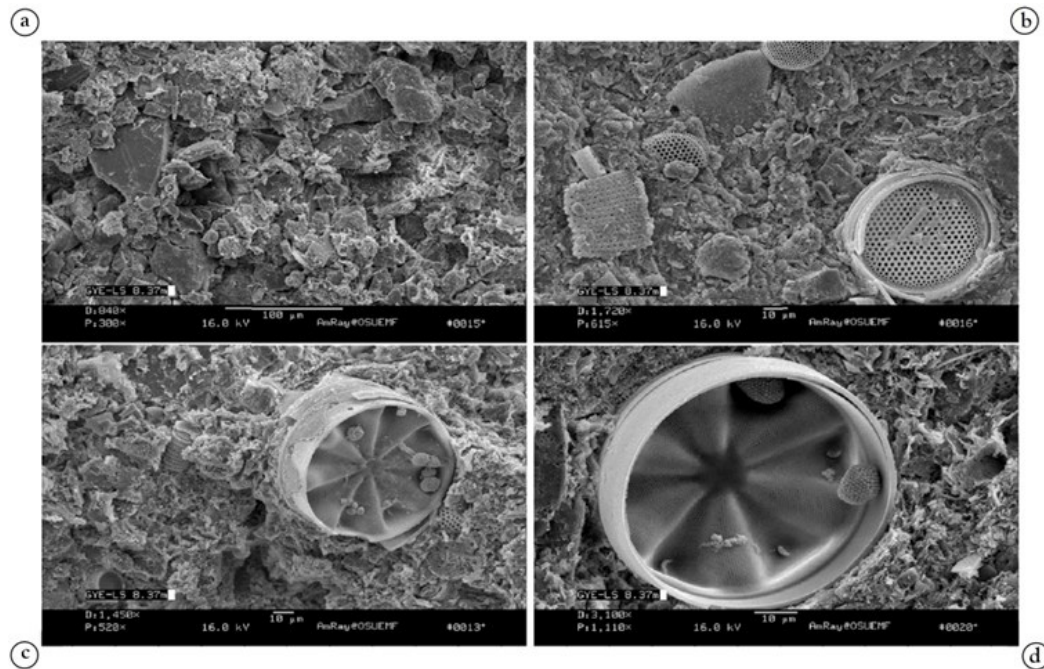


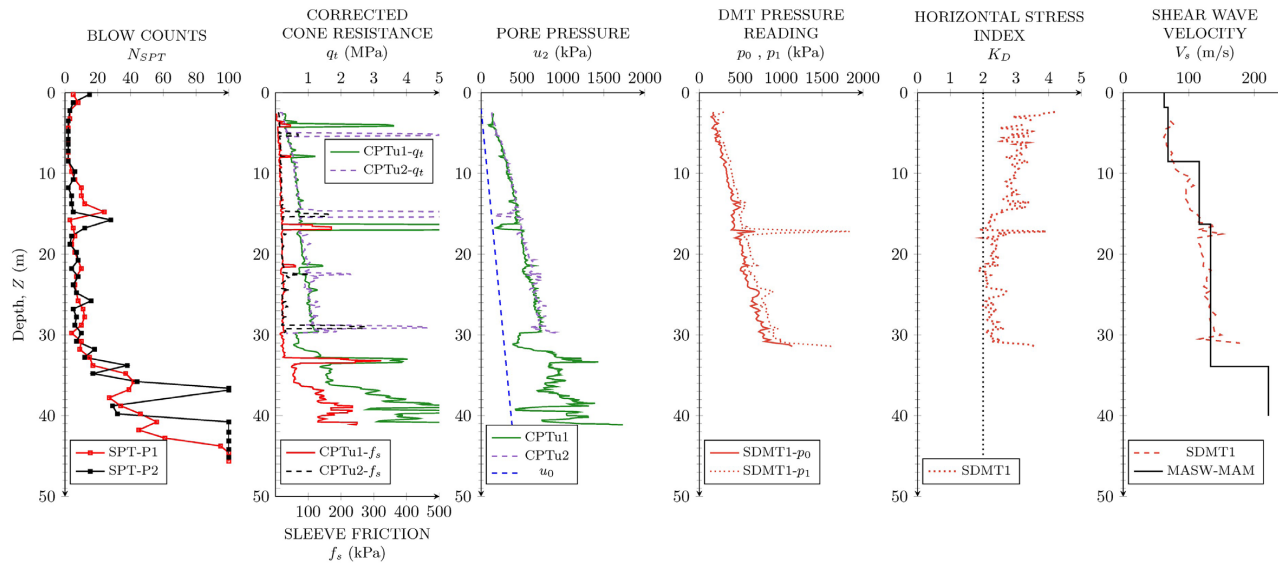
**Figure 2.** Scanning electron micrographs of Kennedy Norte sediment: (a) Sample with thin sand lamina; (b) silty clay with diatoms and diatom fragments; (c) diatomaceous smectite-rich clay matrix surrounds larger very fine sand-size diatoms; (d) well preserved diatom skeleton with micropores (<0.5 mm) (Vera-Grunauer, 2014).



**Table 1.** Summary of the field investigations performed at the Murano site.

Field test	Depth <sup>1</sup> (m)	Dissipation test depth (m)	Disturbed samples	SPT per borehole	GWT depth (m)	Test date
P1	46.00	-	45	45	1.80	14/11/2018
P2	45.00	-	45	45	2.00	08/11/2018
CPTu1	41.00	10.60; 13.45	-	-	2.05	12/11/2018
CPTu2	30.00	8.00; 12.00	-	-	1.82	09/11/2018
MASW+MAM	80.50	-	-	-	-	-
SDMT1	31.40	8.00	-	-	3.24	05/08/2018

<sup>1</sup> For MASW+MAM survey, the value corresponds to receiver spread length.

**Figure 3.** Measured parameters for geotechnical and geophysical tests at the Murano site.

DMT test site. The CPTu test can also be used to estimate the GWT through  $u_2$  in the thin sandy layers; in this case, GWT is at about 2.05 m for CPTu1 and 1.82 m for CPTu2. For boreholes P1 and P2, GWT was measured at 1.80 and 2.00 m of depth respectively. CPTu tests and boreholes were performed roughly in the same wet period (Table 1), which justifies the good agreement between GWT results. On the contrary, SDMT1 was conducted in the Ecuadorian dry season, explaining the GWT variation due to seasonal fluctuations. In addition, despite Guayas River and its Estuarine Complex are influenced by sea level fluctuations, tidal variation should not influence the GWT level due to the low permeability of these fine-grained deposits.

The  $K_D$  profile shown in Figure 3 gives information on the stress history of the deposits (Marchetti, 1980):

$$K_D = (p_0 - u_0) / \sigma'_{v0} \quad (1)$$

where the hydrostatic pore water pressure ( $u_0$ ) is obtained using the GWT profile estimated from DMT and the vertical effective stress ( $\sigma'_{v0}$ ) is estimated from DMT using the soil

unit weight ( $\gamma$ ) by Marchetti & Crapps (1981) chart. The complete  $\gamma$  profile is provided in the subsequent section.

As shown in Equation 1,  $K_D$  can be regarded as an amplified in situ coefficient of earth pressure at rest ( $K_0$ ) since  $(p_0 - u_0)$  is an “amplified” horizontal effective stress ( $\sigma'_{h0}$ ) due to penetration. According to Marchetti et al. (2001) the horizontal stress index  $K_D$  is noticeably reactive to stress history, prestraining/aging and structure, scarcely felt by  $q_t$  from CPT. In normally consolidated (NC) clays, usually identified with an overconsolidation ratio  $OCR \approx 1$ , the value of  $K_D$  is approximately equal to 2, and this justifies that the  $K_D$  profile is similar in shape to the  $OCR$  profile (Jamiolkowski et al., 1988). At the Murano site the  $K_D$  profile provides a value of  $K_D \approx 3$  within the upper 15 m, and of  $K_D \approx 2$  in the bottom layer (15–30 m) that can be associated to a NC behavior. The higher  $K_D$  values revealed in the upper 15 m can be associated to the stress history of this layer and potentially to a “structure-induced overconsolidation” (i.e. “apparent overconsolidation”), representing the Guayaquil diatomaceous naturally cemented clays. As documented by Vera-Grunauer (2014) and Torres et al. (2018), this sediment seems to have a greater proportion of diatomaceous

material and may initially have had a higher organic matter content. This resulted in local cementation of the sediment by framboidal pyrite.

Finally, the SDMT- $V_s$  profile is compared to the MASW+MAM- $V_s$  interpretation, highlighting a good agreement between the geophysical and geotechnical methods. The passive measurements also provide an ambient noise curve, detecting a peak frequency at 0.796 Hz, which corresponds to an elastic period  $T_e = 1.256$  s. This value correctly matches the seismic microzonation study (Vera-Grunauer, 2014) that identifies the Murano area as a D3A zone, namely estuarine deltaic deposits with  $T_e < 1.6$  s.

Other direct measurements obtained at the site are related to CPTu and DMT dissipation tests, as for the coefficient of consolidation in horizontal direction ( $c_h$ ) (Robertson et al., 1992; Marchetti & Totani, 1989). Figure 4a shows the results of the CPTu pore water pressure ( $u_2$ ) with time ( $t$ ) together with the points corresponding to the measured time for the 50% of dissipation ( $t_{50}$ ). Figure 4b illustrates the profile of the non-corrected 1<sup>st</sup> DMT reading ( $A$ ) with the time ( $t$ ) in combination with the contraflexure point of the curve ( $t_{flex}$ ). The  $c_h$  values obtained by dissipation tests are equal to  $4.20 \cdot 10^{-6}$  and  $5.20 \cdot 10^{-6}$  m<sup>2</sup>/sec for CPTu1 and to  $1.70 \cdot 10^{-6}$  and  $1.40 \cdot 10^{-6}$  m<sup>2</sup>/sec for CPTu2, assuming a value of the rigidity index equal to 70 according to Mayne (2007). The  $c_h$  value obtained in the clayey layer by DMT is equal to  $2.6 \cdot 10^{-5}$  m<sup>2</sup>/sec.

### 3 Geotechnical characterization of the test site using in situ and laboratory tests

#### 3.1 Soil classification

Laboratory and in situ testing were analyzed to obtain a detailed soil classification. Figure 5 shows the borehole log using USCS soil classification (ASTM, 2017), the soil

composition, the Atterberg limits (liquid limit  $w_L$ , plastic limit  $w_p$ ), the plasticity index ( $I_p$ ), the water content ( $w$ ) and the liquidity index ( $I_L$ ), the CPT soil behavior type index ( $I_c$ ) and the DMT material index ( $I_D$ ). The water content was considered as a minimum value, due to the possible changes of the natural conditions of the collected SPT disturbed samples. However, the use of the SPT Raymond sampler provided the advantage to have a quite continuous profile of the index laboratory parameters (i.e.  $w_L$ ,  $w_p$ ,  $I_p$ ,  $w$ ,  $I_L$ ), detecting any eventual sudden change in the stratigraphy (Stroud, 1988).

Although the liquidity index values are not usually presented in percentage, this is herein done just to show the liquidity index values in Figure 5 along with the other physical indexes. The soil stratigraphy is apparently quite uniform up to approximately 33-37 m, showing mainly clays with high plasticity (mean  $I_p > 40\%$ ), liquidity index (mean  $I_L > 120\%$ ) and liquid limit (mean  $w_L > 70\%$ ). In particular, from 0 to 15 m, the predominance of silt and clay soil is observed, characterized by an average  $I_p$  of 46% and  $w$  of about 86%. The cohesive deposits continue to prevail from 15 to 30-37 m, but the percent of sand starts to increase and the  $I_p$  and  $w$  values decrease, staying in a range of 30-50% and 70-90%, respectively. Below 30-37 m of depth, the percentage of sand continues to increase up to 60%, and also a relevant presence of gravel (37-54%) is encountered. Consequently, Atterberg limits and water content values decrease. A first order estimate of the void ratio may be also obtained from  $w$  assuming the soil in saturated conditions. Thus, for a given specific gravity value ( $G_s = 2.67$ ), determined via laboratory tests, and the water content profile obtained from SPT retrieved samples, the void ratio value is approximately equal to 2.36 up to 15 m and to 2.10 between 15 and 32 m. The large void ratio is probably due to process of “clay bonding”, since the clay particles of the Guayaquil deltaic estuarine deposits may adhere to the large surface of diatoms, as reported by Vera-Grunauer (2014).

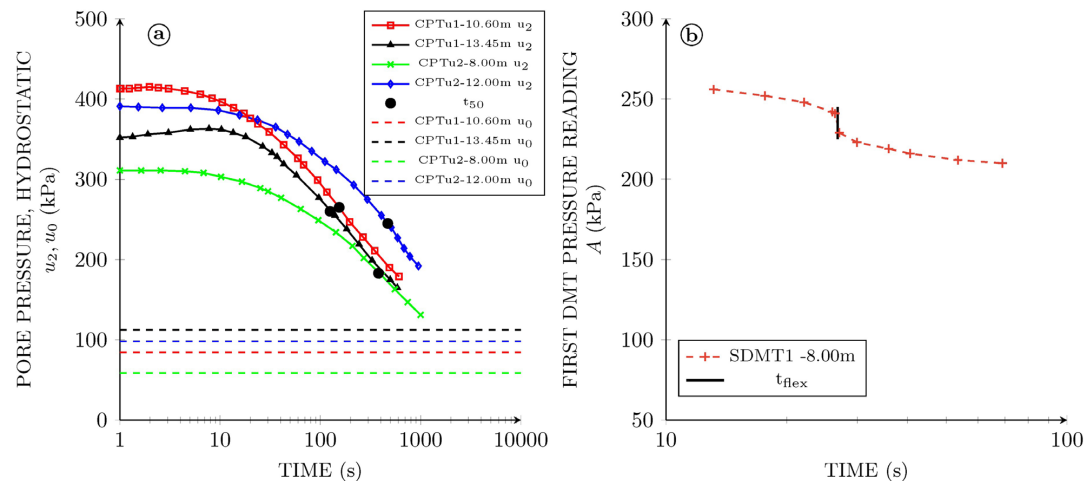


**Figure 4.** Dissipation tests from: (a) CPTu tests; (b) DMT test.

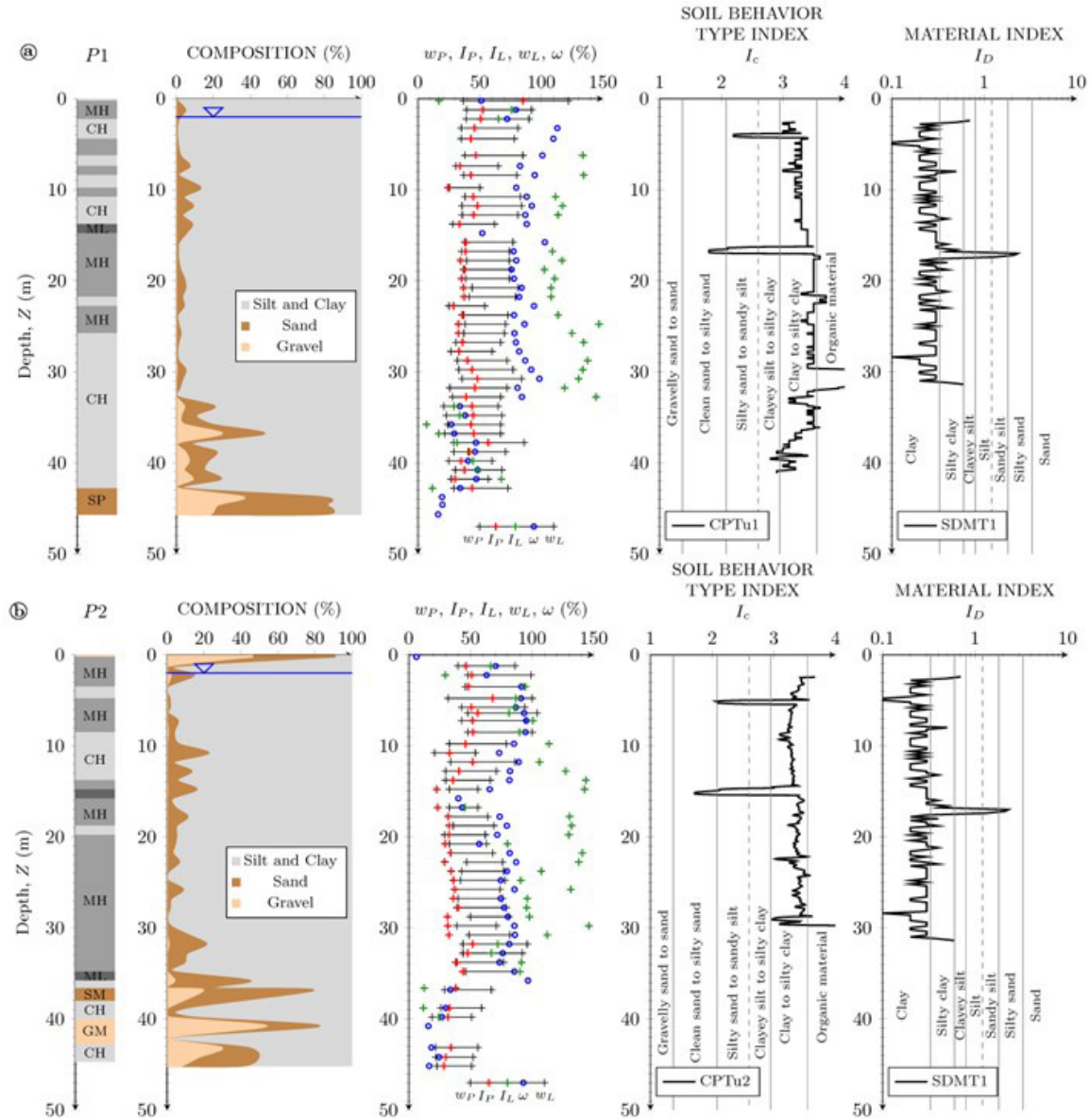


**Figure 5.** Soil classification using USCS method, CPTu and DMT interpretations, soil composition and basic properties for boreholes: (a) P1; (b) P2.

The  $I_c$  and  $I_D$  profiles, estimated using Robertson & Cabal (2015) and Marchetti et al. (2001) respectively, are in broad agreement with the soil stratigraphy obtained from the boreholes and the lab testing, since in situ tests detect on average a clay layer up to 40 m depth with a thin silty sand lens between 15 and 17 m depth. However, there is no perfect correspondence between the CPT-DMT geotechnical description and the grading curves (i.e., soil composition percent), since both  $I_c$  and  $I_D$  are parameters related to the mechanical soil response and not strictly to the grain size distribution of the soil deposits (e.g.: Boncio et al., 2020). The integrated information of gradations and index properties may find better agreement with the  $I_c$  and  $I_D$  values. For example,

correspondence to low-plastic deposits by P2 (Figure 5b) is noticed for the silty sands detected by CPTu2 at about 15 m.

Finally, it can be observed that for most of the soil samples within the upper 30-37 m depth,  $w$  is generally higher than 70%, recording also values bigger than 100%. Particularly, the highest  $I_p$ ,  $w_L$ ,  $w_p$  and  $w$  values are concentrated in the upper 15 m depth. This information is in line with the results by Vera-Grunauer (2014), who performed scanning electron micrographs for soil samples taken at sites close to the studied area. Vera-Grunauer (2014) observed that the microporous structure of diatoms consisted of open pores with a diameter less than  $0.5 \mu\text{m}$  which generates a large specific surface and allows the absorption of a large amount of water.

As described by Díaz-Rodríguez & González-Rodríguez (2013) and Caicedo et al. (2018) for the Mexico City and Bogota clays, the increment in diatom content raises the liquid limit and water content. Therefore, it is probable that the high values of the water content in the upper 15 m depth could be explained by the high presence of the diatoms, as mentioned above.

### 3.2 Strength and compressibility

The total unit weight ( $\gamma$ ) is an important parameter because it indirectly shows an idea of the field state of soil stress at any desired depth (Rodríguez et al., 2015). Recommended  $\gamma$  values were proposed by Look (2007) for cohesive soils, from soft organic with  $\gamma \approx 14 \text{ kN/m}^3$  to soft non-organic with  $\gamma \approx 16 \text{ kN/m}^3$  and, to stiff to hard with  $\gamma$  between 18 to  $20 \text{ kN/m}^3$ . Robertson & Cabal (2015) determined that the unit weight values are in direct proportion of  $q_t$  and the friction ratio  $R_f$ , with values around  $12.5 \text{ kN/m}^3$  for organic material and  $17.5 \text{ kN/m}^3$  for clays. Moreover, Mayne (2016) established a direct relationship between  $\gamma$  and  $f_s$ , for an average value of  $17.5 \text{ kN/m}^3$  in clays and  $13.5 \text{ kN/m}^3$  in diatomaceous mudstone.

At the Murano site the  $\gamma$  profiles obtained from CPTu and DMT interpretations (Figure 6), according to Robertson & Cabal (2015) and Marchetti & Crapps (1981) charts respectively, provide unit weight values that increases with the depth into the homogeneous clay from 14 to  $17 \text{ kN/m}^3$ , due to increased effective vertical stress ( $\sigma'_{v0}$ ). Actually, soil unit weights should be obtained by intact samples. The main scope of CPTu and DMT charts is not an accurate estimation of  $\gamma$ , but the possibility of constructing an approximate

$\sigma'_{v0}$  profile, needed in the interpretation of in situ tests (Robertson & Cabal, 2015; Marchetti et al., 2001).

Undrained shear strength ( $s_u$ ) coupled with total stress analysis is often used to examine the failure state of geotechnical structures under undrained conditions in Guayaquil City (Vera-Grunauer, 2014). At the Murano site, Brown & Hettiarachchi (2008), Robertson (2010) and Marchetti (1980) correlations were used to estimate  $s_u$  from SPT, CPTu and DMT, respectively, although SPT is suited for the use in evaluating strength and compressibility of loose to dense granular soils, with extended applications to stiff to hard clays and silts (e.g. Stroud, 1988; Mayne et al., 2009). CPTu and DMT give similar profiles, while SPT provides lower values within the upper 20 m depth, moving closer to DMT and CPTu prediction at greater depth (Figure 6).

Penetration test results are most commonly used to estimate the soil settlement, using the constrained modulus ( $M$ ), which depends on the stress state, soil type, and overconsolidation ratio. These dependencies are incorporated into CPT and DMT empirical correlations since  $M$  from CPT (Robertson, 2009) is related to the  $I_c$  and the in situ vertical stress, and  $M$  from DMT (Marchetti, 1980) is a function of the  $I_D$ , of the  $K_D$  and of the dilatometer modulus ( $E_D$ ). The in-situ predictions are still in close agreement with each other between 7 and 15 m depth ( $M \approx 2.5 \text{ MPa}$ ), while at greater depths, DMT always provides higher values compared to CPT (Figure 6). According to the numerous case histories available in the literature (e.g., Monaco et al., 2014; Monaco & Calabrese, 2006; Schmertmann, 1986, 1988; Mayne, 2005; Berisavljević, 2017), usually the measured settlements are in good agreement with the DMT-predicted values thanks to the high reliability of the DMT constrained modulus  $M$ , a working strain modulus.  $M$  by DMT is therefore associated

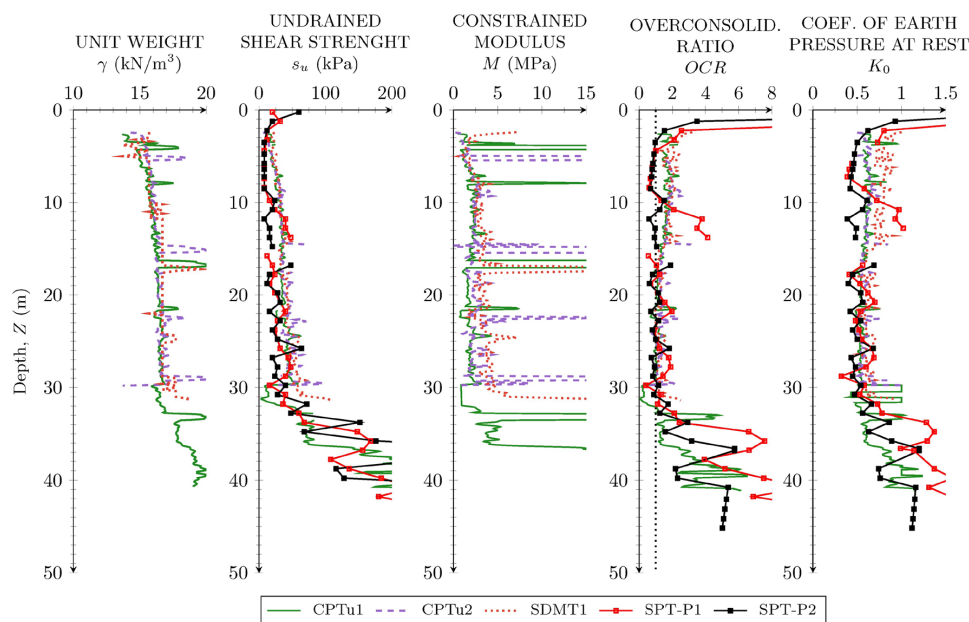


**Figure 6.** Geotechnical parameters estimated from laboratory and in situ tests.



with an intermediate strain level, more appropriate for the settlement calculations. In contrast, penetration tests, like CPT, working at higher strains due to the considerable distortion induced by the CPT conical tip, produce a less reliable  $M$  estimation (Baligh & Scott, 1975; Mayne, 2001).

For evaluating the overconsolidation, the abovementioned strong dependence between  $K_D$  and stress history in clay supported the use of DMT to obtain a more reliable estimate of  $OCR$ , using the Marchetti (1980) formula, rather than from CPT and SPT. However, the  $OCR$  predictions of fine-grained soils were also provided for CPT, using the normalized  $q_t$  values (Kulhawy & Mayne, 1990), and for SPT, using SHANSEP approach and site parameters, selected for the D3 estuarine deltaic zone of Guayaquil (Vera-Grunauer, 2014). A good agreement was shown between CPT and DMT for the entire profile, estimating  $OCR \approx 2$  within the upper 15 m and a value of  $OCR \approx 1$  (or slightly higher than 1) approximately between 15 and 30 m. This confirms the behavior preliminarily observed in the  $K_D$  profile (see Figure 3), being potentially due to the “apparent overconsolidation” of the diatomaceous naturally cemented Guayaquil clays.

For the estimation of the coefficient of earth pressure at rest ( $K_0$ ), the use of pressurimeter and/or flat dilatometer tests is recommended by the literature (e.g., Mayne et al., 2009), considering they can be considered as “horizontal-expansion” tests. Specifically, for the DMT the horizontal stress index ( $K_D$ ), having been regarded as an amplified  $K_0$  (see Equation 1), can provide reliable estimates in clayey deposits by a correlation obtained experimentally by Marchetti (1980), and later theoretically by Yu (2004):

$$OCR = (0.5 \cdot K_D)^{1.56} \quad (2)$$

Estimates of  $K_0$  can be also provided by CPT and SPT tests for low plastic fine-grained soils, using the  $OCR$  values estimated by each own test (Kulhawy & Mayne, 1990), as follow:

$$K_0 = 0.5 \cdot (OCR)^{0.5} \quad (3)$$

However, the “weak” dependency of SPT and CPT from the stress history together with the considerable scatter in the CPT and SPT database used to determine  $OCR$  and  $K_0$  can only provide an order of magnitude of these parameters (Robertson & Cabal, 2015).

The comparison of  $K_0$  profiles, shown in Figure 6, provides  $K_0 \approx 0.8$  by DMT in the upper 15 m depth and lower values by SPT and CPT, while  $K_0$  estimations by all the in-situ tests are consistent at greater depth, providing an average NC value of 0.6 between 15 and 30 m depth. This difference between the geotechnical behavior of the upper 15 m-thick layer and the lower 15 m-thick layer, as detected

by  $K_D$ ,  $OCR$ ,  $K_0$  and index parameters ( $w_L$ ,  $w_P$ ,  $I_P$ ,  $w$ ), may be potentially interpreted as a different concentration of diatoms, higher in the top layer than in the bottom. This assumption finds a consistency with the analyses of Vera-Grunauer (2014) and Torres et al. (2018) that in the Guayaquil estuarine complex revealed the abundant presence of diatoms in the upper 15-20 m depth.

### 3.3 Permeability

In situ tests were also used to determine permeability. Robertson (2010) developed a correlation between  $I_c$  and the coefficient of permeability ( $k$ ) to obtain an entire but approximate permeability profile that is not sensitive to the anisotropy of the soil. However, better estimation of the horizontal permeability ( $k_h$ ) can be provided by dissipation tests from both CPTu and DMT. Teh & Houlsby (1991), Parez & Fauriel (1988) and Robertson (2010) relationships were used for CPTu tests, once  $t_{50}$ , and consequently  $c_h$ , were estimated from dissipation curves (Figure 4). These three correlations provide similar values, and therefore for clarity in Figure 7 only Robertson (2010) estimation is shown. Similarly, for DMT test  $t_{flex}$  and  $c_h$  were used to estimate  $k_h$  according to Marchetti & Totani (1989).

The results obtained at the Murano site show that in the layer at 8.00 m depth horizontal permeability  $k_h$  obtained from DMT1 dissipation tests ( $k_h \approx 10^{-7}$  m/s, silty clay with  $I_D = 0.21$ ) is one order magnitude higher than  $k_h$  from

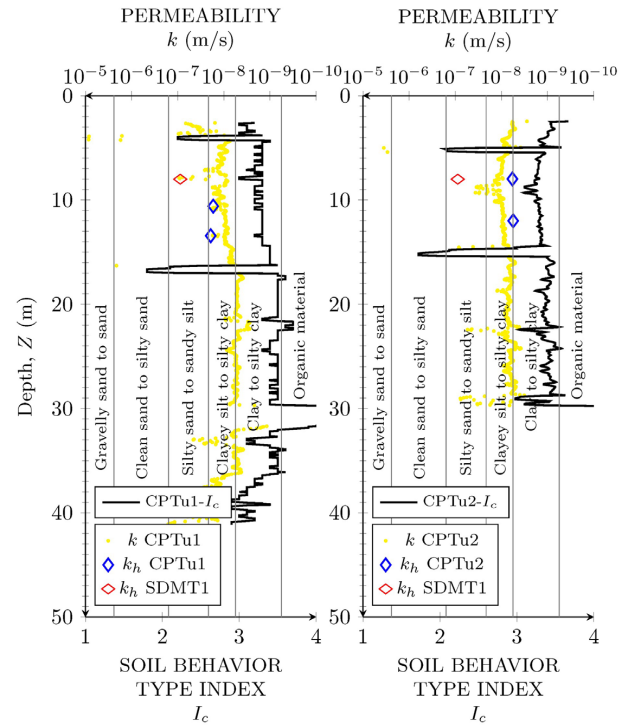


**Figure 7.** Permeability estimates together with soil behavior index profiles for CPTu1 and CPTu2.



CPTu2 (clay to silty clay with  $I_c = 3.29$ ). The continuous  $k$  profile derived from  $I_c$  has been found in broad agreement with the results of CPTu dissipation tests at the Murano site. Higher permeability is encountered in sandy soils ( $k_h \approx 10^{-6}$  m/s) while lower values are confined to soft clay ( $k_h \approx 10^{-8}$  m/s, slightly lower between 15 and 30 m depth) in reasonable agreement with permeability ranges obtained by Holtz et al. (1981). Probably, the higher horizontal permeability for the upper 15 m depth is related to its higher diatom content, when compared to the lower layer.

#### 4. Dynamic soil properties at the test site using geotechnical and geophysical measurements

##### 4.1 Shear wave velocity

The estimation of the shear wave velocity ( $V_s$ ) is fundamental in geotechnical engineering design, not only for site classification and soil-structure interaction, but also for earthquake analysis and site response. Penetration tests can be used for predicting  $V_s$  through some measured parameters. In particular, DMT allows to estimate the small strain shear

modulus ( $G_0$ ), based on the intermediate parameters  $I_D$ ,  $K_D$ ,  $M$  (Marchetti et al., 2008):

$$G_0 = M \cdot 26.177 \cdot K_D^{-1.0066} \text{ for clays } (I_D \leq 0.6) \quad (4)$$

$$G_0 = M \cdot 15.686 \cdot K_D^{-0.921} \text{ for silt } (0.6 < I_D < 1.8) \quad (5)$$

$$G_0 = M \cdot 4.5613 \cdot K_D^{-0.7967} \text{ for sands } (I_D \geq 1.8) \quad (6)$$

$V_s$  can be then obtained referring to the theory of elasticity:

$$V_s = \sqrt{G_0 / \rho} \quad (7)$$

Where  $\rho$  is the density of the soil that can be calculated from the unit weight determined by Marchetti & Crapps (1981) chart at each depth.

Several authors have developed and recommended correlations for SPT, expressed as a function of  $N_{SPT}$ ,  $N_{60}$ , depth ( $Z$ ), soil type and geological age (Table 2). Finally, for CPT several correlations are available to predict  $V_s$ , that are

**Table 2.** Main available equations to estimate  $V_s$  from SPT.

Author	Soil Type <sup>2</sup>	$V_s$ correlation	Geological description
Wair et al. (2012)	All soils	$V_s = 26 \cdot N_{60}^{0.215} \cdot \sigma'_{v0}^{0.275}$	Holocene
	All soils	$V_s = 34 \cdot N_{60}^{0.215} \cdot \sigma'_{v0}^{0.275}$	Pleistocene
	<b>Clays and silts</b>	<b><math>V_s = 23 \cdot N_{60}^{0.17} \cdot \sigma'_{v0}^{0.32}</math></b>	<b>Holocene</b>
	Clays and silts	$V_s = 29 \cdot N_{60}^{0.17} \cdot \sigma'_{v0}^{0.32}$	Pleistocene
	Sands	$V_s = 27 \cdot N_{60}^{0.23} \cdot \sigma'_{v0}^{0.23}$	Holocene
	Sands	$V_s = 35 \cdot N_{60}^{0.23} \cdot \sigma'_{v0}^{0.25}$	Pleistocene
Imai & Yoshimura (1970)	All soils	$V_s = 76 \cdot N_{SPT}^{0.33}$	-
Kalteziotis et al. (1992)	<b>All soils</b>	<b><math>V_s = 76.2 \cdot N_{SPT}^{0.24}</math></b>	-
	Sands and silts	$V_s = 49.1 \cdot N_{SPT}^{0.502}$	-
	Clays	$V_s = 76.55 \cdot N_{SPT}^{0.445}$	-
Ohsaki & Iwasaki (1973)	All soils	$V_s = 81.4 \cdot N_{SPT}^{0.39}$	-
	Sands	$V_s = 59.4 \cdot N_{SPT}^{0.47}$	-
Iyisan (1996)	All soils	$V_s = 51.5 \cdot N_{SPT}^{0.516}$	Deep alluvial deposits
Jinan (1987)	All soils	$V_s = 116.10 \cdot (N_{SPT} + 0.32)^{0.202}$	Soft Holocene deposits
Dikmen (2009)	<b>All soils</b>	<b><math>V_s = 58 \cdot N_{SPT}^{0.39}</math></b>	<b>Quaternary alluvium</b>
	Sands	$V_s = 73 \cdot N_{SPT}^{0.33}$	Quaternary alluvium
	Clays	$V_s = 44 \cdot N_{SPT}^{0.48}$	Quaternary alluvium
	Silt	$V_s = 60 \cdot N_{SPT}^{0.36}$	Quaternary alluvium

<sup>2</sup> For groups of formulas, the best used is highlighted.

related to numerous parameters like tip resistance (cone tip resistance  $q_c$  or corrected cone tip resistance  $q_t$ ),  $f_s$ , confining stress,  $Z$ , soil type, and geologic age (Table 3).

Figure 8a provides the comparison between  $V_s$  measured (MASW+MAM and SDMT) and  $V_s$  predicted by DMT (Marchetti et al., 2008), that shows a reasonable agreement. There is a slight overestimation of DMT predicted values, more pronounced in the upper 15 m that could be related to the higher concentration of the diatoms as previously detected by  $K_D$  (through  $K_0$  and  $OCR$ ) that is noticeable more reactive to stress history, structure and prestraining/aging, scarcely felt by the cone resistance  $q_c$  (or the corrected cone resistance  $q_t$ ) from CPT (Amoroso, 2014). A large number of correlations have been developed for SPT, involving the soil type, the geological description, and sometimes the in-situ stress. This results in a wide variability (Figure 8b) within the  $V_s$  profiles, as previously noted by other authors in different sites (e.g.: Fabbrocino et al., 2015; Akin et al., 2011). This is confirmed also for the soft clay deposits of Murano test site (Figure 8b, e.g.: Jinan, 1987) where, the estimated values are up to two times higher than the measured ones.

Similar behavior (Figure 8c) is observed with the  $V_s$  correlations developed for CPT test. This is confirmed also by Robertson (2012) that estimates values up to four times the measured ones. The arisen uncertainty could be due to the dependency to numerous and different parameters mentioned above that CPT and SPT parameters may not

capture correctly. However, it is possible to select the best SPT- $V_s$  and CPT- $V_s$  predictions for soft clay deposits using the formulas proposed by Wair et al. (2012), Dikmen (2009) and Kalteziotis et al. (1992) for SPT test (Figure 8d). Interestingly, the last two equations developed for all types of soils are in better agreement with the measured  $V_s$  profile than those made exclusively for clays. The selected Wair et al. (2012) equation is valid for Holocene clays and silts. For CPT test, Bouckovalas et al. (1989) and Vera-Grunauer (2014) resulted to fit better with  $V_s$  measurements, and they are valid for very soft clays and for clays with diatoms, respectively (Figure 8c). In particular, Vera-Grunauer (2014) proposed a site-specific correlation for the D3 estuarine deltaic zone of Guayaquil. All together the measured (SDMT, MASW+MAM) and selected-predicted (Marchetti et al., 2008; Wair et al., 2012; Dikmen, 2009; Kalteziotis et al., 1992; Bouckovalas et al., 1989; Vera-Grunauer, 2014)  $V_s$  data presented reasonable agreement identifying  $V_s$  values increasing in the 30 m depth in range of 50-180 m/s.

#### 4.2 Stiffness decay curves

Finally, in situ tests were used to evaluate stiffness decay curves ( $G$ - $\gamma$  curves). In particular, this opportunity is offered by SDMT that allows to estimate the in-situ variation of soil stiffness with the level of deformation, as preliminarily suggested by Marchetti et al. (2008) and then

**Table 3.** Main available equations to estimate  $V_s$  from CPT.

Author	$V_s$ (or $G_0$ ) correlation <sup>3</sup>	Geological description
Robertson (2012)	$V_s = \alpha_{vs} \cdot (q_t - \sigma'_{v0})^{0.5} / p_a$ ; $\alpha_{vs} = 10^{0.55 \cdot I_c + 1.68}$	Holocene and Pleistocene soils, mostly uncemented
Hegazy & Mayne (1995)	$V_s = [10.1 \log(q_t) - 11.4]^{1.67} \cdot f_s / q_t \cdot 100$	All types of soils
Simonini & Cola (2000)	$G_0 = 49.2 \cdot q_c^{0.51}$	Sand, silt and silty clay of Venice Lagoon
Andrus et al. (2007)	$V_s = 2.27 \cdot q_t^{0.412} \cdot I_c^{0.989} Z^{0.033} \cdot ASF$ ; $ASF = 1.00$	<b>Holocene soils</b>
	$V_s = 2.62 \cdot q_t^{0.395} \cdot I_c^{0.912} Z^{0.124} \cdot SF$ ; $SF = 1.12$	Pleistocene soils
Madiari & Simoni (2004)	$V_s = 140 \cdot q_c^{0.30} \cdot f_s^{-0.13}$	<b>Holocene cohesive soils</b>
	$V_s = 268 \cdot q_c^{0.21} \cdot f_s^{0.02}$	Holocene incoherent soils
	$V_s = 182 \cdot q_c^{0.33} \cdot f_s^{-0.02}$	Pleistocene cohesive soils
	$V_s = 172 \cdot q_c^{0.35} \cdot f_s^{-0.05}$	Pleistocene incoherent soils
Bouckovalas et al. (1989)	$G_0 = 28.0 \cdot q_c^{1.40}$	Very soft clays
Vera-Grunauer (2014)	$V_s = \sqrt{\eta \cdot q_c} e^{\alpha}$	Clays with diatoms
	$\alpha = [(3N_{kc} - 4) / 4] - [1 / (2\beta)]$ ;	
	$\eta = 3g / [2N_{kc} \cdot \gamma_s \cdot (1 + \nu)]$	

<sup>3</sup> Legend: see List of Symbols. For groups of formulas, the best used is highlighted.

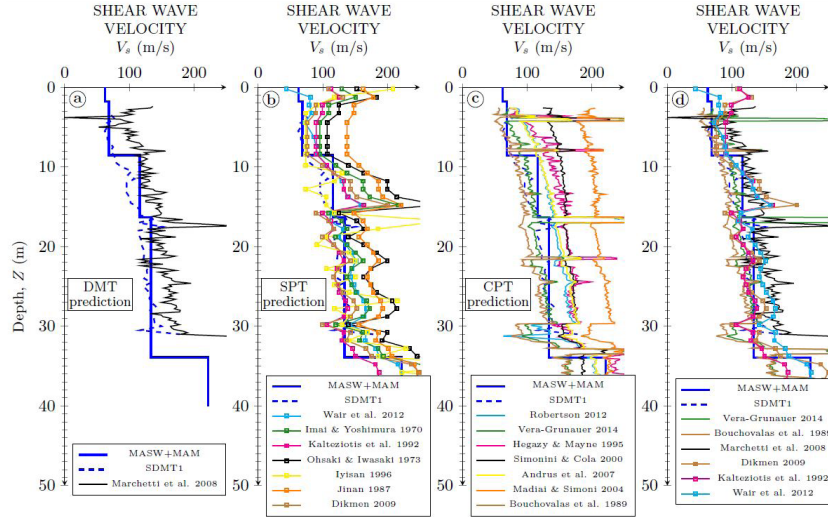


**Figure 8.** Comparison of  $V_s$  measured and  $V_s$  predicted by: (a) DMT; (b) SPT; (c) CPTu; (d) comparison of  $V_s$  measured and  $V_s$  predicted using the best correlations. The plots correspond to borehole P1, CPTu1 and SDMT1 tests.

tested by Amoroso et al. (2014) and Di Mariano et al. (2019). The method proposes firstly to assess the small strain modulus  $G_0$  through the theory of elasticity using  $V_s$ .

Then it is necessary to evaluate a working strain shear modulus  $G_{DMT}$  starting from the constrained modulus ( $M$  also named  $M_{DMT}$ ) obtained from the usual DMT test through the theory of elasticity:

$$G_{DMT} = M_{DMT} \cdot (1 - 2\nu) / [2 \cdot (1 - \nu)] \quad (8)$$

where  $\nu$  = Poisson's ratio, assumed equal to 0.3 for all layers.

Amoroso et al. (2014) proposed an equation to determine a hyperbolic stress-strain equation to represent the non-linear soil behavior through a normalized decay curve ( $G / G_0$ - $\gamma$  curve) by SDMT data:

$$G / G_0 = 1 / [1 + (G / G_{DMT} - 1) \cdot (\gamma / \gamma_{DMT})] \quad (9)$$

where  $G$  = shear modulus;  $\gamma$  = shear strain;  $\gamma_{DMT}$  = shear strain associated with the working strain DMT modulus for which Amoroso et al. (2014) suggested a range of values based on the soil type.

In this particular case, being Murano site composed by soft clays, it is recommendable to use a value of  $\gamma_{DMT} = 2\%$ . Moreover, to consider the effect of the confining stress and the different geotechnical properties of the entire soil profile into the assessment of the  $G / G_0$ - $\gamma$  curves, seven homogeneous strata were identified from 3.50 to 31 m depth, as reported in Figure 9. The  $G / G_0$ - $\gamma$  curves estimated in the upper 15.5 m have a similar behavior, while the deeper  $G / G_0$ - $\gamma$  curves decay much faster. This aspect is related to the higher values of  $K_D$ , and hence of  $OCR$  and  $K_p$ , detected

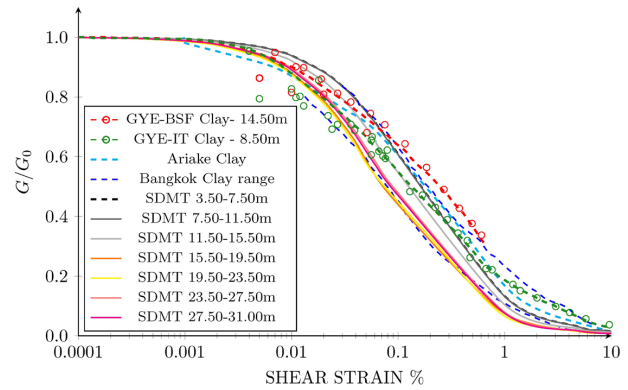


**Figure 9.**  $G$ - $\gamma$  decay curves for Guayaquil clays obtained by SDMT tests and comparison with results of laboratory curves.

for the upper layer, confirming a possible relationship with the different concentration of diatoms.

Figure 9 also plots two  $G/G_0$ - $\gamma$  curves developed for Guayaquil clays in geological zone D3A whose samples were retrieved at Baseball Stadium Field (BSF-dashed red line), in the Kennedy Norte sector, on structure-induced OC diatomaceous clays and at Trinitaria Island (TI-dashed green line) on NC clays according to Vera-Grunauer (2014). The cyclic response of TI samples was evaluated by means of cyclic triaxial and simple shear tests while, for BSF clay, the decay curve was estimated from cyclic triaxial data. The conditions of the clay structure were modeled in the following way: to reproduce the conditions of the BSF clay, the recompression method was used during the consolidation stage and the SHANSEP procedure was applied to model the normally consolidated soil. As reported by Vera-Grunauer (2014), the lower decay of BSF clay is due to the influence of pyrite cementation in its soil fabric. Other laboratory curves are included in Figure 9 for naturally cemented alluvial

clays with diatoms: Bangkok clay (Teachavorasinskun et al., 2002) and Ariake clay (Nagase et al., 2006). A reasonable agreement is possible to detect by comparing the entire group of literature curves with  $G / G_0$ - $\gamma$  curves by SDMT. However, the best fitting can be found between Guayaquil (BSF) and Bangkok (upper limit) laboratory tests and SDMT prediction within the upper 15.5 m, probably due to the higher content of diatoms. Below that depth, SDMT assessment fits well with the lower limit of Bangkok clays.

## 5 Conclusions

The deep site campaign performed in Guayaquil (Ecuador) at the Murano site allowed to provide a better soil characterization for soft clays in presence of diatoms:

- Index properties looked to be potentially influenced by the diatom content: the microstructure and porous shape of diatoms increased the average  $I_p$  and  $w$  values in the upper 15 m depth, influencing the interpretation provided by USCS classification. This aspect is less visible from  $I_c$  (CPTu) and  $I_D$  (DMT);
- The parameters of resistance, compressibility and stress history provided reliable values in the Guayaquil clays using both CPT and DMT, while SPT usually detected lower values being not particularly effective in soft soils;
- The analysis of the  $OCR$  profiles by CPTu and DMT confirmed an apparent overconsolidation in the upper 15 m ( $OCR \approx 2$ ) that could be explained by the presence of pyrite cementation in soil structure. This type of mineralogy is typical of marine environments; the main factor for the production of the cementing agent is the bacterial reduction of sulfate which is closely linked to the presence of diatoms. Similar observations emerged from  $K_D$  (and  $K_0$ ) values obtained only by DMT:  $K_D$  decreases from 3 to 2 moving from the upper 15 m to the lower layer, while  $K_0$  decreases from 0.8 to 0.6 in the same depth intervals. The above findings are in agreement with Vera-Grunauer (2014) and Torres et al. (2018) who both identified soft clays with diatoms in the upper 15-20 m in Guayaquil Bay. However, direct measurements of diatom content are not available at the Murano site, and therefore further research studies are necessary to confirm this hypothesis;
- In terms of permeability, the CPTu and DMT dissipation tests are in broad agreement with the  $k$  estimations obtained from  $I_c$ . The upper 15 m-layer revealed slightly higher values when compared to the permeability of the layer between 15 and 30 m depth, potentially associating this behavior to the porous shape of diatoms, more abundant in the top clayey layer;
- The comparison between predicted and measured  $V_s$  values suggested that DMT prediction is more reliable

than CPT and SPT predictions. The high number of  $V_s$  correlations developed for CPT and SPT test detected a wide variability within the  $V_s$  profile of the soft clays, having estimates up to two-four times the measured values. The arisen uncertainty could be due to the dependency to numerous and different parameters related to the geological age, soil type and in situ stress state that CPT and SPT parameters may not capture correctly. At the same time, DMT (through  $K_D$ ) is well correlated by a single correlation to stress history, prestraining/aging and structure scarcely felt by  $q_c$  and  $N_{SPT}$  (Amoroso, 2014);

- The nonlinear soil behavior of the soft clays at Murano site was presented by means of literature data and direct SDMT data interpretation. The  $G / G_0$ - $\gamma$  decay curves in the estuarine deltaic clays (zone D3) resulted in good agreement using SDMT and cyclic triaxial tests, identifying a similar behavior in the curves of upper 15.5 m, while the deeper  $G / G_0$ - $\gamma$  curves decay much faster. The behavior of the curves resulted related to the higher values of  $K_D$ , and hence of  $OCR$  and  $K_0$ , detected for the upper layer, confirming a possible relationship with the different concentration of diatoms. The use of SDMT in estimating stiffness decay curves could be therefore advantageous for the geotechnical design, although further investigation is needed to better understand the influence of diatoms content on decay curves.

## Acknowledgements

Special thanks to Studio Prof. Marchetti (Italy) for kindly providing the SDMT apparatus and to Prof. Maurizio Mulas (Escuela Superior Politécnica del Litoral, Ecuador) for sharing scientific geological information of the studied area.

## Declaration of interest

The authors declare that they have no known competing financial interests or personal relationships that could have appeared to influence the work reported in this paper.

## Authors' contributions

Bosco Intriago Álvarez: conceptualization, data curation, formal analysis, writing – original draft. Hernán Bazurto Palma: conceptualization, formal analysis, writing – original draft. Davide Besenon: formal analysis, funding acquisition, investigation, methodology, writing – review & editing. Xavier Vera-Grunauer: supervision, validation, investigation, writing – review & editing. Sara Amoroso: conceptualization, methodology, investigation, supervision, validation, writing – review & editing.



## List of symbols

$ASF$	Age scaling factor
$C_E$	Energy correction factor
$c_h$	Consolidation in horizontal direction
$CPT_u$	Cone penetration test with pore pressure measurement – piezocone test.
$c_v$	Consolidation in vertical direction
$DMT$	Flat Dilatometer Test
$E_D$	Dilatometer modulus
$f_s$	Sleeve friction resistance
$g$	Gravity
$G$	Shear modulus
$G_{DMT}$	Working strain shear modulus
$GWT$	Ground water level
$G_0$	Small strain shear modulus
$I_c$	Soil behavior type index
$I_D$	Material index
$I_L$	Liquidity index
$I_P$	Plasticity index
$k$	Coefficient of permeability
$K_D$	Horizontal stress index
$k_h$	Horizontal coefficient of permeability
$k_v$	Vertical coefficient of permeability
$K_0$	In situ earth pressure coefficient
$M$	Constrained modulus
$MAM$	Microtremor Array Measurement
$MASW$	Multichannel Analysis of Surface Waves
$M_{DMT}$	Constrained modulus (DMT)
$NC$	Normally consolidated
$N_{kc}$	Vera-Grunauer (2014) correlation factor
$N_{kt} s_u$	reduction factor
$N_{SPT}$	SPT blow counts
$N_{60}$	Energy corrected SPT blow count
$OCR$	Over Consolidation Ratio
$p_a$	Atmospheric pressure
$p_0$	Corrected first DMT reading
$p_1$	Corrected DMT second reading
$q_c$	Cone resistance
$q_t$	Corrected cone resistance
$R_f$	Friction ratio
$SDMT$	Seismic Dilatometer Test
$SF$	Scaling factor
$SHANSEP$	Stress History and Normalized Soil Engineering Properties
$S,m$	Vera-Grunauer (2014) parameters site
$SPT$	Standard Penetration Test
$s_u$	Undrained shear strength
$t$	Time in the dissipation test
$Te$	Elastic period
$t_{flex}$	Contraflexure point in the dissipation curve
$TI$	Trinitaria Island
$t_{50}$	Time for the 50% of the dissipation
$USCS$	Unified Soil Classification System
$u_0$	Hydrostatic pore water pressure

$u_2$	Pore water pressure at base of sleeve
$V_s$	Shear wave velocity
$w$	Water content
$w_L$	Liquid limit
$w_P$	Plastic limit
$Z$	Depth
$\beta$	Ratio between undrained shear strength and effective vertical stress
$\gamma$	Total unit weight / shear strain
$\gamma_{DMT}$	Shear strain associated with the working strain DMT modulus
$\gamma_s$	Volumetric weight
$\rho$	Density
$\sigma'_{h0}$	Horizontal effective stress
$\sigma'_{v0}$	Vertical effective stress
$\sigma_{v0}$	Total vertical stress
$\nu$	Poisson's constant

## References

- Akin, M.K., Kramer, S.L., & Topal, T. (2011). Empirical correlations of shear wave velocity ( $V_s$ ) and penetration resistance (SPT-N) for different soils in an earthquake-prone area (Erbaa-Turkey). *Engineering Geology*, 119(1-2), 1-17. <http://dx.doi.org/10.1016/j.enggeo.2011.01.007>.
- Amoroso, S. (2014). Prediction of the shear wave velocity  $V_s$  from CPT and DMT at research sites. *Frontiers of Structural and Civil Engineering*, 8(1), 83-92. <http://dx.doi.org/10.1007/s11709-013-0234-6>.
- Amoroso, S., Monaco, P., Lehane, B., & Marchetti, D. (2014). Examination of the potential of the seismic dilatometer (SDMT) to estimate in situ stiffness decay curves in various soil types. *Soils and Rocks*, 37(3), 177-194.
- Andrus, R.D., Mohanan, N.P., Piratheepan, P., Ellis, B.S., & Holzer, T.L. (2007). Predicting shear-wave velocity from cone penetration resistance. In *Proceedings of the 4th International Conference on Earthquake Geotechnical Engineering: Vol. 2528*. Thessaloniki. Springer.
- ASTM D2487. (2017). *Standard Classification of Soils for Engineering Purposes (Unified Soil Classification System)*. ASTM International, West Conshohocken, PA.
- Baligh, M.M., & Scott, R.F. (1975). Quasi-static deep penetration in clays. *Journal of Geotechnical and Geoenvironmental Engineering*, 101(11), 1119-1133.
- Benítez, S., Álvarez, V., Vera-Grunauer, X., & Mera, W. (2005). *Geological study of Guayaquil city*. UCSG.
- Benítez, S.B. (1990). Stratigraphy of the Cayo and Guayaquil formations in the Chongón-Colonche Cordillera: towards a redefinition. *Geociencias*, 3, 7-11. [in Spanish].
- Benítez, S.B. (1995). Geodynamic evolution of the south Ecuadorian coastal province in the upper tertiary cretaceous. *Géologie Alpine*, 71, 3-163. [in French].
- Berisavljević, D. (2017). *Geotechnical soil modeling based on the parameters obtained by seismic* [PhD thesis]. University of Belgrade at Serbia.

- Boncio, P., Amoroso, S., Galadini, F., Galderisi, A., Iezzi, G., & Liberi, F. (2020). Earthquake-induced liquefaction features in a late quaternary fine-grained lacustrine succession (Fucino Lake, Italy): implications for microzonation studies. *Engineering Geology*, 272, 105621. <http://dx.doi.org/10.1016/j.enggeo.2020.105621>.
- Bouckovalas, G., Kalteziotis, N., Sabatakakis, N., & Zervogiannis, C. (1989). Shear wave velocity in a very soft clay-measurements and correlations. In *Proceedings of the 12th International Conference Soil Mechanics Foundation Engineering (ICSMFE)* (pp. 191-194). Rotterdam: A.A. Balkema Publishers.
- Brown, T., & Hettiarachchi, H. (2008). Estimating shear strength properties of soils using SPT blow counts: an energy balance approach. In *GeoCongress 2008: Characterization, Monitoring, and Modeling of GeoSystems* (pp. 364-371). Reston, VA: ASCE. [http://dx.doi.org/10.1061/40972\(311\)46](http://dx.doi.org/10.1061/40972(311)46).
- Caicedo, B., Mendoza, C., López, F., & Lizcano, A. (2018). Behavior of diatomaceous soil in lacustrine deposits of Bogotá, Colombia. *Journal of Rock Mechanics and Geotechnical Engineering*, 10(2), 367-379. <http://dx.doi.org/10.1016/j.jrmge.2017.10.005>.
- Chunga, K., Ochoa-Cornejo, F., Mulas, M., Toulkeridis, T., & Menéndez, E. (2019). Characterization of geological faults related to cortical earthquakes of Guayaquil Gulf (Ecuador). *Andean Geology*, 46(1), 66-81. [in Spanish]
- Di Mariano, A., Amoroso, S., Arroyo, M., Monaco, P., & Gens, A. (2019). SDMT-based numerical analyses of deep excavation in soft soil. *Journal of Geotechnical and Geoenvironmental Engineering*, 145(1), 04018102. [http://dx.doi.org/10.1061/\(asce\)gt.1943-5606.0001993](http://dx.doi.org/10.1061/(asce)gt.1943-5606.0001993).
- Díaz-Rodríguez, J.A., & González-Rodríguez, R.R. (2013). Influence of diatom microfossils on soil compressibility. In *Proceedings of the International XVIII Conference on Soil Mechanics and Geotechnical Engineering* (pp. 325-328). Presses des Ponts, CFMS & ISSMGE.
- Dikmen, Ü. (2009). Statistical correlations of shear wave velocity and penetration resistance for soils. *Journal of Geophysics and Engineering*, 6(1), 61-72.
- Egüez, A., Alvarado, A., Yepes, H., Machette, M.N., Costa, C.H., Dart, R.L., & Bradley, L.A. (2003). Database and map of Quaternary faults and folds of Ecuador and its offshore regions. In US Geological Survey. *US Geological Survey Open-File Report*. US Geological Survey.
- Fabbrocino, S., Lanzano, G., Forte, G., de Magistris, F.S., & Fabbrocino, G. (2015). SPT blow count Vs. shear wave velocity relationship in the structurally complex formations of the Molise Region (Italy). *Engineering Geology*, 187, 84-97.
- Hegazy, Ya., & Mayne, Pw. (1995). Statistical correlations between Vs and cone penetration data for different soil types. In *Proceedings of the International Symposium on Cone Penetration Testing, CPT* (pp. 173-178). Linköping. SGS.
- Holtz, R.D., Kovacs, W.D., & Sheahan, T.C. (1981). *An introduction to geotechnical engineering*. Prentice Hall.
- Imai, T., & Yoshimura, Y. (1970). Elastic wave velocity and soil properties in soft soil. *Tsuchito-Kiso*, 18(1), 17-22. [in Japanese]
- Iyisan, R. (1996). Correlations between shear wave velocity and in-situ penetration test results. *Teknik Dergi*, 7, 371-374. [in Turkish]
- Jamiolkowski, M., Ghionna, V.N., Lancellotta, R., & Pasqualini, E. (1988). New correlations of penetration tests for design practice. In *Proceedings of the International Symposium on penetration testing; ISOPT-1* (pp. 263-296). Rotterdam: A.A. Balkema Publishers.
- Jinan, Z. (1987). Correlation between seismic wave velocity and the number of blow of SPT and depth. *Chinese Journal of Geotechnical Engineering*, 92-100.
- Kalteziotis, N., Sabatakakis, N., & Vassiliou, J. (1992). Evaluation of dynamic characteristics of Greek soil formations, In *Second Hellenic Conference on Geotechnical Engineering* (pp. 239-246). Conference on Geotechnical Engineering (in Greek).
- Kulhawy, F.H., & Mayne, P.W. (1990). *Manual on estimating soil properties for foundation design*. Electric Power Research Inst.
- Look, B.G. (2007). *Handbook of geotechnical investigation and design tables*. CRC Press/Balkema.
- Losic, D., Pillar, R.J., Dilger, T., Mitchell, J.G., & Voelcker, N.H. (2007). Atomic force microscopy (AFM) characterization of the porous silica nanostructure of two centric diatoms. *Journal of Porous Materials*, 14(1), 61-69.
- Lunne, T., Berre, T., & Strandvik, S. (1997). Sample disturbance effects in soft low plastic Norwegian clay. In *Proceedings of the Conference on Recent Developments in Soil and Pavement Mechanics* (pp. 81-102). Rotterdam: A.A. Balkema Publishers.
- Madiai, C., & Simoni, G. (2004). Shear wave velocity-penetration resistance correlation for Holocene and Pleistocene soils of an area in central Italy. In *Proceedings of the 2nd International Conference on Geotechnical Site Characterization (ISC'2)* (pp. 687-1694). Amsterdam: IOS Press.
- Marchetti, S. (1980). In situ tests by flat dilatometer. *Journal of the Geotechnical Engineering Division*, 106(3), 299-321.
- Marchetti, S., & Crapps, D.K. (1981). *Flat dilatometer manual*. Schmertmann and Crapps Inc.
- Marchetti, S., & Totani, G. (1989). Ch evaluation from DMTA dissipation curves. In *Proceedings of the 12th International Conference on Soil Mechanics and Foundation Engineering* (pp. 281-286). Rio de Janeiro, A.A. Balkema Publishers.
- Marchetti, S., Monaco, P., Totani, G., & Calabrese, M. (2001). The flat dilatometer test (DMT) in soil investigations. In *Proceedings of the 2nd International Flat Dilatometer Conference* (pp. 7-48). Reston, VA: ASCE. ISSMGE committee TC16.
- Marchetti, S., Monaco, P., Totani, G., & Marchetti, D. (2008). In situ tests by seismic dilatometer (SDMT). In *Proceedings of the From Research to Practice in*

- Geotechnical Engineering* (pp. 292-311). Reston, VA: ASCE. [https://doi.org/10.1061/40962\(325\)7](https://doi.org/10.1061/40962(325)7).
- Mayne, P.W. (2001). Stress-strain-strength-flow parameters from enhanced in-situ tests. In *Proceedings of the International Conference on In Situ Measurement of Soil Properties and Case Histories* (pp. 27-47). Bali.
- Mayne, P.W. (2005). Unexpected but foreseeable mat settlements on Piedmont residuum. *ISSMGE International Journal of Geoengineering Case Histories*, 1(1), 5-17.
- Mayne, P.W. (2006). In-situ test calibrations for evaluating soil parameters. In *Proceedings of the 2nd International Workshop on Characterization and Engineering Properties of Natural Soils* (pp. 1601-1652). London: Taylor & Francis Group.
- Mayne, P.W. (2007). *Cone penetration testing state-of-practice* (NCHRP Project 20-05). Transportation Research Board.
- Mayne, P.W. (2016). Evaluating effective stress parameters and undrained shear strengths of soft-firm clays from CPT and DMT. *Australian Geomechanics Journal*, 51(4), 27-55.
- Mayne, P.W., Coop, M.R., Springman, S., Huang, A.-B., & Zornberg, J. (2009). Geomaterial behavior and testing. In *Proceedings of the 17th International Conference on Soil Mechanics and Geotechnical Engineering* (pp. 2777-2872). Rotterdam, The Netherlands: IOS Press.
- Monaco, P., & Calabrese, M. (2006). DMT-Predicted Vs. Observed Settlements: A Review of the Available Experience. In *Proceedings of the 2nd International Conference on Flat Dilatometer* (pp. 244-252). Washington, D.C.
- Monaco, P., Amoroso, S., Marchetti, S., Marchetti, D., Totani, G., Cola, S., & Simonini, P. (2014). Overconsolidation and stiffness of Venice lagoon sands and silts from SDMT and CPTU. *Journal of Geotechnical and Geoenvironmental Engineering*, 140(1), 215-227. [http://dx.doi.org/10.1061/\(ASCE\)GT.1943-5606.0000965](http://dx.doi.org/10.1061/(ASCE)GT.1943-5606.0000965).
- Nagase, H., Shimizu, K., Hiro-Oka, A., Tanoue, Y., & Saitoh, Y. (2006). Earthquake-induced residual deformation of Ariake clay deposits with leaching. *Soil Dynamics and Earthquake Engineering*, 26(2-4), 209-220.
- Ohsaki, Y., & Iwasaki, R. (1973). On dynamic shear moduli and Poisson's ratios of soil deposits. *Soil and Foundation*, 13(4), 61-73.
- Parez, L., & Fauriel, R. (1988). The piezocone improvements made to soil recognition. *Revue Française de Géotechnique*, 13-27 (in French).
- Robertson, P.K. (2009). Interpretation of cone penetration tests-a unified approach. *Canadian Geotechnical Journal*, 46(11), 1337-1355.
- Robertson, P.K. (2010). Estimating in-situ soil permeability from CPT & CPTu. In *Memorias Del 2nd International Symposium on Cone Penetration Testing*. Pomona, California: California State Polytechnic University.
- Robertson, P.K. (2012). Discussion of Influence of particle size on the correlation between shear wave velocity and cone tip resistance. *Canadian Geotechnical Journal*, 49(1), 121-123.
- Robertson, P.K., & Cabal, K.L. (2015). *Guide to cone penetration testing for geotechnical engineering* (6th ed.). Gregg Drilling and Testing Inc.
- Robertson, P.K., Sully, J.P., Woeller, D.J., Lunne, T., Powell, J.J.M., & Gillespie, D.G. (1992). Estimating coefficient of consolidation from piezocone tests. *Canadian Geotechnical Journal*, 29(4), 539-550. <http://dx.doi.org/10.1139/t92-061>.
- Rodríguez, J.F., Auvinet, G., & Martínez, H.E. (2015). Settlement analysis of friction piles in consolidating soft soils. *DYNA Journal Engineering*, 82(192), 211-220. <https://doi.org/http://dx.doi.org/10.15446/dyna.v82n192.47752>.
- Salocchi, A.C., Minarelli, L., Lugli, S., Amoroso, S., Rollins, K.M., & Fontana, D. (2020). Liquefaction source layer for sand blows induced by the 2016 megathrust earthquake (Mw 7.8) in Ecuador (Boca de Briceño). *Journal of South American Earth Sciences*, 103, 102737.
- Schmertmann, J.H. (1986). Dilatometer to compute foundation settlement. In *Proceedings of the In Situ* (pp. 303-321). Gainesville, FL: Schmertmann & Crapps Inc.
- Schmertmann, J.H. (1988). Dilatometers settle in. *Civil Engineering*, 58(3), 68.
- Shiwakoti, D.R., Tanaka, H., Tanaka, M., & Locat, J. (2002). Influences of diatom microfossils on engineering properties of soils. *Soil and Foundation*, 42(3), 1-17.
- Simonini, P., & Cola, S. (2000). Use of piezocone to predict maximum stiffness of Venetian soils. *Journal of Geotechnical and Geoenvironmental Engineering*, 126(4), 378-382.
- Stroud, M.A. (1988). The standard penetration test—its application and interpretation. In *Conference on Penetration Testing in the UK*. London: Thomas Telford.
- Teachavorasinskun, S., Thongchim, P., & Lukkunaprasit, P. (2002). Shear modulus and damping of soft Bangkok clays. *Canadian Geotechnical Journal*, 39(5), 1201-1208.
- Teh, C.I., & Houlsby, G.T. (1991). An analytical study of the cone penetration test in clay. *Geotechnique*, 41(1), 17-34. <http://dx.doi.org/10.1680/geot.1991.41.1.17>.
- Torres, G., Recalde, S., Narea, R., Troccoli, L., & Rentería, W. (2018). Spatio-temporal variability of phytoplankton and oceanographic variables in El Golfo de Guayaquil during 2013-15. *Revista del Instituto de Investigación de la Facultad de Ingeniería Geológica, Minera. Metalúrgica y Geográfica*, 20(40), 70-79. [in Spanish].
- Vera-Grunauer, X. (2014). *Seismic response of a soft, high plasticity, diatomaceous naturally cemented clay deposit* [PhD thesis]. University of California at Berkeley.
- Wair, B.R., DeJong, J.T., & Shantz, T. (2012). *Guidelines for Estimation of Shear Wave Velocity Profiles*. Pacific Earthquake Engineering Research Center.
- Yu, H.-S. (2004). James K. Mitchell Lecture. In situ soil testing: from mechanics to interpretation. In *Proceedings of the 2nd International Conference on Geotechnical Site Characterization (ISC'2)* (pp. 3-38). Rotterdam, Netherlands: Millpress.

## Vacuum preloading and PVDs in soft soils beneath embankments: 3D coupled analysis incorporating overall stability study

José Leitão Borges<sup>1#</sup> 

Article

### Keywords

Prefabricated vertical drains  
Vacuum preloading  
Soft soil  
Three-dimensional modelling  
Overall stability  
Mechanical-hydraulic coupled analysis

### Abstract

Although embankments on soft soils with prefabricated vertical drains (PVDs) under vacuum preloading have been widely studied, there is a lack of studies in the literature in which overall stability is analysed through three-dimensional (3D) mechanical-hydraulic coupled modelling. In order to contribute to overcome such deficiency, this paper presents 3D numerical analyses of an embankment on soft soils incorporating PVDs and vacuum preloading. A finite element code, which includes 3D fully coupled analysis, is used and a method for overall stability study – which uses the 3D numerical results obtained with the finite element code – is presented and applied. A parametric study is performed in order to analyse the influence of the magnitude of the vacuum preload and the staged construction of the embankment (time of vacuum application before completion of the embankment). Overall stability, excess pore pressures, settlements, horizontal displacements and stress levels are analysed.

## 1. Introduction

Due to the geotechnical characteristics of the soft soils, such as low strength, high compressibility and low permeability, a number of techniques are available in practice to improve the behaviour of embankments built on such soils. Such improvement techniques provide one or more of the following effects: increase of overall stability, consolidation acceleration and reduction of long-term settlements.

The two techniques most used in practice when the main purpose is to accelerate the consolidation are: (i) use of prefabricated vertical drains (PVDs) (Holtz et al., 1991; Hird et al., 1992; Chai et al., 1995; Borges, 2004; Shen et al., 2005; Lin & Chang, 2009; Liu & Rowe, 2015; Zhang et al., 2015); (ii) preloading, which can typically be performed by an embankment surcharge or vacuum suction (Zhang et al., 2018; Lam et al., 2015; Bergado et al., 2002; Cascone & Biondi, 2013; Long et al., 2015; Indraratna et al., 2016; Mesri & Khan, 2012; Rujikiatkamjorn et al., 2008).

Surcharge preloading combined with PVDs is a popular technique to further increase the consolidation acceleration or reduction of the construction time (Lam et al., 2015). Typically, the PVDs are installed into the soft ground, followed by the construction of the embankment and the surcharge

application. However, this technique is often limited in terms of the magnitude of the surcharge that can be applied, due to overall instability of the embankment. In that case, the use of PVDs combined with vacuum preloading is an alternative that solves the problems of the conventional surcharge preloading (Saowapakpiroon et al., 2010; Rujikiatkamjorn et al., 2008; Long et al., 2015; Chai et al., 2005; Chai & Rondonuwu, 2015; Saowapakpiroon et al., 2010; Indraratna et al., 2012). The advantage of the vacuum application is that gradients of pore pressure are induced in the ground – provoking therefore the consolidation process (pore pressure reduction and effective mean stress increase) – maintaining a constant total stress, instead of what happens in conventional surcharge preloading. Besides a better performance in terms of stability, the vacuum technique also provides lower outward and upward displacements in the lateral regions of the embankment.

Although PVDs combined with vacuum preloading have been widely studied, there is a lack of studies in the literature in which overall stability is analysed through three-dimensional mechanical-hydraulic coupled modelling. In this paper, in order to contribute to overcome such deficiency, three-dimensional numerical analyses are performed and a method for overall stability study – which uses the 3D results of a finite element code – is proposed and applied.

#Corresponding author. E-mail address: leitao@fe.up.pt

<sup>1</sup>Universidade do Porto, Construct, Faculdade de Engenharia, Porto, Portugal.

Submitted on July 25, 2021; Final Acceptance on April 21, 2022; Discussion open until November 30, 2022.

<https://doi.org/10.28927/SR.2022.072821>



This is an Open Access article distributed under the terms of the Creative Commons Attribution License, which permits unrestricted use, distribution, and reproduction in any medium, provided the original work is properly cited.



A parametric study is performed so that the influence of the following parameters is studied: magnitude of the vacuum preload; staged construction of the embankment (time of vacuum application before completion of the embankment). Overall stability, excess pore pressures, settlements, horizontal displacements and stress levels are analysed.

## 2. Finite element code

The finite element code used herein was developed by Borges (1995). The initial version (2-D version) was presented in 1995 and several improvements were subsequently developed and implemented, particularly a 3D version (Borges, 2004). Among other features, the code incorporates fully mechanical-hydraulic coupled analysis (Biot consolidation theory) (Borges, 1995; Lewis & Schrefler, 1987; Britto & Gunn, 1987) and the  $p$ - $q$ - $\theta$  critical state model for soil constitutive simulation (Borges, 1995; Lewis & Schrefler, 1987).

The  $p$ - $q$ - $\theta$  model is an extension of the Modified Cam-Clay model into the three-dimensional stress space that uses the Mohr-Coulomb surface as the critical state criterion, while in the Modified Cam-Clay model the Drucker-Prager surface is utilised. Therefore, in the  $p$ - $q$ - $\theta$  model, the parameter that defines the slope of the critical state line,  $M$ , is not constant (as happens in the Modified Cam-Clay model) and depends on the angular stress invariant  $\theta$  and effective friction angle,  $\phi'$ , as follows (Lewis & Schrefler, 1987; Borges, 1995):

$$M = \frac{3 \sin \phi'}{\sqrt{3} \cos \theta + \sin \phi' \sin \theta} \quad (1)$$

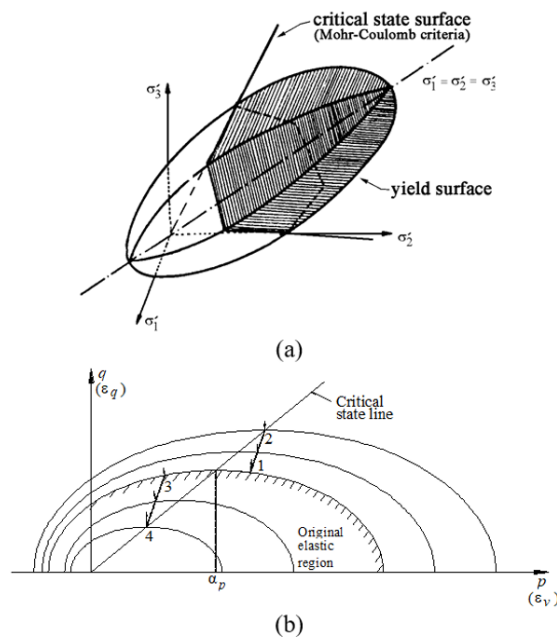


**Figure 1.** Yield and critical state surfaces of the  $p$ - $q$ - $\theta$  critical state model in (a) principal effective stress space and (b)  $p$ - $q$  space.

The Mohr-Coulomb criterion is defined when  $M$ , given by Equation 1, is introduced in the equation of the critical state line

$$q = M \cdot p \quad (2)$$

where  $p$  is the effective mean stress and  $q$  the deviatoric stress.

The yield and critical state surfaces of the  $p$ - $q$ - $\theta$  model in the principal effective stress space and in the  $p$ - $q$  plane are shown in Figure 1. Depending on the over-consolidation ratio, hardening behaviour or softening behaviour is modelled. Hardening occurs in normally consolidated or lightly over-consolidated clays (stress path 1-2, in Figure 1b) while softening occurs in moderately to strongly over-consolidated clays (stress path 3-4, in Figure 1b).

The finite element code has been used to analyse a wide range of geotechnical structures involving consolidation (Borges, 1995; Borges & Cardoso, 2001, 2002; Costa, 2005; Domingues, 2006; Costa et al., 2007; Marques, 2008; Borges et al., 2009; Guerra, 2009; Azevedo, 2010; Borges & Marques, 2011; Caramelo, 2011; Monteiro, 2011; Pinto, 2011; Alves, 2012; Gonçalves, 2012; Borges & Guerra, 2014; Santos, 2014; Barros, 2015; Borges & Gonçalves, 2016; Borges & Almeida, 2018; Marques, 2021).

Comparing numerical and field results, good agreements were obtained in the modelling of several case studies, such as: (i) two trial geosynthetic-reinforced embankments on soft soils (Borges, 1995), one constructed up to failure and the other, also incorporating prefabricated vertical drains, observed until the end of consolidation; (ii) two embankments on soft soils reinforced with stone columns, one in the Gold Coast Highway of Australia (Marques, 2021), and the other in the northern railway of Portugal (Domingues, 2006); (iii) a braced excavation in very soft ground carried out in the City of San Francisco (Costa et al. 2007; Costa, 2005).

For 3D analysis, two types of the 20-noded brick element are used: (i) the coupled element (Figure 2a), for

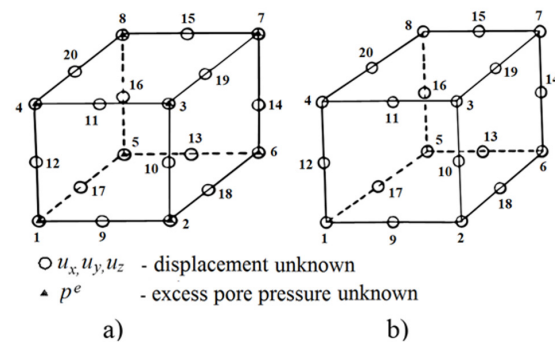


**Figure 2.** 20-noded brick element: (a) coupled element, with 60 displacement degrees of freedom and 8 excess pore pressure degrees of freedom; (b) non-coupled element, with 60 displacement degrees of freedom.

the soft soil, where consolidation is considered; (ii) the non-coupled element (Figure 2b), for the embankment material. All the twenty nodes of the coupled element have displacement degrees of freedom while only the 8 vertex nodes have excess pore pressure degrees of freedom. The 20 nodes of a non-coupled element have only displacement degrees of freedom.

### 3. Overall stability analysis

#### 3.1 Preamble

Especially due to their simplicity, limit equilibrium methods have been commonly used in practice to evaluate overall stability of embankments on soft soils. Theoretically, however, because rigid-plastic behaviour is tacitly assumed for the materials (soils and other materials – geosynthetics or soil-cement, for instance, if reinforcement is used), the use of such methods may raise some limitations, since strains before overall failure, as well as stress redistribution due to elastoplastic behaviour of the materials, are not taken into account in the analysis.

An alternative approach that overcomes such limitations is the use of finite element (FE) modelling (Rowe & Soderman, 1987; Borges, 1995; Borges & Cardoso, 2002; Hinchberger & Rowe, 2003; Chen et al., 2015; Da Silva et al., 2017). In the context of embankments on soft soils, the finite element modelling in stability studies has been mostly based on two-dimensional analysis. However, in many cases, the embankment behaviour is clearly three-dimensional, like, for instance, when PVDs, stone or soil-cement columns are installed into the soft ground. Although in a macro-level one may say that an embankment on soft soils incorporating PVDs is approximately a plane strain problem (if its longitudinal length is large), in fact it is clearly a 3D problem – both mechanical and hydraulic – in a slice of the domain between two vertical planes normal to the longitudinal direction, one containing one row of drain centres and the other equidistant from two rows of drains (Borges & Almeida, 2018). Under these conditions, the 3D finite element analysis only needs to simulate such slice of the domain, where, due to symmetry conditions, zero-displacement conditions in the longitudinal direction are set on the boundary planes normal to the longitudinal direction. Also due to symmetry conditions, water flow crossing such planes, modelled as impermeable boundaries, is not allowed.

A method for 3D overall stability analysis, which uses the results of the finite element code, is presented and applied in this paper. This method is an extension for 3D analysis from the 2D method presented by Borges & Cardoso (2002) and can be applied when the 3D domain of the finite element analysis is a slice between two vertical planes normal to the longitudinal direction of the problem (like for PVDs beneath embankments, as mentioned).

#### 3.2 Proposed method for 3D overall stability analysis

For any stage of a 3D problem whose FE domain is a slice between two vertical planes normal to the longitudinal direction ( $z$ -axis in Figure 3), using the finite element results, the stability analysis program computes the overall safety factor,  $F$ , by analysing the stability along a large number of potential slip cylindrical surfaces whose axes are parallel to  $z$ -axis and cross-sections are circular (Figure 3). The slip surfaces are chosen with criterion; their cross-sections are defined considering a mesh of circle centres and, for each centre, several concentric circles with the radius varying from a minimum to a maximum value. The smallest value of safety factor obtained defines the critical slip surface and quantifies the problem safety.

For a particular potential failure surface, the proposed method firstly determines the intersection points of the cylindrical surface with the edges of the finite elements of the 3D-mesh. Therefore, the potential failure surface is divided into small polygons (typically, a quadrilateral; Figure 4), each of them located inside of only one of the finite elements of the mesh.

Thereafter, the average values of  $\sigma'_x$ ,  $\sigma'_y$ ,  $\sigma'_z$  and  $\tau_{xy}$ ,  $\tau_{yz}$ ,  $\tau_{zx}$ , normal and shear stresses in the  $xyz$ -space (where  $z$  is the longitudinal direction), at each of those polygons, are computed extrapolating from stresses at the Gauss points of the corresponding finite element.

Considering the slip surface divided into polygons, the safety factor is computed as follows:

$$F = \frac{\sum_{i=1}^N \tau_{fi} A_i}{\sum_{i=1}^N \tau_i A_i} \quad (3)$$

where:  $\tau_i$  – projection of the acting shear stress at the  $i$ -polygon on the slip direction (i.e. normal to  $z$ -axis), determined from

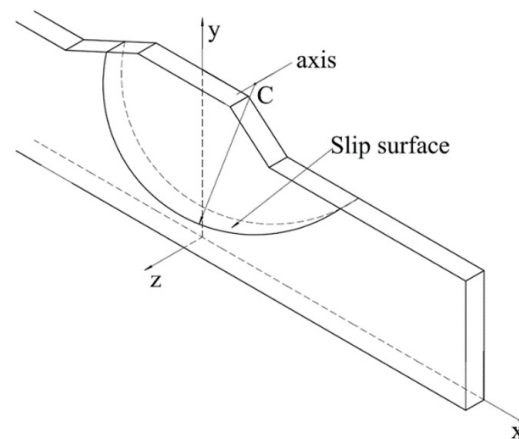
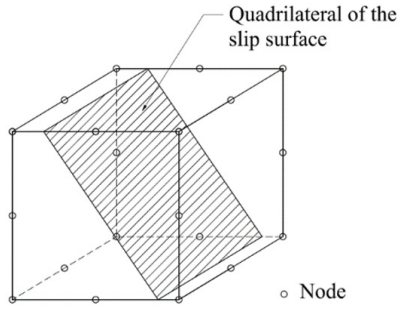


Figure 3. 3D scheme of a potential slip cylindrical surface.



**Figure 4.** Quadrilateral of the slip surface within a 20-noded brick element.

effective stresses  $\sigma'_x$ ,  $\sigma'_y$  and  $\tau_{xy}$ , known the angle that the  $i$ -polygon plane makes with  $x$ -axis (it should be noted that  $\tau_i$ , normal to  $z$ -axis, is not function of  $\sigma'_x$ ,  $\tau_{yz}$  and  $\tau_{zx}$ );  $\tau_{fi}$  – soil shear strength at  $i$ -polygon;  $A_i$  –  $i$ -polygon area;  $N$  – number of mesh elements intersected by the failure surface.

Taking into account that a critical state model is used in the finite element analysis, the soil shear strength  $\tau_{fi}$  – which varies with the consolidation – is calculated by the following equation of the critical state soil mechanics (Britto & Gunn, 1987; Borges & Santos, 2020):

$$\tau_{fi} = \frac{1}{2} M \cdot \exp\left(\frac{\Gamma - v_i}{\lambda}\right) \quad (4)$$

where  $M$  is obtained by Equation 1 and  $v_i$ , the specific volume of soil at  $i$ -polygon, is calculated as follows:

$$v_i = \Gamma - k \ln p_i - (\lambda - k) \ln \alpha_{pi} \quad (5)$$

At the  $i$ -polygon,  $\alpha_{pi}$  is the  $p$ -value of the centre of the yield surface in  $p$ - $q$  plane (Figure 1b), extrapolated from  $\alpha_p$ -values at Gauss points;  $p_i = (\sigma'_{xi} + \sigma'_{yi} + \sigma'_{zi})/3$  is the effective mean stress;  $\lambda$ ,  $k$  and  $\Gamma$  are parameters of the  $p$ - $q$ - $\theta$  model (soil properties), defined as follows:  $\lambda$ , slope of normal consolidation line and critical state line;  $k$ , slope of swelling and recompression line;  $\Gamma$ , specific volume of soil on the critical state line at mean normal effective stress equal to 1 kPa.

When the problem is symmetric and the finite element mesh does not include the entire domain, if part of the slip surface is outside the FE mesh (Figure 5), a complementary symmetric surface is considered, so that the results of such part are obtained from the complementary surface.

#### 4. Description of the problem

The problem comprises the construction of a 3.0 m-high symmetric embankment, with a 15 m-wide crest, 1/1.5 ( $V/H$ ) inclined slopes and large longitudinal length (Figure 6). The

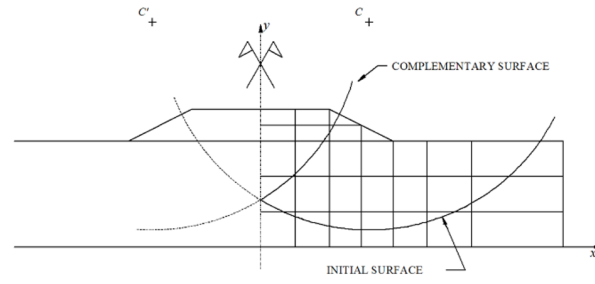


**Figure 5.** Slip surface of a symmetric problem that does not include the entire domain.

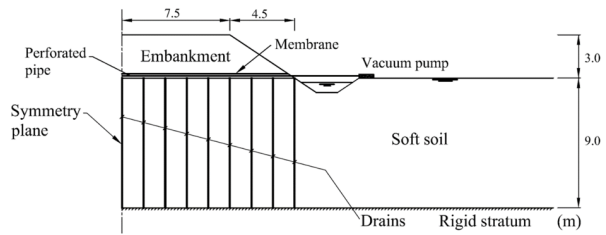


**Figure 6.** Vertical cross section of the problem.

soft ground is a 9 m-thick saturated clay lying on a rigid and impermeable stratum. The water level is at the ground surface. PVDs ( $100 \times 5 \text{ mm}^2$ ) are installed at 1.5 m spacing in a square pattern and combined with vacuum preloading. Similarly to what was installed in a case study for a storage yard at Tianjin Port, China (Rujikiatkamjorn et al., 2008), a 0.30 m sand blanket is supposed to serve as a platform for placing horizontal perforated pipes required for applying and redistributing the vacuum pressure (Figure 6). Horizontal drainage (pipes wrapped in geotextile filters) covered with impermeable membranes is laid to connect the PVDs to the vacuum pump. Parameters related to the PVDs are shown in Table 1.

Regarding the time evolution of the embankment fill and the vacuum application, five cases (C1-C5) are considered (Figure 7), so that the overall stability of the embankment is analysed, as well as the influence of the magnitude of the vacuum pressure and time of vacuum application before completion of the embankment (staged construction). The duration of the embankment construction is 11 days for cases C1 and C2 and 50 days for cases C3, C4 and C5. Vacuum pressure is not applied in cases C1 and C5 (only PVDs are used). A vacuum pressure of -60 kPa is applied in cases C2 and C3 while -90 kPa is applied in case C4. The duration of vacuum application after the end of construction – 60 days for cases C2 and C3 and 30 days for case C4 – was set so that the embankment settlement after the end of vacuum application is negligible. For case C2 – which has the same constructive sequence as case C1 – this corresponds to withdraw the vacuum application at the instant in which its

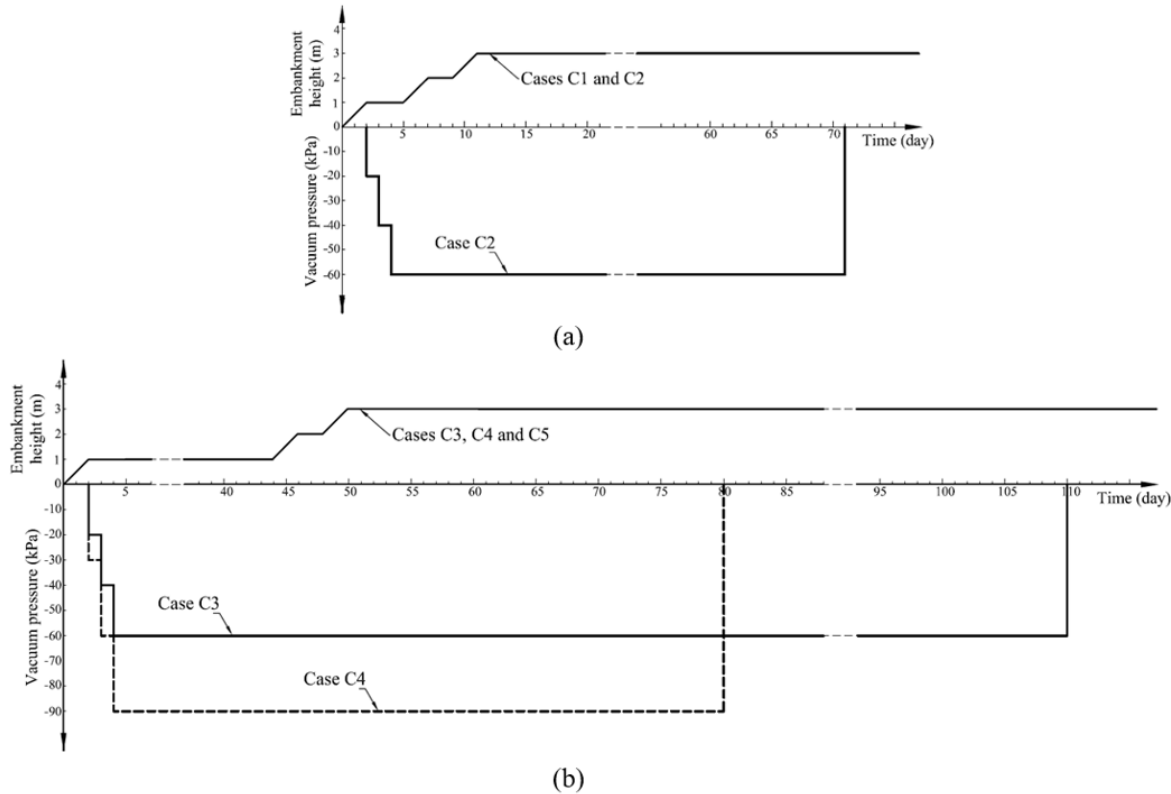


**Figure 7.** Staged construction and vacuum pressure: (a) cases C1 (without vacuum) and C2; (b) cases C3, C4 and C5 (without vacuum).

**Table 1.** Parameters related to the PVDs.

Spacing	1.5 m
Vertical length	9.0 m
Cross-section of PVD	100 × 5 mm <sup>2</sup>
Discharge capacity, $q_w$	130 m <sup>3</sup> / year (per drain)
Cross-section of mandrel	120 × 60 mm <sup>2</sup>
Cross-section of smear zone	240 × 120 mm <sup>2</sup>

settlement is approximately equal to the long-term settlement of the case without vacuum application (case C1).

Considering the variation of only one parameter, the magnitude of the vacuum pressure is the unique parameter that varies from case C1 (vacuum pressure,  $p_v = 0$ ) to case C2 ( $p_v = -60$  kPa), as well as from case C5 ( $p_v = 0$ ) to cases C3 ( $p_v = -60$  kPa) and C4 ( $p_v = -90$  kPa). Regarding the other parameter analysed, the time of vacuum application before completion of the embankment, its influence can be analysed comparing the results of cases C2 and C3.

Figure 8 shows the three-dimensional finite element mesh of the problem.

The displacement boundary conditions are defined taking into account that the soft clay lays on a rigid stratum ( $y = 0$  plane, where displacements are set as zero in the three directions,  $x$ ,  $y$  and  $z$ ). On the other hand, symmetry conditions imply: (i) zero displacement in  $x$ -direction for nodes on the  $x = 0$  plane; (ii) zero displacement in  $z$ -direction for nodes

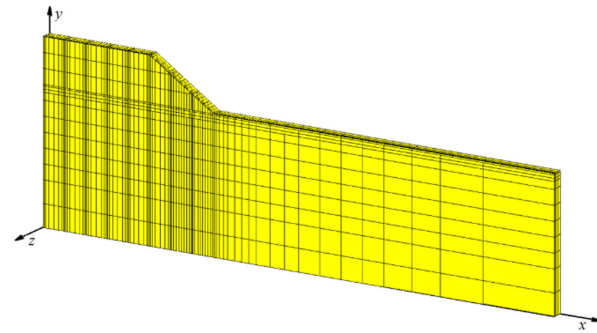


**Figure 8.** 3D finite element mesh of the problem.

on the  $z = 0.75$  m plane, vertical plane containing one row of drain centres; (iii) zero displacement in  $z$ -direction for nodes on the  $z = 0$  plane, vertical plane equidistant from two rows of drains in  $x$ -direction. Assuming that the horizontal displacement can be set as zero at nodes which are enough distant from the embankment, the plane of  $x = 36$  m is considered as the lateral boundary with zero displacement in  $x$ -direction.

In hydraulic terms, to simulate the vacuum pressure, negative values for excess pore pressure are set on the drainage surfaces defined by the drains considered as sheets, namely on the following planes:  $x = 0$ ,  $x = 1.5$ ,  $x = 3.0$ ,  $x = 4.5$ ,  $x = 6.0$ ,  $x = 7.5$ ,  $x = 9.0$ ,  $x = 10.5$  and  $x = 12$  m,



with  $y$ -coordinate ranging from 0 to 9 m and  $z$ -coordinate from 0.70 to 0.75 m (which means that centres of the drains are located on the  $z = 0.75$  m boundary plane and each drain is installed with its larger dimension, 0.10 m, in  $z$ -direction). The vacuum pressure was assumed to be constant along the entire depths of PVDs, as observed in the case study described by Rujikiatkamjorn et al. (2008). The well resistance was neglected due to the very high discharge capacity of the drain, i.e.,  $q_w > 120$  m<sup>3</sup>/year (Indraratna & Redana, 2000).

The constitutive behaviour of soils (embankment material and clay) is simulated with the  $p$ - $q$ - $\theta$  critical state model whose parameters are indicated in Table 2 ( $\lambda$ , slope of normal consolidation line and critical state line;  $k$ , slope of swelling and recompression line;  $\Gamma$ , specific volume of soil on the critical state line at mean normal effective stress equal to 1 kPa;  $N$ , specific volume of normally consolidated soil at mean normal effective stress equal to 1 kPa). Table 2 also shows other geotechnical properties:  $\gamma$ , unit weight;  $\nu'$ , Poisson's ratio for drained loading;  $\phi'$ , angle of friction defined in effective terms;  $c'$ , cohesion defined in effective terms;  $k_h$  and  $k_v$ , coefficients of permeability in horizontal and vertical directions. Table 3 indicates for the clay the variation with depth of the at-rest earth pressure coefficient,  $K_0$ , and undrained shear strength,  $c_u$  ( $\sigma'_{v0}$ , at-rest vertical effective stress), obtained from Equations 4 and 5. The clay is moderately over-consolidated to depth of 3 m and normally consolidated from 3 to 9 m. The values adopted for the clay

are similar to those used by Finno et al. (1991) regarding an excavation in soft soils constructed in Chicago, USA.

As to the smear zone, its cross-section is set as twice the area of the mandrel (Table 1), as considered by Lam et al. (2015). According to Bo et al. (2003), the ratio of horizontal permeability in the undisturbed zone and horizontal permeability in the smear zone ( $k_h/k_s$ ) can vary from 1.5 to 5 depending on the type of drain, soil properties and installation procedures. In this study  $k_h/k_s$  is set as 2.

## 5. Analysis of results

One of the limitations usually existent in the design of embankments over soft ground is the low shear strength of the soft soils, which limits the load magnitude that can be applied with adequate safety for short term stability. In order to analyse stability for cases C1-C5, Figure 9 depicts overall safety factor ( $F$ ) versus time, calculated from the 3D finite element results with the computer program for stability analysis described in Section 3.2. Figure 10 depicts the critical slip surfaces – and corresponding overall safety factors – at the end of construction and end of consolidation. Tables 4 and 5 illustrate the sums of acting and resisting forces along such critical surfaces. The parts of sums along the soft soil (foundation) and the fill (embankment) are also indicated.

These results show that, at the end of construction, the safety factor is very low for case C1 ( $F = 1.09$ ), the case with

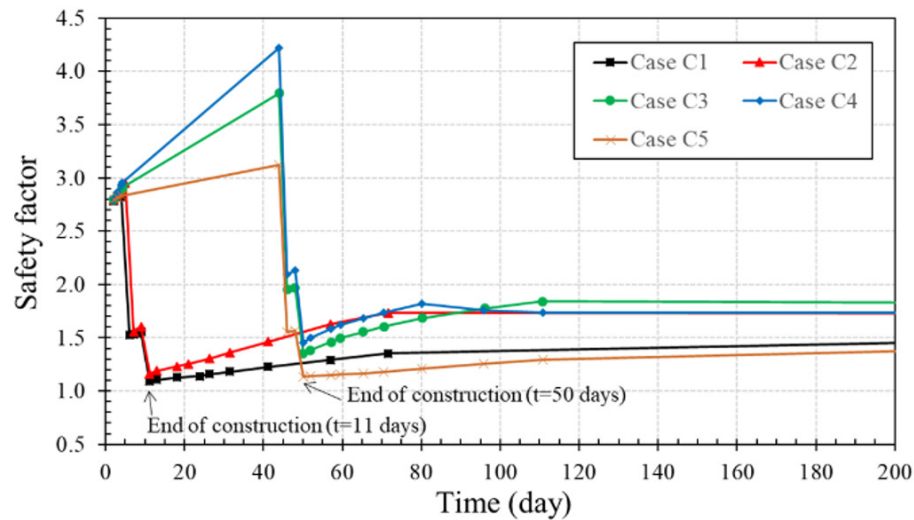
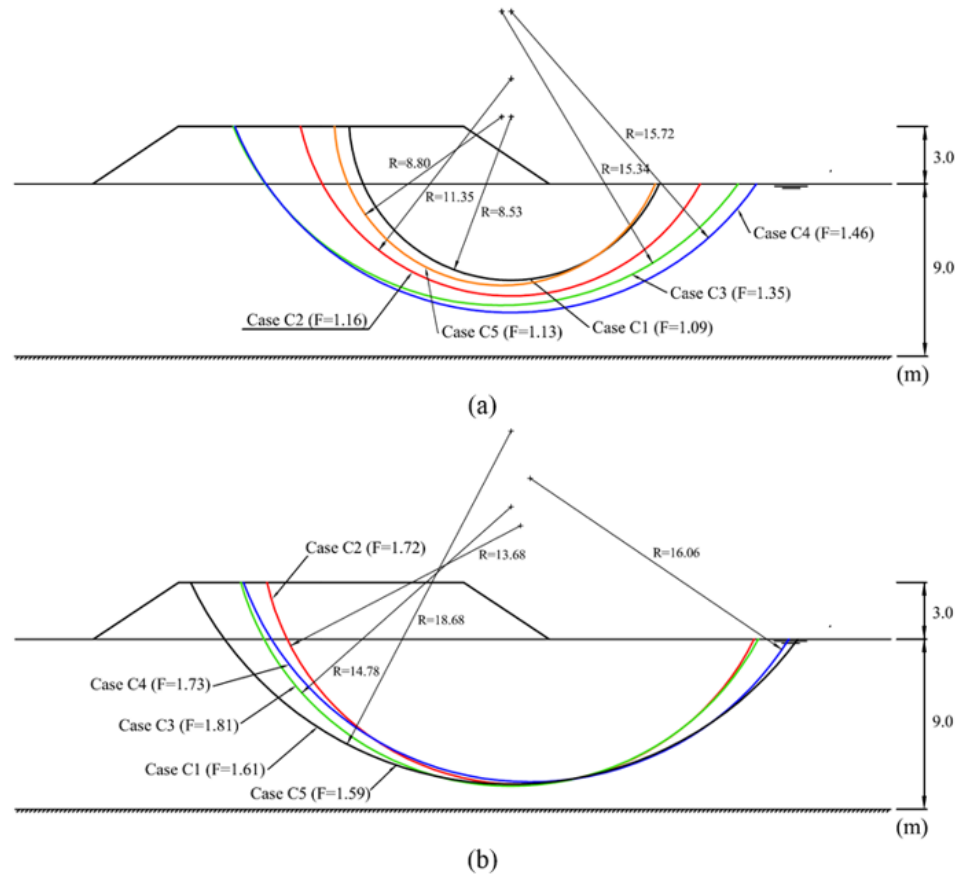


Figure 9. Overall safety factor versus time, for cases C1-C5.

Table 2. Geotechnical properties of the clay and embankment soil.

	$\gamma$ (kN/m <sup>3</sup> )	$\nu'$	$\phi'$ (°)	$c'$ (kPa)	$k_h$ (m/s)	$k_v$ (m/s)	$p$ - $q$ - $\theta$ critical state model			
							$\lambda$	$k$	$\Gamma$	$N$
Clay	16	0.25	26	0	$10^{-9}$	$10^{-9}$	0.18	0.025	3.05	3.158
Embankment	20	0.30	35	0	-	-	0.03	0.005	1.80	1.817



**Figure 10.** Critical slip surfaces for cases C1-C5: (a) end of construction; (b) end of consolidation.

**Table 3.** At rest earth pressure coefficient,  $K_0$ , and undrained shear strength,  $c_u$ , of the clay.

Depth (m)	$K_0$	$c_u$ (kPa)
0 - 3	0.9 - 0.5	13.0 - 4.9
$\geq 3$	0.5	$0.272\sigma'_{v0}$

a short time of construction (11 days) and without vacuum pressure. Although vacuum pressure is applied in case C2, its safety factor ( $F = 1.16$ ) is only slightly higher than that of case C1. This shows that the effect of vacuum preloading on the safety is not efficient enough during construction unless a higher time of construction is considered. This is corroborated comparing cases C3-C5, whose construction time includes a pause period of 42 days after 1 m of embankment height (Figure 7b). For the case without vacuum pressure (case C5), the safety factor is also low ( $F = 1.13$ ), while, for cases C3 and C4,  $F$  increases significantly, taking values of 1.35 and 1.46, respectively. This is explained by the higher gradients of excess pore pressure in cases C3 and C4, determined by the hydraulic boundary conditions on the PVDs, where excess pore pressure is set as -60 kPa and -90 kPa, respectively – while, for case C5, excess pore pressure is set as zero. The higher the gradients of excess pore pressure, the higher the

acceleration of the consolidation during the pause period and, therefore, the higher the values of  $F$ . As shown in Figure 9, in cases C3 and C4,  $F$  significantly increases during the pause period (until day 44) and diminishes during the subsequent phases of loading (embankment construction from 1 m to 2 m height – days 45 and 46 – and from 2 m to 3 m – days 49 and 50).

It should be noted that, at the beginning of the pause period of cases C3-C5, the maximum positive value of excess pore pressure is about 20 kPa (1 m of embankment height), which means that, for case C5 (without vacuum pressure, i.e. with minimum excess pore pressure equal zero), the gradients of excess pore pressure are relatively low and therefore the effect of consolidation during the pause period is lower than in cases C3 and C4 (Figure 9). This explains why the value of  $F$  at the end of construction in case C5 ( $F = 1.13$ ) is only slightly higher than in case C1 ( $F = 1.09$ ), despite its longer construction period.

The low values of  $F$  at the end of construction (3 m of embankment height) for the cases without vacuum application (slightly higher than 1, the value of overall failure) also show that the traditional technique of embankment surcharge (embankment fill with a higher height than 3 m, in this case) could not be applied in the current embankment, due to

**Table 4.** Critical slip surfaces at the end of construction for cases C1-C5: overall safety factor ( $F$ ) and sums of acting and resisting forces.

	$X_0$ (m)	$Y_0$ (m)	$R$ (m)	Sum of acting forces (kN)			Sum of resisting forces (kN)			$F$
				Total $\sum_{i=1}^N \tau_i A_i$	Foundation $\sum_{i=1}^{N1} \tau_i A_i$	Embankment $\sum_{i=1}^{N2} \tau_i A_i$	Total $\sum_{i=1}^N \tau_{fi} A_i$	Foundation $\sum_{i=1}^{N1} \tau_{fi} A_i$	Embankment $\sum_{i=1}^{N2} \tau_{fi} A_i$	
Case C1	10.0	12.5	8.53	138.67	126.91	11.76	151.06	135.20	15.86	1.09
Case C2	10.0	14.5	11.35	177.83	166.35	11.48	207.01	190.25	16.76	1.16
Case C3	9.5	18.0	15.34	230.52	220.22	10.30	311.20	294.37	16.83	1.35
Case C4	10.0	18.0	15.72	242.93	234.96	7.97	354.92	339.68	15.24	1.46
Case C5	9.5	12.5	8.80	145.39	136.04	9.35	164.36	149.17	15.19	1.13

$R$  – radius;  $(X_0, Y_0)$  – co-ordinates of centre;  $N=N_1+N_2$

**Table 5.** Critical slip surfaces at the end of consolidation for cases C1-C5: overall safety factor ( $F$ ) and sums of acting and resisting forces.

	$X_0$ (m)	$Y_0$ (m)	$R$ (m)	Sum of acting forces (kN)			Sum of resisting forces (kN)			$F$
				Total $\sum_{i=1}^N \tau_i A_i$	Foundation $\sum_{i=1}^{N1} \tau_i A_i$	Embankment $\sum_{i=1}^{N2} \tau_i A_i$	Total $\sum_{i=1}^N \tau_{fi} A_i$	Foundation $\sum_{i=1}^{N1} \tau_{fi} A_i$	Embankment $\sum_{i=1}^{N2} \tau_{fi} A_i$	
Case C1	10.0	20.0	18.68	291.62	293.38	-1.76	470.55	452.23	18.32	1.61
Case C2	10.5	15.0	13.68	259.47	256.25	3.22	446.59	425.03	21.56	1.72
Case C3	10.0	16.0	14.78	280.09	277.12	2.97	506.21	478.78	27.43	1.81
Case C4	11.0	17.5	16.06	291.66	289.88	1.78	505.18	480.43	24.75	1.73
Case C5	10.0	20.0	18.68	289.41	289.78	-0.37	460.64	441.21	19.43	1.59

$R$  – radius;  $(X_0, Y_0)$  – co-ordinates of centre;  $N=N_1+N_2$

overall instability. Surcharges of 60 and 90 kPa (equivalent to the vacuum preloads applied in cases C2-C4) correspond to additional fill heights of 3 and 4.5 m, respectively. These embankment heights, added to the 3 m high embankment, meant, therefore, that 6 m and 7.5 m high embankments needed to be constructed. As said, for these heights, with the same staged construction conditions, overall failure of the embankment would occur, contrary to what happens in the cases with vacuum application. As mentioned in section 1, this is one of the advantages of the vacuum technique when compared with the traditional technique of embankment surcharge.

After the end of construction, due to the consolidation process, the safety factor increases in all five cases (Figure 9), showing higher increase rates in the cases with vacuum preloading, which is due to the higher gradients of excess pore pressure at the end of construction due to the negative excess pore pressure on the PVDs, as explained above and shown below (Figures 11-15). At the end of consolidation,  $F$  takes higher values for the cases with vacuum application. This is explained by a certain improvement effect due to the preloading, determined by different stress paths during the construction and post-construction periods. Therefore, due to the elastoplastic behaviour of the soil, different effective stress redistributions occur which explains the differences in the results. This effect also reflects itself in lower deviatoric (distortion) strains within the soft soil at the end of consolidation

in the cases with vacuum application, which determines lower horizontal displacements under the embankment toe and lower settlements, as shown below.

After the end of vacuum application, the safety factor practically does not change for cases C2 and C3 and slightly diminishes for case C4, which means that, at the instant of the vacuum withdrawal, the consolidation is globally processed for the load of the 3 m-high embankment. This is corroborated below in the analysis of the settlements.

Figures 11-15 show the distributions of excess pore pressure at the end of construction and 1 month after the end of construction, for cases C1-C5. These figures depict results both on 3D axonometric perspectives where the vertical plane that contains one row of drain centres ( $z = 0.75$  m plane) is visible (left side figures), and on 3D perspectives where the vertical plane equidistant from two rows of drains ( $z = 0$  plane) is shown (right side figures). The scale of the colours is the same in all these figures, so that the results can be better compared. The shape of the isovalue lines clearly shows the three-dimensional condition of the problem, with drainage occurring both horizontally and vertically toward the several drainage surfaces (PVDs and upper drainage surface). At the end of construction, the highest value of excess pore pressure – which, as expected, takes place on the vertical plane equidistant from two rows of drains ( $z = 0$ ) near the  $x = 0$  symmetry plane –, occurs for case C1 (67.64 kPa) and is slightly higher than the maximum values of cases

C5 (64.63 kPa) and C2 (64.22 kPa) and significantly higher than those of cases C3 and C4 (49.29 kPa and 42.27 kPa, respectively). Therefore, similarly to the results of the stability,

these results show that, comparing with case C1 (without vacuum pressure), in case C2 the vacuum application does not significantly affect the maximum value of excess pore

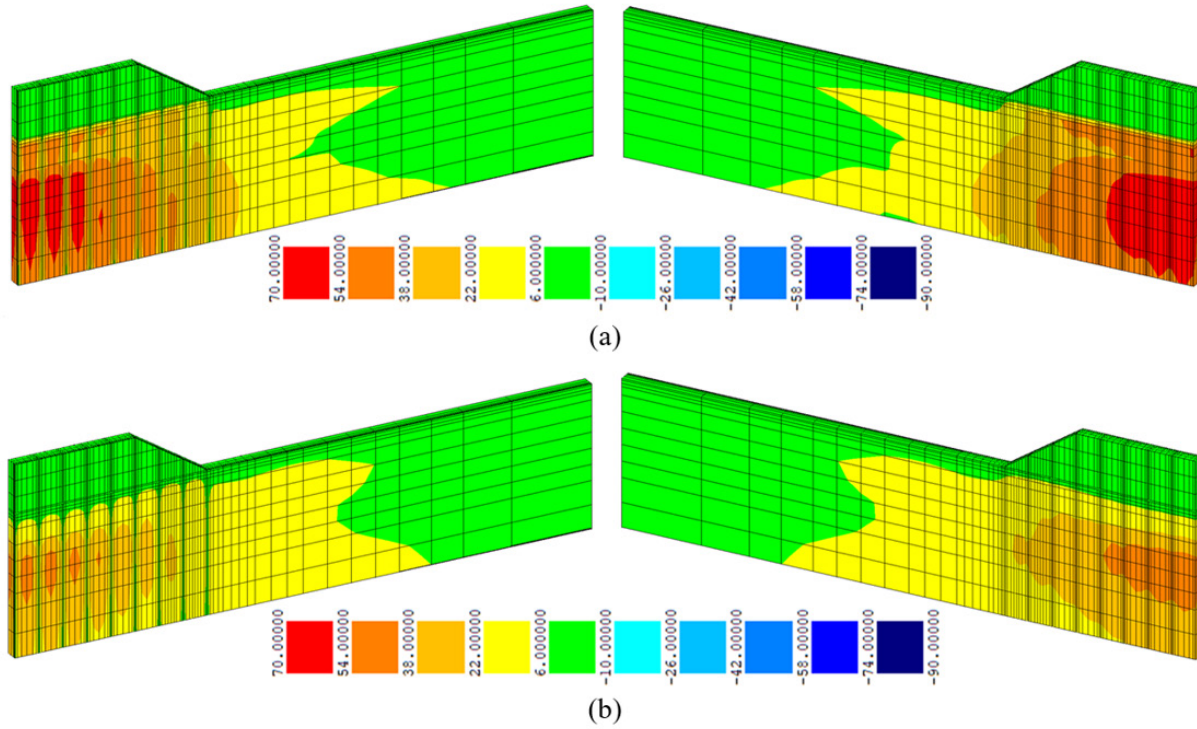


**Figure 11.** Excess pore pressure ( $u$ ) for case C1 (without vacuum pressure;  $u_{min} = 0$ ): (a) end of construction ( $t = 11$  days) ( $u_{max} = 67.64$  kPa); (b) 1 month after the end of construction ( $u_{max} = 47.72$  kPa).

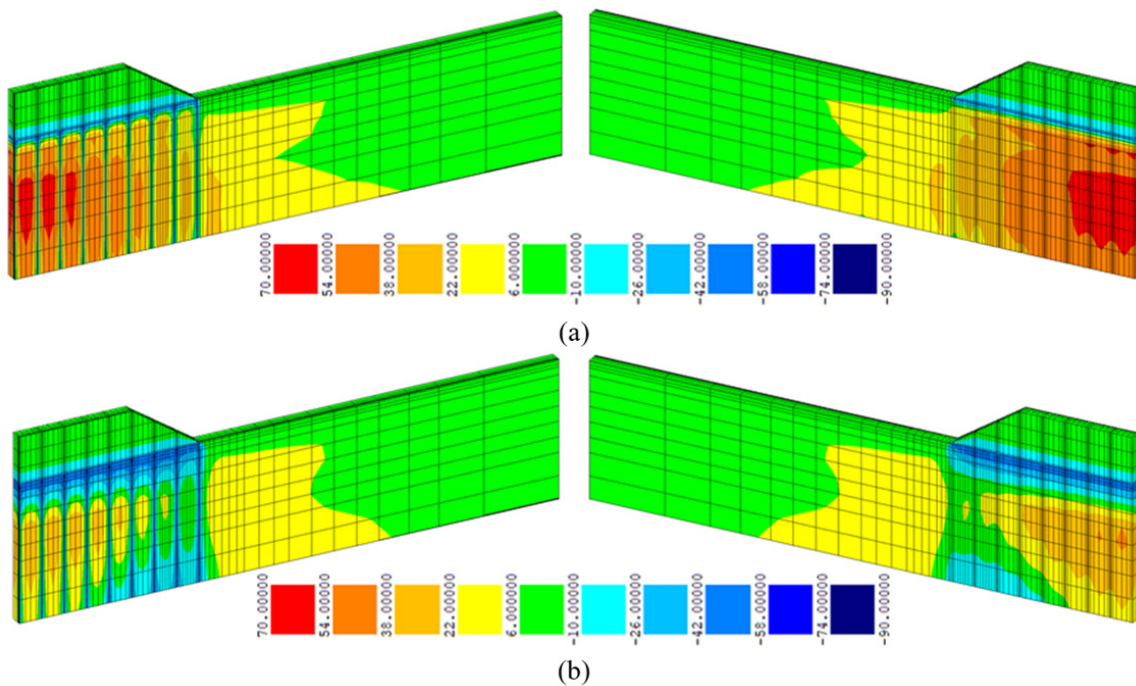


**Figure 12.** Excess pore pressure ( $u$ ) for case C2 (vacuum pressure = -60 kPa;  $u_{min} = -60$  kPa): (a) end of construction ( $t = 11$  days) ( $u_{max} = 64.22$  kPa); (b) 1 month after the end of construction ( $u_{max} = 40.47$  kPa).



pressure during the construction period (due to its short time of construction), contrarily to what happens in cases C3 and C4 compared to case C5. After the construction period, when the problem is characterized by a transient flow of water, the isovalue lines (which geometrically coincide with

the equipotential lines) have a regular shape, normal to the flow lines of water.

It should be noted that, due to the elastoplastic behaviour of the soil, there are stress redistributions – both within the embankment material and within the soft soil – which are

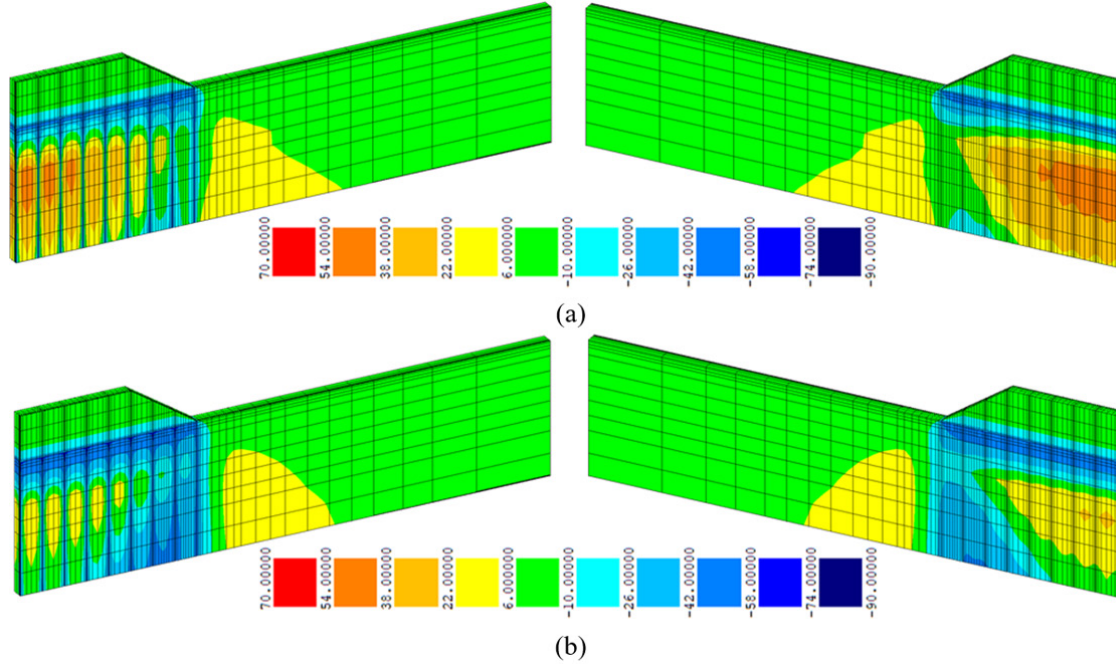


**Figure 13.** Excess pore pressure ( $u$ ) for case C3 (vacuum pressure = -60 kPa;  $u_{min} = -60$  kPa): (a) end of construction ( $t = 50$  days) ( $u_{max} = 49.29$  kPa); (b) 1 month after the end of construction ( $u_{max} = 25.31$  kPa).

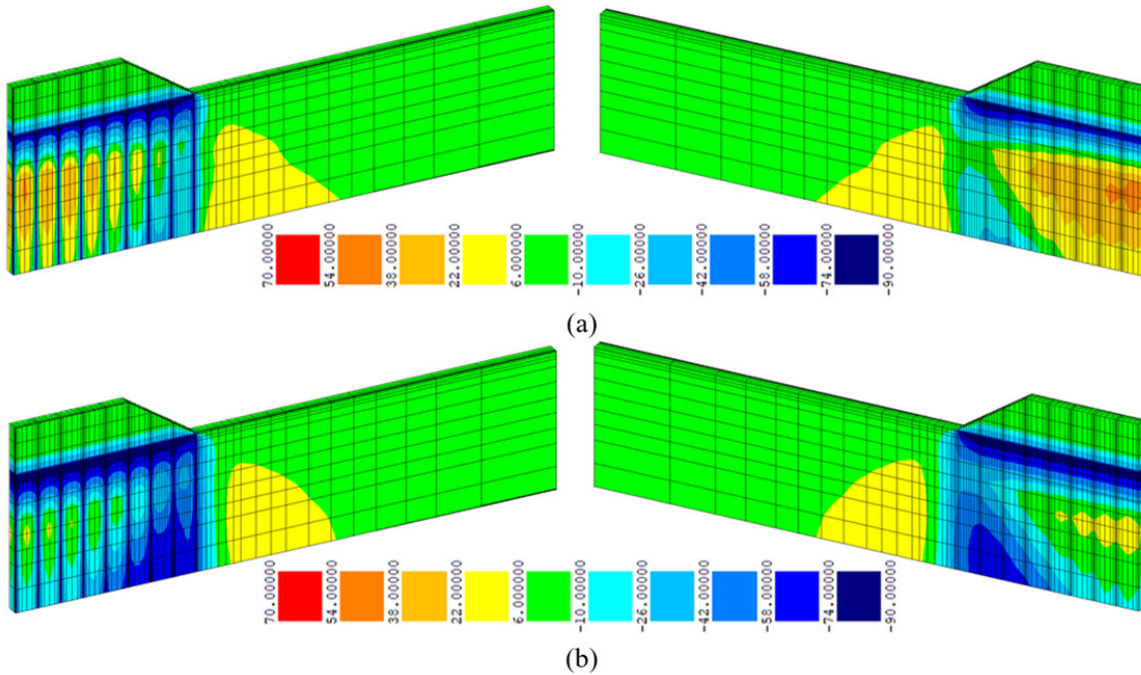


**Figure 14.** Excess pore pressure ( $u$ ) for case C4 (vacuum pressure = -90 kPa;  $u_{min} = -90$  kPa): (a) end of construction ( $t = 50$  days;  $u_{max} = 42.27$  kPa); (b) 1 month after the end of construction ( $u_{max} = 17.25$  kPa).

globally related to the unconfined behaviour of the problem (occurrence of outward horizontal displacements in the lateral areas and non-uniform settlements at the embankment base). This implies that, globally, due to such stress redistributions, the total vertical stress transferred to the foundation soil tends to increase a little at the central zone under the embankment, while it tends to diminish in the lateral zones (Borges, 1995, 2004). This is why maximum values of excess pore pressure at the end of construction, for cases C1, C2 and C5, are a little higher than 60 kPa (value of 3 m height of embankment material) in the central zone of the foundation soil (Figures 11, 12 and 15).

The following figures depict for cases C1-C5: the evolution in time of settlement at the midpoint of the embankment base

(Figure 16); vertical displacements on the soft soil surface, at the end of construction and end of consolidation (Figure 17); horizontal displacements under the embankment toe, at the end of construction and end of consolidation (Figure 18).

The results of Figure 16 show that, after the end of vacuum application, the settlement at the midpoint of the embankment base practically does not change for case C2 and slightly diminishes for cases C3 and C4. This means that, in case C2, the instant of the vacuum withdrawal approximately corresponds to the time the consolidation is globally processed for the final load of the 3-m-high embankment. In cases C3 and C4, as said, after the end of the vacuum application, the ground surface has lifted a bit, which means that, in these cases, the time needed for the consolidation of the final load

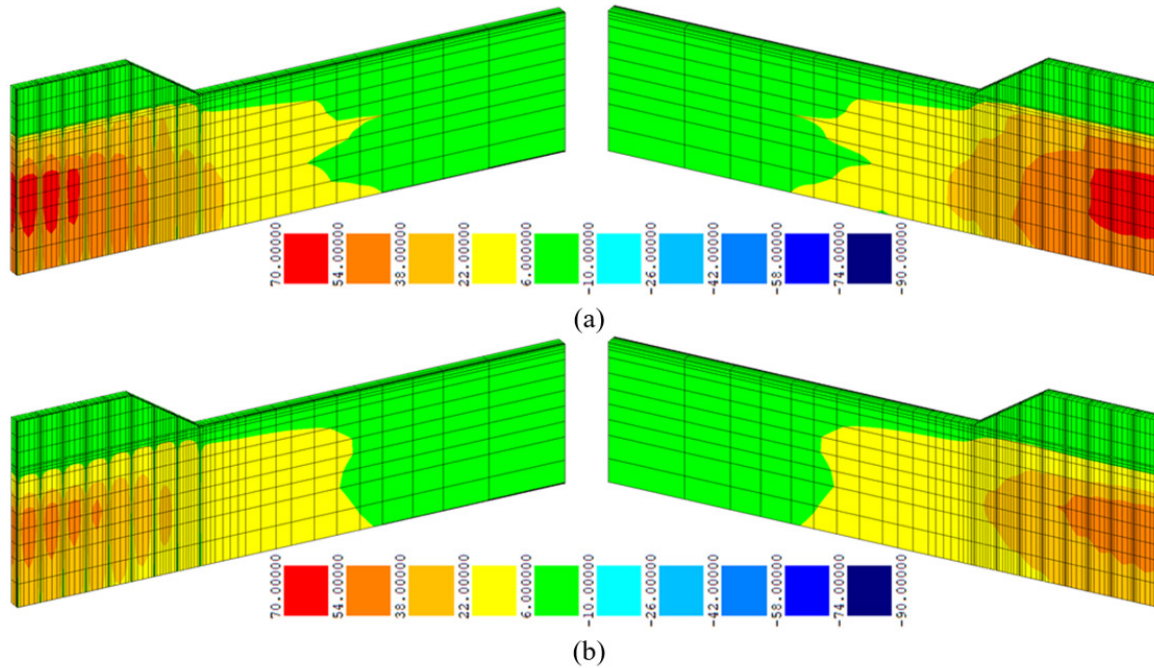


**Figure 15.** Excess pore pressure ( $u$ ) for case C5 (without vacuum pressure;  $u_{min} = 0$ ): (a) end of construction ( $t = 50$  days;  $u_{max} = 64.63$  kPa); (b) 1 month after the end of construction ( $u_{max} = 48.94$  kPa).

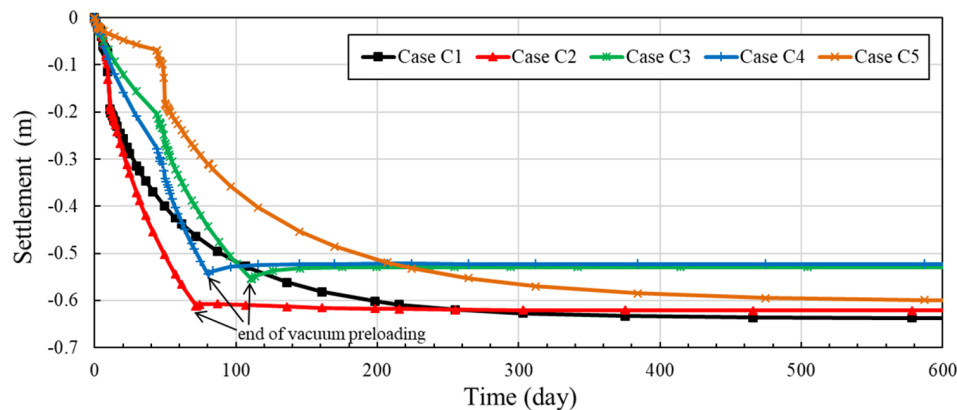


**Figure 16.** Settlement versus time at midpoint of the embankment base (co-ordinates:  $x = 0$ ;  $y = 9$  m;  $z = 0$ ).

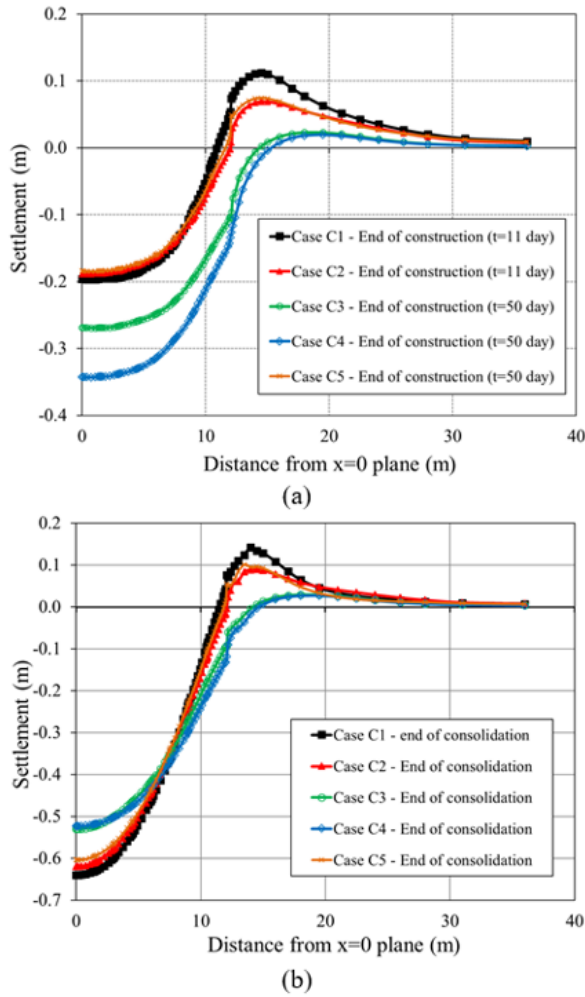


**Figure 17.** Vertical displacements on the soft soil surface ( $y = 9$  m;  $z = 0$ ): (a) end of construction; (b) end of consolidation.

of the 3 m-high embankment is a little shorter. Therefore, if the duration of vacuum application in cases C3 and C4 was a little shorter, negligible settlements could still be obtained after the end of vacuum application.

The results also show (Figures 16 and 17b) that the values of long-term settlement for cases C3 and C4 (52.9 cm and 52.2 cm, respectively) are significantly smaller than that of case C5 (60.4 cm). This reduction of long-term settlement (as well as reduction of horizontal displacements under the embankment toe, as shown below) is justified by a certain improvement effect of the soft soil – hardening effect (Borges, 2004; Borges & Almeida, 2018) – due to the vacuum application during the pause period for cases C3 and C4. Since the stress level of soft soil globally reduces during the pause period in cases C3 and C4, after that period, at the end of construction and for the post-construction period, stress levels are therefore also lower (as shown below). The lower the stress levels the lower the deviatoric (distortion)

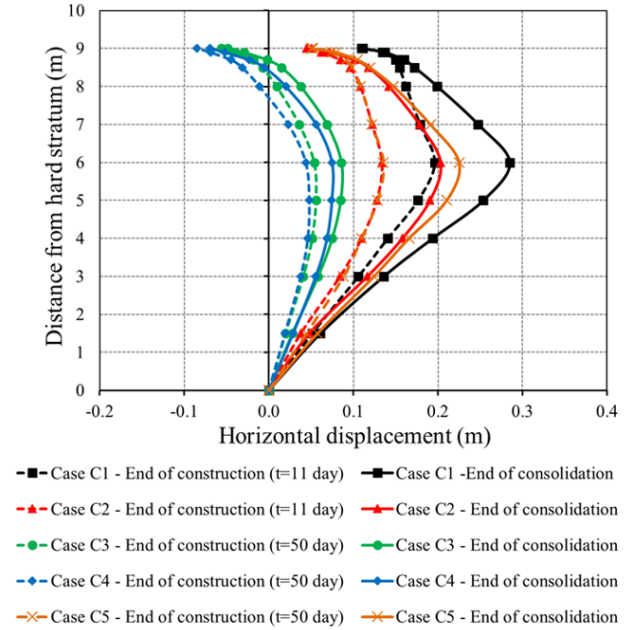


**Figure 18.** Horizontal displacements under the embankment toe ( $x = 12$  m;  $z = 0$ ).

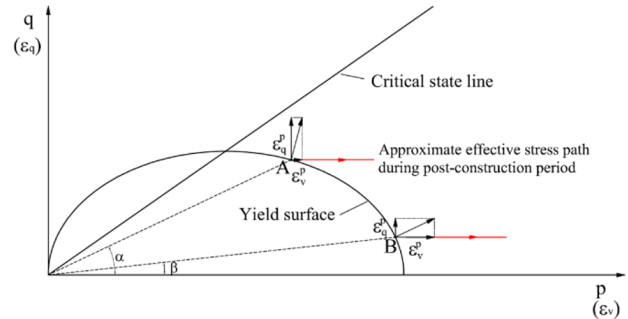


**Figure 19.** Yield and critical state surfaces of the  $p$ - $q$ - $\theta$  critical state model in the  $p$ - $q$  plane.

strains and, therefore, the smaller the settlements and the horizontal displacements at the end of consolidation.

In order to better illustrate this issue, Figure 19 shows, in  $p$ - $q$  plane, the yield and critical state surfaces of the  $p$ - $q$ - $\theta$  model (used to model the constitutive behaviour of soil);  $p$  is the effective mean stress and  $q$  the deviatoric stress. In the  $p$ - $q$  plane, the yielding function is an ellipse. Two different stress states, points A and B, are depicted in Figure 19, with different values of stress level,  $SL$  ( $SL$  is higher at point A, since the angle  $\alpha$  is higher than  $\beta$ ). Since the plastic strain vector is normal to the yield surface, plastic deviatoric strain is higher at point A than at point B; i.e. the higher the stress level the higher the deviatoric strain. Therefore, once deviatoric strain ( $\epsilon_q$ ) implies outward horizontal displacement and settlement under the embankment, this is why settlements (as well as horizontal displacements under the embankment toe, as shown below) at the end of consolidation are larger for the cases without vacuum application (cases C1



and C5) and for case C2 (without a pause period after 1 m embankment construction), than for cases C3 and C4.

Regarding the vertical displacements on the soft soil surface (Figure 17), although maximum long-term settlements are lower for cases C3 and C4 (as commented above), their settlements at the end of construction are significantly larger than those of cases C1, C2 and C5. This is explained by their higher acceleration of consolidation during the construction period, due to higher gradients of excess pore pressure, as explained above, determining therefore significant consolidation settlements during that period. This is logically in consonance with the results of the safety factor,  $F$ , analysed above.

As to the upward displacements in the lateral regions of the embankment (Figure 17) and horizontal displacements under the toe (Figure 18), they are significantly smaller for cases C3 and C4 than for cases C1, C2 and C5. As said in section 1, one advantage of the vacuum application is its induction of

gradients of pore pressure in the ground maintaining a constant total stress. This therefore determines that the volume reduction provoked by the corresponding process of consolidation is associated with downward vertical displacements and inward horizontal displacements. This effect is contrary to what happens in the loading phases where upward vertical displacements in the lateral regions and outward horizontal displacements occur, which justifies the lower values for cases C3 and C4. On the other hand, as explained above regarding Figure 19, since stress levels are lower in cases C3 and C4, lower plastic deviatoric strains and higher plastic volumetric strains also occur, which increase the mentioned reduction effect of the outward horizontal displacements in the lateral regions of the embankment, as well as of the upward displacements.

Figure 20 shows colour maps of stress level for cases C1-C5 at the end of construction and end of consolidation (the figures depict results on 3D perspectives where the vertical

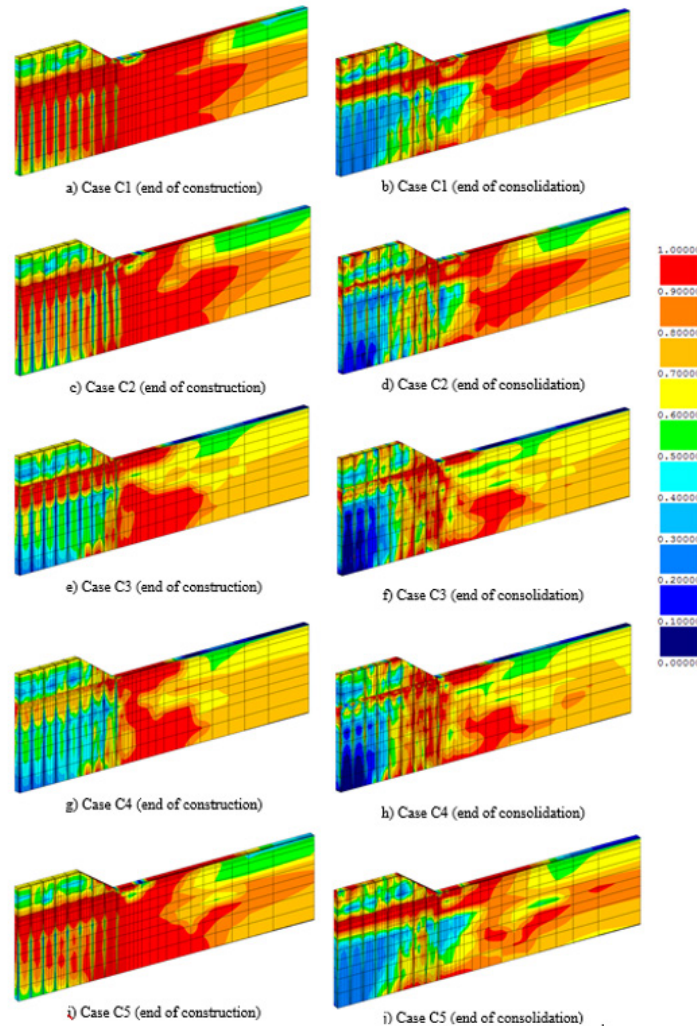


**Figure 20.** Stress level ( $SL$ ) at the end of construction and end of consolidation, for cases C1-C5: (a) case C1 (end of construction); (b) case C1 (end of consolidation); (c) case C2 (end of construction); (d) case C2 (end of consolidation); (e) case C3 (end of construction); (f) case C3 (end of consolidation); (g) case C4 (end of construction); (h) case C4 (end of consolidation); (i) case C5 (end of construction); (j) Case C5 (end of consolidation).

plane that contains one row of drain centres is visible). Stress level,  $SL$ , measures the proximity to the soil critical state and is defined as follows:

$$SL = \frac{q}{pM} \quad (6)$$

where  $p$  is the effective mean stress,  $q$  the deviatoric stress and  $M$  the parameter that defines the slope of the critical state line in the  $p$ - $q$  plane, as said above (Section 2). In normally consolidated soils,  $SL$  ranges from zero to 1, the latter being the critical state level. In over-consolidated soils, because of the peak strength behaviour, the stress level may be higher than 1.

The results of Figure 20 are logically in consonance with the results of stability analysed above. At the end of construction, the area with high values of stress level (due to the increase of deviatoric stress,  $q$ , during the loading phases) is much lower in cases C3 and C4 than in case C5 (and in cases C1 and C2). As said above, this difference is related with the consolidation effect due to the vacuum application during the construction period for cases C3 and C4, which increases the effective mean stress,  $p$ , and therefore reduces  $SL$  (see equation 6).

During the post-construction period, the effective stress path is globally characterized by an increase of the effective mean stress and a low variation of the deviatoric stress (Borges, 1995, 2004; Borges & Almeida, 2018). This implies that a generalised reduction of stress level occurs in all cases in response to the consolidation (Figure 20). However, this reduction is logically lower for cases C3 and C4, since, for these cases, part of the consolidation effect occurs during the construction period, as mentioned. Comparing all five cases, differences in the stress level maps are much less significant at the end of consolidation than at the end of construction, which, as expected, corroborates the results of safety factor,  $F$ , analysed above.

## 6. Conclusions

A computer code based on the finite element method was used to model 3D fully mechanical-hydraulic coupled analyses of an embankment on soft soils incorporating PVDs combined with vacuum preloading. A method for 3D overall stability study – which uses the numerical results obtained by the finite element code – was also proposed and applied. A parametric study was performed so that the influence of the magnitude of the vacuum preload and the staged construction of the embankment (time of vacuum application before completion of the embankment) was studied. The following conclusions can be highlighted:

- (1) At the end of construction, the safety factor was very low for the case without vacuum application and with a short time of construction (case C1). In

the case with vacuum application and the same time of construction (case C2), the safety factor was only slightly higher. This showed that the effect of vacuum preloading on the safety is not efficient enough during construction unless a higher time of construction is considered. This was corroborated comparing cases C3-C5, whose construction time included a pause period of 42 days after 1 m of embankment height. For the case without vacuum pressure (case C5), the safety factor,  $F$ , was also low, while, for cases C3 and C4,  $F$  significantly increased.

- (2) After the end of construction, the safety factor increased in all five cases, with higher increase rates for the cases with vacuum preloading (C2, C3 and C4). This is explained by the higher gradients of excess pore pressure at the end of construction in these cases, determined by the boundary conditions of excess pore pressure on the PVDs (-60 kPa for cases C2 and C3, and -90 kPa for case C4).
- (3) Long term settlements for cases C3 and C4 were significantly smaller than those of cases C1, C2 and C5. This is justified by a certain improvement effect of the soft soil, associated to lower stress levels, due to the vacuum application during the pause period.
- (4) When vacuum pressure is applied, the volume reduction provoked by the corresponding process of consolidation is associated with downward vertical displacements and inward horizontal displacements in the lateral regions of the embankment – contrarily to what happens in the loading phases. This justifies that upward displacements in the lateral regions and outward horizontal displacements under the embankment toe were significantly smaller for cases C3 and C4 than for the other cases.
- (5) At the end of construction, the area with high values of stress level was much lower in the cases with vacuum application and a longer time of construction (cases C3 and C4). This is justified by the consolidation acceleration during the pause period for these cases, determined by the hydraulic boundary conditions on the PVDs.
- (6) During the post-construction period, a generalised reduction of stress level occurred in all cases in response to the consolidation.

## Acknowledgements

This work was financially supported by: Base Funding - UIDB/04708/2020 of the CONSTRUCT - Instituto de I&D em Estruturas e Construções - funded by national funds through the FCT/MCTES (PIDDAC).

## Declaration of interest

The author has no conflicts of interest to declare.

## List of symbols

$c'$	Cohesion defined in effective terms
$c_u$	Undrained shear strength
$k_h$	Coefficient of permeability in horizontal direction
$k_v$	Coefficient of permeability in vertical direction
$p$	Effective mean stress
$p_i$	Effective mean stress at $i$ -polygon
$p_v$	Vacuum pressure
$q$	Deviatoric stress
$q_w$	Discharge capacity of the drain
$t$	Time
$u$	Excess pore pressure
$u_{max}$	Maximum excess pore pressure
$A_i$	Area of the $i$ -polygon
$F$	Overall safety factor
$K_0$	At-rest earth pressure coefficient
$M$	Parameter that defines the slope of the critical state line in the $p$ - $q$ plane
$N$	Number of mesh elements intersected by the failure surface
$N$	Specific volume of normally consolidated soil at mean normal effective stress equal to 1 kPa
$SL$	Stress level
$\alpha_p$	$p$ -value of the centre of the yield surface in $p$ - $q$ plane
$\alpha_{pi}$	$\alpha_p$ -value at $i$ -polygon
$\gamma$	Soil unit weight
$\varepsilon_q$	Deviatoric strain
$\varepsilon_v$	Volumetric strain
$\theta$	Angular stress invariant
$k$	Slope of swelling and recompression line
$\lambda$	Slope of normal consolidation line and critical state line
$v_i$	Specific volume of soil at $i$ -polygon
$\nu'$	Poisson's ratio for drained loading
$\sigma'_{v0}$	At-rest vertical effective stress
$\sigma'_x$	Normal effective stress in the $x$ -direction
$\sigma'_y$	Normal effective stress in the $y$ -direction
$\sigma'_z$	Normal effective stress in the $z$ -direction
$\tau_{fi}$	Soil shear strength at $i$ -polygon
$\tau_i$	Projection of the acting shear stress at the $i$ -polygon on the slip direction (i.e. normal to $z$ -axis)
$\tau_x, \tau_y, \tau_z$	Shear stresses in the $x$ - $y$ - $z$ space
$\phi'$	Angle of friction defined in effective terms
$\Gamma$	Specific volume of soil on the critical state line at mean normal effective stress equal to 1 kPa
FE	Finite element
PVD	Prefabricated vertical drain

## References


- Alves, A.N. (2012). *Cylindrical diaphragm walls in deep excavations in soft soils* [Unpublished MSc thesis]. University of Porto (in Portuguese).
- Azevedo, M.S. (2010). *Cylindrical excavations in soft soils retained by slurry walls* [Unpublished MSc thesis]. University of Porto (in Portuguese).
- Barros, L. (2015). *Berlin-type retaining walls combined with jet-grout or cutter soil mixing walls: Analysis by the finite element method* [Unpublished MSc thesis]. University of Porto (in Portuguese).
- Bergado, D.T., Balasubramaniam, A.S., Jonathan Fannin, R., & Holtz, R.D. (2002). Prefabricated vertical drains (PVDs) in soft Bangkok clay: a case study of the new Bangkok International Airport project. *Canadian Geotechnical Journal*, 39(2), 304-315. <http://dx.doi.org/10.1139/t01-100>.
- Bo, M.W., Chu, J., Low, B.K., & Choa, V. (2003). *Soil improvement: prefabricated vertical drain techniques*. Singapore: Thomson Learning.
- Borges, J.L. (1995). *Geosynthetic-reinforced embankments on soft soils - Analysis and design* [Unpublished PhD Thesis]. Faculty of Engineering, University of Porto (in Portuguese).
- Borges, J.L. (2004). Three-dimensional analysis of embankments on soft soils incorporating vertical drains by finite element method. *Computers and Geotechnics*, 31(8), 665-676. <http://dx.doi.org/10.1016/j.compgeo.2004.11.001>.
- Borges, J.L., & Almeida, F. (2018). Sidewalls and PVDs below embankments on soft soils – three-dimensional analysis by FEM. *Geosynthetics International*, 25(6), 630-643. <http://dx.doi.org/10.1680/jgein.18.00030>.
- Borges, J.L., & Cardoso, A.S. (2001). Structural behaviour and parametric study of reinforced embankments on soft clays. *Computers and Geotechnics*, 28(3), 209-233. [http://dx.doi.org/10.1016/S0266-352X\(00\)00021-5](http://dx.doi.org/10.1016/S0266-352X(00)00021-5).
- Borges, J.L., & Cardoso, A.S. (2002). Overall stability of geosynthetic-reinforced embankments on soft soils. *Geotextiles and Geomembranes*, 20(6), 395-421. [http://dx.doi.org/10.1016/S0266-1144\(02\)00014-6](http://dx.doi.org/10.1016/S0266-1144(02)00014-6).
- Borges, J.L., & Gonçalves, M.S. (2016). Jet-grout column-reinforced soft soils incorporating multilayer geosynthetic-reinforced platforms. *Soil and Foundation*, 56(1), 57-72. <http://dx.doi.org/10.1016/j.sandf.2016.01.005>.
- Borges, J.L., & Guerra, G.T. (2014). Cylindrical excavations in clayey soils retained by jet grout walls: numerical analysis and parametric study considering the influence of consolidation. *Computers and Geotechnics*, 55, 42-56. <http://dx.doi.org/10.1016/j.compgeo.2013.07.008>.
- Borges, J.L., & Marques, D.O. (2011). Geosynthetic-reinforced and jet grout column-supported embankments on soft soils: numerical analysis and parametric study. *Computers and Geotechnics*, 38(7), 883-896. <http://dx.doi.org/10.1016/j.compgeo.2011.06.003>.
- Borges, J.L., & Santos, R.M. (2020). Bottom reinforcement in braced excavations: coupled analysis and new method for basal-heave stability study. *Soils and Rocks*, 43(2), 199-217. <http://dx.doi.org/10.28927/SR.432199>.
- Borges, J.L., Domingues, T.S., & Cardoso, A.S. (2009). Embankments on soft soil reinforced with stone columns:

- numerical analysis and proposal of a new design method. *Geotechnical and Geological Engineering*, 27(6), 667-679. <http://dx.doi.org/10.1007/s10706-009-9266-z>.
- Britto, A.M., & Gunn, M.J. (1987). *Critical soil mechanics via finite elements*. Ellis Horwood Limited, England.
- Caramelo, T.A. (2011). *Embankments on soft soils reinforced with jet grout columns and geosynthetics* [Unpublished MSc thesis]. Faculty of Engineering, University of Porto (in Portuguese).
- Cascone, E., & Biondi, G. (2013). A case study on soil settlements induced by preloading and vertical drains. *Geotextiles and Geomembranes*, 38, 51-67. <http://dx.doi.org/10.1016/j.geotexmem.2013.05.002>.
- Chai, J., & Rondonuwu, S.G. (2015). Surcharge loading rate for minimizing lateral displacement of PVD improved deposit with vacuum pressure. *Geotextiles and Geomembranes*, 43(6), 558-566. <http://dx.doi.org/10.1016/j.geotexmem.2015.07.012>.
- Chai, J., Miura, N., Sakajo, S., & Bergado, D. (1995). Behavior of vertical drain improved subsoil under embankment loading. *Soil and Foundation*, 35(4), 49-61. [http://dx.doi.org/10.3208/sandf.35.4\\_49](http://dx.doi.org/10.3208/sandf.35.4_49).
- Chai, J.C., Carter, J.P., & Hayashi, S. (2005). Ground deformation induced by vacuum consolidation. *Journal of Geotechnical and Geoenvironmental Engineering*, 131(12), 1552-1561. [http://dx.doi.org/10.1061/\(ASCE\)1090-0241\(2005\)131:12\(1552\)](http://dx.doi.org/10.1061/(ASCE)1090-0241(2005)131:12(1552)).
- Chen, J.F., Li, L.Y., Xue, J.F., & Feng, S.Z. (2015). Failure mechanism of geosynthetic-encased stone columns in soft soils under embankment. *Geotextiles and Geomembranes*, 43(5), 424-431. <http://dx.doi.org/10.1016/j.geotexmem.2015.04.016>.
- Costa, P.A. (2005). *Braced excavations in soft clayey soils: Behavior analysis including the consolidation effects* [Unpublished MSc Thesis]. Faculty of Engineering, University of Porto (in Portuguese).
- Costa, P.A., Borges, J.L., & Fernandes, M.M. (2007). Analysis of a braced excavation in soft soils considering the consolidation effect. *Geotechnical and Geological Engineering*, 25(6), 617-629. <http://dx.doi.org/10.1007/s10706-007-9134-7>.
- Domingues, T.S. (2006). *Foundation reinforcement with stone columns in embankments on soft soils: Analysis and design* [Unpublished MSc Thesis]. Faculty of Engineering, University of Porto (in Portuguese).
- Finno, R.J., Harahap, I.S., & Sabatini, P.J. (1991). Analysis of braced excavations with coupled finite element formulations. *Computers and Geotechnics*, 12(2), 91-114. [http://dx.doi.org/10.1016/0266-352X\(91\)90001-V](http://dx.doi.org/10.1016/0266-352X(91)90001-V).
- Gonçalves, M.A. (2012). *Embankments on soft soils reinforced with jet-grout columns and multilayer geosynthetic-reinforced load transfer platforms* [Unpublished MSc Thesis]. Faculty of Engineering, University of Porto (in Portuguese).
- Guerra, G.T. (2009). *Self-supported jet-grout walls in cylindrical excavations* [Unpublished MSc Thesis]. University of Porto (in Portuguese).
- Hinchberger, S.D., & Rowe, R.K. (2003). Geosynthetic reinforced embankments on soft clay foundations: predicting reinforcement strains at failure. *Geotextiles and Geomembranes*, 21(3), 151-175. [http://dx.doi.org/10.1016/S0266-1144\(03\)00006-2](http://dx.doi.org/10.1016/S0266-1144(03)00006-2).
- Hird, C.C., Pyrah, I.C., & Russell, D. (1992). Finite element modelling of vertical drains beneath embankments on soft ground. *Geotechnique*, 42(3), 499-511. <http://dx.doi.org/10.1680/geot.1992.42.3.499>.
- Holtz, R.D., Jamiolkowski, M., Lancellotta, R., & Pedroni, S. (1991). *Prefabricated Vertical Drains: Design and Performance*. London: Heinemann-CIRIA.
- Indraratna, B., & Redana, I.W. (2000). Numerical modeling of vertical drains with smear and well resistance installed in soft clay. *Canadian Geotechnical Journal*, 37(1), 133-145. <http://dx.doi.org/10.1139/t99-115>.
- Indraratna, B., Kan, M.E., Potts, D., Rujikiatkamjorn, C.W., & Sloan, S.W. (2016). Analytical solution and numerical simulation of vacuum consolidation by vertical drains beneath circular embankments. *Computers and Geotechnics*, 80, 83-96. <http://dx.doi.org/10.1016/j.compgeo.2016.06.008>.
- Indraratna, B., Rujikiatkamjorn, C., Balasubramaniam, A.S., & McIntosh, G. (2012). Soft ground improvement via vertical drains and vacuum assisted preloading. *Geotextiles and Geomembranes*, 30, 16-23. <http://dx.doi.org/10.1016/j.geotexmem.2011.01.004>.
- Lam, L.G., Bergado, D.T., & Hino, T. (2015). PVD improvement of soft Bangkok clay with and without vacuum preloading using analytical and numerical analyses. *Geotextiles and Geomembranes*, 43, 547-557. <http://dx.doi.org/10.1016/j.geotexmem.2015.07.013>.
- Lewis, R.W., & Schrefler, B.A. (1987). *The finite element method in the deformation and consolidation of porous media*. New York: John Wiley and Sons, Inc.
- Lin, D.G., & Chang, K.T. (2009). Three-dimensional numerical modelling of soft ground improved by prefabricated vertical drains. *Geosynthetics International*, 16(5), 339-353. <http://dx.doi.org/10.1680/gein.2009.16.5.339>.
- Liu, K.-W., & Rowe, R.K. (2015). Numerical modelling of prefabricated vertical drains and surcharge on reinforced floating column-supported embankment behaviour. *Geotextiles and Geomembranes*, 43(6), 493-505. <http://dx.doi.org/10.1016/j.geotexmem.2015.05.006>.
- Long, P.V., Nguyen, L.V., Bergado, D.T., & Balasubramaniam, A.S. (2015). Performance of PVD improved soft ground using vacuum consolidation methods with and without airtight membrane. *Geotextiles and Geomembranes*, 43, 473-483. <http://dx.doi.org/10.1016/j.geotexmem.2015.05.007>.
- Marques, D.O. (2008). *Reinforcement of foundation soils with jet-grout columns and geosynthetics* [Unpublished

- MSc Thesis]. Faculty of Engineering, University of Porto (in Portuguese).
- Marques, D.O. (2021). *Embankments on soft soils reinforced with stone columns: numerical and experimental analysis* [Unpublished PhD Thesis]. Faculty of Engineering, University of Porto (in Portuguese).
- Mesri, G., & Khan, A.Q. (2012). Ground Improvement using vacuum loading together with vertical drains. *Journal of Geotechnical and Geoenvironmental Engineering*, 138(6), 680-689. [http://dx.doi.org/10.1061/\(ASCE\)GT.1943-5606.0000640](http://dx.doi.org/10.1061/(ASCE)GT.1943-5606.0000640).
- Monteiro, A.S. (2011). *Excavations in clayey soils retained by jet-grout walls reinforced with steel beams* [Unpublished MSc Thesis]. University of Porto (in Portuguese).
- Pinto, M.S. (2011). *Excavations supported by reinforced concrete walls and slab bands* [Unpublished MSc Thesis]. University of Porto (in Portuguese).
- Rowe, R.K., & Soderman, K.L. (1987). Stabilization of very soft soils using high strength geosynthetics: the role of finite element analyses. *Geotextiles and Geomembranes*, 6, 53-80. [http://dx.doi.org/10.1016/0266-1144\(87\)90057-4](http://dx.doi.org/10.1016/0266-1144(87)90057-4).
- Rujikiatkamjorn, C., Indraratna, B., & Chu, J. (2008). 2D and 3D numerical modeling of combined surcharge and vacuum preloading with vertical drains. *International Journal of Geomechanics*, 8(2), 144-156. [http://dx.doi.org/10.1061/\(ASCE\)1532-3641\(2008\)8:2\(144\)](http://dx.doi.org/10.1061/(ASCE)1532-3641(2008)8:2(144)).
- Santos, R.M. (2014). *Basal-heave stability of strutted excavations in soft soils: Safety analysis by the finite element method* [Unpublished MSc Thesis]. University of Porto (in Portuguese).
- Saowapakpi boon, J., Bergado, D.T., Youwai, S., Chai, J.C., Wanthong, P., & Voottipruex, P. (2010). Measured and predicted performance of prefabricated vertical drains (PVDs) with and without vacuum preloading. *Geotextiles and Geomembranes*, 28(1), 1-11. <http://dx.doi.org/10.1016/j.geotexmem.2009.08.002>.
- Shen, S.L., Chai, J.C., Hong, Z.S., & Cai, F.X. (2005). Analysis of field performance of embankments on soft clay deposit with and without PVD improvement. *Geotextiles and Geomembranes*, 23(6), 463-485. <http://dx.doi.org/10.1016/j.geotexmem.2005.05.002>.
- Silva, E.M., Justo, J.L., Durand, P., Justo, E., & Vazquez-Boza, M. (2017). The effect of geotextile reinforcement and prefabricated vertical drains on the stability and settlement of embankments. *Geotextiles and Geomembranes*, 45(5), 447-461. <http://dx.doi.org/10.1016/j.geotexmem.2017.07.001>.
- Zhang, Z., Ye, G., & Xing, H. (2015). Consolidation analysis of soft soil improved with short deep mixed columns and long prefabricated vertical drains (PVDs). *Geosynthetics International*, 22(5), 366-379. <http://dx.doi.org/10.1680/jgein.15.00018>.
- Zhang, Z., Ye, G., & Xu, Y. (2018). Comparative analysis on performance of vertical drain improved clay deposit under vacuum or surcharge loading. *Geotextiles and Geomembranes*, 46(2), 146-154. <http://dx.doi.org/10.1016/j.geotexmem.2017.11.002>.



## A case study of bearing capacity of piles partially embedded in rock

Marília Dantas da Silva<sup>1#</sup> , Roberto Quental Coutinho<sup>1</sup> ,

Bernadete Ragoni Danziger<sup>2</sup> 

Article

### Keywords

Bearing capacity  
Root piles  
Pile in rocks  
Dynamic tests on piles

### Abstract

In the design of piles partially embedded in rock, the main factors that influence the strength and deformability of the rock and the transmission of loads from pile to rock are of utmost relevance to pile behavior. Most empirical methods were developed based on data from specific regions. Differences in geological conditions, drilling methods and other features are not considered in most procedures. The article deals with a case of piles partially embedded in rock located in the town of São Lourenço da Mata, Pernambuco, Brazil. The rock mass consists of ancient deposits, formed mainly by granites of different compositions, gneiss and schists. The deposits have been deformed by several tectonic processes. Results from 99 dynamic loading tests enabled comparison between the mobilized lateral and pile toe resistance, with the estimated capacity obtained from the design methods known in the literature. In the prediction, the lateral shear resistance due to pile penetration in residual soil was also considered. Because failure was not reached in the dynamic tests, the estimated capacity was higher than the mobilized resistance. The resistances mobilized by the pile shaft friction in soil, by the pile shaft friction in rock and by the mobilized toe resistance in rock in the dynamic loading tests are compared to design methods known in the literature. Five static loading tests indicated failure loads greater than the mobilized resistance in the dynamic methods. The comparisons allow recommendations of the most consistent design methods to use in similar cases in practice.

## 1. Introduction

The bearing capacity of piles embedded in rock is difficult to predict. Few documented cases are available in the literature. This is the main reason for the lack of accuracy of the known design methods. Most methods present many uncertainties, leading to very conservative estimations. The lack of a more complete characterization of the rock and of an adequate number of tests are the reason for conservative design. The mobilized resistance in service conditions is usually many times lower than the available resistance.

Some authors, such as Rosenberg & Journeaux (1976), Horvath (1978) and Meigh & Wolski (1979) do not consider the toe resistance in rock when estimating the bearing capacity. Rowe & Armitage (1987) and Seidel & Collingwood (2001), consider that most of the working load is absorbed by the lateral resistance of the pile shaft in rock. Due to uncertainties regarding the proper cleaning of the base of the borehole and the concrete/rock interface behavior, toe resistance is

usually not considered in design. Toe resistance can only be considered if installation procedures ensure adequate cleaning of the bottom hole or when the load tests ensure mobilization of toe resistance (ABNT, 2019).

Empirical methods are based on data from specific regions and usually with a limited mechanical characterization of local rocks. Other aspects not considered, such as geological formations and differences in drilling methods, make empirical methods often unsuited for engineering applications. Few methods employ a rock quality index, such as the RQD, which considers rock mass discontinuities that influence shear strength (Xu et al., 2020).

This article analyzes a case study of a database consisting of 99 dynamic and 5 static tests on piles partially embedded in mainly granitic rock. The objective of the paper is to compare the mobilized resistance obtained in several dynamic loading tests and the conventional failure load in a small number of static loading tests to the capacity predicted by the design methods.

<sup>#</sup>Corresponding author. E-mail address: mariliadantas@hotmail.com

<sup>1</sup>Universidade Federal de Pernambuco, Grupo de Engenharia Geotécnica de Desastres e Planícieis, Recife, PE, Brasil.

<sup>2</sup>Universidade Estadual do Rio de Janeiro, Instituto Alberto Luiz Coimbra de Pós-graduação e Pesquisa de Engenharia, Rio de Janeiro, RJ, Brasil.

Submitted on October 2, 2021; Final Acceptance on June 3, 2022; Discussion open until November 30, 2022.

<https://doi.org/10.28927/SR.2022.075521>



This is an Open Access article distributed under the terms of the Creative Commons Attribution License, which permits unrestricted use, distribution, and reproduction in any medium, provided the original work is properly cited.

The piles consisted of cast-in-place root piles excavated through soil and drilled in rock. A driving recoverable steel casing penetrated as far as the bedrock. From this level, the boring method involved compressed air assisted down-the-hole hammer drilling.

Dynamic tests were carried out according to NBR 13208 (ABNT, 2007). Pile resistance in soil/rock interface was obtained at blows with increasing energy. A pile driving analyzer (PDA) was used for data acquisition.

The dynamic test was analyzed by CAPWAP (Case Pile Wave Analysis Program) and some tests were also analyzed using the DINEXP program, in order to better investigate the mobilized resistance. Empirical methods available for piles partially embedded in rock were applied and compared to the test results.

The static loading tests were performed with a first slow maintained loading up to 1.2 times the service load (stabilized settlement criteria) followed by complete unloading. Second short-duration load increments (quick loading) were then proceeded up to twice the service load. The static loading tests gave some insight into the ratio conventional failure (extrapolated) bearing capacity to dynamic mobilized resistance.

The article discusses the main results and offers design suggestions.

## 2. Capacity estimation of piles partially embedded in rock

The load applied to the pile top is reduced along the shaft by the shear resistance on pile soil and pile rock contact surface. For heavy loads, part of the load is also transferred to the pile tip and the shear mobilized along the shaft may reach its residual value in part or throughout the whole length. Differences in this behavior are mainly due to rock features in the rock mass along the pile shaft. A proper rock characterization is then essential for ultimate capacity evaluation.

Lateral resistance results from the adhesion produced by the pile concrete at the hole's lateral interface, followed by shear at the pile-rock interface when initial adhesion is lost. Tip loading results from direct contact and transmission of the load from the pile to the rock (Goodman, 1989). Considering the three components of resistance (shear at pile soil interface, shear at pile rock contact and toe resistance), the toe resistance is commonly disregarded in piles embedded in rock due to the uncertainties regarding the clearance of the bottom hole (ABNT, 2019). Because pile displacement to reach peak lateral resistance in rock is much smaller than in soil, the lateral soil resistance is also disregarded in several methods. In the present article soil resistance was estimated by semi-empirical formulations used in Brazil (Aoki & Velloso, 1975; Décourt & Quaresma, 1978; Cabral, 1986).

The skin friction is usually estimated as a function of sleeve friction measured during the CPT tests. If CPT

tests are not available, the use of correlations established between the cone tip resistance with  $N_{60}$  from SPT can be used instead (Aoki & Velloso, 1975). Some other methods estimate pile soil lateral resistance directly from the  $N_{60}$  from SPT, according to Décourt & Quaresma (1978). Correction factors are necessary to consider installation procedures and scale effects. Aoki & Velloso (1975) consider the lateral soil resistance ( $Q_{l,s}$ ) given by Equation 1:

$$Q_{l,s} = U \sum \tau_{l,s} \Delta L \quad (1)$$

$U$  is the perimeter of the pile shaft,  $\tau_{l,s}$  is the shear soil resistance,  $\Delta L$  is the pile penetration in the soil layer.

Aoki & Velloso (1975) estimates soil resistance at the pile shaft using Equation 2:

$$\tau_{l,s} = \frac{\alpha k N_L}{F_2} \quad (2)$$

$k$  and  $\alpha$  are CPT x SPT correlation values depending on soil type,  $N_L$  is the average  $N_{60}$  value for a given soil layer with a  $\Delta L$  penetration and  $F_2$  is a factor expressing the installation and scale effects.

Décourt & Quaresma (1978) method, modified by Décourt (1996), suggests shear resistance using Equation 3:

$$\tau_{l,s} = (3.33\bar{N} + 10) \beta' \quad (kPa) \quad (3)$$

$\bar{N}$  is the average  $N_{60}$  value for the whole shaft penetration in soil, and  $\beta'$  is a coefficient given by Décourt (1996).

Cabral (1986) estimates the lateral resistance by Equation 4:

$$\tau_{l,s} = \beta_0 \beta_1 N_L \quad (kPa) \quad (4)$$

$\beta_0$ ,  $\beta_1$  are coefficients given by Cabral (1986) and  $N_L$  is the average  $N_{60}$  value for a given layer.

For the load capacity of piles embedded in rock, most authors correlate the lateral shear resistance ( $\tau_{l,r}$ ) and/or unit tip resistance ( $q_{p,r}$ ) with the uniaxial compressive strength of the intact rock ( $q_u$ ), given in Equation 5 and Equation 6.

$$\tau_{l,r} = \alpha q_u^\beta \quad (MPa) \quad (5)$$

$$q_{p,r} = N q_u^\rho \quad (MPa) \quad (6)$$

$\alpha$  and  $N$  are factors related to the quality of the rock mass and  $\beta$  and  $\rho$  are empirical parameters, Table 1.

The methods from AASHTO (1996), Cabral & Antunes (2000), España (2011) and Xu et al. (2020) proposed further considerations to estimate the bearing capacity of piles partially embedded in rock.

AASHTO (1996) does not consider the resistance contribution in soil. Toe resistance is considered only when the estimated settlement is greater than 1 cm. The total lateral and the toe resistance in rock are given by Equation 7 and Equation 8:

**Table 1.** Empirical coefficients for shear resistance in rock mass.

Reference	Shaft friction (MPa)
Rosenberg & Journeaux (1976)	$\tau_{max} = 0.36(q_u)^{0.52}$
Horvath (1978)	$\tau_{max} = 0.21(q_u)^{0.5}$
Meigh & Wolski (1979)	$\tau_{max} = 0.22(q_u)^{0.6}$
Poulos & Davis (1980)	$\tau_{max} = 0.05 f_{cj}$ or $\tau_{max} = 0.05 q_u$
Rowe & Armitage (1987)	$\tau_{max} = 0.45(q_u)^{0.5}$ or $\tau_{max} = 0.6(q_u)^{0.5}$
Zhang & Einstein (1998)	$\tau_{max} = 0.80(q_u)^{0.5}$ or $\tau_{max} = 0.40(q_u)^{0.5}$

$f_{cj}$  is the uniaxial compressive strength of the concrete at de age of j days in MPa.

$$Q_{l,r} = \pi \phi_r L_r (0.144 \tau_{l,r}) \quad (7)$$

$$Q_{p,r} = N_{ms} q_u A_t \quad (8)$$

$\phi_r$  is the pile diameter in rock and  $L_r$  the pile length in rock,  $\tau_{l,r}$  is the shear resistance in rock,  $N_{ms}$  depends on rock type and quality,  $q_u$  is the uniaxial compressive strength of the intact rock and  $A_t$  is pile toe section.

The method by Cabral & Antunes (2000) considers the lateral friction contribution in soil. However, it is necessary that the soil provides adequate resistance and an elastic displacement greater than  $\delta_0$ , given in Equation 9.

$$\delta_0 = 2mm + 0.2\% \phi_s \quad (9)$$

$\phi_s$  is the pile diameter in soil.

The resistance at pile tip and the lateral shear of the pile embedded in rock are estimated by Equation 10 and Equation 11.

$$q_{p,r} = n \cdot q_u \leq 0.4 f_{ck} \quad (10)$$

$$\tau_{l,r} = 2.5 \text{ to } 3.5\% q_{p,r} < f_{ck} / 15 \quad (11)$$

$n$  is a correction factor that considers the rock alteration degree and the presence of small fractures in rock mass, as in Table 2 ( $f_{ck}$  is the concrete characteristic compressive strength).

The method proposed by España (2011) should not be applied to highly fractured rock ( $q_u < 1$  MPa) presenting an RQD <10% or to a highly weathered rock. For the tip resistance, España (2011) proposes an adaptation of the allowable stress of a shallow foundation in the same rock, increased by a factor of two.

España (2011) highlights that the allowable stress in shallow foundations depends on  $q_u$ , type of rock, degree of alteration and discontinuities spacing. The allowable stress is given by Equation 12.

**Table 2.**  $n$  values, Cabral & Antunes (2000).

Rock alteration degree	Variation Interval	Mean value
Highly weathered	0.07 - 0.13	0.1
Weathered	0.24 - 0.36	0.3
Moderately weathered to sound	0.48 - 0.60	0.54

$$P_{v,adm} = p_0 \alpha_1 \alpha_2 \alpha_3 \sqrt{\frac{q_u}{p_0}} \text{ (MPa)} \quad (12)$$

where  $\alpha_1$ ,  $\alpha_2$ ,  $\alpha_3$  are parameters depending on rock type, alteration degree and discontinuities spacing and  $p_0$  is the reference stress of 1 MPa. These parameters should represent the rock mass at a depth of  $1.5 \phi_r$  below toe.

The dimensionless parameters are estimated as follows:

The parameter  $\alpha_1$  can be determined in the laboratory, from specimens tested in traction, Equation 13:

$$\alpha_1 = \sqrt{\frac{10 \sigma_t}{q_u}} \quad (13)$$

$\sigma_t$  is the rock tensile strength.

In case of no available tests, España (2011) recommends the values in Table 3.

In cases of a different rock at pile toe or doubts about classification,  $\alpha_1$  shall be 0.4.

For  $\alpha_2$ , the worst condition of the rock alteration degree found to a depth of  $1.5 \phi_r$  from the tip must be considered. Values are shown in Table 4.

Regarding the influence of the discontinuity spacing ( $\alpha_3$ ), distinction between two forms of characterization must be identified: from the observation of the discontinuities emerging on an outcrop and from the RQD value.

For this analysis, the reference zone shall be the rock volume located below the foundation to a depth of  $1.5 \phi_r$  and  $\alpha_3$  determined as the minimum value from the following relationships (Equation 14 and Equation 15):

$$\alpha_{3a} = \sqrt{\frac{S}{1m}} \quad (14)$$

$$\alpha_{3b} = \sqrt{\frac{RQD \%}{100}} \quad (15)$$

$S$  is the discontinuity spacings.

The toe resistance  $q_{p,r}$  obtained from the allowable  $P_{v,adm}$  is given by Equation 16.

$$q_{p,r} = 2 P_{v,adm} \text{ (MPa)} \quad (16)$$

If the embedded length ( $L_r$ ) is significant and the rock mass has the same quality as that occurring under the tip, España (2011) proposes the application of an embedded factor to the tip resistance through Equation 17:

**Table 3.** Value of  $\alpha_1$ , España (2011).

Group	Designation	$\alpha_1$
1	Rock with well-developed structure	1
2	Igneous and metamorphic rocks*	0.8
3	Sedimentary** and some metamorphic rocks	0.64
4	Poorly consolidated rocks	0.4

(\*) Except rocks indicated in groups 1 and 3; (\*\*) Except rocks indicated in groups 1 and 4.

**Table 4.** Value of  $\alpha_2$ , España (2011).

Alteration degree	Designation	$\alpha_2$
I	Sound rock	1
II	Slightly weathered rock	0.7
III	Moderately weathered rock	0.5

$$d_f = 1 + 0.4 \frac{L_r}{\phi_r} \leq 2 \quad (17)$$

For the determination of shear strength in rock ( $\tau_{l,r}$ ), España (2011) suggests 10% of the tip resistance, Equation 18:

$$\tau_{l,r} = 0.1 q_{p,r} \text{ (MPa)} \quad (18)$$

Xu et al. (2020) recommend Equation 19 and Equation 20 to predict shear resistance in rock, in MPa.

$$\tau_{l,r} = 0.532 (\sigma_{cm3})^{0.425} \quad (19)$$

$$\sigma_{cm3} = q_u \cdot 10^{0.013 RQD - 1.34} \quad (20)$$

### 3. Back-analyses of the dynamic test

The force and velocity signals obtained in dynamic loading tests are usually analyzed with CAPWAP program, described by Goble et al. (1980). CAPWAP gives the resistance mobilized by the foundation soil in the instrumented blow.

The signals from CAPWAP were reprocessed with DINEXP, a similar program developed by Costa (1988). While CAPWAP is a commercial program, DINEXP routines are known in detail, Danziger (1991). This aspect enables a full understanding of signal matching by using DINEXP. As the uniqueness of CAPWAP results is questioned by some authors, the use of the two programs reduces possible uncertainties about the results (Danziger et al., 1996).

Costa (1988) applied the FEM in the formulation of DINEXP. The soil is represented by nonlinear springs with elastic-perfect plastic behavior, with dynamic resistance simulated by viscous elements (dash pots) with resistance directly proportional to particle velocity. The program was first conceived for application with the Smith (1960) model, alternative models known as Smith modified by Goble (1986) or Simons & Randolph (1985) can be adopted

instead. The time integration of the differential equilibrium equation system is made by the explicit central difference algorithm. The program includes a graphical routine that allows visualization of all calculated variables during the analysis for each node, particularly helpful to back-analysis purposes.

## 4. Case study

The case in study consists of the foundations of a football stadium covering an area of 130,000 m<sup>2</sup>. The stadium's "ring" structure occupies an extensive area. Significant variations in the stratigraphic profile are found. The soil and rock mass present layers of variable thicknesses associated with the geological-geotechnical model layout. The columns have service loads ranging from 1000 kN to 9000 kN, spanning 8-12 m. In part of the stadium the top of the rock mass is covered by alluvium, colluvium and/or residual soil. In other parts, there are rock outcrops.

### 4.1 Site characterization

The foundation consists of ancient deposits, mainly formed by granites of different compositions, gneiss and schists, intensely deformed by several superimposed tectonic processes.

The foundation is laid on metaigneous rocks with a predominantly monzogranitic composition. It comprises deformed granite presenting subvertical foliation, slightly micaceous, with predominance of quartz and feldspar. The rock alteration results in layers of silty sand and sandy silt, with low clay content. Figure 1a illustrates the overview of the site area and Fig. 1b its division in sectors. The location of the rotary drilling borings is shown in the sectors with pile foundations in rock.

The subsoil investigation was carried out by percussion borings and rotary drilling (SPT/SM). Seismic profiles were made to characterize the bedrock and to estimate the mechanical properties of the foundation.

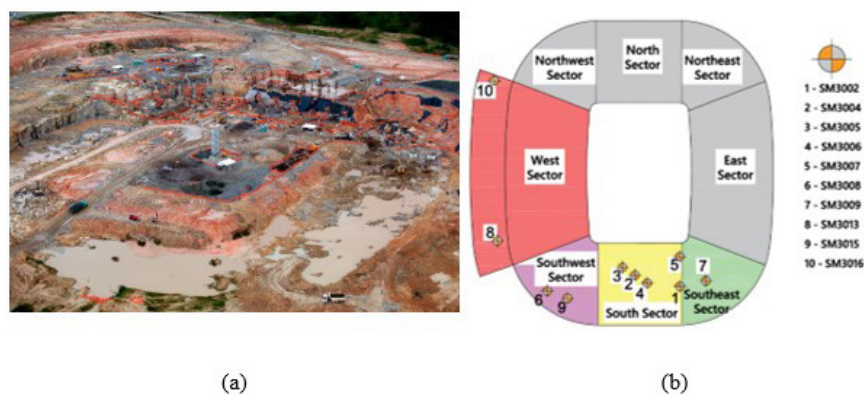
A complementary geophysical campaign was carried out. Rotary drillings identified the bedrock ranging from 0 to 12.7 m depth. In the first meters, the rock mass revealed poor quality, low recovery, highly weathered and intensively fractured.

Figure 2 shows a typical subsurface profile and rock section.

The complexity of the stratigraphy was verified with an alteration of the rock mass starting in the fractures, resulting in lateral contacts between soil and rock and the occurrence of numerous boulders in the soil mass.

With the samples taken from the rock, laboratory tests were carried out to obtain the index properties (absorption, porosity, natural and saturated specific weight) and mechanical properties (uniaxial compressive strength of the intact rock).





**Figure 1.** (a) site view; (b) area subdivided in different sectors.

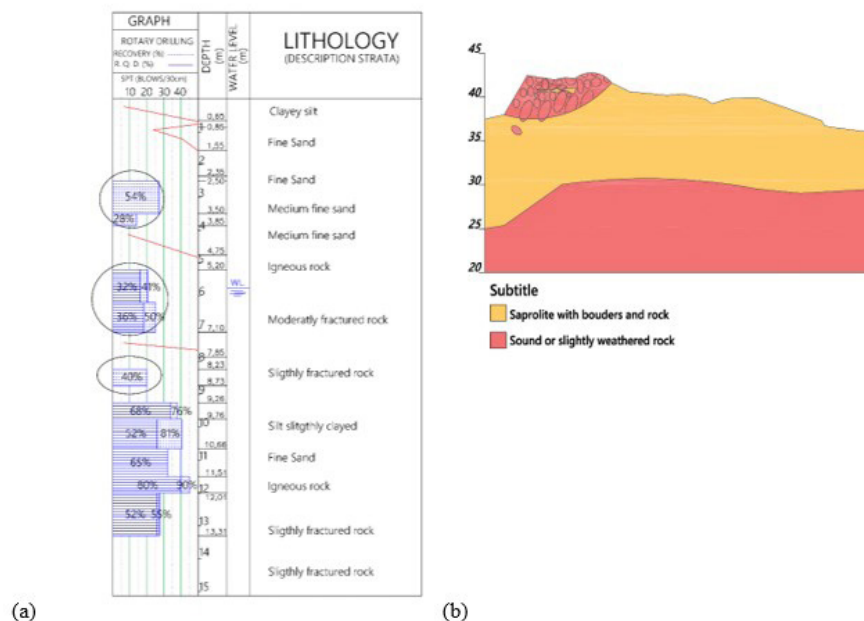


**Figure 2.** (a) percussion boring and rotary drilling; (b) typical section- Southeast Sector.

The strong presence of boulders makes the investigation analyses much more difficult.

Some samples obtained from rotary drilling underwent petrographic analysis and uniaxial compressive strength tests that varied over a wide range [12.27-121.39 MPa], indicating the need to observe other features of the rock mass. This range is investigated later for the different sectors. The observed behavior did not indicate mechanical parameters improving with depth.

Figure 3 illustrates the rocky features in the Southeast Sector, with major weathering and variable aspect, intense heterogeneity and highly fractured, with the presence of boulders and a very irregular surface.

Figure 4 illustrates the bedrock features in the South Sector. They are sub-vertical, of tectonic origin, with the occurrence of a sub-horizontal system, relief joints, forming a



**Figure 3.** Aspect of slope of Southeast Sector.

preferential percolation path, resulting in a very heterogeneous weathered profile. These features result in a spheroidal alteration system with boulders and a very fractured rock.

In the Southwest Sector the rock is composed of deformed granite, very foliated, with an irregular surface. The contact of soil and weathered rock is very heterogeneous and abrupt. The rock surface is very fractured, with the presence of saprolite and boulders.

An alluvial cover in the West Sector is overlaid by an existing landfill.

The geological structures are presented in the form of fractures and fractured zones, from which the alteration in the rock mass advances. A geological fault in an approximate ENE-WSW (east northeast, west southwest) direction was observed.



**Figure 4.** South Sector with occurrence of boulders on its surface, zones of weathered and fractured rock.

## 4.2 Foundation characteristics and testing results

Two foundation solutions were adopted, depending on bedrock depth. Shallow foundations on rock were designed for bedrock to a depth of 5 m or less, and root piles for deeper depths. Figure 5a shows a general scheme of root piles embedded in rock and Figure 5b shows the foundation at shallow depths.

The estimated pile length was 4 m to 5 m in sound rock. The actual embedment length increased where unfavorable geological features occur due to severe weathering, revealed by rotary drilling or during pile installation.

A total of 99 dynamic load tests were analyzed by the CAPWAP program. Better quality signals were also selected and analyzed by DINEXP program. Table 5 summarizes the main pile design information and Table 6 includes the data obtained during ground investigation and installation of the tested piles, including the wide range of  $q_u$  values and statistical distributions for the different sectors.

Table 6 shows that the Southeast, Southwest and South Sectors showed a certain uniformity in the distribution of  $q_u$  of the intact rock, the  $RQD$  and pile length penetration in rock. In the West Sector, in addition to the lower average value of  $q_u$ , its variability also significantly exceeded the other sectors. However, pile penetration in rock presented the smallest mean value contrary to what might be expected. The lower penetration in rock was probably due to the higher  $RQD$  compared to the other sectors. This is an indication of the importance of geological features, other than  $q_u$  of the rock samples.

The recommendations from NBR 6122 (ABNT, 2019) were followed during piling installation. During the dynamic load test according to NBR 13208 (ABNT, 2007) the piles were subjected to twice the working load. In cases of imminent

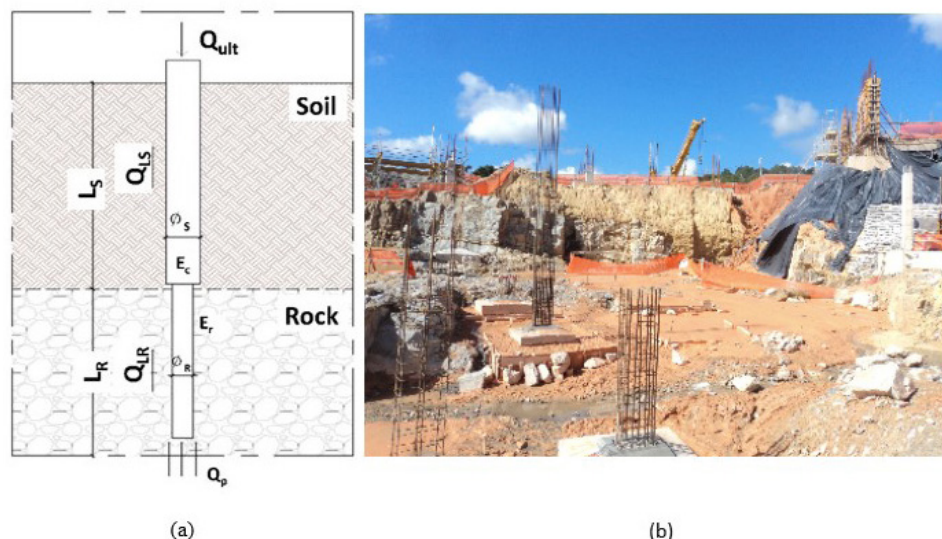


**Figure 5.** (a) general scheme of root piles embedded in rock; (b) foundation at shallow depths.



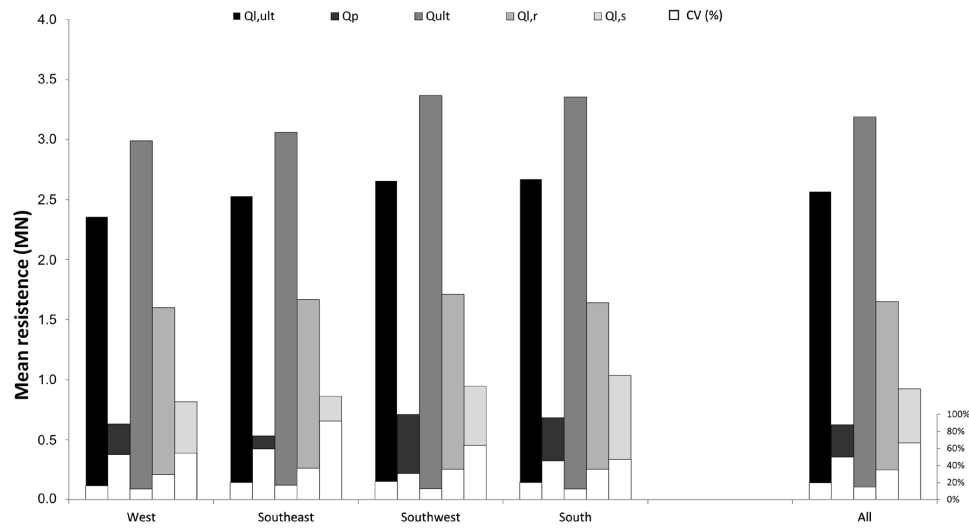


**Figure 6.** CAPWAP mobilized resistance (mean value) and its distribution in soil and rock.

**Table 5.** Characteristic of the root piles drilled in rock.

$\phi_s$ (mm)	$\phi_r$ (mm)	$L_s$ (m)	$L_r$ (m)	Design Load (kN)
	310	1 to 12.2	3 to 8	1.100

**Table 6.** Statistical distribution of  $q_u$ ,  $RQD$ , pile length in soil and in rock.

Sector	Statistical Distribution	$q_u$ (MPa)	$RQD$ (%)	$L_s$ (m)	$L_r$ (m)
West	Mean	58.4	67%	5.4	4.7
	SD	38.4	25%	1.7	0.7
	CV	66%	38%	32%	15%
Southeast	Mean	97.5	42%	4.1	6.9
	SD	28.0	1.4%	1.9	1.3
	CV	29%	- *	46%	19%
Southwest	Mean	99.6	51%	4.6	5.3
	SD	24.2	14%	2.6	0.5
	CV	25%	28%	56%	9%
South	Mean	90.8	48%	8.3	5.5
	SD	19.3	19%	2.3	1
	CV	21%	39%	28%	18%

(\*) For the Southeast Sector only two samples were available, and the coefficient of variation could not be estimated. SD is the standard deviation and CV is the coefficient of variation.

structural damage or when unsatisfactory conditions were observed, loading was interrupted to ensure safety. The test results provided the maximum mobilized load for the blow of higher energy. The behavior of the tested piles was satisfactory. No failure or condition of significant settlements for the service load was reached.

According to Reese & O'Neill (1999), the toe resistance is mobilized for pile displacement of around 5% of the pile diameter in rock. Only 14 out of 99 tested piles had

displacements (DMX) of 8 mm-12 mm, which corresponds to between 2.5% and 3.9% of the pile diameter embedded in rock. Only 20% of the total mobilized capacity was resisted by the pile toe. The West Sector, with a broader variability, displayed greater displacements during the tests. Figure 6 presents the statistical distribution of CAPWAP results for the 99 piles.

The mobilized lateral shear observed in rock was tentatively compared to  $q_u$ . Unfortunately, a simple relationship between the mobilized lateral shear and  $q_u$ , or  $RQD$ , was not reached in the case in study, contrary to Juvêncio et al. (2017) findings.

Juvêncio et al. (2017) presented an interpretation of dynamic tests on cast-in-place piles in gneissic rock in Rio de Janeiro. The authors obtained a relationship between  $q_u$  and the  $RQD$ . Values of mobilized lateral shear in dynamic tests of piles partially embedded in gneissic rock were compared to the  $q_u$  values derived from the  $RQD$  correlation. An expression of prediction of mobilized shear resistance was proposed by Juvêncio et al. (2017) for pile design in gneissic rock in Equation 21. Juvêncio et al. (2017) emphasized that since failure was not reached in the dynamic tests, the use of Equation 21 is a conservative approach.

$$\tau_{l,r} = \alpha (5 + 0.6RQD)^\beta \tau_{l,r} \text{ in MPa, } RQD \text{ in \%} \quad (21)$$

Juvêncio et al. (2017) suggested the values of 0.2 and 0.3 for the empirical adjustment parameters  $\alpha$  and  $\beta$ , very close to Horvath (1978). They also found that in the Rio de Janeiro gneiss, which is only slightly fractured,  $RQD$  has a direct relationship with weathering.

In fact, the results of the statistical distribution of  $q_u$  and  $RQD$  in Table 6 did not indicate a direct relation, especially in the West Sector. The rock mass in the present case is formed mainly by granites of different compositions, gneiss and schists, with marked weathering and intense fragmentation.

Those were probably the reason for the difficulty to establish a correlation in the present case. Dynamic test interpretation in terms of total mobilized resistance was the alternative in the following sections.

The lowest mobilized total resistance in Figure 6 was found in the West Sector, with the lower mean and most variable  $q_u$ . All sectors presented the same approximate percentage (nearly 20%) of load mobilization at the pile toe. The largest contribution of the mobilized capacity was the 50% lateral resistance in rock. However, the lateral resistance mobilized in soil of nearly 28% should not be disregarded. A significant value of lateral resistance in soil occurred also in Sectors West and Southwest, with a pile length in soil comparable to that in rock.

In relation to the coefficient of variation, the lowest values were observed for the total mobilized resistance,  $Q_{ult}$ . A wide dispersion was found for the tip resistance  $Q_p$ . Regarding lateral resistance, it is found that, although the main contribution is due to rock, its variability was much smaller than that in soil. Lateral mobilized resistance in soil ( $Q_{l,s}$ ) presented a mean coefficient of variation of 67%, due to the high variability in soil profile. For the lateral resistance in the rock ( $Q_{l,r}$ ) the coefficient of variation was much lower, close to 35%. Experience shows that the variability of tip resistance in soil mass is reasonably higher than that occurring in the shaft. The same was observed in the present analyses in the mobilized resistance in rock.

Another set of analyses were carried out with DINEXP program. The distribution of lateral resistances in rock and in soil and the corresponding statistical distribution were obtained and compared to CAPWAP analyses. Figure 7 shows the statistical results.

Unlike CAPWAP results, the Southeast Sector presented the lowest total mobilized resistance in DINEXP analyses. As the CAPWAP program was applied to 99 tests and DINEXP to 46, the difference in the mean value, close to 7%, is of no significance, especially when the uniqueness of CAPWAP results is taken into account (e.g. Danziger et al., (1996)).

The statistical distribution of mobilized resistances obtained by CAPWAP in a group of 99 tested piles is very close to the DINEXP in a group of 46 piles. The smallest coefficients of variation of DINEXP analyses were also found in the total mobilized resistance,  $Q_{ult}$  in Figure 7. A high dispersion range was found in the mobilized toe resistance,  $Q_p$ , with a coefficient of variation of 62%, much higher than that of the CAPWAP, but consistent with the experience with static and dynamic tests. The lateral resistance transferred to the soil ( $Q_{l,s}$ ) in the analyses with DINEXP also indicated low uniformity, with a coefficient of variation of 50%. For the lateral resistance mobilized in rock ( $Q_{l,r}$ ) the coefficient of variation was much lower, 33%, very similar to CAPWAP results.

Both programs indicated that lateral capacity in soil should not be disregarded.

Juvêncio et al. (2017) also observed a significant contribution of the residual soil overlying the rock in the lateral capacity of the 30 dynamic tests of partially embedded piles in a granitic rock with a gradual weathered degree of alteration.

The measured and estimated force and/or velocity at the pile top indicated a very good match with the application of both CAPWAP and DINEXP program. The results confirmed the literature indications: lateral capacity is the main contribution of resistance mobilization of piles partially embedded in

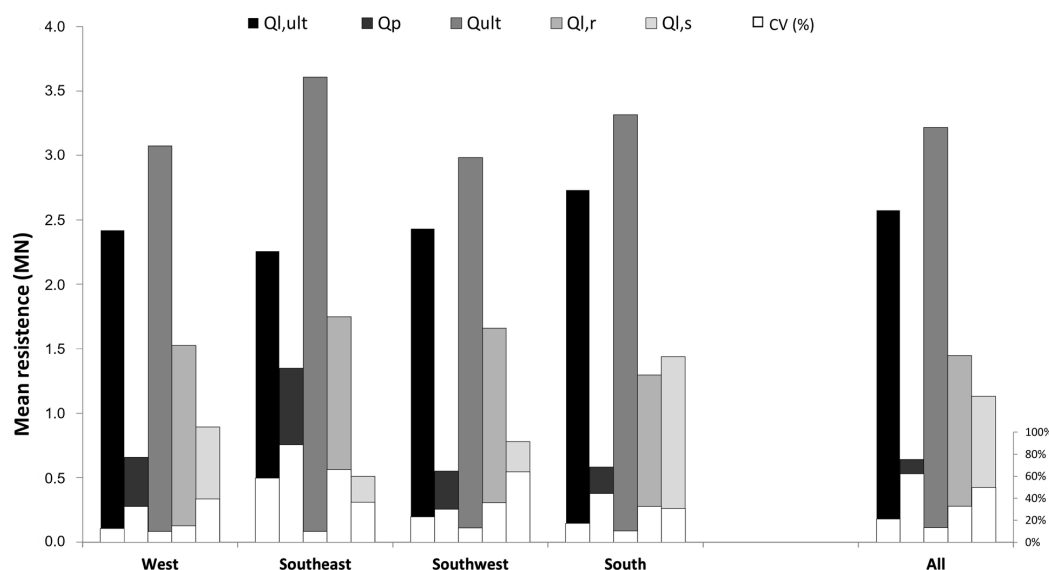


Figure 7. Mobilized mean resistance by DINEXP analysis and its distribution in soil and rock for 46 tested piles.

rock, reaching nearly 80% in the present case analyzed by CAPWAP and by DINEXP. The percentage of mobilization at the pile toe remained close to 20% for both programs. The contribution of each component of total resistance was 20%, 52% and 28% for mobilized tip resistance in rock, lateral resistance in rock and lateral resistance in soil for CAPWAP analyses and 20%, 45% and 35% for DINEXP.

Despite being disregarded in the literature, a significant contribution of lateral resistance in soil was found not only in this case in Recife but also in the database interpreted by Juvêncio et al. (2017) in Rio de Janeiro. The soil contribution, although smaller compared to lateral capacity in rock, reveals room for optimization in the design of deep foundations in root piles in rocks.

#### 4.3 Bearing capacity estimation

The methods summarized in Section 2 were applied to the 99 tested piles. Some limitations of the methods are summarized below.

For Rosenberg & Journeaux (1976), the  $q_u$  was limited to  $5 \leq q_u / P_{atm} \leq 340$  and  $P_{atm} = 0.1 \text{ MPa}$ . As the  $q_u$  results exceeded this range, the upper limit  $q_u = 34 \text{ MPa}$  was applied in the estimations. For the methods of Horvath (1978), Meigh & Wolski (1979) and Zhang & Einstein (1998), the lateral capacity is related to the smallest value between  $q_u / P_{atm}$  and  $f_{ck} / P_{atm}$ . Once the  $q_u$  was higher than the characteristic compressive strength of the pile concrete,  $q_u > f_{ck}$ , the characteristic strength of the concrete was used.

The correlation by Rowe & Armitage (1987) was established for  $q_u \leq 30 \text{ MPa}$ , thus the upper limit of 30 MPa was used for all piles.

For the AASHTO (1996) method, lateral resistance is given by the smallest value between  $q_u / P_{atm}$  and  $f_{ck} / P_{atm}$ , but here a reduction factor based on the  $RQD$  is used. For Cabral & Antunes (2000) and Poulos & Davis (1980) methods, the  $q_u$  defined in each sector for each pile was maintained. The method proposed by España (2011) uses coefficients related

to the rock type, degree of weathering of the rock mass and discontinuity spacings to determine the allowable stress ( $P_{v,adm}$ ).

In the application of the Xu et al. (2020) method, the  $q_u$  of the intact rock was used, associated to the  $RQD$  and the influence of the discontinuity of the rock mass.

The load capacity of the tested piles was estimated by the selected methods and compared to the mobilized resistance obtained by the DINEXP program.

The comparison between the estimated and the mobilized capacity from the dynamic load testing was established for the lateral resistance in soil, lateral resistance in rock, toe resistance in rock and total capacity.

The estimation of lateral capacity in soil ( $Q_{l,s}$ ) was predicted and compared to the mobilized capacity in Table 7 in terms of its statistical distribution and in Figure 8 for each of the 46 tested piles analyzed by DINEXP program.

Figure 8 indicates the ratio estimated to mobilized lateral capacity in soil between 2.7 and 5.5, revealing much higher estimated capacities than the mobilized ones. Similar results were found by Juvêncio et al. (2017).

The estimation of lateral capacity in rock ( $Q_{l,r}$ ) was predicted by Rosenberg & Journeaux (1976), Horvath (1978), Meigh & Wolski (1979), Poulos & Davis (1980), Rowe & Armitage (1987), Cabral & Antunes (2000), AASHTO (1996), Zhang & Einstein (1998), España (2011) and Xu et al. (2020). The estimated and mobilized capacities in rock are presented in Table 8 and in Figure 9 the values are indicated for each of the 46 tested piles analyzed by the DINEXP program.

Similar results were found by Juvêncio et al. (2017) who justified that failure values were not reached in the dynamic tests due mainly to the limited delivered energy. Another reason that contributed to the low mobilized values compared to predicted failure values is that the design methods were conceived for sedimentary rocks, with failure values more easily reached in load testing (Juvêncio et al., 2017).

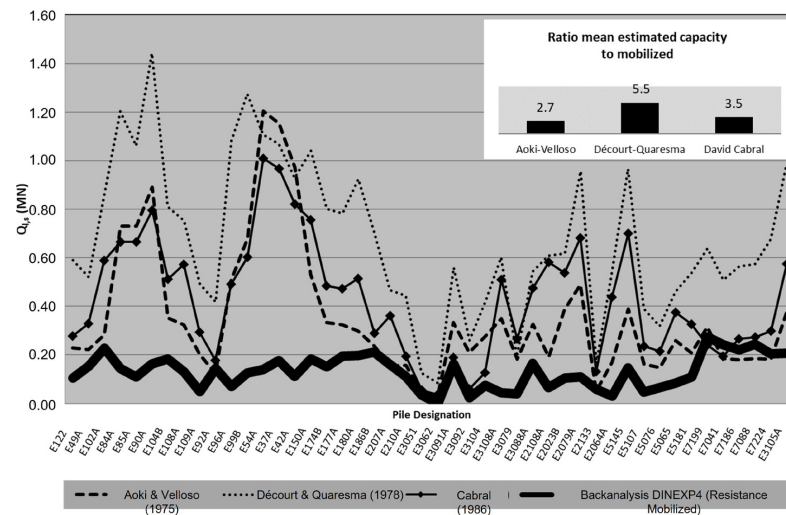
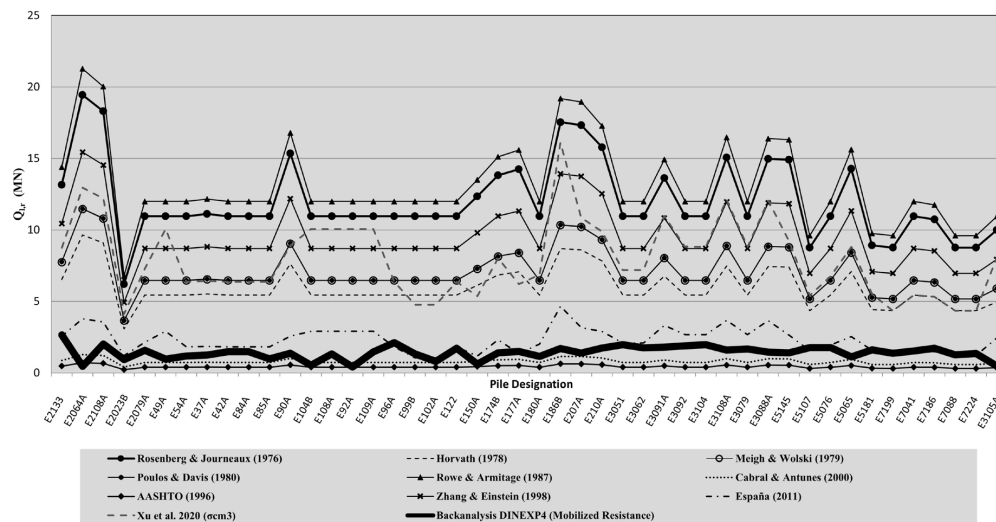
The toe capacity in rock ( $Q_p$ ) was predicted by Poulos & Davis (1980), Rowe & Armitage (1984), Cabral & Antunes

**Table 7.** Statistical distribution of mobilized and estimated lateral capacity of soil,  $Q_{l,s}$  (kN).

Statistical Distribution	Sector	Aoki & Velloso (1975)	Décourt (1996)	Cabral (1986)	Mobilized Resistance
Mean	West	221.2	492.8	312.3	163.4
SD		76.8	177.6	146.8	83.6
CV		35%	36%	47%	51%
Mean	Southeast	137.2	439.7	383.7	51
SD		75.8	240.5	230.1	18.6
CV		55%	55%	60%	36%
Mean	Southwest	236.7	478.5	254.9	83.3
SD		129.8	285.9	213.2	74.5
CV		55%	60%	84%	89%
Mean	South	479.9	921.4	610.6	143.8
SD		318.3	360	408.2	44.1
CV		66%	39%	67%	31%

**Table 8.** Statistical distribution of mobilized and estimated lateral resistance of pile in rock,  $Q_{l,r}$  (kN).

Statistical Distribution	Sector	Rosenberg & Journeaux (1976)	Horvath (1978)	Meigh & Wolski (1979)	Poulos & Davis (1980)	Rowe & Armitage (1987)	AASHTO (1996)	Zhang & Einstein (1998)	Cabral & Antunes (2000)	España (2011)	Xu et al. (2020)	Mobilized Capacity
Mean	West	10586.00	5254.3	6238.8	6250.4	11583.3	387.5	8406.9	702.4	1697.9	5955.2	1497.0
SD		2322.7	1152.8	1368.8	1371.4	2541.5	85	1844.5	154.1	523.7	1773.8	225.2
CV		22%	22%	22%	22%	22%	22%	22%	22%	31%	30%	15%
Mean	Southeast	16970.9	8423.4	10001.7	10020.4	18569.7	621.3	13477.4	1126.0	3309.4	11303.6	1713.5
SD		3352.8	1664.2	1976.0	1979.7	3668.7	122.7	2662.7	222.5	653.8	2233.2	1130.2
CV		20%	20%	20%	20%	20%	20%	20%	20%	20%	20%	66%
Mean	Southwest	12054.5	5983.20	7104.3	7117.5	13190.2	441.3	9573.1	799.8	2815.4	9337.2	1626.0
SD		1945.4	965.6	1146.5	1148.7	2128.7	71.2	1544.9	129.1	606.8	1920.7	458.9
CV		16%	16%	16%	16%	16%	16%	16%	16%	22%	21%	28%
Mean	South	12007.3	5959.8	7076.4	7089.7	13138.6	439.6	9535.6	796.7	2210.3	7841.3	1270.2
SD		2498.20	1240.0	1472.3	1475.0	2733.5	91.5	1983.9	165.7	845.2	2677.0	412.4
CV		21%	21%	21%	21%	21%	21%	21%	21%	38%	34%	32%


**Figure 8.** Estimated and mobilized lateral capacity in soil for each pile.

**Figure 9.** Estimated lateral capacity and mobilized capacity in rock.

(2000), AASHTO (1996) and España (2011). The estimated and mobilized toe capacity are presented in Table 9 and in Figure 10 for each tested pile analyzed by DINEXP program.

The estimated and the mobilized total capacity ( $Q_{ti}$ ) are presented in Table 10 and in Figure 11 for the 46 tested piles analyzed by the DINEXP program. Only the lateral resistance in rock ( $Q_{l,r}$ ) and the toe resistance in rock ( $Q_p$ ) were considered in the estimations. Results from the loading tests included the whole mobilized capacity in rock and the lateral resistance in soil ( $Q_{l,s}$ ).

Four out of ten methods applied do not consider the toe resistance contribution: Rosenberg & Journeaux (1976), Horvath (1978), Meigh & Wolski (1979) and Xu et al. (2020). Even with this conservative approach, the application of all

these design methods resulted in estimated capacity much greater than the mobilized resistance obtained in the tests.

Figure 11 shows the great variations found. It seems clear that the methods of Rosenberg & Journeaux (1976), Rowe & Armitage (1987) and Zhang & Einstein (1998) presented very high estimates of total bearing capacity compared to the other methods. The application of the methods from España (2011), Cabral & Antunes (2000) and AASHTO (1996) resulted in estimates with closer agreement to the mobilized load in the tests.

#### 4.4 Static load testing

The static load testing did not characterize the soil failure. Some extrapolation methods were adopted to obtain

**Table 9.** Statistical distribution of mobilized and estimated toe resistance in rock,  $Q_p$  (kN).

Statistical Distribution	Sector	Poulos & Davis (1980)	Rowe & Armitage (1987)	AASHTO (1996)	Zhang & Einstein (1998)	Cabral & Antunes (2000)	España (2011)	Mobilized Resistance
Mean	West	603.5	2263.2	72.5	1012.1	322.1	539	643.8
SD		-	-	-	-	-	69.3	209.8
CV		-	-	-	-	-	13%	33%
Mean	Southeast	603.5	2263.2	72.5	1012.1	322.1	662.7	1323.2
SD		-	-	-	-	-	-	1174.2
CV		-	-	-	-	-	-	89%
Mean	Southwest	603.5	2263.2	72.5	1012.1	322.1	790.1	537.7
SD		-	-	-	-	-	79.2	314.3
CV		-	-	-	-	-	10%	58%
Mean	South	603.5	2263.2	72.5	1012.1	322.1	626.4	570.5
SD		-	-	-	-	-	205.6	241.9
CV		-	-	-	-	-	33%	42%

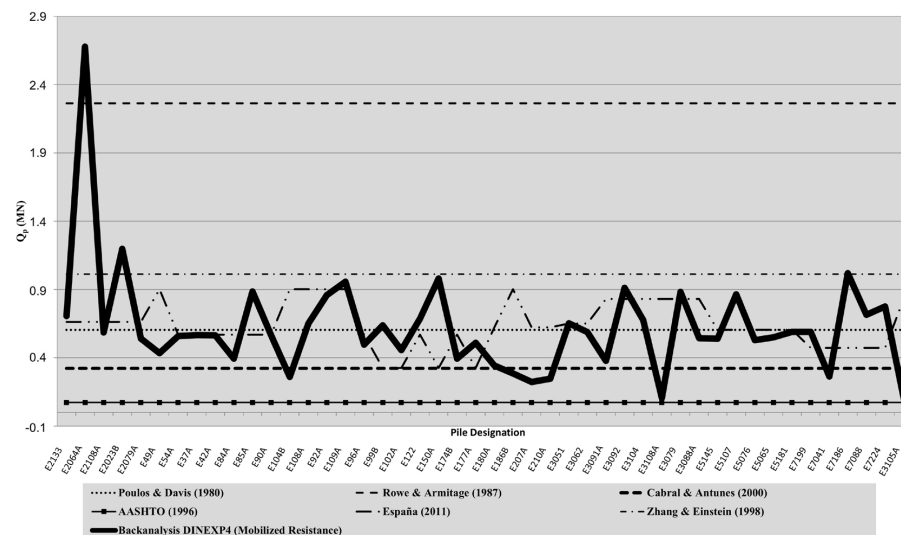


**Figure 10.** Estimated and mobilized toe capacity in rock.



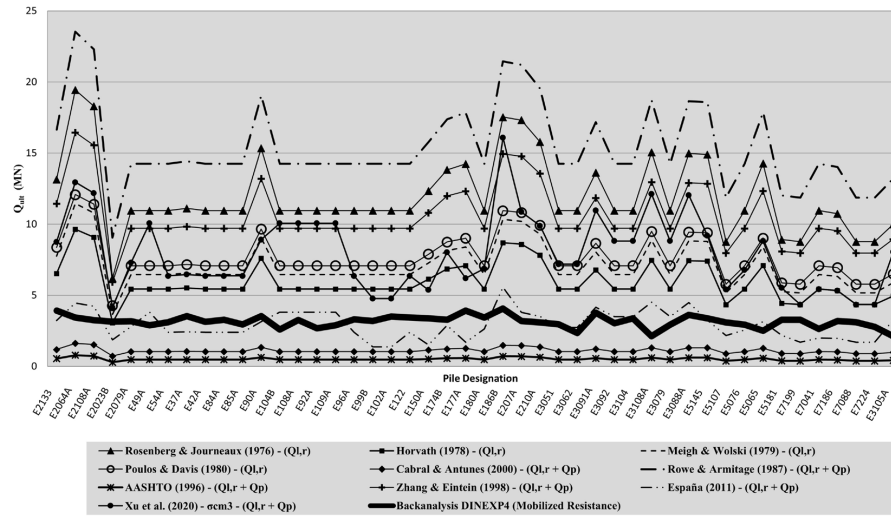


Figure 11. Estimated and mobilized total bearing capacity.

Table 10. Statistical distribution of mobilized and estimated total bearing capacity,  $Q_{ult}$  (kN).

Statistical Distribution	Sector	Rosenberg & Journeaux (1976)	Horvath (1978)	Meigh & Wolski (1979)	Poulos & Davis (1980)	Rowe & Armitage (1987)	AASHTO (1996)	Zhang & Einstein (1998)	Cabral & Antunes (2000)	España (2011)	Xu et al. (2020)	Mobilized Resistance
Mean	West	10586.0	5254.3	6238.8	6853.9	13846.4	460	9419.0	1024.5	2236.9	5955.2	3016.2
SD		2322.7	1152.8	1368.8	1371.4	2541.5	85	1844.5	154.1	576	1773.8	294.1
CV		22%	22%	22%	20%	18%	18%	20%	15%	26%	30%	10%
Mean	Southeast	16970.9	8423.4	10001.7	10623.9	20832.9	693.8	14489.6	1448.1	3972.1	11303.6	3537.3
SD		3352.8	1664.2	1976.0	1979.7	3668.7	122.7	2662.7	222.5	653.8	2233.2	345.1
CV		20%	20%	20%	19%	18%	18%	18%	15%	16%	20%	10%
Mean	Southwest	12054.5	5983.2	7104.3	7721.1	15453.4	513.8	10585.2	1121.9	3605.6	9401.5	2926.7
SD		2129.7	1057.1	1255.1	1257.5	2330.3	78	1691.3	141.3	520.2	4168.6	666.6
CV		18%	18%	18%	16%	15%	15%	16%	13%	14%	44%	23%
Mean	South	12007.3	5959.8	7076.4	7693.2	15401.7	512.1	10547.7	1118.8	2836.7	7841.3	3250.8
SD		2498.2	1240.0	1472.3	1475.0	2733.5	91.5	1983.9	165.7	1005.0	2677.0	337.1
CV		21%	21%	21%	19%	18%	18%	19%	15%	35%	34%	10%

a conventional failure load: Terzaghi (1943), Van Der Veen (1953), Chin (1970, 1971), Davisson (1972), Décourt (1996) and ABNT (2019). Due to the lack of an experimental value for pile concrete modulus, the value of 25 GPa was considered in the interpretation of the pile elastic shortening by Davisson (1972) and ABNT (2019) methods.

For each pile two extrapolated conventional failure loads were indicated in Table 11. The column designated by S provides the results extrapolated from the slow maintained loading and the column designated by Q shows the results extrapolated from the quick maintained load.

Except for pile E184, the quick tests indicate a higher failure load compared to the slow maintained tests, as expected (Lopes et al., 2021).

Only Pile E122 was submitted to both dynamic and static testing, the former three (3) months before the static test. The conventional failure load from the static tests shown in Table 11 were very similar, except for Chin (1970, 1971)

and Décourt (1996) methods. Excluding those two methods, the mean conventional failure load for the slow maintained test for pile E 122 is 3890 kN and the mobilized resistance by CAPWAP analysis is 3432 kN, the former being 12% greater than the latter. If the quick maintained static load testing is considered, the convention failure load is 4396 kN, a value 28% greater than the CAPWAP result.

In Table 12 the mobilized resistance from the CAPWAP of a pile very close to that of the static tested piles are compared. The piles with compared results have the same penetration in rock. The CAPWAP mobilized resistance of pile E7041 is compared to the conventional failure load of rapid test on pile E 7043. Pile E5065 is compared to E5043, E5107 to E5103 and E 186B to E184. Only the pile E122 is compared to itself. All the conventional failure loads in Table 12 correspond to the mean value considering the results from the cited methods, except Chin (1970, 1971) and Décourt (1996). The choice of the rapid maintained test



**Table 11.** Extrapolated conventional failure loads for the slow and quick maintained static loading tests interpreted for the 5 tested piles.

Method	E7043 (KN)		E5043 (KN)		E5103 (KN)		E184 (KN)		E122 (KN)	
	S	Q	S	Q	S	Q	S	Q	S	Q
Terzaghi (1943)	6400	7030	3920	5100	3350	3416	5200	2948	3900	4390
Van Der Veen (1953)	6664	7350	4410	5880	3430	3430	*	2940	3920	4410
Chin (1970, 1971)	10000	12500	10000	10000	5000	10000	10000	5000	10000	10000
Davisson (1972)	6540	7248	3628	5200	3200	3377	5250	2940	3855	4385
Décourt (1996)	9716	11681	8400	8529	5554	5858	11947	4537	9048	6818
ABNT (2019)	6598	7300	2499	5390	3300	3403	5255	2948	3890	4400

(\*) Inconsistent extrapolated value.

**Table 12.** Mobilized resistance compared to conventional failure load from static test.

Pile	E7041	E7043	E5065	E5043	E5107	E5103	E186B	E184	E122	E122
	$Q_{ult}$ (mobilized)	$Q_{ult,mean}$ (extrapolated)	$Q_{ult}$ (mobilized)	$Q_{ult,mean}$ (extrapolated)	$Q_{ult}$ (mobilized)	$Q_{ult,mean}$ (extrapolated)	$Q_{ult}$ (mobilized)	$Q_{ult,mean}$ (extrapolated)	$Q_{ult}$ (mobilized)	$Q_{ult,mean}$ (extrapolated)
Mobilized and Conventional Failure Load (KN)	2643	7232	2500	5392	3090	3407	4069	2948	3432	4396
Ratio Conventional Failure load to Mobilized Load (%)	2.7		2.2		1.1		0.72		1.3	

instead of the slow maintained test in Table 12 is a result of the higher load reached in the test, allowing a much reliable interpretation of the extrapolated conventional failure load.

Comparing the results from pile E122, the only submitted to both dynamic and static loading test, to the mean value from the remaining tests (except E184), it can be observed the following: a value of the ratio conventional failure load to mobilized resistance of 1.3 for pile E122 and 2 for the remaining piles.

As long as pile E122 presented a conventional failure load in the quick static load test 1.13 times the value obtained in the slow maintained load, the following can be inferred: the expected conventional static failure load in a slow maintained load is close to 1.2 to 1.8 times the mobilized values obtained in the dynamic test in this case study. The results of the static load testing reassure room for optimization in the design of deep foundations in root piles in rocks.

## 5. Conclusions

All tested piles presented a satisfactory mobilized capacity in the dynamic load tests.

The CAPWAP analysis applied to 99 piles produced similar results as the equivalent program DINEXP applied to 46 out of the 99 tested piles, presenting a good accuracy, with similar resistance distribution at toe, lateral resistance in soil and lateral resistance in rock.

The mobilized resistance from shaft penetration in soil was between 28% and 35% of the total mobilized resistance. However, many design methods do not consider this component in their estimations.

Despite the inclusion of a more complete characterization of the rock mass, España (2011) and Xu et al. (2020) design methods did not produce a predictive capacity closer to that mobilized in the tests. Yet España (2011) presented results that can be considered in an analysis in which the rock characterization is well performed. The other methods including a much simpler rock characterization, such as Cabral & Antunes (2000) and AASHTO (1996), resulted in an estimation closer to the mobilized resistance for lateral capacity in rock.

The bearing capacity design methods of an empirical nature indicated results against safety for the piles partially penetrating rocks in this case study. The methods from

Rosenberg & Journeaux (1976), Rowe & Armitage (1987) and Zhang & Einstein (1998) should not be applied to similar situations as that presented.

An alternative suggestion for design proposals for piles in similar conditions to those analyzed in the paper is a composition involving the Aoki & Velloso (1975) method for shaft penetration in soil and España (2011), Cabral & Antunes (2000) or AASHTO (1996) for the shaft penetration in rock.

The expected conventional static failure load in a slow maintained load is close to 1.2 to 1.8 times the mobilized values obtained in the dynamic tests. The static load testing reaffirms the conclusions obtained in this case study.

## Acknowledgements

To the REAGEO Project promoted by the National Institute for the Recovery of Slopes and Plains and the company Geomec for providing the dynamic loading test signals.

## Declaration of interest

There are no conflicting interests.

## Author's contributions

Marília Dantas da Silva: data curation, conceptualization, methodology, validation, writing - original draft. Roberto Quental Coutinho: validation, supervision, writing - reviewing and editing. Bernadete Ragoni Danziger: data curation, validation, supervision, writing - reviewing and editing.

## List of symbols

$A_t$	pile toe section
$d_f^t$	embedded factor to the tip resistance
$F_2$	factor expressing the influence of installation and scale effects
$f_{ck}$	concrete characteristic strength in compression
$k$	CPT x SPT correlation value depending on soil type
$L_r$	pile length in rock
$N$	factor related to the quality of the rock mass
$\bar{N}$	average $N_{60}$ value for the whole shaft penetration in soil
$n$	correction factor that considers the rock alteration degree and the presence of small fractures in rock mass
$N_L$	average $N_{60}$ value for a given soil layer with a $\Delta L$ penetration
$N_{ms}$	coefficient that depends on rock type and quality
$P_{v,adm}$	allowable stress by method proposed by España (2011) uses coefficients related to the rock type, degree

	of weathering of the rock mass and discontinuity spacings.
$p_0$	reference stress (1 MPA)
$Q_{l,r}$	lateral resistance in rock
$Q_{l,s}$	lateral resistance in soil
$Q_p$	toe resistance in rock
$Q_{p,r}$	resistance at pile tip
$q_{p,r}$	rock unit tip resistance
$q_u$	uniaxial compressive strength of the intact rock
$Q_{ult}$	mobilized total capacity
$S$	spacing (in meters) between discontinuities
$U$	perimeter of the pile shaft section
$\alpha$	CPT x SPT correlation values depending on soil type
$\alpha$	factor related to the quality of the rock mass
$\alpha_1, \alpha_2, \alpha_3$	dimensionless parameters depending on rock type, alteration degree and discontinuities spacing, respectively
$\beta$	empirical parameter
$\beta'$	coefficient given by Décourt (1996)
$\beta_0, \beta_1$	coefficients given by Cabral (1986)
$\Delta L$	penetration in each soil layer
$\delta_0$	elastic displacement in mm
$\rho$	empirical parameter
$\sigma_{cm3}$	resistance compressive of rock mass using RQD and considering the influence of discontinuities given by Xu et al. (2020)
$\sigma_t$	is the rock tensile strength
$\tau_{l,r}$	unit shear resistance
$\tau_{l,s}$	shear soil resistance
$\tau_{máx}$	the shear resistance in rock
$\phi_r$	the pile diameter in rock
$\phi_s$	he diameter of pile penetrated in soil

## References

- AASHTO. (1996). *Standard Specifications for Highway Bridges*. American Association of State Highway and Transportation Officials, Washington, D.C.
- ABNT NBR 13208. (2007). *Dynamic Testing of Piles – Test Method*. ABNT – Associação Brasileira de Normas Técnicas, Rio de Janeiro, RJ (in Portuguese).
- ABNT NBR 6122. (2019). *Design and execution of foundations*. ABNT – Associação Brasileira de Normas Técnicas, Rio de Janeiro, RJ (in Portuguese).
- Aoki, N., & Velloso, D.A. (1975). An approximate method to estimate the bearing capacity of piles. In *Proceedings of the 5th Pan. Conference on Soil Mechanics and Foundations: Vol. 5* (pp. 367-374). Buenos Aires.
- Cabral, D.A. (1986). The use of root piles as foundation of normal works. In *Proceedings of the Brazilian Conference on Soil Mechanics and Foundation Engineering: Vol. 6* (pp. 71-82). Porto Alegre. (in Portuguese).
- Cabral, D.A., & Antunes, W.R. (2000). A suggestion for bearing capacity estimation of piles embedded in rock.

- In *Proceedings of the Conference on Geot. Eng. Special Found: Vol. 4*. São Paulo. (in Portuguese).
- Chin, F.K. (1970). Discussion: Pile tests. Arkansas River Project. *Journal of the Soil Mechanics and Foundations Division*, 97(SM7), 930-932.
- Chin, F.K. (1971). Discussion of pile test. Arkansas River Project. *Journal for Soil Mechanics and Foundation Engineering*, 97(SM6), 930-932.
- Costa, A.M. (1988). *DINEXP Program developed*. CENPES/Petrobras.
- Danziger, B.R. (1991). *Dynamic Analysis of Driven Piles* [Unpublished doctoral dissertation]. Coppe/UFRJ.
- Danziger, B.R., Costa, A.M., Lopes, F.R., & Pacheco, M.P. (1996). A discussion on the uniqueness of CAPWAP-type analyses. In *Proceedings of the 5th International Congress on the Application of Stress-Wave Theory to Piles: Vol. 1* (pp. 394-408). Miami.
- Davisson, M.T. (1972). *High capacity piles* (Proceedings, Lecture Series. Innovations in Foundation Construction, pp. 52). ASCE, Illinois.
- Décourt, L. (1996). Analysis of deep foundations: piles. In Hachich. *Foundations: theory and practice* (pp. 265-301) Editora Pini Ltda. (in Portuguese).
- Décourt, L., & Quaresma, A. (1978). Pile load capacity from SPT values. In *Proceedings of the VI Brazilian Conference Cobramseg: Vol. 1* (pp. 45-53). Rio de Janeiro (in Portuguese).
- España. (2011). *Guia de cimentaciones en obras de carretera*. Ministerio de Fomento, Centro de Publicaciones.
- Goble, G.G., Rauche, F., & Likins, G.E. (1980). The Analise of Pile Driving – A State of the Art Report. In *Proceedings of the 2nd International Conference on the Application of Stress – Wave Theory to Piles* (pp. 131-161). Stockholm.
- Goble. (1986). *Notes on the course of Application of Stress Wave in Driven Piles*. PUC. (in Portuguese).
- Goodman, R.E. (1989). *Introduction to Rock Mechanics*. John Wiley & Sons.
- Horvath, R. (1978). *Field load test data on concrete-to-rock bond strength for drilled pier foundations* (Publication 78-07). University of Toronto.
- Juvêncio, E.L., Lopes, F.R., & Nunes, A.L.L.S. (2017). An Evaluation of the Shaft Resistance of Piles Embedded in Gneissic Rock. *Soils and Rocks, São Paulo*, 40(1), 61-74.
- Lopes, F.R., Santa Maria, P.E.L., Danziger, F.A.B., Martins, I.S.M., & Tassi, M.C. (2021). A proposal for static load tests on piles: the Equilibrium Method. *Soils and Rocks, São Paulo*, 44, 1-10.
- Meigh, A.C., & Wolski, W. (1979). Design parameters for weak rock. In *Proceedings of the 7th European Conference on Soil Mechanics and Foundation Engineering: Vol. 5* (pp. 59-79). London. British Geotechnical Society, Brighton.
- Poulos, H.G., & Davis, E.H. (1980). *Pile Foundation Analysis and Design*. John Wiley & Sons.
- Reese, L.C., & O'Neill, M.W. (1999). *Drilled Shafts: construction procedures and design methods* (Report FHWA-IF-99-025). Federal Highway Administration.
- Rosenberg, P., & Journeaux, N. (1976). Friction and end bearing tests on bed rock for high-capacity socket design. *Canadian Geotechnical Journal*, 13(3), 324-333.
- Rowe, R.K., & Armitage, H.H. (1984). *The design of piles socketed into weak rock* (Report GEOT-11-84). University of Western Ontario.
- Rowe, R.K., & Armitage, H.H. (1987). A design method for drilled piers in soft rock. *Canadian Geotechnical Journal*, 24(1), 126-142.
- Seidel, J.P., & Collingwood, B. (2001). A new socket roughness factor for prediction of rock socket shaft resistance. *Canadian Geotechnical Journal*, 38, 138-153.
- Simons, H.A., & Randolph, M.F. (1985). A new approach to one dimensional pile driving analysis. In *Proceedings of the 5th International Congress on Numerical Methods in Geomechanics*. Nagoya.
- Smith, E.A.L. (1960). Pile driving analysis by the Wave Equation. *Journal of the Soil Mechanics and Foundations Division*, 127(I), 1145-1193.
- Terzaghi, K. (1943). *Theoretical soil mechanics*. John Wiley & Sons.
- Van Der Veen, C. (1953). The bearing capacity of a pile. In *International of the 3rd Conference of Soil Mechanics and Foundation Engineering: Vol. 2* (pp. 84-90). Zurich: ICOSOMEF.
- Xu, J., Gong, W., Gamage, R.P., Zhang, Q., & Dai, G. (2020). A new method for predicting the ultimate shaft resistance of rock-socketed drilled shafts. *Proceedings of the Institution of Civil Engineers–Geotechnical Engineering*, 173(2), 169-186. <http://dx.doi.org/10.1680/jgeen.18.00221>.
- Zhang, L., & Einstein, H.H. (1998). End bearing capacity of drilled shafts in rock. *Journal of Geotechnical and Geoenvironmental Engineering*, 124(7), 574-584.

## An evaluation of reinforcement mechanical damages in geosynthetic reinforced piled embankments

Ennio Marques Palmeira<sup>1</sup> , José Melchior Filho<sup>1#</sup> ,

Ewerton Clayton Alves Fonseca<sup>2</sup> 

Article

### Keywords

Geosynthetics  
Reinforcement  
Piled embankments  
Mechanical damage

### Abstract

The use of geosynthetic reinforcement in piled embankments over soft soils is an effective solution for the reduction of settlements and to increase the embankment stability. The most efficient position for the reinforcement layer is on the pile cap or head. However, a direct contact of the reinforcement with sharp edges may damage it, compromising its efficiency to transfer loads to the piles. This paper investigates the possibility of mechanical damages in geosynthetic reinforcements on pile caps by large scale laboratory tests. Tests with and without pieces of nonwoven geotextile protective layer between the caps and the reinforcements were executed. Wide strip tensile tests were performed on exhumed reinforcement specimens after the tests to assess tensile strength and stiffness variations. A statistical analysis of the results shows reductions in tensile strength of unprotected reinforcement layers of up to 28%. A mechanical damage index is introduced and its correlation with calculated reduction factors is investigated. The use of a piece of a thick geotextile layer to protect the reinforcement against mechanical damage can be effective. However, the geotextile product must be properly specified and installed with due care.

## 1 Introduction

The design of embankments on soft soils must guarantee not only the embankment stability but also that its settlements due to soft soil consolidation will not compromise its function. In this context, the use of piles to transfer the embankment load (self-weight and surcharges) to deeper strong layers can be an effective solution to minimize settlements and increase the overall stability of the embankment. The presence of the piles as rigid elements compared to the soft soil compressible nature causes arching of the fill material between the piles, yielding to the transference of loads to the piles and reduction of stresses acting on the surface of the soft subgrade. However, the solution must be properly designed to guarantee an effective mechanism of load transfer to the piles and from them to a stiffer soil layer underneath the soft soil.

The use of geosynthetic reinforcement in piled embankments has increased significantly in the last 4 decades. The reasons for this are that the presence of the geosynthetic

layer improves the load transfer to the piles and reduces even further the stresses transmitted to the soft foundation soil. In addition, the reinforcement increases the safety of the embankment against global failure. However, the interaction between fill material, reinforcement and piles is complex and different analytical and numerical studies can be found in the literature to address this problem (Low et al., 1994; Russel & Pierpoint, 1997; Filz & Smith, 2006; Filz & Smith, 2007; Abusharar et al., 2009; Sloan et al., 2011; Zhuang et al., 2014; van Eekelen., 2015; Fattah et al., 2015; Fattah et al., 2016a, b; Fonseca & Palmeira, 2018; Fonseca et al., 2018; Al-Taie et al., 2019). Standards and guidelines can also be found to help the design and construction of such works complying with technical requirements and appropriate safety margins (BSI, 2010; EBGE0, 2011; FHWA, 2017; van Eekelen, 2016).

Figure 1 shows the typical deformation pattern of a bottom reinforcement layer in a geosynthetic reinforced piled embankment after consolidation of the soft soil. The most efficient position for the reinforcement layer is on the pile caps or heads, when the former is not present (Fonseca

\*Corresponding author: E-mail address: melchior\_filho@hotmail.com

<sup>1</sup>Universidade de Brasília, Departamento de Engenharia Civil e Ambiental, Brasília, DF, Brasil.

<sup>2</sup>Universidade Federal Tecnológica do Paraná, Departamento de Construção Civil, Campo Mourão, PR, Brasil.

Submitted on January 11, 2022; Final Acceptance on May 21, 2022; Discussion open until: November 30, 2022.

<https://doi.org/10.28927/SR.2022.000522>



This is an Open Access article distributed under the terms of the Creative Commons Attribution License, which permits unrestricted use, distribution, and reproduction in any medium, provided the original work is properly cited.

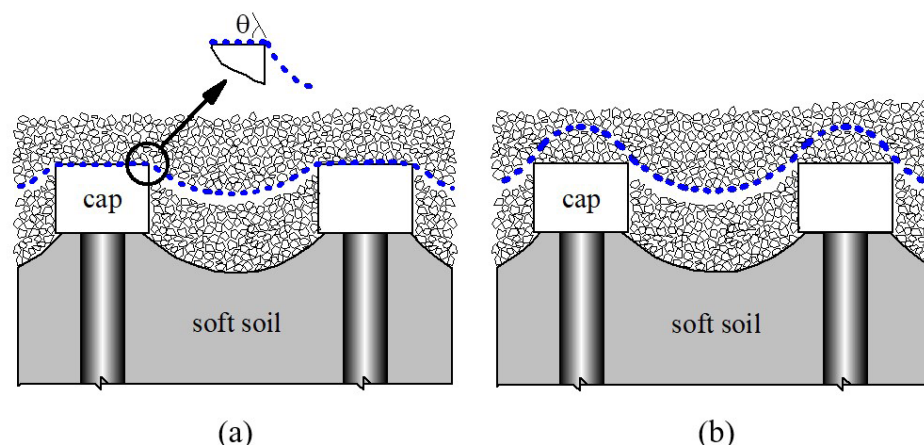


**Figure 1.** Typical deformation patterns of the bottom reinforcement layer in a piled embankment: (a) reinforcement initially in contact with cap; (b) reinforcement above cap.

& Palmeira, 2018). However, this direct contact between the reinforcement and a rigid body, usually with sharp edges, defects, and lack of proper finishing, may damage the reinforcement along the edges of the cap or pile head to the point of tearing the reinforcement entirely along the cap or pile perimeter, as exemplified in Figure 2a. This damaging mechanism is particularly relevant under repeated loading, which is likely to occur during the construction of the embankment and during its operational life in embankments for highways and railways, for instance. To avoid or minimize this possibility of mechanical damage, a protective thick nonwoven geotextile layer can be installed between the reinforcement and the cap/pile, as shown in Figure 2b. However, it should be pointed out that both Figures 2a,b were from the same work. So, the torn geogrid reinforcement in Figure 2a was also protected by a geotextile layer. Therefore, due care must be taken in the specification of the protective geotextile layer and construction practice to avoid failure of the reinforcement in contact with the cap. van Eekelen (2016) recommends caps with beveled edges to avoid or minimize such damages. Some recommendations are more restrictive, establishing that the reinforcement layer must be placed some minimum distance above the pile cap/head to avoid direct contact between them (EBGEO, 2011). Almeida & Marques (2011) recommend a 150 mm thick sand layer to be installed between the reinforcement and the pile cap. BSI (2010) also recommends a layer of sand between reinforcement and caps. It should be pointed out that even with the reinforcement above the cap (Figure 1b), some level of mechanical damage of the reinforcement should be expected due to the abrasive nature of the interaction between soil and reinforcement, particularly under repeated loading and in the long-term. Thus, appropriate reduction factors for the relevant mechanical properties of the reinforcement must be chosen to avoid problems such as those shown in Figure 2a.

Several works on geosynthetic mechanical damage can be found in the literature (Azambuja, 1994; Richardson, 1998; Hufenus et al., 2002; Huang, 2006; Bathurst & Miyata, 2015; Pinho-Lopes et al., 2018; Fleury et al., 2019, for instance). These works have investigated the intensity and/or estimate appropriate reduction factors by laboratory and field tests. Some studies involved the use of standard laboratory tests to evaluate mechanical damages to reinforcements under repeated loading (Cho et al., 2006; Yoo et al. 2009; Rosete et al., 2013; Gonzalez-Torre et al., 2014). Large scale field tests have also been performed to investigate mechanical damages of geosynthetic reinforcements (Austin, 1997; Richardson, 1998; Hsieh & Wu, 2001; Hufenus et al., 2002; Cho et al., 2006; Fleury et al., 2019). However, the authors of the present paper are not aware of any study on damage to reinforcements in piled embankments on soft soils.

Due to the relevance of the problem described above, this paper aimed at investigating the intensity and consequences of mechanical damages of reinforcements in contact with the edge of rigid bodies, such as in the case of concrete caps in piled embankments. An evaluation of the contribution of a thick nonwoven geotextile layer between the cap and the reinforcement was also investigated.

## 2. Experimental

### 2.1. Equipment

A large equipment developed for tests on large scale models of geosynthetic reinforced piled embankments (Fonseca, 2017; Melchior Filho, 2022) was used in this research. Figure 3 shows the geometrical characteristics of the equipment, which consists of a large rigid container (1000 mm × 1000 mm × 450 mm), made of steel, to confine



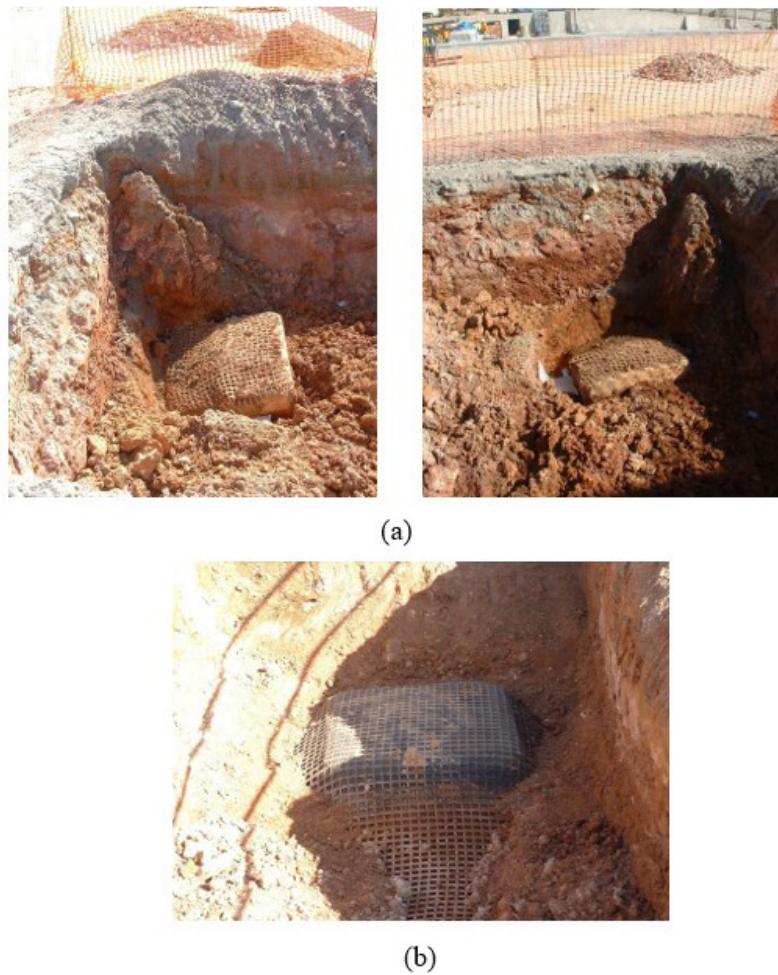


**Figure 2.** Example of failure of the reinforcement due to mechanical damage (a) reinforcement failure along cap perimeter; (b) protective geotextile layer between cap and geogrid reinforcement. (courtesy of Dr. Alberto Ortigão).

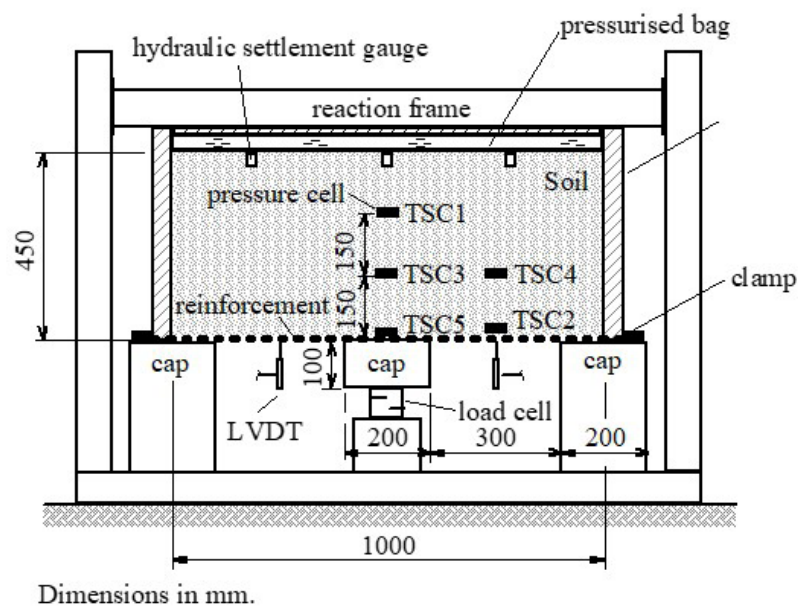


**Figure 3.** Equipment used in the tests.

the fill material, a reaction frame (1800 mm × 1500 mm × 1500 mm) to provide reaction to the load applied on the fill surface and a set of concrete caps (square in plan, 200 mm × 200 mm) located under the container. The spacing between centres of caps was equal to 500 mm. This spacing was chosen to simulate a typical value found under prototype conditions. The surface vertical surcharge is applied by a pressurized rubber bag that covers the entire plan area of the fill layer. The reinforcement layer is anchored along the perimeter of the container by a rigid steel clamping system. The internal walls of the container were lubricated with double layers of plastic film and grease to minimize friction with the fill layer. Tests with a single reinforcement layer and two layers at the bottom region of the fill were carried out. In all tests with a single reinforcement layer this layer was installed directly on the caps. In tests with two reinforcement layers, the bottom layer was installed directly on the caps and the upper layer was installed 50 mm above the bottom one. Figure 4a shows a general view of the equipment during one of the tests and Figure 4b shows one of the caps used in the test, which can be considered as having a much smoother and better finishing condition than those expected in the field (Figure 2a and Figure 4c). Despite having been manufactured under laboratory-controlled conditions, the

caps still had defects and protrusions capable of damaging the reinforcement.

The instrumentation used in the tests consisted of a load cell to measure loads on the central pile cap, displacement transducers to measure vertical displacements of the reinforcement layer between caps, hydraulic settlement gauges to measure fill surface settlements and pressure cells distributed in the fill mass. The average reinforcement strains were obtained from measurements of movements of markers attached to the reinforcement layer. Additional information on equipment, instrumentation and testing methodology can be found in Melchior Filho (2022).

The study can be viewed as an investigation of mechanical damage of a reinforcement in contact with the edges of a rigid body in a general sense or as model scale study of a reinforced piled embankment. Considering the latter case, the dimensions of the test would simulate typical prototype conditions with a geometric scale factor ( $\lambda$ ) ranging from 3 to 5. Hence, all the relevant typical dimensions and properties of the materials were scaled accordingly. However, as mentioned above, to some extent the tests can also simulate a prototype ( $\lambda = 1$ ) field situation with regard to the possibility of damage, under similar conditions, of a reinforcement in contact with a rigid body, but in this case under a smaller surcharge (40 kPa, which was the maximum surcharge applied

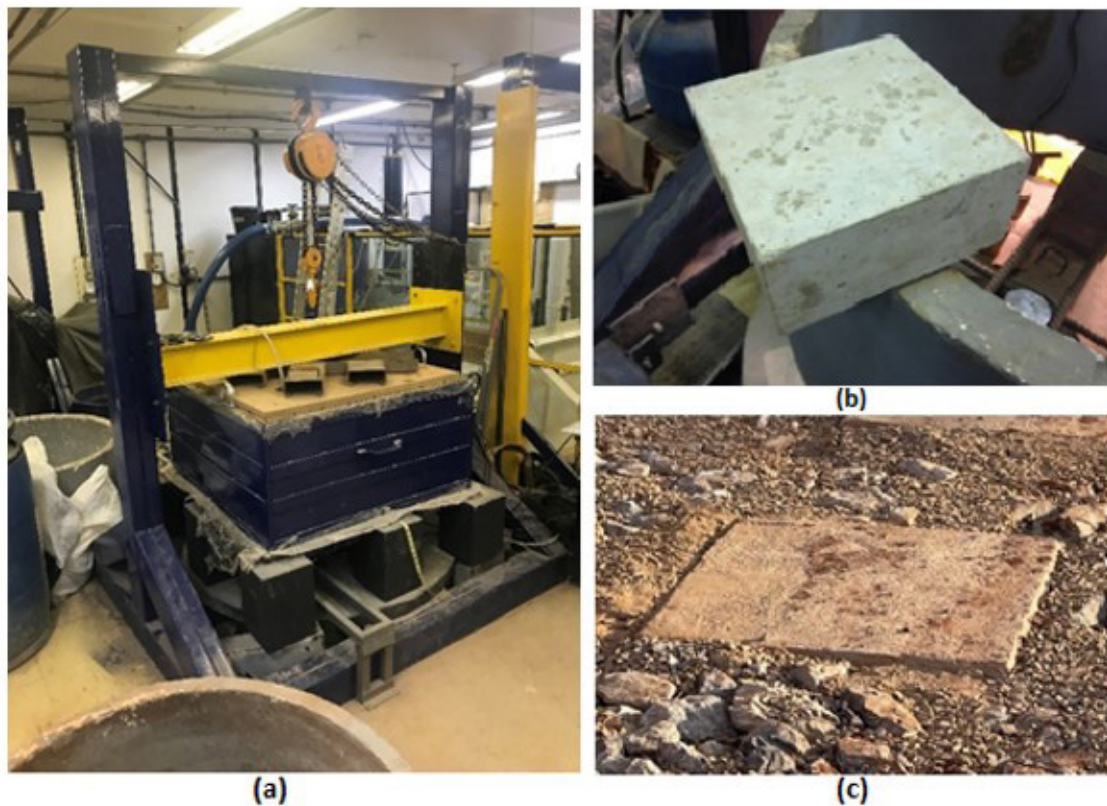


**Figure 4.** General view of the equipment during one of the tests performed: (a) general view; (b) view of a concrete cap; (c) typical cap surface in the field.

on the top of the fill layer) and with the actual mechanical and physical properties of the materials tested.

The maximum vertical surcharge applied on the top of the fill layer was equal to 40 kPa, which would simulate a surcharge of 200 kPa under prototype conditions in a model scale test with  $\lambda = 5$ . Following the stabilization of the instrumentation readings after the application of the last loading stage, the tests were disassembled, and specimens of the reinforcements were collected for tensile tests. Figure 5 depicts the locations (with respect to the cap borders) where these specimens were collected. A tensile test machine manufactured by EMIC was used in these tests, which were executed according to ASTM D4595

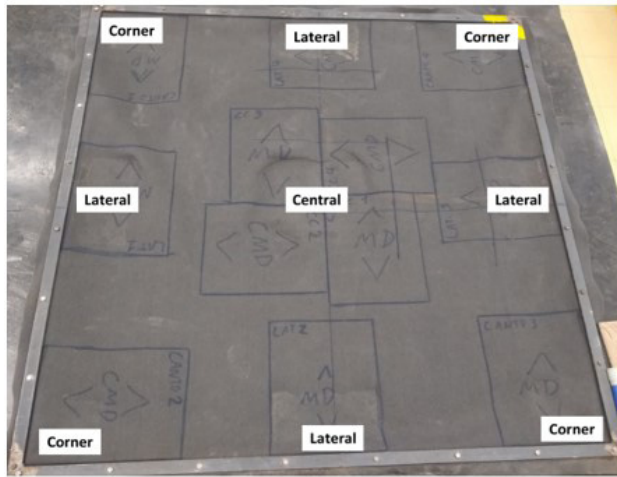


**Figure 5.** Locations of the specimens collected for tensile tests.

**Table 1.** Properties of the fill material.

$\phi'$ ( $^{\circ}$ ) <sup>(1)</sup>	43
$D_{50}$ (mm) <sup>(2)</sup>	7.1
$D_{85}$ (mm) <sup>(2)</sup>	10.4
$C_u$	2.56
$\gamma_d$ (kN/m <sup>3</sup> )	16.0
$I_D$ (%)	65
$G_s$ <sup>(3)</sup>	2.73

Notes: (1)  $\phi'$  = friction angle using a medium size direct shear box (300 mm  $\times$  300 mm  $\times$  175 mm),  $D_n$  = diameter for which n% of the remaining particles have smaller diameters,  $C_u$  = coefficient of uniformity ( $= D_{60}/D_{10}$ ),  $\gamma_d$  = dry unit weight,  $I_D$  = relative density,  $G_s$  = soil particle specific gravity; (2) According to NBR 7181; (3) According to NBR 6458.

**Table 2.** Relevant properties of the geosynthetic reinforcements.

Polymer	GG	MGR	GTX	GTA	GTB	GTC
	PET	PE	PP	PP	PET	PET
$M_A$ (g/m <sup>2</sup> )	NA	130	400	300	75	185
Aperture (mm)	20 $\times$ 20	4 $\times$ 4	NA	NA	NA	NA
$T_{max}$ (kN/m)	17.2/10.5	13.76/13.54	18.19/18.08	15.6	5.6/5.1	10.1/6.0
$\varepsilon_{max}$ (%)	6.4/7.1	21.0/28.3	86.1/102.5	67	71.1/53.7	9.6/13.2
$J_{5\%}$ (kN/m)	280/152	80.2/59.1	31.5/23.8	29	38/29	113/65

Notes: Results from wide-strip tensile tests as per ASTM D4595 (ASTM, 2017) or D6637 (ASTM, 2015), depending on the reinforcement considered; Numbers on the left of the slash are values along the machine direction, whereas numbers on the right are values along the cross-machine direction; NA = not applicable or not available.

or ASTM D6637 (ASTM 2015, 2017), depending on the reinforcement type.

## 2.2 Materials

The fill material employed consisted of an uniform gravel, classified as GP according to the Unified Soil Classification System, with angular grains, an average particle diameter of 7.10 mm and a coefficient of uniformity equal to 2.56. The fill material was prepared under a loose state, with a dry unit weight of 16.0 kN/m<sup>3</sup>, yielding to a relative density of 65%. The friction angle of the fill material obtained in medium size (300 mm  $\times$  300 mm  $\times$  175 mm specimen size) direct shear tests is equal to 43°. Table 1 presents the relevant geotechnical properties of the gravel.

Six reinforcements consisting of a geogrid (code GG), a polymeric mesh (code MGR) and 4 geotextiles (codes GTX, GTA, GTB and GTC) were tested. These reinforcements were tested in the research activities carried out by Fonseca (2017) and Melchior Filho (2022). The main properties of these materials are listed in Table 2. Geogrid GG is a polyester product with square apertures, 20 mm  $\times$  20 mm wide, and a tensile stiffness at 5% strain ( $J_{5\%}$ ) equal to 280 kN/m and 152 kN/m along machine (MD) and cross-machine (CMD) directions, respectively. The polymeric mesh (code MGR) is made of polyester, with square apertures 4 mm wide and  $J_{5\%}$  of 80.2 kN/m along MD and 59.1 kN/m along CMD. Geotextiles GTX and GTA are nonwoven, needle-punched, geotextiles, made from polypropylene, with masses per unit area of 400 g/m<sup>2</sup> and 300 g/m<sup>2</sup>, respectively. Reinforcements GTB and GTC are polymeric materials, made from polyester, similar to woven geotextiles, with masses per unit area equal to 75 g/m<sup>2</sup> and 185 g/m<sup>2</sup>, respectively. In a real piled embankment, nonwoven geotextiles would not be suitable reinforcements due to their low tensile strength and stiffness in comparison with available geogrids and woven geotextiles. However, they were used in the present work to simulate reinforcements that would present typical mechanical properties commonly found under prototype conditions of piled embankments on soft soils, as well as to cover a wide range of reinforcement mechanical properties. Table 3 summarizes the types of tests that were performed. Duplicates of tests were carried out to assess the repeatability of the results obtained.



**Table 3.** Types of tests carried out.

Test code	Reinforcement	No. of reinforcement layers	Test description
GTX-1	GTX	1	Test with one layer of GTX.
GTX-1 (R)		1	Repetition of test GTX-1.
GTX-2		2	Test with two layers of GTX.
GTX-2 (R)		2	Repetition of test GTX-2.
MGR-1	MGR	1	Test with one layer of MGR.
MGR-2		2	Test with two layers of MGR.
MGR-1 (P1)		1	Test with one layer of MGR and a protective geotextile layer with $M_A = 450 \text{ g/m}^2$ .
MGR-1 (P2)		1	Test with one layer of MGR and a protective geotextile layer with $M_A = 900 \text{ g/m}^2$ .
GG-1	GG	1	Test with one layer of GG.
GTA-1	GTA	1	Test with one layer of GTA.
GTB-1	GTB	1	Test with one layer of GTB.
GTC-1	GTC	1	Test with one layer of GTC.

Notes:  $M_A$  = mass per unit area.

If a geometrical scale factor of 5 is assumed, the reinforcements will present tensile stiffness values ranging from 725 kN/m to 7000 kN/m along machine direction and from 595 kN/m to 3800 kN/m along cross-machine direction under prototype conditions. With respect to tensile strength, under the same scale factor, the ranges would be 132 kN/m to 455 kN/m along machine direction and 128 kN/m to 452 kN/m along cross-machine direction. Values 64% smaller for the ranges above are obtained if a geometrical scale factor ( $\lambda$ ) of 3 is considered (scale factor equal to  $\lambda^2$  for reinforcement tensile strength and stiffness). If the tests are viewed as simulations of full-size problems of contact between different reinforcements and a rigid body, the properties of the reinforcement to be considered would be those in Table 2. In this case, the stress level expected on the reinforcement due to the maximum surface surcharge of 40 kPa plus the fill self-weight would be equivalent to that caused by an embankment approximately 2.9 m high. However, under such assumption only reinforcements GG, GTX, and GTA should be considered, for being actual geosynthetics, although the latter two are nonwoven products. The other reinforcements (MGR, GTB and GTC) would be too weak and extensible for most situations in practice and were tested in the current study only to attend modelling requirements in case the experiment is viewed as a model study.

Some testes were carried out with a geotextile protective layer between the reinforcement MGR and the concrete pile cap. In these tests, nonwoven, needle-punched geotextiles, made of polyester, with masses per unit area of 450 g/m<sup>2</sup> and 900 g/m<sup>2</sup> were employed as protective layers.

As mentioned before, after the tests, exhumed specimens of the reinforcements were subjected to wide-strip tensile tests and a statistical analysis (Student's *t* Test) was carried out based on results under virgin and damaged conditions to evaluate possible changes in reinforcement tensile properties

with a level of confidence of 95%. Based on these analyses, reduction factors (RF) for the damage mechanisms simulated were estimated.

### 3. Results and discussions

#### 3.1 Effect of mechanical damage on reinforcement tensile strength

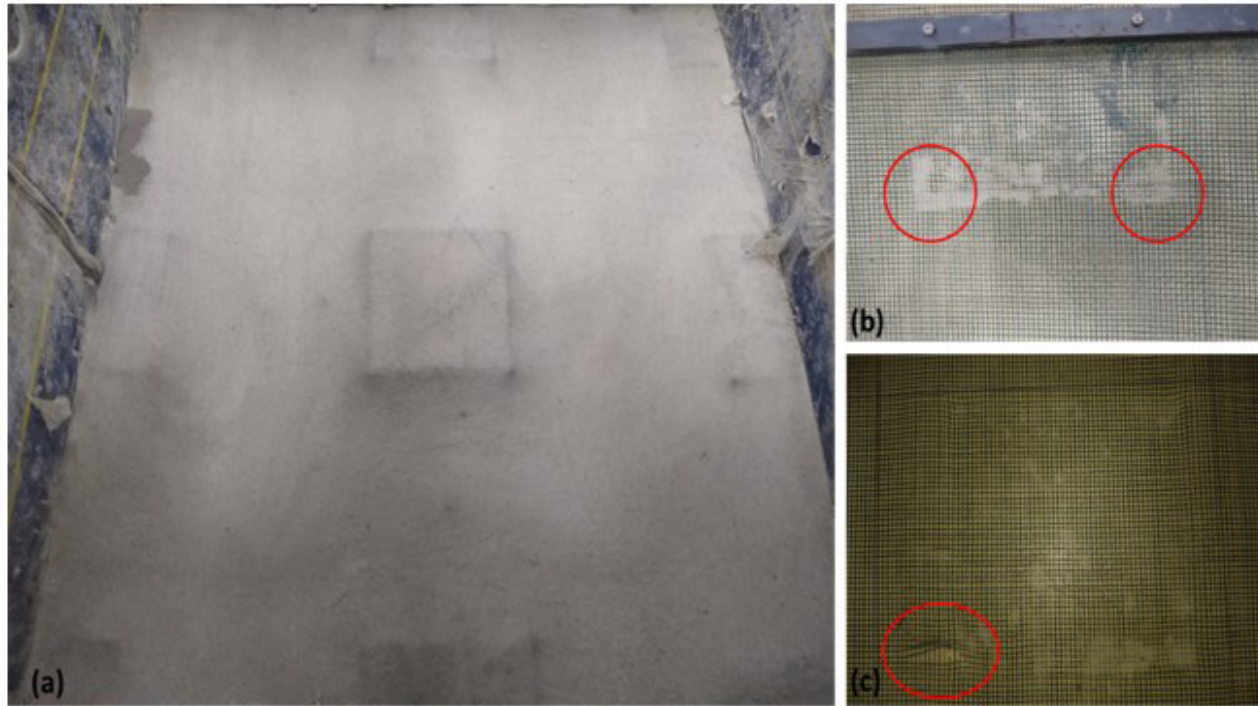
Table 4 presents mean values of reinforcement tensile strength ( $T_{max}$ ) of specimens collected at different locations (see Figure 5) after the tests. Some variations in tensile strength with respect to the strength of virgin reinforcements (Table 2) can be observed due to mechanical damages. Figure 6 shows images of reinforcements after some of the tests, where points of reinforcement distresses along the edges of the caps can be observed.

Table 5 shows the results of statistical significance if the mean values of all specimens (virgin and damaged) are compared. A statistically significant variation of  $T_{max}$  along the cross-machine direction can be observed for all tests without the protective layer of geotextile beneath the reinforcement, except for tests GTA-1 and GG-1. No statistically significant variations were observed for tests on GTX along the machine direction. On the other hand, without the presence of the geotextile protection layer, there was statistically significant variations in the tensile strength of reinforcement MGR in both directions, independent on the number of reinforcement layers present. The bottom reinforcement layer in test MGR-2 (test with 2 reinforcement layers) presented significant variation in its tensile strength, suggesting that the presence of the additional layer 50 mm above did not significantly influence the mechanical damages to the bottom layer for the conditions of the tests. It should be pointed out that the

**Table 4.** Tensile strength after the tests.

Test	Location (see Figure 5)	$T_{max}$ (kN/m)		Test	Location (see Figure 5)	$T_{max}$ (kN/m)	
		MD	CMD			MD	CMD
GTX-1	Central	14.76	20.79	MGR-1	Central	9.03	10.12
	Lateral	14.59	20.95		Lateral	10.38	11.43
	Corner	14.33	21.09		Corner	13.28	12.24
GTX-1 (R)	Central	17.10	21.55	MGR-2	Central	9.37	12.93
	Lateral	17.45	20.38		Lateral	9.74	12.08
	Corner	19.87	20.80		Corner	10.23	12.53
GTX-2	Central	17.58	20.42	MGR-1 (P1)	Central	13.46	13.69
	Lateral	16.93	21.44		Lateral	12.76	12.63
	Corner	15.67	23.05		Corner	12.22	13.11
GTX-2 (R)	Central	18.96	18.42	MGR-1 (P2)	Central	12.10	13.48
	Lateral	20.85	21.44		Lateral	13.04	12.52
	Corner	20.49	23.05		Corner	12.18	13.10

Notes:  $T_{max}$  = tensile strength after the test from wide-strip tensile tests (ASTM 2017); For exact location of specimens see Figure 5; Values of tensile strengths are mean values at each specimen location.



**Figure 6.** Images of some reinforcements at the end of the tests: (a) View of the central cap and the deformed reinforcement; (b), (c) Local damages in reinforcement.

maximum vertical displacements between caps in test MGR-2 were only 6% (along MD) and 12% (along CMD) smaller than those measured in test MGR1, for which the variations in tensile strength were also statistically significant (Table 5).

The results for tests on MGR protected with geotextile layer in Table 5 (tests MGR-1 (P1) and MGR-1 (P2)) presented no statistically significant differences, even for the lighter ( $M_A = 450 \text{ g/m}^2$ ) protective geotextile, showing that the nonwoven geotextile layer used was effective in minimizing the effects of mechanical damage on reinforcement tensile strength.

### 3.2 Effect of mechanical damage on reinforcement tensile stiffness

Table 6 presents the mean results of reinforcement tensile stiffness ( $J_{5\%}$ ) at the end of the test at different locations, whereas Table 7 shows the statistical significance of the variations in results. Unfortunately,  $J_{5\%}$  values at the end of the test are not available for reinforcements GG, GTA, GTB and GCT. In practice, variations of reinforcement tensile stiffness will increase the settlement of the base of the embankment between caps. In ten out of twelve cases



**Table 5.** Statistical significance of tensile strength variation.

Test	Direction	$T_{max-v}$ (kN/m)	$T_{max}$ (kN/m)	Significance
GTX-1	MD	18.19	14.56	NS
	CMD	18.08	20.94	S
GTX-1 (R)	MD	18.19	18.14	NS
	CMD	18.08	20.91	S
GTX-2	MD	18.19	16.73	NS
	CMD	18.08	21.08	S
GTX-2 (R)	MD	18.19	20.10	NS
	CMD	18.08	20.97	S
MGR-1	MD	13.76	10.90	S
	CMD	13.54	11.26	S
MGR-2	MD	13.76	9.78	S
	CMD	13.54	12.51	S
MGR-1 (P1)	MD	13.76	12.81	NS
	CMD	13.54	13.14	NS
MGR-1 (P2)	MD	13.76	12.77	NS
	CMD	13.54	13.03	NS
GG-1	MD	15.43	15.73	NS
	CMD	8.88	8.70	NS
GTA-1	MD	14.10	13.28	NS
	CMD	19.78	19.28	NS
GTB-1	MD	6.00	3.78	S
	CMD	5.02	2.88	S
GTC-1	MD	10.38	9.96	S
	CMD	6.44	6.80	S

Notes:  $T_{max-v}$  = virgin tensile strength from wide-strip tensile tests;  $T_{max}$  = tensile strength after the test from wide-strip tensile tests; MD = machine direction; CMD = cross-machine direction; NS = not statistically significant with 95% confidence level; S = statistically significant with 95% confidence level.

**Table 6.** Tensile stiffness ( $J_{5\%}$ ) at different locations after the test.

Test	Location	$J_{5\%}$ (kN/m)		Test	Location	$J_{5\%}$ (kN/m)	
		MD	CMD			MD	CMD
GTX-1	Central	30.92	32.47	MGR-1	Central	63.73	53.92
	Lateral	32.74	34.45		Lateral	68.89	52.23
	Corner	27.25	23.35		Corner	66.90	50.84
GTX-1 (R)	Central	34.67	25.21	MGR-2	Central	65.80	51.99
	Lateral	30.09	21.66		Lateral	60.41	46.85
	Corner	33.07	22.14		Corner	60.74	50.78
GTX-2	Central	35.63	30.78	MGR-1 (P1)	Central	68.33	55.63
	Lateral	28.62	30.41		Lateral	67.19	53.95
	Corner	26.19	28.70		Corner	64.64	53.52
GTX-2 (R)	Central	35.85	26.74	MGR-1 (P2)	Central	67.03	62.65
	Lateral	39.12	30.32		Lateral	79.36	65.01
	Corner	37.14	29.21		Corner	85.22	60.18

Notes:  $J_{5\%}$  = secant tensile stiffness at 5% strain; The values of  $J_{5\%}$  are mean values at each specimen location.

(MD and CMD considered) the statistical significance was the same for both  $T_{max}$  and  $J_{5\%}$  variations (Tables 5, 7). In this sense, it should be noted that reduction factors are commonly applied only to  $T_{max}$  in design, although some statistically significant variations in  $J_{5\%}$  were observed (Table 7). No statistically significant variation in tensile stiffness was observed in the tests with GTX, except for the tests with two reinforcement layers, where increases in  $J_{5\%}$  were obtained

along the cross-machine direction. These increases can be a consequence of variations in mass per unit area of GTX in combination with the influence of the impregnation of the geotextile by dust resulting from abrasion of the gravel particles during loading. The measurement of mass per unit area of GTX after the tests confirmed its impregnation by gravel dust. The impregnation of nonwoven geotextiles can increase their tensile stiffness, as observed by Mendes et al.

**Table 7.** Statistical significance of tensile stiffness variation.

Test	Direction	$J_{5\%-v}$ (kN/m)	$J_{5\%}$ (kN/m)	Significance
GTX-1	MD	31.54	30.30	NS
	CMD	23.84	30.09	NS
GTX-1 (R)	MD	31.54	32.61	NS
	CMD	23.84	23.00	NS
GTX-2	MD	31.54	30.15	NS
	CMD	23.84	29.96	S
GTX-2 (R)	MD	31.54	37.37	NS
	CMD	23.84	28.76	S
MGR-1	MD	80.20	66.51	S
	CMD	59.12	52.33	S
MGR-2	MD	80.20	62.32	S
	CMD	59.12	49.87	S
MGR-1 (P1)	MD	80.20	66.72	S
	CMD	59.12	54.37	S
MGR-1 (P2)	MD	80.20	77.20	NS
	CMD	59.12	62.61	NS

Notes:  $J_{5\%-v}$  = secant tensile stiffness at 5% strain of virgin specimens;  $J_{5\%}$  = secant tensile stiffness at 5% strain after the test; NS = not statistically significant with 95% confidence level; S = statistically significant with 95% confidence level.

(2007). On the other hand, significant reductions in tensile stiffness were noted in tests on MGR in both directions, except for test MGR-1(P2), where a heavier (900 g/m<sup>2</sup>) protective geotextile layer was used between the reinforcement and the cap. This result shows that heavy nonwoven geotextiles would be required for an effective protection of the reinforcement layer. It can be noted in Figure 2a that tearing of the geogrid reinforcement took place despite the presence of a geotextile protective layer, which was also torn along the cap perimeter. The image in this figure suggests that a light geotextile may have been used for protection, and its failure corroborates what was observed in the present study regarding the need for heavier protective geotextile layers.

#### 4. Reduction factors

The results of the tensile tests carried out on virgin and damage reinforcement specimens allow the evaluation of reduction factors for tensile strength and stiffness for the reinforcements tested. The reduction factors are defined as:

$$RF_T = \frac{T_{max-v}}{T_{max}} \quad (1)$$

$$RF_{J5\%} = \frac{J_{5\%-v}}{J_{5\%}} \quad (2)$$

Where  $RF_T$  = reduction factor for tensile strength,  $RF_{J5\%}$  = reduction factor for tensile stiffness (secant, at 5% tensile strain),  $T_{max-v}$  = tensile strength of virgin reinforcement,  $T_{max}$  = tensile strength of damaged reinforcement,  $J_{5\%-v}$  = tensile

stiffness of virgin reinforcement and  $J_{5\%}$  = tensile stiffness of damaged reinforcement.

The reduction factors for the different reinforcements tested are presented in Figure 7. In general, rather similar values of reduction factors were obtained in machine and cross-machine directions, ranging from 1.03 to 1.74 for  $RF_T$  and from 1.04 to 1.29 for  $RF_{J5\%}$  (considering only values greater than 1), depending on the direction considered (MD or CMD). It should be pointed out that values of  $RF_T$  slightly greater than one could just be considered as one, since the statistical analysis did not show any relevant difference between tensile strengths of virgin and damaged specimens in these cases. However, values between 1.27 and 1.74 can be noted because of statistically relevant consequences of damages in the reinforcements after the tests. A few values of reduction factors smaller than one were observed in the case of geotextiles and this may be attributed to more significant variations of masses per unit area of the geotextiles at the locations where the specimens were collected in comparison with the average mass per unit area and, to some extent, the influence of geotextile impregnation by soil particles, as commented before.

Values of reduction factors commonly used in design to account for mechanical damages in geotextiles depend on the soil type, soil particle dimensions and shape, construction characteristics and geotextile mass per unit area (Jewell & Greenwood, 1988; Azambuja, 1994). In comparison with the gravel particle sizes in the present study, except for reinforcement GG, all the other reinforcements can be considered similar to geotextiles. For such cases, Figure 8a shows the variation of  $RF_T$  with reinforcement mass per unit area for tests with unprotected reinforcements. It can be noted that the lighter the reinforcement the greater the reduction factor obtained.

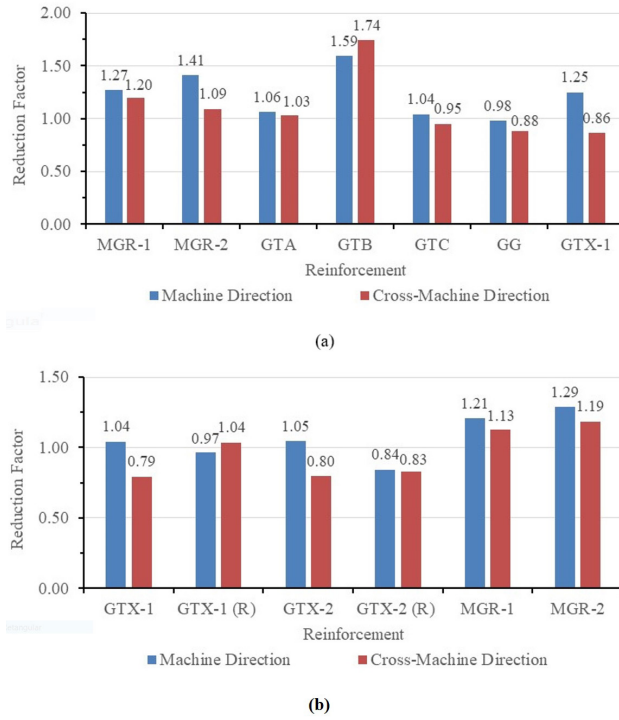


**Figure 7.** Reduction factors: (a) for tensile strength; (b) for tensile stiffness at 5% tensile strain.

Despite some scatter, the reduction factor value tends to unity for masses per unit area greater than 150 g/m<sup>2</sup> for the scaling conditions of the tests. This suggests the need for much heavier geotextiles under prototype conditions. Despite the smaller number of test results, the same pattern of larger values of  $RF_{J5\%}$  (1.04 to 1.29) for smaller masses per unit area can be noted in Figure 8b.

A similar trend of results can be observed when the reduction factors are plotted against the reinforcement tensile strength under virgin conditions ( $T_{max-v}$ ) for unprotected reinforcements, as shown in Figure 9. There is also a trend of reduction  $RF_T$  and  $RF_{J5\%}$  with increasing  $T_{max-v}$ . This behavior would be expected also for the nonwoven geotextiles tested, since the tensile strength of nonwoven, needle-punched, geotextiles is proportional to its mass per unit area.

The values of reduction factors back analyzed for reinforcement MGR with protective nonwoven geotextile layers are depicted in Figure 10 as a function of the protective layer mass per unit area ( $M_p$ ). It can be noted that the geotextile protective layers were effective in reducing the effects of damages to MGR on its reinforcement strength (Figure 10a), bearing in mind that the differences between tensile strengths of damaged and virgin reinforcements did not have statistical significance (Table 5). However, that was not the case for the variations in tensile stiffness of MGR protected by the lighter geotextile (Figure 10b and Table 7). Despite the limited number of experimental data, the results obtained

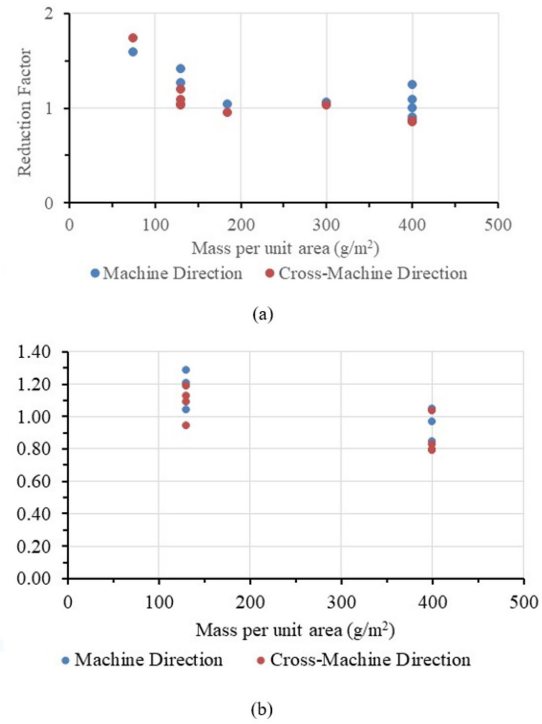


**Figure 8.** Reduction factors for tensile strength for geotextile like reinforcements versus mass per unit area: (a)  $RF_T$ ; (b)  $RF_{J5\%}$ .

suggest that nonwoven geotextile protective layers heavier than 450 g/m<sup>2</sup>, for the test scale) would be necessary. Under prototype conditions, a mass per unit area of the protective layer larger than 2000 g/m<sup>2</sup> would be recommended.

## 5. Mechanical damage index

It would be expected the effects of the mechanical damage to a tensioned and deformed geosynthetic reinforcement in contact with a mechanically aggressive rigid body edge to be a function of the geosynthetic surface characteristics, reinforcement tensile force, loading type (cyclic or static), inclination of the reinforcement with the horizontal direction at the reinforcement-edge contact (Figure 1a) and surface characteristics of the body edge. A dimensionless index to try to assess the level of reinforcement mechanical damage under such conditions can be expressed as:

$$MDI = \zeta_{es} \zeta_{rs} \zeta_l \frac{T}{T_{max-v}} \theta \quad (3)$$

Where  $MDI$  = mechanical damage index,  $T$  = expected mobilized reinforcement tensile force (undamaged conditions),  $T_{max-v}$  = reinforcement tensile strength under virgin conditions,  $\theta$  = inclination (in radians) of the reinforcement with the horizontal direction at the reinforcement-edge contact point

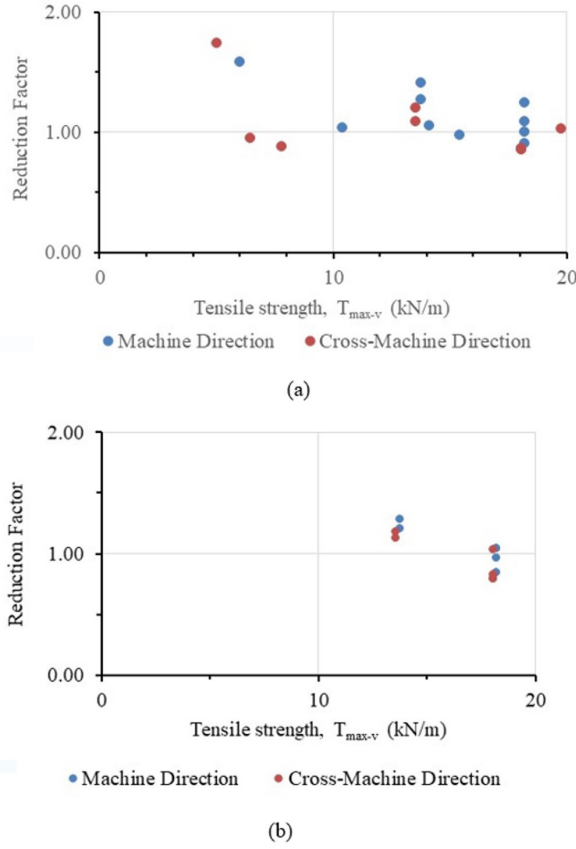


**Figure 9.** Reduction factors versus reinforcement tensile strength: (a)  $RF_T$ ; (b)  $RF_{J5\%}$ .

(Figure 1a),  $\zeta_{es}$  = parameter to account for the aggressiveness of the body edge,  $\zeta_l$  = parameter to consider the type of loading (=1 for static permanent loading and > 1 for cyclic loading) and  $\zeta_{rs}$  = parameter to account for reinforcement surface characteristics (level of protection against damages).

The value of  $T$  can be obtained as a function of the expected reinforcement strain at the contact between reinforcement and cap edge and the tensile stiffness of the reinforcement. In analytical methods for geosynthetic reinforced piled embankments the value of  $T$  is commonly obtained as a function of the average reinforcement tensile strain, which is smaller than that value at the reinforcement-cap (or pile head) edge. The value of  $\theta$  can be estimated based on the deformed shape of the reinforcement between caps. Analytical methods usually assume a parabolic or a catenary deformed shape for the reinforcement (BSI, 2010; Sloan 2011; Zhuang et al., 2014; van Eekelen, 2015, for instance). Fonseca et al. (2018) found little difference between predictions from these two shapes. The parameters  $\zeta_{es}$ ,  $\zeta_{rs}$  and  $\zeta_l$  should be equal or greater than one and determined from a large number of tests with different loading types and reinforcement and body edge surface conditions (smooth, rough, beveled etc.).

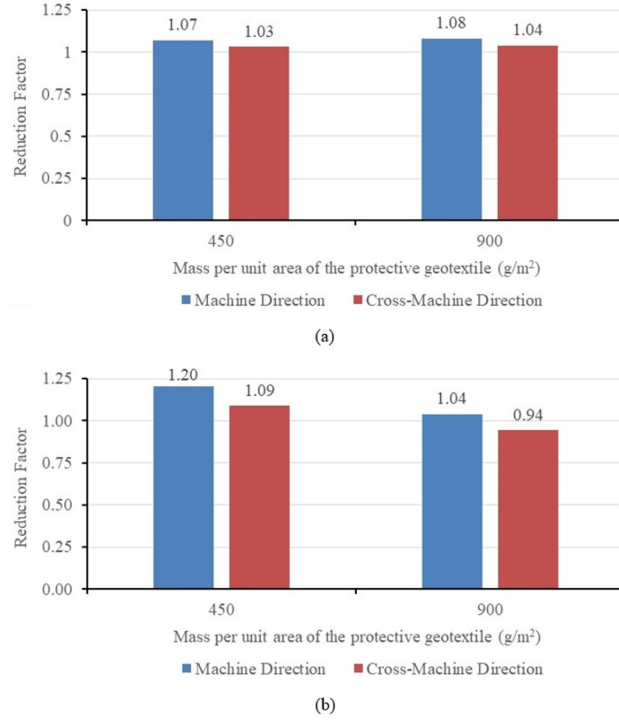


**Figure 10.** Reduction factors for geotextile protected reinforcement MGR: (a)  $RF_T$ ; (b)  $RF_{J5\%}$ .

In the present study, the value of  $T$  used in Equation 3 was estimated based on the average reinforcement strain ( $\epsilon$ ) measured during the tests (Melchior Filho, 2022 and Fonseca & Palmeira, 2018) and the reinforcement tensile stiffness ( $J$ ,  $T = \epsilon J$ ). For the sake of simplicity, in the present study the values of  $\zeta_{es}$ ,  $\zeta_{rs}$  and  $\zeta_l$  are assumed as equal to 1. The angle  $\theta$  (expressed in radians) was calculated by the following expression for a parabolic deformed shape of the reinforcement between caps:

$$\theta = \tan^{-1} \left( \frac{4\delta_{max}}{s-a} \right) \quad (4)$$

Where  $\delta_{max}$  = maximum reinforcement settlement between caps,  $s$  = centre to centre distance between caps and  $a$  = cap width.

Figure 11 shows the variation of reduction factors for tensile strength ( $RF_T$ ) with  $MDI$  for unprotected and geotextile protected reinforcements from tests with a single layer of reinforcement. The results in this figure show  $RF_T$  values close to unity for  $MDI$  smaller than 0.08. Above this value a greater scatter of  $RF_T$  values can be noted with  $RF_T$  values between 1 and 1.74. Despite the rather limited number of results, larger values of  $RF_T$  are noted for larger  $MDI$  values. Values of the former very close to unity were obtained for the geotextile protected reinforcements and values of  $MDI$

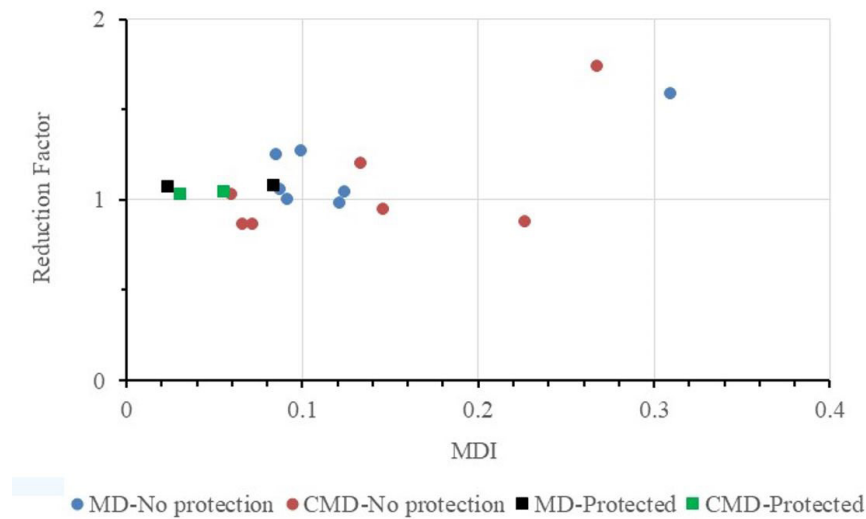


**Figure 11.** Reduction factor  $RF_T$  versus  $MDI$  for protected and unprotected reinforcements.

between 0.02 and 0.08. For the unprotected reinforcements, the results suggest that values of  $RF_T$  greater than 1.8 should be employed in designs where the reinforcement will be in contact with the cap or pile head for large values of  $MDI$ . Bearing in mind that monotonic loading was used in the tests carried out in this research, larger reduction factors would be necessary in case of cyclic loadings or for thinner fill layers.

## 6. Conclusions

This paper presented the results of an investigation aiming at quantifying the mechanical damage to geosynthetic reinforcements in reinforced piled embankment applications. The results and conclusions obtained may be extended to other situations of geosynthetic reinforcement in contact with mechanically aggressive rigid bodies. The main conclusions obtained in this investigation are summarized as follows.

Different intensities of damage were identified depending on the type and properties of the reinforcement tested and the damages influenced the values of reinforcement tensile strength and stiffness. Back analyzed reduction factors for the conditions of the tests varied between values slightly smaller than one and 1.74. The values smaller than one obtained are attributed to variations in mass per unit of the specimens in comparison to the average mass per unit area. In practice, reduction factor values must be greater than one. The larger the values of reinforcement mass per unit area of geotextile like reinforcements the smaller the back analyzed reduction factors for tensile strength and stiffness. These reduction factors also decreased with increasing tensile strength of the reinforcement under virgin conditions.

The protection of the reinforcement with a nonwoven geotextile layer was effective in reducing the mechanical damages, with back analyzed reduction factors for tensile

strength smaller than 1.08 under the conditions of the tests. The statistical analysis showed no statistical relevance for the differences between tensile strengths of virgin and damaged reinforcements in tests with geotextile protection. However, in terms of prototype conditions, heavy nonwoven geotextiles will be required for an effective protection of the reinforcement against mechanical damages. The results obtained in the present work suggest that values of mass per unit area larger than 2000 g/m<sup>2</sup> under prototype conditions should be employed, particularly bearing in mind that the caps tested in the present work were smoother and with much better finishing than those typically found in the field.

The definition of a mechanical damage index was preliminarily introduced as a function of deformed geometry of the reinforcement, mobilized tensile force, tensile strength and parameters considering the mechanical aggressiveness of the cap, reinforcement surface characteristics and loading conditions. The ranges of possible values for the latter three parameters remain to be established based on a larger number of tests under different conditions. For the test conditions of the present work, a satisfactory correlation was observed between the mechanical damage index and the required reduction factor for reinforcement tensile strength.

The results obtained in this research highlight the importance of the use of appropriate reduction factors to account for the effects of mechanical damages of the reinforcement. This is particularly relevant in the case of repeated loading conditions, which can occur still during embankment construction, as well as for the durability and proper performance of the reinforcement during the project service life. Further research on appropriate values of reduction factors to be used in case of repeated loading is certainly necessary. Although the use of protective nonwoven geotextile layers between the reinforcement and the pile cap may be



effective, heavy geotextile layers are required. In this context, the installation of the reinforcement some distance above the cap is safer and even so appropriate reduction factors must be employed. Eventually, besides the use of reduction factors, the use of protective geotextile layers may also be recommendable depending on the project characteristics.

## Acknowledgements

The authors are indebted to the University of Brasília and to the National Council for Scientific and Technological Development (CNPq) for their support for the research activities described in this paper.

## Declaration of interest

The authors have no conflicts of interest to declare. All co-authors have observed and affirmed the contents of the paper and there is no financial interest to report.

## Authors' contributions

Ennio Marques Palmeira: conceptualization, methodology, visualization, formal analysis, writing – review & editing. José Melchior Filho: conceptualization, supervision, data gathering, data validation, formal analysis, writing – original draft. Ewerton Clayton Alves Fonseca: conceptualization, supervision, data gathering, data validation, formal analysis, writing – review & editing.

## List of symbols and abbreviations

$a$	Pile cap width (mm)
$C_u$	Soil uniformity coefficient (dimensionless)
$D_n$	Diameter for which $n$ (%) in mass of the remaining particles have smaller diameters (mm)
$G_s$	Soil particle specific gravity (dimensionless)
$J_{5\%}$	Secant tensile stiffness at 5% strain of damaged reinforcement (kN/m)
$J_{5\%-v}$	Secant tensile stiffness at 5% strain of virgin reinforcement (kN/m)
$M_A$	Geosynthetic mass per unit area (g/m <sup>2</sup> )
$T$	Mobilized reinforcement tensile load (kN/m)
$T_{max}$	Tensile strength of damaged reinforcement (kN/m)
$T_{max-v}$	Tensile strength of virgin (undamaged) reinforcement (kN/m)
$RF_T$	Reduction factor for tensile strength (dimensionless)
$RF_{J5\%}$	Reduction factor for tensile stiffness at 5% strain (dimensionless)
$s$	Pile spacing (mm)
$\delta_{max}$	Maximum settlement of the reinforcement between caps (mm)
$\gamma_d$	Dry soil unit weight (kN/m <sup>3</sup> )
$\phi'$	Soil friction angle (degrees)

$\theta$	Inclination of the reinforcement to the horizontal at the contact with the cap (radians)
$\zeta_l$	Parameter for loading type (dimensionless)
$\zeta_{es}$	Parameter for cap edge surface (dimensionless)
$\zeta_{rs}$	Parameter for reinforcement surface (dimensionless)


## References

- ABNT NBR 6458. (2016). *Gravel grains retained on the 4,8 mm mesh sieve – Determination of the bulk specific gravity, apparent specific gravity and water absorption*. ABNT - Associação Brasileira de Normas Técnicas, Rio de Janeiro, RJ (in Portuguese).
- ABNT NBR 7181. (2016). *Soil – Grain Size Analysis*. ABNT - Associação Brasileira de Normas Técnicas, Rio de Janeiro, RJ (in Portuguese).
- Abusharar, S.W., Zheng, J.-J., Chen, B.-G., & Yin, J.-H. (2009). A simplified method for analysis of piled embankment reinforced with geosynthetics. *Geotextiles and Geomembranes*, 27(1), 39-52. <http://dx.doi.org/10.1016/j.geotexmem.2008.05.002>.
- Almeida, M.S.S., & Marques, M.E.S. (2011). Construction methods in Brazilian extremely soft soils. In *Proceedings of the Pan-Am CGS Geotechnical Conference* (16 p.). Toronto, Ontario, Canada.
- Al-Taie, E.T., Al-Kalali, H.H., & Fattah, M.Y. (2019). Evaluation of settlement and bearing capacity of embankment on soft soil with reinforced geogrids. *International Journal of Engineering Research & Technology (Ahmedabad)*, 8(6), 99-103. <http://dx.doi.org/10.17577/IJERTV8IS060044>.
- Austin, R. (1997). The effect of installation activities and fire exposure on geogrid performance. *Geotextiles and Geomembranes*, 15(4-6), 367-376. [http://dx.doi.org/10.1016/S0266-1144\(98\)80009-5](http://dx.doi.org/10.1016/S0266-1144(98)80009-5).
- ASTM D6637. (2015). *Standard test method for determining tensile properties of geogrids by the single or multi-rib tensile method*. ASTM International, West Conshohocken, PA.
- ASTM D4595. (2017). *Standard test method for tensile properties of geotextiles by the wide-width strip method*. ASTM International, West Conshohocken, PA.
- Azambuja, E. (1994). *Investigação do dano mecânico em geotêxteis não tecidos* [Masters dissertation]. Universidade Federal do Rio Grande do Sul.
- Bathurst, R.J., & Miyata, Y. (2015). Reliability-based analysis of combined installation damage and creep for the tensile rupture limit state of geogrid reinforcement in Japan. *Soil and Foundation*, 55(2), 437-446. <http://dx.doi.org/10.1016/j.sandf.2015.02.017>.
- BSI BS 8006. (2010). *Code of practice for strengthened/reinforced soils and other fills*. British Standards Institution, United Kingdom.
- Cho, S.D., Lee, K.W., Cazzuffi, D.A., & Jeon, H.Y. (2006). Evaluation of combination effects of installation damage and creep behavior on long-term design strength of

- geogrids. *Polymer Testing*, 25(6), 819-828. <http://dx.doi.org/10.1016/j.polymertesting.2006.04.007>.
- EBGEO. (2011). *Recommendations for design and analysis of earth structures using geosynthetic reinforcements - EBGEO*. Germany: EBGEO.
- Fattah, M.Y., Zabar, B.S., & Hassan, H.A. (2015). Soil arching analysis in embankments on soft clays reinforced by stone columns. *Structural Engineering and Mechanics*, 56(4), 507-534. <http://dx.doi.org/10.12989/sem.2015.56.4.507>.
- Fattah, M.Y., Mohammed, H.A., & Hassan, H.A. (2016a). Load transfer and arching analysis in reinforced embankment. *Structures and Buildings, Proceedings - Institution of Civil Engineers*, 169(11), 797-808. <http://dx.doi.org/10.1680/jstbu.15.00046>.
- Fattah, M.Y., Zabar, B.S., & Hassan, H.A. (2016b). Experimental analysis of embankment on ordinary and encased stone columns. *International Journal of Geomechanics*, 16(4), 04015102. [http://dx.doi.org/10.1061/\(ASCE\)GM.1943-5622.0000579](http://dx.doi.org/10.1061/(ASCE)GM.1943-5622.0000579).
- Federal Highway Administration – FHWA. (2017). *Ground modification methods reference manual* (Vol. 2, No. FHWA-NHI-16-028, 542 p.). Washington: Federal Highway Administration, US Department of Transportation.
- Filz, G.M., & Smith, M.E. (2006). *Design of bridging layers in geosynthetic-reinforced column-supported embankments* (46 p.). Charlottesville, VA, USA: Virginia Transportation Research Council.
- Filz, G.M., & Smith, M.E. (2007). Net vertical loads on geosynthetics reinforcement in column-supported embankments. In *Proceedings of the Soil Improvement* (Geotechnical Special Publication, No. 172). Reston, VA, USA: Geo-Institute of ASCE. [http://dx.doi.org/10.1061/40916\(235\)1](http://dx.doi.org/10.1061/40916(235)1).
- Fleury, M.P., Santos, E.C.G., Lins da Silva, J., & Palmeira, E.M. (2019). Geogrid installation damage caused by recycled construction and demolition waste. *Geosynthetics International*, 26(6), 641-656. <http://dx.doi.org/10.1680/jgein.19.00050>.
- Fonseca, E.C.A. (2017). *Estudo experimental do comportamento de aterros estacados reforçados com geossintéticos* [PhD thesis]. Departamento de Engenharia Civil e Ambiental, Universidade de Brasília.
- Fonseca, E.C.A., & Palmeira, E.M. (2018). Evaluation of the accuracy of design methods for geosynthetic reinforced piled embankments. *Canadian Geotechnical Journal*, 56(6), 761-773. <http://dx.doi.org/10.1139/cgj-2018-0071>.
- Fonseca, E.C.A., Palmeira, E.M., & Barrantes, M.V. (2018). Load and deformation mechanisms in geosynthetic-reinforced piled embankments. *International Journal of Geosynthetics and Ground Engineering*, 4(32), 1-12. <http://dx.doi.org/10.1007/s40891-018-0150-x>.
- Gonzalez-Torre, I., Calzada-Perez, M.A., Vega-Zamanillo, A., & Castro-Fresno, D. (2014). Damage evaluation during installation of geosynthetics used in asphalt pavements. *Geosynthetics International*, 21(6), 377-386. <http://dx.doi.org/10.1680/gein.14.00025>.
- Hsieh, C. W., & Wu, J. H. (2001). Installation survivability of flexible geogrids in various pavement subgrade materials. *Transportation Research Record: Journal of the Transportation Research Board*, 1772(1), 190-196. <http://dx.doi.org/10.3141/1772-23>.
- Huang, C.C. (2006). Laboratory simulation of installation damage of a geogrid. *Geosynthetics International*, 13(3), 120-132. <http://dx.doi.org/10.1680/gein.2006.13.3.120>.
- Hufenus, R., Ruegget, R., & Flum, D. (2002). Geosynthetics for reinforcement – resistance to damage during installation. In D. Cazzuffi, J. Greenwood, M. Heibbaum, D. Leshchinsky & F. Tatsuoka (Eds.), *Proceedings of the 7th International Conference on Geosynthetics* (Vol. 2, pp. 1387-1390). USA: International Geosynthetics Society (IGS).
- Jewell, R.A., & Greenwood, J.H. (1988). Long term strength and safety in steep soil slopes reinforced by polymer materials. *Geotextiles and Geomembranes*, 7(1-2), 81-118. [http://dx.doi.org/10.1016/0266-1144\(88\)90020-9](http://dx.doi.org/10.1016/0266-1144(88)90020-9).
- Low, B.K., Tang, S.K., & Choa, V. (1994). Arching in piled embankments. *Journal of Geotechnical Engineering*, 120(11), 1917-1938. [http://dx.doi.org/10.1061/\(ASCE\)0733-9410\(1994\)120:11\(1917\)](http://dx.doi.org/10.1061/(ASCE)0733-9410(1994)120:11(1917)).
- Melchior Filho, J. (2022). *Estudo da interação solo-reforço geossintético em aterros estacados por meio de ensaios de grandes dimensões* [PhD thesis]. University of Brasília (in progress).
- Mendes, M.J.A., Palmeira, E.M., & Matheus, E. (2007). Some factors affecting the in-soil load–strain behaviour of virgin and damaged nonwoven geotextiles. *Geosynthetics International*, 14(1), 39-50. <http://dx.doi.org/10.1680/gein.2007.14.1.39>.
- Pinho-Lopes, M., Paula, A.M., & Lopes, M.L. (2018). Long-term response and design of two geosynthetics: effect of field installation damage. *Geosynthetics International*, 25(1), 98-117. <http://dx.doi.org/10.1680/jgein.17.00036>.
- Richardson, G. (1998). Field evaluation of geosynthetic survivability in aggregate road base. *Geotechnical Fabrics Report*, 16(7), 34-38.
- Rosete, A., Mendonça Lopes, P., Pinho-Lopes, M., & Lopes, M.L. (2013). Tensile and hydraulic properties of geosynthetics after mechanical damage and abrasion laboratory tests. *Geosynthetics International*, 20(5), 358-374. <http://dx.doi.org/10.1680/gein.13.00022>.
- Russel, D., & Pierpoint, N. (1997). *An assessment of design methods for piled embankments* (Ground Engineering, Vol. 30, No. 10, pp. 39-44). London, United Kingdom: EMAP Construct Limited.
- Sloan, J.A. (2011). *Column-supported embankments: full-scale tests and design recommendations* [PhD thesis]. Virginia Polytechnic Institute and State University.
- Sloan, J.A., Filz, G.M., & Collin, J.G. (2011). A generalized formulation of the adapted Terzaghi method of arching in column-supported embankments. In J. Han & D.

- E. Alzamora (Eds.), *Proceedings of the Geo-Frontiers: Advances in Geotechnical Engineering* (Geotechnical Special Publication, No. 211, pp. 798-805). Reston, VA, USA: Geo-Institute of ASCE. [http://dx.doi.org/10.1061/41165\(397\)82](http://dx.doi.org/10.1061/41165(397)82).
- van Eekelen, S.J.M. (2015). *Basal reinforced piled embankments* [PhD thesis]. Technical University of Delft.
- van Eekelen, S.J.M. (2016). The 2016-update of the dutch design guideline for basal reinforced piled embankments. *Procedia Engineering*, 143, 582-589. <http://dx.doi.org/10.1016/j.proeng.2016.06.077>.
- Yoo, H., Jeon, H.Y., & Chang, Y.C. (2009). Evaluation of engineering properties of geogrids for soil retaining walls. *Textile Research Journal*, 80(2), 184-192. <http://dx.doi.org/10.1177/0040517508093442>.
- Zhuang, Y., Wang, K.Y., & Liu, H.L. (2014). A simplified model to analyze the reinforced piled embankments. *Geotextiles and Geomembranes*, 42(2), 154-165. <http://dx.doi.org/10.1016/j.geotexmem.2014.01.002>.

## Soil-water characteristic curve of polypropylene fibre-reinforced sandy soil

Cíntia Lopes de Castro<sup>1#</sup> , Anderson Borghetti Soares<sup>1</sup> ,

Marcos Fábio Porto de Aguiar<sup>2</sup> 

Article

### Keywords

Fibre reinforcement  
Soil-water characteristic curve  
Filter paper technique  
Matric suction

### Abstract

Fibre reinforcement is considered a good alternative for improving the geotechnical properties of soil. However, studies that investigate its behaviour, accounting for the unsaturated condition, and the hydraulic behaviour of soil mixtures with fibre, are limited. Therefore, the current study evaluates the impact of the inclusion of polypropylene fibres on the hydraulic behaviour of soil through geotechnical characterisation, scanning electron microscopy (SEM), macroporosity and microporosity tests, and filter paper tests. The soil-water characteristic curve (SWCC) of different mixtures of fibre-reinforced soil was adjusted by the models enshrined in the literature, using polypropylene fibres of length 6 mm, diameter 18  $\mu$ m, and fibre contents 0.25% (SF025), 0.75% (SF075), 1.0% (SF100), and 1.25% (SF125) relative to the dry weight of the soil. The results indicated a transition from unimodal to bimodal shape in the SWCC for the polypropylene fibre-reinforcement, suggesting that their inclusion altered the soil structure. The same bimodal behaviour of SWCC was observed in all reinforced samples that produced similar values of air-entry suction and residual volumetric water content, but with increased water retention for the same level of suction for higher fibre content. The results of the tension table test indicated an increase in the volume of macropores with an increase in fibre content and a decrease in micropore volumes. These results agree with the compaction tests, which showed a decrease in the dry maximum density with an increased fibre content, whereas the optimum water content increased.

## 1. Introduction

Applying polypropylene fibres to layers of soil in geotechnical projects, such as landfills on soft soils, slopes, and covers for sanitary landfills or surface foundations, improve the mechanical behaviour of these structures, particularly through increased strength, ductility, and tenacity, and in limiting post-peak reduction in resistance (Al-Refeai, 1991; Consoli et al., 2009; Yilmaz, 2009; Falorca & Pinto, 2011; Olgun, 2013; Chen et al., 2015; Festugato et al., 2017; Mirzababaei et al., 2018).

Fibre-reinforced soils are subjected to variations in moisture on site, often in their unsaturated state. However, studies investigating the hydromechanical behaviour of fibre-reinforced soils under unsaturated conditions are limited (Al-Mahbashi et al., 2020). Therefore, the study of this condition is important and necessary to understand the behaviour to determine their geotechnical properties.

The soil-water characteristic curve (SWCC), also referred to as the retention curve, is a key property for implementing unsaturated soil mechanics in engineering practice. The SWCC is a measure of the variations in the water storage capacity within the macropores and micropores of the soil undergoing matric suction variation (Fredlund et al., 2012). Malekzadeh & Bilsel (2014) investigated the effects of including polypropylene fibres in the SWCC of expansive soil. The results showed that fibre-reinforcement increased the adhesion between soil particles and the air-entry suction values.

Several in situ and laboratory techniques can be used to measure the suction. Different suction measurement techniques have been employed by Southen & Kerry Rowe (2007), Miguel & Bonder (2012), and Priono et al. (2016). Among them, the filter paper technique has been widely used to obtain the SWCC of porous materials because suction measurements can be easily performed at a low cost, and a wide suction interval can be measured (Leong et al., 2002).

#Corresponding author. E-mail address: cintia.civil@gmail.com

<sup>1</sup>Universidade Federal do Ceará, Departamento de Engenharia Hidráulica e Ambiental, Fortaleza, CE, Brasil.

<sup>2</sup>Instituto Federal de Educação, Ciência e Tecnologia do Ceará, Fortaleza, CE, Brasil.

Submitted on April 30, 2021; Final Acceptance on May 10, 2022; Discussion open until November 30, 2022.

<https://doi.org/10.28927/SR.2022.070021>



This is an Open Access article distributed under the terms of the Creative Commons Attribution License, which permits unrestricted use, distribution, and reproduction in any medium, provided the original work is properly cited.

The filter paper test is performed by placing the soil in contact with a filter paper that can absorb the water in the soil until a certain balance condition is attained, such that the matric potentials of water in the soil and porous material are equal.

SWCC may be influenced by various factors, such as void ratio, soil type, soil structure, particle size distribution, stress state, mineralogy, degree of weathering, and pore size distribution (Yang et al., 2004; Zhou & Jian-lin, 2005; Priono et al., 2016).

Moreover, SWCCs may display unimodal and bimodal shapes (Burger & Shackelford, 2001; Li & Zhang, 2009; Satyanaga et al., 2013; Li et al., 2014; Wijaya & Leong, 2017). Unimodal curves exhibit a single desaturation stretch, whereas bimodal curves display two stretches of desaturation, and consequently exhibit two air-entry values: the first corresponds to a pore family of relatively large pores and the second to another family of small pores (Gitirana Junior & Fredlund, 2004).

Generally, bimodal SWCC is attributed to double porosity in the soil, which may appear as a result of the bimodal distribution of the particle sizes, compaction, or other characteristics such as cracks in the earth (Li & Zhang, 2009; Satyanaga et al., 2013; Li et al., 2014). In soils with double porosity, the pores are largely governed by the layout of coarse and fine particles, resulting in large (macropores) and small pores (micropores), respectively (Burger & Shackelford, 2001).

The SWCC is obtained by adjusting the experimental points using mathematical equations. Many researchers have proposed adjustment models that are valid for certain soil types and suction ranges (Van Genuchten, 1980; Fredlund & Xing 1994; Gitirana Junior & Fredlund, 2004).

Gitirana Junior & Fredlund (2004) proposed a set of equations, which includes the adjustment of bimodal curves with two air-entry values and two residual points. The other models can be adapted to bimodal curves using the equations for two stretches joined by junction suction, that is, considering two unimodal curves. Various equations for adjusting the unimodal and bimodal characteristic curves and for determining the adjustment parameters have been proposed by Satyanaga et al. (2013), Li et al. (2014), Wijaya & Leong (2016), and Leong (2019).

The current study presents the behaviour of the SWCC of polypropylene fibre-reinforced soil, based on the results of an experimental program developed with a mixture of sandy soil with different polypropylene fibre contents, and investigates the influence of the fibres on the hydraulic behaviour of mixtures. Fibre reinforcement in sandy soil can affect the structure of the composite, changing the macro and microporosity, and consequently, the mechanical and hydraulic properties, such as the saturated permeability, unsaturated permeability, and soil-water retention (SWR) curve. These changes in the structure result in different drainage conditions and water retention capacities, which are fundamental to the

performance of unsaturated soils, such as landfill waste cover, foundations, and slopes with reinforced soils.

## 2. Materials and methods

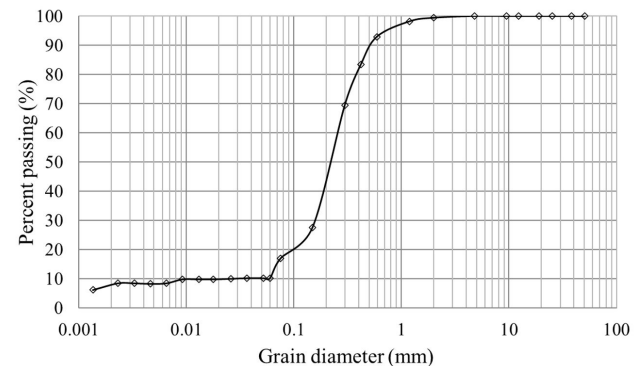
The soil used in the study was collected from the Geotechnics and Foundations Test Field (GECEF), Federal University of Ceará (UFC) in Fortaleza, Ceará State, Northeast Brazil. Disturbed samples were collected at a depth of 10 cm using shovel and picks, and thereafter they were sent to the laboratory and packed in plastic bags in sufficient quantities for reinforcement with fibres, according to NBR 6457 (ABNT, 2016a).

Table 1 presents the results of the geotechnical characterisation of the soil and grading curve, according to NBR 7181 (ABNT, 2016c), ASTM D7928 (ASTM, 2021b), and ASTM D6913 (ASTM, 2017b), as shown in Figure 1. This soil was classified as poorly graded silty sand (SM-SP) according to the Unified Soil Classification System (USCS). The liquid limit, NBR 6459 (ABNT, 2017), plastic limit, NBR 7180 (ABNT, 2016b), and ASTM D4318 (ASTM, 2017a), indicate that the soil has non-plastic (NP) characteristics.

The polypropylene fibre contents analysed were 0% (SN), 0.75% (SF075), 1.0% (SF100), and 1.25% (SF125) of the dry weight of the soil. The polypropylene fibres used in this study consisted of extremely fine filaments produced through an extrusion process. The fibres were of length 6 mm, diameter 18  $\mu\text{m}$ , specific weight 0.91  $\text{g}/\text{cm}^3$ , tensile

**Table 1.** Physical properties of soil.

Property	Value
Specific gravity	2.56
Coarse sand ( $0.6 < \text{diameter} < 2 \text{ mm}$ )	7.0%
Medium sand ( $0.2 < \text{diameter} < 0.6 \text{ mm}$ )	51.0%
Fine sand coefficient ( $0.06 < \text{diameter} < 0.2 \text{ mm}$ )	32.0%
Silt ( $0.002 < \text{diameter} < 0.06 \text{ mm}$ )	2.0%
Clay ( $\text{diameter} < 0.002 \text{ mm}$ )	8.0%
Uniformity coefficient ( $C_u$ )	28.9
Curvature coefficient ( $C_c$ )	12.4



**Figure 1.** Particle size distribution curve.



shear strength 300 MPa, elastic modulus 3 GPa, and shear elongation of 80%, with a circular section (Figure 2).

## 2.1 Experimental program

The experimental program included compaction characterisation tests, filter paper tests, scanning electron microscopy (SEM), and macroporosity and microporosity tests.

### 2.1.1 Sample preparation

To homogenise the material, the dry components of the mixture (soil and fibre) were first manually mixed, after which water was added, and the mixture was visually verified. The compaction test according to NBR 7182 (ABNT, 2020) and ASTM D698 (ASTM, 2021a), with normal Proctor energy, was performed for the natural soil and soil–fibre mixtures, and test samples were moulded using the values obtained for the optimum water content ( $w$ ) and corresponding maximum dry unit weights ( $\gamma_{d, \max}$ ), which are provided in Table 2. Figure 3 shows the compaction curves obtained for the natural soil and soil–fibre mixtures.

The test samples were compacted inside aluminium rings of diameter 5 cm and height 2 cm to attain the density corresponding to the maximum dry apparent specific weight. Figure 3 shows an increase in the optimum water content and a reduction in the maximum dry weight by increasing the fibre content. This behaviour in the compaction curves was observed for mixtures of natural fibre with different soils

by Oliveira Junior (2018) and Ayala (2020), indicating an increase in the porosity of the mixture.

### 2.1.2 Filter paper technique

The filter paper technique was adopted according to ASTM D 5298 (ASTM, 2016). A Whatman No. 42 filter paper was placed directly from the box over the sample surface. Curves were obtained by drying the samples. After the equalisation period between the filter paper and the seven-day soil, the gravimetric moisture of the filter paper was measured, and the matric suction ( $\Psi$ ) was obtained from the calibration equations proposed by Chandler et al. (1992), as follows, in Equations 1 and 2:

For filter paper moisture < 47%:

$$\Psi \text{ (kPa)} = 10^{4.842 - 0.0622w} \quad (1)$$

For filter paper moisture > 47%:

$$\Psi \text{ (kPa)} = 10^{6.050 - 2.48 \text{ Log} w} \quad (2)$$

The samples were homogenised at the optimal water content and dynamically compacted into three layers in a metallic ring of diameter 5 cm and height 2 cm. The filter paper technique is suitable for suction values between 10–29000 kPa (Marinho, 1994).



Figure 2. Polypropylene fibres.

Table 2. Parameters of compaction curves.

Sample	w (%)	$\gamma_{d, \max}$ (kN/m <sup>3</sup> )
N	9.6	19.09
SF025	10.5	18.60
SF075	10.6	18.31
SF100	11.3	18.18
SF125	11.5	17.95

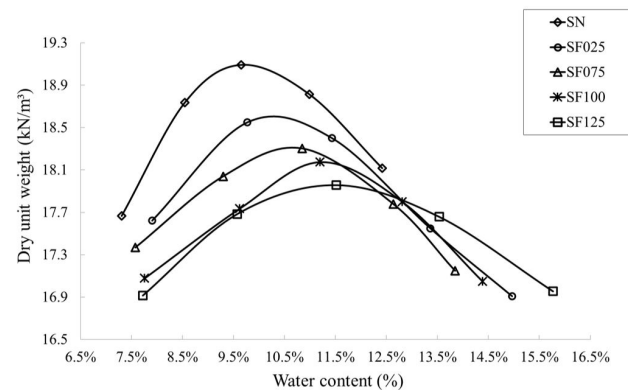


Figure 3. Compaction curves.

### 2.1.3 Soil-water characteristic curve functions

The models proposed by Fredlund & Xing (1994) and Gitirana Junior & Fredlund (2004) (hereafter referred to as FX and GF, respectively) were applied to obtain the adjusted SWCC using the experimental points obtained from the filter paper technique. The equation proposed by Fredlund & Xing (1994) was applied to unimodal SWCCs; however, bimodal SWCCs can be obtained by adaptation, considering the equation applied to two unimodal curves connected by junction suction. Gitirana Junior & Fredlund (2004) proposed an equation for bimodal SWCCs defined by two air-entry values and two residual points, resulting in four curve inflection points.

### 2.1.4 SEM

SEM was used to visualise the soil structure and analyse the shape, distribution, soil–fibre adhesion, and connection between the voids inside the tested samples. Pictures of the samples were enlarged to 120 times their actual size. The samples under analysis were first compacted in a ring of diameter 5 cm and height 2 mm, and dried in an oven at 105 °C.

### 2.1.5 Macro and microporosity testing

The macroporosity and microporosity of the soil samples were determined using a stress table (EMBRAPA, 1997), which is fast, simple, easy to use, and common in agricultural sciences.

In this method, a stress corresponding to a 60 cm high water column, that is, 6 kPa, is applied to the saturated samples, which would cause the water to drain from the macropores. The application of a tension of 6 kPa in sandy soils is sufficient to drain water in the macropores and retain the water in the micropores (Teixeira et al., 2017). After drainage, the samples were oven-dried at 105 °C, and the micropore percentage was determined, corresponding to the remaining water in the soil. The difference between the saturated water percentage (total porosity) and the micropore percentage provides the macropore percentage, as the total porosity is the sum of the macropore and micropore percentages of the soil sample.

## 3. Analysis and results

### 3.1 Soil-water characteristic curve

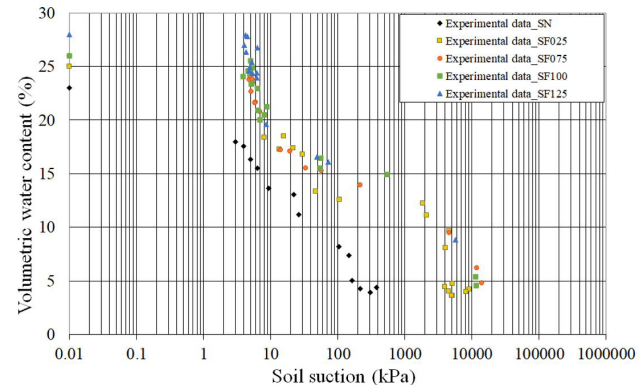
The SWCC obtained by drying the natural soil and soil–fibre mixtures was expressed in terms of suction and volumetric water content. Figure 4 shows the experimental filter paper test results for the natural soil sample and soil–fibre mixtures. The experimental points obtained from the filter paper method for natural soil were observed to tend toward unimodal behaviour, whereas the soil–fibre samples

exhibit a bimodal shape in the SWCC, suggesting that the macrostructure and microstructure of the soil were affected by the inclusion of fibres, resulting in a change in the hydraulic behaviour of the samples.

The SWCCs were adjusted using the FX and GF methods. Figure 5 shows SWCC for the natural soil. The adjustments by both methods used were approximate, indicating that the air-entry suction value was less than 1 kPa and the residual volumetric water content was approximately 2.5%. These values are typical of sandy soils, and agree with the results reported by Fredlund & Xing (1994).

Figures 6 to 9 show the SWCC of the fibre-reinforced soil for the analysed fibre contents (0.25%, 0.75%, 1.0%, and 1.25%, respectively) adjusted by the FX and GF methods. Although a marginal dispersion of the experimental data was identified, the models were adequate, because it was possible to identify the shape of the SWCCs.

Tables 3 and 4 show the parameters adopted for the mathematical adjustment using the equations proposed by Fredlund & Xing (1994) and Gitirana Junior & Fredlund (2004) describing the unimodal SWCCs of the natural soil and bimodal SWCCs of the soil–fibre mixtures. The results revealed that the SWCCs behaved similarly and agreed significantly with the behaviour of the experimental points obtained from the filter paper test. A significant aspect of the



**Figure 4.** Experimental points obtained from the filter paper test on natural soil and soil–fibre mixture.

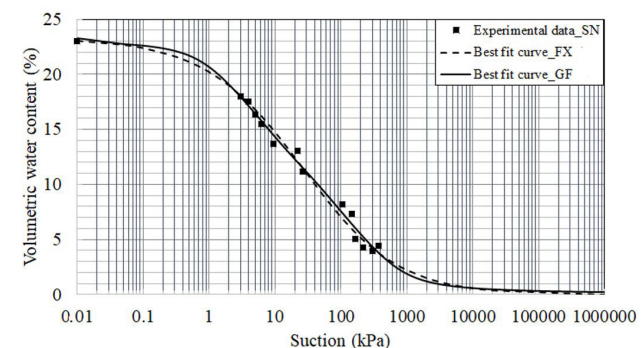


**Figure 5.** SWCC-natural soil.

SWCC analysis is the change in the curve behaviour from unimodal to bimodal shape when the soil is reinforced with polypropylene fibres, suggesting that the macrostructure and microstructure of the soil were affected by the fibre inclusion. The bimodal behaviour of SWCC was observed by Abdallah et al. (2019) in sandy soil (with fines) and lint wool residues.

The analysis of the water retention curves revealed that an increase in the volumetric water content was observed

for the same suction with an increase in the fibre content (Figure 10). This behaviour was also observed in fibre–soil mixtures with clayey and sandy soils and natural and synthetic fibres (Saad, 2016; Gusmão, 2020; Gusmão & Jucá, 2021; Abdallah et al., 2019; Ayala, 2020).

### 3.2 SEM

Figure 11 shows the micrograph results of the compacted samples of the natural soil (Figure 10a) and

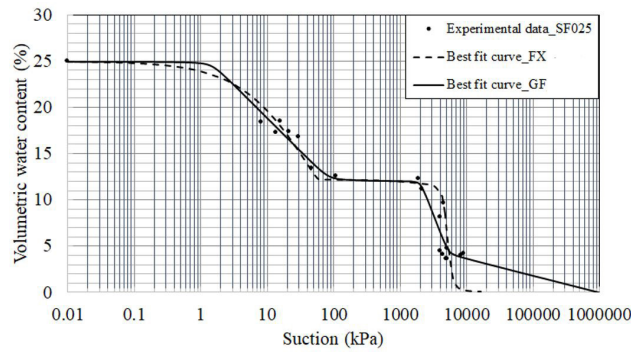


Figure 6. SWCC-SF025.

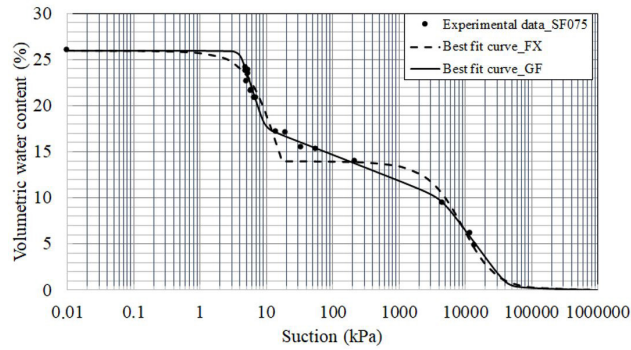


Figure 7. SWCC-SF075.

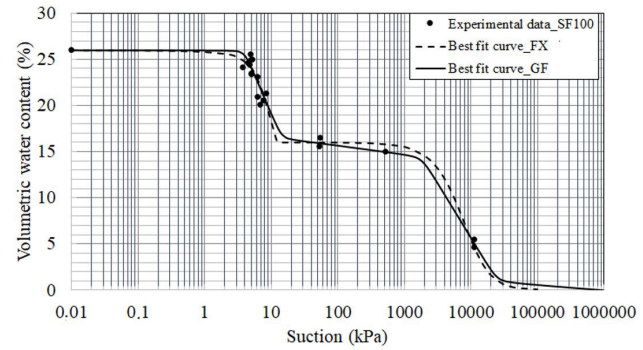


Figure 8. SWCC-F100.

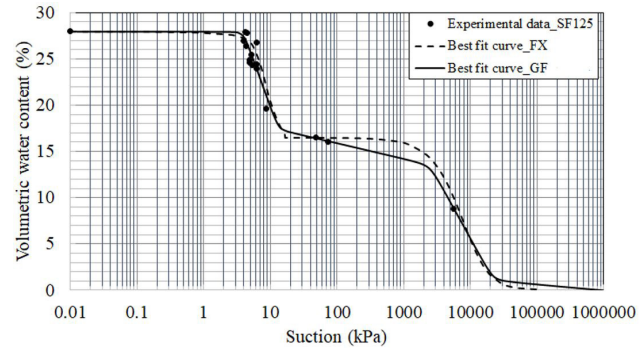


Figure 9. SWCC-SF125.

**Table 3.** Adjustment parameters of the equation proposed by Fredlund & Xing (1994) for the behaviour of the soil–fibre samples.

Sample	Macropores				Micropores			
	$a$ (kPa)	$n$	$m$	$\Psi_r$ (kPa)	$a'$	$n'$	$m'$	$\Psi_r$ (kPa)
SN	29	0.56	2.7	1100	--	--	--	--
SF025	31	0.78	1.68	50	5000	12.1	1.97	11800
SF075	9.5	2.19	0.87	15	10000	1.9	3.62	30000
SF100	7.2	3.68	0.51	12	10000	1.77	3.6	30000
SF125	6.4	6.27	0.25	16.5	10000	1.72	3.71	30000

**Table 4.** Adjustment parameters of the equation proposed by Gitirana Junior & Fredlund (2004) for the behaviour of the soil–fibre samples.

Sample	$\Psi_{bl}$ (kPa)	$\Psi_{rl}$ (kPa)	$\theta_{rl}$ (%)	$\Psi_{b2}$ (kPa)	$\theta_b$ (%)	$\Psi_{r2}$ (kPa)	$\theta_{r2}$ (%)	$a$
SN	1.6	670	0.025	--	--	--	--	0.093
SF025	1.45	84.43	12.1	2031.7	12.1	5293.4	4.15	0.020
SF075	4	9.319	17.52	4410.6	10.2	42275	0.26	0.022
SF100	4	14.19	16.41	1836.4	14.56	24740.2	0.88	0.022
SF125	4	13.06	17.4	2506.6	13.6	21993.3	1.04	0.020



soil–fibre mixtures (Figure 10b–10d). The morphological characteristics indicating the texture, structure, and adhesion between materials can be observed.

The micrograph of natural soil illustrates the presence of voids and irregularly shaped particles. In the micrograph of the soil–fibre mixtures, soil clusters were predominant, causing apparently larger voids compared to those formed in the natural soil. The fibre agglomerations hinder the connection and interlocking between the soil particles, and little adhesion of the materials is observed.

Moreover, the polypropylene fibres disposed in random directions interfere with the continuity of the pores, thereby increasing the desaturation path and the capacity to retain

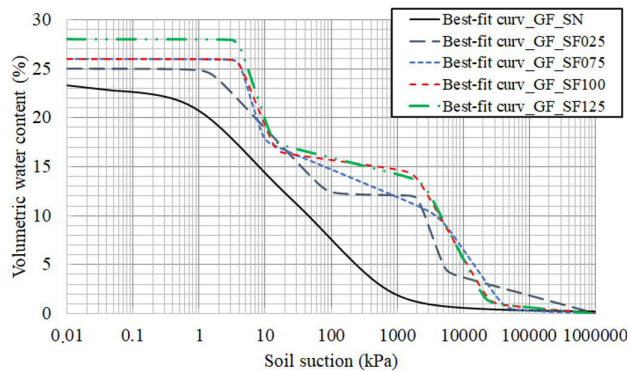


Figure 10. SWR curves with different fibre contents.

macropores. These characteristics justify the increased total porosity of the soil–fibre mixtures and confirm the change in the soil structure, causing an alteration in the shape of the SWCC. In all cases, agglomeration of fibres with large voids was verified, which may explain the macroporosity observed in the tests.

### 3.3 Analysis of macroporosity and microporosity

Macroporosity and microporosity were determined using the stress table method to investigate the relationship between the macropores and micropores of the reinforced samples. Figure 12 shows the test results as percentages of macropores and micropores. The microporosity percentage was significantly higher (approximately 80%) than the macroporosity percentage (approximately 20%). This result was expected, because the amount of added fibre was relatively small compared to that of soil in the sample. These results agree with the compaction curves, which show that increasing the fibre content in the mixture decreased the maximum apparent specific weight and increased the optimal water content.

In addition, the soil was predominantly composed of medium to fine sand, as confirmed in the particle size analysis, thus possibly resulting in the formation of a larger number of small voids, that is, micropores. A sharp increase in macroporosity was observed with the increase in fibre

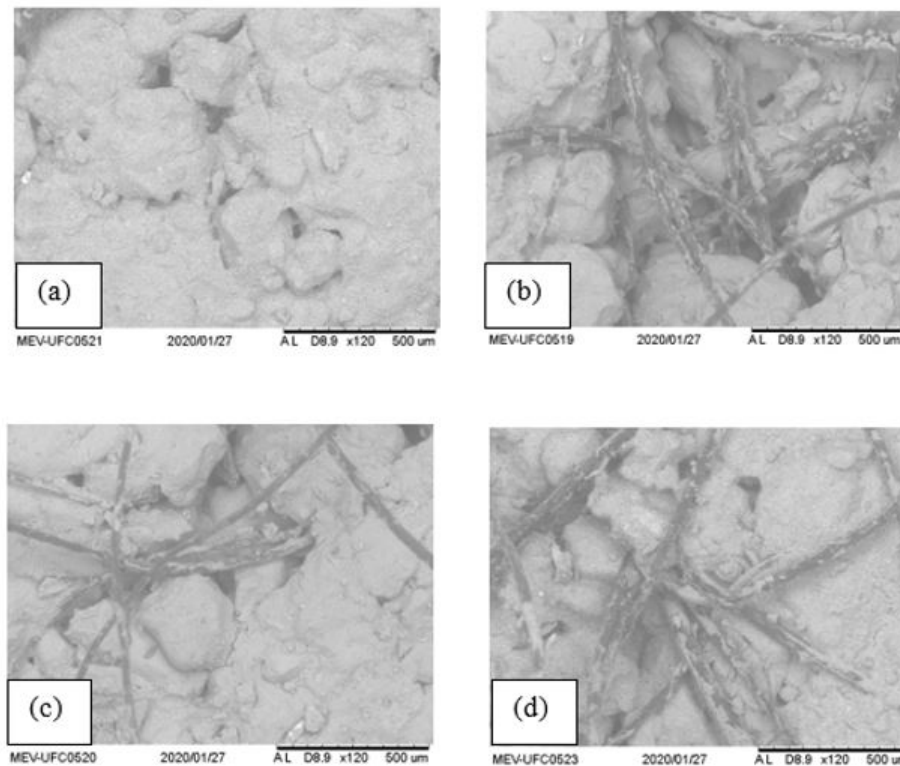
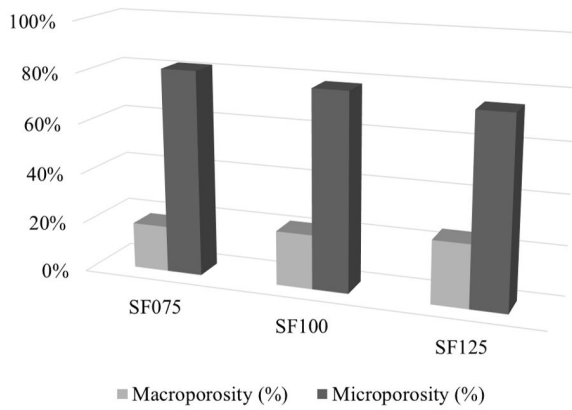


Figure 11. SEM micrograph results ( $\times 120$ ): (a) natural soil; soil–fibre mixtures: (b) SF075, (c) SF100 (d) SF125.



**Figure 12.** Results of the macroporosity and microporosity test.

content, as expected, because the increase in fibre content resulted in the increase of the porosity of the mixture.

#### 4. Conclusion

The geotechnical properties of soil–fibre mixtures are important in geotechnical engineering. Therefore, determining the physical properties of the composites is necessary. The inclusion of fibre in the soil can affect the soil structure and the hydromechanical properties of the composite. This study aimed to evaluate the effect of the addition of propylene fibre to sandy soils on the SWCCs.

The compaction curves showed that the inclusion of propylene fibre resulted in a decrease in the maximum dry weight and an increase in the optimum water content, indicating an increase in the soil porosity. Through SEM, a considerable quantity of voids and irregularity in the shape of the soil particles could be identified. The soil–fibre samples demonstrated a predominance of soil and fibre agglomerations, with apparently larger voids compared to the natural soil. At the soil–fibre interface, a significant number of voids and regions with little adhesion to the materials were apparent, with the formation of fibre clusters that hinder the connection and interlocking between the soil particles and fibres. The results of the macroporosity and microporosity tests using the stress table indicated that the increase in the fibre content in the soil increased the macroporosity of the reinforced samples.

The SWCCs of the natural soil and the soil–polypropylene fibre mixtures were derived from the experimental points obtained through the filter paper technique, and adjusted by the GF method, as it was closer to the experimental points obtained. The results showed that when the soil was reinforced with fibres, the SWCC changed from unimodal to bimodal shape for the fibre contents studied, suggesting that the macrostructure and microstructure of the soil were influenced by the inclusion of fibres, which consequently influenced the hydromechanical behaviour of the soil. Furthermore, an increase in volumetric water content was observed for the

same suction with an increase in fibre content. The results of this study are limited to the SWCC and structure of propylene fibre–soil mixtures, and further research is required to study the complete hydraulic parameters, such as unsaturated and saturated permeabilities, and mixtures with different types of soils and fibres.

#### Acknowledgements

The authors thank Maccaferri for the donation of the polypropylene fibres used in the study, the soil mechanics laboratory team of the Federal Institute of Education, Science and Technology of Ceará (IFCE), and the Federal University of Ceará (UFC), for their support in performing the tests.

#### Declaration of interest

The authors declare that there are no conflicts of interest regarding the publication of this paper.

#### Authors' contributions

Cíntia Lopes de Castro: conceptualisation, methodology, validation, writing - original draft. Anderson Borghetti Soares: supervision, validation, writing - review & editing. Marcos Fábio Porto de Aguiar: supervision, validation, writing—review & editing.

#### List of symbols

$a, a'$	SWCC adjustment parameter;
$m, m'$	SWCC adjustment parameter;
$n, n'$	SWCC adjustment parameter;
SWCC	Soil-water characteristic curve;
$w$	Optimum water content;
$\gamma_{d, max}$	Maximum dry specific weight;
$\theta$	Volumetric water content
$\theta_b$	Volumetric water content at air-entry value;
$\theta_r$	Volumetric water content in residual state
$\theta_{r1}$	First volumetric water content in residual state
$\theta_{r2}$	Second volumetric water content in residual state.
$\Psi$	Matric suction;
$\Psi_b$	Air-entry value;
$\Psi_{b1}$	First air-entry value
$\Psi_{b2}$	Second air-entry value
$\Psi_r$	Residual state of air-entry value
$\Psi_{r1}$	Residual state of first of air-entry value
$\Psi_{r2}$	Residual state of second air-entry value

#### References

- Abdallah, A., Ugolini, F., Baronti, S., Maienza, A., Camilli, F., Bonora, L., Marteli, F., Primicerio, J., & Ungaro, F. (2019). Potential of recycling wool residues as an



- amendment for enhancing the physical and hydraulic properties of sandy loam soil. *International Journal of Recycling of Organic Waste in Agriculture*, 8(Suppl. 1), 131-143. <http://dx.doi.org/10.1007/s40093-019-0283-5>.
- ABNT NBR 6457. (2016a). *Soil samples - Preparation for compaction and characterization tests*. ABNT - Associação Brasileira de Normas Técnicas, Rio de Janeiro, RJ (in Portuguese).
- ABNT NBR 7180. (2016b). *Soil - Plasticity limit determination*. ABNT - Associação Brasileira de Normas Técnicas, Rio de Janeiro, RJ (in Portuguese).
- ABNT NBR 7181. (2016c). *Soil - Grain size analysis*. ABNT - Associação Brasileira de Normas Técnicas, Rio de Janeiro, RJ (in Portuguese).
- ABNT NBR 6459. (2017). *Soil - Liquid limit determination*. ABNT - Associação Brasileira de Normas Técnicas, Rio de Janeiro, RJ (in Portuguese).
- ABNT NBR 7182. (2020). *Soil - Compaction test*. ABNT - Associação Brasileira de Normas Técnicas, Rio de Janeiro, RJ (in Portuguese).
- Al-Mahbashi, A.M., Al-Shamrani, M.A., & Moghal, A.A.B. (2020). Soil–water characteristic curve and one-dimensional deformation characteristics of fiber-reinforced lime-blended expansive soil. *Journal of Materials in Civil Engineering*, 32(6), 04020125-1-04020125-9. [https://doi.org/10.1061/\(ASCE\)MT.1943-5533.0003204](https://doi.org/10.1061/(ASCE)MT.1943-5533.0003204).
- Al-Refeai, T.O. (1991). Behavior of granular soils reinforced with discrete randomly oriented inclusions. *Geotextiles and Geomembranes*, 10(4), 319-333. [http://dx.doi.org/10.1016/0266-1144\(91\)90009-L](http://dx.doi.org/10.1016/0266-1144(91)90009-L).
- ASTM D5298-03. (2016). *Standard Test Method for Measurement of Soil Potential (Suction) Using Filter Paper*. ASTM International, West Conshohocken, PA.
- ASTM D4318. (2017a). *Standard Test Methods for Liquid limit, Plastic limit and Plastic Index of soils*. ASTM International, West Conshohocken, PA.
- ASTM D6913. (2017b). *Standard Test Methods for Particle-size Distribution (Gradation) of Soils Using the Sieve Analysis*. ASTM International, West Conshohocken, PA.
- ASTM D698:12. (2021a). *Standard Test Methods for Laboratory Compaction Characteristics of Soils using Standard Effort*. ASTM International, West Conshohocken, PA.
- ASTM D7928. (2021b). *Standard Test Methods for Particle-size Distribution of Fine-Grained soils using the sedimentation analysis*. ASTM International, West Conshohocken, PA.
- Ayala, R.J.L. (2020). *Melhoria de Solos com Fibras Provenientes da Indústria Avícola* [Doctoral thesis]. Departamento de Engenharia Civil e Ambiental, Universidade de Brasília.
- Burger, C.A., & Shackelford, C.D. (2001). Soil-water characteristic curves and dual porosity of sand–diatomaceous earth mixtures. *Journal of Geotechnical and Geoenvironmental Engineering*, 127(9), 790-800. [http://dx.doi.org/10.1061/\(ASCE\)1090-0241\(2001\)127:9\(790\)](http://dx.doi.org/10.1061/(ASCE)1090-0241(2001)127:9(790)).
- Chandler, R.J., Crilly, M.S., & Montgomery-Smith, G. (1992). A low cost method of assessing clay desiccation for low-rise buildings. *Proceedings of the Institution of Civil Engineers. Civil Engineering*, 92(2), 82-89. <http://dx.doi.org/10.1680/icien.1992.18771>.
- Chen, M., Shen, S.L., Arulrajah, A., Wu, H.N., Hou, D.W., & Xu, Y.S. (2015). Laboratory evaluation on the effectiveness of polypropylene fibers on the strength of fiber-reinforced and cement-stabilized Shanghai soft clay. *Geotextiles and Geomembranes*, 43(6), 515-523. <http://dx.doi.org/10.1016/j.geotexmem.2015.05.004>.
- Consoli, N.C., Festugato, L., & Heineck, K.S. (2009). Strain-hardening behaviour of fibre-reinforced sand in view of filament geometry. *Geosynthetics International*, 16(2), 109-115. <http://dx.doi.org/10.1680/gein.2009.16.2.109>.
- Empresa Brasileira de Pesquisa Agropecuária – EMBRAPA. (1997). *Manual de métodos de análise de solos* (2. ed., 212 p). Rio de Janeiro/RJ: Embrapa Solos.
- Falorca, I.M.C.F.G., & Pinto, M.I.M. (2011). Effect of short, randomly distributed polypropylene microfibres on shear strength behaviour of soils. *Geosynthetics International*, 18(1), 2-11. <http://dx.doi.org/10.1680/gein.2011.18.1.2>.
- Festugato, L., Menger, E., Benezra, F., Kipper, E.A., & Consoli, N.C. (2017). Fibre-reinforced cemented soils compressive and tensile strength assessment as a function of filament length. *Geotextiles and Geomembranes*, 45(1), 77-82. <http://dx.doi.org/10.1016/j.geotexmem.2016.09.001>.
- Fredlund, D.G., & Xing, A. (1994). Equations for the soil-water characteristic curve. *Canadian Geotechnical Journal*, 31(4), 521-532. <http://dx.doi.org/10.1139/t94-061>.
- Fredlund, D.G., Rahardjo, H., & Fredlund, M.D. (2012). *Unsaturated soil mechanics in engineering practice* (926 p.). New Jersey: John Wiley and Sons.
- Gitirana Junior, G.F.N., & Fredlund, D.G. (2004). Soil-water characteristic curve equation with independent properties. *Journal of Geotechnical and Geoenvironmental Engineering*, 130(2), 209-211. [http://dx.doi.org/10.1061/\(ASCE\)1090-0241\(2004\)130:2\(209\)](http://dx.doi.org/10.1061/(ASCE)1090-0241(2004)130:2(209)).
- Gusmão, L.R.C. (2020). *Influência de ciclos secagem-molhagem no comportamento hidráulico-mecânico de misturas compactadas de solo argiloso com fibras de coco verde* [Master's dissertation]. Programa de Pós-Graduação em Engenharia Civil, Universidade Federal de Pernambuco.
- Gusmão, L.R.C., & Jucá, J.F.T. (2021). Influence of green's coconut fiber in unsaturated behavior of compacted clayey soil. *MATEC Web of Conferences*, 337, 01017. <https://doi.org/10.1051/mateconf/202133701017>.
- Leong, E.C. (2019). Soil-water characteristic curves – Determination, estimation and application. *Japanese Geotechnical Society Special Publication*, 7(2), 21-30. <http://dx.doi.org/10.3208/jgssp.v07.003>.
- Leong, E.C., He, L., & Rahardjo, H. (2002). Factors affecting the filter paper method for total and matric suction

- measurements. *Geotechnical Testing Journal*, 25(3), 321-332. <http://dx.doi.org/10.1520/GTJ11094J>.
- Li, X., & Zhang, L.M. (2009). Characterization of dual-structure pore-size distribution of soil. *Canadian Geotechnical Journal*, 46(2), 129-141. <http://dx.doi.org/10.1139/T08-110>.
- Li, X., Li, J.H., & Zhang, L.M. (2014). Predicting bimodal soil-water characteristic curves and permeability functions using physically based parameters. *Computers and Geotechnics*, 57, 85-96. <http://dx.doi.org/10.1016/j.compgeo.2014.01.004>.
- Malekzadeh, M., & Bilsel, H. (2014). Hydro-mechanical behavior of polypropylene fiber reinforced expansive soils. *KSCE Journal of Civil Engineering*, 18(7), 2028-2033. <http://dx.doi.org/10.1007/s12205-014-0389-2>.
- Marinho, F.A.M. (1994). Suction measurements with the filter paper method. In *Anais do X Congresso Brasileiro de Mecânica dos Solos e Engenharia de Fundações* (pp. 515-522). Fox do Iguaçu.
- Miguel, M.G., & Bonder, B.H. (2012). Soil-water characteristic curves obtained for a colluvial and lateritic soil profile considering the macro and micro porosity. *Geotechnical and Geological Engineering*, 30(6), 1405-1420. <http://dx.doi.org/10.1007/s10706-012-9545-y>.
- Mirzababaei, M., Arulrajah, A., Haque, A., Nimbalkar, S., & Mohajerani, A. (2018). Effect of fiber reinforcement on shear strength and void ratio of soft clay. *Geosynthetics International*, 25(4), 471-480. <http://dx.doi.org/10.1680/jgein.18.00023>.
- Olgun, M. (2013). Effects of polypropylene fiber inclusion on the strength and volume change characteristics of cement-fly ash stabilized clay soil. *Geosynthetics International*, 20(4), 263-275. <http://dx.doi.org/10.1680/jgein.13.00016>.
- Oliveira Júnior, A.I. (2018). *Comportamento geotécnico de misturas compactadas de solo argiloso com fibras curtas de coco* [Master's dissertation]. Programa de Pós-Graduação em Engenharia Civil, Universidade Federal de Pernambuco.
- Priono, Rahardjo, H., Chatterjea, K., Leong, E.C., & Wang, J.Y. (2016). Effect of hydraulic anisotropy on soil-water characteristic curve. *Soil and Foundation*, 56(2), 228-239. <http://dx.doi.org/10.1016/j.sandf.2016.02.006>.
- Saad, S.S.E. (2016). *Mechanical behavior of fibre reinforced unsaturated clay* [Doctoral thesis] University of Bradford, England.
- Satyanaga, A., Rahardjo, H., Leong, E.C., & Wang, J. (2013). Water characteristic curve of soil with bimodal grain-size distribution. *Computers and Geotechnics*, 48, 51-61. <http://dx.doi.org/10.1016/j.compgeo.2012.09.008>.
- Southen, J.M., & Kerry Rowe, R. (2007). Evaluation of the water retention curve for geosynthetic clay liners. *Geotextiles and Geomembranes*, 25(1), 2-9. <http://dx.doi.org/10.1016/j.geotexmem.2006.10.002>.
- Teixeira, P.C., Donagemma, G.K., Fontana, A., & Teixeira, W.G. (2017). *Manual de métodos de análises de solos* (3. ed., 574 p.). Brasília: Empresa Brasileira de Pesquisa Agropecuária, Centro Nacional de Pesquisa de Solos, Ministério da Agricultura e do Abastecimento.
- Van Genuchten, M.T. (1980). A closed-form equation for predicting the hydraulic conductivity of unsaturated soils. *Soil Science Society of America Journal*, 44(5), 892-898. <http://dx.doi.org/10.2136/sssaj1980.03615995004400050002x>.
- Wijaya, M., & Leong, E.C. (2016). Equation for unimodal and bimodal soil-water characteristic curves. *Soil and Foundation*, 56(2), 291-300. <http://dx.doi.org/10.1016/j.sandf.2016.02.011>.
- Wijaya, M., & Leong, E.C. (2017). Modelling the effect of density on the unimodal soil-water characteristic curve. *Geotechnique*, 67(7), 637-645. <http://dx.doi.org/10.1680/jgeot.15.P.270>.
- Yang, H., Rahardjo, H., Leong, E.C., & Fredlund, D.G. (2004). Factors affecting drying and wetting soil-water characteristic curves of sandy soils. *Canadian Geotechnical Journal*, 41(5), 908-920. <http://dx.doi.org/10.1139/t04-042>.
- Yilmaz, Y. (2009). Experimental investigation of the strength properties of sand-clay mixtures reinforced with randomly distributed discrete polypropylene fibers. *Geosynthetics International*, 16(5), 354-363. <http://dx.doi.org/10.1680/jgein.2009.16.5.354>.
- Zhou, J., & Jian-lin, Y. (2005). Influences affecting the soil-water characteristic curve. *Journal of Zhejiang University. Science*, 6A(8), 797-804. <http://dx.doi.org/10.1631/jzus.2005.A0797>.

## Prediction of soil water retention curve based on physical characterization parameters using machine learning

Enzo Aldo Cunha Albuquerque<sup>1</sup> , Lucas Parreira de Faria Borges<sup>1</sup> ,

André Luís Brasil Cavalcante<sup>1#</sup> , Sandro Lemos Machado<sup>2</sup> 

Article

### Keywords

Soil water retention curve  
Physical characterization  
parameters  
Machine learning  
Python

### Abstract

This paper explores the potential of machine learning techniques to predict the soil water retention curve based on physical characterization parameters. Results from 794 water retention and suction points obtained from 51 different soils were used in the algorithm. The soil properties used are the percentages of gravel, sand, silt, and clay, the plasticity index, the porosity, and the relation between the volumetric water content and total suction. The data were used as input for machine learning estimators to predict the volumetric water content of a soil with specified physical characterization parameters and suction, the techniques of artificial intelligence were developed in python. Results show that an extremely randomized trees' estimator can reach a coefficient of determination of 0.99 in the training dataset, with a coefficient of 0.90 in the cross-validation and testing dataset, which measures the generalization capacity. Furthermore, a continuous function can be obtained by fitting a model such as Cavalcante & Zornberg, or van Genuchten, or Costa & Cavalcante (bimodal) to the predictions of the machine learning for use in numerical methods. These results indicate that the proposed machine learning estimator can become an interesting alternative to estimate the soil water retention curve in engineering practice. This work is in progress and the predictions can be improved with the addition of new data. Know how to participate at the end of the paper.

## 1. Introduction

The soil water retention curve is a fundamental soil property that governs many agricultural, environmental, and engineering applications (Khlosi et al., 2016). However, conducting laboratory tests for soil water retention curve (SWRC) determination can be expensive and time-consuming, mainly in places located away from universities and research centers (Achieng, 2019; Haghverdi et al., 2015; Khlosi et al., 2016). An alternative for estimating this curve using physical characterization parameters such as percentage of gravel, sand, silt, clay, plasticity index (*PI*), and porosity (*n*) could contribute to a preliminary assessment of the soil water retention curve requiring less laboratory cost and time.

Other researchers developed procedures and techniques to assess or estimate the properties of unsaturated soils. Costa (2017) developed a model capable of representing the centrifuge permeameter test in order to facilitate obtaining

the hydraulic properties of a soil. He obtained the SWRC and the hydraulic conductivity of the soil requiring a shorter time compared to the filter paper and pressure plate tests and using a single moisture sensor. Arya & Paris (1981), Fredlund et al. (2002) and Vanapalli & Catana (2005) proposed models for estimating the SWRC using grain-size distribution curve and volume-mass properties.

Artificial intelligence is a novel technique that can be used for estimating the SWRC. It has been widely applied in geotechnics as examples are given. Ozelim et al. (2022) proposed a methodological framework to monitor internal erosion in dams based on artificial intelligence, which consist of processing the acoustic data obtained by geophones through artificial intelligence techniques in order to identify anomalies and classify the health status of the dam. Belcher et al. (2015), Fisher et al. (2016, 2017) investigated the erosion events, crack detection and anomaly detection in an experimental earth embankment seismic data using unsupervised, semi-supervised

\*Corresponding author. E-mail address: albrasilc@gmail.com

<sup>1</sup>Universidade de Brasília, Department of Civil and Environmental Engineering, Brasília, DF, Brasil.

<sup>2</sup>Universidade Federal da Bahia, Department of Materials Science and Technology, Salvador, BA, Brasil.

Submitted on January 6, 2022; Final Acceptance on June 14, 2022; Discussion open until November 30, 2022.

<https://doi.org/10.28927/SR.2022.000222>



This is an Open Access article distributed under the terms of the Creative Commons Attribution License, which permits unrestricted use, distribution, and reproduction in any medium, provided the original work is properly cited.

and supervised machine learning techniques. Marjanović et al. (2011) and Tien Bui et al. (2016) used machine learning approach to assess problems of landslide susceptibility.

Machine learning techniques have been used in geotechnical engineering to predict engineering properties of soils based on previously known index properties. Some studies were performed in this subject to predict the compression index of soft soils from the Brazilian coast (Oliveira Filho et al., 2020), to define soil classes by the similarity of the CPT measurements (Carvalho & Ribeiro, 2019, 2020), to predict friction capacity of driven piles in cohesive soil (Prayogo & Susanto, 2018), to construct a site-specific multivariate probability distribution model of soil characteristics using Bayesian machine learning and hybridization between site-specific and generic data (Ching & Phoon, 2019).

Concerning the SWRC prediction using characterization results, one can cite the use of k-nearest-neighbors and sand, silt, and clay percentages and soil bulk density on samples from Belgium and UNSODA database to derive a pedotransfer function (PTF) for van Genuchten's (1980) equation (Haghverdi et al., 2015); support vector machine (SVM) was also employed using a variety of parameters based on 72 samples from Syria to predict PTF at some SWRC points (Khlosi et al., 2016) and SVM and neural networks were applied to suction data to predict the SWRC for one loamy sand soil (Achieng, 2019).

This paper explores the potential use of machine learning techniques, such as extremely randomized trees, random forest, decision trees, logistic regression, support vector machine, multi-layer perceptron, and k-nearest neighbors, to predict the soil water retention curve for different soil types using physical characterization parameters. The database contains 794 measured SWRC points (main drying branch) and related soil characterization properties carried out on a wide variety of soils compiled by the authors. This dataset is divided into training, cross-validation, and test sets used, respectively, to fit, select and evaluate the model. Then, Cavalcante's & Zornberg's (2017), van Genuchten's (1980) and Costa & Cavalcante (2021) functions are fitted to machine learning prediction to obtain a continuum function that can be used in other applications, such as numerical calculus. This study fits the Ordinance number

1.122 from Ministry of Science, Technology, Innovations and Communications from Brazil (Brasil, 2020), which establishes priorities for research, development, and innovation projects to enable technologies such as artificial intelligence to contribute to the innovation base on intensive products in scientific and technological knowledge.

## 2. Materials and methods

### 2.1 Materials

All the compiled dataset containing the SWRC points and the corresponding characterization properties was filtered from the Environmental Geotechnics Laboratory (GEOAMB) (UFBA, 2022) of the Federal University of Bahia (UFBA). Table 1 presents variables' statistical properties. Most of the soil samples are sandy soils, with low percentages of gravel. There are some samples with high clay and silt content. The mean plasticity index is near 13% and only few soils present plasticity above 21%. The samples have porosity between 0.24 and 0.69. The suction covers from 0 up to  $4.10^4$  kPa. Figure 1 illustrates all the SWRC points of the dataset. It can be noted that most points are in the central region of the graph.

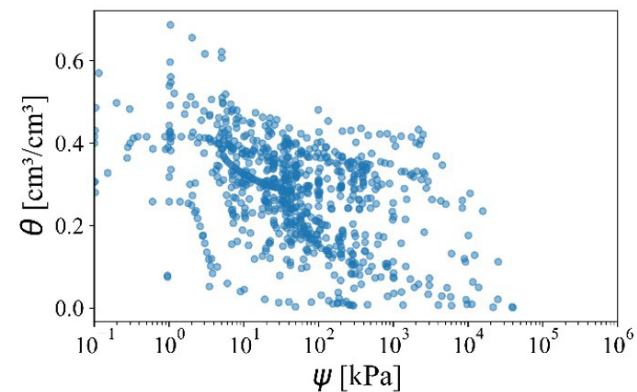


**Figure 1.** All dataset points in one graph of volumetric water content against suction.

**Table 1.** Statistical description of the selected 794 samples.

Variable	Mean	Standard deviation	Minimum	25% <sup>a</sup>	50% <sup>a</sup>	75% <sup>a</sup>	Maximum
Sand (%)	52.22	27.48	1.00	32.00	55.00	73.00	100.00
Clay (%)	26.97	23.00	0.00	8.25	22.00	45.17	89.00
Silt (%)	21.14	16.55	0.00	9.00	19.00	29.30	85.00
Gravel (%)	0.62	1.24	0.00	0.00	0.00	0.08	5.00
Plasticity index (%)	12.78	12.84	0.00	3.00	9.00	21.00	58.00
Porosity	0.48	0.10	0.24	0.42	0.49	0.54	0.69
Volumetric water content, $\theta$ (cm <sup>3</sup> /cm <sup>3</sup> )	0.28	0.12	0.00	0.20	0.30	0.37	0.69
Suction, $\psi$ (kPa)	617.29	2856.69	0.00	10.74	42.17	199.35	39605.60

<sup>a</sup>Quantiles.

The dataset doesn't have all features available. In some experiments, the granulometry, or the plasticity index weren't measured. Within the entire database of the 794 points, there were missing 11 points without percentages of sand, and silt, 37 points without plasticity index, filling with the average value of the attribute was done to solve this. More information about the dataset is available in: <https://geoapps/swrc-ai/report/>

## 2.2 Methods

The potential of machine learning to predict the soil water retention curve was investigated by developing estimators in Python using the scikit-learn library (Pedregosa et al., 2011). Other tools used to subsidize were: pandas (McKinney, 2010), NumPy (Oliphant, 2006), matplotlib (Hunter, 2007), jupyter notebook (Kluyver et al., 2016), and anaconda navigator (Anaconda, 2016).

An overview of the method is shown in Figure 2, adapted from Scikit-learn (2021), it is a typical cross-validation workflow in model training. To develop and choose the machine learning model, the training was done on the training set, after which the evaluation was done on the cross-validation set. When the experiments seem to be successful, the final evaluation was done on the test set (Géron, 2019).

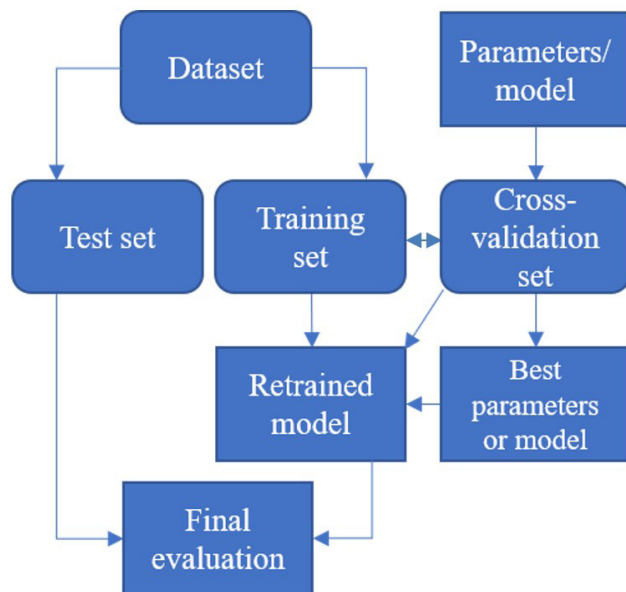
To avoid overfitting, a common practice when performing a supervised machine learning experiment is to hold out part of the available data as a test set. Here, 20% of the data (159 points) were used (Géron, 2019; Scikit-learn, 2021). The data were randomly divided into training and test set using a stratified shuffle split because most suction data are between  $10^2$  and  $10^3$  kPa. This creates divisions that preserve the same percentage in each interval of suctions defined in

Figure 3 and allows to assess generalization performance across the entire suction range.

It's necessary for most machine learning estimators that the data are scaled, and the missing ones are filled. They can misbehave if the individual features do not more or less resemble standard normally distributed data (Géron, 2019). So, the data were scaled by standardization, removing the mean and scaling to unit variance. Only 1.4% of the sand and silt percentages data and 4.6% of plasticity index data were missing, as it was a small amount, this was adjusted by filling in with the mean value of each feature.

When evaluating different estimators or different hyperparameter settings of estimators, there is still a risk of overfitting on the test set because the estimators can be chosen by the test performance or the parameters can be tweaked until the model performs optimally (Géron, 2019). This way, knowledge about the test can be part of the model, and evaluation metrics no longer report on generalization performance (Scikit-learn, 2021). To solve this problem, another part of the dataset was held out. This part is the cross-validation set, and the evaluation was done using the 5-fold cross-validation (Breiman & Spector, 1992). The hyperparameter space was searched to achieve the best cross-validation score, using the grid search cross-validation to exhaustively consider all parameter combinations provided and select the best combination.

As an example, some hyperparameters of a decision tree are: *min\_samples\_split*, minimum number of samples a node must have before it can be split; *min\_samples\_leaf*, minimum number of samples a leaf node must have; *max\_features*, maximum number of features that are evaluated for splitting at each node. The *n\_estimators*, *random\_state*, *ccp\_alpha* hyperparameters controls the number of decision trees ensemble, the randomness, and the pruning of the trees, respectively. Increasing *min\_samples\_split*, or *min\_samples\_leaf* or *ccp\_alpha* hyperparameters or reducing



**Figure 2.** Flowchart of a typical cross-validation workflow.

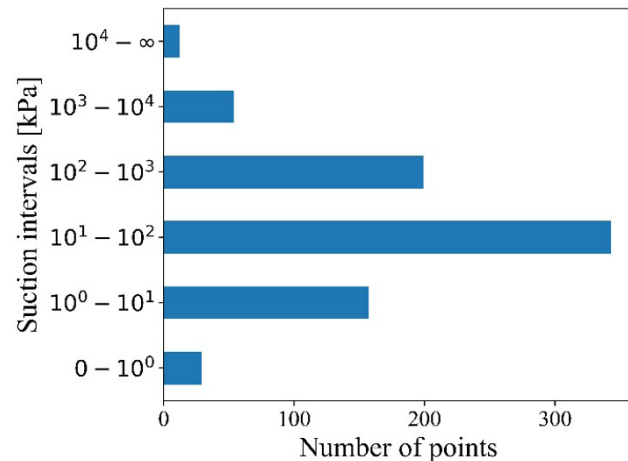


**Figure 3.** Suction intervals of all the datasets.



*max\_features* hyperparameter will regularize the model (Scikit-learn, 2021; Géron, 2019).

The training was divided into two phases. Phase 1 was characterized by fitting various types of machine learning estimators, such as logistic regression, multilayer-perceptron with adam and different activation functions: ReLU, hyperbolic tangent, sigmoid and identity (Kingma & Ba, 2015), support vector machine with different kernels: linear, polynomial, radial basis function and sigmoid (Smola & Schölkopf, 2004), k-nearest-neighbors, decision tree, random forest (Kam, 1995), and extremely randomized trees (extra trees) (Geurts et al., 2006), with default settings of scikit-learn. More about each model can be seen in Géron's book (Géron, 2019) and Scikit-Learn user guide (Scikit-learn, 2021). In phase 2, the best algorithm obtained in phase 1 was selected to fine-tune the hyperparameters of this model with grid search cross-validation tool. Algorithm selection was based on the root mean squared error (*RMSE*) and the coefficient of determination  $R^2$  measured in the evaluation of the model in the 5-fold cross-validation.

Toward facilitating output results application, predicted SWRC points were fitted using three different models. Cavalcante & Zornberg (2017) proposed a model considering one fitting parameter for the soil water retention curve. The study solved Richard's equation – which governs the unsaturated flow through porous media by a rigorous approach – analytically for a one-dimensional flow. The function was deduced as:

$$\theta(\psi) = \theta_r + (\theta_s - \theta_r) e^{(-\delta\psi)} \quad (1)$$

where  $\delta$  = fitting hydraulic parameter [ $M^{-1}LT^2$ ];  $\psi$  = soil suction [ $ML^{-1}T^2$ ];  $\theta_r$  = residual volumetric water content [ $L^3L^{-3}$ ]; and  $\theta_s$  = saturated volumetric water content [ $L^3L^{-3}$ ].

van Genuchten's (1980) proposed a model considering three fitting parameters, and it is described as:

$$\theta(\psi) = \theta_r + \frac{\theta_s - \theta_r}{\left(1 + (a_{vg}\psi)^n\right)^{m_{vg}}} \quad (2)$$

where  $a_{vg}$  = fitting parameter [ $M^{-1}LT^2$ ];  $n$ , and  $m$  are dimensionless fitting parameters [-].

For bimodal soils, Costa & Cavalcante (2021) proposed a model based on the linear superposition principle and on the Cavalcante's & Zornberg's (2017) model, described as:

$$\theta(\psi) = \theta_r + (\theta_s - \theta_r) \left[ \lambda \psi e^{(-\delta_1\psi)} + (1 - \lambda) e^{(-\delta_2\psi)} \right] \quad (3)$$

where  $\delta_1$  and  $\delta_2$  = fitting hydraulic parameter corresponding to the microporous and macroporous regions, respectively [ $M^{-1}LT^2$ ]; and  $\lambda$  = weight factor [-].

Costa & Cavalcante (2020) demonstrated that the  $\delta$  parameter is inversely proportional to the air entry pressure and is given by:

$$\psi_{air} = \frac{\exp(1 - \exp(1))}{\delta} \quad (4)$$

where  $\psi_{air}$  is the air entry value [ $ML^{-1}T^2$ ].

### 3. Analysis and results

The results from phase 1, characterized by the running of a diversity types of machine learning algorithms with scikit-learn default settings, are presented in Table 2. The extra trees and random forest were the best models, achieving cross validation  $R^2$  greater than 0.85 and cross-validation *RMSE* less than 0.05. The decision tree algorithm has  $R^2$

**Table 2.** Phase 1 - Evaluation of different machine learning models with scikit-learn default hyperparameters.

Model	Training <i>RMSE</i>	Cross-validation <i>RMSE</i>	Training $R^2$	Cross-validation $R^2$
Extra trees	0.001	0.040	0.99	0.90
Random forest	0.017	0.046	0.98	0.86
Decision tree	0.001	0.056	0.99	0.79
KNN	0.049	0.068	0.84	0.70
SVM (rbf)	0.081	0.088	0.57	0.49
MLP (relu)	0.087	0.092	0.50	0.44
MLP (logistic)	0.098	0.100	0.37	0.35
LR	0.099	0.101	0.36	0.34
MLP (identity)	0.100	0.101	0.35	0.33
MLP (tanh)	0.097	0.101	0.38	0.33
SVM (linear)	0.100	0.102	0.35	0.32
Dummy	0.124	0.124	0.00	0.00
SVM (poly)	0.090	0.183	0.47	-2.50
SVM (sigmoid)	7.328	7.143	-3516.33	-3383.65

Notes: Extra trees is the extremely randomized trees, KNN is the K-Nearest-Neighbors algorithm, SVM is the Support Vector Machine algorithm and in parenthesis is the kernel used, MLP is the Multi-Layer Perceptron algorithm and in parenthesis is the activation function used.

of 0.99 in training, but it presented an inferior performance in generalization phase. K-nearest neighbors (KNN) is the fourth best algorithm analyzed with 0.70 cross-validation  $R^2$ .

Support vector machine (SVM), multi-layer perceptron (MLP) and logistic regression (LR) didn't perform satisfactorily with default settings. The dummy algorithm is a simple regressor that just uses the mean value of the volumetric water content of the training set, it was used to compare the  $RMSE$  with the other estimators. Using extra trees algorithm, the cross-validation  $RMSE$  was improved in 0.084 compared to that obtained with the dummy algorithm. The SVM with sigmoid kernel and scikit-learn default settings couldn't find a pattern in the training dataset.

The extra trees algorithm was the best model analyzed in phase 1, so it was selected to phase 2. This algorithm is an ensemble of decision trees with all the hyperparameters to control how trees are grown, plus all the parameters to control the ensemble itself. A decision tree is formed by roots nodes and leaf nodes. The root node is the question to make a decision and the leaf node is the answer after all questions (Géron, 2019). Figure 4 presents an example of decision tree, where the root nodes set thresholds towards the leaf node with the corresponding value of volumetric water content. The function used to measure the quality of the split was the mean squared error ( $mse$ ). In Figure 5, the regression of this tree is shown. The extra trees algorithm fits a number of randomized decision trees on various subsamples of the dataset using random thresholds for each feature rather than searching for the best possible thresholds, and uses averaging to join the predictions from each decision tree (Géron, 2019).

The extra trees algorithm was refined by varying the hyperparameters of the forest and trees to generate a model with higher generalization performance. To find this model, the grid search cross-validation was evaluated varying the  $n\_estimators$  from 8 to 40,  $random\_state$  from 0 to 30 in multiples of 2,  $min\_samples\_split$  from 2 to 5,  $min\_samples\_leaf$  from 1 to 4,  $max\_features$  from 1 to 6, and  $ccp\_alpha$  with 0, 0.0001 and 0.0002.

In total 152064 combinations were evaluated, and the hyperparameters of the best estimator were:  $n\_estimators = 24$ ,

$random\_state = 10$ ,  $min\_samples\_leaf = 1$ ,  $min\_samples\_split = 2$ ,  $max\_features = 6$ ,  $ccp\_alpha = 0$ . Figure 6 illustrates the learning curve of the best extra trees model, which tells how the performance of this estimator varies according to the amount of data. The  $R^2$  in the training set reaches the top with  $R^2 = 0.99$ , and the  $R^2$  in validation increases very fast with data reaching  $R^2 = 0.90$ . It displays that the amount of data leverages the generalization capacity of the algorithm, which could reach up until  $R^2 = 0.99$ .

Figure 7 shows the graph of the estimator's evaluation in the test set. High scattering occurs at  $\theta$  ranges with few amounts of data. The coefficient of determination in the test set is  $R^2 = 0.90$ , and the  $\theta$  error in a 95% confidence interval is between  $0.029 \text{ cm}^3/\text{cm}^3$  to  $0.043 \text{ cm}^3/\text{cm}^3$ . This order of magnitude can negatively influence the results depending on the soil type, especially in low porosity soils, where a volumetric water content variation of this magnitude can be significant in the saturated zone of the curve. However, the algorithm will decrease this error as new data is computed.

An interesting aspect is that the decision tree-based estimators (such as extra trees) provide the relative importance of each parameter for the prediction of volumetric water content by the model. Feature importance is a weighted average of how much the trees nodes that use that feature reduce Gini impurity, then the results are scaled to add up to 1 (Géron, 2019). Table 3 presents this result, indicating that suction is the most significant feature, followed by porosity, and percentage of sand.

Suction is the most relevant variable because it makes the volumetric water content vary from dry to saturated and this makes it out of scale. The other variables have similar importance to each other, despite the percentage of gravel and silt that have feature importance close to zero, probably because the granulometry are linearly dependent on the fourth-dimensional hyperplane where the sum of all the percentages results 100%.

Figure 8 illustrates some predictions of the model for a (a) sandy, (b) silty, and (c) clayey soil. Visually, there is a good adherence between predicted and experimental results. The model is able to predict the SWRC with the

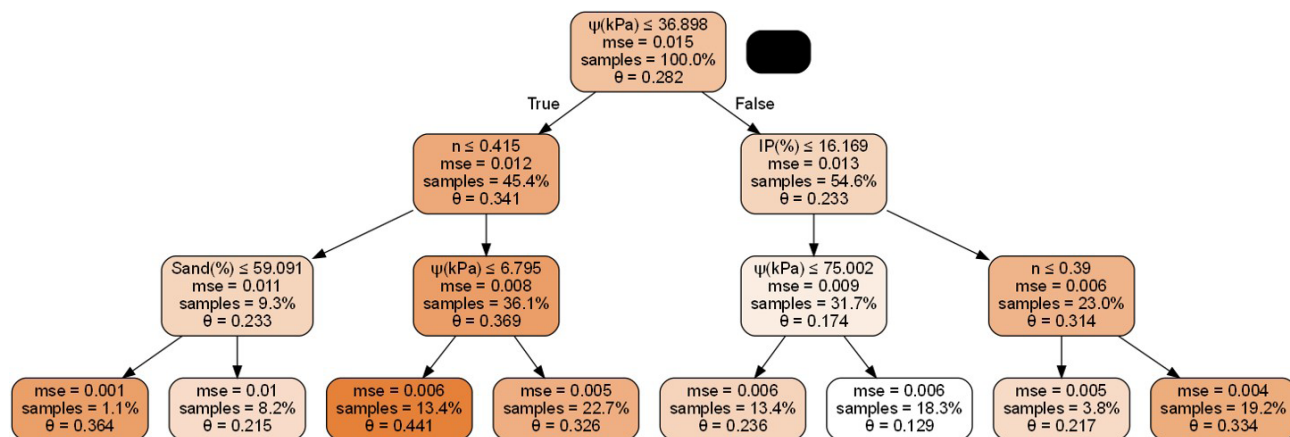
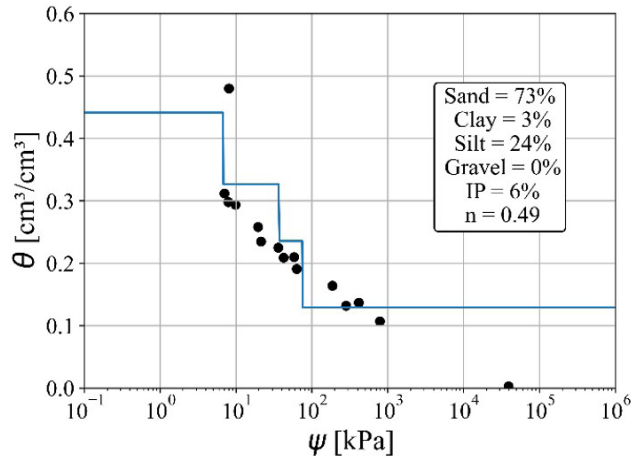
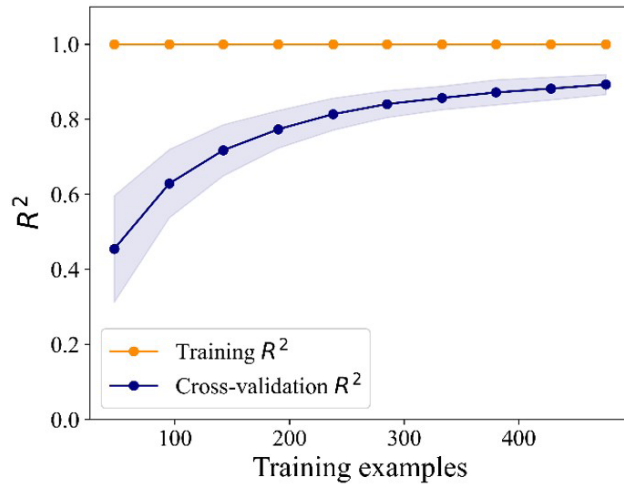


Figure 4. A decision tree example.



**Figure 5.** A decision tree regression example.



**Figure 6.** Learning curve of extremely randomized trees.

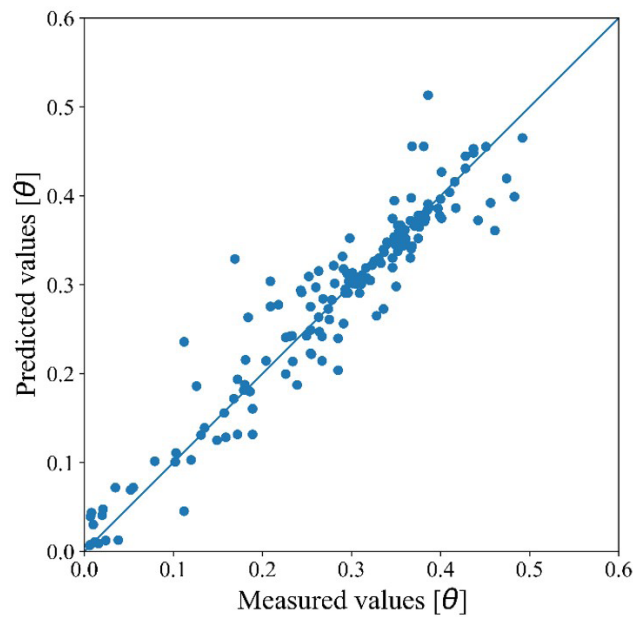


**Figure 7.** Evaluation in the test set of extremely randomized trees.

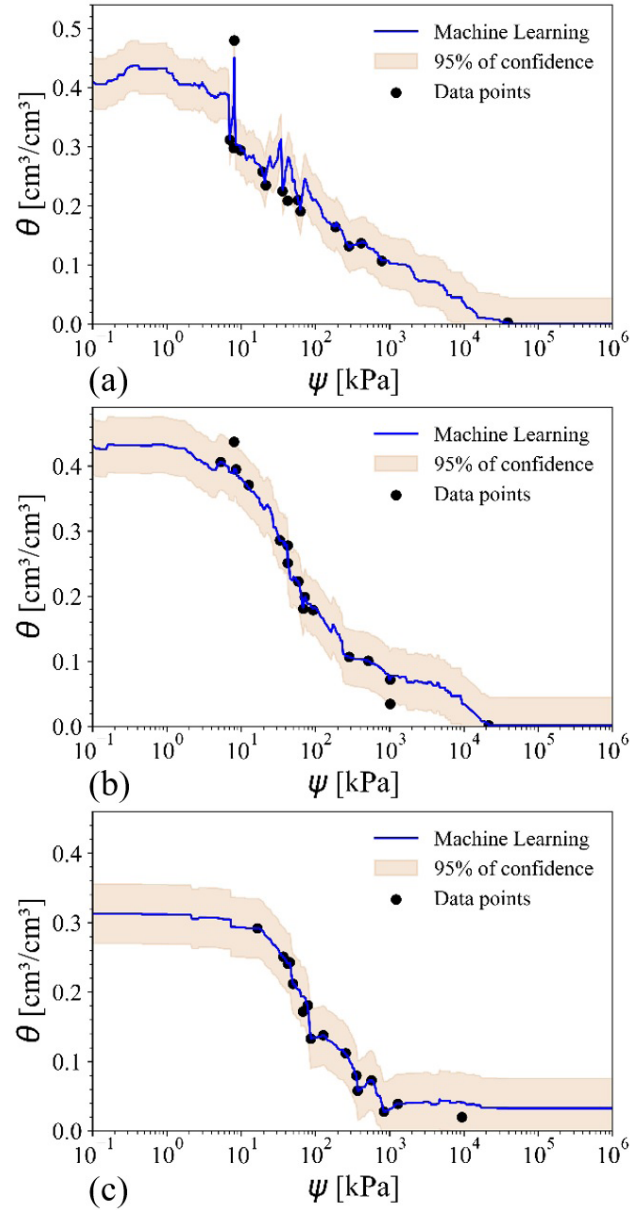


**Figure 8.** Prediction of the soil water retention curve with extremely randomized trees machine learning algorithm: (a) for a sandy soil with 73% of sand; (b) for a silty soil with 85% of silt; (c) for a clayey soil with 89% of clay.

**Table 3.** Feature importance for predicting the soil water retention with extremely randomized trees.

Feature	Feature importance
Suction $\psi$	0.427
Porosity $n$	0.155
% Sand	0.127
% Clay	0.103
Plasticity index $PI$	0.085
% Gravel	0.058
% Silt	0.045

three well-defined sections, presenting the saturated zone, the desaturation zone and the residual zone. Some points are far from the machine learning predictions because part of the data was used for testing the model. In Figure 8a, there are some valleys and picks, and probably the first point is an outlier. In some areas, increasing suction causes an increase in volumetric water content, which is not physically defensible. This occurs because the algorithm tries to better fit the data of different types of soils and due to measurement errors.

To overcome these deficiencies and obtain a continuous and smooth curve, a model of soil water retention can be

fitted to the predictions of the machine learning model. The saturated volumetric water content parameter was set equal to the porosity. The graphics on the left of the Figure 9 show the adjustment of Cavalcante's & Zornberg's (2017) function to machine learning predictions, and on the right are the adjustment of van Genuchten's (1980) function. Cavalcante's & Zornberg's (2017) function fits well the predicted silty soil presented, but got lower coefficient of determination  $R^2$  for the sandy and clayey soils. van Genuchten's (1980) model present a visually pleasing performance to fit the sandy and silty soils analyzed; machine learning and the curves almost

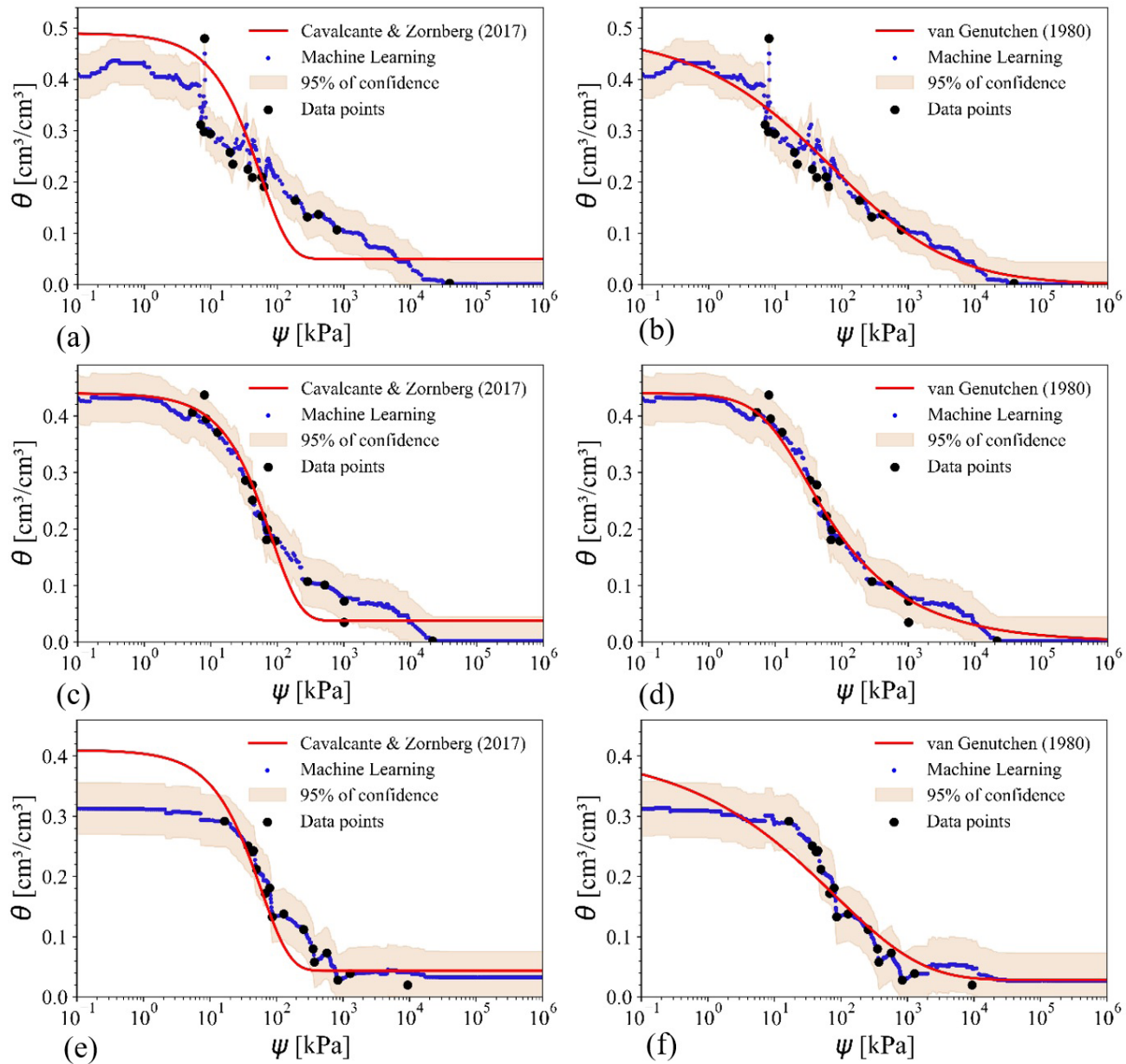


**Figure 9.** Prediction of the soil water retention curve with Cavalcante & Zornberg (2017) and with van Genuchten (1980) fitting extremely randomized trees prediction with saturated volumetric water content equal to porosity: (a) and (b) experimental points from dataset for a sandy soil with 73% of sand; (c) and (d) experimental points from dataset for a silty soil with 85% of silt; (e) and (f) experimental points from dataset for a clayey soil with 89% of clay.



**Table 4.** Cavalcante's & Zornberg's (2017) parameters and coefficient of determination of fitting to the machine learning prediction data.

Parameters	Sandy soil	Silty soil	Clayey soil
$\theta_s$ (cm <sup>3</sup> /cm <sup>3</sup> )	0.49	0.44	0.41
$\theta_r$ (cm <sup>3</sup> /cm <sup>3</sup> )	0.05	0.04	0.04
$\delta$ (kPa <sup>-1</sup> )	0.0176	0.0122	0.0170
$R^2$	0.86	0.97	0.84

**Table 5.** van Genuchten's (1980) parameters and coefficient of determination of fitting to the machine learning prediction data.

Parameters	Sandy soil	Silty soil	Clayey soil
$\theta_s$ (cm <sup>3</sup> /cm <sup>3</sup> )	0.49	0.44	0.41
$\theta_r$ (cm <sup>3</sup> /cm <sup>3</sup> )	0.00	0.00	0.03
$a_{vg}$ (kPa <sup>-1</sup> )	0.005	0.084	$1.1 \times 10^{-7}$
$n_{vg}$ (-)	0.401	1.377	0.349
$m_{vg}$ (-)	1.534	0.289	54.245
$R^2$	0.99	0.99	0.96

overlap in all regions. The porosity of the analyzed clayey soil is 0.41 and probably has some measurement error.

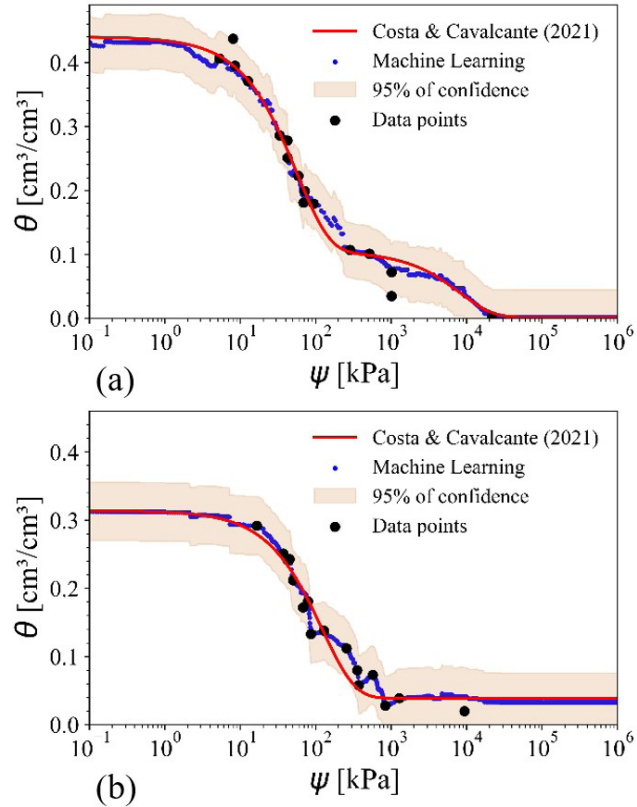
Table 4 and Table 5 presents, respectively, the adjusted parameters and coefficient of determination  $R^2$  for Cavalcante's & Zornberg's (2017) function and van Genuchten's (1980) function. The  $\delta$  parameter is inversely proportional to the air entry pressure as demonstrated by Costa & Cavalcante (2020). So, the sandy and clayey soil fitted with Cavalcante's & Zornberg's (2017) function have similar air entry pressure and the silty soil has a higher air entry pressure. The clayey soil fitted with van Genuchten's (1980) function resulted in unusual parameters of  $a_{vg}$  and  $m$ , this was due to the points predicted by the machine learning model in the saturated zone being far from measured porosity.

For bimodal soils, Costa's & Cavalcante's (2021) model can be used to fit the predictions. Figure 10 shows the fit of the silty and clayey soil with Costa & Cavalcante (2021) function. Comparing with Figure 9c, Costa's & Cavalcante's (2021) function fits better to the silty soil analyzed than Cavalcante's & Zornberg's (2017) function. Table 6 shows the adjusted parameters and coefficient of determination  $R^2$  for Costa's & Cavalcante's (2021) function. The silty soil has microporous that results in an air entry pressure about 1800 kPa, and macroporous with an air entry pressure of 10 kPa. The clayey soil analyzed resulted 22 kPa and  $10^{-4}$  kPa for microporous and macroporous, respectively. This low value of air entry for macroporous was due to the function trying to fit the machine learning data and the saturated volumetric water content of 0.41. The use of bimodal SWRC models is necessary for modeling the entire SWRC of soils with a bimodal pore size distribution, common in many Brazilian tropical formations (Kühn et al., 2021; Futai & Almeida, 2005; Cordão-Neto et al., 2018; Miguel & Bonder, 2012).

Although Cavalcante's & Zornberg's (2017) function didn't model as well as Costa's & Cavalcante's (2021)

**Table 6.** Costa's & Cavalcante's (2021) parameters and coefficient of determination of fitting to the machine learning prediction data.

Parameters	Silty soil	Clayey soil
$\theta_s$ (cm <sup>3</sup> /cm <sup>3</sup> )	0.44	0.41
$\theta_r$ (cm <sup>3</sup> /cm <sup>3</sup> )	0.00	0.04
$\delta_1$ (kPa <sup>-1</sup> )	0.0001	0.0082
$\delta_2$ (kPa <sup>-1</sup> )	0.0178	1758.0848
$\lambda$	0.235	0.742
$R^2$	0.99	0.99


**Figure 10.** Prediction of the soil water retention curve with Costa & Cavalcante (2021) fitting extremely randomized trees prediction with saturated volumetric water content equal to porosity: (a) experimental points from dataset for a silty soil with 85% of silt; (b) experimental points from dataset for a clayey soil with 89% of clay.

and van Genuchten's (1980) functions, its advantages are: analytical solutions for transient unsaturated flow problems and fewer adjusted parameters.

## 4. Conclusion

In this paper, the performance of machine learning models for predicting the soil water retention curve was evaluated using a dataset with 794 measured water retention and suctions points from 51 different soils with a wide range of soil properties. Several models have been trained, such as linear regression, logistic regression, multi-layer



perceptron (with identity, sigmoid, hyperbolic tangent activation functions), support vector machine (with radial basis function, linear and sigmoid kernels), k-nearest-neighbors, decision tree, random forest, and extremely randomized trees (extra trees). Extra trees regressor was the best model with scikit-learn default settings, it was selected by measurement of the performance on the cross-validation dataset referring to root mean squared error (*RMSE*) and coefficient of determination  $R^2$ .

This model was then fine-tuned varying its training hyperparameters. For the training set,  $RMSE = 0.001$  and  $R^2 = 0.99$ . For the cross-validation set,  $RMSE = 0.039$  and  $R^2 = 0.90$ . And for the test set,  $RMSE = 0.037$  and  $R^2 = 0.90$ . The most important features, in decreasing order, for prediction were: suction, porosity, percentage of sand, percentage of clay, plasticity index, percentage of gravel, and percentage of silt.

Alternatives to obtain a continuous and smooth curve from the machine learning model were presented by fitting soil water retention functions. Cavalcante's & Zornberg's (2017) function reached  $R^2$  between 0.84 and 0.97 and has the advantage of having analytical solutions, and fewer parameters. van Genuchten's (1980) function reached  $R^2$  between 0.96 and 0.99. Costa's & Cavalcante's (2021) function reached  $R^2 = 0.99$  in the silty and clayey soils. Its advantages are being able to fit a bimodal soil model to the predictions of the machine learning estimator, and according to Costa & Cavalcante (2021), it's efficient in representing bimodal soils, and mathematically and physically consistent.

In the preliminary stage of design projects, where not much data is readily available, the model developed can be used to predict the engineering behavior of unsaturated soils. It may be utilized to guide the geotechnical engineers throughout the preliminary analyses and design procedures.

It's important to highlight that machine learning models can always be updated by presenting new training soil samples as new data with measured suction, volumetric water content, and corresponding characterization parameters become available.

This is a work in progress and the quality of predictions will be better the greater the collaboration. Instructions on how to collaborate with this project are provided in the Appendix A.

## Acknowledgements

This study was financed in part by the Coordination for the Improvement of Higher Education Personnel – Brazil (CAPES) – Finance Code 001. The authors also acknowledge the support of the National Council for Scientific and Technological Development (CNPq Grant Nos. 435962/2018-3 and 305484/2020-6), the Foundation for Research Support of the Federal District (FAPDF) (Projects 0193.002014/2017-68 and 0193.001563/2017), the National Electric Energy

Agency (ANEEL) and its R&D partners Neoenergia/CEB Distribuição S.A. (Grant number PD-05160-1904/2019, contract CEBD782/2019), and the University of Brasília. The authors also acknowledge the support of GEOAMB for making the data available on its website.

## Declaration of interest

The authors have no conflicts of interest to declare. All co-authors have observed and affirmed the contents of the paper and there is no financial interest to report.

## Authors' contributions

Enzo Aldo Cunha Albuquerque: conceptualization, formal analysis, investigation, methodology, software, validation, visualization, writing - original draft. Lucas Parreira de Faria Borges: software, visualization, writing - review and editing. André Luís Brasil Cavalcante: conceptualization, project administration, supervision, writing - review and editing. Sandro Lemos Machado: conceptualization, resources, supervision, writing - review and editing.

## List of symbols

$a_{vg}$	Fitting parameter of van Genuchten's (1980) function [ $M^{-1}LT^2$ ]
$ccp\_alpha$	Complexity parameter used for minimal cost-complexity pruning
$m_{vg}$	Fitting parameter of van Genuchten's (1980) function [-]
$max\_features$	Number of features to consider when looking for the best split
$min\_samples\_leaf$	Minimum number of samples required to be a leaf node
$min\_samples\_split$	Minimum number of samples required to split an internal node
$mse$	Mean squared error
$n$	Porosity [ $L^3L^{-3}$ ]
$n_{vg}$	Fitting parameter of van Genuchten's (1980) function [-]
$n\_estimators$	Number of trees in the forest
$PI$	Plasticity index
$R^2$	Coefficient of determination
$RMSE$	Root mean squared error
$random\_state$	Random state of parameters initialization
$\delta$	Fitting parameter of Cavalcante's & Zornberg's (2017) function [ $M^{-1}LT^2$ ]
$\theta$	Volumetric water content [ $L^3L^{-3}$ ]
$\theta_s$	Volumetric water content at saturation ( $L^3L^{-3}$ )
$\theta_r$	Residual volumetric water content [ $L^3L^{-3}$ ]
$\psi$	Soil suction [ $ML^{-1}T^2$ ]
$\psi_{air}$	Air entry pressure [ $ML^{-1}T^2$ ]

## References

- Achieng, K.O. (2019). Modelling of soil moisture retention curve using machine learning techniques: artificial and deep neural networks vs support vector regression models. *Computers & Geosciences*, 133, 104320. <http://dx.doi.org/10.1016/j.cageo.2019.104320>.
- Anaconda. (2016). *Anaconda software (No. 2-2.4.0)*. Austin.
- Arya, L.M., & Paris, J.F. (1981). A physicoempirical model to predict the soil moisture characteristic from particle-size distribution and bulk density data. *Soil Science Society of America Journal*, 45(6), 1023-1030. <http://dx.doi.org/10.2136/sssaj1981.03615995004500060004x>.
- Belcher, W., Camp, T., & Krzhizhanovskaya, V. (2015). Detecting erosion events in earth dam and levee passive seismic data with clustering. In *2015 IEEE 14th International Conference on Machine Learning and Applications* (pp. 903-910), Miami, FL, USA. <https://doi.org/10.1109/ICMLA.2015.9>.
- Brasil. Ministério da Ciência, Tecnologia, Inovações e Comunicações – MCTIC. (March 24, 2020). Portaria nº 1.122, de 19 de março de 2020. *Diário Oficial [da] República Federativa do Brasil*.
- Breiman, L., & Spector, P. (1992). Submodel selection and evaluation in regression: the X-random case. *International Statistical Review*, 60(3), 291. <http://dx.doi.org/10.2307/1403680>.
- Carvalho, L.O., & Ribeiro, D.B. (2019). Soil classification system from cone penetration test data applying distance-based machine learning algorithms. *Soils and Rocks*, 42(2), 167-178. <http://dx.doi.org/10.28927/SR.422167>.
- Carvalho, L.O., & Ribeiro, D.B. (2020). Application of kernel k-means and kernel x-means clustering to obtain soil classes from cone penetration test data. *Soils and Rocks*, 43(4), 607-618. <http://dx.doi.org/10.28927/SR.434607>.
- Cavalcante, A.L.B., & Zornberg, J.G. (2017). Efficient approach to solving transient unsaturated flow problems. I: analytical solutions. *International Journal of Geomechanics*, 17(7), 04017013. [http://dx.doi.org/10.1061/\(ASCE\)GM.1943-5622.0000875](http://dx.doi.org/10.1061/(ASCE)GM.1943-5622.0000875).
- Ching, J., & Phoon, K.-K. (2019). Constructing site-specific multivariate probability distribution model using bayesian machine learning. *Journal of Engineering Mechanics*, 145(1), 04018126. [http://dx.doi.org/10.1061/\(ASCE\)EM.1943-7889.0001537](http://dx.doi.org/10.1061/(ASCE)EM.1943-7889.0001537).
- Cordão-Neto, M.P., Hernández, O., Lorenzo Reinaldo, R., Borges, C., & Caicedo, B. (2018). Study of the relationship between hydro-mechanical soil behavior and microstructure of a structured soil. *Earth Sciences Research Journal*, 22(2), 91-101. <http://dx.doi.org/10.15446/esrj.v22n2.65640>.
- Costa, M.B.A. (2017). *Modelagem numérica do fluxo transiente em meio poroso não saturado sob a ação de centrifugação* [Master's dissertation, University of Brasília]. University of Brasília repository (in Portuguese). Retrieved in January 10, 2021, from <https://repositorio.unb.br/handle/10482/24849>.
- Costa, M.B.A., & Cavalcante, A.L.B. (2020). Novel approach to determine soil-water retention surface. *International Journal of Geomechanics*, 20(6), 04020054. [http://dx.doi.org/10.1061/\(ASCE\)GM.1943-5622.0001684](http://dx.doi.org/10.1061/(ASCE)GM.1943-5622.0001684).
- Costa, M.B.A., & Cavalcante, A.L.B. (2021). Bimodal soil-water retention curve and k-function model using linear superposition. *International Journal of Geomechanics*, 21(7), 04021116. [http://dx.doi.org/10.1061/\(ASCE\)GM.1943-5622.0002083](http://dx.doi.org/10.1061/(ASCE)GM.1943-5622.0002083).
- Fisher, W.D., Camp, T.K., & Krzhizhanovskaya, V. (2016). Crack detection in earth dam and levee passive seismic data using support vector machines. *Procedia Computer Science*, 80, 577-586. <http://dx.doi.org/10.1016/j.procs.2016.05.339>.
- Fisher, W.D., Camp, T.K., & Krzhizhanovskaya, V. (2017). Anomaly detection in earth dam and levee passive seismic data using support vector machines and automatic feature selection. *Journal of Computational Science*, 20, 143-153. <http://dx.doi.org/10.1016/j.jocs.2016.11.016>.
- Fredlund, M.D., Wilson, G.W., & Fredlung, D.G. (2002). Use of the grain-size distribution for estimation of the soil-water characteristic curve. *Canadian Geotechnical Journal*, 39(5), 1103-1117. <https://doi.org/10.1139/t02-049>.
- Futai, M.M., & Almeida, M.S.S. (2005). An experimental investigation of the mechanical behaviour of an unsaturated gneiss residual soil. *Geotechnique*, 55(3), 201-213. <http://dx.doi.org/10.1680/geot.2005.55.3.201>.
- Géron, A. (2019). *Hands-on machine learning with Scikit-Learn, Keras, and Tensorflow: concepts, tools, and techniques to build intelligent systems*. Beijing: O'Reilly Media.
- Geurts, P., Ernst, D., & Wehenkel, L. (2006). Extremely randomized trees. *Machine Learning*, 63(1), 3-42. <http://dx.doi.org/10.1007/s10994-006-6226-1>.
- Haghverdi, A., Leib, B.G., & Cornelis, W.M. (2015). A simple nearest-neighbor technique to predict the soil water retention curve. *Transactions of the ASABE*, 58(3), 697-705. <http://dx.doi.org/10.13031/trans.58.10990>.
- Hunter, J.D. (2007). Matplotlib: a 2D graphics environment. *Computing in Science & Engineering*, 9(3), 90-95. <http://dx.doi.org/10.1109/MCSE.2007.55>.
- Kam, T.H. (1995). Random decision forests. In *Proceedings of 3rd International Conference on Document Analysis and Recognition* (pp. 278-282), Montreal, QC, Canada.
- Khlosi, M., Alhamdoosh, M., Douaik, A., Gabriels, D., & Cornelis, W.M. (2016). Enhanced pedotransfer functions with support vector machines to predict water retention of calcareous soil. *European Journal of Soil Science*, 67(3), 276-284. <http://dx.doi.org/10.1111/ejss.12345>.
- Kingma, D.P., & Ba, J.L. (2015). Adam: a method for stochastic optimization. In *Proceedings of the 3rd International Conference on Learning Representations, ICLR 2015 - Conference Track Proceedings* (pp. 1-15), San Diego, CA.

- Kluyver, T., Ragan-Kelley, B., Pérez, F., Granger, B., Bussonnier, M., Frederic, J., Kelley, K., Hamrick, J., Grout, J., Corlay, S., Ivanov, P., Avila, D., Abdalla, S., & Willing, C. (2016). Jupyter Notebooks: a publishing format for reproducible computational workflows. In *Positioning and Power in Academic Publishing: Players, Agents and Agendas - Proceedings of the 20th International Conference on Electronic Publishing, ELPUB 2016* (pp. 87-90). Amsterdam: IOS Press. <https://doi.org/10.3233/978-1-61499-649-1-87>.
- Kühn, V.O., Lopes, B.C.F., Caicedo, B., & Cordão-Neto, M.P. (2021). Micro-structural and volumetric behaviour of bimodal artificial soils with aggregates. *Engineering Geology*, 288, 106139.
- Marjanović, M., Kovačević, M., Bajat, B., & Voženilek, V. (2011). Landslide susceptibility assessment using SVM machine learning algorithm. *Engineering Geology*, 123(3), 225-234. <http://dx.doi.org/10.1016/j.enggeo.2011.09.006>.
- McKinney, W. (2010). Data structures for statistical computing in Python. In *Proceedings of the 9th Python in Science Conference* (pp. 56-61), Austin, Texas.
- Miguel, M.G., & Bonder, B.H. (2012). Soil–water characteristic curves obtained for a colluvial and lateritic soil profile considering the macro and micro porosity. *Geotechnical and Geological Engineering*, 30(6), 1405-1420. <http://dx.doi.org/10.1007/s10706-012-9545-y>.
- Oliphant, T. (2006). *A guide to NumPy*. USA: Trelgol Publishing.
- Oliveira Filho, A.G., Totola, L.B., Bicalho, K.V., & Hisatugu, W.H. (2020). Prediction of compression index of soft soils from the Brazilian coast using artificial neural networks and empirical correlations. *Soils and Rocks*, 43(1), 109-121. <https://doi.org/10.28927/sr.431109>.
- Ozelim, L.C., Borges, L.P.F., Cavalcante, A.L.B., Albuquerque, E.A.C., Diniz, M.S., Góis, M.S., Costa, K.R.C.B., Sousa, P.F., Dantas, A.P.N., Jorge, R.M., Moreira, G.R., Barros, M.L., & Aquino, F.R. (2022). Structural health monitoring of dams based on acoustic monitoring, deep neural networks, fuzzy logic and a CUSUM control algorithm. *Sensors*, 22(7), 1-25. <http://dx.doi.org/10.3390/s22072482>.
- Pedregosa, F., Varoquaux, G., Gramfort, A., Michler, V., Thirion, B., Grisel, O., Blondel, M., Prettenhofer, P., Weiss, R., Dubourg, V., Vanderplas, J., Passos, A., Cournapeau, D., Brucher, M., Perrot, M., & Duchesnay, E. (2011). Scikit-learn: machine learning in Python. *Journal of Machine Learning Research*, 12, 2825-2830. <http://dx.doi.org/10.1289/EHP4713>.
- Prayogo, D., & Susanto, Y.T.T. (2018). Optimizing the prediction accuracy of friction capacity of driven piles in cohesive soil using a novel self-tuning least squares support vector machine. *Advances in Civil Engineering*, 2018, 6490169. <http://dx.doi.org/10.1155/2018/6490169>.
- Scikit-learn. (2021). *User guide*. Retrieved in January 10, 2021, from [https://scikit-learn.org/stable/user\\_guide.html](https://scikit-learn.org/stable/user_guide.html)
- Smola, A.J., & Schölkopf, B. (2004). A tutorial on support vector regression. *Statistics and Computing*, 14(3), 199-222. <http://dx.doi.org/10.1023/B:STCO.0000035301.49549.88>.
- Tien Bui, D., Tuan, T.A., Klempe, H., Pradhan, B., & Revhaug, I. (2016). Spatial prediction models for shallow landslide hazards: a comparative assessment of the efficacy of support vector machines, artificial neural networks, kernel logistic regression, and logistic model tree. *Landslides*, 13(2), 361-378. <http://dx.doi.org/10.1007/s10346-015-0557-6>.
- Universidade Federal da Bahia – UFBA. (2022). Retrieved in January 6, 2022, from <http://www.geoamb.eng.ufba.br/dados/buscaSolos.php>
- van Genuchten, M.T. (1980). A closed-form equation for predicting the hydraulic conductivity of unsaturated soils. *Soil Science Society of America Journal*, 44(5), 892-898.
- Vanapalli, S.K., & Catana, M.C. (2005). Estimation of the soil-water characteristic curve of coarse-grained soils using one point measurement and simple properties. In *International Symposium on Advanced Experimental Unsaturated Soil Mechanics*, Trento, Italy.

## Appendix A. How to collaborate.

To add new data to the machine learning set, one should sign up at the website (<https://www.geofluxo.com/>) and go to the restricted area, then to applications, Figure A1.

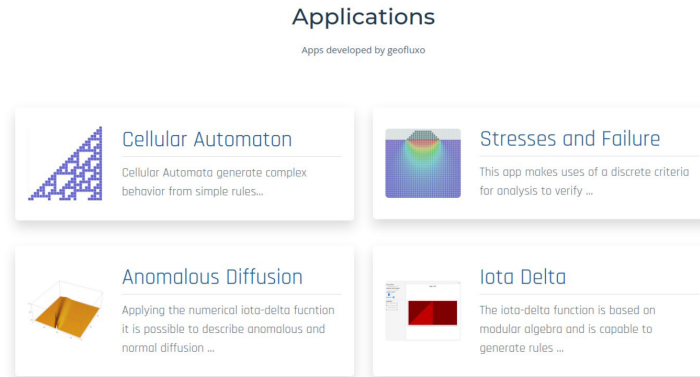


Figure A1. Applications page at <https://geofluxo.com/geoapps/>.

Then, one should select the SWRC AI application. On the application page, (<https://geofluxo.com/geoapps/swrc-ai/>) it is possible to insert the inputs and come up with the outputs values plus the chart with the artificial intelligence fit.

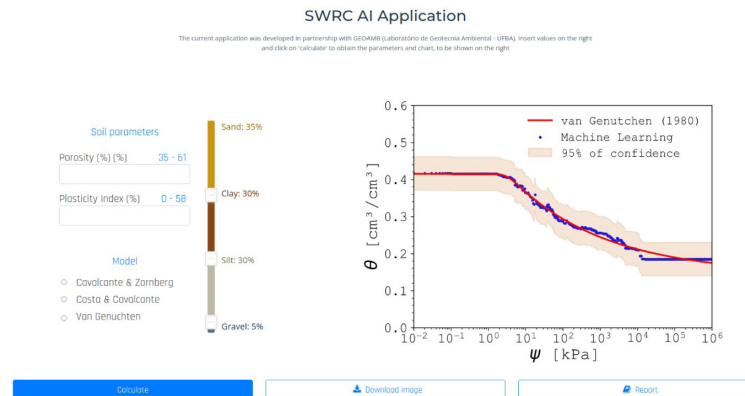


Figure A2. SWRC AI application page.

If the user scrolls down and hit the form button, Figure A3, he will be redirected to a webpage that does not host the application itself, but allows the user to collaborate with new data to the dataset.



Figure A3. SWRC AI form button.

Once the user access the form page at <https://geofluxo.com/geoapps/swrc-ai/form/>, it is possible to write an introduction about the data, the percentages of gravel, sand, clay and silt, porosity, plasticity index, and insert several points of suction and volumetric water content.

SWRC AI  
Form

Form

This form allows to insert data that describes the soil water retention curve, granulometry and physical indexes to calibrate the models based on Artificial Intelligence. The data may come from laboratory or field experimentation.

Circumstantial description of data

Granulometric Cruve

Gravel (%)

0

Sand (%)

0

Silt (%)

0

Clay (%)

0

Physical Indexes

Porosity (%)

0

Plasticity index (%)

0

Soil Water retention curve

Moisture (%)

Suction (kPa)

0

0

0

0

0

0

0

0

0

0

-

+

Save the data

Figure A4. SWRC AI form.

Once the form is submitted, the admins will accept or deny the new dataset. If accepted, the new dataset will integrate the next machine learning training session.



## Lining forces in tunnel interaction problems

António M. G. Pedro<sup>1#</sup> , José C. D. Grazina<sup>2</sup> , Jorge N. V. Almeida e Sousa<sup>2</sup>

Article

### Keywords

Twin tunnels  
Lining forces  
Numerical modelling

### Abstract

In big cities the construction of new tunnels in close proximity to existing ones is unavoidable given the densely and growing occupation of the subsoil. The interaction between tunnels in such conditions is well identified in the literature and has been thoroughly investigated in the past. However, most of those studies are focused on the effect of the ground conditions and relative position between tunnels on the ground movements and often disregard the impact induced by the second excavation on the lining forces of both tunnels. To provide further insight into this subject a numerical study of the sequential excavation of side-by-side twin tunnels is presented in this paper. The study also assesses the influence of parameters that have not been covered in the previous studies, namely the stiffness of the lining and the initial stress conditions. The results confirm that significant interaction occurs when the tunnels are spaced less than one diameter, where a considerable increase on both hoop forces and bending moments, particularly on the lining of the existing tunnel, is observed after the second excavation. For a spacing higher than two diameters the interaction between tunnels is almost negligible. The magnitude of the lining forces and of the interaction effects are also dependent of the stiffness of the linings and of the initial stress conditions.

## 1. Introduction

Having an efficient and sustainable transportation network is a fundamental condition for the development of a city (Admiraal & Cornaro, 2016). Given the increasing occupation at ground surface and the growing environment awareness the most frequently adopted solution consists on building these networks in the subsoil (Cui & Nelson, 2019). However, in large cities the underground space is also congested by the existence of different types of infrastructures (Bobylov, 2016), which often leads to the construction of new tunnels in close proximity to existing ones, or to the construction of twin tunnels close to each other. In this case, one of the most important aspects in the design stage is to assess the existence of interaction between tunnels and how it might affect the ground deformations and the forces on its linings.

Evidences of twin tunnel interaction have been reported by many case studies (e.g. Bartlett & Bubbers, 1970; Cording & Hansmire, 1975; Nyren, 1998; Afifipour et al., 2011; Ocak, 2014; Fagnoli et al., 2015; Elwood & Martin, 2016; Wan et al., 2017), which concluded, based on the monitoring data, that the second tunnel (2T) excavation induced higher movements than those associated with the construction of the existing/first tunnel (1T). Mair & Taylor (1997) justified

this behaviour with the disturbed ground conditions where the 2T is excavated and identified the pillar width between tunnels as a key parameter in the interaction. Numerical (e.g. Addenbrooke & Potts, 2001; Ng et al., 2004; Do et al., 2015), centrifuge (Wu & Lee, 2003; Divall & Goodey, 2015) and small-scale (Kim et al., 1998; Chapman et al., 2007) models reached similar conclusions and observed that the interaction between tunnels was particularly relevant for a ratio of the pillar width ( $L$ ) to the diameter of tunnel ( $D$ ) smaller than one ( $L/D < 1.0$ ). A compilation and a thorough review of the studies published in the literature about the influence of twin tunnelling on the ground deformations was presented by Do et al. (2014b) and, more recently, by Islam & Iskander (2021). However, as stated by Do et al. (2014b), most of those studies are focused on the deformations measured at ground surface, while the evaluation of the lining forces induced by the 2T excavation on both tunnels is often disregarded or seen as a minor aspect. Following a strategy similar to the previous studies the aim of this paper is to contribute to a better knowledge of these aspects by performing a thorough numerical analysis. The influence of crucial parameters, such as the stiffness of the lining and the initial stress conditions, on the lining forces of both tunnels were also assessed. For that purpose, a series of 2D numerical analyses of the sequential

<sup>#</sup>Corresponding author. E-mail address: amgpedro@dec.uc.pt

<sup>1</sup>Universidade de Coimbra, Instituto para a Sustentabilidade e Inovação em Estruturas de Engenharia, Departamento de Engenharia Civil, Coimbra, Portugal.

<sup>2</sup>Universidade de Coimbra, Departamento de Engenharia Civil, Coimbra, Portugal.

Submitted on November 15, 2021; Final Acceptance on June 3, 2022; Discussion open until November 30, 2022.

<https://doi.org/10.28927/SR.2022.077221>



This is an Open Access article distributed under the terms of the Creative Commons Attribution License, which permits unrestricted use, distribution, and reproduction in any medium, provided the original work is properly cited.

excavation of side-by-side twin tunnels was carried out using the in-house finite element program, UCGeoCode, developed at the Department of Civil Engineering of the University of Coimbra (Sousa, 1998; Grazina, 2009).

## 2. Background on lining forces induced by twin tunnelling

Table 1 summarizes the main results published in the literature that refer the impact of side-by-side twin tunnelling in the stresses and forces acting on the lining. From the thirteen research studies compiled eleven are based on numerical analysis (2D and 3D) and only two (Adachi et al., 1993; Kim et al., 1998) used 1g small-scale models, highlighting the lack and need of real monitoring data to support their conclusions. However, it is worth mentioning the recent study conducted by Cheng et al. (2020) which, in spite of analysing a piggyback (one tunnel above the other) rather than a side-by-side configuration, compared the numerical results against field measurements with the results showing a good agreement in terms of the hoop forces predicted in the 1T.

The initial research on the topic was performed by Ghaboussi & Ranken (1977) and Soliman et al. (1993) and confirmed its relevance with the results showing a significant increase of the forces in the lining of the 1T after the excavation of the 2T. The lining of the 2T also presented higher forces when compared with those determined in a greenfield scenario, i.e., without the presence of the 1T, although of smaller magnitude. However, in those studies a linear elastic model was adopted for the soil, which is an unrealistic assumption. In the following studies, more realistic constitutive models were adopted for the soil, with the majority considering the elastic-perfectly plastic Mohr-Coulomb failure criterion or equivalent. These studies mainly assessed the influence of the distance between tunnels (pillar width) and, recurring to 3D analysis, the lagged distance between the two excavation faces. In line with the elastic results, and despite the differences among the analysis, all studies concluded that significant interaction occurred for  $L/D < 1.0$ , with a considerable increase of the lining forces in

the 1T while a moderate increase was observed on the 2T. In all cases the maximum variations of the lining forces were observed at the pillar springline (i.e. the springline closest to the other tunnel). Most studies also observed that for  $L/D > 2.0$  there is no noticeable variation on the lining forces of both tunnels, suggesting that this ratio corresponds to the maximum interaction distance between tunnels. Kim et al. (1998) results showed that the stiffness of the lining has a reduced influence on the bending moments of the 1T, but these results were obtained employing very flexible supports, which are not ideal to characterise the lining behaviour (Peck et al., 1972). The effect of the initial stress conditions was also not thoroughly analysed with most studies using a constant depth of the tunnel and a coefficient of earth pressure at rest ( $K_0$ ) value of about 0.5. The exceptions are the elastic study of Ghaboussi & Ranken (1977) where a moderately increase of the lining forces was observed for greater depths and the research performed by Adachi et al. (1993) which found that the interaction between tunnels appears to increase with the increase of the overburden. Despite using significantly higher and even non-constant  $K_0$  values, Ng et al. (2004) and Liu et al. (2008) obtained results similar to those presented by the other studies and did not investigate the influence of using different initial stress conditions.

All these studies represent a valid effort towards understanding how the lining of the tunnels are affected by twin tunnelling, since it is extremely unlikely to be able to investigate based on real cases due to the rigid geometry configurations that are usually imposed and due to the absence of monitoring data available. As a result, the most common option to analyse the problem is by conducting vast numerical studies where the influence of the different parameters is analysed through parametric studies.

## 3. Methodology employed

Figure 1 shows the layout of the geometry adopted in all 2D plane strain analyses. For the reference analyses a depth of the tunnel axis ( $H$ ) of 19 m (cover of 16 m) was adopted, while the circular tunnels had a diameter

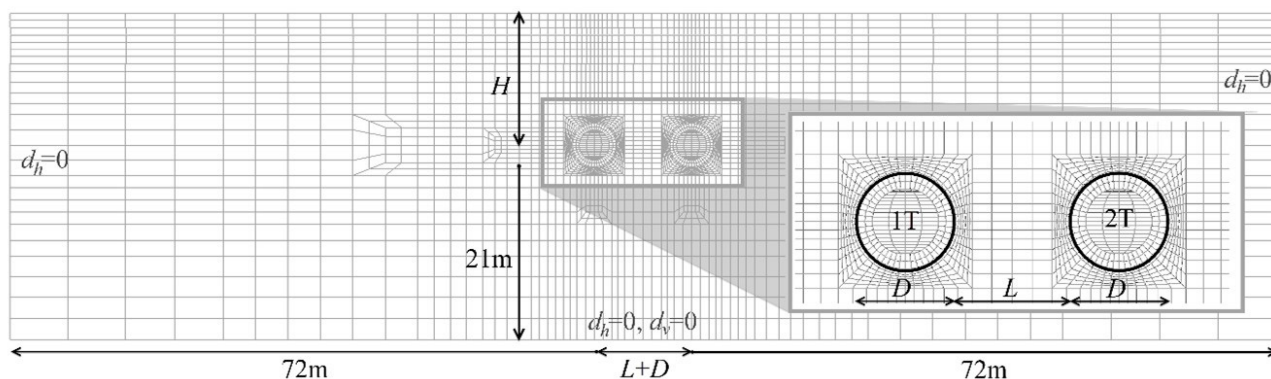


**Figure 1.** Layout of the geometry and finite element mesh for the model with  $L/D = 1.0$ .

**Table 1.** Summary of the relevant studies about pressures and lining forces induced by twin tunnelling.

References	Geotechnical soil model	Tunnel geometry	Method of analysis	Main results about pressures and lining forces
Ghaboussi & Ranken (1977)	Linear elastic $K_0 = 0.5$	$D = (?)$ m $H/D = 1.5$ ; 5.5 $L/D = 0.25$ to 1.0	Numerical 2D Excavation in full section	Increase of forces in the lining in the zone around the pillar springline in both tunnels; Interaction more relevant for deep tunnels; Suggest no interaction for $L/D > 2.0$
Soliman et al. (1993)	Linear elastic Stiffness of the ground varied $K_0 = 0.5$	$D = 10$ m $H/D = 3.5$ $L/D = 0.25$ ; 0.5	Numerical 2D / 3D Excavation in full section	Increase of forces in the lining of both tunnels; Bending moments are more affected by the 2T excavation but no trend was observed with the increase of stiffness of the ground
Adachi et al. (1993)	Sand $c' = 0$ kPa; $\phi' = 30^\circ$ $K_0 \approx 0.7$	$D = 130$ mm $H/D = 1.0$ to 4.5 $L/D = 0.5$ to 2.0	Small scale 1g model Excavation in full section by reducing the diameter	Interaction between tunnels increases with the increase of the overburden. Interaction still occurs for $L/D = 2.0$
Kim et al. (1998)	Speswhite kaolin clay $S_u \approx 20$ kPa $K_0 \approx 0.5$	$D = 70$ mm $H/D = 3.2$ $L/D = 0.4$ ; 1.0	Small scale 1g model Simulation of an EPB-TBM	Interaction between tunnels was observed with an increase of the bending moments on the 1T at the pillar springline
Ng et al. (2004)	Drucker-Prager (equivalent Mohr-Coulomb: $c' = 5$ kPa; $\phi' = 22^\circ$ ) $K_0 = 1.5$	$D \approx 8.6$ m (Oval) $H/D = 2.3$ $L/D = 1.0$	Numerical 3D NATM modelling with 2 side-drifts and variable lagged distance	Increase of the lining forces (bending and hoop) of the 1T with the increase of the lagged distance; The lining forces on both tunnels are minimum for a zero lagged distance
Hage Chehade & Shahrour (2008)	Mohr-Coulomb ( $c' = 3$ kPa; $\phi' = 33^\circ$ ) $K_0 = 0.5$	$D = (?)$ m $H/D = 2.5$ $L/D = 1.0$ to 4.0	Numerical 2D ( $\beta = 0.5$ ) Excavation in full section	No interaction was detected on the hoop forces while a residual increase was observed on the bending moments for $L/D < 2.0$
Liu et al. (2008)	Mohr-Coulomb ( $c' = 500$ kPa; $\phi' = 38^\circ$ ) $K_0$ varies with depth and direction	$D \approx 10$ m (Oval) $H/D = 1.5$ ; 3.0 $L/D = 1.0$ ; 2.0	Numerical 3D NATM modelling with excavation in full section	Stresses in the 1T lining increase after the 2T excavation; Interaction increases with the decrease of the pillar width
Hossaini et al. (2012) (Section 1)	Mohr-Coulomb ( $c' = 0$ kPa; $\phi' = 35^\circ$ ) $K_0 = 0.43$	$D = 6.9$ m $H/D = 1.9$ $L/D = 0.5$ to 1.5	Numerical 3D Simulation of an EPB-TBM	Increase of forces (bending and hoop) in the lining of 1T after the 2T excavation; Minimum interaction for $L/D > 1.5$
Do et al. (2014a)	Mohr-Coulomb ( $c' = 0$ kPa; $\phi' = 37^\circ$ ) $K_0 = 0.5$	$D = 94$ m $H/D = 2.1$ $L/D = 0.25$ to 3	Numerical 2D ( $\beta = 0.3$ ) Excavation in full section	Relevant increase of the hoop forces on both tunnels (mainly on 1T) while only a slight variation observed on the bending moments; Interaction is relevant for $L/D < 1.0$ and more relevant if in a jointed lining; Negligible interaction for $L/D > 2.0$
Do et al. (2015)	CY soil model ( $c' = 0$ kPa; $\phi' = 37^\circ$ ) $K_0 = 0.5$	$D = 9.4$ m $H/D = 2.1$ $L/D = 0.25$ to 2	Numerical 3D Simulation of an EPB-TBM considering a lagged distance of 10D	Relevant increase of the lining forces (bending and hoop) on the 1T; Slight decrease of the lining forces (bending and hoop) on the 2T; Negligible interaction for $L/D > 1.0$
Do et al. (2016)	CY soil model ( $c' = 0$ kPa; $\phi' = 37^\circ$ ) $K_0 = 0.5$	$D = 9.4$ m $H/D = 2.1$ $L/D = 0.25$	Numerical 3D Simulation of an EPB-TBM considering variable lagged distance	Increase of the hoop forces of both tunnels with the lagged distance, while the opposite occurs for the bending moments; The lining forces on both tunnels are minimum for a zero lagged distance

Table 1. Continued...

References	Geotechnical soil model	Tunnel geometry	Method of analysis	Main results about pressures and lining forces
Shivaiei et al. (2020)	Modified Cam-Clay ( $M = 1.14$ ; $\kappa = 0.011$ ; $\lambda = 0.048$ ) $K_0 = 0.55$	$D = 6.9$ m $H/D = 2.75$ $L/D = 1.2$	Numerical 3D (coupled-consolidation) Simulation of an EPB-TBM Consolidation of the soil after the complete excavation of each tunnel	Increase of the lining permeability from impermeable to fully permeable originates an increase of the lining forces (bending and hoop) on both tunnels, which is more relevant on the 1T on the pillar side;
Cheng et al. (2020)	Mohr–Coulomb ( $c' = 5$ kPa; $\phi' = 33.3^\circ$ ) $K_0 = 0.7$	$D = 6.1$ m $H/D = 3.5$ (1T) $L/D = 0.4$ (2T above 1T)	Numerical 2D ( $\beta = 0.1$ ) Excavation in full section Piggyback configuration	Good agreement of the hoop forces between the numerical predictions and the field measurement

( $D$ ) of 6 m and were spaced of a distance ( $L$ ) which varied between a minimum value of 1.5 m and a maximum value of 24 m, corresponding to extreme  $L/D$  ratios of 0.25 and 4.0, respectively. A continuous lining with 0.3 m thick was considered in both tunnels. Different values for the depth and diameter of the tunnels and for the thickness of the lining were adopted to assess their influence on the lining forces.

The finite element meshes employed in the analyses were different according with the geometries adopted. In all cases the tunnels were centred in the mesh and both the soil and the lining were discretized with quadrilateral solid elements, each with eight nodal points and four Gauss points for displacement and stress evaluation, respectively. To ensure the complete stabilisation of both stress and strain fields induced by the excavations a lateral distance of 72 m was adopted, measured from the centrelines of the nearest tunnel to the model external right/left border, while the bottom boundary was placed at 21 m below the invert of the tunnels (Figure 1). In terms of boundary conditions, no horizontal displacements ( $d_h = 0$ ) were allowed along the lateral boundaries of the mesh, while at the bottom the displacements were constrained in both directions ( $d_h = 0$ ,  $d_v = 0$ ). No restriction of displacements was imposed at the top of the model, coincident with the ground surface. Drained conditions were assumed in all analyses and consequently no hydraulic boundaries were prescribed. In order to improve the accuracy of the results a high discretization and density of elements around the tunnels and on the linings was adopted (Figure 1).

In line with the most recent studies (Table 1) a perfectly plastic non-associated Mohr–Coulomb yield criterion was adopted for describing the soil strength. For the stiffness a modified version of the power law proposed by Janbu (1967), where the deformability modulus varies throughout the analysis with the minimum principal effective stress (Equation 1), was employed.

$$E_s = E_0 + A \times p_{\text{ref}} \times \left( \frac{\sigma'_3}{p_{\text{ref}}} \right)^n \quad (1)$$

The values adopted for the soil parameters are presented in Table 2 and were established having as reference the values employed by the previous studies in order to facilitate the comparison of results. As for the lining a linear elastic behaviour, characterised by a Poisson's ratio ( $\nu_l$ ) of 0.2 and a Young's modulus ( $E_l$ ) of 30 GPa, was adopted to simulate the pre-cast concrete segments.

To establish the initial geostatic stresses in the model the vertical stresses were calculated assuming a unit weight of 20 kN/m<sup>3</sup> while the horizontal stresses were determined by considering a constant  $K_0$  of 0.6.

Modelling the excavation of a tunnel in 2D requires simplifications and assumptions in order to account for the 3D effects of the excavation of the tunnel. From the diverse approaches available in the literature (Möller, 2006) the stress reduction method is the most common and was adopted in the present study. This method simulates the excavation in two stages. In the first, the elements inside the tunnel are removed and the initial ground pressure ( $p_0$ ) acting on the tunnel contour, is reduced of  $(1 - \beta) \times p_0$ . In the second stage the lining is installed and the remaining load,  $\beta \times p_0$ , applied so that a final equilibrium state is achieved. As demonstrated by Möller & Vermeer (2006) the selection of an appropriate load reduction factor ( $\beta$ ) is one of the difficulties of the method. Their study concluded that the adoption of one single  $\beta$ -value is not suitable for reproducing both the lining forces and the displacements observed in the 3D calculations and suggested using  $\beta$ -values between 0.3 and 0.4 to properly match the displacements, while for the lining forces higher values, in the range of 0.5 to 0.7, are recommended. Given the purpose of this investigation a value of 0.6, in line with the suggestion of Möller & Vermeer (2006), was adopted in all analyses. For modelling the sequential excavation of



both tunnels this procedure was adopted separately for each tunnel, first for the left tunnel (1T) and then for the right tunnel (2T), resulting in a total of four stages.

#### 4. Influence of the pillar width

The influence of the pillar width on the hoop force and bending moment of both tunnels for the final stage (i.e. after the 2T excavation) is illustrated in the radial diagrams presented in Figure 2, for six  $L/D$  ratios, varying from 0.25 to 4.0. For ease of comparison the values obtained in greenfield conditions, i.e., immediately after the 1T excavation (stage 2), are also superimposed on the figures. As expected and in agreement with the results of Möller (2006), the hoop forces obtained in greenfield conditions are always compressive and symmetrical in relation to the tunnel centreline, exhibiting higher values at the springline, of around 654 kN/m, in correspondence with the squat of the lining caused by the  $K_0$  being smaller than one. At the invert the hoop forces are slightly higher ( $\approx 445$  kN/m) than those determined at the crown ( $\approx 383$  kN/m) as a result of the higher geostatic pressure. The bending moments in greenfield conditions exhibit a maximum negative value at the springline ( $\approx -64$  kNm/m) and a slightly smaller positive value at the invert and crown ( $\approx 61$  kNm/m). The inversion of sign of the bending moment is also associated with the deformation shape of the lining and occurs around the shoulder and knee of the lining, being positive (sagging) within these locations and negative (hogging) in the other parts of the lining.

Figure 2 shows that for  $L/D > 2.0$  the final lining forces on both tunnels are similar to those determined for greenfield conditions, implying that the 2T excavation had a minimal impact on the lining forces and consequently the interaction effects appear to be minimal. For smaller  $L/D$

the lining forces surpass those determined for greenfield conditions and increase with the decrease of the pillar width, reaching a maximum for  $L/D = 0.25$ . This behaviour is in agreement with the results of Do et al. (2014a, 2016) and confirms that the interaction between tunnels leads to an increase of the lining forces in both of them. The increase in both hoop forces and bending moments is more relevant in the 1T with the highest variations observed on the side of the 2T, with a maximum at the pillar springline, as noted by Kim et al. (1998). In the 2T the lining forces variations are smaller but are also primarily concentrated around the pillar springline (i.e., springline closest to the 1T in this case).

To facilitate the comprehension of the results the maximum absolute values of the lining forces ( $F_{Final}$ ) are normalised by the respective greenfield values ( $F_{Greenfield}$ ) and replotted in Figure 3 against the  $L/D$  ratio. The plot confirms that maximum interaction occurs for tunnels closely spaced and tend to decrease with the increase of the pillar width, being residual for  $L/D = 2.0$  and negligible for  $L/D > 3.0$ . The trend observed for both lining forces is similar in each tunnel with the bending moments presenting a slightly more pronounced decay. For the 1T (solid lines) a maximum increase of about 30% and 27% is observed on the hoop force and bending moment, respectively, for a  $L/D = 0.25$ . However, for the same  $L/D$ , the increase in the 2T lining forces (dashed lines) is considerably smaller and does not surpass 12%, with the bending moment being slightly higher in this case.

#### 5. Stiffness of the lining

The forces acting on the lining are influenced by the relative stiffness between the soil and the lining, which can be evaluated by recurring to two dimensionless coefficients,

**Table 2.** Soil parameters adopted in the reference analysis.

$\gamma$ (kN/m <sup>3</sup> )	$\phi'$ (°)	$c'$ (kPa)	$\psi$ (°)	$E_0$ (kPa)	$A$	$n$	$p_{ref}$ (kPa)	$v_s$	$K_0$
20	35	5	5	5000	400	0.5	100	0,3	0.6

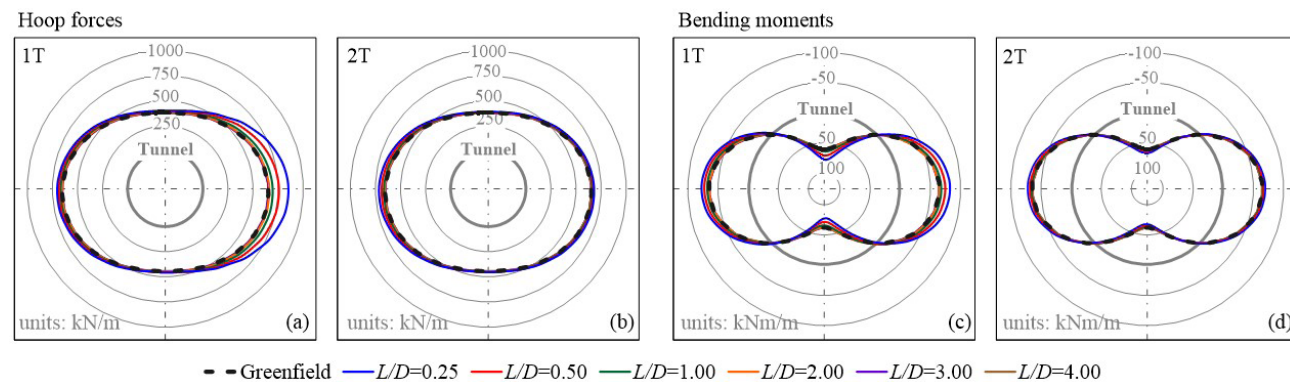


**Figure 2.** Radial diagrams of the hoop forces and bending moments acting on the lining for the reference analyses on both tunnels.



the compressibility ( $c$ ) and the flexibility ( $f$ ) ratios (Peck et al., 1972), as expressed in the following equations:

$$c = \frac{E_s \times R \times (1 - \nu_l^2)}{E_l \times t (1 + \nu_s) (1 - 2\nu_s)} \quad (2)$$

$$f = \frac{E_s \times R^3 \times (1 - \nu_l^2)}{6 \times E_l \times I \times (1 + \nu_s)} \quad (3)$$

where  $E_l$  and  $\nu_l$  are the Young's modulus and Poisson's ratio of the lining and  $E_s$  and  $\nu_s$  are the equivalent values of the soil determined for the depth of the tunnel axis.  $R$  is the radius of the tunnel and  $t$  and  $I$  refer to the thickness and moment of inertia of the lining cross-section. The compressibility ratio ( $c$ ) is a measure of the extensional stiffness of the soil relative to that of the lining under a uniform external pressure, while the flexibility ratio ( $f$ ) is associated with the relative

flexural stiffness under a state of pure shear. The results of Peck et al. (1972) show that the flexibility ratio is particularly relevant when analysing the lining behaviour. As confirmed by Kim et al. (1998) tests, for flexibility ratios higher than 10 the lining can be considered flexible and no substantial variations on the bending moments values should be expected.

In order to clarify the influence of the stiffness of the lining three sets of analyses were carried out. In these the geometrical characteristics of the tunnels and linings were chosen so that preferably stiffer, though realistic, linings were obtained, while the stiffness properties of both soil and lining were kept equal to the reference values to better isolate and assess the effects of the variable parameters. In Set A, the thickness ( $t$ ) of the lining was varied from 0.15 to 0.6 m, while keeping the diameter of the tunnel constant with 6 m. In set B, diameters of the tunnel of 4, 6 and 8 m were adopted under a constant aspect ratio,  $D/t$ , equal to 20. In the third set (Set C) two additional analyses were performed to explore extreme scenarios, one with a tunnel diameter of 4 m and  $D/t = 10$  representing a very stiff lining, and the other with a diameter of 8 m and  $D/t = 40$  corresponding to a flexible lining. The geometrical characteristics of the tunnels and linings employed in the three sets of analyses are presented in Table 3.

The results of the lining forces are presented in Figure 4 for the three sets of analyses. In the radial diagrams the hoop forces and bending moments obtained in greenfield conditions are represented, while in the other plots the final normalized maximum values are plotted against the  $L/D$  ratio for both tunnels. The results of Set A are displayed on the left side (corresponding to plots (a), (b), (e) and (f)) while Set B and C are depicted on the right (corresponding to plots (c), (d), (g) and (h)). Looking at the effect on the hoop forces, and in spite of the significant variation of the thickness of the lining considered in the analyses, the results obtained in greenfield conditions are similar with only a maximum variation of about 8% observed at the tunnel springlines between the two extreme cases analysed, 15 and 60 cm thick (Figure 4a). These results can be related with the compressibility ratio, which is small and of the same magnitude in all analyses, indicating that the lining is considerably stiffer than the soil. Furthermore, the interaction effects observed in the hoop force after the

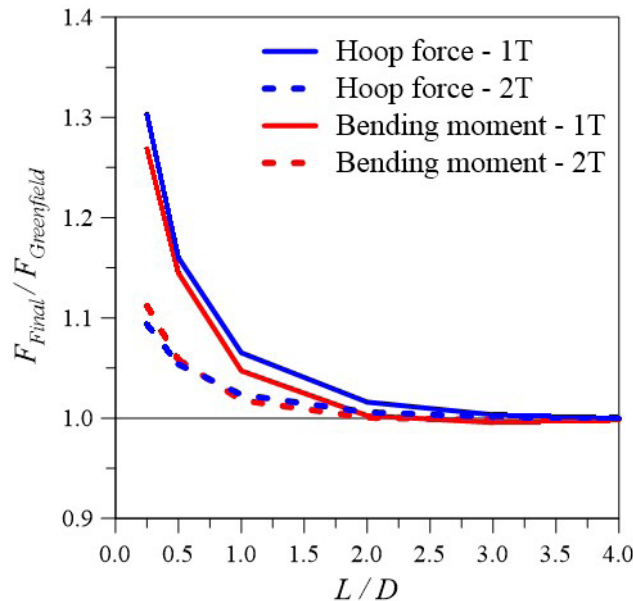


**Figure 3.** Influence of the pillar width on the lining forces.

**Table 3.** Geometrical characteristics of the tunnels and linings employed in the analyses.

Set	A					B			C	
Designation	$t=15\text{cm}$	$t=20\text{cm}$	$t=30\text{cm}$	$t=40\text{cm}$	$t=60\text{cm}$	$D4-D/t=20$	$D6-D/t=20$	$D8-D/t=20$	$D4-D/t=10$	$D8-D/t=40$
$D$ (m)	6	6	6	6	6	4	6	8	4	8
$C$ (m)	16	16	16	16	16	16	16	16	16	16
$H$ (m)	19	19	19	19	19	18	19	20	18	20
$t$ (cm)	15	20	30	40	60	20	30	40	40	20
$D/t$	40	30	20	15	10	20	20	20	10	40
$c$	$3.8 \times 10^{-2}$	$2.8 \times 10^{-2}$	$1.9 \times 10^{-2}$	$1.4 \times 10^{-2}$	$9.4 \times 10^{-3}$	$1.8 \times 10^{-2}$	$1.9 \times 10^{-2}$	$1.9 \times 10^{-2}$	$9.2 \times 10^{-3}$	$3.8 \times 10^{-2}$
$f$	12.0	5.1	1.5	0.6	0.2	1.5	1.5	1.5	0.2	12.3

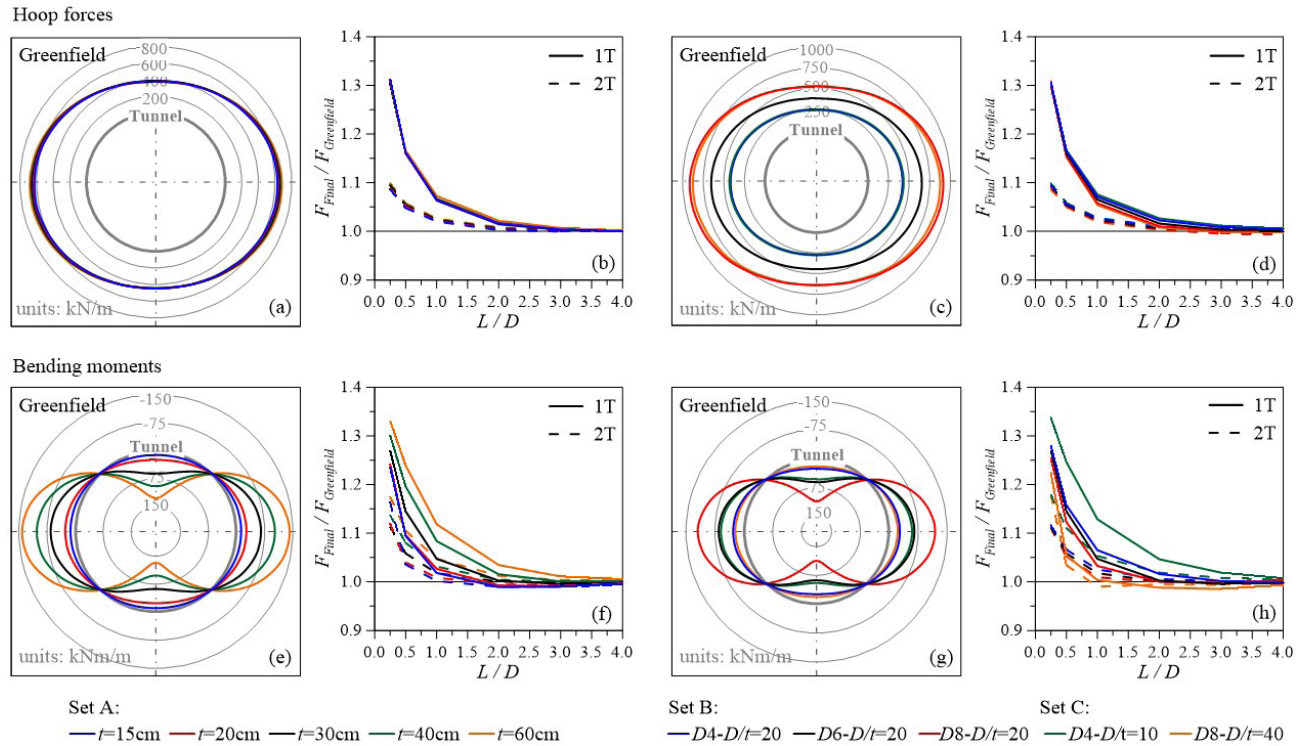


**Figure 4.** Influence of the thickness and of the tunnel lining aspect ratio on the lining forces.

2T excavation are also almost independent of the thickness of the lining with a similar behaviour observed in all cases (Figure 4b). Naturally, and as mentioned in the previous section, the interaction affects mainly the 1T, although the increase of forces cannot be neglected for  $L/D < 2.0$  in both tunnels. Figure 4c shows that the diameter of the tunnel under a constant aspect ratio only scales the magnitude of the hoop forces, while its overall behaviour remains equal. As expected, a higher diameter of the tunnel corresponds to higher hoop forces since the excavated soil mass increases considerably. In similarity with the previous results and in agreement with the compressibility ratio interpretation it is also verified that the influence of the thickness on the hoop force is also minimal when the diameter of the tunnel is varied. The results of the tunnel interaction (Figure 4d) show that despite all analyses presenting a similar value for  $L/D = 0.25$  a slightly higher decay, predominantly observed in the 1T, is visible with the increase of the tunnel diameter. Nevertheless, the overall behaviour is very similar in all analyses and suggests that the hoop forces are not significantly affected by changing the geometrical characteristics of the lining, particularly if linings with small compressibility ratios are considered.

In contrast with the observed in the hoop forces, the bending moments values are influenced by the thickness of the lining in greenfield conditions and tend to increase considerably for thicker linings (Figure 4e). In agreement with Peck et al. (1972) results, as the thickness reduces the

lining becomes flexible and the bending moments became smaller and uniform. The thickness of the lining also influences the bending moment distribution when the 2T is excavated. Figure 4f shows that for greater thicknesses the interaction increases in magnitude and extends to a further distance, reaching  $L/D = 3.0$  for a thickness of 60 cm. The increase in magnitude is observed in both tunnels, although continues greater in the 1T. As shown in Figure 4g, the diameter of the tunnel under constant aspect ratio (Set B) also affects the bending moments in greenfield conditions. As the diameter of the tunnel increases the bending moments also increase, though the overall behaviour remains similar in all cases, with the maximum absolute values observed at the springlines. The extreme cases analysed in Set C confirmed the influence of the thickness on the bending moments, with higher values obtained in the stiffer lining ( $D4-D/t=10$ ) and smaller in the flexible lining ( $D8-D/t=40$ ) in comparison with the results of the analyses with the same diameter and  $D/t = 20$ . Also in this case the interaction effects observed in the bending moments depend on the diameter of the tunnel under constant aspect ratio as it can be seen by the results of Set B (Figure 4f). For  $D/t = 20$  the interaction between tunnels tends to decrease slightly when larger diameters are considered, though it is still relevant in both tunnels for  $L/D < 2.0$ . The two extreme cases analysed in Set C clearly show that the interaction effects tend to increase in magnitude and extension (negligible only for  $L/D > 3.0$ ) when stiffer

linings are considered and is minor and only relevant for  $L/D < 1.0$  when flexible linings are employed.

## 6. Initial stress conditions

The initial stress conditions are a fundamental aspect in tunnelling since their orientation and value directly influences the distribution and magnitude of the forces acting on the lining. In order to further explore this aspect two additional sets of analyses were performed. In Set D, the effect of the overburden was analysed by varying the cover ( $C$ ) of the tunnel from 8 to 32 m, while keeping a constant  $K_0$  value equal to 0.6. In the second set (Set E) the cover was kept constant as 16 m while the  $K_0$  value was varied from 0.4 to 1.2 in order to evaluate the influence of the lateral stresses. All other parameters were unchanged and kept equal to those employed in the reference analyses.

The results of the lining forces are presented in Figure 5 for the two sets of analyses. In the radial diagrams the hoop forces and bending moments obtained in greenfield conditions are represented, while in the other plots the final normalized maximum values are plotted against the  $L/D$  ratio for both tunnels. The results of Set D are displayed on the left side (corresponding to plots (a), (b), (e) and (f)) while Set E is depicted on the right (corresponding to plots (c), (d), (g) and (h)). Figure 5a shows that the increase in overburden translates in an almost proportional increase of the hoop forces in greenfield conditions, with the minimum values observed

for a cover of 8 m and the maximum for 32 m. The overburden of the tunnels marginally influences the interaction effects on the hoop forces, which continue to be significant for  $L/D < 1.0$  and negligible for  $L/D > 3.0$  (Figure 5b). The exception is the analysis with the minimum cover of 8 m, where a higher decay of the interaction is visible, suggesting that for shallower tunnels the interaction only occurs when the tunnels are closely spaced ( $L/D < 2.0$ ). This result is in agreement with Adachi et al. (1993) observations and is justified by the impossibility of the typical yielding zones observed in shallower tunnels fully develop and transfer load to the other tunnel due to the small cover.

The influence of the  $K_0$  on the hoop forces for greenfield conditions is plotted in Figure 5c. With the increase of the  $K_0$  the behaviour of the lining is modified and the hoop forces at the crown and invert tend to increase due to the higher lateral stresses, while the forces at the springline remain approximately constant since the overburden is equal in all analyses. For a  $K_0 = 1.0$  an almost uniform hoop force is observed throughout the entire lining, with just a slight increase in depth due to the higher geostatic stresses, while for a  $K_0 = 1.2$  the maximum hoop forces became located at the invert and crown. The analysis of the interaction plot (Figure 5d) shows that the maximum hoop forces in the lining present a similar behaviour for  $K_0$  smaller than 1.0, with the typical increase of forces on both tunnels, higher in the 1T, with the decrease of the pillar width. However, for a  $K_0 \geq 1.0$  a considerable modification occurs with the

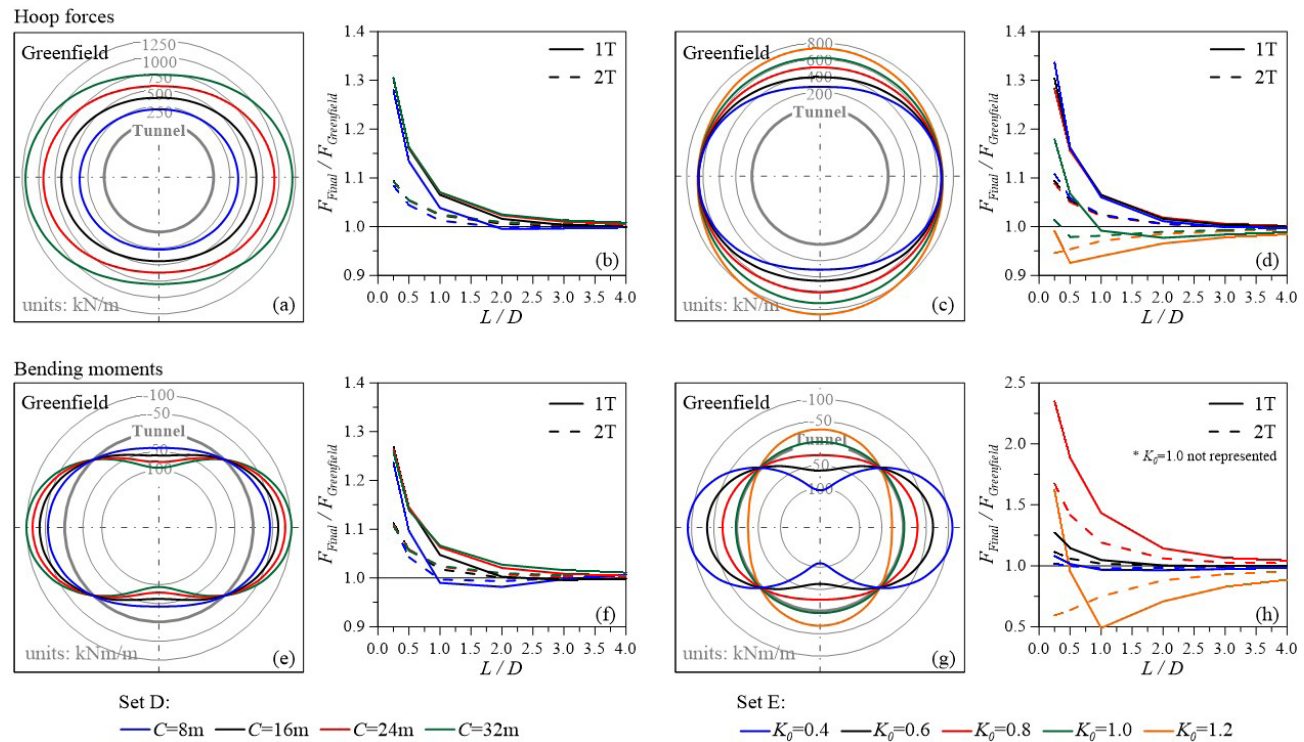


**Figure 5.** Influence of the cover and of the  $K_0$  on the lining forces.



final maximum forces becoming inclusively smaller than those determined in greenfield conditions, for almost all  $L/D$  ratios when  $K_0 = 1.0$  and for all pillar widths when  $K_0 = 1.2$ . Naturally, with the increase of the pillar width all analyses tend to converge towards zero interaction. In order to understand the behaviour observed when  $K_0 \geq 1.0$  the distribution of hoop forces acting on the lining of both tunnels for the final stage are plotted in Figure 6 for the most relevant pillar widths ( $L/D = 0.25, 0.5, 1.0$  and  $2.0$ ). From the plot it is possible to verify that with the 2T excavation the hoop forces in both tunnels tend to increase at the pillar springline and to decrease at the crown and invert with the decrease of the pillar width. Consequently, and in contrast with the previous analyses where the maximum hoop forces always occurred at the pillar springline, when  $K_0 \geq 1.0$  the maximum values in the greenfield and final stages do not occur at the same location. As a result, an overall relative reduction in the final hoop forces can occur in the lining as shown in Figure 5h, since only the maximum values are considered in the plot, regardless of their location at the lining. However, it should be noted that in some parts of the lining, namely at the pillar springline, a substantial increase of forces should be expected due to the 2T excavation.

The influence of the overburden on the bending moments is also presented in Figure 5. The greenfield results show that the increase of the cover translates in moderately higher bending moments as a result of the higher stresses, though the overall behaviour of the lining remains unchanged (Figure 5e). The interaction effects observed in the bending moments after the 2T excavation depend on the overburden

of the tunnel and present a similar trend to that observed on the hoop forces but with a slightly more pronounced decay (Figure 5f). For the analysis with a cover of 8 m the influence of the presence of the 1T is just relevant for  $L/D < 1.0$ , confirming that shallower tunnels only interact if closely spaced.

Figure 5g shows that the  $K_0$  value influences the bending moments distribution in greenfield conditions. For  $K_0 < 1.0$  the lining squats and consequently positive bending moments are obtained at crown and invert, while negative values are determined at the springlines. However, when  $K_0 > 1.0$  the lining deformation shifts from squatting to egging, with the consequent inversion of signal of the bending moments. In the particular case where  $K_0 = 1.0$  the bending moments are nearly zero due to the almost symmetrical loading. The  $K_0$  value also affects significantly the bending moments induced by the 2T excavation as it can be seen in Figure 5h. With the increase of the  $K_0$  value up to 1.0 a significant increase of the bending moments is observed on both tunnels. For a  $K_0 = 0.8$  an increase of the bending moments of nearly 230% and 170% is observed in the 1T and 2T, respectively, and even higher variations are obtained for a  $K_0 = 1.0$  (not represented in the figure). However, these increases are exponentiated by the almost zero values determined in greenfield conditions and correspond to final bending moments of moderate magnitude as it can be seen in Figure 7. In contrast, for a  $K_0 = 0.4$  almost no interaction between tunnels is observed with only a slight increase of forces obtained for  $L/D = 0.25$ . The different behaviour observed for  $K_0 = 1.2$  in both tunnels, is again justified by

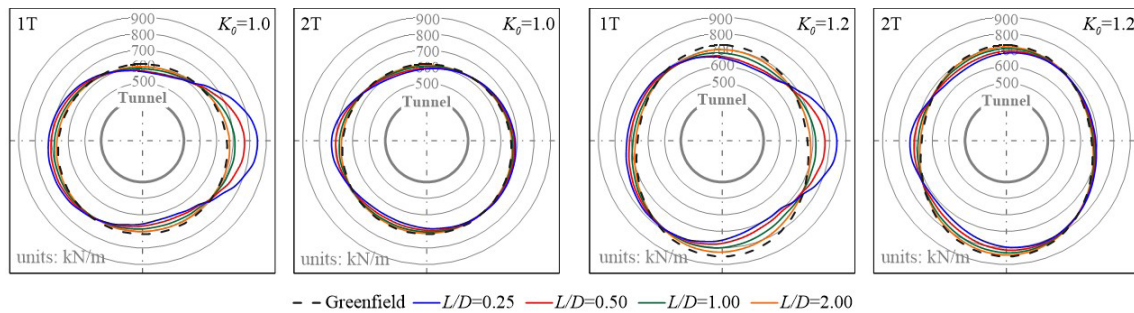


**Figure 6.** Radial diagrams of the hoop force acting on the lining for the  $K_0 = 1.0$  and  $K_0 = 1.2$  analyses.

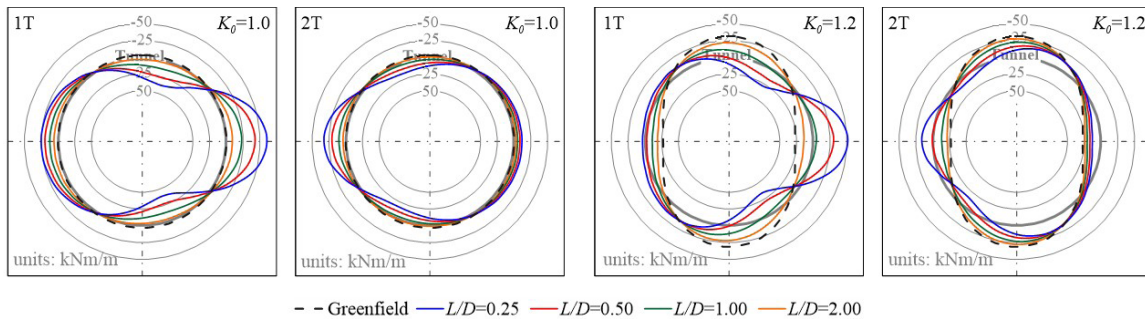


**Figure 7.** Radial diagrams of the bending moment acting on the lining for the  $K_0 = 1.0$  and  $K_0 = 1.2$  analyses.

the different location in the lining of the maximum absolute values of bending moment as can be seen in Figure 7. Also in this case, the excavation of the 2T originates an increase of bending moments at the pillar springline and a decrease at the invert and crown, inverting the position where the maximum values were observed in greenfield conditions.

## 7. Conclusions

It is well recognised that the excavation of a tunnel in close proximity to an existing one induces in the soil higher deformations due to the interaction effects between the tunnels. Furthermore, the second excavation also has an impact on the lining forces of both tunnels which is necessary to assess in order to design a lining capable to withstand the variations of forces induced by the excavation. In order to assess the influence of the flexibility and compressibility of the tunnel and of the initial stress conditions on the lining forces of both tunnels a series of 2D numerical analyses of side-by-side twin tunnels is carried out in this paper for a vast range of pillar widths and tunnel geometries. Based on the achieved results the following conclusions can be drawn:

- The results confirm that the 2T excavation induces higher hoop forces and bending moments on the linings of both tunnels, with the interaction being significant for  $L/D < 1.0$ , residual for  $L/D = 2.0$  and negligible for  $L/D > 3.0$ . The concentration of forces is essentially located at the pillar springline and is more relevant in the 1T, nearly 30%, although it cannot be neglected in the 2T where an increase of about 12% was still obtained for the same conditions;
- The thickness of the lining and the diameter of the tunnel marginally affected the increase of the hoop forces caused by tunnel interaction. In contrast, the bending moments are considerably influenced by those factors and an increase of the magnitude and of the extension of the interaction is observed when stiffer linings are employed;
- The increase of the overburden also does not influence the interaction between tunnels with similar curves being obtained for the lining forces. The exception was obtained for shallower tunnels suggesting that interaction only occurs if the tunnels are closely spaced due to the impossibility of the yielding zones above the tunnels to fully develop;
- The  $K_0$  value influences considerably the lining behaviour and the interaction between tunnels. For  $K_0 < 1.0$  the interaction is visible on the bending moments and increases with the increase of the  $K_0$  value, while no noticeable differences in the interaction are observed in the hoop forces. For  $K_0 \geq 1.0$  the lining deformation changes from squatting to egging in greenfield conditions and the maximum hoop forces and bending moments become located

at the invert and crown. With the 2T excavation a reduction on both forces is observed at these locations while an increase is visible at the pillar springline. As a result, an overall relative reduction in the final forces occurs in the lining for all pillar widths if  $K_0 = 1.2$  and for almost all  $L/D$  ratios if  $K_0 = 1.0$ .

The difficulties of finding real case studies where parameters such as the geometry and/or stiffness of the tunnel and/or the initial stress conditions vary significantly throughout the route makes this and the previous numerical studies valuable exercises in order to understand the behaviour of twin tunnels and to estimate the possible impact of a second excavation on an existing tunnel.

## Declaration of interest

The authors have no conflicts of interest to declare. All co-authors have observed and affirmed the contents of the paper and there is no financial interest to report.

## Authors' contributions

António Manuel Gonçalves Pedro: conceptualization, data curation, methodology, supervision, validation, writing – original draft. José Carlos Duarte Grazina: conceptualization, data curation, methodology, validation, writing – original draft. Jorge Nuno Veiga de Almeida e Sousa: conceptualization, methodology, validation, writing – review & editing.

## List of symbols

$c$	Compressibility ratio
$c'$	Soil cohesion
$d_h$	Horizontal displacement at model boundaries
$d_v$	Vertical displacement at model boundaries
$f$	Flexibility ratio
$n$	Parameter of the Janbu's law
$p_0$	Initial ground pressure
$p_{ref}$	Reference stress (= 100 kPa)
$t$	Thickness of the lining
$A$	Parameter of the Janbu's law
$C$	Cover of the tunnel
$D$	Diameter of the tunnel
$E_l$	Young's modulus of the lining
$E_s$	Soil deformability modulus
$E_0$	Soil deformability modulus at ground surface
$F_{Final}$	Final maximum hoop force / bending moment value
$F_{Greenfield}$	Greenfield maximum hoop force / bending moment value
$H$	Depth of the tunnel axis
$I$	Inertia of the tunnel lining
$K_0$	At-rest earth pressure coefficient
$L$	Pillar width
$M$	Stress ratio (Cam-clay model)




$R$	Radius of the tunnel
$S_u$	Undrained strength
$\beta$	Load reduction factor
$\gamma$	Unit weight of the soil
$\phi$	Angle of shear resistance
$\kappa$	Slope of the swelling line (Cam-clay model)
$\lambda$	Slope of the normal compression (Cam-clay model)
$\nu_l$	Poisson's ratio of the lining
$\nu_s$	Poisson's ratio of the soil
$\sigma'_3$	Minimum principal effective stress
$\psi$	Soil dilatancy angle

## References

- Adachi, T., Kimura, M., & Osada, H. (1993). Interaction between multi-tunnels under construction. In *Proceedings of the 11th Southeast Asian Geotechnical Conference* (pp. 51-60). Singapore.
- Addenbrooke, T.I., & Potts, D. (2001). Twin tunnel interaction: surface and subsurface effects. *International Journal of Geomechanics*, 1(2), 249-271. <http://dx.doi.org/10.1016/j.tust.2015.11.013>.
- Admiraal, H., & Cornaro, A. (2016). Why underground space should be included in urban planning policy – And how this will enhance an urban underground future. *Tunnelling and Underground Space Technology*, 55, 214-220. <http://dx.doi.org/10.1016/j.tust.2015.11.013>.
- Afifipour, M., Sharifzadeh, M., Shahriar, K., & Jamshidi, H. (2011). Interaction of twin tunnels and shallow foundation at Zand underpass, Shiraz metro, Iran. *Tunnelling and Underground Space Technology*, 26(2), 356-363. <http://dx.doi.org/10.1016/j.tust.2010.11.006>.
- Bartlett, J.V., & Bubbers, B.L. (1970). Surface movements caused by bored tunnelling. In *Proceedings Conference on Subway Construction* (pp. 513-539), Budapest.
- Bobylyev, N. (2016). Underground space as an urban indicator: measuring use of subsurface. *Tunnelling and Underground Space Technology*, 55, 40-51. <http://dx.doi.org/10.1016/j.tust.2015.10.024>.
- Chapman, D.N., Ahn, S.K., & Hunt, D.V. (2007). Investigating ground movements caused by the construction of multiple tunnels in soft ground using laboratory model tests. *Canadian Geotechnical Journal*, 44(6), 631-643. <http://dx.doi.org/10.1139/t07-018>.
- Cheng, W., Li, G., Ong, D.E.L., Chen, S., & Ni, J.C. (2020). Modelling liner forces response to very close-proximity tunnelling in soft alluvial deposits. *Tunnelling and Underground Space Technology*, 103, 103455. <https://doi.org/10.1016/j.tust.2020.103455>
- Cording, E.J., & Hansmire, W. (1975). Displacements around soft ground tunnels, general report: Session IV, Tunnels in soil. In *Proceedings of the 5th Pan American Conference on Soil Mechanics and Foundation Engineering* (pp. 571-633), Buenos Aires: Sociedad Argentina de Mecánica de Suelos e Ingeniería de Fundaciones.
- Cui, J., & Nelson, J.D. (2019). Underground transport: an overview. *Tunnelling and Underground Space Technology*, 87, 122-126. <http://dx.doi.org/10.1016/j.tust.2019.01.003>.
- Divall, S., & Goodey, R.J. (2015). Twin-tunnelling-induced ground movements in clay. *Geotechnical Engineering*, 168(3), 247-256. <http://dx.doi.org/10.1680/geng.14.00054>.
- Do, N., Dias, D., & Oreste, P. (2015). 3D numerical investigation on the interaction between mechanized twin tunnels in soft ground. *Environmental Earth Sciences*, 73(5), 2101-2113. <http://dx.doi.org/10.1007/s12665-014-3561-6>.
- Do, N., Dias, D., & Oreste, P. (2016). 3D numerical investigation of mechanized twin tunnels in soft ground—Influence of lagging distance between two tunnel faces. *Engineering Structures*, 109, 117-125. <http://dx.doi.org/10.1016/j.engstruct.2015.11.053>.
- Do, N., Dias, D., Oreste, P., & Djeran-Maigre, I. (2014a). 2D numerical investigations of twin tunnel interaction. *Geomechanics and Engineering*, 6(3), 263-275. <http://dx.doi.org/10.12989/gae.2014.6.3.263>.
- Do, N.-A., Dias, D., Oreste, P., & Djeran-Maigre, I. (2014b). Three-dimensional numerical simulation of a mechanized twin tunnels in soft ground. *Tunnelling and Underground Space Technology*, 42, 40-51. <http://dx.doi.org/10.1016/j.tust.2014.02.001>.
- Elwood, D.E.Y., & Martin, C.D. (2016). Ground response of closely spaced twin tunnels constructed in heavily overconsolidated soils. *Tunnelling and Underground Space Technology*, 51(Suppl. C), 226-237. <http://dx.doi.org/10.1016/j.tust.2015.10.037>.
- Fargnoli, V., Boldini, D., & Amorosi, A. (2015). Twin tunnel excavation in coarse grained soils: observations and numerical back-predictions under free field conditions and in presence of a surface structure. *Tunnelling and Underground Space Technology*, 49, 454-469. <http://dx.doi.org/10.1016/j.tust.2015.06.003>.
- Ghaboussi, J., & Ranken, R.E. (1977). Interaction between two parallel tunnels. *International Journal for Numerical and Analytical Methods in Geomechanics*, 1(1), 75-103.
- Grazina, J. (2009). *Dynamic modelling of elastoplastic massifs with viscous coupling. Application to flexible retaining walls under seismic loading*. [Doctoral thesis, University of Coimbra]. University of Coimbra's repository (in Portuguese). <http://hdl.handle.net/10316/12076>
- Hage Chehade, F., & Shahrour, I. (2008). Numerical analysis of the interaction between twin-tunnels: influence of the relative position and construction procedure. *Tunnelling and Underground Space Technology*, 23(2), 210-214. <http://dx.doi.org/10.1016/j.tust.2007.03.004>.
- Hossaini, S.M., Shaban, M., & Talebinejad, A. (2012). Relationship between twin tunnels distance and surface subsidence in soft ground of Tabriz Metro, Iran. In N. Aziz & B. Kininmonth (Eds.), *12th Coal Operators' Conference* (pp. 163-168). University of Wollongong.
- Islam, M.S., & Iskander, M. (2021). Twin tunnelling induced ground settlements: a review. *Tunnelling and Underground*

- Space Technology*, 110, 103614. <https://doi.org/https://doi.org/10.1016/j.tust.2020.103614>
- Janbu, N. (1967). *Settlement calculations based on the tangent modulus concept. Three guest lectures at Moscow State University*. Technical University of Norway.
- Kim, S.H., Burd, H.J., & Milligan, G.W.E. (1998). Model testing of closely spaced tunnels in clay. *Geotechnique*, 48(3), 375-388. <http://dx.doi.org/10.1680/geot.1998.48.3.375>.
- Liu, H.Y., Small, J.C., & Carter, J.P. (2008). Full 3D modelling for effects of tunnelling on existing support systems in the Sydney region. *Tunnelling and Underground Space Technology*, 23(4), 399-420. <http://dx.doi.org/10.1016/j.tust.2007.06.009>.
- Mair, R.J., & Taylor, R.N. (1997). Bored tunnelling in the urban environment. In A.A. Balkema (Ed.), *Proceedings of the 14th International Conference on Soil Mechanics and Foundation Engineering, State-of-the-art Report and Theme Lecture* (Vol. 4, pp. 2353-2385). Balkema.
- Möller, S., & Vermeer, P. (2006). Prediction of settlements and structural forces in linings due to tunnelling. In *Proceedings of the 5th International Conference of TC 28 of the ISSMGE* (pp. 621-627). The Netherlands, 15-17 June 2005.
- Möller, S.C. (2006) *Tunnel induced settlements and structural forces in linings*. [Doctoral thesis, University of Stuttgart]. University of Stuttgart's repository. [https://www.igs.uni-stuttgart.de/dokumente/Mitteilungen/54\\_Moeller.pdf](https://www.igs.uni-stuttgart.de/dokumente/Mitteilungen/54_Moeller.pdf)
- Ng, C.W.W., Lee, K.M., & Tang, D.K.W. (2004). Three-dimensional numerical investigations of new Austrian tunnelling method (NATM) twin tunnel interactions. *Canadian Geotechnical Journal*, 41(3), 523-539. <http://dx.doi.org/10.1139/T04-008>.
- Nyren, R. (1998). *Field measurements above twin tunnels in London Clay*. [Doctoral thesis. Imperial College London]. Imperial College London's repository. <https://spiral.imperial.ac.uk/handle/10044/1/8573>
- Ocak, I. (2014). A new approach for estimating of settlement curve for twin tunnels. In *Proceedings of the World Tunnel Congress '14*, Foz do Iguaçu, Brazil.
- Peck, R.B., Hendron, A., & Mohraz, B. (1972). State of the art of soft-ground tunneling. In K.S. Lane & L.A. Garfield (Eds.), *Proceedings of the 1st Rapid Excavation and Tunnelling Conference* (Vol. 1, pp. 259-286). AIME.
- Shivaci, S., Hataf, N., & Pirastehfar, K. (2020). 3D numerical investigation of the coupled interaction behavior between mechanized twin tunnels and groundwater – A case study: shiraz metro line 2. *Tunnelling and Underground Space Technology*, 103, 103458. <https://doi.org/https://doi.org/10.1016/j.tust.2020.103458>
- Soliman, E., Duddeck, H., & Ahrens, H. (1993). Two- and three-dimensional analysis of closely spaced double-tube tunnels. *Tunnelling and Underground Space Technology*, 8(1), 13-18. [http://dx.doi.org/10.1016/0886-7798\(93\)90130-N](http://dx.doi.org/10.1016/0886-7798(93)90130-N).
- Sousa, J.N.V.A. (1998). *Túneis em maciços terrosos: comportamento e modelação numérica* [Doctoral thesis, University of Coimbra]. University of Coimbra's repository (in Portuguese). <http://hdl.handle.net/10316/1874>
- Wan, M.S.P., Standing, J.R., Potts, D.M., & Burland, J.B. (2017). Measured short-term ground surface response to EPBM tunnelling in London Clay. *Geotechnique*, 67(5), 420-445. <http://dx.doi.org/10.1680/jgeot.16.P.099>.
- Wu, B., & Lee, C. (2003). Ground movements and collapse mechanisms induced by tunneling in clayey soil. *International Journal of Physical Modelling in Geotechnics*, 3(4), 15-29. <http://dx.doi.org/10.1680/ijpmg.2003.030402>.

## Estimative of shaft and tip bearing capacities of single piles using multilayer perceptrons

Luciana Barbosa Amâncio<sup>1#</sup> , Silvrano Adonias Dantas Neto<sup>2</sup> ,

Renato Pinto da Cunha<sup>1</sup> 

Article

### Keywords

Multilayer perceptrons  
Pile shaft bearing capacity  
Pile tip bearing capacity  
Standard Penetration Test  
Instrumented load tests

### Abstract

There are an increasing number of studies that use the artificial neural networks (ANN) as a prediction tool in the field of foundations with satisfactory results. In this paper, multilayer perceptrons are used to develop prediction models for the shaft and tip bearing capacities of single piles based on a supervised training using the error back propagation algorithm. Results from static load tests carried out on 95 instrumented single piles executed in different regions of Brazil were used in the ANN modelling. The prediction models of shaft and tip bearing capacities of single piles were obtained portraying indicated in the validation phase determination coefficients equal to 95% and 99%, respectively. To demonstrate their applicability and efficiency, such models were used to estimate the bearing capacity of single piles unused in the models' development, as well as groups of two and three piles. The results demonstrated that the neuron models were much closer to the values of the bearing capacities measured in single pile tests and groups of piles, than the estimated results using semi-empirical methods. As a result of overestimating the predicted bearing capacities in relation to the results of the load tests, it is recommended to use models applying reduction factors of 0.88 for single piles, and 0.75 for groups of up to three piles.

## 1. Introduction

Pile foundations are responsible for transmitting loads from the superstructure to the ground, so that deformations do not affect the usage of the project. This transmission occurs through two mechanisms: friction (between the side of the pile and the ground) and reaction of the pile tip.

The bearing capacity of single pile ( $Q_r$ ) is defined by Cintra & Aoki (2010) as the sum of the maximum loads that can be supported by shaft and tip resistance. According to Fellenius (2016, 2021), a pile design based on "the bearing capacity is with a factor of safety of two or better, so we will have no settlement" is an inadequate, because the bothersome settlement is that caused by other factors than the pile loads, such as, fills, groundwater table lowering, neighboring structures, regional subsidence, etc.

The value of  $Q_r$  can be determined based on parameters taken from field and laboratory testing, by means of theoretical and or semi-empirical methods. Given the problems in obtaining the ground strength to adopt theoretical methods, the designer often resorts to semi-empirical methods which

use Standard Penetration Test (SPT) results to estimate the bearing capacity of different types of deep foundations, also taking into account the particular executive methods of each pile. Amann (2010) criticizes the indiscriminate use of such formulations without taking due care to the adjustments referring to the characteristics of the geotechnical profile on the development site of a specific design.

Studies developed by Maya et al. (2013), Probst et al. (2018), Amann et al. (2018), Carvalho & Santos (2019), Pereira et al. (2020), Silva (2020) indicate that there is high dispersion between the values of pile bearing capacity assessed by traditional semi-empirical methods and those ones obtained in dynamic and static load tests.

The static load test is an efficient way to check the bearing capacity of single piles assessed by using semi-empirical methods and, when in instrumented piles, it allows to analyze the load transfer mechanism from the pile to the surrounding soil. In the last decade several researchers have discussed the results of instrumentation performed on different types of piles (Tran et al., 2012; Seo et al., 2013; Haque et al., 2014; Musarra & Massad, 2015; Bohn et al., 2017; Bersan et al., 2018; Narsavage, 2019 and Akl & Mossaad, 2021).

<sup>#</sup>Corresponding author. E-mail address: lucianab@ufpi.edu.br

<sup>1</sup>Universidade de Brasília, Departamento de Engenharia Civil e Ambiental, Brasília, DF, Brasil.

<sup>2</sup>Universidade Federal do Ceará, Departamento de Engenharia Hidráulica e Ambiental, Fortaleza, CE, Brasil.

Submitted on November 25, 2021; Final Acceptance on June 3, 2022; Discussion open until November 30, 2022.

<https://doi.org/10.28927/SR.2022.077821>



This is an Open Access article distributed under the terms of the Creative Commons Attribution License, which permits unrestricted use, distribution, and reproduction in any medium, provided the original work is properly cited.

Quite an alternative used to improve the prediction process of deep foundation behavior has been to apply Artificial Neural Networks (ANN). Moayedi et al. (2020) reviewed the literature in which they found a total of 121 articles about the applicability of ANN in pile bearing capacity (lateral and axial). Pham et al. (2020), Chen et al. (2020), Kardani et al. (2020), Zhang et al. (2020), Benali et al. (2018), Maizir (2017) and Momeni et al. (2014, 2015) applied of ANN when predicting the piles bearing capacity. Most ANN models developed in the studies estimate the bearing capacity of piles or the shaft bearing capacity or tip bearing capacity and, in most cases, for the same soil profile.

There are different types of artificial neural networks for solving problems in geotechnical engineering being the multilayer perceptrons the most used (Tizpa et al., 2015; Kiran et al., 2016; Dantas Neto et al., 2017; Ebtehaj et al., 2018; Zhang et al., 2019; Darbor et al., 2019; De Granrut et al., 2019). What makes this neural network attractive is the presence of hidden layers and the high degree of connectivity which allows it to be capable of understanding the complex behavior of several multivariable phenomenon in geotechnical engineering.

Given the applicability of multilayer perceptrons and the scarcity of neuron models to predict the pile shaft bearing capacity depending on the depth and the pile tip bearing capacity of different types of piles and various geotechnical profiles, and in order to mitigate the restrictions found in semi-empirical methods, the purpose of this article is to propose neuron models that are able to estimate the shaft and tip bearing capacities of

single piles and even analyze the applicability of such models in predicting the failure load for groups of piles.

## 2. Materials and methods

### 2.1 Data collection

The first step of modeling with artificial neural networks is to define the variable that could influence the studied phenomenon, in this case the load transfer mechanism from the pile to the ground. This phenomenon is influenced by several factors, such as, for example: the pile's geometry, type of pile, installation process, initial stress status of ground and the loading background undergone by the pile (Bohn et al., 2017; Cooke et al., 1979).

Studies such as those by Benali et al. (2018), Maizir (2017) and Momeni et al. (2014, 2015) who used the artificial neural networks to predict the pile bearing capacity were developed by addressing between 35 and 260 field tests (Standard Penetration Test, Cone Penetration Test, Pile Driving Analyzer, Static Load Test), the used variables being related only to the pile's geometry and data take from those tests.

In this article, it was decided to use as input and output variables of the neuron models, developed to estimate shaft and tip bearing capacities of single piles, the information gained from results of static load tests piles, under axial compression effort, instrumented along the length and *SPT* boreholes. A database includes 95 single piles installed in different regions of Brazilian territory, as shown in Figure 1.

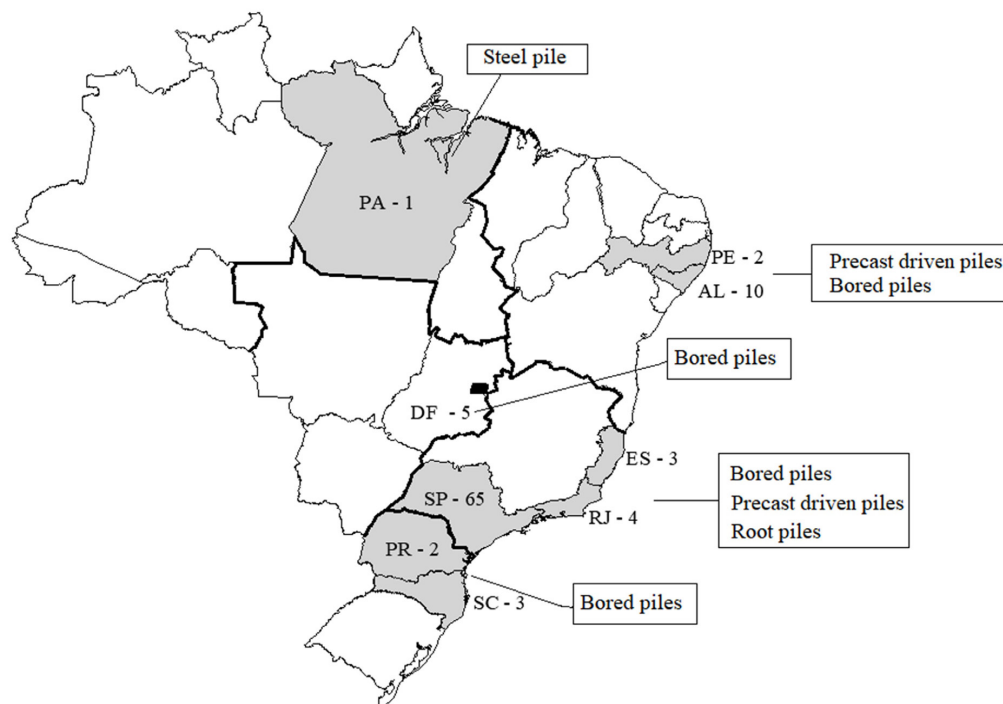


**Figure 1.** Distribution used instrumented piles on the Brazilian territory.

It is noted that, of the five Brazilian regions in question, the Southeast region concentrated the majority (72 piles), while the North, Midwest and South regions have the smallest quantities, that is, one, five and five piles, respectively.

It should be mentioned that the use of a database with information from different regions in Brazil and, consequently, installed in different geological conditions, gives the proposed neuron models more applicability and representativeness from a practical viewpoint.

## 2.2 Definition of neuron model variables

In this article, the output variables are the shaft and tip bearing capacities of single piles. To discover the input variables, the available information that influences the ground-pile interaction was found in the database (Pham et al., 2020; Chen et al., 2020; Benali et al., 2018; Maizir, 2017 and Momeni et al., 2014, 2015), and consequently, is responsible for mobilizing the shaft and tip bearing capacities of piles, namely: pile geometry (diameter and length); pile type; soil type; *SPT* test rate and type of loading applied to the static load test. All procedures and criteria used to define the input and output variables considered are described below.

### 2.2.1 Shaft and tip bearing capacities of pile

The shaft ( $Q_s$ ) and tip ( $Q_p$ ) bearing capacities of piles are provided by the instrumentation of the piles undergoing static load tests. It is important to emphasize that all piles were instrumented, 97% with strain gauges installed at different levels. In addition, the maximum loads applied to the piles are higher than the failure load defined by the Brazilian Standard (ABNT, 2019).

Only in cases where the piles were not instrumented at the tip or had problems at this instrumented level while applying the loads, it was decided to extrapolate the last segment of the pile until reaching the tip, as shown in Figure 2. It is noteworthy that the extrapolations correspond to less than 12% of the total length of the piles.

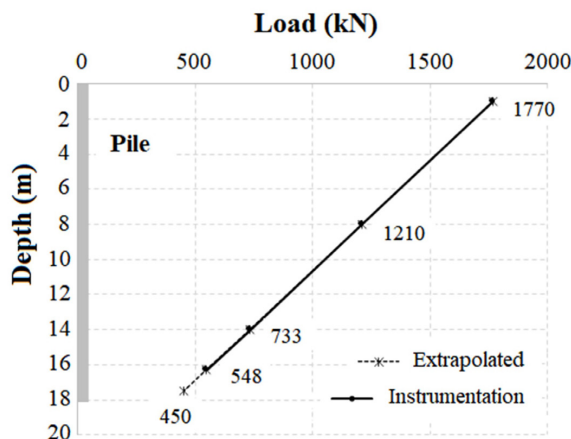


Figure 2. Load distributions in instrumented pile.

It should be stressed that, since this is an analysis in terms of bearing capacity, the only results of interest are those corresponding to the ultimate load applied in the static load test.

### 2.2.2 Pile type

The input variable, when considering the pile type, was included in the models developed in two ways: the first, *PT1*, based on the classification by Velloso & Lopes (2010); and the second, *PT2*, corresponding to a proposal of the study herein, in which it was decided to separate pile types by their material (precast driven, steel and concrete piles), including piles with similar modeling methodologies, as in the case of micro-piles and root piles.

Tables 1 and 2 provided the values adopted for variables *PT1* and *PT2*, respectively, used to develop the neuron models in this study. It was found from the analyses in these tables that the models proposed for predicting the shaft and tip bearing capacities of single piles include a large variety of pile types, considering the main pile construction methods currently adopted in Brazil and abroad (Velloso & Lopes, 2010; Van Impe, 2003).

### 2.2.3 Pile geometry

In this study, pile geometry was represented by the diameter ( $D$ ) and embedded length ( $L_e$ ), which directly influence the prediction process of the shaft and tip bearing capacities of piles. The diameter values of the piles used in developing the neuron models range from 88.9 mm to 1200 mm, while the embedded lengths vary from 3.5 m to 51 m. For piles with rectangular or square sections and for steel piles the diameter was calculated based on the circumscribed area.

Table 1. Adopted values for *PT1*.

Pile type	Value
Major displacement	1
Minor displacement	2
Substitution	3
Without displacement	4

Table 2. Adopted values for *PT2*.

Pile type	Value
Precast concrete	1
Steel	2
Injected	3
Bored with displacement	4
Continuous flight auger	5
Bored	6
Bored with stabilizer	7



### 2.2.4 Soil type

In the models estimating the shaft and tip bearing capacities of piles, the three variables adopted to represent the soil type were as follows:  $\%Sand_{ac}$ ,  $\%Silt_{ac}$  and  $\%Clay_{ac}$ . The definitions for such variables were based on those proposed by Araújo et al. (2016), who used the artificial neural networks to predict settlements in single piles, as described in Equations 1, 2 and 3.

$$\%Sand_{ac} = \sum_1^n \frac{\Delta L_{sand}}{\Delta L_e} \quad (1)$$

$$\%Silt_{ac} = \sum_1^n \frac{\Delta L_{silt}}{\Delta L_e} \quad (2)$$

$$\%Clay_{ac} = \sum_1^n \frac{\Delta L_{clay}}{\Delta L_e} \quad (3)$$

where,  $n$  is the number of pile sections;  $\%Sand_{ac}$ ,  $\%Silt_{ac}$  and  $\%Clay_{ac}$  are the factors representing the occurrence of accumulated layers of sand, silt and clay, respectively;  $\Delta L_e$  is the length in meters of the pile section; and  $\Delta L_{sand}$ ,  $\Delta L_{silt}$  and  $\Delta L_{clay}$  are the lengths in meters of the sections occurring sand, silt and clay, respectively.

Some geotechnical profiles contain layers with marine clay or organic clay, and in such cases, they were considered as clay. Stony soils were not to be found and are, therefore, not considered in the neuron models developed.

For prediction models of shaft and tip bearing capacity of single piles, two alternatives were evaluated, as follows:

- (a) Percentage values for of sandy, silty and clayey fractions

Three input variables were proposed to represent the soil type in the models that estimate shaft and tip bearing capacities of piles:  $G_{sand}$ ,  $G_{silt}$  and  $G_{clay}$ . Table 3 provided the values to be adopted for each one of the three variables according of the prevailing material type at the depth of the single pile tip.

- (b) Values tabulated for each soil type ( $S$ )

The soil types adopted are the same proposed in the semi-empirical method of Aoki & Velloso (1975) and the values are displayed in Table 4.

For piles supported on silty organic clay the variable soil type was simplified as silty clay. As there were no stony soils present along the depth of the piles, no soil type was found at the tip, and for this reason it was not included in the developed neuron models.

It is also important to stress that no pile analyzed is supported or embedded in weathered or unaltered rock and in such cases, the models proposed herein do not apply.

**Table 3.** Combinations for percentage values representing soil types in the models developed for estimating the tip bearing capacity.

Soil	$G_{sand}$ (%)	$G_{silt}$ (%)	$G_{clay}$ (%)
Sand	100	0	0
Silty sand	60	40	0
Clayey sand	60	0	40
Clayey-silty sand	60	20	20
Silty-clay sand	60	20	20
Silt	0	100	0
Clayey silt	0	60	40
Sandy silt	40	60	0
Sandy clay silt	20	60	20
Clayey sandy silt	20	60	20
Clay	0	0	100
Sandy clay	40	0	60
Silty clay	0	40	60
Silty sandy clay	20	20	60
Sandy silt clay	20	20	60

**Table 4.** Adopted values for  $S$ .

Soil type	Value
Sand	1
Silty sand	2
Clay-silt sand	3
Clay sand	4
Silty-clay sand	5
Silt	6
Sandy silt	7
Clay sand silt	8
Clayey silt	9
Sandy clay silt	10
Clay	11
Sandy clay	12
Silty sand clay	13
Silty clay	14
Sandy silt clay	15

### 2.2.5 Soil resistance index

By being aware that the shaft bearing capacity is a value accumulated along the length of the pile, it is understood that the resistance index used in models that estimate the value of this load must also be accumulated. As a result, the variable is known as  $NF_{ac}$  and obtained through Equation 4.

$$NF_{ac} = (N \times \Delta L_e) \quad (4)$$

where,  $N$  is the number of blow counts/last 30 cm of penetration in a typical  $SPT$  test.

In relation to the tip bearing capacity, it was decided to assess three different variables,  $NP1$ ,  $NP2$  and  $NP3$  calculated according to the values of the  $SPT(N)$  index.  $NP1$  is equal to the  $N$  value corresponding to a layer immediately 1m below the tip of the pile.  $NP2$  is the arithmetic mean of three (3)  $N$  values corresponding to the layer 1 m before the tip, the pile tip layer, and the layer 1 m below the tip.  $NP3$  is the average value of  $N$  in the interval between four (4) diameters above the tip and one diameter below. It is worth mentioning that these definitions come from already established semi-empirical methods (Aoki & Velloso, 1975; Décourt & Quaresma, 1978; Teixeira, 1996).

### 2.2.6 Water Level ( $WL$ )

Teixeira & Albiero (1994) confirmed that saturation increases by around 30% the settlements and reduces the bored pile bearing capacity, evidencing that the variation in moisture alters the load transfer mechanism, and this is the reason why the water level was included in the neuron models as being the accumulated value of depth of the water level, based on the elevation detected in the geotechnical profile.

### 2.2.7 Loading Type ( $LT$ )

The instrumented piles belonging to the database underwent a static load test with slow loading ( $SML$  - Slow Maintained Load) and or quick ( $QML$  - Quick Maintained Load). The value of 1 was adopted to represent the  $SML$  loading and 2 for the  $QML$  loading, both in the models developed to estimate the shaft and tip bearing capacities of piles. Of the 95 piles studied, 56 were carried out in slow maintained conditions whereas 39 in quick conditions.

## 3. Development of the prediction model

The QNET2000 program (Vesta Services, 2000) was used to develop the neuron models proposed herein. This is a multilayer perceptron computer code that uses the error back propagation algorithm to correct the synaptic weights still in the training phase, with the artificial neurons being able to activate using four types of trigger functions: sigmoid, hyperbolic tangent, hyperbolic secant and gaussian.

It is very common when solving geotechnical problems to use the sigmoid or hyperbolic tangent functions, as can be confirmed in the studies by Dantas Neto et al. (2014), Araújo et al. (2015), Santiago (2018), Maizir et al. (2015), Momeni et al. (2015) and Nejad & Jaksa (2017). In this study, the neurons of all neural network layers were triggered using the sigmoid function (Haykin, 2008). After choosing the trigger function, the following must be defined: the input variables of each neuron model proposed; data handling, training, testing and validation of different architectures and, based on established criteria, the configuration with the best performance.

### 3.1 Combinations of variables

Nine (9) input variables were adopted for neuron models that estimate the shaft bearing capacity:  $D$ ,  $NF_{ac}$ ,  $WL$ ,  $PT1$ ,  $PT2$ ,  $\%Sand_{ac}$ ,  $\%Silt_{ac}$ ,  $\%Clay_{ac}$  and  $LT$ . The combinations with those input variables are:

- MQS1:  $Q_S = f(D, NF_{ac}, WL)$
- MQS2:  $Q_S = f(D, NF_{ac}, WL, PT1)$
- MQS3:  $Q_S = f(D, NF_{ac}, WL, PT2)$
- MQS4:  $Q_S = f(D, NF_{ac}, WL, PT2, \%Sand_{ac}, \%Silt_{ac}, \%Clay_{ac})$
- MQS5:  $Q_S = f(D, NF_{ac}, WL, PT2, \%Sand_{ac}, \%Silt_{ac}, \%Clay_{ac}, LT)$

It is noticeable that the construction of these models began in the simplest manner (MQS1) with only three (3) variables, gradually adding more input variables until reaching the more complex models containing eight (8) input variables (MQS5). It was therefore possible to separately assess the influence of each input variable in the obtained results.

In the neuron models that estimate the tip bearing capacity, the input variables are:  $D$ ,  $PT1$ ,  $PT2$ ,  $G_{sand}$ ,  $G_{silt}$ ,  $G_{clay}$ ,  $S$ ,  $NP1$ ,  $NP2$ ,  $NP3$ ,  $WL$  and  $LT$ . The combinations with these input variables are:

- MQP1:  $Q_P = f(D, NP1)$
- MQP2:  $Q_P = f(D, NP2)$
- MQP3:  $Q_P = f(D, NP3)$
- MQP4:  $Q_P = f(D, NP1, PT1)$
- MQP5:  $Q_P = f(D, NP1, PT2)$
- MQP6:  $Q_P = f(D, NP1, PT2, S)$
- MQP7:  $Q_P = f(D, NP1, PT2, G_{sand}, G_{silt}, G_{clay})$
- MQP8:  $Q_P = f(D, NP1, PT2, WL)$
- MQP9:  $Q_P = f(D, NP1, PT2, LT)$

The models were created in the same way as the neuron models developed to estimate the shaft bearing capacity.

### 3.2 Data handling

The sigmoid function, chosen as a trigger function for the developed models, has the benefits of being continuous and distinguishable through its domain, enabling the application of the generalized delta rule (Widrow & Hoff, 1960) to modify synaptic weights. However, its use requires standardizing the values of output variables in an interval belonging to its image set, in this case, the interval (0.1).

Therefore, both output and input variables were standardized by linear interpolation between the values 0.15 and 0.85 and the maximum and minimum values of each of these variables.

### 3.3 Training, testing and validation

The purpose of the  $RNA$  training phase is to adjust in the best possible way the values of the synaptic weights, so that the output values estimated by the  $RNA$  are as close as possible to their actual corresponding values, but without losing generalizing capacity (Haykin, 2008).

To start training, two adjustment parameters must be chosen to adjust the synaptic weights:  $\eta$  (learning rate), which influences the convergence of the error back algorithm propagation; and the factor  $\alpha$  (momentum), which minimizes the algorithm's instability during this convergence, as applied by Dantas Neto et al. (2014, 2017) and Araújo et al. (2015) who used QNET2000 in their studies, by adopting  $\alpha = 0.8$  and  $0.01 \leq \eta \leq 0.30$ .

Unlike those authors, this choice was to include the "test" stage in all developed models, this being a stage that occurs simultaneously with training using data not included in the set adopted in that training.

During training the so-called overfitting may occur, meaning that the neural network stored the peculiarities and noise levels, but lost the generalizing capacity (Haykin, 2008). To detect overfitting, as recommended by Nejad & Jaksa (2011, 2017), the early stopping technique was used, that is, the training process is interrupted when the error in the test stage increases even when the number of iterations increases.

In the validation phase, output neurons are calculated with the synaptic weights obtained during the training phase, but using information as yet unknown by the artificial neural network, which is why it is possible to assess the generalizing capacity (Haykin, 2008) of the tested neural network at this stage.

There are no explicit rules to determine the quantity of data used at each of these stages (training, testing and validation), but it was decided to use the same proportion between training, testing and validation adopted by Maizir (2017), Kordjazi et al. (2015) and Tarawneh (2013), i.e., 70%, 15% and 15%, respectively. In this work the examples are randomly separated.

### 3.4 Criterion for definition of the ANN architecture

The architecture of an artificial neural network is related to how the neurons are structured. The performance of the architectures tested in this study is assessed by the values of root mean square error (Equation 5),  $RMSE$ , and coefficient of determination (Equation 6),  $R^2$ , obtained in the

validation phase. These measurements were used in several works (Pham et al., 2020; Chen et al., 2020; Benali et al., 2018; Maizir, 2017 and Momeni et al., 2014, 2015).

$$RMSE = \sqrt{\frac{1}{m} \sum_{i=1}^m (y_i - \bar{y}_i)^2} \quad (5)$$

$$R^2 = 1 - \frac{\sum_{i=1}^m (y_i - \bar{y}_i)^2}{\sum_{i=1}^m (y_i - \bar{y})^2} \quad (6)$$

where  $m$  inferred the number of examples,  $y_i$  and  $\bar{y}_i$  were the actual and predicted outputs, respectively, and  $\bar{y}$  was the average value of the  $y_i$ .

Considering these concepts, the architectures with correlations closest to 1.0 were selected, totaling 14 models, five of which are to the predictions of the shaft bearing capacity and nine tip bearing capacity, the results of which will be presented and discussed below.

## 4. Results and discussions

The architectures, iteration numbers and coefficient of determination values obtained in the validation phase, referring of the models developed to prediction of the shaft and tip bearing capacities of single piles are presented in Tables 5 and 6, respectively.

In Table 5 it is apparent that an increase in the quantity of input variables requires more hidden layers and, consequently, more neurons in these layers to achieve the same correlations as the simpler models. In relation to the iterations, it is noticeable that for more complex architectures more iterations are required, the only exception being model MQS3, which differs only in the input variable  $PT$  of MQS2. However, the number of iterations between them differs by approximately 50%, in contrast to the expected behavior that would be an increase in iterations, since the  $PT1$  variable assumes only four values while  $PT2$  variable has seven possibilities.

**Table 5.** Performance indices obtained in the validation phase for neuron models developed to estimate the shaft bearing capacity.

Model	Input variables	Architecture	Iteration	$R^2$	$RMSE$
MQS1	$Q_S = f(D, NF_{ac}, WL)$	3:2:1	800	0.86	0.235
MQS2	$Q_S = f(D, NF_{ac}, WL, PT1)$	4:4:1	15000	0.91	0.227
MQS3	$Q_S = f(D, NF_{ac}, WL, PT2)$	4:4:1	7600	0.93	0.184
MQS4	$Q_S = f(D, NF_{ac}, WL, PT2, \%Sand_{ac}, \%Silt_{ac}, \%Clay_{ac})$	7:4:2:1	26000	0.94	0.175
MQS5	$Q_S = f(D, NF_{ac}, WL, PT2, \%Sand_{ac}, \%Silt_{ac}, \%Clay_{ac}, LT)$	8:4:2:1	20000	0.95	0.158

**Table 6.** Performance indices obtained in the validation phase for the neuron models developed to estimate the tip bearing capacity of piles.

Model	Input variables	Architecture	Iteration	$R^2$	$RMSE$
MQP1	$Q_P = f(D, NP1)$	2:2:1	200	0.89	0.102
MQP2	$Q_P = f(D, NP2)$	2:3:1	1700	0.50	0.175
MQP3	$Q_P = f(D, NP3)$	2:1:1	1400	0.88	0.161
MQP4	$Q_P = f(D, NP1, PT1)$	3:4:1	30000	0.77	0.064
MQP5	$Q_P = f(D, NP1, PT2)$	3:6:1	90000	0.99	0.177
MQP6	$Q_P = f(D, NP1, PT2, S)$	4:2:1	3000	0.86	0.095
MQP7	$Q_P = f(D, NP1, PT2, G_{sand}, G_{silt}, G_{clay})$	6:4:1	78000	0.90	0.094
MQP8	$Q_P = f(D, NP1, PT2, WL)$	4:3:1	37300	0.87	0.170
MQP9	$Q_P = f(D, NP1, PT2, LT)$	4:3:1	30300	0.86	0.057

The analysis of the coefficient of determination in Table 5 show that model MQS1, even with few input variables, has already achieved satisfactory results, i.e., a coefficient of determination of 0.86. This affirmation is based on the conclusions reported by Pham et al. (2020), Chen et al. (2020), Benali et al. (2018), Maizir (2017) and Momeni et al. (2014, 2015).

Nevertheless, when including the input variables  $PT1$  and  $PT2$  there was an increase in the coefficient of determination from 0.86 to 0.91 and 0.93, the largest being for variable  $PT2$ . This means that the idea to separate the pile types, both by constructive methodology and their material, is close to the models' responses for the desired value. There is also an increase, albeit smaller, in the coefficient of determination, when adding the input variables that represent the soil type ( $\%Sand_{ac}$ ,  $\%Silt_{ac}$  and  $\%Clay_{ac}$ ) and loading type ( $LT$ ), arriving at a coefficient of determination equal to 0.95. Thus, the MQS5 model is proposed herein to estimate the shaft bearing capacity.

Regarding the root mean square error, the values shown in Table 5 are acceptable when compared to the results found by Pham et al. (2020) and Chen et al. (2020) who applied artificial neural networks to estimate the bearing capacity of single piles. The MQS5 model has the lowest root mean square error.

Table 6 shows that, even when increasing the quantity of input variables, it was possible to achieve good results with only one hidden layer. The models with the highest number of iterations are the models MQP5 and MQP7 that have the largest quantity of neurons in the hidden layer and input layer, respectively. No relation was detected between the quantity of neurons of the hidden layer and the number of iterations.

On analyzing the coefficient of determination values in Table 6, it is apparent that the first three models were evaluated to predict the tip bearing capacity of piles, MQP1, MQP2 and MQP3 in which only the input variable is modified with regard to the soil index. The lowest value belongs to model MQP2 and the highest to model MQP1, which means that variable  $NP1$  better represents the soil index in the developed neuron models for the tip load.

Including variable  $PT1$  in model MQP1 there was a decrease in the coefficient of determination from 0.89 to 0.77, and by repeating the procedure for input variable  $PT2$  it increased to 0.99. As in the case of the model proposed to predict the shaft bearing capacity of piles, pile type  $PT2$  provides answers closer to the desired value also for the tip load. Other input variables were added to model MQP5, but there was no increase in the coefficient of determination value, so model MQP5 is proposed herein to estimate the tip bearing capacity of piles.

The root means square error values obtained in the models developed to estimate the tip bearing capacity, shown in Table 6, are also acceptable. Model MQP9 has the smallest root mean square error and was not chosen because the coefficient of determination is only 0.88.

Figure 3a demonstrates the evolution of the coefficient of determination in function of the iterations for model MQS5, in which the convergence of the curves is noticeable, referring to training and testing performed in the training phase. Figure 3b illustrates the coefficient of determination for model MQS5 in the validation phase for 20000 iterations.

Figure 3c shows the evolution of the coefficient of determination as a result of the iterations for model MQP5, in which a similarity is noticeable of the curves referring to training and testing during the training phase. Figure 3d



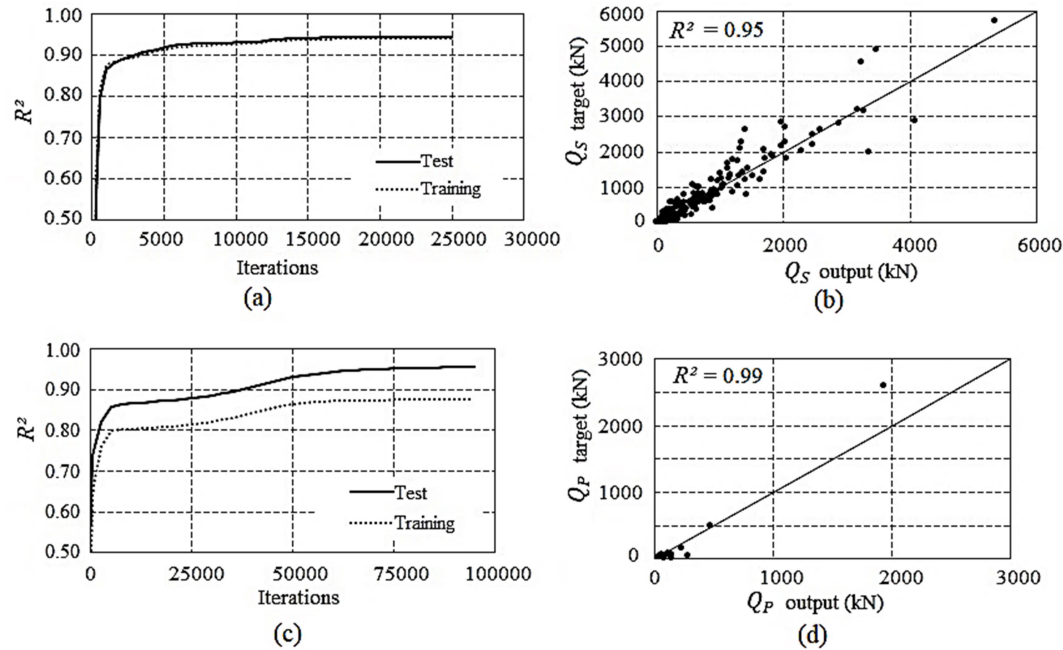


**Figure 3.** Coefficient of determination for models proposed.

illustrates the coefficient of determination for model MQP5 in the validation phase.

## 5. Model application

The models proposed in this article were used to estimate the bearing capacity of three (3) single piles (two bored and one continuous flight auger type) as well as in groups of up to three piles implemented in the Experimental Research Site of foundations and in situ testing of the University of Brasília (Figure 4).

The geotechnical profile and pile characteristics are provided in Figure 5 and were compiled in the study by Anjos (2006). This is a geotechnical profile consisting of three layers: the first, from 0 to 3.5 m, has porous clayey sand; the second, between 3.5 and 8.5 m, provides sandy clay, and from 8.5 m the soil has a siltier texture (Mota, 2003).

The two bored piles (single) were tested until there was a 10% displacement in diameter. One of them placed on only a slightly resistant material with a view to assessing only the shaft bearing capacity. And two consecutive tests were performed on the pile supported on soil (in which it was possible to assess the shaft bearing capacity and tip bearing capacity), the first being a slow maintained load test (*SML*) and the second a quick maintained load (*QML*).

In relation to continuous flight auger piles, Anjos (2006) installed one single pile, a group with two and another with three piles, all subject to slow loading (*SML*). The spacing between the piles in groups was three times the diameter with a rigid crown block in no contact with the ground.

Figure 6 shows the shaft bearing capacity-depth curves corresponding to the semi-empirical methods of Aoki & Velloso (1975) and Décourt & Quaresma (1978) and model proposed in this works. Figure 6a refers to the bored pile E1 and Figure 6b to the continuous flight auger pile E3.

Note that the shaft bearing capacity calculated by the proposed models are higher than those obtained by the semi-empirical methods. Knowing that the semi-empirical methods usually underestimate the shaft bearing capacity, it is possible to infer that the proposed model provides more realistic values.

Figure 7 shows the comparison between the values found in the load test and semi-empirical methods (Aoki & Velloso, 1975; Décourt & Quaresma, 1978) and those obtained from the models proposed in this study. The bearing capacity of the pile groups was considered equal to multiplying between the quantity of piles and the single pile bearing capacity (Cintra & Aoki, 2010).

It is found that for bored single piles the proposed models overestimate the bearing capacity obtained in the static load test, but the difference in percentage terms between the values for the proposed methods and the load test value varies between 3% and 30%, while the method by Aoki & Velloso (1975) shows that this difference ranges from 59% to 83%, and between 38% and 64% for the method by Décourt & Quaresma (1978).

For the single continuous flight auger pile the result achieved with the proposed neuron models can be considered very close to the load test value, since the values calculated by the methods of Aoki & Velloso (1975) and Décourt &



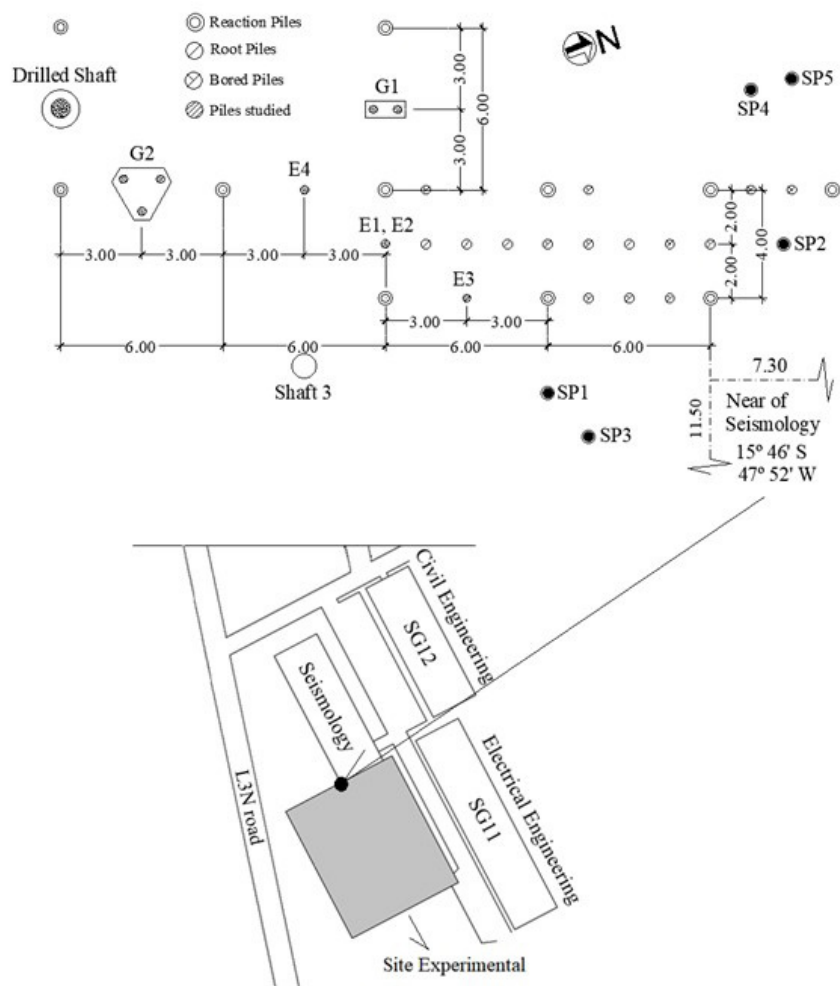


Figure 4. Location map of the site experimental and the piles studied.

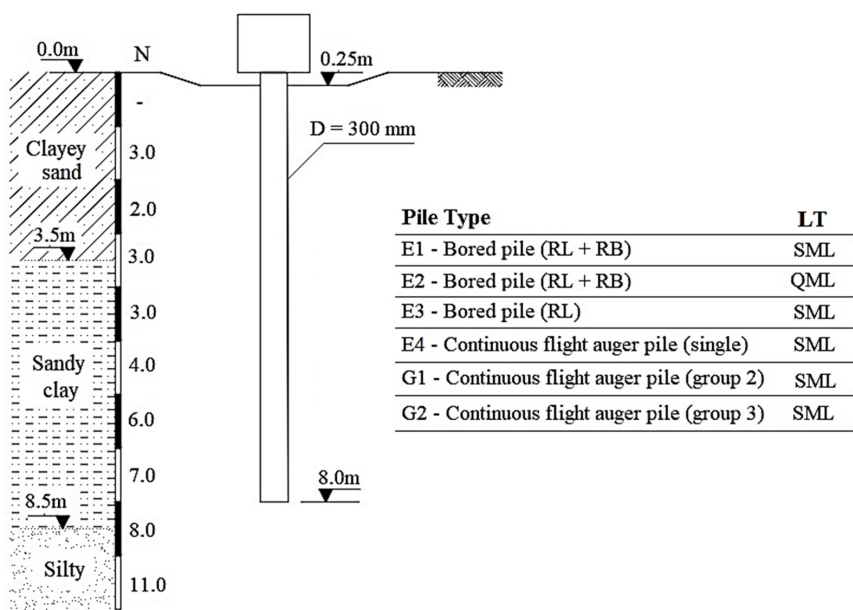
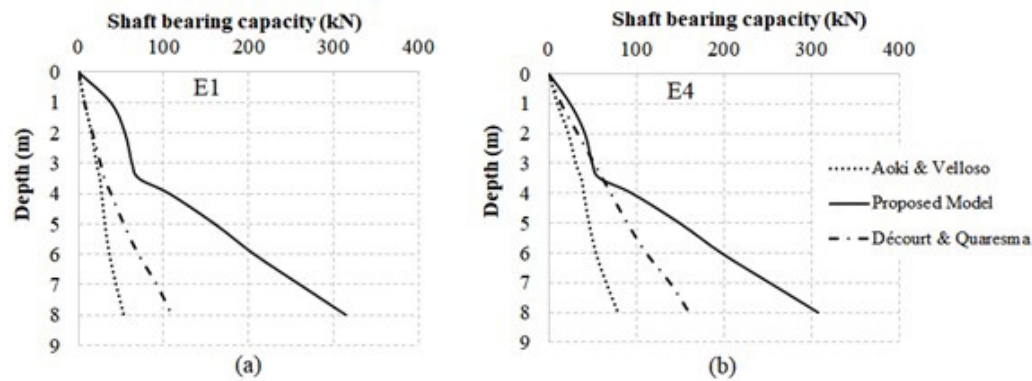
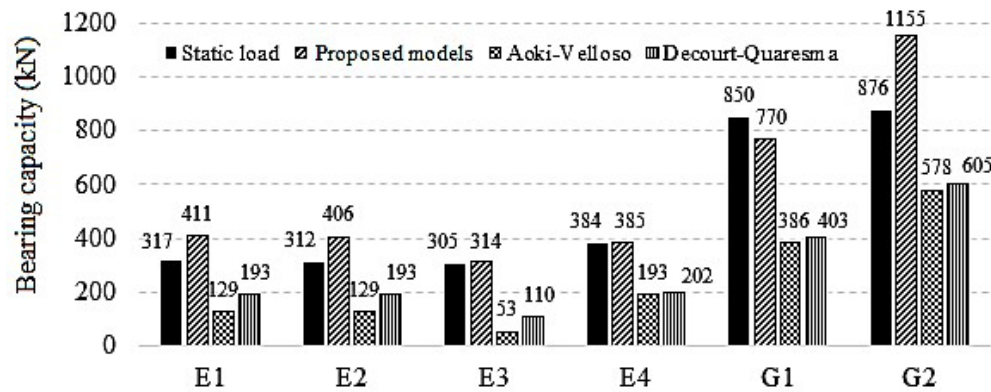


Figure 5. Geotechnical profile for single piles and in groups. Adapted from Mota (2003).



**Figure 6.** Comparison between the shaft bearing capacity estimated by the proposed models and the values obtained from semi-empirical methods.



**Figure 7.** Comparison between the bearing capacity estimated by the proposed models and the values obtained from load testing and semi-empirical methods.

Quaresma (1978) are approximately 50% lower than the desired value.

With regard to the groups consisting of two and three continuous flight auger piles, it is apparent that the proposed neuron models underestimate by only 9% and overestimate by 32% the values obtained from the static load tests on those groups, respectively. However, for the semi-empirical methods of Aoki & Velloso (1975) and Décourt & Quaresma (1978), this same difference is around 55% for the group with two piles and 33% for the three-pile group.

Accordingly, it can be said that the proposed models reproduce more satisfactorily the bearing capacity both for single piles and groups than the semi-empirical models considered. The difference between the values found for the proposed methods and the load test value varies between 9% and 32%, while for the method by Aoki & Velloso (1975) this interval is between 34% and 83% and for the Décourt & Quaresma method (1978) it is between 31% and 64%.

## 6. Conclusions

According to the results, it can be concluded that the multilayer perceptron is a tool that can estimate the shaft bearing capacity and tip bearing capacity of single piles, based on variables relating to pile geometry and soil type (information collected from boreholes), with a relatively simple architecture.

The neural model proposed to estimate the shaft bearing capacity has eight (8) input variables ( $D$ ,  $NF_{ac}$ ,  $WL$ ,  $PT2$ ,  $\%Sand_{ac}$ ,  $\%Silt_{ac}$ ,  $\%Clay_{ac}$ ,  $LT$ ) and provided a coefficient of determination equal to 95% between the desired value and the calculated value. On the other hand, the model that estimates the tip bearing capacity has only three input variables ( $D$ ,  $NPI$ ,  $PT2$ ) with 99% coefficient of determination.

The coefficient of determination obtained from the neuron models that estimate the shaft bearing capacity and tip bearing capacity of single piles range from 0.8 to 0.99, an interval of coefficient of determination similar as those obtained by authors when assessing the applicability of

artificial neural networks in the ability to predict the pile bearing capacity. However, the neuron models proposed proved to help the calculation of the shaft bearing capacity according to depth and not only the total value of bearing capacity. Moreover, have the potential to be applicable to seven types of piles and different geotechnical profiles.

When analyzing the results from the neuron models for single piles and groups of piles, it was observed that the proposed methods are more efficient than the semi-empirical methods applied in Brazilian foundation engineering practice, since the dispersion in the results is less when the results achieved are compared to the static load test values.

In general, the proposed models overestimate the bearing capacity, which can be explained by the fact that the models were based on the ultimate load applied during the static load test. Therefore, the recommendation is to use correction factors of around 0.88 for single piles and approximately 0.75 for groups. To improve these values, it is recommended an improved analysis with more data and distinct geotechnical conditions.

## Acknowledgements

The authors thank the University of Brasília, Federal University of Ceará, Federal University of Piauí and Coordination of Improvement of Higher Education Personnel (CAPES) for the incentive and support of the research. They are also indebted to colleagues from the research group on foundations, in situ testing and retaining structures, GPFees (<https://rpcunha.wixsite.com/gpfees>) from the University of Brasília.

## Declaration of interest

The authors have no conflicts of interest to declare. All co-authors have observed and affirmed the contents of the paper and there is no financial interest to report.

## Authors' contributions

Luciana Barbosa Amâncio: conceptualization, data curation, formal analysis, investigation, methodology, visualization, writing – original draft. Silvrano Adonias Dantas Neto: conceptualization, data curation, supervision, validation, writing – review & editing. Renato Pinto da Cunha: conceptualization, methodology, supervision, validation, writing – review & editing.

## List of symbols

$m$	Number of examples
$n$	Number of pile sections
$y_i$	Actual outputs
$\hat{y}_i$	Predicted outputs

$\bar{y}$	Average value of the $y_i$ .
$ANN$	Artificial Neural Networks
$D$	Pile dDiameter
$G_{sand}$	Percentage values for of sandy fractions
$G_{silt}$	Percentage values for of silty fractions
$G_{clay}$	Percentage values for of clayey fractions
$L_e$	Embedded length
$LT$	Loading Type
$N$	Number of blow counts/last 30 cm of penetration in SPT test
$NF_{ac}$	Soil resistance index along the shaft
$NP1$	Soil resistance index at tip 1
$NP2$	Soil resistance index at tip 2
$NP3$	Soil resistance index at tip 3
$PT1$	Pile type 1
$PT2$	Pile type 2
$QML$	Quick Maintained Load
$Q_r$	Bearing capacity
$Q_s$	Shaft bearing capacity
$Q_p$	Tip bearing capacity
$S$	Soil type
$SML$	Slow Maintained Load
$SPT$	Standard Penetration Test
$R^2$	Coefficient of determination
$RMSE$	Root mean square error
$WL$	Water Level
$\%Sand_{ac}$	Factor representing the occurrence of accumulated layers of sand
$\%Silt_{ac}$	Factor representing the occurrence of accumulated layers of silt
$\%Clay_{ac}$	Factor representing the occurrence of accumulated layers of clay
$\alpha$	Momentum
$\eta$	Learning rate
$\Delta L_{clay}$	Length of the section occurring clay
$\Delta L_e$	Length of the section
$\Delta L_{sand}$	Length of the section occurring sand
$\Delta L_{silt}$	Length of the section occurring silt

## References

- ABNT NBR 6122. (2019). *Design and construction of foundations*. ABNT - Associação Brasileira de Normas Técnicas, Rio de Janeiro, RJ (in Portuguese).
- Akl, S.A.Y., & Mossaad, M.E. (2021). Detecting piston effect on drilled shafts side resistance using instrumented pile load tests. *KSCE Journal of Civil Engineering*, 25(3), 822-832. <http://dx.doi.org/10.1007/s12205-021-0914-z>.
- Amann, K.A.P. (2010). *Unified semiempirical methodology for estimating the load capacity of piles* [Doctoral thesis, University of São Paulo]. University of São Paulo's repository (in Portuguese). <https://doi.org/10.11606/T3.2010.tde-21102010-094919>.

- Amann, K.A.P., Kuboyama, C.T., & Silva, C.O. (2018). Metodologia para a avaliação estatística da aplicabilidade de métodos semi-empíricos de cálculo da capacidade resistente última de estacas. In *16º Congresso Nacional de Geotecnia* (pp. 1-12). Ponta Delgada, Açores. SPG. (in Portuguese).
- Anjos, G.J.M. (2006). *Experimental study of the behavior of bored pile foundations founded in tropical soils* [Doctoral's thesis, University of Brasília]. University of Brasília's repository (in Portuguese). <https://repositorio.unb.br/handle/10482/5660>.
- Aoki, N., & Velloso, D.A. (1975). An approximate method to estimate the bearing capacity of piles. In *Proceedings of the 5º Pan-American Conference of Soil Mechanics and Foundation Engineering* (Vol. 1, pp. 367-376). Buenos Aires, October 1975. ISSMGE
- Araújo, C.B.C., Dantas Neto, S.A., & Anjos, G.J.M. (2016). Estimativa de recalque em estacas utilizando redes neurais artificiais. In *18º Congresso Brasileiro de Mecânica dos Solos e Engenharia Geotécnica* (pp. 1-8), Belo Horizonte. ABMS. (in Portuguese).
- Araújo, C.B.C., Dantas Neto, S.A., & Souza Filho, F.A. (2015). Streamflow forecasting for the dam Orós/CE from hydrometeorological data using perceptrons. *Revista Brasileira de Meteorologia*, 30, 37-46. <http://dx.doi.org/10.1590/0102-778620140048>.
- Benali, A., Nechnech, A., Boukhatem, B., Hussein, M.N., & Karry, M. (2018). Neural networks and principle component analysis approaches to predict pile capacity in sand. *MATEC Web of Conferences*, 149, 02025. <https://doi.org/10.1051/mateconf/201714902025>.
- Bersan, S., Bergamo, O., Palmieri, L., Schenato, L., & Simonini, P. (2018). Distributed strain measurements in a CFA pile using high spatial resolution fibre optic sensors. *Engineering Structures*, 160, 554-565. <http://dx.doi.org/10.1016/j.engstruct.2018.01.046>.
- Bohn, C., Santos, A.L., & Frank, R. (2017). Development of axial pile load transfer curves based on instrumented load tests. *Journal of Geotechnical and Geoenvironmental Engineering*, 143(1), 04016081. [http://dx.doi.org/10.1061/\(asce\)gt.1943-5606.0001579](http://dx.doi.org/10.1061/(asce)gt.1943-5606.0001579).
- Carvalho, C.A., & Santos, D.A.F. (2019). Análise geotécnico-estrutural de resultados de prova de carga estática em estacas. *Engineering and Science*, 7(1), 61-72 (in Portuguese). <http://dx.doi.org/10.6008/CBPC2318-3055.2019.001.0007>.
- Chen, W., Sarir, P., Bui, X.N., Nguyen, H., Tahir, M.M., & Armaghani, D.J. (2020). Neuro-genetic, neuro-imperialism and genetic programming models in predicting ultimate bearing capacity of pile. *Engineering with Computers*, 36(3), 1101-1115. <http://dx.doi.org/10.1007/s00366-019-00752-x>.
- Cintra, J.C.A., & Aoki, N. (2010). *Fundações por estacas: projeto geotécnico*. Oficina de Textos (in Portuguese).
- Cooke, R.W., Price, G., & Tarr, K. (1979). Jacked piles in London clay: a study of load transfer and settlement under working conditions. *Geotechnique*, 29(2), 113-147.
- Dantas Neto, S.A., Indraratna, B., Oliveira, D.A.F., & Assis, A.P. (2017). Modelling the shear behaviour of clean rock discontinuities using artificial neural networks. *Rock Mechanics and Rock Engineering*, 50(7), 1817-1831. <http://dx.doi.org/10.1007/s00603-017-1197-z>.
- Dantas Neto, S.A., Silveira, M.V., Amâncio, L.B., & Anjos, G.J.M. (2014). Pile settlement modeling with multilayer perceptrons. *The Electronic Journal of Geotechnical Engineering*, 19, 4517-4528.
- Darbor, M., Faramarzi, L., & Sharifzadeh, M. (2019). Performance assessment of rotary drilling using non-linear multiple regression analysis and multilayer perceptron neural network. *Bulletin of Engineering Geology and the Environment*, 78(3), 1501-1513. <http://dx.doi.org/10.1007/s10064-017-1192-3>.
- De Granrut, M., Simon, A., & Dias, D. (2019). Artificial neural networks for the interpretation of piezometric levels at the rock-concrete interface of arch dams. *Engineering Structures*, 178, 616-634. <http://dx.doi.org/10.1016/j.engstruct.2018.10.033>.
- Décourt, L., & Quaresma, A. (1978). Capacidade de carga de estacas a partir de valores de SPT. In *6º Congresso Brasileiro de Mecânica dos Solos e Engenharia de Fundações* (Vol. 6, pp. 45-53), Rio de Janeiro. ABMS (in Portuguese).
- Ebtehaj, I., Bonakdari, H., Moradi, F., Gharabaghi, B., & Khozani, Z.S. (2018). An integrated framework of Extreme Learning Machines for predicting scour at pile groups in clear water condition. *Coastal Engineering*, 135, 1-15. <http://dx.doi.org/10.1016/j.coastaleng.2017.12.012>.
- Fellenius, B.H. (2016). Fallacies in piled foundation design. In P.D. Long (Ed.), *Proceedings of the Geotechnics for Sustainable Infrastructure Development Geotec Hanoi* (pp. 41-46), Hanoi.
- Fellenius, B.H. (2021). *Basics of foundation design*. Retrieved in November 25, 2021, from <https://www.fellenius.net>.
- Haque, M.N., Abu-Farsakh, M.Y., Chen, Q., & Zhang, Z. (2014). Case study on instrumenting and testing full-scale test piles for evaluating setup phenomenon. *Transportation Research Record: Journal of the Transportation Research Board*, 2462(1), 37-47. <http://dx.doi.org/10.3141/2462-05>.
- Haykin, S. (2008). *Neural networks and learning machines* (3rd ed.). Prentice Hall.
- Kardani, N., Zhou, A., Nazem, M., & Shen, S.L. (2020). Estimation of bearing capacity of piles in cohesionless soil using optimised machine learning approaches. *Geotechnical and Geological Engineering*, 38(2), 2271-2291. <http://dx.doi.org/10.1007/s10706-019-01085-8>.
- Kiran, S., Lal, B., & Tripathy, S.S. (2016). Shear strength prediction of soil based on probabilistic neural network. *Indian Journal of Science and Technology*, 9(41), 1-6. <http://dx.doi.org/10.17485/ijst/2016/v9i41/99188>.

- Kordjazi, A., Nejad, F.P., & Jaksa, M.B. (2015). The evaluation of ultimate axial-loading capacity of piles using artificial intelligence methods. In *Proceedings of the 16<sup>o</sup> ECSMGE Geotechnical Engineering for Infrastructure and Development* (pp. 3929–3934), Edinburgh. BGA, SIMSG & ISSMGE. <https://doi.org/10.1680/ecsmge.60678>.
- Maizir, H. (2017). Evaluation of shaft bearing capacity of single driven pile using neural network. In *Proceedings of the International Multiconference of Engineers and Computer Scientists 2017* (Vol. 1, pp. 36-39), Hong Kong, March 2017. IMECS.
- Maizir, H., Gofar, N., & Kassim, K.A. (2015). Artificial neural network model for prediction of bearing capacity of driven pile. *Jurnal Teknik Sipil ITB*, 22(1), 49-56. <http://dx.doi.org/10.5614/jts.2015.22.1.6>.
- Maya, A.P.B., González, Y.V. & Ramírez, O.E. (2013). Comparative evaluation of load capacity in deep foundations. Analytical formulations and load tests. *Boletín de Ciencias de la Tierra*, (33), 93-110 (in Spanish).
- Moayedi, H., Mosallanezhad, M., Rashid, A.S.A., Jusoh, W.A.W., & Muazu, M.A. (2020). A systematic review and meta-analysis of artificial neural network application in geotechnical engineering: theory and applications. *Neural Computing & Applications*, 32(2), 495-518. <http://dx.doi.org/10.1007/s00521-019-04109-9>.
- Momeni, E., Nazir, R., Armaghani, D.J., & Maizir, H. (2014). Prediction of pile bearing capacity using a hybrid genetic algorithm-based ANN. *Measurement*, 57, 122-131. <http://dx.doi.org/10.1016/j.measurement.2014.08.007>.
- Momeni, E., Nazir, R., Armaghani, D.J., & Maizir, H. (2015). Application of artificial neural network for predicting shaft and tip resistances of concrete piles. *Earth Sciences Research Journal*, 19(1), 85-93. <http://dx.doi.org/10.15446/esrj.v19n1.38712>.
- Mota, N.M.B. (2003). *Ensaio avançados de campo na argila porosa não saturada de Brasília: interpretação e aplicação em projetos de fundação*. [Unpublished doctoral's thesis]. University of Brasília (in Portuguese).
- Musarra, M., & Massad, F. (2015). Static load tests in an instrumented rock socket barrette pile. *Soils and Rocks*, 38(2), 163-177.
- Narsavage, P.A. (2019). Optimizing the design of driven pile foundations with instrumented static load tests. In *Proceedings of the 8<sup>o</sup> International Conference on Case Histories in Geotechnical Engineering* (pp. 74-87), Philadelphia. ASCE. <http://dx.doi.org/10.1061/9780784482094.008>.
- Nejad, F.P., & Jaksa, M.B. (2011). Prediction of pile behavior using artificial neural networks based on standard penetration test data. In *13<sup>o</sup> International Conference of the IACMAG* (pp. 564-569), Melbourne, May 2011. IACMAG.
- Nejad, F.P., & Jaksa, M.B. (2017). Load-settlement behavior modeling of single piles using artificial neural networks and CPT data. *Computers and Geotechnics*, 89, 9-21. <http://dx.doi.org/10.1016/j.compgeo.2017.04.003>.
- Pereira, A.B., Porto, T.B., Gomes, R.C., dos Santos, R.L.R., & Rabelo, J.M.G. (2020). Performance analysis of semiempirical bearing capacity prediction methods applied to precast concrete piles based on sandy clay. *Brazilian Journal of Development*, 6(2), 5948-5976. <http://dx.doi.org/10.34117/bjdv6n2-049>.
- Pham, T., Ly, H., Tran, V., Giap, L., Vu, H., & Duong, H. (2020). Prediction of pile axial bearing capacity using artificial neural network and random forest. *Applied Sciences (Basel, Switzerland)*, 10(5), 1871. <http://dx.doi.org/10.3390/app10051871>.
- Probst, C.A., Aguiar, M.F.P., Mendes, G.C.M., & Oliveira, F.H.L. (2018). Análise comparativa de métodos de determinação da capacidade de carga em estacas hélice contínua com ensaios de prova de carga estática realizados em Uberaba-MG. In *19<sup>o</sup> Congresso Brasileiro de Mecânica dos Solos e Engenharia Geotécnica*, Salvador. ABMS (in Portuguese).
- Santiago, D.L.G. (2018). *Cimentaciones con pilas y pilotes: análisis de la capacidad de carga, en suelos cohesivos y no cohesivos, con redes neuronales* [Tesis de Licenciatura]. Universidad Nacional Autónoma de México (in Spanish). <https://repositorio.unam.mx/contenidos/70191>.
- Seo, H., Prezzi, M., & Salgado, R. (2013). Instrumented static load test on rock-socketed micropile. *Journal of Geotechnical and Geoenvironmental Engineering*, 139(12), 2037-2047. [http://dx.doi.org/10.1061/\(ASCE\)GT.1943-5606.0000946](http://dx.doi.org/10.1061/(ASCE)GT.1943-5606.0000946).
- Silva, R.R.C. (2020). Análise de métodos de previsão de capacidade de carga em estaca raiz a partir do comportamento em ensaios de carregamento estático e dinâmico. *Revista Tecnologia*, 41(2), 1-14 (in Portuguese). <https://doi.org/10.5020/23180730.0.10788>.
- Tarawneh, B. (2013). Pipe pile setup: database and prediction model using artificial neural network. *Soil and Foundation*, 53(4), 607-615. <http://dx.doi.org/10.1016/j.sandf.2013.06.011>.
- Teixeira, A.H. (1996). Projeto e execução de fundações. In *3<sup>o</sup> Seminário de Engenharia de Fundações Especiais e Geotecnia* (pp. 33-50). São Paulo: ABEF (in Portuguese).
- Teixeira, C.Z., & Albiero, J.H. (1994). Comportamento de estacas escavadas instrumentadas em um solo colapsível. In *10<sup>o</sup> Congresso Brasileiro de Mecânica dos Solos e Engenharia de Fundações* (Vol. 1, pp. 95-102), Foz do Iguaçu. ABMS (in Portuguese).
- Tizpa, P., Chenari, R.J., Fard, M.K., & Machado, S.L. (2015). ANN prediction of some geotechnical properties of soil from their index parameters. *Arabian Journal of Geosciences*, 8(5), 2911-2920. <http://dx.doi.org/10.1007/s12517-014-1304-3>.
- Tran, K.T., McVay, M., Herrera, R., & Lai, P. (2012). Estimating static tip resistance of driven piles with bottom pile instrumentation. *Canadian Geotechnical Journal*, 49(4), 381-393. <http://dx.doi.org/10.1139/t2012-001>.



- Van Impe, W.F. (2003). Screw piling: still a challenging discussion topic? In *Proceedings of the International Geotechnical Seminar on Deep Foundations on Bored and Auger Piles* (pp. 3-8), Ghent, June 1-4. W. Van Impe.
- Velloso, D.A., & Lopes, F.R. (2010). *Fundações - volume único*. Oficina de Textos (in Portuguese).
- Vesta Services. (2000). *QNET2000. Version V2k build 721*. Winnetka: Vesta Services.
- Widrow, B., & Hoff, M.E. (1960). Adaptive switching circuits. In *Proceedings of the IRE WESCON Convention Record* (Vol. 4, pp. 96-104), New York: Institute of Radio Engineers.
- Zhang, J., Cao, X., Xie, J., & Kou, P. (2019). An improved long short-term memory model for dam displacement prediction. *Mathematical Problems in Engineering*, 2019, 6792189. <http://dx.doi.org/10.1155/2019/6792189>.
- Zhang, J., Hu, J., Li, X., & Li, J. (2020). Bayesian network based machine learning for design of pile foundations. *Automation in Construction*, 118, 103295. <http://dx.doi.org/10.1016/j.autcon.2020.103295>.

## Simplified model for dam rockfill creep and influence of constructive delay of concrete face

Renato Santos Paulinelli Raposo<sup>1#</sup> , Yasletty Zamora Hernández<sup>2</sup> ,

André Pacheco de Assis<sup>1</sup> 

Article

### Keywords

Concrete Face Rockfill Dams  
Creep  
Slab

### Abstract

Advances in equipment and tools implemented for geotechnics have been allowing design to be supported by numerical simulations. However, even with sophisticated resources, the dam geotechnical engineering industry still lacks few information on laboratory parameters as in the case of Concrete Face Rockfill Dams (CFRD). It is necessary to simplify the use of back-analysis that represent real CFRD, in search of tools that can be applied in the industry. The objectives include the simplification of the behavior of the linear modules associated with a linear coefficient representing the vertical creep and evaluation of the influence of the constructive delay of the concrete face in a specific case. The text goes through examples of real CFRD simulations, as a theoretical background. The CFRD calibration model includes an elegant representation of the vertical orthotropic rockfill creep with only two calibration parameters. The displacements obtained from a CFRD are represented with a linear elastic constitutive model with linear vertical deformation in time. The result is well adjusted both in the construction phase and during filling. Further on, six different slab constructive delay sequencing arrangements were simulated. The study uses a numerical device that makes it possible to drive the concrete slab in its correct design thickness. Among the stress results, the step-by-step sequencing of the slab following the rockfill reached the worst horizontal stresses, reaching almost 45 MPa, which exceeds the typical compressive strengths of conventional concretes that can affect the structural integrity of the slab. The results suggest that step-by-step sequencing should be avoided. In the case studied, the balanced behavior could be achieved in a concreting scenario maintaining the constructive delay of the slab with at least half the height of the dam. It is important to point out that all this work considerations serve for a specific example. Any generalization should be avoided or associated with broader complementary studies, as each dam is a unique work and must be studied individually, case by case.

## 1. Introduction

Concrete-faced rockfill dams (CFRD) have proven to be quite safe in terms of slope stability, commonly with safety factors above seven. Robustness is also evidenced in seismic zones, as the rockfill does not develop additional pore pressures under these conditions (ICOLD, 2010). For example, when an earthquake measuring 8 on the Richter scale occurred in 2008, the epicenter was about 20 km away from the 156 m-high Zipingpu Dam in China, which stood firm. Despite some localized damage to the slab and crest, the structure remained safe and stable (Cruz et al., 2014). ICOLD (2010) cites some examples of problems not related to rockfill masses, such as: foundation erosion due to overtopping, regressive internal tubular erosion (piping) of

the foundations or failures in hydraulic mechanisms such as spillways, water intakes, diversion galleries etc. Even with advances in numerical simulation methods, rockfill dam designs require many simplifications, mainly due to difficulties in laboratory tests on larger particle sizes. In general, it is practically impossible to obtain the material properties by direct methodology. Its dimensioning involves complex phenomena of water propagation over time and its criteria are predominantly semi-empirical (Pinto, 2007). The problem may be more complex when the material is not completely flooded, as in the case of CFRD. Deformation arrangements not foreseen in the design generated surprising cases of large ruptures in sealing slabs. Over the last few decades, advances in equipment and tools implemented for geotechnics are increasingly allowing projects to be supported by numerical

<sup>#</sup>Corresponding author. E-mail address: renatopaulinelli@gmail.com

<sup>1</sup>Universidade de Brasília, Departamento de Engenharia Civil e Ambiental, Brasília, DF, Brasil.

<sup>2</sup>Universidade Estadual do Norte Fluminense, Laboratório de Engenharia Civil, Campos dos Goytacazes, RJ, Brasil.

Submitted on August 8, 2021; Final Acceptance on June 21, 2022; Discussion open until November 30, 2022.

<https://doi.org/10.28927/SR.2022.074221>



This is an Open Access article distributed under the terms of the Creative Commons Attribution License, which permits unrestricted use, distribution, and reproduction in any medium, provided the original work is properly cited.

simulations. Several works have used numerical simulations to study the types of failure and the main causes of failure of these dams (Chen et al., 2019; Pramthawee et al., 2017; Wei & Zhu, 2015; Xavier et al., 2007; Yao et al., 2019; Zhang et al., 2004; Zhou et al., 2016). However, the availability of advanced and sophisticated resources may take time to reach the dam geotechnical engineering industry.

The difficulty in forecasting new projects reinforces the growing trend to revise design criteria using back analysis based on technical bases based on the performance of previous works. The creep of the CFRD rockfill develops throughout construction, during filling and later in the operation of the dam. The main motivation of the study is based on the search for simplicity in a constitutive model that can represent the behavior reality of rockfill creep. The technical means have expanded the database on the deformability behavior of rockfills, before, during and after filling the reservoir.

Dams are checked over time. As main information: the vertical and horizontal displacements within the embankment, crest settlements and displacement readings of the slabs during the first filling. Even with the volume of data checked, according to Basso (2007), the constitutive laws are unrealistic in relation to the data read in the field, due to different rockfill regions if the construction phases are considered. The constructive stresses are low near the sides of the backrests and the filling of the reservoir promotes a rotation of stress mainly in the first third of the upstream slope. The main objective of the present work is to propose and validate a consolidated calibration methodology for rockfill creep applied to dams with a concrete face that considers deformability in time and propagated flow of reservoir filling from the back analysis of Swedish boxes and displacements in the slab. The deformability behavior of rockfill is treated by its macroscopic phenomena with two main parameters of a simplified constitutive model: deformability modulus and creep that depend on time, wetting and stress magnitude.

### 1.1 Collapse and creep in rockfill

The use of three-dimensional simulations for CFRD projects is a practice that is spreading recently. According to a study by Frutuoso (2007), most designs were built with two-dimensional simulations and linear elastic models. This practice ends up ignoring the influence of the effect of the shoulder and the non-linearity of geotechnical materials. According to Naylor et al. (1981), the ideal model to simulate CFRD would be:

- Non-linear stress-strain relationships
- Several stress paths
- Time effect, with deformations such as consolidation and creep
- Anisotropy, especially in compacted soils
- Dilatancy, as shear stresses can also cause volume increase
- Increased material stiffness during loading.

The criteria proposed by Sherard & Cooke (1987) continue to be followed by most designers today, nearly thirty years after publication. Cost and schedule challenges have forced bolder projects and advances in three-dimensional analysis help to adapt to classical criteria.

### 1.2 Compressibility model for rockfill

The one-dimensional model was proposed by Oldecop & Alonso (2001), which has the proposal to represent rockfill deformability. The breakage and rearrangement of rockfill particles depend not only on the acting stresses, but also on the relative air humidity conditions, which fills the gaps in the rock blocks. The great contribution of this work is the observation that the rockfill collapse in environments with 100% relative air humidity is the same as observed in flooded samples. According to the authors, rockfill has an intrinsic dependence on deformation over time and the crack propagation speed in general has two main variables: stress level and moisture content. The rock pores can have a determining influence on the deformability of rockfills. The work of Oldecop & Alonso (2003) complemented the model with the addition of new results of controlled consolidation tests. Improvements in its constitutive equations generated gains in the formulation, such as the correction of a hardening that does not depend on the initial formulation and has an excellent adherence to experimental results.

Oldecop & Alonso (2007) demonstrated that the long-term behavior of deformations can be linear in relation to the logarithm of time, if the materials are granular and the consolidation tests are long-term in large diameters. The macroscopic behavior can be explained from the phenomenon of crack propagation, with successive breakage of grains subjected to stress, whose microcracks are influenced by issues such as relative humidity.

## 2. Proposed Rockfill deformability modeling in CFRD

The proposed deformability model considers two mechanical parameters to be calibrated: a constant deformability modulus ( $E$ ) in the MPa unit and an additional constant deformation percentage in the vertical direction during construction (creep) in the %/year unity.

The stress and deformation response of the model follows the linear elastic modulus, which takes the proposal of deformability over time to a very simple level. The purpose of this interpretation is to verify the possibility of adjusting the deformability of the slab before and during filling, even in a linear elastic model. The Young's modulus represents the isotropic deformability with the linear-elastic ABAQUS® Mechanical model, Elasticity.

The paper does not use the hyperbolic model, even though it is widely used to represent the behavior of rockfill.

Also, the transverse anisotropic nature of the rockfill was not considered. These are simplifying assumptions due to the indication of satisfactory results between read and measured vertical displacements with elastic deformability and creep models. The model is complex due to the three-dimensional geometry that involves stepwise construction and finite element mesh separation.

The additional parameter in the vertical direction is linked to the control variable ( $S'$ ), which controls the forced reduction of the vertical volume. The range is between 0 and 100%, in the percentage missing in relation to the total of the parameter during construction. This is implemented as orthotropic thermal expansion in the vertical direction, since the variable  $S'$  is the temperature in the ABAQUS® Mechanical model, Expansion. During construction, this constructive fluency follows a line in time as a boundary condition:

$$S'(t) = 1 - \frac{t - t_0}{t_f - t_0} \quad (1)$$

Where:

$S'$  = control variable for missing percentage of creep [dimensionless]

$t$  = constructive time variable [time];

$t_0$  = construction start time constant [time].

$t_f$  = time constant at the end of construction [time].

The other parameters are arbitrated and constant:

- Poisson values were adopted with a value of 0.3, including for slab and plinth
- the concrete material is linear elastic with Young's Modulus adopted as 20 GPa
- the unit weight is 20 kN/m<sup>3</sup> for rockfill and 25 kN/m<sup>3</sup> for concrete

- the heat flux arbitrated values of 100 K·m·W<sup>-1</sup> for thermal conductivity and 1 J·K<sup>-1</sup>·kg<sup>-1</sup> for specific heat, which does not influence the analysis at all, because the temperature variation is imposed.

In this work it was chosen not to add any shear strength to the models, assuming that the CFRDs have no recent history of slope instability.

## 2.1 Geometry

The geometry of the dam model is based on previous study presented by Raposo (2016), maintaining aspects as height (200 m), shape of the valley, concrete face thickness, width of the berm, dimensions of the plinth, slopes. Only half of the model is mounted. The dam geometry is separated into three major fundamental parts shown in Figure 1, the rockfill dam body (white), a replaceable rockfill face layer (blue) and the slab (grey). The image also defines the Swedish boxes positions (red circle) and horizontal construction lines, each with a 10 m lift.

In addition to the X, Y and Z axes, a rotated reference is defined, where the Y' and X' plane is parallel to the shoulder plane. The vertical plane perpendicular to the Axis Z is sliced with 16 out of 16 m, propagates through the entire model. The slab thickness followed empirical criteria like those adopted for designing the Campos Novos and Barra Grande dams (Frutuoso, 2007). The thickness is reduced from the base to the top, with a change in the middle of the slab. The thickness adopted is 100 cm at the base, 50 cm in the middle and then 30 cm at the crest.

## 2.2 Interfaces and separation of materials

The ABAQUS® software allows mesh detachment between different parts, allowing differential movements

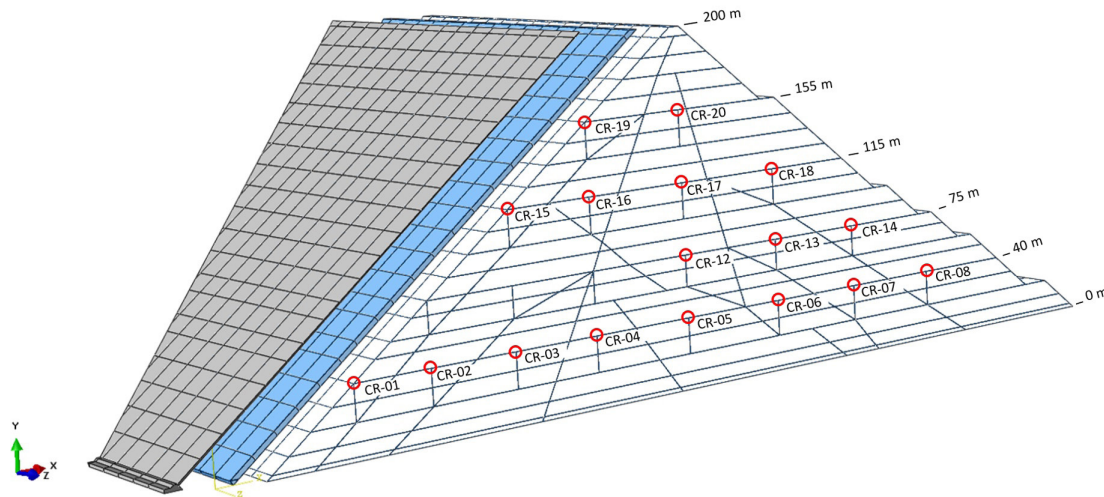


Figure 1. 3D geometry rockfill dam.

between the slab strips and between the slab and rockfill. The slab strips have a simply supported interface, both with its adjacent strip and with the blue layer and the plinth itself. According to the British Standard BS 5975 (BSI, 1996), the minimum value for the coefficient of friction in the contact between concrete/concrete and concrete/soil is 0.4, thus, it was adopted the value of friction at 0.5.

The blue layer in Figure 1 is divided into sets of 21 horizontal bands which composes a set. In each complete set it has bands stuck together with its adjacent one using the “tie” type interface. Each set, in turn, is also tied to the white part, joined with a “tie” type constraint. The interface between the rockfill dam body and the replaceable rockfill face layer is bonded with a “tie” type constraint. The interface between the concrete plinth and slab with the face rockfill replaceable layer is only a friction penalty of 0.5 as shown in Figure 2.

The regions are delimited from the Settlement Swedish Boxes (CR) shown by Cruz & Pereira (2007). To respect the

design and stress ranges, the areas of influence for each of the instrument regions were separated. The rockfills on the faces are the same as in the CR-01 region. The regions will be gradually grouped respecting the sectorization guidelines of Sherard & Cooke (1987) as presented in Figure 3.

### 2.3 Boundary and loading conditions

The boundary conditions of the three-dimensional model include displacement restrictions. The base of the model has three directions restrictions. The symmetry plane is restricted in the horizontal direction of the Y Axis. The abutment plane has a sectorization in the vicinity of the slab with restriction only in the normal plane (Z' axis) apart from a wider region with restriction in the normal and horizontal directions (Z' and X' axes), outside the region close to the slab. Reservoir filling is applied in five steps with conventional triangular hydrostatic diagram. Specific weight of water and gravity are rounded to 10 kN/m<sup>3</sup> and 10 m/s<sup>2</sup>.

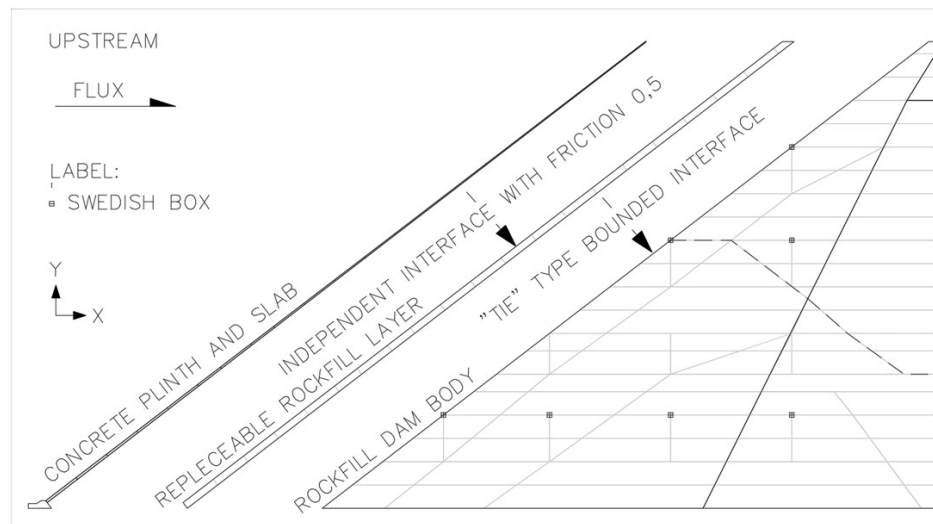


Figure 2. Interfaces between geometric parts.

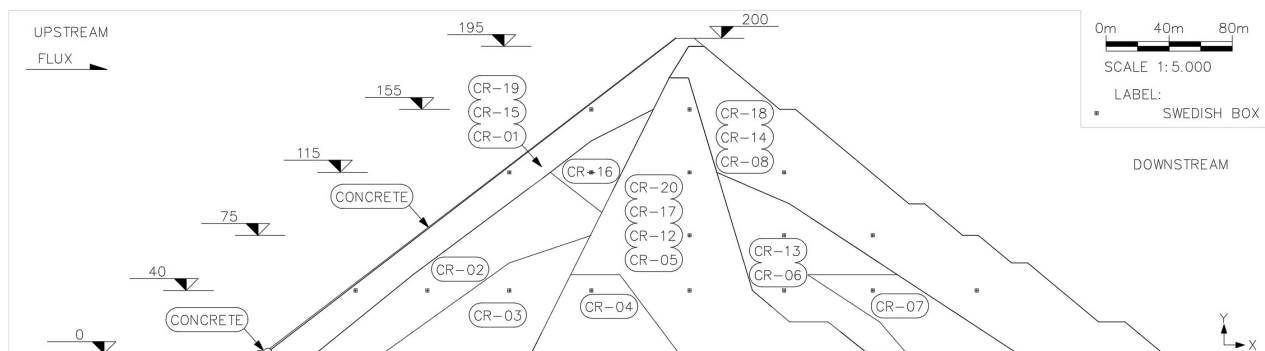


Figure 3. Geometric separation of materials.



## 2.4 Mesh

The tetrahedral rockfill elements are of the C3D4T type and the hexahedral concrete elements are of the C3D8R type, with approximate sizes of 5 m. The formulation of its matrix is coupled with temperature, transient and considering geometric nonlinearity with updating of the stiffness matrix at each increment. The mesh density study is not detailed here, but consisted in finding a finite element size based on the previous study presented by Raposo (2016).

## 2.5 Rockfill sequencing

The reference dam model was built in two phases, the first is highlighted in gray in Figure 4. In these analyses, the initial time is  $t_0 = 0$  days and the final time is  $t_f = 620$  days, as on Table 1, which are the input data for the imposition of vertical settlement in Equation 1. Raise times were based on the work by Cruz & Pereira (2007).

## 2.6 Slab construction delays

The study of the influence of the slab construction delay was carried out with six different scenarios, one by

one, arrangements of substitutions were being founded for each slab delay. The first scenario is named Step-by-step model, where the slab is activated following the dam body without initial embankment. The slab is activated with the rockfill at elevation 30 m. From then on, the slab is activated following each elevation step by step. The replacement of the sacrificial layer occurs level by level.

The second scenario is named 0/4 delay model. It considers a sectoring of the initial embankment (grey region in Figure 4), and the slab being activated step by step with the rockfill after the middle of the embankment. The three replacements of the rockfill surface layers start at step 13, as shown in Figure 5a. The first slab level is activated at step 14 and from on, the slab is lifted following the step-by-step embankment of the downstream slope.

The 1/4 delay model represents slab raising with the order of a quarter of the dam height, in relation to the rockfill raising. The five replacements of the rockfill surface layers start at step 18, according to Figure 5b. The 2/4 delay model represents slab raising with the order of half of the dam height. This model requires, at least, four replacements of the sacrificial rockfill surface layer, starting at step 23. The second, third and fourth replacements are at steps 27, 31 and 34, respectively, as shown in Figure 5c. The 3/4 delay

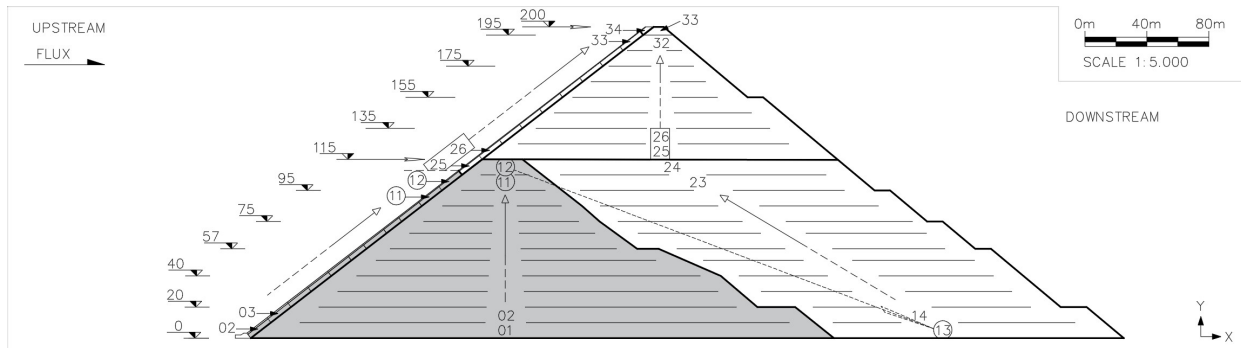
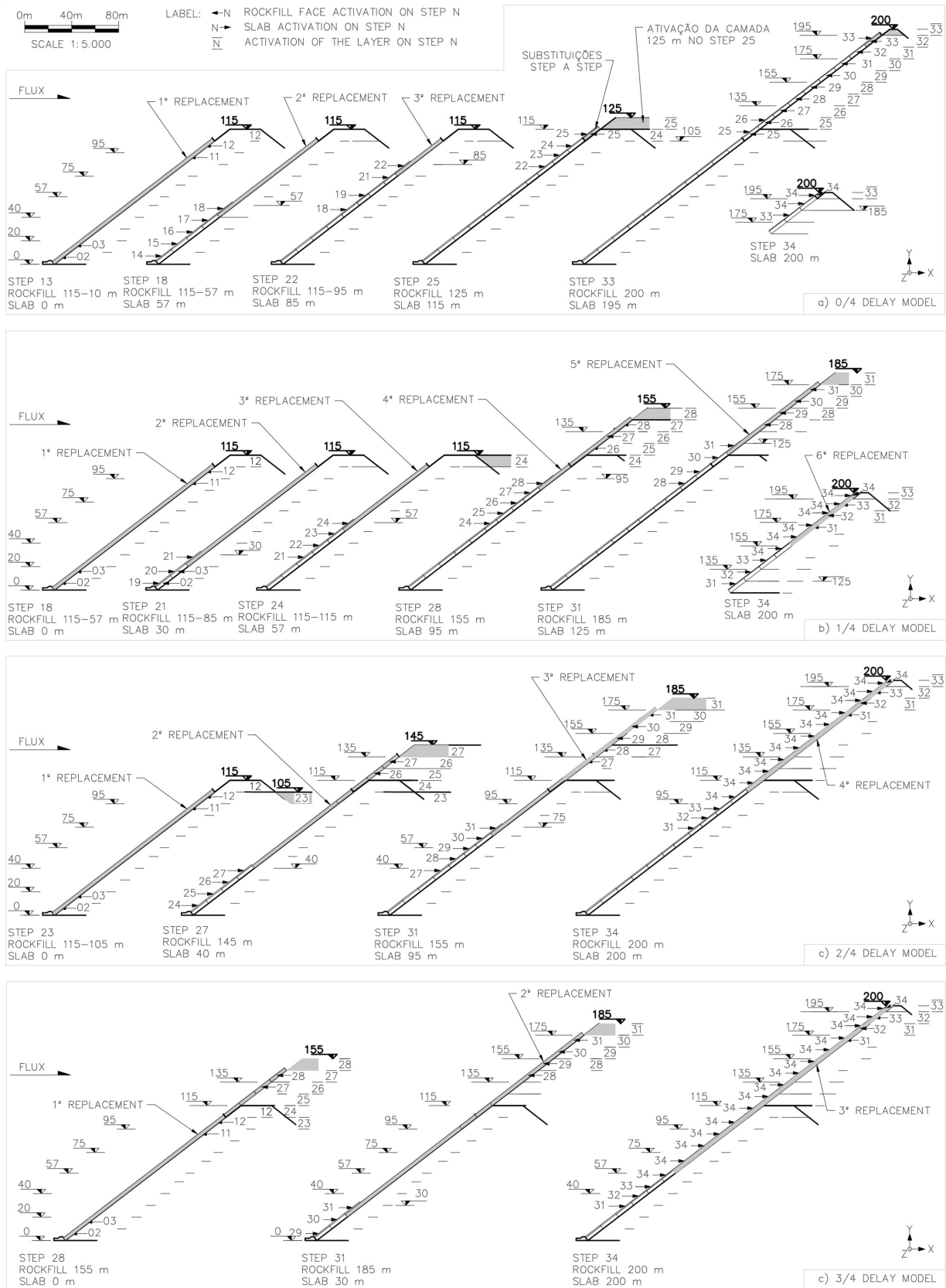


Figure 4. Standard elevation sequence from 01 to 34. Gray region first.

Table 1. Construction Steps of Rockfill.

First raise in gray (0 m to 115 m)			Downstream up to 115 m			Elevation above 115 m.		
Step	Height (m)	Days	Step	Height (m)	Days	Step	Height (m)	Days
1	010	10	13	115-010	230	25	125	380
2	020	30	14	115-020	240	26	135	440
3	030	50	15	115-030	250	27	145	480
4	040	70	16	115-040	260	28	155	520
5	050	90	17	115-050	270	29	165	540
6	057	110	18	115-057	280	30	175	560
7	065	130	19	115-065	290	31	185	580
8	075	150	20	115-075	300	32	195	600
9	085	170	21	115-085	305	33	200	610
10	095	190	22	115-095	310	34	Face Final	620
11	105	210	23	115-105	315			
12	115	220	24	115-115	320			

# Simplified model for dam rockfill creep and influence of constructive delay of concrete face



**Figure 5.** Sequencing of replacements and activation of the slab: (a) 0/4 delay model, (b) 1/4 delay model, (c) 2/4 delay model and (d) 3/4 delay model.

model represents raising the slab with the order of three quarters of the height of the dam. In this case, there were three replacements of the rockfill surface layers, according to Figure 5d. In the 4/4 delay model, the slab is only activated after the full height of the dam. Only two replacements of the rockfill surface layers were required in the last two steps.

### 3. Adjustments and calibration

The slab activation requires forced geometric adjustments that ensures activation of a concrete face with the correct thickness. The artifice consists of replacing a new layer on the rockfill face, with a completely new mesh (blue layer in Figure 1). Each replacement aligns the outer face with the original undeformed geometry. The inner face is fitted with the geometry already deformed from the fixed link (constraint: tie). The substitution generates a thickness change in the

rockfill face layer, that changes the stress field. Therefore, a second substitution is necessary to drive the slab in thickness to grant minimum residual stresses.

The vertical slab strips can move in independent directions with some friction between them. For future studies, it would be possible to think of some numerical implementation that adjusts the parametric activation of the slab thickness. The slab would have some differential curvature that follows the displacements of the rockfill base, maintaining the thickness.

#### 3.1 Slab thickness adjustment example

The concrete face sequencing used for calibration considers a slab delay of half of the dam height (2/4 delay model). Step 22 (Figure 6a) precedes the first replacement of the surface layer that occurs in the 23rd step (Figure 6b) without

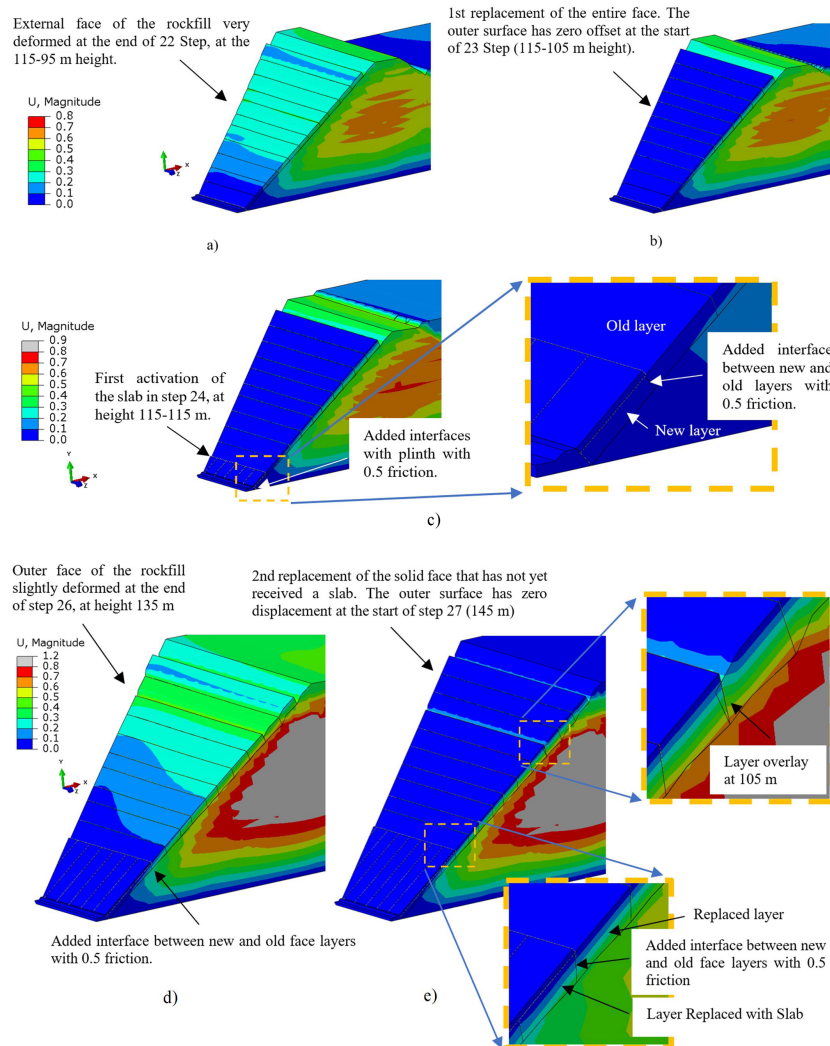


**Figure 6.** Replacing artifice, (a) step 22, before first replacement of the rockfill face and (b) step 23, showing face with zero displacement in 2/4 delay model. (c) activation of the first raising of the slab in step 24. (d) step 26, before second replacement and (e) step 27, adjusted face.

the concrete slab. The results images were extracted from the 2/4 delay model with ten times exaggeration. The slab starts to be activated in step 24 (Figure 6c), always in conjunction with the replacement of the rockfill surface layer immediately below and activation of the interface with the next layer. Step 26 (Figure 6d) presents accumulated displacements on the rockfill face, so the layer is replaced in step 27 (Figure 6e). A face remained linked to the previous displacement, creating an overlapping of layers at elevation 105 m. This condition was kept as it is because the sequential lifting of the slab does not reach the height of the inconsistency.

Step 30 precedes the third replacement of the surface layer. The inconsistency remains at an elevation of 105 m. The step 33 precedes the last activation of the slab, its level is at an elevation of 95 m. The activation of the rest of the slab in step 34 is still presented. The entire slab is activated at once.

### 3.2 Calibration Results

The calibration was obtained by a central section of the dam for the 1/2 delay model. The parameter results of Young Modulus ( $E$ ) and Vertical Deformation per year (creep) are shown in Table 2. According to the proposed methodology, Figure 7a and Figure 7b show the results of the calibrated model that compares the displacement curves obtained from Settlement Swedish Box (CR) with displacements calculated during the construction phase. Figure 8 shows the face displacement in the slab due to reservoir filling.

### 4. Stresses and displacements

Detailed stresses and displacements are shown only for the 1/2 delay model. The stress S33 is with a maximum in the order of 33 MPa (Figure 9a) and maximum total

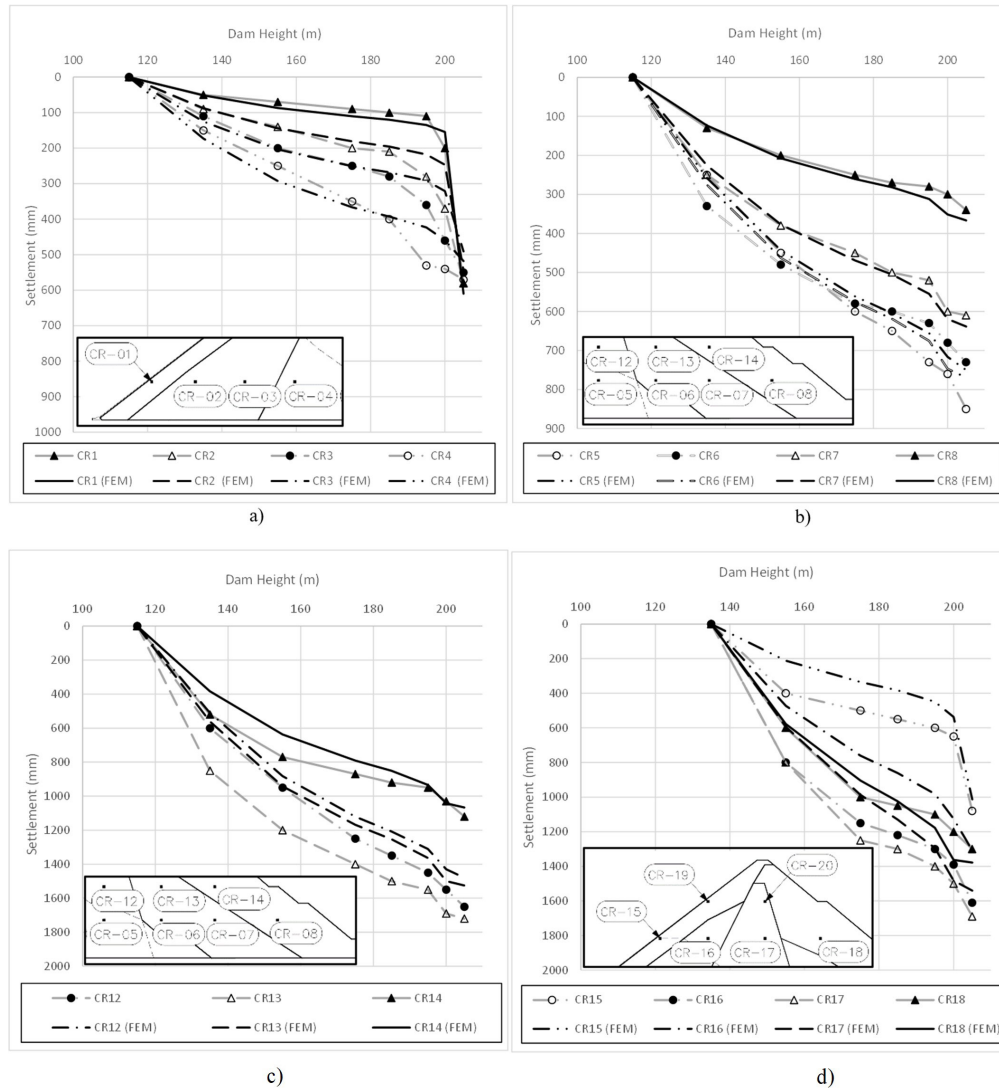


**Figure 7.** Displacements in the Swedish boxes positions (a) CR-01 to CR-04, (b) CR-05 to CR-08, (a) CR-12 to CR-14 and (b) CR-15 to CR-18. FEM calculated vs measured by Cruz & Pereira (2007).

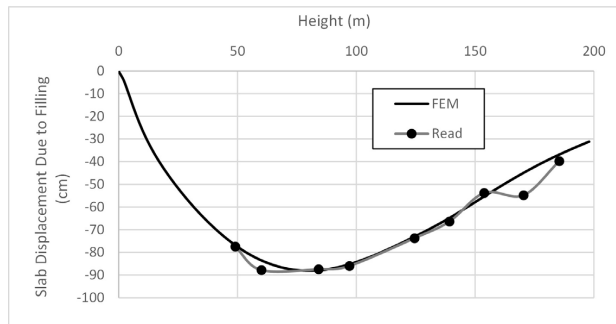


**Figure 8.** Displacement in the slab due to reservoir filling. FEM calculated vs measured from Xavier et al. (2007).

displacements in the order of 1 m (Figure 9b). Stress curves  $S_{11'}$  (longitudinal of the slab) get close to 6 MPa in the axis of symmetry (Figure 9c), except for the peaks of dimension 105 m. Transverse and shear stress curves are residual, without any suggestion for important bending moments. The curves in Figure 9d show the right axis displacement and the left displacement. The deviation is almost entirely in the range between -1% and 1%, slightly surpassing the range near the plinth.

All six scenarios show greater stresses in the shoulder-to-shoulder direction. Other stresses, including bending moment, are residual. Thus, the displacements (Figure 10a)

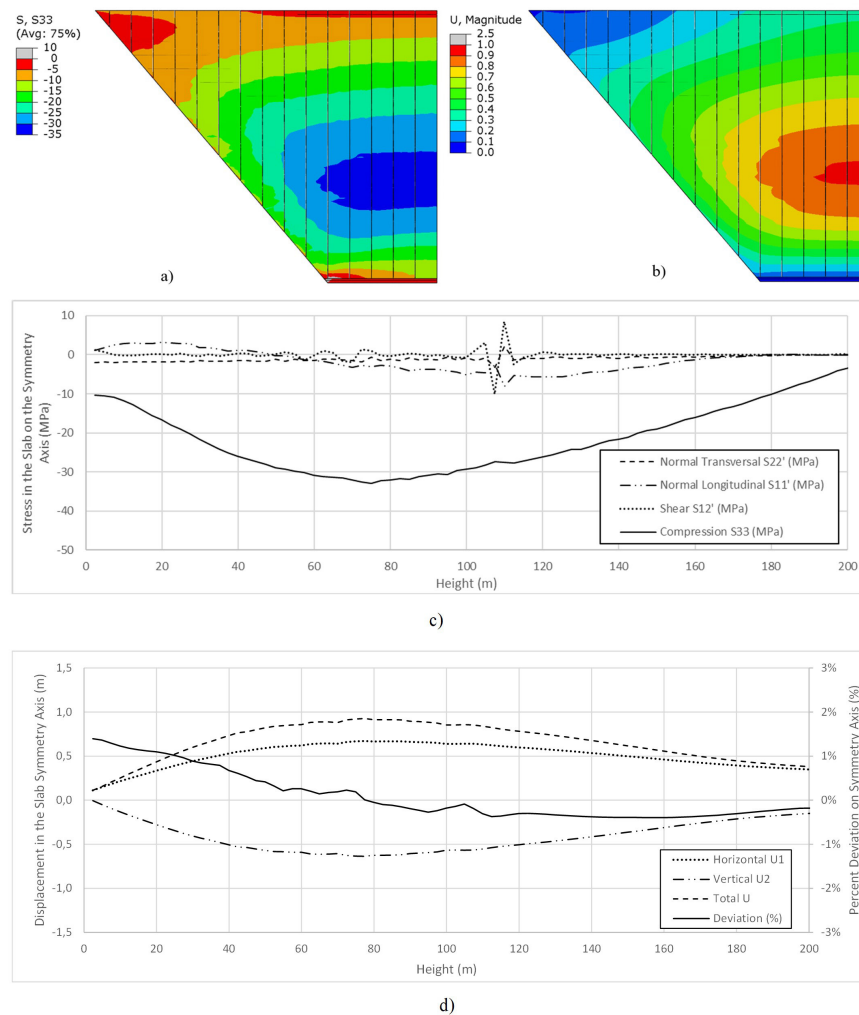


**Figure 9.** (a) horizontal stress  $S_{33}$  (MPa), (b) total displacements  $U$  (m), (c) slab stresses in the dam symmetry line (MPa) and (d) displacements (m) and deviation (%) in the slab in the dam symmetry line in the 2/4 delay model.

**Table 2.** Parameters calibrated using the 1/2 delay model.

REGION		UPSTREAM								CORE				DOWNSTREAM			
CR	01	15	19	02	16	03	04	05	12	17	20	06	13	07	14	18	08
$E$ (MPa)		80		100	80	100	180		180			80		80		80	
Creep (%/year)		0		1	1.77	0.59	0.88		1.77			1.77		1.18		0.59	



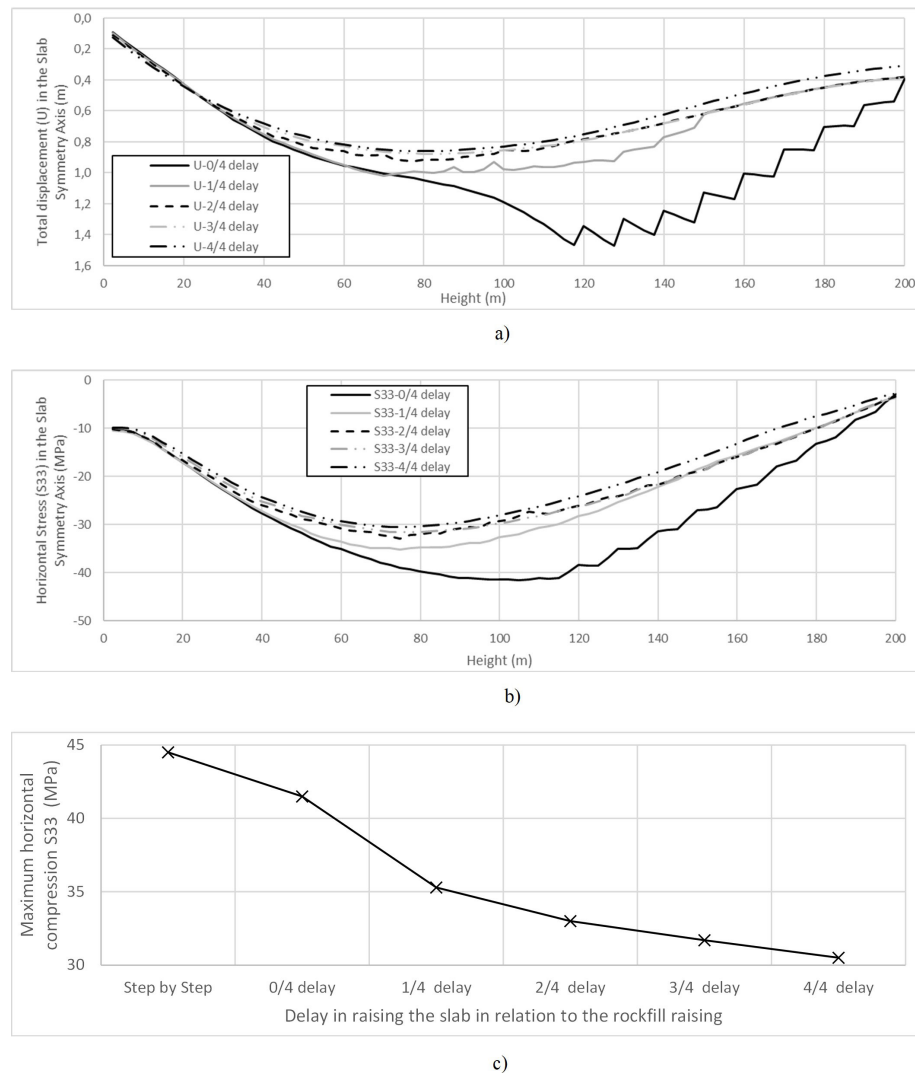


**Figure 10.** (a) Slab symmetry axis total displacement ( $U$ ) at five different slab delays, (b) slab symmetry axis horizontal compressions ( $S_{33}$ ) at five different slab delays, (c) synthesis of maximum results of horizontal compressions ( $S_{33}$ ) at six different slab delays.

and stresses  $S_{33}$  (Figure 10b) are presented comparing five different slab delays. All five scenarios start after the first gray landfill phase of Figure 4. In plot, it is noticeable that the curves with minor delay of the slab stand out from the others. Comparatively, it is possible to plot a synthesis of maximum horizontal stress in Figure 10c, including Step-by-Step. It is possible to observe that the presence of a greater reduction in stress  $S_{33}$  when there is a delay of at least a quarter of the slab in relation to the rockfill.

## 5. Conclusions

The forced linear reduction of vertical volume in time is implemented with a device of using orthotropic thermal expansion for coupling with linear mechanical behavior. Sophisticated constitutive models would involve an even greater difficulty for calibration. Furthermore, without massive

support of laboratory results, any more far-fetched results would inevitably fall back on a semi-empirical approach to estimating and fixing parameters that cannot be calibrated.

Restricted to the analyzed cases and starting from the purely behavioral view, the linear calibration presented a suitable result for the objectives of the work to serve as a basis for the sequencing studies. The worst sequencing arrangements would be step-by-step and zero delay where the slab strips are concreted, following each step of the rockfill raising. In these scenarios, stresses build up right at the beginning of the rockfill mass elevation. One of the models reached horizontal stress values that reach 45 MPa, which far exceeds the compressive strengths typical of conventional concretes. As highlighted, this expressive result becomes a point of attention regarding the structural integrity of the slab and this sequencing should really be avoided. The advantage of this condition could be associated with possible gains in terms

of a more closed work schedule, with some anticipation of filling the reservoir. This evaluation serves as a provocation that may suggest induction of cracking in the slab.

At least, all considerations need to be taken with parsimony and caution, each dam is a unique work and must be analyzed individually, case by case. In other words, these simulations are based on a database of settlement Swedish box results and slab displacements, for a very specific example of a dam.

## Acknowledgements

The authors would like to thank the financial support of the Brazilian National Research Council (CNPq) and Post-Graduation Agency of Brazil (CAPES).

## Declaration of interest

The authors have no conflicts of interest to declare. All co-authors have observed and affirmed the contents of the paper and there is no financial interest to report.

## Authors' contributions

Renato Santos Paulinelli Raposo: conceptualization, data curation, visualization, software, investigation, methodology, writing – original draft. Yasletty Zamora Hernández: formal analysis, supervision, visualization, writing – original draft. André Pacheco de Assis: supervision, validation, writing – review and editing.

## List of symbols

<i>CFRD</i>	Concrete Face Rockfill Dams
<i>CR</i>	Settlement Swedish Boxes
<i>E</i>	Young's modulus
<i>S'</i>	Control variable for missing percentage of creep
<i>S</i>	Stress
<i>t</i>	Constructive time variable
<i>t<sub>f</sub></i>	Time constant at the end of construction
<i>t<sub>0</sub></i>	Construction start time constant
<i>U</i>	Total displacement

## References

- Basso, R.V. (2007). *Stress-strain study for one rockfill aiming concrete face rockfill dam* [Master's dissertation, University of São Paulo]. University of São Paulo's repository. <https://doi.org/10.11606/D.3.2007.tde-07082007-112420>.
- BSI BS 5975. (1996). *Code of practice for falsework friction*. British Standards Institution, London.
- Chen, Y., Gu, C., Shao, C., & Qin, X. (2019). Parameter sensitivity and inversion analysis for a concrete face rockfill dam based on CS-BPNN. *Advances in Civil Engineering*, 2019, 1-17. <http://dx.doi.org/10.1155/2019/9742961>.
- Cruz, P., Materón, B., & Freitas, M. (2014). *Barragens de enrocamento com face de concreto* (2. ed.). Oficina de Textos.
- Cruz, P.T., & Pereira, R.F. (2007). The rockfill of Campos Novos – CFRD. In *Proceedings of 3rd Symposium on Concrete Face Rockfill Dams* (pp. 207–216). Florianopolis, October 2007. CBDB.
- Frutuoso, A. (2007). *Análises tridimensionais de barragens de enrocamento com face de concreto com objetivo de otimizar os critérios de projeto* [PhD thesis, University of Brasília]. University of Brasília's repository (in Portuguese). <https://repositorio.unb.br/handle/10482/1582>.
- International Commission on Large Dams – ICOLD. (2010). *Concrete face rockfill dams: concepts for design and construction* (Bulletin 141). Paris.
- Naylor, D.J., Pande, G.N., Simpson, B., & Tabb, R. (1981). Finite element in geotechnical engineering. *International Journal for Numerical and Analytical Methods in Geomechanics*, 6(4), 491-492. <http://dx.doi.org/10.1002/nag.1610060409>.
- Oldecop, L.A., & Alonso, E.E. (2001). A model for rockfill compressibility. *Geotechnique*, 51(2), 127-139. <http://dx.doi.org/10.1680/geot.2001.51.2.127>.
- Oldecop, L.A., & Alonso, E.E. (2003). Suction effects on rockfill compressibility. *Geotechnique*, 53(2), 289-292. <http://dx.doi.org/10.1680/geot.2003.53.2.289>.
- Oldecop, L.A., & Alonso, E.E. (2007). Theoretical investigation of the time-dependent behaviour of rockfill. *Geotechnique*, 57(3), 289-301. <http://dx.doi.org/10.1680/geot.2007.57.3.289>.
- Pinto, N.L.S. (2007). Very high CFRDs: behaviour and design features. In *Proceedings of 3rd Symposium on Concrete Face Rockfill Dams* (pp. 43-49). Florianopolis, October 2007. CBDB.
- Pramthawee, P., Jongpradist, P., & Sukkarak, R. (2017). Integration of creep into a modified hardening soil model for time-dependent analysis of a high rockfill dam. *Computers and Geotechnics*, 91, 104-116. <http://dx.doi.org/10.1016/J.COMPGeo.2017.07.008>.
- Raposo, R.S.P. (2016). *Estudo tridimensional dos efeitos devido a força de percolação em barragens de enrocamento com face de concreto* [Master's dissertation, University of Brasília]. University of Brasília's repository (in Portuguese). <https://repositorio.unb.br/handle/10482/22604>.
- Sherard, L., & Cooke, B. (1987). Concrete-face rockfill dam: I. Assessment. *Journal of Geotechnical Engineering*, 113(10), 1096-1112. [http://dx.doi.org/10.1061/\(ASCE\)0733-9410\(1987\)113:10\(1096\)](http://dx.doi.org/10.1061/(ASCE)0733-9410(1987)113:10(1096)).
- Wei, K., & Zhu, S. (2015). Application of an elastoplastic model to predict behaviors of concrete-faced rockfill dam under complex loading conditions. *Journal of Civil Engineering and Management*, 21(7), 854-865. <https://doi.org/10.3846/13923730.2014.893911>.
- Xavier, L.V., Albertoni, S.C., Antunes, J., Gasparetto, M., & Pereira, R.F. (2007). Concrete face rockfill dams-studies on face stresses through mathematical models.

- In *Proceedings of 3rd Symposium on Concrete Face Rockfill Dams* (pp. 129–138), Florianopolis, October 2007. CBDB.
- Yao, F., Guan, S., Yang, H., Chen, Y., Qiu, H., Ma, G., & Liu, Q. (2019). Long-term deformation analysis of Shuibuya concrete face rockfill dam based on response surface method and improved genetic algorithm. *Water Science and Engineering*, 12(3), 196-204. <http://dx.doi.org/10.1016/j.wse.2019.09.004>.
- Zhang, B., Wang, J.G., & Shi, R. (2004). Time-dependent deformation in high concrete-faced rockfill dam and separation between concrete face slab and cushion layer. *Computers and Geotechnics*, 31(7), 559-573. <http://dx.doi.org/10.1016/J.COMPGEO.2004.07.004>.
- Zhou, M.Z., Zhang, B.Y., & Jie, Y.X. (2016). Numerical simulation of soft longitudinal joints in concrete-faced rockfill dam. *Soil and Foundation*, 56(3), 379-390. <http://dx.doi.org/10.1016/J.SANF.2016.04.005>.

## Contribution for a root pile installation control approach using a digital odometer

José Melchior Filho<sup>1#</sup> , Alfran Sampaio Moura<sup>2</sup> ,

Fernando Feitosa Monteiro<sup>1</sup> 

Article

### Keywords

Root piles  
Static load testing  
Bearing Capacity

### Abstract

A root pile is a form of injection pile (cast-in-place with pressure, with very distinct construction aspects from the known micropile type). During the mortar shaft development, these piles are inserted using distinct injection pressures of up to 500 kPa. Static load tests are typically used to control root piles, which can be an expensive and time-consuming testing procedure. Static load tests were performed on eight monitored piles with diameters of 350 and 410 mm to investigate root pile performance control during pile installation. This research presents a refined and developed alternative methodology for confirming root pile performance using a digital odometer attached to the drill rig's rotatory head. The methodology consists of monitoring variables obtained during pile installation related to pile bearing capacity. Moreover, empirical equations with simple and relevant applications to estimate root pile bearing capacity during installation are proposed. The developed equations produced results consistent with the values obtained from static load testing on the test piles. Therefore, the results suggest that the proposed methodology is a viable alternative for root pile performance control.

## 1. Introduction

Pile foundations have been used as load-bearing and load transferring systems for many years. More recently, the increased demand for housing and building has compelled companies to improve pile construction productivity, resulting in the development of numerous innovative pile installation techniques.

In the last decade, root piles have become a widespread alternative (Moura et al., 2015; Lima & Moura, 2016; Monteiro et al., 2019), especially in pile foundation strengthening and complex geological circumstances involving rock strata profiles (Ding et al., 2017). Single root pile testing is frequently included in project specifications for large construction projects. Compression static load testing is the most common type of root pile performance control and certainly, the most reliable method to determine bearing capacity and load-settlement relationships (Russo, 2012). The static load test is simple to perform and analyze. However, practical issues arise when performing static load tests with limited access, such as the reaction system setup, which can be time-consuming and expensive.

Many researchers have investigated the performance of root piles, such as Cadden et al. (2004), Huang et al. (2007), Moura et al. (2015), Lima & Moura (2016), Monteiro et al. (2019). Other studies were conducted focusing on other types of piles but also sharing other important conclusions (Lin et al., 2004; Liang & Yang, 2006; Herrera et al., 2009; Basu et al., 2010; Alzo'Ubi & Ibrahim, 2018; Pari et al., 2019). However, root pile installation control has rarely been studied directly. Monteiro et al. (2019) proposed an alternative approach to the root pile installation control, helping in the decision-making during field construction concerning the definition of the pile length to be installed. The preliminary methodology proposed by the authors consists of monitoring installation variables related to the root pile bearing capacity and using them as inputs of empirical equations developed in their research.

The undrained soil shear strength can be determined from the measurement of torque and assuming a prescribed shear stress profile along the potential cylindrical failure surface. Therefore, it can be emphasized that torque is a variable that must influence the soil shear strength (Cabalar et al., 2020; Baroni & Almeida, 2022). Regarding pile foundation construction, it can be verified that torque measurements are

<sup>#</sup>Corresponding author. E-mail address: melchior\_filho@hotmail.com

<sup>1</sup>Universidade de Brasília, Programa de Pós-graduação Programa de Pós-graduação, Brasília, DF, Brasil.

<sup>2</sup>Universidade Federal do Ceará, Departamento de Engenharia Hidráulica e Ambiental, Fortaleza, CE, Brasil.

Submitted on November 14, 2021; Final Acceptance on July 21, 2022; Discussion open until November 30, 2022.

<https://doi.org/10.28927/SR.2022.077121>



This is an Open Access article distributed under the terms of the Creative Commons Attribution License, which permits unrestricted use, distribution, and reproduction in any medium, provided the original work is properly cited.

often performed during the installation of continuous flight auger piles. However, this measurement is not performed in the field during the root pile installation due to the lack of built-in equipment in the drilling system for torque measurement.

The current research establishes the literature gap filled by the alternative approach to the root pile installation control proposed by Monteiro et al. (2019) and proposes an improved method for assessing root pile performance. For this purpose, root pile installation variables related to bearing capacity were monitored, and data was collected in experimental fields using a wireless sensor (a speedometer coupled with four magnets) connected to the rotating head of a drill rig. The data was used to develop three empirical equations to estimate the ultimate bearing capacity ( $Q_{ult}$ ) of root piles and evaluate their performance during installation.

The improvements in this research aim to obtain more accurate field data (i.e. with fewer embedded errors due to using four magnets instead of only one) and to develop a better model with better statistical performance than that proposed by Monteiro et al. (2019). This was achieved by upgrading data acquisition equipment, adding a few more piles to the monitored group, and introducing the injection pressure variable in the proposed empirical equations. The methodology was tested and calibrated on eight root piles with lengths between 7.7 to 18 m, installed in 5 different experimental fields in the city of Fortaleza, State of Ceará, Brazil. In order to conduct pile performance assessment during their installation, it is necessary to estimate  $Q_{ult}$ , which requires one (or more) expressions to determine minimum pile length.  $N_{SPT}$  blow counts, pile geometry, drill bit penetration (advancing) velocity, and drill bit linear velocity were monitoring variables suggested by Monteiro et al. (2019) to estimate pile length and  $Q_{ult}$ , which were also contemplated in the development of the current research.

## 2. Root pile installation procedure

The installation of root piles comprises the following stages, as shown in Figure 1: (i) determining pile location; (ii) positioning of equipment and verification of verticality and inclination angle; (iii) drilling; (iv) inserting reinforcement bar; (v) filling pile hole with mortar; (vi) removing drill pipe with simultaneous application of compressed air.

Root piles possess a specific installation procedure that, depending on local conditions and soil characteristics, provides various advantages over other piles. Some advantages of this type of pile can be described as minimal vibration, drilling in rock strata, and small-sized equipment, which allows it to be operated in sites with limited heights and on varying slopes. However, root pile performance is currently controlled only after installation via static load tests.

## 3. Methodology

In this study, a wireless digital speedometer was used to monitor the variables of interest during pile installation. Figure 2 shows the monitoring apparatus installed on the rotating head of the drill rig. The diameter of the rotary drill was manually informed to the speedometer in each case so that the sensor (odometer) could log each complete lap performed by the rotary drill (with the help of the four magnets). Each time a magnet passes by the sensor, it registers a quarter of the linear length of the circumference previously informed to the speedometer. This approach allowed monitoring the linear distance the rotary drill performed during pile installation.

The drilling rod used to drill the last meter of pile length was also subdivided into sections of 10 and 20 cm (as shown in Figure 3), aiming to track the advancing velocity ( $V_a$ ) and

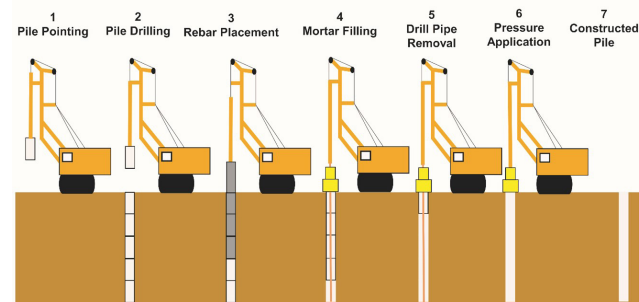


Figure 1. Root pile installation stages.

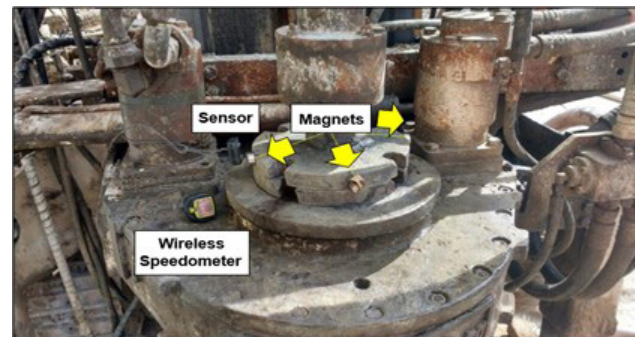


Figure 2. Monitoring equipment.



Figure 3. Marked sections on the last meter of the drilling rod.



linear velocity ( $V_b$ ) of the rotary drill during the drilling of these sections. This installation control procedure was only applied during the last meter of pile length due to constructive productivity. In case this procedure is implemented for the entire pile shaft, a considerable constructive production reduction would be observed.

Many semi-empirical bearing capacity methods present a relation between pile bearing capacity and  $N_{SPT}$  values. In some methods, the  $N_{SPT}$  value of the soil underneath the pile toe is considered for computing the toe bearing capacity (Meyerhof, 1976; Décourt & Quaresma, 1978; Bazaraa & Kurkur, 1986; Shariatmadari et al., 2008). On the other hand, other often employed methods consider only the soil at the toe level (Aoki & Velloso, 1975; Cabral, 1986; Alonso, 1996), which will depend on the pile failure mechanism being considered. Therefore, in this research, the latter assumption was considered. It could also be mentioned that pile diameters range from 0.31 to 0.41 m, which are relatively small diameters regarding the pile stress bulb below the pile tip level.

The number of rotations performed was calculated as the relationship between the linear distance traveled by the rotary drill and its circumferential length. This was used to determine the frequency (i.e., number of rotations per minute) and the rotary drill's angular velocity ( $\omega_r$ ), as shown in Equation 1. Since the rotary drill and the drill bit are mechanically attached (as seen in Figure 2), their angular velocities ( $\omega_r$  and  $\omega_b$ ) are equivalent:

$$2\pi f = \omega_r = \omega_b \quad (1)$$

The drill bit's radius ( $R_b$ ) is a known variable. Hence, the drill bit's linear velocity ( $V_b$ ) can be obtained (Equation 2):

$$V_{\dot{u}} = \omega R \quad (2)$$

The development of the empirical equations for the performance control of root piles during installation was initiated by selecting variables that would be comfortably obtained in the field since the goal is to propose an empirical method with simple application in the performance assessment process.

Two variables related to pile bearing capacity were obtained during the monitoring of test piles: (i) drill bit's linear velocity ( $V_b$ ), which is associated with shaft bearing capacity ( $Q_s$ ); and (ii) drill bit's advancing velocity ( $V_a$ ), associated with toe bearing capacity ( $Q_{toe}$ ).

Following what was suggested by Monteiro et al. (2019), in addition to  $V_a$  and  $V_b$ , other variables were also considered: Toe resistance index ( $N_{SPT, toe}$ , which corresponded to the average  $N_{SPT}$  value at the pile tip, that is, last meter); Average shaft resistance index ( $N_{SPT, shaft}$ , average  $N_{SPT}$  values along pile shaft); Pile diameter ( $D$ ); Pile length ( $L$ ); Pile perimeter ( $U$ ); and Pile toe cross-sectional area ( $A_p$ ). Energy corrections were not applied to the  $N_{SPT}$  values in this research.

However, Décourt et al. (1989) describe that the Brazilian SPT average efficiency is about 72%.

In static load tests, the ultimate bearing capacity ( $Q_{ult}$ ) is reached when a rapid movement happens under constant or slight load increase. However, it is quite uncommon for a pile to reach a plunging failure load (Fellenius, 2021). In this study, static load tests were performed, and Van der Veen's extrapolation was applied (van der Veen, 1953) since a distinct plunging ultimate load ( $Q_u$ ) was not obtained for most of the monitored piles.

In order to correlate the monitored variables and pile ultimate load ( $Q_u$ ), it was necessary to estimate the load distribution along shaft and toe (Monteiro et al., 2019). The Brazilian standard NBR 6122 states that shaft resistance should correspond to 80% of the total load for bored piles, and the rest should be provided by the toe (ABNT, 2010).

Since no instrumentation of the static load tests was performed in this research, three distinct scenarios were considered: (i) shaft resistance carrying 80% of total bearing capacity and toe resistance, the other 20%, as suggested by NBR 6122 ( $Q_u, 80/20$ ); (ii) toe resistance carrying 10% and shaft resistance, 90% of total load capacity ( $Q_u, 90/10$ ); and (iii) shaft alone carries the load (100% of total bearing capacity,  $Q_u, 100/0$ ). These are all viable alternatives, and choosing the expression to be applied in a real case will depend on the personal decision of the engineer, who could also use them all to evaluate potential field situations.

Multiple linear regression analysis (MLR) was used to establish the relationship between one dependent variable and several independent variables, following the generic expression shown in Equation 3:

$$Y = a_0 + a_1 X_1 + a_2 X_2 + \dots + a_n X_n \quad (3)$$

where:

$Y$  is the dependent variable (in this case,  $Q_{toe}$  or  $Q_s$ );

$X_1, X_2, \dots, X_n$  are the independent variables;

$a_1, a_2, \dots, a_n$  are coefficients of the independent variables (regression coefficients); and

$a_0$  is a constant that represents the portion of  $Y$  not explained by the independent variables.

The final expressions were obtained through the least-squares method (slightest deviation between observed and predicted values) and should be solved considering multiple linear functions of three variables,  $X_1$ ,  $X_2$ , and  $X_3$  (Equations 4 to 7):

$$\sum Y = n.a_0 + a_1 \sum X_1 + a_2 \sum X_2 + a_3 \sum X_3 \quad (4)$$

$$\sum YX_1 = a_0 \sum X_1 + a_1 \sum X_1^2 + a_2 \sum X_1X_2 + a_3 \sum X_1X_3 \quad (5)$$

$$\sum YX_2 = a_0 \sum X_2 + a_1 \sum X_2X_1 + a_2 \sum X_2^2 + a_3 \sum X_2X_3 \quad (6)$$

$$\sum YX_3 = a_0 \sum X_3 + a_1 \sum X_3 X_1 + a_2 \sum X_3 X_2 + a_3 \sum X_3^2 \quad (7)$$

Using the field data as inputs for variables  $Y$ ,  $X_1$ ,  $X_2$ , and  $X_3$ , the multiple linear regression model was implemented, and the coefficients  $a_0$ ,  $a_1$ ,  $a_2$ , and  $a_3$  were determined. An exponential model with log-transformation of variables was used in this step, considering that the relation between bearing capacity variables in usual prediction methods is not linear. Equations 8 and 9 show how this log transformation was implemented:

$$Y = a_0 * X_1^{a_1} * X_2^{a_2} * \dots * X_n^{a_n} \quad (8)$$

$$\ln(Y) = \ln(a_0) + a_1 * \ln(X_1) + a_2 * \ln(X_2) + \dots + a_n * \ln(X_n) \quad (9)$$

Hence, the three empirical equations to assess performance control of root piles during the installation step were established as below (Equations 10, 11, and 12):

$$Q_u = Q_s + Q_{toe} \quad (10)$$

$$Q_{toe} = a'_0 \cdot (A_p)^{a_1} \cdot (V_a)^{a_2} \cdot (N_{SPT, toe})^{a_3} \quad (11)$$

$$Q_s = a''_0 \cdot (V_b)^{a_4} \cdot (U.L)^{a_5} \cdot (p)^{a_6} \cdot (\bar{N}_{SPT, shaft})^{a_7} \quad (12)$$

where:

$p$  is the injection pressure.

#### 4. Site description and soil profile

In this study, root pile foundations were installed and monitored in five construction sites in northeastern Fortaleza, State of Ceará, Brazil. Standard penetration tests and rock core borings were conducted at all five sites.

At site A, where test piles P1 and P2 were installed, the groundwater level is found at -3 m. A clayey silt layer is found between the ground surface and a depth of 5 m, with  $N_{SPT}$  values varying from 16 to 60. Below, there is a 10-m-thick layer of sandstone with  $RQD$  (Rock Quality Designation index) ranging from 43% to 54%, with  $N_{SPT}$  values ranging from 48 to 60. (Figure 4)

At Site B, where test piles P3 and P4 were installed, a clayey sand layer is found between the ground surface and a depth of 11 m, with  $N_{SPT}$  values varying between 3 and 60. Then, a 5-m-thick layer of silty clay soil, with  $N_{SPT}$  values ranging from 29 to 60, is found. The bedrock was located at -16 m and the groundwater level at -1.2 m. (Figure 5)

Site C (test pile P5) has its groundwater level located between -6.7 m to -7.4 m. A silty sand layer is found between the ground surface and -4 m, with  $N_{SPT}$  values varying between

2 and 4. An 8-m-thick clayey sand layer is found below this silty sand, with  $N_{SPT}$  values between 4 and 9. Finally, a layer of sandy clay with  $N_{SPT}$  values from 9 to 42 was located, between -12m and -22 m. (Figure 6)

Site D (test piles P6 and P7) has a 11-m-thick top layer of silty sand, with  $N_{SPT}$  values between 6 and 60. Below, an 8-m-thick layer of clayey silt with  $N_{SPT}$  values from 7 to 59 is encountered. Water is found between -3.85 m and -4 m. (Figures 7 and 8)

Finally, Site E (test pile P8) has a clayey sand upper layer, identified from ground surface to -10 m, with  $N_{SPT}$

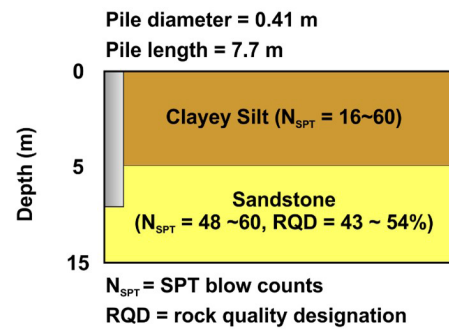


Figure 4. Soil profile at Site A (test piles P1 and P2).

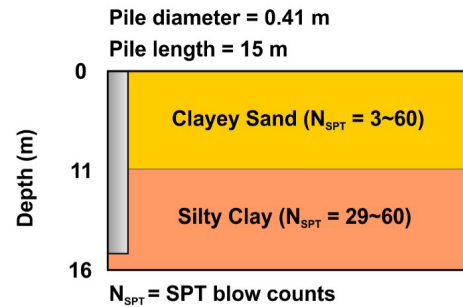


Figure 5. Soil profile at Site B (test piles P3 and P4).

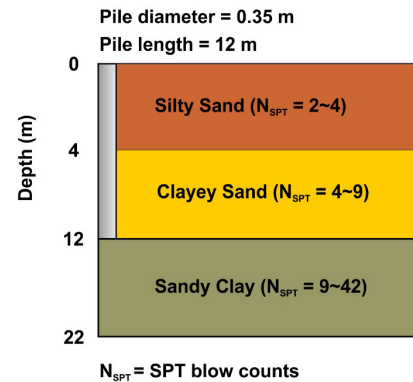


Figure 6. Soil profile at Site C (test pile P5).

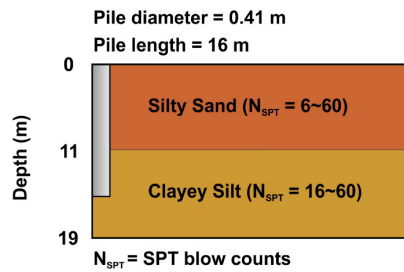


Figure 7. Soil profile at Site D (test pile P6).

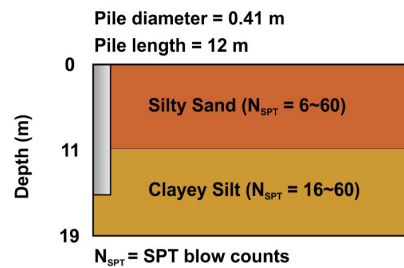


Figure 8. Soil profile at Site D (test pile P7).

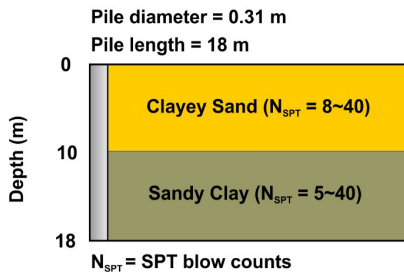


Figure 9. Soil profile at Site E (test pile P8).

values from 8 to 40. A sandy clay layer with  $N_{SPT}$  values of 5 to 40 is also found to have a depth of 18 m (Figure 9).

## 5. Static load tests

The test piles were subjected to static load tests ten days after installation, and the vertical settlement was assessed by four dial gauges installed on their heads (two on each side). The piles were connected to two reference beams, and the load was applied in increments of 20% of the expected final load and then sustained until the settlement rate between two consecutive readings was not higher than 5%.

The piles were unloaded in five stages after reaching the maximum load (except for pile P5). The geometry of the 8 test piles, maximum applied load, injection pressure, and maximum displacement measured are shown in Table 1. The curves “applied load versus settlement” obtained from the static load tests for test piles P1 to P4 are shown in Figure 10. Figure 11 shows the results for test piles P5 to P8.

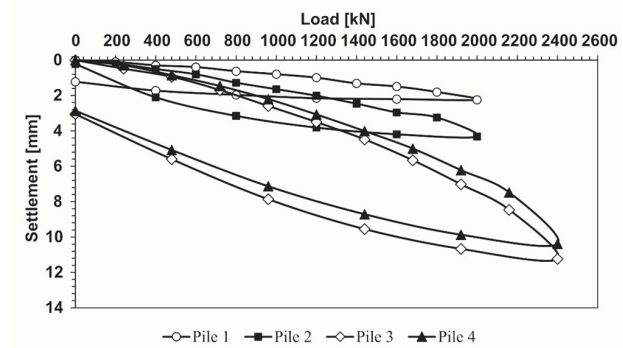


Figure 10. Results from static load tests for piles P1, P2, P3, and P4.

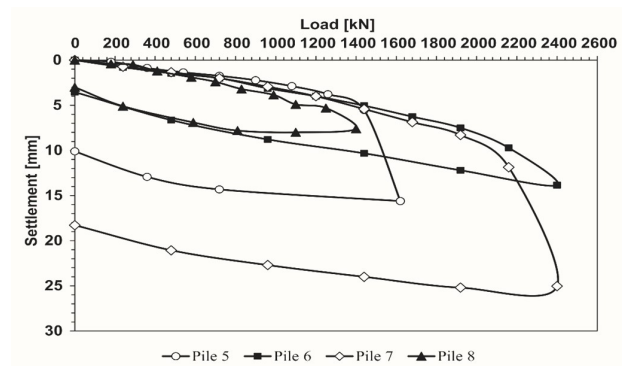


Figure 11. Results from static load tests for piles P5, P6, P7, and P8.

Test piles P5, P6, and P8 had the friction along the shaft completely mobilized, evidenced by a sudden increase in the settlements around the maximum applied load. Piles P1, P2, P3, P4, and P7 showed similar behavior, with settlements primarily controlled by shaft resistance.

For most test piles, a distinct plunging ultimate load ( $Q_u$ ) was not obtained, so the Van der Veen extrapolation was applied. The extrapolated values for  $Q_u$  are presented in Table 2.

## 6. Monitoring results

The piles were monitored, and the variables of interest were logged during the installation phase. Information related to the drill bit's linear velocity ( $V_b$ ) and drill bit's advancing velocity ( $V_a$ ) was captured by the data acquisition device (a speedometer) while drilling the marked section (i.e., the last meter of the drilling rod). Part of the data used in this research was cataloged by Monteiro et al. (2019), and the primary dataset was changed through data from different test piles. Monitored data is shown in Table 3.

In this study, in soil depths where  $N_{SPT}$  values were high and the installation had no remarkable hindrances, the  $N_{SPT}$  were designated as 60 (the arbitrated maximum). Also, it is worth mentioning that due to unexpected events in the field, adjustments in the marked sections were necessary for test piles P3, P4, P5, P6, and P7 (see Table 3).

**Table 1.** Results of performed load tests.

Site	Test pile	$L$ (m)	$d$ (m)	Max. applied load (kN)	Settlement (mm)	$p$ (kPa)
A	P1	7.7	0.41	2000	2.24	400
	P2	7.7	0.41	2000	4.32	400
B	P3	15.0	0.41	2400	11.24	300
	P4	15.0	0.41	2400	10.38	300
C	P5	12.0	0.35	1620	15.61	300
D	P6	16.0	0.41	2400	13.85	300
	P7	12.0	0.41	2400	25.04	300
E	P8	8.0	0.31	1400	7.60	300

**Table 2.** Extrapolated ultimate load ( $Q_u$ ).

Site	Pile	$Q_u$ (kN)
A	P1	3000
	P2	3200
B	P3	3100
	P4	2900
C	P5	1550
D	P6	2450
	P7	2150
E	P8	1800

Test piles P1 and P2 (both installed in Site A) had higher excavation times (i.e., lower advancing velocities) because pile toes reached the bedrock (sandstone). Test piles P5 (Site C) and P7 (Site D) were installed in soils with similar USCS classifications (clayey silt, silty sand, clayey sand, and sandy clay), and fair compliance between  $N_{SPT}$  values and advancing velocity ( $V_a$ ) was detected for both sites. When comparing test piles P5 and P7,  $V_a$  was 7.4% smaller, and  $N_{SPT}$  values for pile toe were higher for P7. This led to the conclusion that there is an inversely proportional correlation between these two variables: the higher the standard penetration resistance, the lower the advancing velocity.

During the installation of test piles P5 and P7, high values for the variable frequency ( $f$ ) were observed. It is evident that this variable has a direct relationship with drill bit's linear velocity ( $V_b$ ). Thus, the smaller the  $N_{SPT}$  value, the higher the frequency ( $f$ ) and the drill bit's linear velocity. Therefore, pile load bearing capacity can be deemed to be inversely proportional to the drill bit's linear velocity ( $V_b$ ) and to the frequency ( $f$ ).

Table 4 displays the average values of the monitored variables and the ultimate load for each test pile.

## 7. Development and validation of the empirical equations

A multiple linear regression analysis was used to develop the empirical equations. Test piles P1, P2, P3, P5, and P7 were randomly selected to obtain the equations

(calibration step), and test piles P4, P6, and P8 were used in the validation phase.

As mentioned in section 3, the three contemplated scenarios were named as  $Q_{u, 80/20}$ ,  $Q_{u, 90/10}$ , and  $Q_{u, 100/0}$ . Equations 13, 14, and 15 display the proposed expressions for the field performance control of root piles:

$$Q_{u, 80/20} = \frac{81.61 \cdot (A_p)^{0.015} \cdot (N_{SPT, toe})^{0.404}}{(V_a)^{0.08}} + \frac{1,666.94 \cdot (U.L)^{0.0064} \cdot (p)^{0.0036} \cdot (\bar{N}_{SPT, shaft})^{0.1578}}{(V_b)^{0.5492}} \quad (13)$$

$$Q_{u, 90/10} = \frac{40.80 \cdot (A_p)^{0.015} \cdot (N_{SPT, toe})^{0.404}}{(V_a)^{0.08}} + \frac{2,168.02 \cdot (U.L)^{0.0022} \cdot (p)^{0.0044} \cdot (\bar{N}_{SPT, shaft})^{0.15}}{(V_b)^{0.5271}} \quad (14)$$

$$Q_{u, 100/0} = \frac{2,508.88 \cdot (U.L)^{0.0064} \cdot (p)^{0.0037} \cdot (\bar{N}_{SPT, shaft})^{0.1402}}{(V_b)^{0.5492}} \quad (15)$$

In the proposed equations, the variables had a tangible, physical meaning: the higher the perimeter, pile length, or average shaft resistance index, the higher the shaft resistance. In contrast, the greater the drill bit's linear velocity, the lower the shaft resistance.

$V_a$  could be considered negligible for the database analyzed. However, this variable can present a more significant relationship to the pile tip bearing capacity for a more extensive dataset. On the other hand,  $V_b$  presents a reasonable correlation with the pile shaft bearing capacity. One of the limitations of this research is associated with the quantity of the analyzed dataset. However, it is essential to mention that minimal experimental data are available on loading full-scale root piles due to the difficulties and cost of full-scale load tests. It is worth mentioning that this work proposes a simplified procedure for the installation control of root piles, helping

**Table 3.** Data logged for monitored variables.

Site	Pile	Drilled length (m)	Time (s)	$V_a$ (x10 <sup>-3</sup> m/s)	$f$ (Hz)	$\omega_b$ (rad/s)	$V_b$ (m/s)	$N_{SPT, toe}$	$N_{SPT, shaft}$
A	P1	0.1	38.00	2.63	2.01	12.60	1.95	60	50
		0.2	51.00	3.92	2.50	15.72	2.44		
		0.2	78.00	2.56	2.15	13.50	2.09		
		0.2	72.00	2.78	2.25	14.13	2.19		
	P2	0.1	27.00	3.70	1.76	11.08	1.72	60	52
		0.2	50.00	4.00	2.67	16.76	2.60		
		0.2	56.00	3.57	1.36	8.55	1.33		
B	P3	0.2	54.00	3.70	2.65	16.62	2.58	60	33
		0.1	11.22	8.91	2.55	16.00	2.48		
		0.1	8.27	12.10	1.15	7.24	1.12		
		0.2	19.28	10.40	0.99	6.21	0.96		
	P4	0.1	4.76	21.00	2.00	12.57	1.95	60	32
		0.2	9.78	20.40	1.95	12.24	1.90		
		0.2	15.84	12.60	1.20	7.56	1.17		
C	P5	0.2	29.00	5.20	3.99	25.10	3.89	10	6
		0.2	43.00	4.70	4.06	25.48	3.95		
D	P6	0.3	30.00	1.00	2.05	12.86	1.99	39	22
		0.2	27.00	7.40	2.44	15.32	2.37		
	P7	0.3	38.00	7.90	1.61	10.14	1.57	22	22
		0.2	44.00	4.50	4.38	27.52	4.27		
E	P8	0.1	16.00	6.25	1.79	11.25	1.69	40	19
		0.2	39.00	5.13	1.71	10.77	1.62		
		0.2	41.00	4.88	1.71	10.73	1.61		
		0.2	37.00	5.41	1.72	10.81	1.62		

**Table 4.** Average monitoring variables values.

Pile	Drilled length (m)	Time (s)	$v_a$ (m/s)	Frequency (Hz)	$\omega$ (rad/s)	$V_b$ (m/s)	$N_{SPT, toe}$	$N_{SPT, shaft}$	$Q_u$ (kN)
1	0.175	59.75	2.97	2.23	13.99	2.17	60	50	3000
2	0.175	46.75	3.74	2.11	13.25	2.05	60	52	3200
3	0.133	12.92	10.50	1.56	9.81	1.52	60	33	3100
4	0.167	10.13	18.00	1.72	10.79	1.67	60	32	2900
5	0.175	36.00	4.95	4.03	25.29	3.92	10	7	1550
6	0.250	28.50	8.70	2.24	14.09	2.18	39	22	2450
7	0.250	41.00	6.20	3.00	18.83	2.92	22	22	2150
8	0.175	33.25	5.41	1.73	10.89	1.63	40	19	1800

in the decision-making during field construction with the definition of the pile length to be installed.

Since most of the root pile bearing capacity was mobilized essentially by shaft resistance, due to the installation process and proposed scenarios of load mobilization, the pile essentially behaves as a friction pile. Therefore, it is expected that  $N_{SPT}$  along with the shaft and  $V_b$  values, presents higher exponent values when compared to the  $V_a$  parameter exponent value. The geotechnical interpretation of these equations is that the pile shaft bearing capacity is preponderant. Therefore, pile tip mobilization is significantly lower than pile skin friction mobilization.

The proposed equations were tested with new data (validation dataset – test piles P4, P6, and P8), and the outputs (predicted values) were compared with results from performed load tests, as shown in Table 5.

Table 5 shows percentage errors between 0.2% (P6) and 65.1% (P8) were found. The predicted values for bearing capacity of test pile P4 were slightly higher than the reference values (bearing capacity obtained from static load tests) for two of the proposed load distribution scenarios (90/10 and 100/0), with an absolute error of 17.1%. For test pile P6, an absolute error of 16.7% was found when comparing predicted pile bearing capacity with reference values, which were slightly lower than what was estimated. As for test pile P8,



**Table 5.** Load test results and predicted values (from proposed equations) for the 3 considered scenarios.

Scenario	Pile 4			Pile 6			Pile 8		
	$Q_s$ (kN)	$Q_{toe}$ (kN)	$Q_u$ (kN)	$Q_s$ (kN)	$Q_{toe}$ (kN)	$Q_u$ (kN)	$Q_s$ (kN)	$Q_{toe}$ (kN)	$Q_u$ (kN)
$Q_{u,80/20}$	2404	328	2732	2039	293	2332	2079	304	2383
$Q_{u,90/10}$	2811	164	2975	2309	146	2455	2642	152	2794
$Q_{u,100}$	3147	0	3147	2579	0	2579	2972	0	2972
Load test $Q_u$ (kN)			2900			2450			1800

the predicted values were higher than the reference ones, with the most significant error (65.1%).

It is worth mentioning that using the proposed method in cases involving clayey soils must be done under careful judgment, for a considerable disturbance of the soil happens due to SPT blows. Eurocode 7 (BSI, 2007) recommends that, for fine soils, SPT tests should be taken into account only for qualitative assessments since no prevailing consensus regarding the precise effects of SPT blows on these soils has been reached.

Since the bearing capacity values obtained with the proposed equations showed a fair agreement with the reference values (static load tests), it was possible to conclude that there is indeed a correlation between pile bearing capacity and the adopted variables. It should be noted, however, that the aim of this research was to propose an alternative approach for the root pile installation control, with the goal of assisting engineers in the decision-making process during pile installation by employing variables that may be easily collected in the field as inputs.

## 8. Conclusions

A methodology based on monitoring variables to confirm the root pile length during installation was refined and developed. The technique is based on monitoring installation variables (drill bit's advancing and linear velocities) and classical concepts coupled with measurements made during fieldwork. The pressure injection variable was inserted into the empirical formulas, and enhanced monitoring procedures and equipment were implemented. The control methodology was based on the alternative approach of root pile installation control originally proposed by Monteiro et al. (2019), assisting in the decision-making process during field installation on the pile length to be constructed.

This approach is simple to implement and produces immediate interpretation. It is also specially designed for the real-world construction of root pile sites, providing a technically and economically viable preliminary installation control with reasonable accuracy regarding the root pile bearing capacity estimate during pile installation.

The non-destructive approach of this method allows engineers to perform and manage root pile performance control without damaging structures, saving valuable field

resources. This is especially important when static load tests are unavailable for some reason because the predictions were remarkably comparable to those obtained by static load tests.

Nevertheless, it is crucial to note that this technique has a limited range of applications and is currently limited to root pile lengths of up to 20 m with a maximum bearing capacity of 2,500 kN. Further research is required and recommended so that the dataset can be expanded, and broader-spectrum equations can be determined.

## Acknowledgements

This research was carried out under the auspices of the Foundations Group (Professors, M.Sc. Students, and Technicians) of the Post-Graduation Program in Civil Engineering – Geotechnical Engineering of the Federal University of Ceará (POSDEHA/UFC). All the authors would like to express their gratitude to the engineering contractors, FUNDAÇÕES GEOBRASIL and TECNORD, for the invaluable partnership in the field, and to CNPq Foundation for the financial aid granted to the first author.

## Declaration of interest

The authors have no conflicts of interest to declare. All co-authors have observed and affirmed the contents of the paper and there is no financial interest to report.

## Authors' contributions

José Melchior Filho: conceptualization, methodology, data gathering, visualization, formal analysis, writing - original draft. Alfran Sampaio Moura: conceptualization, formal analysis, supervision, data validation. Fernando Feitosa Monteiro: formal analysis, investigation, writing - review & editing.

## List of symbols

$a_0$	Dependent variables constant
$a_n$	Independent variables coefficients
$a_1$	Linear regression coefficient
$a_2$	Linear regression coefficient
$a_3$	Linear regression coefficient

$a_4$	Linear regression coefficient
$a_5$	Linear regression coefficient
$a_6$	Linear regression coefficient
$a_7$	Linear regression coefficient
$a'_0$	Linear regression constant
$a''_0$	Linear regression constant
$A_p$	Pile toe cross sectional area
$D$	Pile diameter
$f$	Frequency
$L$	Pile length
$N_{SPT}^{shaft}$	Average shaft N-value
$N_{SPT}^{toe}$	Toe resistance N-value
$p$	Air injection pressure
$Q_s$	Pile shaft resistance
$Q_p$	Pile toe resistance
$Q_{ult}$	Pile ultimate bearing capacity
$Q_u$	Plunging ultimate load
$R_b$	Drill bit radius
$RQD$	Rock Quality Designation index
$U$	Pile perimeter
$V_a$	Drill bit advancing velocity
$V_b$	Drill bit linear velocity
$\omega_b$	Drill bit angular velocity
$\omega_r$	Drill rod angular velocity
$X_n$	Independent variables
$Y$	Dependent variable

## References

- ABNT NBR 6122. (2010). *Foundation Design and Installation*. ABNT - Associação Brasileira de Normas Técnicas, Rio de Janeiro, RJ (in Portuguese).
- Alonso, U.R. (1996). Estacas hélice contínua com monitoração eletrônica: previsão da capacidade de carga através do ensaio SPT-T. In *Anais do 3º Seminário de Engenharia de Fundações Especiais e Geotecnia* (Vol. 2, pp. 141-151). São Paulo: ABMS (in Portuguese).
- Aoki, N., & Velloso, D.A. (1975). An approximate method to estimate vertical load capacity of piles. In *Proceedings of the 5th Panamerican Conference on Soil Mechanics and Foundation Engineering* (Vol. 1, pp. 367-376), Buenos Aires. CSMFE.
- Alzo'ubi, A.K., & Ibrahim, F. (2018). Predicting the pile static load test using backpropagation neural network and generalized regression neural network: a comparative study. *International Journal of Geotechnical Engineering*, 15(7), 1-12. <http://dx.doi.org/10.1080/19386362.2018.1519975>.
- Bazaraa, A.R., & Kurkur, M.M. (1986). N-values used to predict settlements of piles in Egypt. In *Proceedings of the Specialty Conference In Situ '86* (Vol. 1, pp. 462-474), Syracuse. ASCE.
- Baroni, M., & Almeida, M.S.S. (2022). Undrained shear strength correlation analysis based on vane tests in the Jacarepaguá Lowlands, Brazil. *Soils and Rocks*, 45(2), 1-12. <http://dx.doi.org/10.28927/SR.2022.072721>.
- Basu, P., Prezzi, M., & Basu, D. (2010). Drilled displacement piles: current practice and design. *DFI Journal*, 4(1), 3-20. <http://dx.doi.org/10.1179/dfi.2010.001>.
- BSI. (2007). *Eurocode 7: Geotechnical Design – Part 2: Ground Investigation and Testing*. British Standard Institution, Milton Keynes, UK.
- Cabral, D.A. (1986). O uso da estaca raiz como fundação de obras normais. In *Anais do 11º Congresso Internacional de Mecânica dos Solos e Engenharia de Fundações* (Vol. 6, pp. 71-82), Porto Alegre. ABMS (in Portuguese).
- Cadden, A., Gomez, J., & Bruce, D. (2004). Micropiles: recent advances and future trends. In *Proceedings of the 1st Conference on Current Practices and Future Trends in Deep Foundations* (Vol. 1, pp. 140-165), Los Angeles. ASCE. [https://doi.org/10.1061/40743\(142\)9](https://doi.org/10.1061/40743(142)9)
- Cabalar, A.F., Khalaf, M.M., & Isik, H. (2020). A comparative study on the undrained shear strength results of fall cone and vane shear tests in sand-clay mixtures. *Arabian Journal of Geosciences*, 13(11), 1-11. <http://dx.doi.org/10.1007/s12517-020-05351-5>.
- Décourt, L., & Quaresma, A.R. (1978). Capacidade de carga de estacas a partir de valores de SPT. In *Anais do 6º Congresso Internacional de Mecânica dos Solos e Engenharia de Fundações* (Vol. 1, pp. 45-53), Rio de Janeiro. ABMS (in Portuguese).
- Décourt, L., Belicanta, A., & Quaresma Filho, A.R. (1989). Brazilian experience on SPT. In *Anais do 12º Congresso Brasileiro de Mecânica dos Solos e Engenharia Geotécnica* (Vol. 1, pp. 49-54), Rio de Janeiro. ABMS, CBMR, ISRM & SPG (in Portuguese).
- Ding, H., Su, L., Lai, J., & Zhang, Y. (2017). Development and prospect of root piles in tunnel foundation reinforcement. *Civil Engineering Journal*, 26(3), 250-266. <http://dx.doi.org/10.14311/CEJ.2017.03.0022>.
- Fellenius, B.H. (2021). *Basics of foundation design*. Retrieved in September 16, 2021, from <http://www.fellenius.net/papers/412%20The%20Red%20Book,%20Basics%20of%20Foundation%20Design%202021.pdf>
- Herrera, R., Jones, L.E., & Lai, P. (2009). Driven concrete pile foundation monitoring with embedded data collector system. In *Proceedings of the 1st International Foundation Congress and Equipment Expo* (pp. 78-84), Orlando. ASCE. [https://doi.org/10.1061/41021\(335\)78](https://doi.org/10.1061/41021(335)78).
- Huang, Y., Hajduk, E.L., Lipka, D.S., & Adams, J.C. (2007). Micropile load testing and installation monitoring at the CATS vehicle maintenance facility. In *Proceedings of the GeoDenver 2007* (Vol. 1, pp. 28-38), Denver. ASCE. [https://doi.org/10.1061/40902\(221\)28](https://doi.org/10.1061/40902(221)28).
- Liang, R., & Yang, S.M. (2006). Quality control method for pile driving. *Journal of Geotechnical and Geoenvironmental Engineering*, 132(8), 1098-1104. [http://dx.doi.org/10.1061/\(ASCE\)1090-0241\(2006\)132:8\(1098\)](http://dx.doi.org/10.1061/(ASCE)1090-0241(2006)132:8(1098)).

- Lin, G., Hajduk, E.L., & Lipka, D.S., & NeSmith, W. (2004). Design, monitoring, and integrity testing of drilled soil displacement piles (DSDP) for a gas-fired power plant. In *Proceedings of the GeoSupport 2004* (Vol. 1, pp. 17-29), Orlando. ASCE. [https://doi.org/10.1061/40713\(2004\)17](https://doi.org/10.1061/40713(2004)17).
- Lima, D.R., & Moura, A.S. (2016). Executive control of root piles from field measurements. *Ciência & Engenharia*, 25(2), 95-104 (in Portuguese).
- Meyerhof, G.G. (1976). Bearing capacity and settlement of pile foundations. *Journal of the Geotechnical Engineering Division*, 91(1), 67-75.
- Moura, A., Lima, R., & Monteiro, F. (2015). A preliminary proposal: executive control of root piles. *The Electronic Journal of Geotechnical Engineering*, 20(26), 12906-12920.
- Monteiro, F.F., Moura, A.S., & Aguiar, M.F.P. (2019). An alternative approach to the executive control of root piles. *Soils and Rocks*, 42(3), 289-299. <http://dx.doi.org/10.28927/SR.423289>.
- Pari, S.A.A., Habibagahi, G., Ghahramani, A., & Fakharian, A. (2019). Improve the design process of pile foundations using construction control techniques. *International Journal of Geotechnical Engineering*, 14(6), 636-646. <http://dx.doi.org/10.1080/19386362.2019.1655622>.
- Russo, G. (2012). Experimental investigations and analysis on different pile load testing procedures. *Acta Geotechnica*, 8(1), 17-31.
- Shariatmadari, N., Eslami, A., & Karimpour-Fard, M. (2008). Bearing capacity of driven piles in sands from SPT-applied to 60 case histories. *Iranian Journal of Science and Technology, Transaction B: Engineering*, 32(2), 125-140.
- van der Veen, C. (1953). The bearing capacity of a pile. In *Proceedings of the 3rd International Conference on Soil Mechanics and Foundation Engineering* (Vol. 2, pp. 84-90), Zurich.

## Effect of steel slag on the mechanical behavior of surficial yellow marl of Tabriz

Hossein Soltani-Jigheh<sup>1#</sup> , Hamed Golmohammadi<sup>2</sup> , Manouchehr Tajrostami<sup>3</sup> 

Article

### Keywords

High plastic fine-grained soil  
Steel slag  
CBR  
Atterberg limits  
Strength  
Freeze-thawing

### Abstract

Fine-grained soils usually have low shear strength and bearing capacity and high swelling potential in the wet state, therefore, they have often to be stabilized by additives. The main objective of this study is to determine the possible effects of ground-granulated blast-furnace slag on the physical and mechanical properties of fine-grained soil. For this purpose, a number of Atterberg, compaction, California bearing ratio (CBR), unconfined compression and freeze-thaw tests were conducted on fine-grained soil. Steel slag (SS) inclusion reduced plasticity index of soil from 44% to 20% when slag content increased from 0% to 55.0%. Moreover, the slag addition improved soil CBR with maximum improvement rate in the sample consists to 55% slag. This increment in CBR was about 140% and 154% for 2.54 mm and 5.08 mm penetration respectively. In addition, slag inclusion raised soil strength with a maximum increment of 132% for clay mixed with 55% slag. Water content and volume changes in freeze-thaw cycles also decreased with increasing percentage of SS, therefore mixtures durability increased.

## 1. Introduction

Soft depositional soils, in general, have very low strength and high compressibility and they may swell and shrink due to wetting and drying phenomenon. In permafrost regions, freeze-thaw phenomenon greatly affects characteristics of these soils. Thus, it is occasionally required to stabilize soft soils via mechanical or chemical techniques. In chemical techniques, additive materials such as lime, cement, etc. were added to soils (Sharma & Sivapullaiah, 2012), which is not reasonable since they release CO<sub>2</sub> into the environment (Sharma & Sivapullaiah, 2012), thus encouraging engineers to find alternatives for these stabilizers.

On the other hand, in the world, annually large volumes of iron used in the steel industry produces waste and garbage of an undesirable type, called steel slag (SS) or industrial waste (Yong-Feng et al., 2020). Several researchers suggested using blast furnace slag for various applications in civil engineering. Some researchers have been focused on compaction, unconfined compressive strength, consolidation, CBR and Atterberg limit properties of soil-slag mixtures (Wild et al., 1996; Manso et al., 2013; Yadu & Tripathi, 2013; Akinwumi, 2014; Goodarzi & Salimi, 2015; Sharma & Sivapullaiah, 2012, 2017; Chandra & Lavanya, 2017; Montenegro-Cooper et al., 2019; Mozejko & Francisca, 2020).

Regarding compaction, SS inclusion increases maximum dry density and decreases optimum moisture of soils and the changes in these parameters are high as the slag amount increases (Yadu & Tripathi, 2013; Akinwumi, 2014; Chandra & Lavanya, 2017; Mozejko & Francisca, 2020).

Liquid and plastic limits of soils decrease by adding SS, and leads to reduce of plasticity index (Wild et al., 1996; Manso et al., 2013; Yadu & Tripathi, 2013; Akinwumi, 2014; Goodarzi & Salimi, 2015; Chandra & Lavanya, 2017).

Consolidation tests demonstrated that swelling pressure and free swelling index of soils reduce due to slag inclusion (Yadu & Tripathi, 2013; Sharma & Sivapullaiah, 2017; Afrasiabian et al., 2021) and their CBR values enhance (Yadu & Tripathi, 2013; Chandra & Lavanya, 2017; Bera et al., 2019). Moreover, adding SS to soils improves their unconfined compressive strength (Wild et al., 1996; Manso et al., 2013; Yadu & Tripathi, 2013; Akinwumi, 2014; Goodarzi & Salimi, 2015; Afrasiabian et al., 2021).

Previous researches revealed a lack of studies on the behavior of steel slag-stabilized soil under freeze-thaw cycles. The main objective of this research is to investigate the effect of SS on the physical properties including volume change, water absorption and durability of fine-grained soils due to freeze-thaw phenomenon. In addition to these tests, CBR

<sup>#</sup>Corresponding author. E-mail address: hsoltani@azaruniv.ac.ir

<sup>1</sup>Azərbaycan Şahid Mədanı Universiteti, Dəniz İnşaatı Departmanı, Tabriz, İran.

<sup>2</sup>Azərbaycan Şahid Mədanı Universiteti, Dəniz İnşaatı Departmanı, Tabriz, İran.

<sup>3</sup>İslami Azad Universiteti, Dəniz İnşaatı Departmanı, Tabriz Şubəsi, Tabriz, İran.

Submitted on May 21, 2021; Final Acceptance on July 21, 2022; Discussion open until November 30, 2022.

<https://doi.org/10.28927/SR.2022.071821>



This is an Open Access article distributed under the terms of the Creative Commons Attribution License, which permits unrestricted use, distribution, and reproduction in any medium, provided the original work is properly cited.

and unconfined compressive strength tests were performed on the soil-slag mixtures.

## 2. Materials and Methods

### 2.1 Materials and sample preparation

A high plastic cohesive soil was retrieved from the north east of Tabriz city in East Azerbaijan province, Iran. At shallow depth, this yellow soil has low strength, bearing capacity and high compressibility, and it is often subjected to periodically freeze-thaw phenomenon. About 93% of soil particles are finer than 0.075 mm, as per ASTM D422 (ASTM, 2007), and its liquid limit and plasticity index are 87% and 43%, respectively. According to Unified Soil Classification System, the soil categorized as CH according to ASTM D2487 (ASTM, 2017).

Steel slag with mean grain particle of 0.24 mm used as a soil stabilizer. Chemical components of SS are  $\text{SiO}_2$  (37.6%),  $\text{Al}_2\text{O}_3$  (13.5%),  $\text{CaO}$  (38.23%),  $\text{MgO}$  (7.63%),  $\text{Fe}_2\text{O}_3$  (0.6%),  $\text{MnO}$  (1.2%) and other (1.34%). Figure 1 presents the grain size distributions of Tabriz soil and steel slag.

The slag was added to clay in a weight percentage of 15%, 25%, 35%, 45% and 55% and the mixtures were named MS15, MS25, MS35, MS45 and MS55, respectively. The specific gravity of the natural soil was 2.41 and the values corresponding to the mixtures were 2.47, 2.53, 2.58, 2.62 and 2.66, respectively (ASTM, 2014). For better moisture absorption, the mixtures were kept in plastic bags for 24 hours in 23 °C and, then, utilized to perform the tests. All samples for CBR, freeze-thaw and unconfined compressive strength (UCS) tests were prepared with 95% of maximum dry density (MDD) and at optimum moisture content (OMC).

### 2.2 Conducted tests

Plasticity characteristics of the samples were determined according to ASTM D4318 (ASTM, 2010) and Standard Proctor

compaction tests were carried out on soil samples following ASTM D698 (ASTM, 2012) to obtain MDD and OMC. CBR of soaked samples was measured according to ASTM D1883 (ASTM, 2016a). Compressibility characteristics were evaluated in oedometer test on samples 75 mm in diameter and 21 mm in height, according to ASTM D2435 (ASTM, 2020). Cylindrical specimens with 50 mm in diameter and 100 mm in height were prepared for UCS tests, according to ASTM D2166/D2166M (ASTM, 2016b). Soil samples were compacted in four layers in a special mould, also scratching the interface of layers in a proper way to prevent the formation of weak planes.

Freeze-thaw tests were conducted on two similar compacted samples with 101.6 mm in diameter and 120.0 mm in height, according to ASTM D560 (ASTM, 2016c). After extraction, samples were placed on water saturated felt pads on the carrier. Both samples were kept in a freezer at a constant temperature of -23 °C for 24 h and, then, moved to a moisture room with the constant temperature of 23 °C for 23 h. Eight freeze-thaw cycles were performed. Some of the samples deteriorated after five cycles. One of the samples was used to determine the volume change and water absorption by measuring its height, diameter and weight. The loss of soil weight during freeze-thaw cycles was measured in the other one.

## 3. Results and Discussions

### 3.1 Consistency characteristics

Liquid Limit (LL), Plastic Limit (PL) and Plasticity Index (PI) values explain that all plasticity parameters decreased with an increase in SS content (Figure 2). Maximum decrease was observed in the mixture with 55% SS, in which LL, PL and PI values reduced from 87%, 43% and 44% to 45%, 25% and 20%, respectively; therefore, slag inclusion decreased these parameters about 42%, 18% and 24%, respectively.

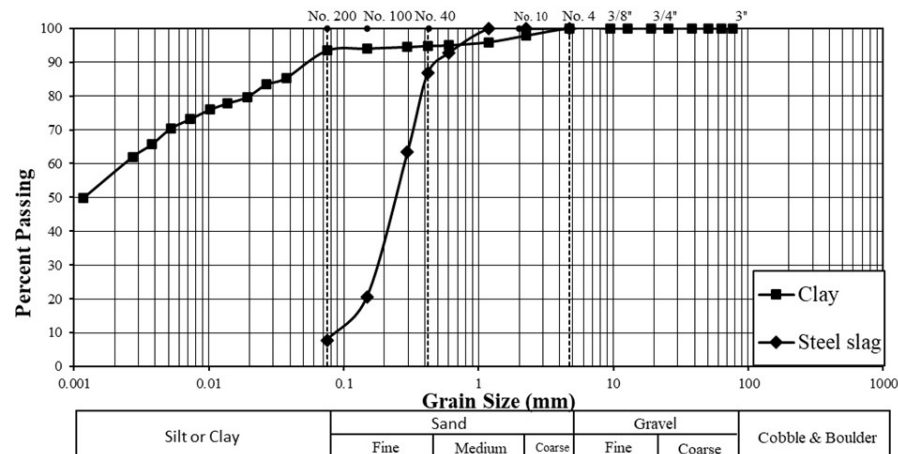
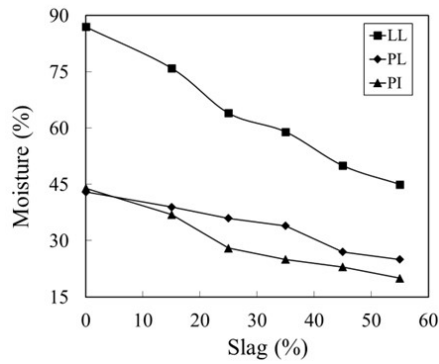


Figure 1. Grain size distributions of Tabriz soil and steel slag.





**Figure 2.** Effect of SS content on the Atterberg limits of the used soil.

In fact, adding SS increased the coarse-grained part of mixture, and in turn reduced the liquid and plastic limits and plasticity index of the soil. A similar trend was observed by Sivrikaya et al. (2014).

### 3.2 Compaction characteristics

Compaction curves of the mixtures revealed that adding SS led to an increase in MDD and a decrease in OMC (Figure 3). Maximum increment and decrement in MDD and OMC values are those of the mixture including 55% slag, which are about 15% and 56%, respectively. The increase in MDD by SS inclusion is mainly due to the higher specific gravity of the slag in comparison to the clay; on the other hand, coarse-grains need less water for compaction. The results reported on slag stabilized clay (Sivrikaya et al., 2014; Mozejko & Francisca, 2020) and on lime-slag treated black clay (Osinubi & Eberemu, 2006) are in agreement with those obtained in this research.

### 3.3 Consolidation test

Void ratio versus effective stress curves illustrate that the mixtures have different initial densities and void ratio at the end of loading step (Figure 4), implying that the samples exhibit different compressibility behaviour. Butterfield (1979) presented a method for interpreting the oedometer test result. So that one can obtain the yielding point from the intersection of two straight lines from curve plotted as  $\ln v$  against  $\log p'$ . In vertical axis  $v$  is specific volume, which equals with  $1 + e$ ; in which  $e$  is void ratio.

The effect of slag was investigated using the intersection point of two lines, according to the method above (Figure 5a). It was observed that increasing slag content higher pressure was required to reach the yield point (Figure 5b). For example, by adding 55% slag the yielding point increased from 68 kPa to 98 kPa.

Both the values of the  $C_c$  and  $C_s$  decrease significantly when the percentage of SS varies from 0 to 55% (Figure 6a).

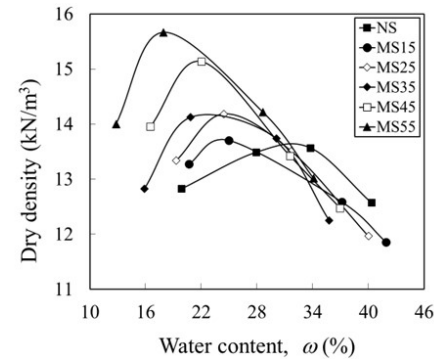


**Figure 3.** Effect of SS additive on the dry density-water content relation of soil.

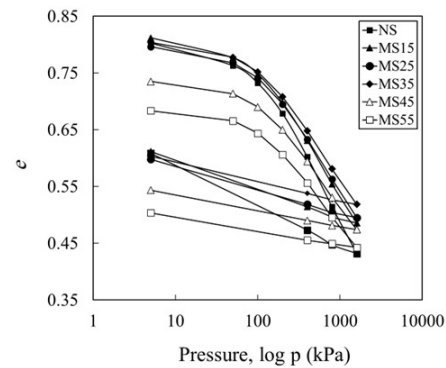


**Figure 4.** Void ratio versus stress curve.

This is due to the partial substitution of clay by the slag, which is less compressible.

Settlement of samples as a function of slag percentage under different stresses are seen in Figure 6b. In general, slag inclusion decreased the soil's compressibility, with the decreasing rate depending on the stress level. For example, at  $p' = 50$  kPa, adding 55% slag reduced the settlement from 0.461 mm to 0.221 mm. Similarly, the values at  $p' = 1600$  kPa reduced from 4.295 mm to 2.952 mm; therefore, 55% slag reduced the settlement about 52% and 31.2%, respectively. Since the slag particles have large stiffness as compared with the clay ones, thus by an increase in the slag content, total stiffness of the sample increased and consequently settlements reduced. Moreover, by raising the slag percentage, the mixture initial void ratio decreased (Figure 4). To explain the effect of slag on the compressibility of mixtures, the inter-granular void ratio ( $e_s$ ), according to Monkul & Önal (2006), was computed using Equation 1:

$$e_s = \frac{e + \frac{G_{s(mix)} \times F_c}{G_{sc} \times 100}}{\frac{G_{s(mix)}}{G_{ss}} \times \left(1 - \frac{F_c}{100}\right)} \quad (1)$$

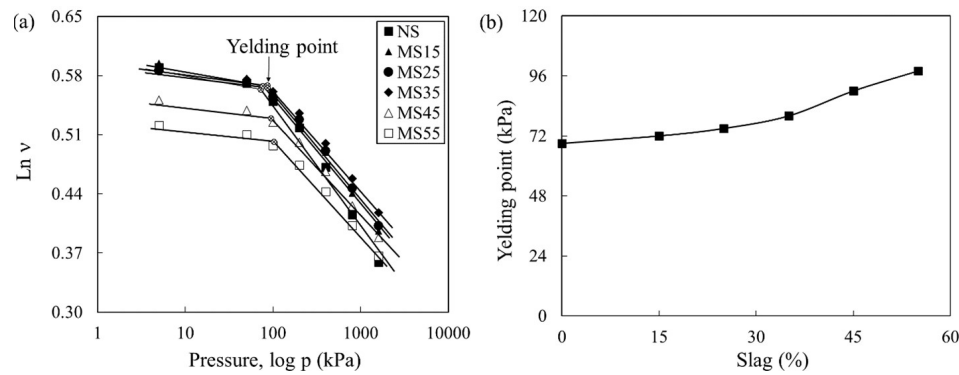


Figure 5. (a)  $\ln v$  versus  $\log p'$  of samples; (b) Consolidation yield stress versus slag content.

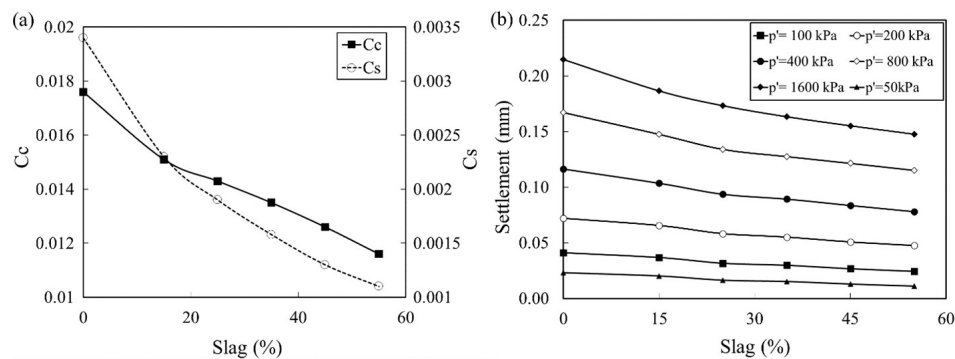


Figure 6. (a) Compression and swelling indices; (b) settlement values; versus slag content.

Figure 7 shows that by increasing the slag content the inter-granular void ratio decreases, which means that the slag grains tend to contact and the applied forces transform by the chain of slag grains, and as a result, the settlement decreased and strength improved.

In addition, due to adding 15% and 25% slag, free swelling of soil reduced about 58% and 92%, respectively, and samples with 35%, 45% and 55% slag did not show any swelling (Figure 8). The slag inclusion also diminished the soil's swelling pressure. For example, adding 15% and 25% of slag reduced the swelling pressure from 19 kPa to 16 kPa and 6.9 kPa, respectively. In the other mixtures, the swelling pressure reduced to zero.

The decrease in compressibility and swelling characteristics of soil with an increase in SS content is due to replacing the clay particles by the SS material. This material has low compressibility and low water absorption, which has been led to mentioned results. These results are consistent with those reported for expansive soils by Rao et al. (2009).

### 3.4 CBR

CBR is one of the most important tests to assess bearing capacity of sub-base and base layers. As shown in Figure 9, applied stress to samples versus penetration

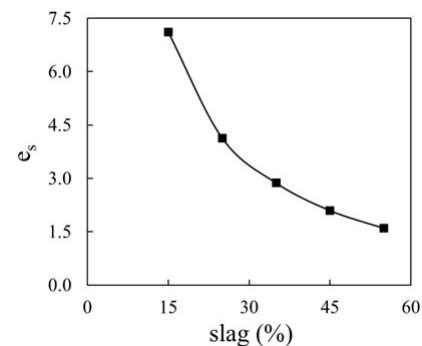


Figure 7. Effect of slag content on the inter-granular void ratio.

values indicate that by increasing slag percentage in the sample, the amount of suffered stress increased. Moreover, CBR values corresponding to penetrations of 2.54 mm and 5.08 mm indicated that slag addition improved the bearing capacity of the soil (Figure 9b). The highest improvement was observed for the mixture consisting of 55% SS, with values of 140% and 154%, respectively, for penetration of 2.54 mm and 5.08 mm. The reason for the CBR enhancement is due to increase in the maximum unit weight of the stabilized specimens and decrease in the void ratio of mixtures, due to

the addition of slag to clay. These results are in agreement with results reported by Laxmikant & Tripathi (2013), which worked on stabilization of soft soil with slag and fly ash, and by Takhelmayum et al. (2013), who researched the soil stabilization using fine and coarse GGBS.

### 3.5 Unconfined compression tests

Stress-strain curves of samples displayed that adding steel slag to the soil improves the strength and changes the behavior pattern of mixtures from ductile to brittle (Figure 10). Therefore, in the MS55 mixture the UCS value increased about 132%. The failure pattern of this sample is

completely brittle as compared to the ductile behavior of plain clay. In general, when the samples are subjected to freeze-thaw phenomenon, their strengths drop off suddenly (Figure 10b). This reduction is relatively low for samples with high slag content. Effect of slag inclusion is obvious in improvement of strength after freeze-thawing phenomenon. For plain clay, by applying one cycle freeze-thaw, the UCS value diminished from 175 kPa to 50 kPa, while for MS55, it reduced from 406 kPa to 194 kPa. The reduction in UCS due to freeze-thaw was 71% and 52% respectively for NS and MS55.

The relationships of UCS, failure strain and secant deformation modulus of specimens with slag content for

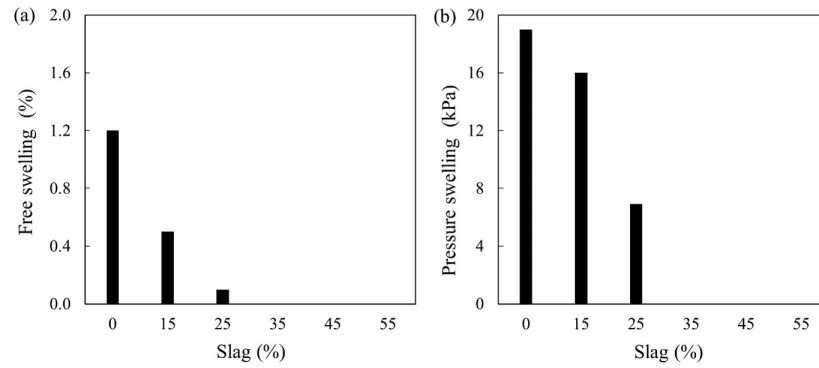


Figure 8. Effect of percentage of SS on: (a) the free swelling; (b) the pressure swelling.

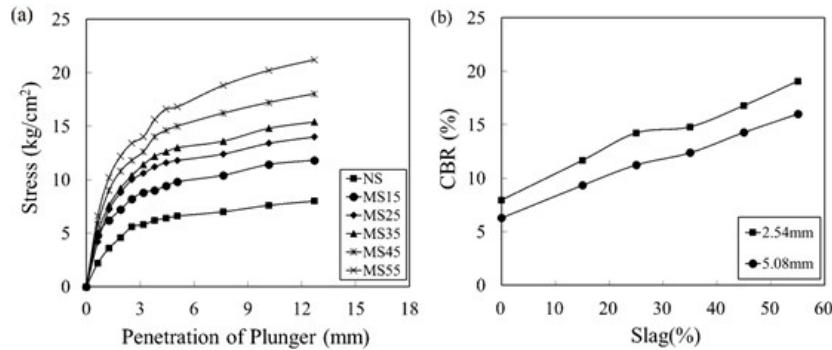


Figure 9. (a) Stress-penetration depth of samples; (b) CBR values versus slag content.

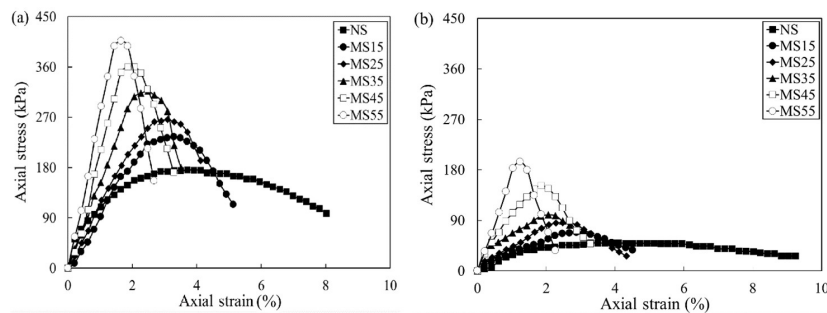


Figure 10. Effect of slag content on the stress-strain behavior of soils: (a) without freezing and thawing cycles; (b) after cycles.

unfrozen and frozen samples are presented in Figure 11. By use of a regression analysis, as listed in Table 1, linear functions suggested for UCS and failure strain parameters and a power function obtained for unconfined compression strength.  $R^2$  shows that these models may use as a useful engineering tool to describe the relationship between geotechnical characteristic in terms of slag percentage for clayey soils.

By adding more slag to clay, like that described for clay-sand mixtures by Soroush & Soltani-Jigheh (2009), the soil structure becomes contact structure; in other word, when the slag content is high the slag particles are in contact together. In fact, as the slag percentage increases, the force applied to the soil mixture is sustained by the slag particles rather than clay particles. Therefore, the improvement in strength may be due to (i) decrease of fine-grained part of soil and increase of slag material with high friction and hardness, (ii) inducing soil cementation by pozzolanic compounds of soil and SS reaction (Yi et al., 2015; Yong-Feng et al., 2020; Mozejko & Francisca, 2020). It should be noted that the source of calcium is calcium hydroxide contributed by the slag.

The secant deformation modulus ( $E_{50}$ ) increased as the slag content increased. This means that the deformation and flexibility of the specimens reduced. For example, by increasing the 55% slag to the soil, the  $E_{50}$  value for unfrozen and frozen samples increased from 7.14 MPa to 27.1 MPa and 2.94 MPa to 16.37 MPa, respectively. Regression analysis provided exponential functions for frozen and unfrozen samples as seen in Table 1.

### 3.6 Freeze-Thaw tests

The freezing-thaw cycle is a weathering process that significantly alters the geotechnical properties of the soil. This phenomenon changes the volume, strength, bearing capacities and microstructure of clays (Eigenbrod, 1996; Czurda & Hohmann, 1997). In this study, the water content of soil samples was measured during the freeze-thaw cycles (Figure 12a). The amount of water absorption during the tests decreased with increasing the amount of SS. Figure 12b shows that the soil samples volume also decreased with increasing number of freeze-thaw cycles. The highest reduction in volume change was obtained in the sample stabilized with 55% SS content. Also it was observed that with increasing slag percentage freezing-thaw cycles has less effect on the volume changes and water absorption of the samples. Since water absorption of slag is less than that of the clay, SS behaves like sand and reduces water content and volume changes of mixtures.

Moreover, the weight loss of soil due to freeze-thaw was determined by weighing the specimen before and after brushing process for each cycle. The samples with a higher amount of slag are more resistant to brushing and lose less weight. Also with increasing slag the weight loss of samples decreases, so that, the weight loss in NS (natural soil) and MS55 is 68% and 26%, respectively. It should be noted that the pure sample and MS15 were destroyed in cycle 4 (Figure 13).

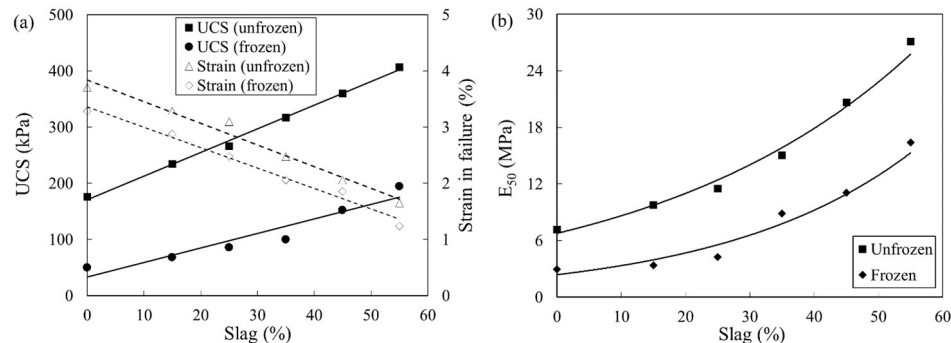
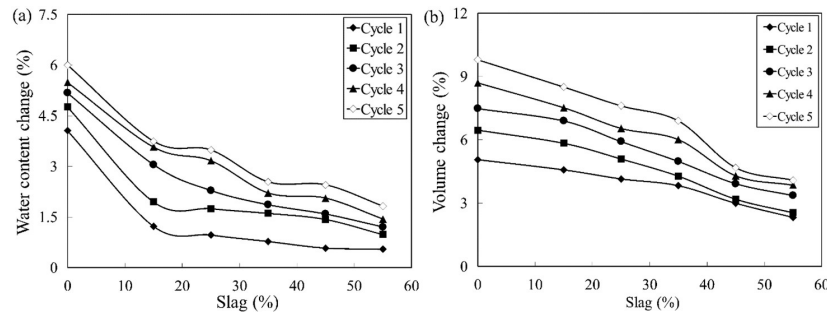


Figure 11. Relationship between slag content and: (a) UCS and failure strain; (b)  $E_{50}$ .

Table 1. Linear regression of UCS and failure strain and  $E_{50}$  with SS content.

Samples	y Parameter	Correlation with SS (%)*	Coefficient $R^2$
Unfrozen	UCS	$y = 4.2088 \text{ SS (\%)} + 170.6$	0.996
	Failure strain	$y = -0.0386 \text{ SS (\%)} + 3.8384$	0.9764
	$E_{50}$	$y = 6.7704e^{0.0243 \text{ SS (\%)}}$	0.9878
Frozen	UCS	$y = 2.5873 \text{ SS (\%)} + 32.942$	0.9093
	Failure strain	$y = -0.0364 \text{ SS (\%)} + 3.362$	0.9843
	$E_{50}$	$y = 2.3881e^{0.0338 \text{ SS (\%)}}$	0.9352

\*SS (%) refers to steel slag percentage.



**Figure 12.** Effect of freeze-thaw cycles on: (a) water content change; (b) volume change.

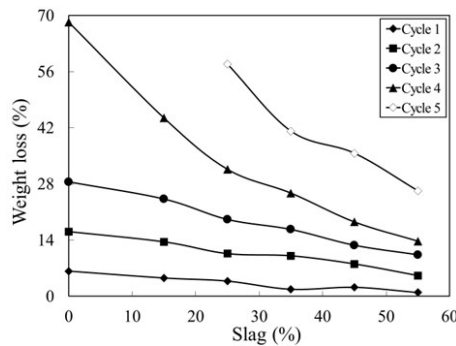


**Figure 13.** Effect of freeze-thaw cycles on soil loss weight of stabilized soil SS.

- The amount of water absorption and volume changes in freeze-thaw cycles decreased with increasing SS content; thus, the mixtures' durability increased;
- Due to slag inclusion, the freeze-thaw induced weight loss of soil decreased, so that this parameter diminished from 68% to 26% by adding 55% slag to the clay.

To avoid accumulation of steel slag in the environment and solving the technical problems of the soil, the use of soil-slag mixture was developed as a way to stabilize the soil. Therefore, the use of slag as soil stabilizing materials to increase bearing capacity and strength as an appropriate method is suggested.

## Declaration of interest

The authors declare that they have no known competing financial interests or personal relationships that could have appeared to influence the work reported in this paper.

## Authors' contributions

Hossein Soltani-Jigheh: data curation, writing – review & editing. Hamed Golmohammadi: writing – original draft preparation. Manouchehr Tajrostami: investigation.

## List of symbols

CBR	California bearing ratio
$C_c$	Compression index
CH	Fat clay
$C_s$	Swell index
$e$	Void ratio
$e_0$	Initial void ratio
$e_s$	inter-granular void ratio
$E_{50}$	Secant deformation modulus
$F_c$	clay content in the mixture
$G_s$	Specific gravity
$G_{s(mix)}$	specific gravities of the mixture
$G_{ss}$	Specific gravity of the clay
$G_{sc}$	Specific gravity of the slag
LL	Liquid limit
PI	Plasticity index
PL	Plastic limit

## 4. Conclusion

In this paper, a comprehensive experimental study conducted to know the stabilizing effect of steel slag on the properties plastic, strength and durability of fine-grained soils and the obtained main results are the following:

- By adding slag content from 0 to 55%, the liquid limit and plasticity index reduced 42% and 24%, respectively. Moreover, the addition of slag increased the MDD and decreased the OMC of the soil;
- In low stresses, the effect of steel slag on the settlement reduction was very high and by increasing of the stress level, its effect diminished. The compressibility and swelling indices of clay decreased by adding 55% slag about 34% and 67%, respectively;
- Adding 15% and 25% slag content, free swelling of soil reduced about 58% and 92%, respectively and clay mixtures with slag amount more than 25% did not show swelling;
- With increasing slag from 0 to 55% in clay, CBR values enhanced;
- The unconfined strength of clay increased from 175 kPa to 406 kPa by adding 55% slag. Under frozen condition, the  $UCS$  values reduced to 50 kPa and 194 kPa, respectively;



## References

- Afrasiabian, A., Salimi, M., Movahedrad, M., & Vakili, A.H. (2021). Assessing the impact of GBFS on mechanical behaviour and microstructure of soft clay. *International Journal of Geotechnical Engineering*, 15(3), 327-337. <http://dx.doi.org/10.1080/19386362.2019.1565393>.
- Akinwumi, I. (2014). Soil modification by the application of SS. *Periodica Polytechnica. Civil Engineering*, 58(4), 371-377. <http://dx.doi.org/10.3311/PPci.7239>.
- ASTM D422. (2007). *Standard Test Method for Particle-Size Analysis of Soils*. ASTM International, West Conshohocken, PA. <https://doi.org/10.1520/D0422-63R07E02>.
- ASTM D4318-10. (2010). *Standard Test Methods for Liquid Limit, Plastic Limit, and Plasticity Index of Soils*. ASTM International, West Conshohocken, PA. <https://doi.org/10.1520/D4318-17E01>.
- ASTM D698. (2012). *Standard Test Methods for Laboratory Compaction Characteristics of Soil Using Standard Effort (12400 ft-lbf/ft<sup>3</sup> (600 kN-m/m<sup>3</sup>))*. ASTM International, West Conshohocken, PA. <https://doi.org/10.1520/D0698-12E02>.
- ASTM D854. (2014). *Standard Test Methods for Specific Gravity of Soil Solids by Water Pycnometer*. ASTM International, West Conshohocken, PA. <https://doi.org/10.1520/D0854-14>.
- ASTM D1883-16. (2016a). *Standard Test Method for California Bearing Ratio (CBR) of Laboratory-Compacted Soils*. ASTM International, West Conshohocken, PA. <https://doi.org/10.1520/D1883-16>.
- ASTM D2166/D2166M-16. (2016b). *Standard Test Method for Unconfined Compressive Strength of Cohesive Soil*. ASTM International, West Conshohocken, PA. [https://doi.org/10.1520/D2166\\_D2166M-16](https://doi.org/10.1520/D2166_D2166M-16).
- ASTM D560/D560M-16. (2016c). *Standard Test Methods for Freezing and Thawing Compacted Soil-Cement Mixtures*. ASTM International, West Conshohocken, PA. [https://doi.org/10.1520/D0560\\_D0560M-16](https://doi.org/10.1520/D0560_D0560M-16).
- ASTM D2487-17. (2017). *Standard Practice for Classification of Soils for Engineering Purposes (Unified Soil Classification System)*. ASTM International, West Conshohocken, PA. <https://doi.org/10.1520/D2487-17E01>.
- ASTM D2435/D2435M-11. (2020). *Standard Test Methods for One-Dimensional Consolidation Properties of Soils Using Incremental Loading*. ASTM International, West Conshohocken, PA. [https://doi.org/10.1520/D2435\\_D2435M-11R20](https://doi.org/10.1520/D2435_D2435M-11R20).
- Bera, A.K., Das, A., & Patra, S. (2019). Influence of granulated blast furnace slag contents on California bearing ratio value of clay GBFS mixture. In *Proceedings of the Ground Improvement Techniques and Geosynthetics* (pp. 277-284). Singapore: Springer. [http://dx.doi.org/10.1007/978-981-13-0559-7\\_31](http://dx.doi.org/10.1007/978-981-13-0559-7_31).
- Butterfield, R. (1979). A natural compression law for soils (an advance on  $e-\log p'$ ). *Geotechnique*, 29(4), 469-480. <http://dx.doi.org/10.1680/geot.1979.29.4.469>.
- Chandra, J.V., & Lavanya, P.M. (2017). Effect of granulated blast furnace slag in the stabilization of expansive soil for the pavement sub-grades. *International Research Journal of Engineering and Technology*, 4(5), 1735-1739.
- Czurda, K.A., & Hohmann, M. (1997). Freezing effect on shear strength of clayey soils. *Applied Clay Science*, 12(1-2), 165-187. [http://dx.doi.org/10.1016/S0169-1317\(97\)00005-7](http://dx.doi.org/10.1016/S0169-1317(97)00005-7).
- Eigenbrod, K.D. (1996). Effects of cyclic freezing and thawing on volume changes and permeabilities of soft fine-grained soils. *Canadian Geotechnical Journal*, 33(4), 529-537. <http://dx.doi.org/10.1139/t96-079-301>.
- Goodarzi, A., & Salimi, M. (2015). Stabilization treatment of a dispersive clayey soil using granulated blast furnace slag and basic oxygen furnace slag. *Applied Clay Science*, 108, 61-69. <http://dx.doi.org/10.1016/j.clay.2015.02.024>.
- Laxmikant, Y., & Tripathi, R. (2013). Stabilization of soft soil with granulated blast furnace slag (GBS) and fly ash (FA). *International Journal of Research in Engineering and Technology*, 2(2), 115-119. <http://dx.doi.org/10.15623/ijret.2013.0202005>.
- Manso, J.M., Ortega-López, V., Polanco, J.A., & Setién, J. (2013). The use of ladle furnace slag in soil stabilization. *Construction & Building Materials*, 40, 126-134. <http://dx.doi.org/10.1016/j.conbuildmat.2012.09.079>.
- Monkul, M.M., & Önal, O. (2006). A visual basic program for analyzing oedometer test results and evaluating intergranular void ratio. *Computers & Geosciences*, 32(5), 696-703. <http://dx.doi.org/10.1016/j.cageo.2005.09.005>.
- Montenegro-Cooper, J.M., Celemin-Matachana, M., Cañizal, J., & González, J.J. (2019). Study of the expansive behavior of ladle furnace slag and its mixture with low quality natural soils. *Construction & Building Materials*, 203, 201-209. <http://dx.doi.org/10.1016/j.conbuildmat.2019.01.040>.
- Mozejko, C.A., & Francisca, F.M. (2020). Enhanced mechanical behavior of compacted clayey silts stabilized by reusing steel slag. *Construction & Building Materials*, 239, 117901. <http://dx.doi.org/10.1016/j.conbuildmat.2019.117901>.
- Osinubi, K.J., & Eberemu, O.A. (2006). Hydraulic conductivity of compacted lateritic soil treated with blast furnace slag. *The Electronic Journal of Geotechnical Engineering*, 11, 1-16. <http://dx.doi.org/10.1504/IJEW.2013.050522>.
- Rao, A.S., Sridevi, G., & Rao, M.R. (2009). Heave studies on expansive clays with stabilized granulated blast furnace slag cushion. In *Proceedings of the Indian Geotechnical Conference 2009* (pp. 109-113). New Delhi: Allied Publishers.
- Sharma, A.K., & Sivapullaiah, P. (2012). Improvement of strength of expansive soil with waste granulated blast furnace slag. In *Proceedings of the GeoCongress* (pp. 15-17). Oakland: ASCE. <http://dx.doi.org/10.1061/9780784412121.402>.

- Sharma, A.K., & Sivapullaiah, P. (2017). Swelling behaviour of expansive soil treated with fly ash–GGBS based binder. *Geomechanics and Geoengineering*, 12(3), 191-200. <http://dx.doi.org/10.1080/17486025.2016.1215548>.
- Sivrikaya, O., Yavascan, S. & Cecen, E. (2014). Effects of ground granulated blastfurnace slag on the index and compaction parameters of clayey soils. *Acta geotechnica Slovenica*, 11(1), 19-27.
- Soroush, A., & Soltani-Jigheh, H. (2009). Pre-and post-cyclic behavior of mixed clayey soils. *Canadian Geotechnical Journal*, 46(2), 115-128. <http://dx.doi.org/10.1139/T08-109>.
- Takhelmayum, G., Savitha, A.L., & Gudi, K. (2013). Experimental studies on soil stabilization using fine and coarse GGBS. *International Journal of Emerging Technology and Advanced Engineering*, 3(3), 919-921. <http://dx.doi.org/10.1007/s12594-018-1019-2>.
- Wild, S., Kinuthia, J., Robinson, R., & Humphreys, I. (1996). Effects of ground granulated blast furnace slag (GGBS) on the strength and swelling properties of lime-stabilized kaolinite in the presence of sulphates. *Clay Minerals*, 31(3), 423-433. <http://dx.doi.org/10.1180/claymin.1996.031.3.12>.
- Yadu, L., & Tripathi, R. (2013). Effects of granulated blast furnace slag in the engineering behaviour of stabilized soft soil. *Procedia Engineering*, 51, 125-131. <http://dx.doi.org/10.1016/j.proeng.2013.01.019>.
- Yi, Y., Li, Ch., & Liu, S. (2015). Alkali-Activated Ground-Granulated Blast Furnace Slag for Stabilization of Marine Soft Clay. *Journal of Materials in Civil Engineering*, 27(4):04014146. [http://dx.doi.org/10.1061/\(ASCE\)MT.1943-5533.0001100](http://dx.doi.org/10.1061/(ASCE)MT.1943-5533.0001100).
- Yong-Feng, D., Tong-Wei, Z., Yu, Z., Qian-Wen, L., & Qiong, W. (2020). Mechanical behaviour and microstructure of SS-based composite and its application for soft clay stabilisation. *European Journal of Environmental and Civil Engineering*, 10(22), 8210. <http://dx.doi.org/10.3390/app10228210>.

## Use of low-cost accelerometers for landslides monitoring: results from a flume experiment

Malena D'Elia Otero<sup>1#</sup> , Ana Elisa Silva de Abreu<sup>1</sup> , Amin Askarinejad<sup>2</sup> ,

Marcela Penha Pereira Guimarães<sup>3</sup> , Eduardo Soares de Macedo<sup>3</sup> ,

Alessandra Cristina Corsi<sup>3</sup> , Rynaldo Zanotele Hemery de Almeida<sup>3</sup> 

Article

### Keywords

Landslides early warning system  
Accelerometer  
Micro-electrical-mechanical-system  
Geotechnical monitoring  
Natural hazards

### Abstract

Early Warning Systems (EWS) are non-structural measures for landslides disaster prevention. They are based on the detection of impending failure signals. The results of a landslide simulation experiment where accelerometers were used to identify pre-failure signals are presented in this paper. Landslide was simulated in a tilting flume filled with sandy soil. During the experiment, the flume was fixed at 30° inclination and water percolated through the soil until it slid. Accelerometers were embedded into the soil and recorded acceleration data from the beginning of the experiment until failure. Acceleration data were analyzed in time domain aiming at estimating translational velocity of the movement. Angular variation was also estimated from acceleration data. The experiment was recorded with a camera and pictures were used for Particle Image Velocimetry (PIV) analysis, in order to validate the estimated translational velocity. Results showed that accelerometers can identify pre-failure signals before any macroscopic movement could indicate impending failure in fast to very fast landslides, showing their potential to be used in EWS. Validation of estimated velocities was not always possible due to PIV setup constraints and the velocity of the mass movement simulated. In fact, the estimated translational velocities seem to be unreliable. On the other hand, the results suggest that acceleration data and angular position variation trend and rate can be incorporated into EWS.

## 1. Introduction

Landslide disaster prevention involves forecasting landslides enough time in advance to allow for actions to be taken towards reducing the possible damages. This prediction can be made in spatial or temporal terms (Intrieri et al., 2019). A spatial prediction relates the distribution of previous and potential landslides with the frequency of those events in the past. One of the most important products of this type of prediction for disaster prevention is the susceptibility maps, developed with computational models, such as SHALSTAB, TRIGRS, among others, as in Melo et al. (2021) and Craig & Augusto Filho (2020).

A temporal prediction is related to time of failure determination methods. For a regional scale prediction, rainfall monitoring is commonly used, as in Bandeira & Coutinho (2015), whereas slope scale prediction focuses on geotechnical instrumentation monitoring. As stated by Intrieri et al. (2019), a traditional and reliable approach for

landslide early warning is to monitor slope displacement and to analyze its derivatives (velocity and acceleration). The most used method to forecast the time of failure was developed by Fukuzono (1985), who defined a linear relationship between the time of failure and the inverse of velocity: failure moment can be inferred when that value approximates to zero. This method has been largely applied as detailed by Intrieri et al. (2019).

Regarding the monitoring issue, Yin et al. (2010), Stähli et al. (2015) and Askarinejad & Springman (2017) emphasized the need of using remote real time, high resolution and automatized sensors, considering failure can happen at high speed and pre-failure signals can be measured only a short time before rupture. Askarinejad et al. (2018) identified previous signals in a real scale landslide simulation experiment 2.5 h before failure happened (accelerating increase of horizontal pressure) and more significantly 23 min before failure for surface displacements and 30 min before for subsurface deformations. Because the precursors detection

<sup>#</sup>Corresponding author. E-mail address: m211338@dac.unicamp.br

<sup>1</sup>Universidade Estadual de Campinas, Geosciences Department, Campinas, SP, Brasil.

<sup>2</sup>Delft University of Technology, Department of Geo-sciences and Engineering, Delft, South Holland, The Netherlands.

<sup>3</sup>Instituto de Pesquisas Tecnológicas, Investigation, Risk, Environmental Management Section, São Paulo, SP, Brasil.

Submitted on December 14, 2021; Final Acceptance on July 13, 2022; Discussion open until November 30, 2022.

<https://doi.org/10.28927/SR.2022.078621>



This is an Open Access article distributed under the terms of the Creative Commons Attribution License, which permits unrestricted use, distribution, and reproduction in any medium, provided the original work is properly cited.

depends on the measurement resolution and the type of the employed sensors, as well as on the triggering mechanism and the material type, it is important to perform experiments in controlled conditions to analyze whether monitoring sensors can identify pre-failure signals with sufficient time for actions to be taken.

In this sense, accelerometers are promising devices for landslide early detection. Technological developments have allowed manufacturing these sensors at lower costs allowing remote monitoring. Previous papers describe the use of accelerometers for landslide precursor detection and characterization purposes, such as Arnhardt et al. (2007), Azzam et al. (2010), De Dios et al. (2009), Segalini & Carini (2013), Ooi et al. (2014), Uchimura et al. (2015), Khoa et al. (2017), Giri et al. (2018), Dikshit & Satyam (2019), Ruzza et al. (2020), Sheikh et al. (2021) and Towhata et al. (2021).

Arnhardt et al. (2007) and Azzam et al. (2010) suggest implementing accelerometers in a rockslide EWS, however, they do not present results from this instrumentation. De Dios et al. (2009) tested in laboratory conditions a column sensor built with triaxial accelerometers buried for slope tilt measurements, similar to those developed by Segalini & Carini (2013). Like Giri et al. (2018), Ooi et al. (2014) monitored soil movements with accelerometers associated with gyroscopes to measure translational and rotational components in landslides simulated in a flume. Giri et al. (2018) also proposed a criterion to establish slow and rapid translational landslides and identify failure types through sensor readings. Khoa et al. (2017) used experimentally triaxial accelerometers to calculate slope angles and classify three types of movement: collision, slide down and rolling down. Ruzza et al. (2020) developed a low-cost pipe for tilt measurements built with an arrangement of triaxial accelerometers, similar to De Dios et al. (2009) and Segalini & Carini (2013). The instrument performance was successfully checked in laboratory experiments.

Literature review suggests that there is no consensus yet on how to employ accelerometers for landslide monitoring. Some works focused on using accelerometers associated with other sensors to characterize landslides qualitatively and to better understand the movement itself, like Ooi et al. (2014), Khoa et al. (2017) and Giri et al. (2018), whereas other authors used accelerometers in a similar fashion as inclinometers (De Dios et al., 2009; Segalini & Carini, 2013; Ruzza et al., 2020). Uchimura et al. (2015) developed an EWS based on tiltmeters, which are, in principle, dampened accelerometers, and tilting variation, mostly being used in Asian countries recently, as in Dikshit & Satyam (2019), Sheikh et al. (2021) and Towhata et al. (2021).

These previous works confirmed that accelerometers are strong instruments for geotechnical monitoring, mainly to monitor changes in slope tilt and to qualify failure types. Since there is no consensus in how to deploy and use accelerometers, it is crucial to validate their use in laboratory conditions before deploying them in real conditions. This

has been accomplished in the research presented here by simulating landslides in a flume, similar to what was done by other researchers with different sensors (Fukuzono, 1985; Ooi et al., 2014; Uchimura et al., 2015; Giri et al., 2018; Franco et al., 2019).

The main objective of this paper is to disclose the results obtained using low-cost biaxial accelerometers to identify pre-failure signals in a landslide simulated in a small-scale tilting flume experiment, where failure was triggered by percolating water into sandy soil, in a 30° slope. The overall performance of the low-cost accelerometers in detecting failure precursors is presented and discussed.

## 2. Experimental setup

### 2.1 Landslide flume

In this research, the results from one landslide simulated using a flume are presented. The glass side of the flume allows soil observation during the experiments. The flume is 1.60 m long, 0.5 m wide and 0.5 m deep and can be tilted up to 45° with a hydraulic jack (Figure 1). Three sections, namely “Upper part”, “Intermediate part” and “Lower part”, are indicated in this figure. Those terms will be used in this paper to explain the position of the sensors during the experiments. However, there are no internal divisions in the flume.

A perforated water hose was deployed at the base of the flume, to allow water percolation at the base of the soil sample. The water hose was covered with geosynthetic in order to minimize internal soil erosion.

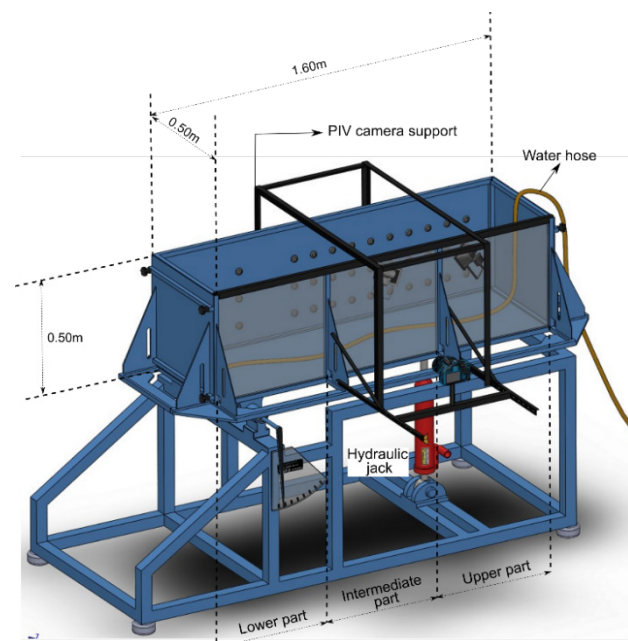


**Figure 1.** Tilting flume used for landslide simulation experiments and its components.

The soil used in this research is a uniform medium sand, with a mean particle diameter of 0.27 mm composed by 96% silica. Soil parameters are:  $D_{10} = 0.16$  mm,  $D_{30} = 0.22$  mm,  $D_{60} = 0.30$  mm,  $e_{max} = 0.92$ ,  $e_{min} = 0.70$ ,  $\gamma_{d,max} = 15.30$  kN/m<sup>3</sup>,  $\gamma_{d,min} = 13.54$  kN/m<sup>3</sup> and  $G = 2.65$ . According to the Unified Soil Classification System (USCS), the soil is classified as poorly graded sand, with uniformity coefficient of 1.90. The internal friction angle of soil is equal to 31° and cohesion is 0 kPa. They were determined using direct shear tests performed with dry soil and normal stresses ranging from 10 to 80 kPa. 30% of total dry soil volume was dyed with black waterproof ink (brand Indian Ink Talens), to enhance particle contrast for PIV analysis.

## 2.2 Landslide simulation experiment

The sample for the landslide simulation experiment was prepared according to the following steps:

1. The flume was filled in horizontal position with 0.3 m height of dry sandy soil, compacted with a wooden hammer in six layers at its maximum dry density;
2. Water supply was switched on to partially saturate the soil. The water supply was switched off when 75% of the soil's height (from bottom to top) was saturated;
3. A slope of 30° was excavated in the lower part of the flume;
4. Camera support was attached to the intermediate part;
5. The lowest door was opened, and the flume was tilted to 30°;
6. Water supply was brought back;
7. Acceleration data and picture acquisitions started simultaneously. This is considered time zero of the experiment ( $t = 0$ ). During the experiment, the lowest

door was kept open, to allow soil to freely move down the flume. The experiment was performed at constant water flow of 4.4 L/min.

## 2.3 Instrumentation

Accelerometers were used for soil monitoring during the experiment. Five micro-electrical-mechanical-system (MEMS) accelerometers (ADXL-321, Analog Devices) were embedded into the soil during the model preparation phase. These accelerometers are biaxial (axes are called in this paper  $u$  and  $v$ ). According to the manufacturer, their main characteristics are: measurement rate of  $\pm 18$  g, bandwidth from 0 to 100 Hz and typical resolution values of 3 mg at 50 Hz. Accelerometers were encapsulated in aluminum alloy square boxes of 2.5 cm width and 1.0 cm height. Data were transmitted through 3 mm diameter flexible cables to a datalogger connected to a computer. Devices were positioned with the  $u$  axis parallel to the main movement direction and  $v$  perpendicular to  $u$  (Figure 2). Five accelerometers were embedded into the soil (numbers 1 to 5) and one accelerometer (number 6) was fixed on the external side of the steel wall. Therefore, accelerometer n. 6 was used as a benchmark of no soil movement.

## 2.4 PIV setup

The camera support is made of steel bars that can be bolted in the intermediate and upper parts and can be removed during sample preparation. Two LED reflectors are attached to the support and the room is darkened during the experiment, in order to keep the light supply constant. The camera used in this research is a Canon EOS Rebel T3i, with 18 MPx resolution, 35 mm of focal length, 1/5 s exposure time and maximum acquisition rate of 1 frame every 5 seconds.

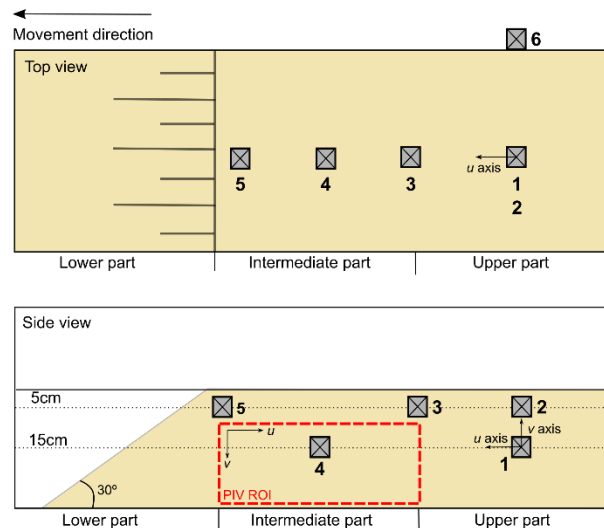


**Figure 2.** Sensors and PIV ROI positions during the experiment.



### 3. Data processing

#### 3.1 Acceleration data processing procedure

Acceleration was measured in two directions and the resultant acceleration was calculated from those values. Analyzing resultant and components separately gives information about how the device moved during the experiment. Two types of movement can be identified by this analysis: in the first type, if the resultant acceleration remains constant with magnitude equals to 1 g, the gravity acceleration on Earth magnitude, it was assumed that no movement or negligible movement happened along the plane defined by accelerometer's  $u$  and  $v$  axes. In this case, although the resultant is constant, concomitant accelerations may happen in both components, indicating that the device had pitched. On the contrary, with decreasing resultant acceleration, it was considered that the device rotated around  $u$  or  $v$  axes, or achieved post-failure high acceleration translational movement. Therefore, focusing on the pre-failure period, it is considered that the device had rolled (rotated around  $u$ ) or yawed (rotated around  $v$ ).

Data were acquired at 4 kHz aiming to identify high frequency impulsive signal, which were supposed to be generated in crack formation, and also low frequency signal related to slow soil movement. First, raw data were analyzed for impulsive acceleration signals identification. After that, two Python routine codes were developed and employed to process accelerometer low frequency signal content and estimate landslide translational velocity from acceleration. The first one corresponds to filtering of acceleration data in time domain and aims to clear possible data outliers and high frequency noise. At this stage, a 4<sup>th</sup> order Butterworth filter was applied, with cutoff frequency of 1 Hz. Processed signals were analyzed for the identification of features that could be indicative of impending failure.

The second routine code was used to calculate the translational velocity from acceleration, by integrating the acceleration over time. Although it may seem like a simple procedure, it is necessary to admit that even when there is no soil movement, acceleration is measured. This acceleration is related to the Earth gravity acceleration projection on each accelerometer axis. Therefore, to calculate velocity, it was necessary to first remove gravity acceleration effects from measured accelerations. Hence, raw data were submitted to two processing steps: one to clear outliers, by using the same Butterworth filter aforementioned (the output of this step was called "filtered data") and another one for gravity offset removal, by applying a 10 s centralized window moving average filter on the "filtered data" (output of this step was called "smoothed data") and subtracting it from filtered data. Finally, the result was integrated to estimate the translational movement velocity.

To employ this translational velocity estimation procedure, it must be assumed that the small amplitude of the accelerometer's initial movement happened approximately

along the plane defined by  $u$  and  $v$  axes. When failure happens, accelerometers can rotate about  $u$  and  $v$  and this assumption is no longer valid.

Angular position over time was also calculated from smoothed data accelerations in  $u$  and  $v$  directions, following Equations 1 and 2:

$$\theta_u = \frac{180 \cdot \arcsin(a_{us})}{\pi} \quad (1)$$

$$\theta_v = \frac{180 \cdot \arccos(a_{vs})}{\pi} \quad (2)$$

where  $\theta_u$  and  $\theta_v$  are estimations of the accelerometer angular position, in degrees, based on smoothed data accelerations  $a_{us}$  (in  $u$  direction) and  $a_{vs}$  (in  $v$  direction). Note that  $\theta_u$  and  $\theta_v$  are equal and correspond exactly to the accelerometer angular position if the plane defined by  $u$  and  $v$  axes is perfectly vertical and the accelerometer is at rest (behaving as an inclinometer).

#### 3.2 PIV data processing procedure

The Particle Image Velocimetry (PIV) is a velocimetry technique developed for experimental fluid mechanics, using double-flash photography of a seeded flow (Adrian, 1991). According to Take (2015), from the late 1990s onwards researchers became aware that this technique was also well-suited for geotechnical engineering applications. Many geotechnical processes such as collapse of shallow foundations or landslides triggering involve granular flow and can, therefore, take advantage of the technique.

Since then, PIV has been widely used in laboratory experiments (Take et al., 2004; Baba & Peth, 2012; Franco et al., 2019) or in field experiments (Akca 2013; Askarinejad et al., 2018). Previous works show that results from PIV technique are similar to those achieved with in situ instruments. Although the values are not exactly the same, good agreement in order of magnitude and rates of change is observed (Askarinejad, 2013; Pei et al., 2019).

In this research, PIV Lab®, a free Matlab tool, developed by Thielicke (2020), was used for PIV analysis. Figure 2 shows the region of interest (ROI) defined to perform the analysis in experiment. Before choosing this ROI, some tests were performed with different ROI sizes. However, the results did not show any significant difference.

### 4. Results

#### 4.1 Soil movement and acceleration results

Figure 3 shows schematically and illustrates with pictures the main experiment events. Landslide happened in a unique event, although a soil block developed during the experiment, but

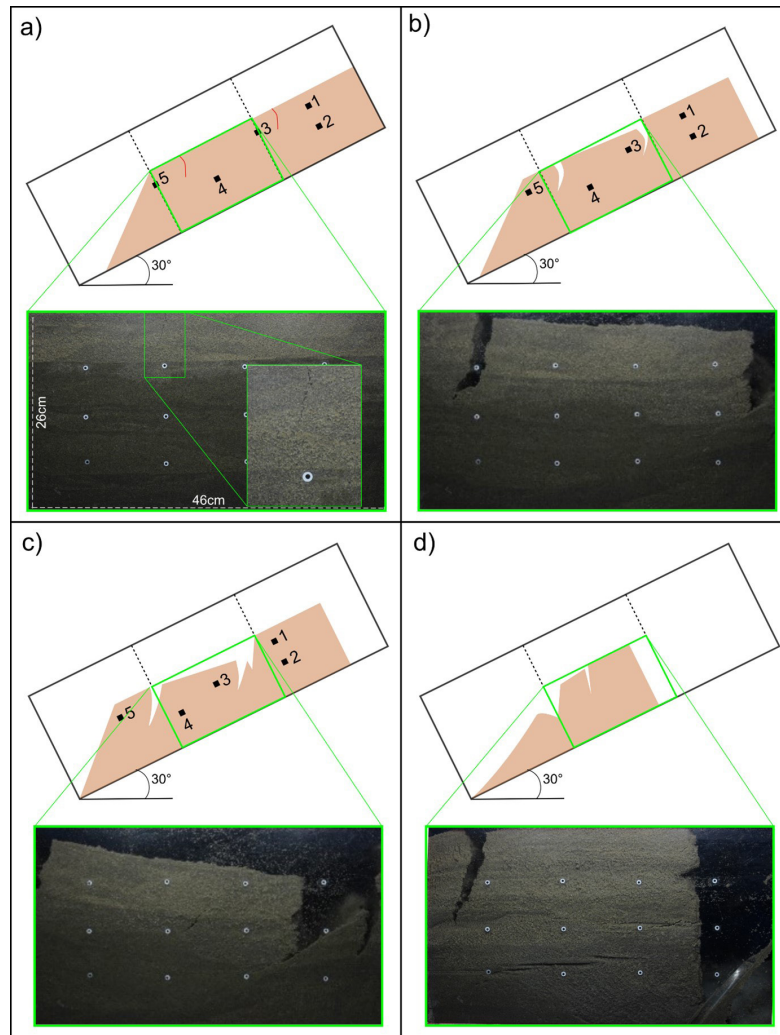
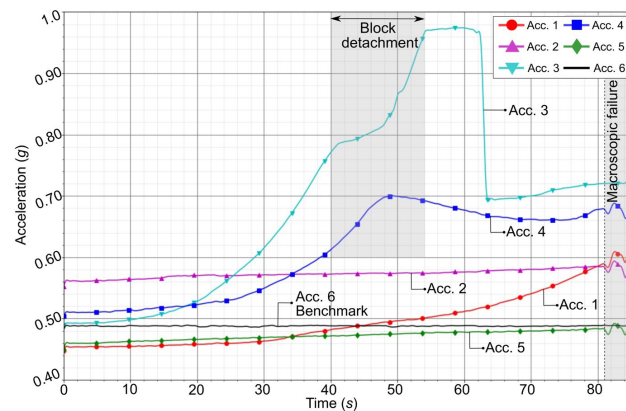


**Figure 3.** Schematic movement evolution during experiment: (a) time = 5 s: cracks started to develop in the intermediate part, defining a block; (b) time = 45 s: block started to move forward; (c) time = 65 s: block stopped moving and remained in the same position until failure; (d) time = 81 s: end of the experiment, all accelerometers fell out of the flume. Pictures were taken in the intermediate part of the flume.

remained in the same position until general failure happened. At 5 s, cracks started to develop in the intermediate part, defining a block (Figure 3a) where accelerometers n. 3 and n. 4 were embedded. From 45 s to 65 s (Figure 3b and Figure 3c), the block moved and remained in that position until failure happened at 81 s (Figure 3d). At the end of the experiment, part of the soil and all accelerometers fell out of the flume.

Figures 4 and 5 show the experiment acceleration results in  $u$  and  $v$  directions respectively and Figure 6 presents the calculated resultant acceleration. Benchmark acceleration is shown in black.

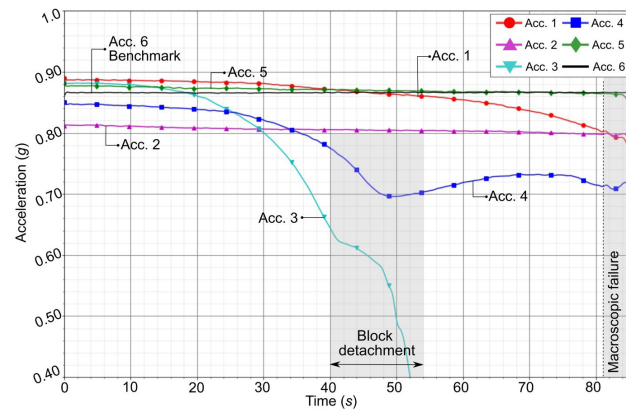
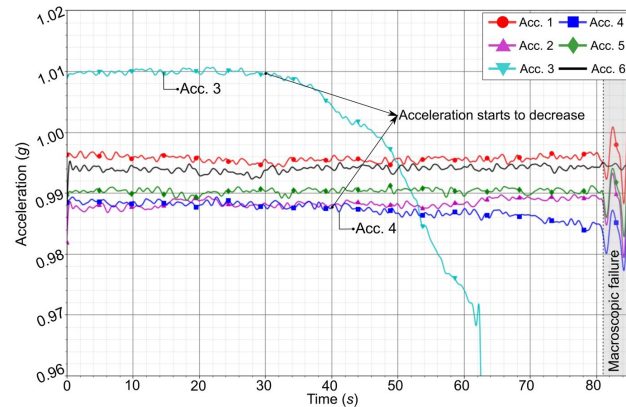
The collected acceleration data were primarily analyzed for the identification of impulsive signal features. Since none of such features could be detected, acceleration results presented in this section focus on low frequency content of those signals. Table 1 summarizes the results achieved with the five accelerometers embedded in the soil.



**Figure 4.** Acceleration results: filtered acceleration component in  $u$  direction for accelerometers n. 1 (red), n. 2 (magenta), n. 3 (cyan), n. 4 (blue), n. 5 (green) and n. 6 (benchmark, black). Block detachment and macroscopic failure are highlighted.

**Table 1.** Summary of acceleration variation and angular responses.

Acc.	Failure or Block detachment time (s)	Acceleration variation start time in component (s)	Difference in time between failure and first signal (s)	Acceleration variation (g)		Angular variation (°)	
				<i>u</i> direction	<i>v</i> direction	<i>u</i> direction	<i>v</i> direction
1	81	5	66	0.130	0.082	9	9
2	81	15	76	0.022	0.014	1.5	1.5
3	45	5	40	0.260	0.290	20	20
4	45	5	40	0.200	0.150	13	13
5	81	5	76	0.025	0.010	1.5	1.5

**Figure 5.** Acceleration results: filtered acceleration component in *v* direction for accelerometers n. 1 (red), n. 2 (magenta), n. 3 (cyan), n. 4 (blue), n. 5 (green) and n. 6 (benchmark, black). Block detachment and macroscopic failure are highlighted.**Figure 6.** Resultant acceleration calculated for accelerometers n. 1 (red), n. 2 (magenta), n. 3 (cyan), n. 4 (blue), n. 5 (green) and n. 6 (benchmark, black). Macroscopic failure is highlighted.

As it can be seen in Figure 4 and Figure 5, all accelerometers experienced acceleration variation in both directions before macroscopic failure happened, in agreement with macroscopic observations. Table 1 shows the time when each device measured acceleration variation and also the magnitude of acceleration variations.

Accelerometers n. 1, n. 2 and n. 5 presented a similar behavior: acceleration started to increase in *u* direction and

decrease in *v* direction until macroscopic failure happened. Accelerometers n. 1 and n. 5 started to identify this behavior at 5 s whilst accelerometer n. 2, at 15 s, indicating that from this time onwards accelerometers started to pitch. Accelerometer n. 1 presented variation at  $10^{-1}$  g, whilst accelerometers n. 2 and n. 5 at  $10^{-2}$  g.

Accelerometers n. 3 and n. 4, located in the intermediate part of the flume, also identified acceleration variation related to block detachment. Both accelerometers started to measure acceleration variation at 5 s, indicating pitching movement, that was more pronounced between 40 s and 55 s, when block detachment happened. Resultant acceleration variation observed in both accelerometers is related to block detachment and indicates rolling or yawing movements because resultant acceleration decreased. After 60 s and before macroscopic failure happened, at 81 s, both accelerometers experienced deceleration, suggesting that deceleration do not necessarily imply in stabilization. Accelerometers n. 3 and n. 4 presented variation at  $10^{-1}$  g.

Resultant accelerations showed in Figure 6 indicate that accelerometers n. 3 and n. 4 experienced rotation (rolling or yawing) from 30 s and 40 s onwards respectively whereas the other accelerometer's resultant acceleration remained constant at 1 g, suggesting that those sensors did not rotate about *u* or *v* directions until failure happened at 81 s.

## 4.2 Translational velocity estimation

PIV analysis was run with PIV Lab® Matlab tool. The tool compares subsequent images from the same ROI and tracks the same pixels in each image to calculate velocity during the time elapsed between those images. The first pair of images that was analyzed are images from 0 s and 5 s. Hence, the result obtained from those images is considered the velocity calculated at  $t = 5$  s. In cases where it is not possible to find the same pixel, velocity vectors are interpolated from surrounding information.

In this research, velocity up to 30 s of the experiment was calculated, as can be seen in Figure 7. From this time onwards analysis was considered unreliable since the quantity of interpolated vectors increased significantly as a result of the low picture acquisition rate. Also, estimated velocity remained constant which is not consistent with the movement observed. Up to 30 s, PIV calculated velocities ranged from  $6.0 \times 10^{-4}$  to



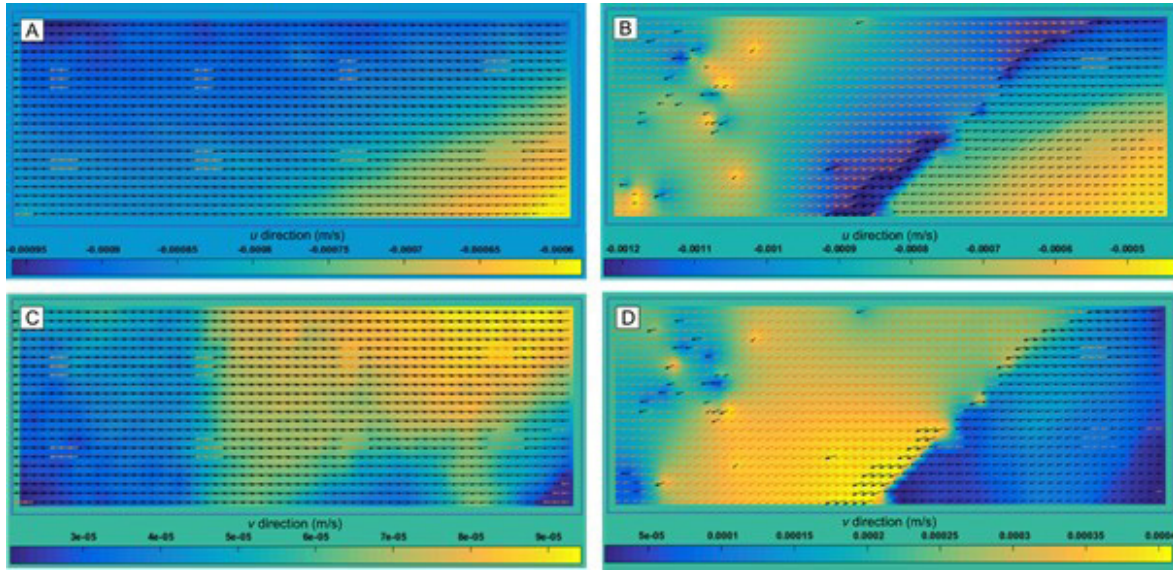


**Figure 7.** PIV Lab graphics output for  $u$  (A and B) and  $v$  directions (C and D). Figures A and C are for  $t=5$  s and B and D for  $t=30$  s.

$1.2 \times 10^{-3}$  m/s in  $u$  direction and from  $3.0 \times 10^{-5}$  to  $4.0 \times 10^{-4}$  m/s in  $v$  direction. This reveals that the simulated landslides were rapid to very rapid according to Hungr et al. (2014).

Unfortunately, translational velocities calculated from accelerometers data resulted in inconsistent results compared to those obtained using the PIV method. Moreover, the benchmark accelerometer remained still during the tests, but the processing procedure estimated velocity fluctuations between 0 and  $10^{-3}$  m/s, although the mean value consistently remained around zero for this sensor. These aspects revealed that the data processing presented in Section 3 did not remove completely the gravity effects on moving accelerometers, probably due to a correlation between translational and rotational movements (and similarity in their frequency content), and to the accelerometer sensitivity to external noise being too high concerning velocity quantification. Nevertheless, the angular position calculation procedure was robust, as presented below.

#### 4.3 Angular position variation in time

Figure 8 shows the angular position variation calculated, which is also presented for each accelerometer in Table 1. Results indicate that angular position started to change before block detachment and general failure happened, showing similar results to those of acceleration trends. Because the magnitude of the angle variation is the same for both axes, only the results of  $u$  direction angle position are presented.

The angular variation results corroborate the results observed with the acceleration variation: the devices measured angular variations that indicate progressive microscopic movements, although at macroscopic scale no remarkable observations could be made for the same time intervals.

Previous works, such as Ooi et al. (2014), Khoa et al. (2017) and Giri et al. (2018), used this angular variation to

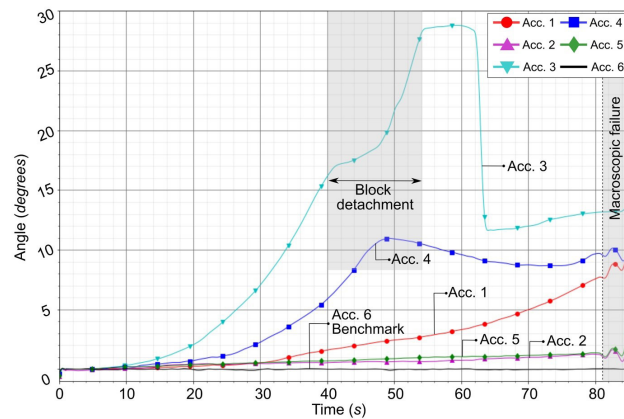


**Figure 8.** Angle variation calculated for accelerometers n. 1 (red), n. 2 (magenta), n. 3 (cyan), n. 4 (blue), n. 5 (green) and n. 6 (benchmark, black). Macroscopic failure and block detachment are highlighted.

qualitatively define the type of soil movement. By analyzing how angular variation occurred, together with other sensors, they indicate if the movement was rotational or translational. However, they did not focus their research on evaluating if the sensors were able to measure variations before rupture happened.

## 5. Discussion

A traditional approach for landslide early warning is to monitor slope deformations and to analyze movement velocity increase, as defined by Fukuzono (1985). Xu et al. (2011) calculated soil velocity and acceleration based on displacement data, proposing a criterion to analyze acceleration increase and establish acceleration threshold values for the development of an EWS.

This research aimed at measuring the acceleration directly, although it was not possible to identify resultant acceleration increase in any sensor during the pre-failure period. As explained in the previous section, velocities calculated from acceleration measurements were not consistent compared to those obtained based on PIV method, indicating that the data processing procedure did not succeed in terms of gravity offset removal. As gravity acceleration is many orders of magnitude higher than the movement acceleration, this could not be quantified. This implies that the proposed measuring and processing method is not capable of indicating an increase in acceleration in the same sense as Xu et al. (2011).

Nevertheless, when analyzing  $u$  and  $v$  components separately, in all cases, acceleration variations can be interpreted as pre-failure signals. Those signals measured in each component are related to small scale movement rather than to the macroscopic failure movement and they imply that the sensors are pitching prior to macroscopic failure. Macroscopically, it is not always possible to observe the whole soil massif moving, however, movement is happening in particle scale and accelerometers were able to capture these movements.

Different acceleration trends observed in each device confirm that, for slope monitoring, it is highly important to work with a sensor network, since different parts of the slope may have different behaviors. The importance of monitoring networks has been demonstrated by Arnhardt et al. (2007), Azzam et al. (2010), Ramesh (2014), Li et al. (2016), Giordan et al. (2019), among others.

Furthermore, it was observed that at particle scale the soil may experience rotation (pitching), even though at macroscopic scale the movement was a translational landslide. This indicates that an Inertial Measurement Unit (IMU) could be used in order to detect both translational and rotational movements. On the other hand, IMU's long-term stability and energy consumption are factors to be considered.

The angular variation observed in the experiment has a progressive growth trend, which predates the landslide and can be interpreted in a similar way as proposed by Fukuzono (1985) for translational velocity. This is in line with the early warning proposal made by Uchimura et al. (2015) and that has been used recently in Asian countries (Dikshit & Satyam, 2019; Xie et al., 2020; Towhata et al., 2021; Sheikh et al., 2021).

## 6. Conclusions

In this research, landslide was simulated in a tilting flume, where movement was triggered by tilting the slope and percolating water into the soil. To monitor soil behavior during the experiment, five low-cost accelerometers were embedded into the soil and images were acquired with an external camera.

By analyzing acceleration data, it became clear that accelerometers measured acceleration variations in each

component that can be interpreted as pre-failure signals which indicate that, at particle scale, pitching happened, although no macroscopic displacement observations were made. In some cases, pre-failure signals were measured more than one minute before failure.

The well-established procedure to estimate time of failure from translational velocity variation in time could not be used in this case, because the procedure to estimate translational velocity from acceleration data did not work properly. This likely happened due to a correlation between rotational and translational movements of the accelerometers, leading to a similarity in their frequency contents that precluded gravity effect removal by the proposed processing procedure based on traditional filtering procedures.

Nevertheless, even using low-cost biaxial accelerometers, it was possible to quantify the angular variation during the experiment. The results suggest that angle variations can be interpreted as pre-failure signals and that landslides EWS could be based directly on acceleration data or on angular position variation trends and rates.

Since no impulsive features were detected and landslide movement happened at very low frequencies, in future research or in field deployments it is not necessary to acquire data at such high rates, as done in this research. Sensor resolution and noise sensibility were also issues concerning velocities quantification. However, improving sensor characteristics implies using more expensive accelerometers and the scope of the research was to test low-cost sensors, economically viable for large area monitoring.

For future works, it is important to test the accelerometers responses in slower movements. It is expected that in field conditions, impending failure signals may be identified earlier than in this research. The use of triaxial sensors is recommended in order to measure yawning and rolling movements.

## Acknowledgements

The research was financed by the São Paulo Research Foundation (FAPESP), processes numbers: 2017/50343-2, 2018/15869-6 and 2019/16458-2. The authors would like to thank FAPESP for the financial support.

## Declaration of interest

The authors have no conflicts of interest to declare. All co-authors have observed and affirmed the contents of the paper and there is no financial interest to report.

## Authors' contributions

Malena D'Elia Otero: data curation, investigation, methodology, visualization, writing - original draft. Ana Elisa Silva de Abreu: conceptualization, supervision, writing



- review & editing. Amin Askarinejad: supervision, writing - review & editing. Marcela Penha Pereira Guimarães: funding acquisition, resources, conceptualization. Eduardo Soares de Macedo: funding acquisition, resources, conceptualization. Alessandra Cristina Corsi: funding acquisition, resources, conceptualization. Rynaldo Zanotele Hemerly de Almeida: data curation, writing - review & editing.

## List of symbols

$D_{10}$	effective grain size
$D_{30}$	sieve size through which 30% (by weight) of the material passes
$D_{60}$	sieve size through which 60% (by weight) of the material passes
$e_{max}$	maximum void index
$e_{min}$	minimum void index
$\gamma_{d,max}$	maximum dry unit weight
$\gamma_{d,min}$	minimum dry unit weight
$G$	density of solids
$u$	accelerometer axis parallel to movement main direction
$v$	accelerometer axis perpendicular to movement main direction
$a_{us}$	smoothed acceleration calculated in $u$ direction
$a_{vs}$	smoothed acceleration calculated in $v$ direction
$\theta_u$	accelerometer angular position estimated in $u$ direction
$\theta_v$	accelerometer angular position estimated in $v$ direction

## References

- Adrian, R.J. (1991). Particle-imaging techniques for experimental fluid-mechanics. *Annual Review of Fluid Mechanics*, 23(1), 261-304. <http://dx.doi.org/10.1146/annurev.fl.23.010191.001401>.
- Akca, D. (2013). Photogrammetric monitoring of an artificially generated shallow landslide. *The Photogrammetric Record*, 28(142), 178-195. <http://dx.doi.org/10.1111/phor.12016>.
- Arnhardt, C., Asch, K., Azzam, R., Bill, R., Fernández-Steeger, T.M., Homfeld, S., Kallash, A., Niemeyer, F., Ritter, H., Toloczyki, M., & Walter, K. (2007). Sensor Based Landslide Early Warning System - SLEWS: development of a geoservice infrastructure as basis for early warning systems for landslides by integration of real-time sensors. In *Early Warning Systems in Earth Management: Kick-Off-Meeting* (pp. 75-88). Technical University Karlsruhe.
- Askarinejad, A., & Springman, S.M. (2017). A novel technique to monitor subsurface movements of landslides. *Canadian Geotechnical Journal*, 55(5), 620-630. <http://dx.doi.org/10.1139/cgj-2016-0338>.
- Askarinejad, A. (2013). *Failure mechanisms in unsaturated silty sand slopes triggered by rainfall* [D.Sc. thesis]. ETH Zurich.
- Askarinejad, A., Akca, D., & Springman, S.M. (2018). Precursors of instability in a natural slope due to rainfall: a full-scale experiment. *Landslides*, 15(9), 1745-1759. <http://dx.doi.org/10.1007/s10346-018-0994-0>.
- Azzam, R., Arnhardt, C., & Fernández-Steeger, T.M. (2010). Monitoring and early warning of slope instabilities and deformations by sensor fusion in self-organized wireless ad-hoc sensor networks. *Journal of Southeast Asian Applied Geology*, 2(3), 163-169.
- Baba, H.O., & Peth, S. (2012). Large scale soil box test to investigate soil deformation and creep movement on slopes by Particle Image Velocimetry (PIV). *Soil & Tillage Research*, 125, 38-43. <http://dx.doi.org/10.1016/j.still.2012.05.021>.
- Bandeira, A.P.N., & Coutinho, R.Q. (2015). Critical rainfall parameters: proposed landslide warning system for the Metropolitan Region of Recife, PE, Brazil. *Soils and Rocks*, 38(1), 27-48. <http://dx.doi.org/10.28927/SR.381027>.
- Craig, A.M.L., & Augusto Filho, O. (2020). Landslide susceptibility mapping of highway slopes, using stability analyses and GIS methods. *Soils and Rocks*, 43(1), 71-84. <http://dx.doi.org/10.28927/SR.431071>.
- De Dios, J.C., Enriquez, J., Victorino, F.G., Mendoza, E.A., Talampas, M.C., & Marciano, J.J. (2009). Design, development and evaluation of a tilt and moisture sensor network for slope monitoring applications. In *TENCON 2009-2009 IEEE Region 10 Conference* (pp. 1-6), Singapore.
- Dikshit, A., & Satyam, N. (2019). Probabilistic rainfall thresholds in Chibo, India: estimation and validation using monitoring system. *Journal of Mountain Science*, 16(4), 870-883. <http://dx.doi.org/10.1007/s11629-018-5189-6>.
- Franco, Y.B., Silva, J.L., & Valentin, C. (2019). A new small-scale test apparatus for modeling buried pipes under axial or lateral soil loading. *Geotechnical Testing Journal*, 43(1), 20180228. <http://dx.doi.org/10.1520/GTJ20180228>.
- Fukuzono, T.A. (1985). A new method for predicting the failure time of a slope. In *Proceedings of the Fourth International Conference and Field Workshop on Landslides* (pp. 145-150). Tokyo: Landslides Society.
- Giordan, D., Wrzesniak, A., & Allasia, P. (2019). The importance of a dedicated monitoring solution and communication strategy for an effective management of a complex active landslides in urbanized areas. *Sustainability*, 11, 946. <http://dx.doi.org/10.3390/su11040946>.
- Giri, P., Ng, K., & Phillips, W. (2018). Laboratory simulation to understand translational soil slides and establish movement criteria using wireless IMU sensors. *Landslides*, 15(12), 2437-2447. <http://dx.doi.org/10.1007/s10346-018-1055-4>.
- Hungr, O., Leroueil, S., & Picarelli, L. (2014). The Varnes classification of landslide types, an update. *Landslides*, 11(2), 167-194. <http://dx.doi.org/10.1007/s10346-013-0436-y>.

- Intrieri, E., Carlà, T., & Gigli, G. (2019). Forecasting the time of failure of landslides at slope-scale: a literature review. *Earth-Science Reviews*, 193, 333-349. <http://dx.doi.org/10.1016/j.earscirev.2019.03.019>.
- Khoa, V.V., Nakano, T., Masanori, H., & Takayama, S. (2017). Detection of landslide disaster by telemetric sensing node network system. In *Proceedings of 11th Asian Control Conference (ASCC)* (pp. 447-452), Gold Coast, QLD, Australia.
- Li, C., Azzam, R., & Fernández-Steege, T.M. (2016). Kalman filters in geotechnical monitoring of ground subsidence using data from MEMS sensors. *Sensors*, 16(7), 1109-1123. <http://dx.doi.org/10.3390/s16071109>.
- Melo, C.R., Guedes, P.A., Amorim, S.F., Alves, F.H.B., & Cirilo, J.A. (2021). Combined analysis of landslide susceptibility and soil water dynamics in a metropolitan area, northeast, Brazil. *Soils and Rocks*, 44(2), e2021051420. <http://dx.doi.org/10.28927/SR.2021.051420>.
- Ooi, G.L., Wang, Y., Tan, P.S., So, C.F., Leung, M.L., Li, X., & Lok, K.H. (2014). An instrumented flume to characterize the initiation features of flow landslides. *Geotechnical Testing Journal*, 37(5), 1-21. <http://dx.doi.org/10.1520/GTJ20130158>.
- Pei, H., Zhang, S., Borana, L., Zhao, Y., & Yin, J. (2019). Slope stability analysis based on real-time displacement measurements. *Measurement*, 131, 686-693. <http://dx.doi.org/10.1016/j.measurement.2018.09.019>.
- Ramesh, M.V. (2014). Design, development, and deployment of a wireless sensor network for detection landslides. *Ad Hoc Networks*, 13, 2-18. <http://dx.doi.org/10.1016/j.adhoc.2012.09.002>.
- Ruzza, G., Guerriero, L., Revellino, P., & Guadagno, F.M. (2020). A multi-module fixed inclinometer for continuous monitoring of landslides: design, development and laboratory testing. *Sensors*, 20(11), 3318. <http://dx.doi.org/10.3390/s20113318>.
- Segalini, A., & Carini, C. (2013). Underground landslide displacement monitoring: a new MEMS based device. In C. Margottini, P. Canuti & K. Sassa (Eds.), *Landslide science and practice* (Vol. 2: Early warning, instrumentation and monitoring, pp. 87-93). Berlin: Springer. [http://dx.doi.org/10.1007/978-3-642-31445-2\\_11](http://dx.doi.org/10.1007/978-3-642-31445-2_11).
- Sheikh, M.R., Nakata, Y., Shitano, M., & Kaneko, M. (2021). Rainfall-induced unstable slope monitoring and early warning through tilt sensors. *Soil and Foundation*, 61(4), 1033-1053. <http://dx.doi.org/10.1016/j.sandf.2021.05.010>.
- Stähli, M., Sättele, M., Huggel, C., McArdell, B.W., Lehmann, P., van Herwijnen, A., Berne, A., Schleiss, M., Ferrari, A., Kos, A., Or, D., & Springman, S.M. (2015). Monitoring and prediction in early warning systems for rapid mass movements. *Natural Hazards and Earth System Sciences*, 15(4), 905-917. <http://dx.doi.org/10.5194/nhess-15-905-2015>.
- Take, W.A. (2015). Thirty-six Canadian Geotechnical Colloquium: advances in visualization of geotechnical processes through digital image correlation. *Canadian Geotechnical Journal*, 52, 1199-1220. <https://doi.org/10.1139/cgj-2014-0080>.
- Take, W.A., Bolton, M.D., Wong, P.C.P., & Yeung, F.J. (2004). Evaluation of landslide triggering mechanisms in model fill slopes. *Landslides*, 1(3), 173-184. <http://dx.doi.org/10.1007/s10346-004-0025-1>.
- Thielicke, W. (2020). *PIVlab: particle image velocimetry (PIV) tool*. Retrieved in December 14, 2021, from <https://www.mathworks.com/matlabcentral/fileexchange/27659-pivlab-particle-image-velocimetry-piv-tool>
- Towhata, I., Goto, S., Goto, S., Akima, T., Tanaka, J., Uchimura, T., Wang, G., Yamaguchi, H., & Aoyama, S. (2021). Mechanism and future risk of slope instability induced by extreme rainfall event in Izu Oshima Island, Japan. *Natural Hazards*, 105(1), 501-530. <http://dx.doi.org/10.1007/s11069-020-04321-0>.
- Uchimura, T., Towhata, I., Wang, L., Nishie, S., Yamaguchi, H., Seko, I., & Qiao, J. (2015). Precaution and early warning surface failure of slopes by using tilt sensors. *Soil and Foundation*, 22(5), 1086-1099. <http://dx.doi.org/10.1016/j.sandf.2015.09.010>.
- Xie, J., Uchimura, T., Wang, G., Shen, Q., Maqsood, Z., Xie, C., Liu, J., Lei, W., Tao, S., Chen, P., Dong, H., Mei, G., & Qiao, S. (2020). A new prediction method for the occurrence of landslides based on the time history of tilting of the slope surface. *Landslides*, 17(2), 301-312. <http://dx.doi.org/10.1007/s10346-019-01283-8>.
- Xu, Q., Yuan, Y., Zeng, Y.P., & Hack, R. (2011). Some new pre-warning criteria for creep slope failure. *Science China. Technological Sciences*, 54(S1), 210-220. <http://dx.doi.org/10.1007/s11431-011-4640-5>.
- Yin, Y., Wang, H., Gao, Y., & Li, X. (2010). Real-time monitoring and early warning of landslides at relocated Wushan Town, the Three Gorges Reservoir, China. *Landslides*, 7(3), 339-349. <http://dx.doi.org/10.1007/s10346-010-0220-1>.

## Methodology for risk management in dams from the event tree and FMEA analysis

Rafaela Baldi Fernandes<sup>1#</sup> , Ana Cristina Castro Fontenla Sieira<sup>1</sup> ,

Armando Prestes Menezes Filho<sup>1</sup> 

Article

### Keywords

Dam  
Failures  
Risk management  
Failure management

### Abstract

Some studies that analyze the risk of dam failures estimate that between 2016 and 2025 about 30 major tragedies should be expected. Failure records between 1900 and 2014 indicate that there is an average of three ruptures every two years, considering only the failures that were officially registered and investigated. It can be said that the potential for dam failures will be driven by the economy, since cost has been the main variable considered in the design, construction, operation, monitoring and closing plan of these structures. As companies reduce investments in maintenance, risk management and failure prevention, there is an incentive for economic recovery, competitiveness of product value and debt reduction, required by investors. The result has been a decrease in specialized labor, to the point that companies no longer have sufficient knowledge about the engineering and operational skills that apply to tailings and water management. Learning from the dams' tragedies is practically non-existent, in Brazil and worldwide, leading to catastrophic environmental and social consequences. Failures will occur as long as they are viewed and treated as unpredictable, thereby lacking risk management. The proposed risk management method, presented in this paper, considers the information of inspection and instrumentation, identifying risks from event trees, separately, intolerable, tolerable and acceptable risks. The intolerable risks are conducted for FMEA-type failure analysis, where severe, intermediate and mild failures are assessed. The objective is to enable the development of an assertive and effective action plan for dam safety management.

## 1. Introduction

The dam rupture scenario has been more frequent than expected worldwide, with an average of two events per year, even if new regulatory and inspection measures are implemented. The main causes are related to the deficiency of geological-geotechnical investigations, hydrological design and management systems, causing deaths, economic loss and, usually, irreversible environmental devastation. In this sense, the regulations on inspections are part of the process and, by themselves, do not constitute a guarantee of safety, being essential the management of routines in operation and maintenance, according to Fernandes (2020).

Dams provide many benefits for society, but the floods resulting from the disruptions produce devastating scenarios, since the extent of flooding is large and places the population downstream in a risk zone. Of an immense number of dams that have failed over the years, according to ICOLD (2001), there are three ruptures that contributed significantly in terms of the number of victims, Vajont in Italy in 1963,

with 2.6 thousand of victims, Johnstown in Pennsylvania in 1889 with 2 thousand and Machhu II in India in 1974 with 2 thousand of victims. Costa (1985) reports that the average number of deaths in dam ruptures is 19 times higher when there is no warning system in place.

A good integrated geotechnical risk management system must consider the involvement of people, with high-performance, qualified and dedicated teams. In relation to the processes used, they need to contain safety management elements, when the operation, maintenance and emergency management routines are established, defining which guidelines to be followed for each emergency level identified in risk situations. In addition, detailed risk management must be based, generally supported by information systems that assist in data control.

The lack of commitment by the company's top management is usually noticeable through the implementation of inadequate management procedures. There is no efficient management without the support of physical and financial resources, and the application of good practices is only achieved if supported

<sup>#</sup>Corresponding author. E-mail address: rafaelacivil@yahoo.com.br

<sup>1</sup>Universidade do Estado do Rio de Janeiro, Departamento de Engenharia Civil, Rio de Janeiro, RJ, Brasil.

Submitted on May 4, 2021; Final Acceptance on July 22, 2022; Discussion open until November 30, 2022

<https://doi.org/10.28927/SR.2022.070221>



This is an Open Access article distributed under the terms of the Creative Commons Attribution License, which permits unrestricted use, distribution, and reproduction in any medium, provided the original work is properly cited.

by the top administrative categories. For the tailings dams, the scenario is expected to be even worse, since the waste constitutes a rejected portion of resources, which does not contemplate direct financial return on the actions linked to its disposal. There is a continuous tendency to reduce costs to a minimum, reducing staff, not conducting research and not investing in monitoring and security. Total quality programs are prioritized for the product and not for the situation of reservoirs and containment structures. However, in the event of disruptions, the costs of damages and reparations, the loss of prestige with society, and the reduction of the company's market value, are much greater than the savings made by neglecting good techniques and practices.

## 2. Risk and failure management

The issues related to the design, construction, operation and maintenance of dams are very specific and depend on variables that must be thoroughly analyzed and evaluated over the life of the structure.

The dangerous condition is a situation with the potential to cause human or environmental damage, and the dangerous event involves a danger and leads to disastrous consequences. The risk, on the other hand, is the combination of the probability of occurrence and the consequence of a dangerous event, being a function of the severity and frequency of a given situation. In other words, according to Whitman (1984) it is the relationship between danger and consequence, being danger defined as the temporal probability of the occurrence of a threat and, consequently, the composition of vulnerability to risk elements, exposure and utility of elements to risk.

Within the risk analysis it is essential to analyze all possible failure modes in order to determine the probability of the occurrence of each scenario. The objective of the risk analysis is to obtain the probability of rupture or failure of the dam, for each failure mode, identifying the most critical paths, that is, the probabilistically most favorable events of occurrence. Companies must give guarantees to society regarding the operation of waste and water deposits, defining tolerable risk limits.

Deterministic analyzes evaluate the nominal case (a scenario), without considering the entire range of plausible results, and do not quantify the probability of the result. Probabilistic analysis, on the other hand, identifies the uncertainties that are fundamental to security and tries to include all plausible scenarios, their probability and their consequences. Generally, this type of uncertainty condition is represented by a normal statistical distribution, and the methods consider a mean, a standard deviation ( $SD$ ) and a coefficient of variation, represented by the ratio of the standard deviation and the mean ( $coV = SD / \text{mean}$ ), as noted in Figure 1 (Lacasse et al., 2019).

According to Londe (1995), the safety margin  $M$ , which is our safety factor ( $FS$ ), is obtained when the resistance load is subtracted and, necessarily, must be

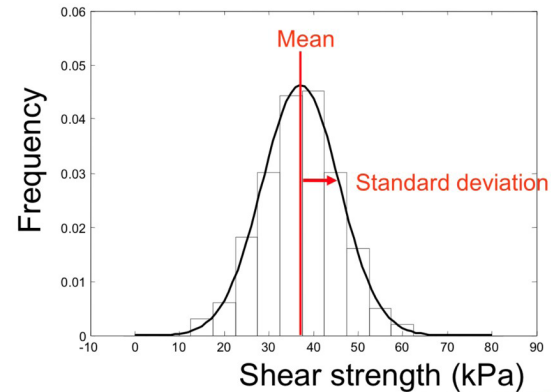


**Figure 1.** Shear tension in the normal distribution. Source: Lacasse et al. (2019).

greater than or equal to zero for a safe condition of project. In Figure 2 the safety margin condition considers the probability of failure ( $P_f$ ), defined as the potential overlap of load and resistance uncertainty distributions, which results in a failure probability. In terms of resistance, the safety factor is the ratio between the resistant and active moments, with values greater than 1.0 representing a greater structural capacity to resist the instabilizing forces, according to their proportionality.

Thus, it is to be expected that, for each situation, given the particularity of each project, there is a safety margin and very different failure probabilities, for small and large uncertainties, as shown in Figure 3.

The legislation of most countries requires the safety factor of a dam to be greater than 1.3 or 1.5. In reality, the safety factor is not the most relevant criterion for ensuring the safety of the dam since it represents a spectrum of probability of failure. A dam with a safety factor of 1.4 may be less vulnerable than one with a safety factor of 1.79, but with a higher level of uncertainty, resulting in a greater probability of failure.

Numerically, a higher safety factor value does not necessarily mean a greater safety margin and the reliability index ( $\beta$ ) must be calculated,  $SD$  being the standard deviation. However, the uncertainties in the parameters that define the safety factor are not an exclusive influence on the final safety of the dam. Other aspects that are not accounted for in the safety factor are the quality of engineering, construction and operation. A good project, careful execution and an operation following international recommendations are factors that directly influence the risk of the dam, in a positive way. In this sense, the reliability index ( $\beta$ ) and the failure probability ( $P_f$ ) can be related, assuming a normal distribution of the failure probability, where the higher the value of  $\beta$ , the lower the probability of failure (Figure 4).

In this way, raising the discussion of uncertainties always leads to a better understanding of what is important for

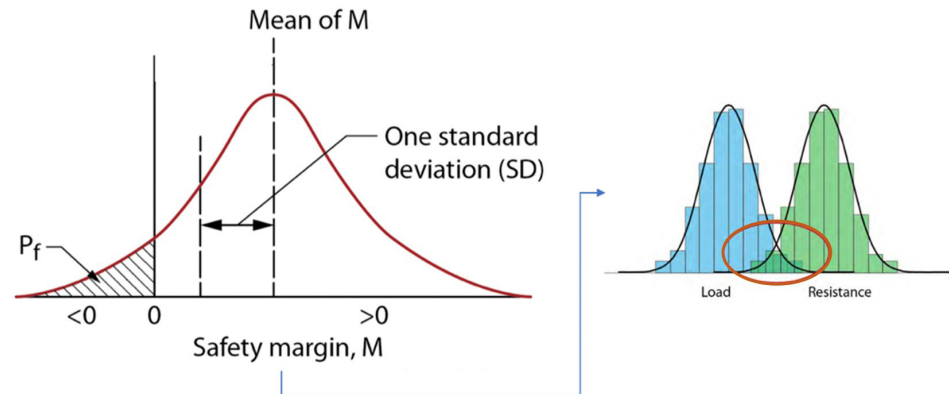


**Figure 2.** Safety margin considering the probability of failure. Source: Londe (1995).

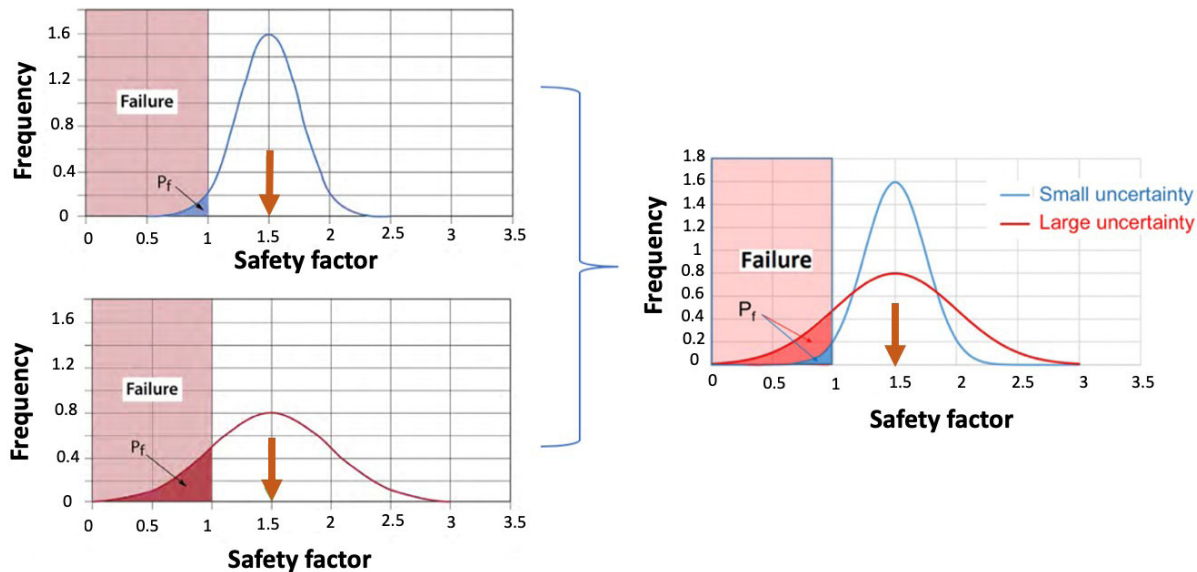


**Figure 3.** Small and large uncertainties in the safety margin. Source: Londe (1995).

the project, safety assessment and performance monitoring, related to the acceptable or not *FS* values. Issues related to what the safety objective should be during the life of a dam, as well as assessments of whether deterministic fixed safety factors are appropriate or not to ensure the same level of safety throughout the life of the dam, should be constantly evaluated. A dam in operation for 50 years represents at least 50 years of experience evaluated under operational and environmental loads and the uncertainties at the time of the design and construction will have changed over time. In this sense, an annual failure probability, based on the performance of the structure and monitoring and inspection data, allows a more consistent comparison of the safety level at different times in the life of a dam than a pre-established and fixed safety factor.

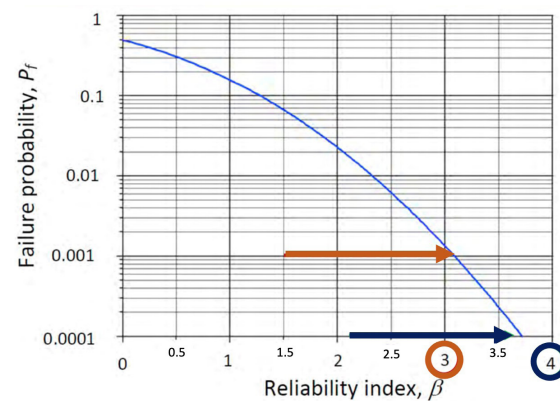


**Figure 4.** Reliability index x Probability of failure. Source: Lacasse et al. (2019).



## 2.1 Risk analysis

Some companies accept risk passively, and others create competitive advantage by exposing them to risks in a prudent and reasoned manner. The definition of risk includes the possibility of loss, damage, disadvantage, negative impact, danger or threat of a specific event. There is no zero risk and all activities involve a certain degree of risk, which must be understood and managed, so that it is minimized to the maximum. The concept of risk has acquired wide social and industrial prominence, constituting an operational concept widely used in engineering and management. According to ABNT (2018), it is associated with an event, being a quantity that results from the combination of the probability and the severity of consequences due to potential failures.

Risk management must be developed in stages, based on the principle of knowing what type of risk is being considered. One step to follow, risk analysis, consider the possibility of identifying the threat and its causes, as well as estimating the risk according to the severity of the damage and the frequency of occurrence. The risk assessment identifies or can be done to reduce the risk situation, followed by the control stage, where the procedures for reduction and mitigation of the event are designed and implemented. Finally, make an analysis of the results obtained, evaluate as previous steps and check if the model is satisfactory. There are several methodologies developed for the elaboration of risk management and the choice is made according to the author's preference.

## 3. Proposed method

Risk assessment, as a whole, is the process in which quantitative or qualitative risk estimation is considered, along with all social, environmental, temporal and other aspects, assessing the consequences of a failure and determining an action plan to mitigate or accept the risk. This analysis must necessarily be performed by specialists in several fields, such as geologists, geotechnical engineers, and hydrologists, hydraulic and structural engineers, among others.

Risk management has been widely used in the industry since the 1960s, according to Kloman (1992), but it was only in the late 1980s that the concept was incorporated into the decision-making process related to dams. However, dam safety management must be very specific, differentiated for each structure, region, country and, mainly, enterprises.

According to Fernandes (2020), the event tree methodology has been very useful for assessing risks in dams as it uses data from field inspection sheets, which are standardized routines and with reasonable frequency. In this way, it can be updated frequently, generating increasingly assertive and directive parameters for the structure being considered, in addition to being orientative for the management issues of dam safety.

The first step is to have a well-defined inspection sheet, with all areas of the structure mapped, as well as an applied list of possible anomalies. Fernandes (2017) presents

a model form, emphasizing that it must be customized according to the particularity of each dam. The perception of possible anomalies associated with the functionality of a structure, and its respective performance, trigger a process of verification of probabilities, determining which decisions or recommendations should be prioritized.

In this item, a new risk analysis methodology is being proposed, based on the event tree model, but totally directed to use in tailings or water dams. Such methodology will be called "proposed method" and basically consists of calculating a probabilistic risk ( $RP$ ), based on events and probabilities resulting from the progression of an anomaly identified in inspection sheets (called inspection probability -  $PI$ ), following a logical and numerical order, depending on the magnitude ( $M$ ), the danger level ( $NP$ ), the anomaly probability ( $PA$ ) and the selected failure mode. In addition, it considers a probabilistic anomaly description (DPR), which allows a better visualization of the associated risks.

For each region of the dam the probable anomalies are listed, which have subsequent coding, as the following example, still being defined, for each one, the magnitude and the level of danger: B – Dam, B.1 – Upstream Slope 1, B.1.1 – Erosions.

Magnitude ( $M$ ) defines a dimension and the evolution of this anomaly, compared to previous inspections and, based on what was verified in the field during use as the basis of the risk analysis. For magnitude, there are the following categories:

- *I*. Insignificant anomaly with no apparent evolution;
- *P*. Small anomaly with evolution over time;
- *M*. Medium anomaly with no apparent evolution;
- *G*. Large anomaly with evident evolution, or large-scale anomaly.

The danger level ( $NP$ ) presents a numerical classification for the anomaly identified, based on the degree of impairment of the stability and safety of the structure, being:

- Normal, anomaly does not compromise dam safety;
- Attention, anomaly does not immediately compromise the safety of the dam, but if it progresses, it can compromise it, and must be controlled, monitored or repaired;
- Alert, anomaly compromises dam safety, and immediate measures must be taken to eliminate it;
- Emergency, anomaly represents a high probability of dam failure.

In this way, at the end of the evaluation, it will be possible to establish a sequence of anomalies, by region, which will present a magnitude and a level of danger, as shown in Table 1. Anomaly probability ( $PA$ ) ranges from 1 to 100%, presented in decimals. Therefore, there will be variations between 0 and 1.0, depending on the magnitude composition and the level of danger presented in the inspection form. It should be noted that the values 0% and 100% can be disregarded because they are extremes and, to guarantee a safety margin in relation to subjectivity when filling out

**Table 1.** Example of list of anomalies, magnitudes and levels of danger by the proposed method.

Code	Local of anomalies	Situation	Magnitude ( <i>M</i> )	Danger level ( <i>NP</i> )
B.1.1	Upstream slope	Erosion	<i>M</i>	1
B.1.4		Incomplete rip-rap, destroyed or displaced	<i>M</i>	1
B.1.6		Trees and huge vegetation	<i>P</i>	1
B.2.5		Sinks and holes	<i>P</i>	1
B.2.12	Downstream slope	Dam overflow	<i>G</i>	1
B.3.5		Protection failure	<i>P</i>	1
B.3.7		Trees and huge vegetation	<i>M</i>	1
B.3.11		Anthills or animal holes	<i>P</i>	1

the inspection form. The ranges must be defined based on the stability analyzes and, according to the potential failures of the structure verified in the history of regular inspections.

As an example, anomaly probability (*PA*) can be defined with a combination of:

- Insignificant magnitude (*I*) with:
  - o Normal *NP* (0) - Probability of 0.10;
  - o Attention *NP* (1) - 0.15;
  - o Alert *NP* (2) -; and
  - o Emergency *NP* (4) - 0.25.
- Small magnitude (*P*) with:
  - o Normal *NP* (0) - Probability of 0.30;
  - o Attention *NP* (1) - 0.40;
  - o Alert *NP* (2) - 0.50; and
  - o Emergency *NP* (4) - 0.55.
- Average magnitude (*M*) with:
  - o Normal *NP* (0) - Probability of 0.60;
  - o Attention *NP* (1) - 0.65;
  - o Alert *NP* (2) - 0.70; and
  - o Emergency *NP* (4) - 0.75.
- Large magnitude (*G*) with:
  - o Normal *NP* (0) - Probability of 0.80;
  - o Attention *NP* (1) - 0.85;
  - o Alert *NP* (2) - 0.90; and
  - o Emergency *NP* (4) - 0.95.

Failure mode (*MF*), also defined as consequence, consists of the last event, subsequent to the progression of the anomaly, which leads the structure to a rupture condition. There are several failure modes that can be considered, such as overtopping, piping, structural problems like instability, liquefaction, deformation, and management issues.

The events are the unfolding of the observations made on the Inspection Sheet, as well as analysis of the photographic report, with the possible and probable sequencing of the anomaly's progression, up to the failure mode considered. The events are successive, that is, event 5, is an offshoot of event 4 which, consequently, is an offshoot of event 3, and so on. The events are defined in sufficient numbers to fully describe the progression of the anomaly to the failure mode. Generally, events are defined as the “nodes” of the tree, and unfold into two branches, or more.

The inspection probability (*PI*) is the product of anomaly probability (*PA*) by the probabilistic percentage attributed to each event. In a general equation:  $PI_n = (PI_{n-1}) \times (PE_{event'n})$ , where “*n*” corresponds to the number of events, and for the first event,  $PI_1 = PA \times PE_{event'1}$ .

The numerical relationship of the probability of occurrence of each event analyzed is based on the photographic report and the observations of the inspection form. The events are complementary, that is, the sum of the branches of each “node” must be 100%. Also, for each event, the sum of the probabilities of all branches is 100%.

If risk analysis is used as a prerequisite for failure analysis, such as FMEA type, according to USACE (2014), it is essential that the final event of the tree consider processes of local and global instability.

Probabilistic risk (*RP*) is the product of anomaly probability (*PA*) by the inspection probability (*PI*) for each event. That is, it is the probability of each branch of the tree. It is interesting to organize them in priority order, that is, from the highest to the lowest probability.

Table 2 shows an example of anomaly probability (*PA*) and failure mode (*MF*) for certain anomalies. Figure 5 shows an example of an event tree for anomaly B.1.1, of erosions in the upstream slope.

After calculating the Probabilistic Risk (*RP*) for each anomaly, the Probabilistic Anomaly Description (*DPR*) is performed, organizing the *RP* of each tree in sequencing, from largest to smallest. The description must be complete, starting with the anomaly and followed by the location where it was found, with the insertion of all events. It is generally easier to describe each block separately, starting with the branch with the fewest events and progressing to the one with the most events, like in Figure 5.

In the end, all the *RP*'s of the trees are compiled and priority sequencing is taken to treat anomalies, based on the probability of failure. This product of the proposed method is risk analysis, that is, the definition of the probabilistic risks of the progressive sequencing of each anomaly, for certain failure modes.

The *RP*'s can be grouped in acceptable and unacceptable zones, as proposed by Brazendale & Bell (1994) and previously presented. In this case, the extremes are defined

LOCALIZATION		ANOMALY	FAILURE MODE (MF)	INSPECTION PROBABILITY (PI)										PROBABILISTIC RISK (RP)	SEQUENCE																																																																																																																																																																																																																																																																																																																																																																																																					
				EVENT 1	PROBAB P11	EVENT 2	PROBAB P12	EVENT 3	PROBAB P13	EVENT 4	PROBAB P14	EVENT 5	PROBAB P15	EVENT 6	PROBAB P16																																																																																																																																																																																																																																																																																																																																																																																																					
Dam (B)	Upstream Slope (B.1)	Erosion (B.1.1)	Anomaly Probability (PA) 0.65			Isolated erosions	0.039	Progressive development of erosions	0.0312	With water	0.0312	Water with sediments	0.00312	Global Instability	0.000156	0.000156	15																																																																																																																																																																																																																																																																																																																																																																																																			
																		0.1	0.065	Multiple erosions	0.026	0.8	0.0312	0.1	0.0312	0.1	0.00156	0.000156	17																																																																																																																																																																																																																																																																																																																																																																																							
																														Superficial erosions	0.2	No progressive development of erosions	0.0208	0.0208	0.0208	0.0208	0.00104	0.00104	11b																																																																																																																																																																																																																																																																																																																																																																													
																																								0.4	No progressive development of erosions	0.2	0.0208	0.1	0.0208	0.0208	0.00104	0.00104	5																																																																																																																																																																																																																																																																																																																																																																			
																																																		0.5	0.0351	0.8	0.2808	0.1	0.2808	0.02808	0.02808	0.001	0.001	9																																																																																																																																																																																																																																																																																																																																																								
																																																													0.585	Deep erosions 0.9	0.2	No progressive development of erosions	0.01872	0.1	0.01872	0.01872	0.001872	0.001872	0.001	0.001	16																																																																																																																																																																																																																																																																																																																																											
																																																																										0.4	No progressive development of erosions	0.8	0.234	0.01872	0.1	0.01872	0.01872	0.01872	0.01872	0.01872	0.01872	0.017	0.017	18																																																																																																																																																																																																																																																																																																																												
																																																																																									0.0047	0.0047	0.0047	0.0047	0.0047	0.0047	0.0047	0.0047	0.0047	0.0047	0.0047	0.0047	0.0047	0.0047	0.0047	0.0047	0.0047	0.0047	0.0047	0.0047	0.0047	0.0047	0.0047	0.0047	0.0047	0.0047	0.0047	0.0047	0.0047	0.0047	0.0047	0.0047	0.0047	0.0047	0.0047	0.0047	0.0047	0.0047	0.0047	0.0047	0.0047	0.0047	0.0047	0.0047	0.0047	0.0047	0.0047	0.0047	0.0047	0.0047	0.0047	0.0047	0.0047	0.0047	0.0047	0.0047	0.0047	0.0047	0.0047	0.0047	0.0047	0.0047	0.0047	0.0047	0.0047	0.0047	0.0047	0.0047	0.0047	0.0047	0.0047	0.0047	0.0047	0.0047	0.0047	0.0047	0.0047	0.0047	0.0047	0.0047	0.0047	0.0047	0.0047	0.0047	0.0047	0.0047	0.0047	0.0047	0.0047	0.0047	0.0047	0.0047	0.0047	0.0047	0.0047	0.0047	0.0047	0.0047	0.0047	0.0047	0.0047	0.0047	0.0047	0.0047	0.0047	0.0047	0.0047	0.0047	0.0047	0.0047	0.0047	0.0047	0.0047	0.0047	0.0047	0.0047	0.0047	0.0047	0.0047	0.0047	0.0047	0.0047	0.0047	0.0047	0.0047	0.0047	0.0047	0.0047	0.0047	0.0047	0.0047	0.0047	0.0047	0.0047	0.0047	0.0047	0.0047	0.0047	0.0047	0.0047	0.0047	0.0047	0.0047	0.0047	0.0047	0.0047	0.0047	0.0047	0.0047	0.0047	0.0047	0.0047	0.0047	0.0047	0.0047	0.0047	0.0047	0.0047	0.0047	0.0047	0.0047	0.0047	0.0047	0.0047	0.0047	0.0047	0.0047	0.0047	0.0047	0.0047	0.0047	0.0047	0.0047	0.0047	0.0047	0.0047	0.0047	0.0047	0.0047	0.0047	0.0047	0.0047	0.0047	0.0047	0.0047	0.0047	0.0047	0.0047	0.0047	0.0047	0.0047	0.0047	0.0047	0.0047	0.0047	0.0047	0.0047	0.0047	0.0047	0.0047	0.0047	0.0047	0.0047	0.0047	0.0047	0.0047	0.0047	0.0047	0.0047	0.0047	0.0047	0.0047	0.0047	0.0047	0.0047	0.0047	0.0047	0.0047	0.0047	0.0047	0.0047	0.0047	0.0047	0.0047	0.0047	0.0047	0.0047	0.0047	0.0047	0.0047	0.0047	0.0047	0.0047	0.0047	0.0047	0.0047	0.0047	0.0047	0.0047	0.0047	0.0047	0.0047	0.0047	0.0047	0.0047	0.0047	0.0047	0.0047	0.0047	0.0047	0.0047	0.0047	0.0047	0.0047	0.0047	0.0047	0.0047	0.0047	0.0047	0.0047	0.0047	0.0047	0.0047	0.0047	0.0047	0.0047	0.0047	0.0047	0.0047	0.0047	0.0047	0.0047	0.0047	0.0047	0.0047	0.0047	0.0047	0.0047	0.0047	0.0047	0.0047	0.0047	0.0047	0.0047	0.0047	0.0047	0.0047	0.0047	0.0047	0.0047	0.0047	0.0047	0.0047	0.0047	0.0047	0.0047	0.0047	0.0047	0.0047	0.0047	0.0047	0.0047	0.0047	0.0047	0.0047	0.0047	0.0047	0.0047	0.0047	0.0047	0.0047	0.0047	0.0047	0.0047	0.0047	0.0047

Figure 5. Anomaly Event Tree B.1.

**Table 2.** Probability example (*PA*) and failure modes (*MF*) for certain anomalies, by the proposed method.

Magnitude ( <i>M</i> )	Danger level ( <i>NP</i> )	Code	Anomaly probability ( <i>PA</i> )	Failure mode ( <i>MF</i> )
<i>I</i>	0	D.3	0.10	Management
<i>P</i>	0	A.8	0.30	Management
<i>P</i>	1	B.1.6	0.40	Structural Problems
<i>P</i>	1	B.3.11	0.40	Structural Problems
<i>P</i>	1	C.1.2	0.40	Overtopping
<i>P</i>	1	C.3.3	0.40	Structural Problems
<i>M</i>	1	A.1	0.65	Structural Problems
<i>M</i>	1	B.1.1	0.65	Piping

as an acceptable risk range, and an unacceptable risk range. In between these two bands, there is the tolerable risk zone. For the proposed method, it is defined that probabilistic risks (*RP*) equal to or greater than 20% represent a great potential for failure and should be considered in a more detailed analysis, as unacceptable risks. Tolerable Risks are those in the range between  $10 \leq RP < 20$  and acceptable risks are those with a value less than 10%.

### 3.1 Failure analysis

The analysis of failure modes of the FMEA type allows anomalies to be assessed from the perspective of the function in the structure where they occur, considering the occurrence, detection and severity. It is an in-depth analysis that allows the identification of the individual failure modes of each anomaly, exploring the consequences of the causes and effects.

The occurrence index (*O*) represents the probability of the occurrence of the anomaly that will result in a failure, that is, the frequency with which these failures can occur per year, ranging from 1 to 10 (Table 3).

The detection index (*D*) considers the possibility of detecting new failure modes before they occur and varies on a scale from 1 to 10 (Table 4). In the case of dams, it is an important index since some failure-triggering mechanisms do not demonstrate clear signs or in time if rupture is avoided. That is why inspections must be carried out by an extremely qualified team, considering the highest evaluation criteria, since the situation involves a high risk and a high potential for damage.

The severity index (*S*) considers the impacts and damage resulting from the failure and also varies on a scale from 1 to 10, with the greater the severity, the greater the associated damage (Table 5). In the context of the word damage, social, environmental and economic impacts are considered, according to Fernandes (2020). According to the FMEA methodology (USACE, 2014), the multiplier interaction between the three indexes occurs with the calculation of the risk potential number (*RPN*), represented in a two-dimensional risk matrix, characteristic of the model.

**Table 3.** Occurrence index (*O*) - Proposed method.

Occurrence index ( <i>O</i> )	Probability of occurrence (events per year)
1	Unlikely ( $\leq 0.01\%$ )
2	Remote ( $> 0.01$ and $\leq 0.1\%$ )
3	Insignificant ( $> 0.1$ and $\leq 1\%$ )
4	Casual ( $> 1$ and $\leq 10\%$ )
5	Frequent ( $> 10$ and $\leq 25\%$ )
6	High ( $> 25$ and $\leq 40\%$ )
7	More high ( $> 40$ and $\leq 60\%$ )
8	Expected ( $> 60$ and $\leq 80\%$ )
9	Likely ( $> 80$ e $\leq 90\%$ )
10	Very likely ( $> 90$ e $\leq 100\%$ )

Source: Fernandes (2020).

**Table 4.** Detection index (*D*) - Proposed method.

Detection index ( <i>D</i> )	Probability of detection
1	Very likely
2	More high
3	High
4	Moderately high
5	Casual
6	Low
7	Very low
8	Remote
9	Very remote
10	Unlikely

Source: Fernandes (2020).

**Table 5.** Severity Index (*S*) – Proposed method.

Severity Index ( <i>S</i> )	Damage and Impacts
1	No damage
2	Isolated damage with slow magnitude
3	Short-term reversible individual damage
4	Long-term reversible individual damage
5	Isolated damage with huge magnitude
6	Short-term reversible collective damage
7	Long-term reversible collective damage
8	Collective damage with huge magnitude
9	Irreversible individual damage
10	Irreversible collective damage

Source: Fernandes (2020).

The uncertainties of the geotechnical behavior of soils, mainly under the action of static and dynamic loads, signal the importance of a probabilistic analysis for an adequate assessment of the stability of the structures. In this way, risk analysis consists of verifying different components of a system, which interact, and the resulting scenarios can be more or less critical. It also allows for the definition and recognition of risks, resulting in a more effective and integrated action plan.

For each system and subsystem that has been assigned a code for the inspection sheet, a function, failure, final effect, cause, control and control type must be established, in addition to the *RPN* calculation.

For the function item, it is desirable to contain transitive verbs that, having incomplete meaning, need a verbal complement to complete their meaning, that is, they need a direct or indirect object. Some examples of transitive verb linked to the object are contained, retain, provide, drain, promote, among others. In this item, something that is related to the anomaly considered for the item is added.

For the failure item, the failure mode is associated in case the system is prevented from exercising the defined function and, generally, it is the direct negation of the function item. If the failure analysis is being used as a next step to the risk analysis by the proposed method, the failure modes defined for the anomaly probability (*PA*), associated with the anomaly considered for the item, can also be used.

The final effect is the consequence of the failure and is the item that must be evaluated together with the severity index (*S*). If the failure analysis is being used as a next step to a risk analysis, the final effect refers to the progressive unfolding of the anomaly, that is, the last event considered, which generally indicates a global or local instability. Each final effect must contain a numerical indicator of severity (*S*).

The cause must be assessed on two scales. On the micro scale, it is usually associated with an anomaly and, in this case, the anomalies listed in the risk analyzes can be used. The progression of anomalies leads to a macro-scale assessment, and generally refers to issues related to the inadequacy of designs, inefficient construction techniques or problems with maintenance of the structure. Each cause must contain a numeric indication of occurrence (*O*). If the failure analysis is being used as a step following a risk analysis, the probability of occurrence is interpreted according to the probabilistic risk (*RP*) of the risk analysis.

In the FMEA matrix of the proposed method, the mild failures are those contemplated in the green portions of the matrix, with the Intermediates in the region in blue and the severe in the orange and red portions. The definition of colors by the proposed method considered that:

- Collective damages are related to severe failures, therefore, severity index  $\geq 6$ ;
- Individual damages are related to intermediate failures, therefore,  $6 > \text{severity index} \geq 3$ ;

- Isolated or undamaged damages are related to mild failures, therefore, severity index  $< 3$ ;
- Occurrence index  $\geq 6$  (high to very likely) combined with severity index  $\geq 9$  are zones of severe failures;
- Occurrence index  $\geq 7$  (high to very likely) combined with severity index  $\geq 9$  are zones of severe failures. The same is true for occurrence index = 6 (high) and severity index 10;
- The definition considered the great impact of the damages and the high probability of the events occurring in the year;
- The demarcation of the other severe, intermediate and mild zones follows the proportion of the severity of each failure when combined with the occurrence of the events.

The action plan established for the control of each cause can be broken down into as many activities as necessary in order to control what is causing a particular failure. In this case, they are listed as control and, generally, measures are established for the adequacy and revision of the project, visual inspections, verification of instrumentation levels, stability analyzes or more particular actions. Control type is generally defined as prevention and detection. Prevention refers to measures that require planning to occur and the involvement of a multidisciplinary team for this action, such as, for example, project adjustments. Detection, on the other hand, refers to activities that must be carried out directly in the structure and that do not require major interventions to be carried out, being, in general, the routine activities already established such as inspection and monitoring. It is desirable that for each cause, at least two controls are established and, consequently, two types of control, one for prevention and the other for detection. Each prevention x detection pair must contain a numeric detection index (*D*).

*RPN* is the multiplication of severity (*S*), occurrence (*O*), detection (*D*) indexes. Table 6 presents an example of FMEA analysis for dam, upstream slope and crest, with the respective indexes and *RPN* calculation, applying the index values established in the proposed method. The FMEA matrix considers the values of severity and occurrence and, for the case of Table 6, Figure 6 has the graphical representation. For this case, item "B = Dam" requires greater attention, as it is in a more critical area. However, in terms of *RPN*, the calculated values B.2.a are higher, but due to the low occurrence, they are in a less critical zone, which still requires attention.

According to the *RPN* ranges obtained in each analysis, a segmentation of the *RPN* should be proposed, at least, in three ranges, such as acceptable risk, tolerable risk and intolerable risk. The higher the *RPN* value, the lower the tolerance for a given event, that is, the greater the assertiveness in the response must be, and immediate measures must be implemented.

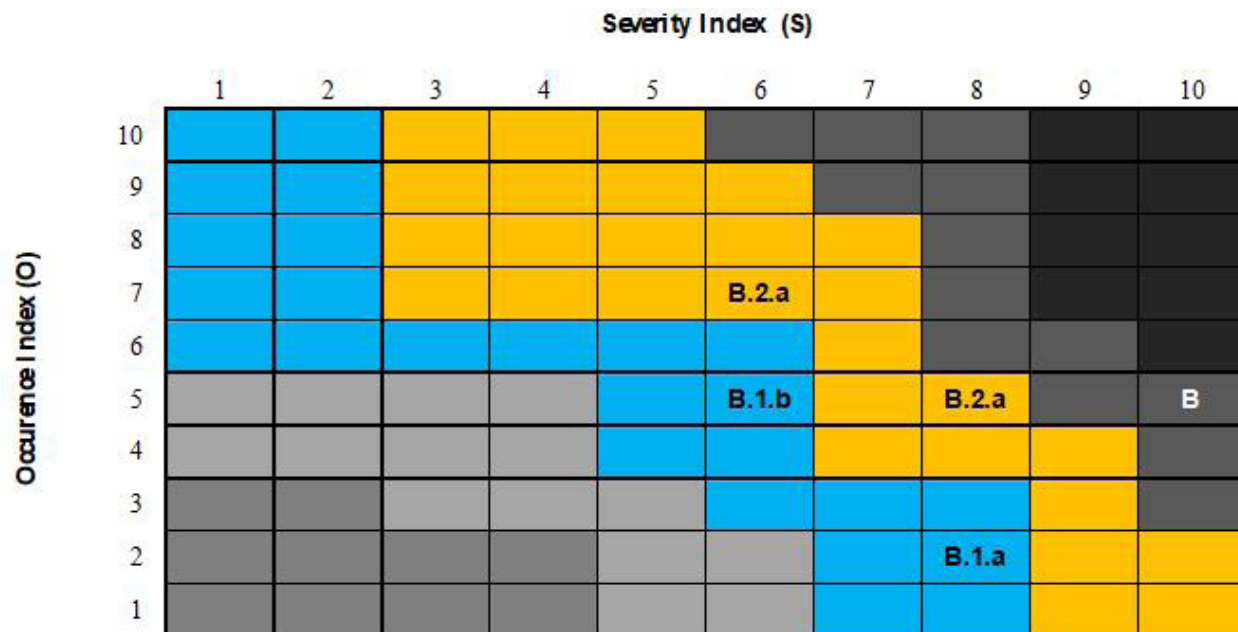
In defining the action plan, a priority order of actions based on the *RPN* could be developed, for example, as follows:

- Priority 0 – B and B.2.a;



**Table 6.** Example of FMEA analysis for dam, slope and crest.

Structure	DPR	Function	Failure	Final effect	(S)	Cause	(O)	Control	Type of control	(D)	RPN
B. Dam		a.Retain water	Insufficient capacity to contain water	Global instability	10	Inadequacy of design and / or construction and / or maintenance	4	Project suitability Visual inspection and instrumentation	Prevention Detection	3	120
B.1 Upstream Slope	Presence of ant, constructions and small burrows in the upstream slope, shallow and to a great extent	9.Retain tailings	Structural instability due to animals	Local instability	3	Ants and animals	3	Adequacy of geometry and constituent materials Visual inspection	Prevention Detection	1	9
		No development of surface erosions in the rip-rap of the upstream slope	4a.Give stability	Structural instability due to erosions	3	Superficial Erosion	3	Adequacy of geometry and constituent materials Visual inspection and instrumentation	Prevention Detection	1	9
B.2 Crest	Small damage at the crest with formation of percolation paths, without water accumulation	3.Retain water	Overtopping (free board)	Global instability	4	Coverage and / or protection failures	3	Adequacy of geometry and constituent materials Visual inspection	Prevention Detection	3	36
	Small damage at the crest with formation of percolation paths, without water accumulation	4. Retain water	Overtopping (free board)	Global instability	4	Coverage and / or protection failures	3	Adequacy of geometry and constituent materials Visual inspection	Prevention Detection	3	36

**Figure 6.** FMEA matrix for the example of dams.

- Priority 1 - B.2.b;
- Priority 2 - B.1.a and B.1.b.

#### 4. Application of the proposed method

In this item, three dams will be evaluated in the light of the methodology described, defined as the proposed method. The identification of the dams, as well as the photographic report of the structures has been deleted to protect the data companies that own the structures, given that there is no authorization for detailed disclosure of the dams. This omission does not compromise the study, since what is discussed and presented is the application of the method based on the inspection form and identification of anomalies.

Dam A is a soil embankment structure with a homogeneous section, 6 m high and 200 m length at the top, built to accumulate water from a food industry, with construction works completed in 1995. Dam B is a concrete structure, with a maximum height of 10 m, 130 m long and a spillway (millenary *TR*), with water accumulation for the purpose of generating electricity, built in 1930. Dam C is a soil embankment dam, with a homogeneous section, 14 m high and 800 m long, built to accumulate residues from a gold mining. The spillway was expanded in 2009 to and the dam was built in 1982.

The inspection of the three structures was carried out between the period of November 2019. The application of the method will be done in stages so that its effectiveness is individually assessed, in the topics described below:

- Dam inspection form that allows identifying anomalies as well as determining the magnitude (*M*) and danger level (*NP*). An example was provided in Fernandes (2017);
- For anomalies identified as first time (*PV*), disappeared (*DS*), decreased (*DI*), remained constant (*PC*) and increased (*AU*), values of *M* and *NP* must be assigned. Categories of *M* and *NP* was described in section 3 of this report with a summary model on Table 1);

- Define the anomaly probability (*PA*) according to intervals defined in section 3, after example on Table 1;
- Define the failure mode (*MF*);
- List the anomalies in sequence of less magnitude (*M*) and danger level (*NP*) for the highest indices, inserting the anomaly probability (*PA*) and failure mode (According example in Table 2);
- Design of the event trees considering the probability of the anomaly (*PA*) to compromise the structure stability (an example was provided in Figure 5);
- Probabilistic risk management (*RP*) of anomalies, like described in the end of general section 3. Definition of acceptable, tolerable and unacceptable risk zones;
- Failure analysis for the unacceptable risks define index like described on Table 3 to 5 on section 3.1. Establish the RPN as the example on Table 6;
- Definition of severe, intermediate and mild failures on a matrix like the one shown on Figure 6. Define the action plan.

In the case of Dam B, for example, 14 anomalies were identified during the field inspection, as shown in Table 7. There is no critical anomaly, that is, a hazard level equal to or greater than 2 (Alert or emergency, as they require an intervention immediate repair). Table 8 shows the ordering of anomalies and the definition of anomaly probability and failure mode.

For the anomalies of Dam B, 150 probabilistic risk Scenarios were identified according to the event tree analysis for proposed method, like the example at Figure 7 and Table 9. For all these scenarios, 6 of which were considered unacceptable, as shown in Table 10. These were directed to the failure analysis of the FMEA type which identified 4 intermediate and 2 mild failures as demonstrated in Table 11 and Figure 8.

A summary of all risk and failure analysis with the application of the proposed method is presented in the Table 12, considering the three dams.

**Table 7.** Dam B anomalies.

Code	Local of anomalies	Situation	Magnitude ( <i>M</i> )	Danger level ( <i>NP</i> )
A.3	Operational infrastructure	Lack of staff training	<i>G</i>	1
A.7		Lack or deficiency of protective fences	<i>P</i>	1
B.1.7	Upstream slope	Erosion	<i>P</i>	1
B.4.1	Downstream area	Irregular constructions	<i>M</i>	1
B.4.3		Erosion	<i>P</i>	1
D.1		Damaged or missing instruments	<i>P</i>	1
D.2	Reservoir	Constructions in protection areas	<i>P</i>	1
D.3		Pollution by sewage, garbage or pesticides	<i>P</i>	1
D.4		Evidence of poor water quality	<i>P</i>	1
D.5		Erosion	<i>P</i>	1
D.7		Collapsing margins	<i>P</i>	1
E.1.6		Grid problems	<i>P</i>	1
E.2.6		Lack of open indicator	<i>P</i>	1
E.4.6	Structure	Deterioration of the railing	<i>P</i>	1

**Table 8.** Dam B anomaly probability and failure mode.

Magnitude ( <i>M</i> )	Danger level ( <i>NP</i> )	Code	Anomaly probability ( <i>PA</i> )	Failure mode ( <i>MF</i> )
<i>P</i>	1	A.7	0.40	Management
<i>P</i>	1	B.1.7	0.40	Structural problems
<i>P</i>	1	B.4.3	0.40	Structural problems
<i>P</i>	1	D.1	0.40	Overtopping
<i>P</i>	1	D.2	0.40	Management
<i>P</i>	1	D.3	0.40	Management
<i>P</i>	1	D.4	0.40	Management
<i>P</i>	1	D.5	0.40	Structural problems
<i>P</i>	1	D.7	0.40	Structural problems
<i>P</i>	1	E.1.6	0.40	Structural problems
<i>P</i>	1	E.2.6	0.40	Structural problems
<i>P</i>	1	E.4.6	0.40	Management
<i>M</i>	1	B.4.1	0.65	Structural problems
<i>G</i>	1	A.3	0.85	Management

**Table 9.** Probabilistic anomaly description for anomaly A.3 for Dam B.

Sequ.	<i>RP</i>	Code	Probabilistic anomaly description ( <i>DPR</i> )
1	0	A.3	Global stability of the structure compromised by the inefficiency of inspections and treatment of readings due to the team not having adequate emergency training
2	0	A.3	Performs regular inspections, with staff without adequate training for emergency
3	0	A.3	Inefficiency of inspections due to the team not having adequate emergency training, with monitoring of instrumentation data
4	0	A.3	Team has emergency training
5	0	A.3	Local stability of the structure compromised by the inefficiency of inspections and treatment of readings due to the team not having adequate emergency training

**Table 10.** Dam B ordering of unacceptable risks.

Code	Anomaly	Probabilistic Anomaly Description ( <i>DPR</i> )	Percentage
B.4.1	Downstream area	Irregular constructions in the downstream region, with no flow obstructions	58.50%
A.3	Operational infrastructure	Operational Infrastructure Global stability of the structure compromised by the inefficiency of inspections and treatment of readings due to the team not having adequate emergency training	28.92%
D.4	Reservoir	Poor water quality in the reservoir, without recreational use	24.00%
A.3	Operational infrastructure	Performs regular inspections, with staff without adequate training for emergency	22.95%
A.3	Operational infrastructure	Inefficiency of inspections due to the team not having adequate emergency training, with monitoring of instrumentation data.	21.42%
B.1.7	Upstream slope	Progressive development of erosions in the upstream slope, without the presence of water, in isolated deep erosion or in the protection	20.74%

- For the case of dam A:
  - o Inspection: 50 anomalies, 35 of which are critical but without understanding what the probability of their progression will generate a failure mode.
  - o Risk analysis: breakdown of 50 anomalies into 749 failure scenarios due to local or global instability, for a given failure mode. Of this total, 45 are prioritized as unacceptable risks, that is, they must be immediately mitigated.
- Failure analysis: out of the 45 unacceptable risks, none are subject to severe failures, and the 33 intermediaries must be prioritized over the 12 mild ones.
- For the case of dam B:
  - o Inspection: 14 anomalies, with no criticism but without understanding what the probability of its progression will generate a failure mode.

**Table 11.** Failure analysis for the unacceptable risk at Dam B.

Structure	DPR	Function	Failure	Final effect	(S)	Cause	(O)	Control	Type of control	(D)	RPN
B. Dam		a.Retain water	Insufficient capacity to contain water	Global instability	10	Inadequacy of design and / or construction and / or maintenance	7	Project suitability Visual inspection and instrumentation	Prevention Detection	3	210
B.1 Upstream slope	Progressive development of erosions in upstream slope, without the presence of water, in isolated deep erosion grooves, or in protection	7.Offer stability	Structural instability due to erosion	Global instability	3	Erosion	5	Adequacy of geometry and constituent materials Visual inspection and instrumentation	Prevention Detection	3	45
B.4 Downstream area	Irregular constructions in the downstream region, with no flow obstructions	1.Offer stability	Structural instability due to irregular constructions	Global instability	3	Irregular constructions downstream from the dam	7	Adequacy of management procedures Visual inspection	Prevention Detection	3	63
D. Reservoir		a.Retain water	Insufficient capacity to contain water	Global instability	10	Inadequacy of design and / or construction and / or maintenance	5	Project suitability Visual inspection and instrumentation	Prevention Detection	3	150
	Poor water quality in the reservoir, without recreational use	4. Store water for energy	Management	Global instability	3	Erosion	5	Adequacy of management procedures Audit	Prevention Detection	3	45

**Table 12.** Application summary of proposed method.

Topic	Dam A		Dam B		Dam C	
Anomaly	<i>NP</i> =0	0	<i>NP</i> =0	0	<i>NP</i> =0	6
	<i>NP</i> =1	15	<i>NP</i> =1	14	<i>NP</i> =1	36
	<i>NP</i> =2	35	<i>NP</i> =2	0	<i>NP</i> =2	4
	<i>NP</i> =3	0	<i>NP</i> =3	0	<i>NP</i> =3	0
	Total	50	Total	14	Total	46
Probabilistic risk ( <i>RP</i> )	749		150		634	
	Unacceptable	45	Unacceptable	6	Unacceptable	17
	Tolerable	76	Tolerable	11	Tolerable	64
	Acceptable	628	Acceptable	133	Acceptable	553
Failure analysis of unacceptable risks	45		6		17	
	Severe	0	Severe	0	Severe	0
	Intermediate	33	Intermediate	4	Intermediate	14
	Mild	12	Mild	2	Mild	3
General failure analysis (Place where anomalies are)	Severe	3	Severe	3	Severe	4
	Intermediate	0	Intermediate	0	Intermediate	0
	Mild	0	Mild	0	Mild	0

- o Risk analysis: breakdown of 14 anomalies into 150 failure scenarios due to local or global instability, for a given failure mode. Of this total, 6 are prioritized as unacceptable risks, that is, they must be immediately mitigated.
- o Failure analysis: out of the 6 unacceptable risks, none is a condition for severe failures, and the 4 intermediaries must be prioritized over the 2 mild ones.
- For the case of dam C:
  - o Inspection: 46 anomalies, 4 of which are critical but without understanding what the probability of its progression will generate a failure mode.
  - o Risk analysis: breakdown of 46 anomalies into 634 failure scenarios due to local or global instability, for a given failure mode. Of this total, 17 are prioritized as unacceptable risks, that is, they must be immediately mitigated.

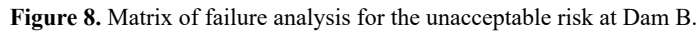


**Figure 7.** Tree events for anomaly A.3 for Dam B.

- confidence in the observational method, a continuous, managed and integrated design process, construction control and monitoring of structures. In many of the failures, the reports indicate a series of constructive breaches in the filter and drain systems, concrete galleries, concrete bypass channels, in addition to critical operational issues over the years of operation. The best practices, the best knowledge and the best available techniques need to be main guidelines, assumed about planning, design, construction, operation, monitoring and closing plan of dams. As these guidelines become clear, and are applied, the industry will no longer depend on assumptions about observational methods, which consider the expertise and particular point of view of engineers and consultants to make important decisions that affect risk.

The frequency and severity of the failures are increasing globally, the majority of which would be preventable if observed due diligence on the part of dam owners and operators. Technical knowledge exists to allow dams to be built and operated at low risk, but the frequency of ruptures leads to lapses in the consistent application of expertise throughout the life of an installation and due to a lack of attention to detail. In Brazil, professional practice and regulatory guidance allow unbridled



All structures present some degree of risk, even after control and, therefore, it is necessary to develop action plans, or contingency plans, to minimize such risks. In these plans, the necessary actions to minimize the risk and mitigate the consequences should the event be addressed, as well as address issues of responsibility and responses to emergencies. The proposed method reduces the subjectivity of filling in dam inspection forms, expanding the understanding of which anomalies are most significant from the point of view of triggering a failure mode. In this way, it allows prioritizing an action plan in a more assertive way, reducing time of operation and maintenance costs, as it increases the effectiveness in controlling anomalies in dam safety management.

The application of the proposed method for the case study of the three dams allows us to conclude that:

- The definition of an action plan based only on the observations of the inspection form has a subjective character, since it will depend on the professional's expertise in surveying the structure's commitment in the face of a certain anomaly;
- As levels of magnitude ( $M$ ) and danger level ( $NP$ ) associated with each anomaly are defined, a pattern is created that reduces subjectivity in the classification of the anomaly and allows the identification of critical anomalies ( $NP \geq 2$ ) that require more immediate intervention. It is noteworthy that until this phase of the method it is not yet defined which anomaly represents the greatest risk, as it is a partial analysis;
- When creating the probabilistic matrix of the combination of magnitude ( $M$ ) with the danger level ( $NP$ ), it is possible to find the anomaly probability ( $PA$ ), an index for entry into the proposed method event trees. The higher the  $PA$ , the closer the anomaly is to the unacceptable risk scenario;
- Failure Mode ( $MF$ ) identification allows to relate the anomaly to the final process of instability in the progression of the anomaly, both from a local and global point of view. Thus, when sequencing the event tree for each anomaly, the objective will always be to predict all scenarios up to the defined failure mode;
- The events in the event tree are broken down based on the observations of the inspection forms and the photographic report and, accordingly, it is important to detail each anomaly marked on the form. The higher the level of details, the more accurate the establishment of the percentages of each event and, consequently, the more assertive the calculation of the probabilistic risk ( $RP$ );
- The definition of probabilistic risks at unacceptable, tolerable and acceptable intervals, allows the action plan to be directed towards a more specific intervention, in order to mitigate anomalies that have a development more directed to the specified failure mode;

- Failure analysis of unacceptable risks, prioritizes anomalies that lead to severe failures within the action plan, followed by intermediate and mild failures. In this way, a robust, directive plan can be used to guide all dam safety management;
- The severe failure action plan should include more immediate mitigating actions in relation to anomalies that correspond to intermediate failures and, in the sequencing, to mild failures;
- The proposed method is a failure and risk analysis tool that must be used in conjunction with other techniques to guarantee the local and global stability of dams;
- For the complete version of this methodology, access the PhD Thesis available at Fernandes (2020).

## Declaration of interest

The authors have no conflicts of interest to declare. All co-authors have observed and affirmed the contents of the paper and there is no financial interest to report.

## Authors' contributions

Rafaela Baldi Fernandes: conceptualization, writing - original draft, data curation. Ana Cristina Castro Fontenla Sieira: writing - review & editing, supervision, validation. Armando Prestes Menezes Filho: writing - review, formal analysis.

## List of symbols

$\beta$	Reliability index
AU	Increased
coV	Coefficient of variation
CMP	Maximum design flood
$D$	Detection Index
DI	Decreased
DPR	Probabilistic Anomaly Description
DS	Disappeared
FMEA	Failure Mode Event Analysis
FS	Safety Factor
$G$	Large Magnitude
$H$	Horizontal
$I$	Insignificant Magnitude
$M$	Safety margin
$M$	Magnitude
$M$	Average Magnitude
MF	Failure Mode
$N$	Number of events
NP	Danger Level
$O$	Occurrence Index
$P$	Small Magnitude
PA	Anomaly Probability
PC	Remained Constant
PE	Anomaly Probability per Event

<i>P<sub>f</sub></i>	Probability of failure
<i>P<sub>I</sub></i>	Inspection Probability
<i>P<sub>V</sub></i>	First Time
<i>R<sub>P</sub></i>	Probabilistic Risk
<i>R<sub>PN</sub></i>	Risk Potential Number
<i>S</i>	Severity Index
<i>SD</i>	Standard deviation
<i>TR</i>	Return Period
<i>V</i>	Vertical

## References

- ABNT NBR 31000. (2018). *Risk Management: Guidelines*. ABNT - Associação Brasileira de Normas Técnicas, Rio de Janeiro, RJ (in Portuguese).
- Brazendale, J., & Bell, R. (1994). Safety-related control and protection systems: standards update. *IEE Computing and Control Engineering J.*, 5(1), 6-12. <http://dx.doi.org/10.1049/cce:19940101>.
- Costa, J.E. (1985). *Floods from dam failures*. Reston: U.S. Geological Survey.
- Fernandes, R.B. (2017). *Manual for preparing emergency action plans for mining dams (PAE)* (1st ed.). Belo Horizonte: Instituto Minere (in Portuguese).
- Fernandes, R.B. (2020). *Methodology for risk management in dams from the Event Tree and FMEA Analysis* [Doctoral thesis, Rio de Janeiro University State]. Rio de Janeiro University's repository (in Portuguese). Retrieved in May 1, 2021, from <http://www.labbas.eng.uerj.br/pgceciv/nova/files/teses/16.pdf>
- International Commission on Large Dams – ICOLD. (2001). *Tailings dams risk of dangerous occurrences: lessons learnt from practical experiences* (Bulletin, No. 121). Paris: ICOLD.
- Kloman, H.F. (1992). Rethinking risk management. *The Geneva Papers on Risk and Insurance - Issues and Practice*, 17(3), 299-313. <http://dx.doi.org/10.1057/gpp.1992.19>.
- Lacasse, S., Nadim, F., Liu, Z.Q., Eidsvig, U.K., Le, T.M.H., & Lin, C.G. (2019). Risk assessment and dams: recent developments and applications. In *Proceedings of the XVII European Conference on Soils Mechanics and Geotechnical Engineering* (Vol. 1, pp. 1-26), Reykjavik Iceland. <https://doi.org/10.32075/17ECSMGE-2019-1110>.
- Londe, P. (1995). Safety concepts applied to rock masses. In C. Fairhurst (Ed.), *Analysis and design methods: principles, practice and projects* (pp. 749-769). Minnesota: University of Minnesota. <https://doi.org/10.1016/B978-0-08-040615-2.50035-6>.
- U.S. Army Corps of Engineers – USACE. (2014). *Engineering and design: safety of dams: policy and procedures, engineering* (Manual, No. 1110-2-1156). Washington: USACE.
- Whitman, R.V. (1984). Evaluating calculated risk in geotechnical engineering. *Journal of Geotechnical Engineering*, 110(2), 143-189. [http://dx.doi.org/10.1061/\(ASCE\)0733-9410\(1984\)110:2\(143\)](http://dx.doi.org/10.1061/(ASCE)0733-9410(1984)110:2(143)).



## GABIÃO BELGO. UMA ESCOLHA PARA ELEVAR A QUALIDADE DA SUA OBRA.



A linha **Belgo GeoTech** traz ao mercado soluções em aço para aplicações geotécnicas. Entre os nossos produtos, disponibilizamos **gabiões**, **malhas talude**, **fibras de aço Dramix®**, **telas de fortificação**, **cordoalhas** e **barras helicoidais**. Mas também oferecemos suporte técnico qualificado para atender a todas as necessidades do seu projeto. **Aqui se faz geotecnia com a força do aço.**



Saiba mais em: [belgogeotech.com.br](http://belgogeotech.com.br)

**BELGO**  
GeoTech

Belgo Bekaert Arames

 ArcelorMittal

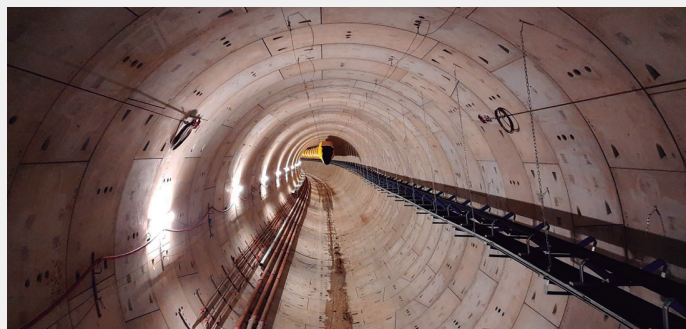
 **BEKAERT**  
better together





TPF - CONSULTORES DE ENGENHARIA E ARQUITETURA, S.A.

# BUILDING THE WORLD, BETTER



## ENGINEERING AND ARCHITECTURAL CONSULTANCY

- > GEOLOGY, GEOTECHNICS, SUPERVISION OF GEOTECHNICAL WORKS
- > EMBANKMENT DAMS, UNDERGROUND WORKS, RETAINING STRUCTURES
- > SPECIAL FOUNDATIONS, SOIL IMPROVEMENT, GEOMATERIALS

[www.tpf.pt](http://www.tpf.pt)





**TRANSFORMATIVE  
ENGINEERING,  
MANAGEMENT,  
AND INNOVATION  
DELIVERING RESULTS**



DF+ IS AN INTEGRATED ENGINEERING CONSULTING FIRM WITH OVER 25 YEARS OF EXPERIENCE IN THE SECTORS OF MINING, INFRASTRUCTURE, AGRIBUSINESS, AND INDUSTRIAL.

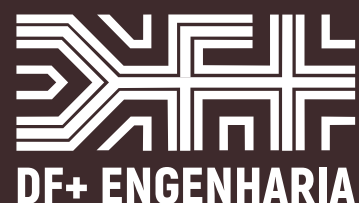
WE DEVELOP PROJECTS BASED ON CONSOLIDATED TECHNICAL SOLUTIONS THAT ENCOMPASS THE STATE OF THE ART IN DIGITAL ENGINEERING.



AV. BARÃO HOMEM DE MELO, 4554 - 5th floor  
ESTORIL, BELO HORIZONTE/MG

**+55 31 2519-1001**

**dfmais.eng.br**  
comercial@dfmais.eng.br





# PIONEERING AND INNOVATION

SINCE 1921

 **TEIXEIRA DUARTE**  
ENGENHARIA E CONSTRUÇÕES, S.A.

PORT FACILITY CONSTRUCTION  
NACALA - MOZAMBIQUE



Building a better world.  
[teixeiraduarteconstruction.com](http://teixeiraduarteconstruction.com)





Safety is our nature

Líder mundial em pesquisa, desenvolvimento, fabricação e comercialização de soluções em aço de alta resistência contra desastres naturais.

Leading research, development, manufacturing and supplying high tensile steel solutions against natural hazards.



Petrópolis/RJ-Brasil

## SEGURANÇA É A NOSSA NATUREZA

**Estabilização de taludes |**  
Slope stabilization

**Queda de rochas |**  
Rockfall

**Escorregamento Superficial |**  
Shallow landslides

**Corridas detríticas |**  
Debris flow

**Escavações subterrâneas |**  
Underground support

Para mais informações, acesse  
[www.geobrugg.com](http://www.geobrugg.com)





# The Best Solution!

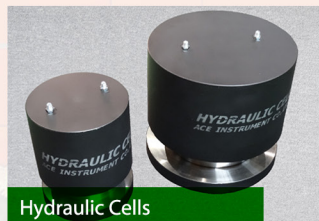
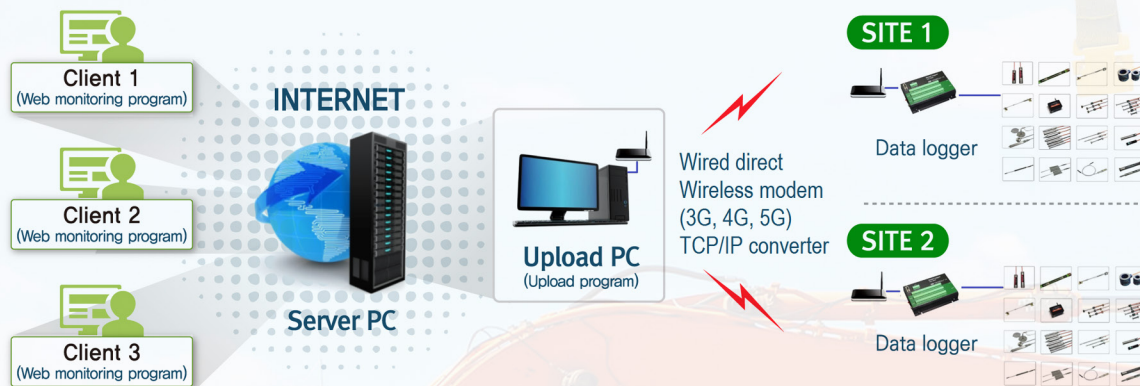
**Tecnilab Portugal, S.A.** will provide you with answers to your Geotechnical engineering needs.

**Tecnilab Portugal, S.A.** is a professional Geotechnical engineering company and has a lot of experience as a professional group that mainly engages in measurement engineering in dam, subway(Metro), harbor, power plant, soft ground and structure construction.

**WE ARE THE DISTRIBUTOR OF PORTUGAL OF ACE INSTRUMENT CO., LTD. IN KOREA.**

**ACE INSTRUMENT CO., LTD.** is a company that obtains worldwide reputation for supplying high precision, high reliability products in all Geotechnical instruments, data logger and in-situ test equipments. Independently developed automatic monitoring system can be used anywhere in the world, including buildings, bridges, ground and any constructions.

## Data Acquisition System & Web Monitoring Program



Sales company



**Tecnilab Portugal, S.A.**

A: Rua Gregorio Lopes, Lote 1512B 1449-041 Lisboa Portugal  
T: +351 217 220 870 F: +351 217 264 550  
www.tecnilab.pt

Manufacturer



**ACE INSTRUMENT CO., LTD.**

The first value in Geotechnical & Structural Instrumentation  
A: 9, Dangjung-ro 27 beon-gil, Gunpo-si, Gyeonggi-do, Korea  
T: +82 31 459 8753-7 F: +82 31 459 8758 E: acens@naver.com  
www.aceinstrument.com



# ENGINEERING AND ENVIRONMENTAL CONSULTANTS



## COBA



## GEOLOGY AND GEOTECHNICS

Hydrogeology • Engineering Geology • Rock Mechanics • Soil Mechanics • Foundations and Retaining Structures • Underground Works • Embankments and Slope Stability  
Environmental Geotechnics • Geotechnical Mapping



- Water Resources Planning and Management
- Hydraulic Undertakings
- Electrical Power Generation and Transmission
- Water Supply Systems and Pluvial and Wastewater Systems
- Agriculture and Rural Development
- Road, Railway and Airway Infrastructures
- Environment
- Geotechnical Structures
- Cartography and Cadastre
- Safety Control and Work Rehabilitation
- Project Management and Construction Supervision



### PORTUGAL

CENTER AND SOUTH REGION  
Av. 5 de Outubro, 323  
1649-011 LISBOA  
Tel.: (351) 210125000, (351) 217925000  
Fax: (351) 217970348  
E-mail: [coba@coba.pt](mailto:coba@coba.pt)  
[www.coba.pt](http://www.coba.pt)

Av. Marquês de Tomar, 9, 6º.  
1050-152 LISBOA  
Tel.: (351) 217925000  
Fax: (351) 213537492

### NORTH REGION

Rua Mouzinho de Albuquerque, 744, 1º.  
4450-203 MATOSINHOS  
Tel.: (351) 229380421  
Fax: (351) 229373648  
E-mail: [engico@engico.pt](mailto:engico@engico.pt)

### ANGOLA

Praceta Farinha Leitão, edifício nº 27, 27-A - 2º Dto  
Bairro do Maculusso, LUANDA  
Tel./Fax: (244) 222338 513  
Cell: (244) 923317541  
E-mail: [coba-angola@netcabo.co.ao](mailto:coba-angola@netcabo.co.ao)

### MOZAMBIQUE

Pestana Rovuma Hotel. Centro de Escritórios.  
Rua da Sé nº114. Piso 3, MAPUTO  
Tel./Fax: (258) 21 328 813  
Cell: (258) 82 409 9605  
E-mail: [coba.mz@tdm.co.mz](mailto:coba.mz@tdm.co.mz)

### ALGERIA

09, Rue des Frères Hocine  
El Biar - 16606, ARGEL  
Tel.: (213) 21 922802  
Fax: (213) 21 922802  
E-mail: [coba.alger@gmail.com](mailto:coba.alger@gmail.com)

### BRAZIL

Rio de Janeiro  
COBA Ltd. - Rua Bela 1128  
São Cristóvão  
20930-380 Rio de Janeiro RJ  
Tel.: (55 21) 351 50 101  
Fax: (55 21) 258 01 026

### Fortaleza

Av. Senador Virgílio Távora 1701, Sala 403  
Aldeota - Fortaleza CEP 60170 - 251  
Tel.: (55 85) 3261 17 38  
Fax: (55 85) 3261 50 83  
E-mail: [coba@esc-te.com.br](mailto:coba@esc-te.com.br)

### UNITED ARAB EMIRATES

Corniche Road - Corniche Tower - 5th Floor - 5B  
P.O. Box 38360 ABU DHABI  
Tel.: (971) 2 627 0088  
Fax: (971) 2 627 0087



## Maccaferri Rockfall barrier installed alongside mesh systems

*Combining different systems to provide the most effective solution for rock faces and soil slopes.*

Maccaferri RB Series of rockfall barriers is specifically designed to retain impacts of falling boulders, protecting people and infrastructure. Maccaferri rockfall barriers are available with energy absorption capacity starting from 35 kJ and up to 9,000 kJ, which is equivalent to the kinetic energy generated by a block of 29 tons falling at 90 km/h.

Maccaferri additionally developed numerous rockfall mitigation and erosion protection system to be implemented directly within the detachment zone. Among those, soil nailing is a technique that combines the use of steel anchors and facing systems to provide global and surficial stability to soil and weathered rocks.

The facing system plays a key role since it restrains the superficial portion of the slope which can mobilise between the anchors, potentially destabilizing the overall slope. Therefore, Maccaferri developed MacMat®, an innovative reinforced 3D geomat that provide surficial stabilization while promoting the revegetation of the slope.

Very often the use of combined solutions such as the two mentioned above leads to the best results. It also provides the most cost-effective balance between technical performance, risk, client value, ease/safety of installation and environmental benefits.



/maccaferri



/maccaferrimatriz



@Maccaferri\_BR



/MaccaferriWorld



/maccaferriworld

**MACCAFERRI**





The Ground is our Challenge

## MAIN ACTIVITY AREAS

Consultancy, Supervision and Training

- Earth Retaining Structures
- Special Foundations
- Ground Improvement
- Foundations Strengthening and Underpinning
- Façades Retention
- Tunnels and Underground Structures
- Slope Stability
- Geological and Geotechnical Investigation
- Demolition

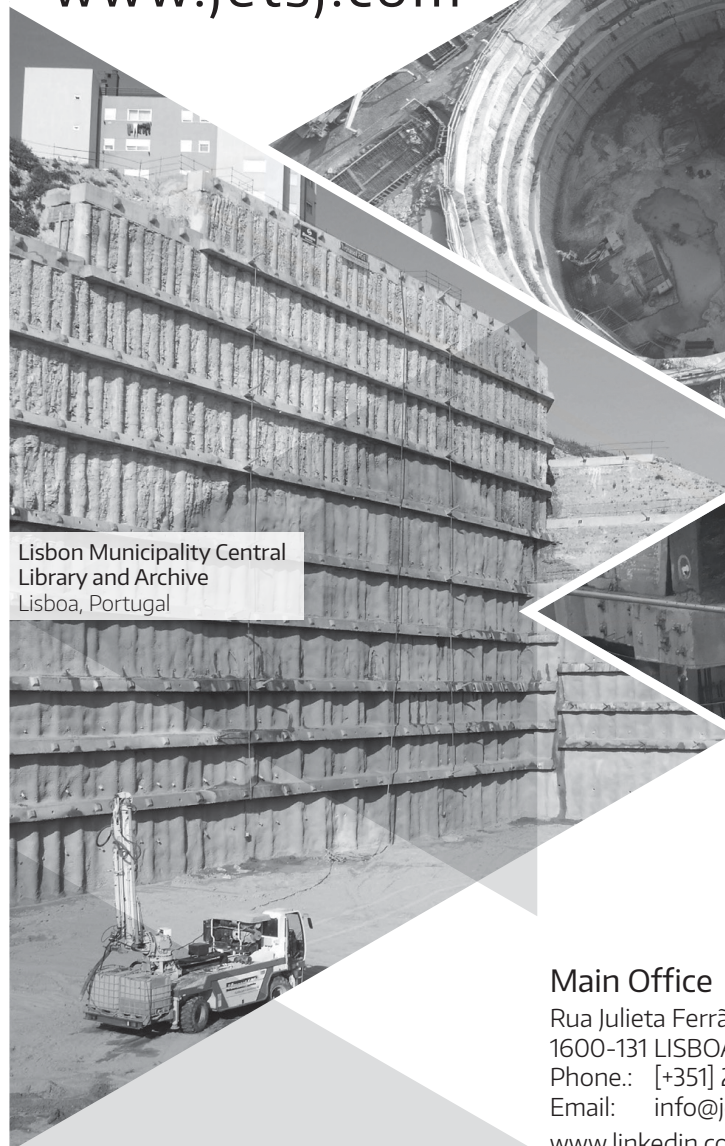
[www.jetsj.com](http://www.jetsj.com)



Tool Plazas P2 and P3  
Santa Catarina, Brazil



Mining Shaft  
Kamsar, Guiné



Lisbon Municipality Central  
Library and Archive  
Lisboa, Portugal



Solar Santana Building  
Lisboa, Portugal

## Main Office

Rua Julieta Ferrão, 12 - Office 1501

1600-131 LISBOA, Portugal

Phone.: [+351] 210 505 150 / 51

Email: [info@jetsj.com](mailto:info@jetsj.com)

[www.linkedin.com/company/jetsj-geotecnia-lda/](http://www.linkedin.com/company/jetsj-geotecnia-lda/)



- > **Prospecção Geotécnica**  
*Site Investigation*
- > **Consultoria Geotécnica**  
*Geotechnical Consultancy*
- > **Obras Geotécnicas**  
*Ground Treatment-Construction Services*
- > **Controlo e Observação**  
*Field Instrumentation Services and Monitoring Services*
- > **Laboratório de Mecânica de Solos**  
*Soil and Rock Mechanics Laboratory*

Certificada ISO 9001 por



# Geocontrole



Parque Oriente, Bloco 4, EN10  
2699-501 Bobadela LRS  
Tel. 21 995 80 00  
Fax. 21 995 80 01  
e.mail: mail@geocontrole.pt  
www.geocontrole.pt

  
**Geocontrole**  
Geotecnia e Estruturas de Fundação SA



## Guide for Authors

Soils and Rocks is an international scientific journal published by the Brazilian Association for Soil Mechanics and Geotechnical Engineering (ABMS) and by the Portuguese Geotechnical Society (SPG). The aim of the journal is to publish original papers on all branches of Geotechnical Engineering. Each manuscript is subjected to a single-blind peer-review process. The journal's policy of screening for plagiarism includes the use of a plagiarism checker on all submitted manuscripts.

Soils and Rocks embraces the international Open Science program and is striving to meet all the recommendations. However, at this moment, the journal is not yet accepting preprints and open data, and has not adopted open peer reviews.

Soils and Rocks provides a manuscript template available at the journal's website.

### 1. Category of papers

Submissions are classified into one of the following categories:

**Article** – an extensive and conclusive dissertation about a geotechnical topic, presenting original findings.

**Technical Note** – presents a study of smaller scope or results of ongoing studies, comprising partial results and/or particular aspects of the investigation.

**Case Study** – report innovative ways to solve problems associated with design and construction of geotechnical projects. It also presents studies of the performance of existing structures.

**Review Article** – a summary of the State-of-the-Art or State-of-the-Practice on a particular subject or issue and represents an overview of recent developments.

**Discussion** – specific discussions about published papers.

Authors are responsible for selecting the correct category when submitting their manuscript. However, the manuscript category may be altered based on the recommendation of the Editorial Board. Authors are also requested to state the category of paper in their Cover Letter.

When submitting a manuscript for review, the authors should indicate the category of the manuscript, and is also understood that they:

- a) assume full responsibility for the contents and accuracy of the information in the paper;
- b) assure that the paper has not been previously published, and is not being submitted to any other journal for publication.

### 2. Paper length

Full-length manuscripts (Article, Case Study) should be between 4,000 and 8,000 words. Review articles should have up to 10,000 words. Technical Notes have a word count limit of 3,500 words. Discussions have a word count limit of 1,000 words. These word count limits exclude the title page, notation list (e.g., symbols, abbreviations), captions of tables and figures, acknowledgments and references. Each single column and double column figure or table is considered as equivalent to 150 and 300 words, respectively.

### 3. Scientific style

The manuscripts should be written in UK or US English, in the third person and all spelling should be checked in accordance with

a major English Dictionary. The manuscript should be able to be readily understood by a Civil Engineer and avoid colloquialisms. Unless essential to the comprehension of the manuscript, direct reference to the names of persons, organizations, products or services is not allowed. Flattery or derogatory remarks about any person or organization should not be included.

The author(s) of Discussion Papers should refer to himself (herself/themselves) as the reader(s) and to the author(s) of the paper as the author(s).

The International System (SI) units must be used. The symbols are recommended to be in accordance with Lexicon in 14 Languages, ISSMFE (2013) and the ISRM List of Symbols. Use italics for single letters that denote mathematical constants, variables, and unknown quantities, either in tables or in the text.

### 4. Submission requirements and contents

A submission implies that the following conditions are met:

- the authors assume full responsibility for the contents and accuracy of the information presented in the paper;
- the manuscript contents have not been published previously, except as a lecture or academic thesis;
- the manuscript is not under consideration for publication elsewhere;
- the manuscript is approved by all authors;
- the manuscript is approved by the necessary authorities, when applicable, such as ethics committees and institutions that may hold intellectual property on contents presented in the manuscript;
- the authors have obtained authorization from the copyright holder for any reproduced material;
- the authors are aware that the manuscript will be subjected to plagiarism check.

The author(s) must upload two digital files of the manuscript to the Soils and Rocks submission system. The size limit for each submission file is 20 MB. The manuscript should be submitted in docx format (Word 2007 or higher) or doc format (for older Word versions). An additional PDF format file of the manuscript is also required upon submission. Currently, the journal is not accepting manuscripts prepared using LaTeX.

The following documents are required as minimum for submission:

- cover letter;
- manuscript with figures and tables embedded in the text (doc or docx format);

manuscript with figures and tables embedded in the text for revision (PDF format);

- permission for re-use of previously published material when applicable, unless the author/owner has made explicit that the image is freely available.

#### 4.1 Cover letter

The cover letter should include: manuscript title, submission type, authorship information, statement of key findings and work novelty, and related previous publications if applicable.

#### 4.2 Title page

The title page is the first page of the manuscript and must include:

- A concise and informative title of the paper. Avoid abbreviations, acronyms or formulae. Discussion Papers should contain the title of the paper under discussion. Only the first letter of the first word should be capitalized.
- Full name(s) of the author(s). The first name(s) should not be abbreviated. The authors are allowed to abbreviate middle name(s).
- The corresponding author should be identified by a pound sign # beside his/her and in a footnote.
- The affiliation(s) of the author(s), should follow the format: Institution, (Department), City, (State), Country.
- Affiliation address and e-mail must appear below each author's name.
- The 16-digit ORCID of the author(s) – mandatory
- Main text word count (excluding abstract and references) and the number of figures and tables

#### 4.3 Permissions

Figures, tables or text passages previously published elsewhere may be reproduced under permission from the copyright owner(s) for both the print and online format. The authors are required to provide evidence that such permission has been granted at the moment of paper submission.

#### 4.4 Declaration of interest

Authors are required to disclose conflicting interests that could inappropriately bias their work. For that end, a section entitled “Declaration of interest” should be included following any acknowledgments and prior to the “Authors’ contributions” section. In case of the absence of conflicting interests, the authors should still include a declaration of interest.

#### 4.5 Authors’ contributions

Authors are required to include an author statement outlining their individual contributions to the paper according to the CASRAI CRediT roles (as per <https://casrai.org/credit>). The minimum requirements of contribution to the work for recognition of authorship are: a) Participate actively in the discussion of results; b) Review and approval of the final version of the manuscript. A section entitled “Authors’ contributions” should be included after the declaration of interest section, and should be formatted with author's name and CRediT role(s), according to the example:

**Samuel Zheng:** conceptualization, methodology, validation. **Olivia Prakash:** data curation, writing - original draft preparation. **Fatima Wang:** investigation, validation. **Kwame Bankole:** supervision. **Sun Qi:** writing - reviewing and editing.

Do not include credit items that do not follow the Taxonomy established by CASRAI CRediT roles.

The authors’ contributions section should be omitted in manuscripts that have a single author.

#### 5. Plagiarism checking

Submitted papers are expected to contain at least 50 % new content and the remaining 50 % should not be verbatim to previously published work.

All manuscripts are screened for similarities. Currently, the Editorial Board uses the plagiarism checker Plagius ([www.plagius.com](http://www.plagius.com)) to compare submitted papers to already published works. Manuscripts will be rejected if more than 20 % of content matches previously published work, including self-plagiarism. The decision to reject will be under the Editors’ discretion if the percentage is between 10 % and 20 %.

**IMPORTANT OBSERVATION:** Mendeley software plug-in (suggested in this guide) for MS-Word can be used to include the references in the manuscript. This plug-in uses a field code that sometimes includes automatically both title and abstract of the reference. Unfortunately, the similarity software adopted by the Journal (Plagius) recognizes the title and abstract as an actual written text by the field code of the reference and consequently increases considerably the percentage of similarity. Please do make sure to remove the abstract (if existing) inside Mendeley section where the adopted reference is included. This issue has mistakenly caused biased results in the past. The Editorial Board of the journal is now aware of this tendentious feature.

#### 6. Formatting instructions

The text must be presented in a single column, using ISO A4 page size, left, right, top, and bottom margins of 25 mm, Times New Roman 12 font, and line spacing of 1.5. All lines and pages should be numbered.

The text should avoid unnecessary italic and bold words and letters, as well as too many acronyms. Authors should avoid to capitalize words and whenever possible to use tables with distinct font size and style of the regular text.

Figures, tables and equations should be numbered in the sequence that they are mentioned in the text.

##### *Abstract*

Please provide an abstract between 150 and 250 words in length. Abbreviations or acronyms should be avoided. The abstract should state briefly the purpose of the work, the main results and major conclusions or key findings.

##### *Keywords*

A minimum of three and a maximum of six keywords must be included after the abstract. The keywords must represent the

content of the paper. Keywords offer an opportunity to include synonyms for terms that are frequently referred to in the literature using more than one term. Adequate keywords maximize the visibility of your published paper.

Examples:

Poor keywords – piles; dams; numerical modeling; laboratory testing

Better keywords – friction piles; concrete-faced rockfill dams; material point method; bender element test

#### List of symbols

A list of symbols and definitions used in the text must be included before the References section. Any mathematical constant, variable or unknown quantity should appear in italics.

### 6.1 Citations

References to other published sources must be made in the text by the last name(s) of the author(s), followed by the year of publication. Examples:

- Narrative citation: [...] while Silva & Pereira (1987) observed that resistance depended on soil density
- Parenthetical citation: It was observed that resistance depended on soil density (Silva & Pereira, 1987).

In the case of three or more authors, the reduced format must be used, e.g.: Silva et al. (1982) or (Silva et al., 1982). Do not italicize “et al.”

Two or more citations belonging to the same author(s) and published in the same year are to be distinguished with small letters, e.g.: (Silva, 1975a, b, c.).

Standards must be cited in the text by the initials of the entity and the year of publication, e.g.: ABNT (1996), ASTM (2003).

### 6.2 References

A customized style for the Mendeley software is available and may be downloaded from this link.

Full references must be listed alphabetically at the end of the text by the first author's last name. Several references belonging to the same author must be cited chronologically.

Some formatting examples are presented here:

#### Journal Article

Bishop, A.W., & Blight, G.E. (1963). Some aspects of effective stress in saturated and partly saturated soils. *Géotechnique*, 13(2), 177-197. <https://doi.org/10.1680/geot.1963.13.3.177>

Castellanza, R., & Nova, R. (2004). Oedometric tests on artificially weathered carbonatic soft rocks. *Journal of Geotechnical and Geoenvironmental Engineering*, 130(7), 728-739. [https://doi.org/10.1061/\(ASCE\)1090-0241\(2004\)130:7\(728\)](https://doi.org/10.1061/(ASCE)1090-0241(2004)130:7(728))

Fletcher, G. (1965). Standard penetration test: its uses and abuses. *Journal of the Soil Mechanics Foundation Division*, 91, 67-75.

Indraratna, B., Kumara, C., Zhu S-P., Sloan, S. (2015). Mathematical modeling and experimental verification of fluid flow through deformable rough rock joints. *International Journal of Geomechanics*, 15(4): 04014065-1-04014065-11. [https://doi.org/10.1061/\(ASCE\)GM.1943-5622.0000413](https://doi.org/10.1061/(ASCE)GM.1943-5622.0000413)

Garnier, J., Gaudin, C., Springman, S.M., Culligan, P.J., Goodings, D., König, D., ... & Thorel, L. (2007). Catalogue of scaling laws and similitude questions in geotechnical centrifuge modelling. *International Journal of Physical Modelling in Geotechnics*, 7(3), 01-23. <https://doi.org/10.1680/ijpmg.2007.070301>

Bicalho, K.V., Gramelich, J.C., & Santos, C.L.C. (2014). Comparação entre os valores de limite de liquidez obtidos pelo método de Casagrande e cone para solos argilosos brasileiros. *Comunicações Geológicas*, 101(3), 1097-1099 (in Portuguese).

#### Book

Lambe, T.W., & Whitman, R.V. (1979). *Soil Mechanics, SI version*. John Wiley & Sons.

Das, B.M. (2012). *Fundamentos de Engenharia Geotécnica*. Cengage Learning (in Portuguese).

Head, K.H. (2006). *Manual of Soil Laboratory Testing - Volume 1: Soil Classification and Compaction Tests*. Whittles Publishing.

Bhering, S.B., Santos, H.G., Manzatto, C.V., Bognola, I., Fasolo, P.J., Carvalho, A.P., ... & Curcio, G.R. (2007). *Mapa de solos do estado do Paraná*. Embrapa (in Portuguese).

#### Book Section

Yerro, A., & Rohe, A. (2019). Fundamentals of the Material Point Method. In *The Material Point Method for Geotechnical Engineering* (pp. 23-55). CRC Press. <https://doi.org/10.1201/9780429028090>

Sharma, H.D., Dukes, M.T., & Olsen, D.M. (1990). Field measurements of dynamic moduli and Poisson's ratios of refuse and underlying soils at a landfill site. In *Geotechnics of Waste Fills - Theory and Practice* (pp. 57-70). ASTM International. <https://doi.org/10.1520/STP1070-EB>

Cavalcante, A.L.B., Borges, L.P.F., & Camapum de Carvalho, J. (2015). Tomografias computadorizadas e análises numéricas aplicadas à caracterização da estrutura porosa de solos não saturados. In *Solos Não Saturados no Contexto Geotécnico* (pp. 531-553). ABMS (in Portuguese).

#### Proceedings

Jamiolkowski, M.; Ladd, C.C.; Germaine, J.T., & Lancellotta, R. (1985). New developments in field and laboratory testing of soils. *Proc. 11th International Conference on Soil Mechanics and Foundation Engineering*, San Francisco, August 1985. Vol. 1, Balkema, 57-153.

Massey, J.B., Irfan, T.Y. & Cipullo, A. (1989). The characterization of granitic saprolitic soils. *Proc. 12th International Conference on Soil Mechanics and Foundation Engineering*, Rio de Janeiro. Vol. 6, Publications Committee of XII ICSMF, 533-542.



Indraratna, B., Oliveira D.A.F., & Jayanathan, M. (2008b). Revised shear strength model for infilled rock joints considering overconsolidation effect. *Proc. 1st Southern Hemisphere International Rock Mechanics Symposium*, Perth. ACG, 16-19.

Barreto, T.M., Repsold, L.L., & Casagrande, M.D.T. (2018). Melhoria de solos arenosos com polímeros. *Proc. 19º Congresso Brasileiro de Mecânica dos Solos e Engenharia Geotécnica*, Salvador. Vol. 2, ABMS, CBMR, ISRM & SPG, 1-11 (in Portuguese).

#### Thesis

Lee, K.L. (1965). *Triaxial compressive strength of saturated sands under seismic loading conditions* [Unpublished doctoral dissertation]. University of California at Berkeley.

Chow, F.C. (1997). *Investigations into the behaviour of displacement pile for offshore foundations* [Doctoral thesis, Imperial College London]. Imperial College London's repository. <https://spiral.imperial.ac.uk/handle/10044/1/7894>

Araki, M.S. (1997). *Aspectos relativos às propriedades dos solos porosos colapsíveis do Distrito Federal* [Unpublished master's dissertation]. University of Brasília (in Portuguese).

Sotomayor, J.M.G. (2018). *Evaluation of drained and non-drained mechanical behavior of iron and gold mine tailings reinforced with polypropylene fibers* [Doctoral thesis, Pontifical Catholic University of Rio de Janeiro]. Pontifical Catholic University of Rio de Janeiro's repository (in Portuguese). <https://doi.org/10.17771/PUCRio.acad.36102>\*

\* official title in English should be used when available in the document.

#### Report

ASTM D7928-17. (2017). Standard Test Method for Particle-Size Distribution (Gradation) of Fine-Grained Soils Using the Sedimentation (Hydrometer) Analysis. *ASTM International, West Conshohocken, PA*. <https://doi.org/10.1520/D7928-17>

ABNT NBR 10005. (2004). Procedure for obtention leaching extract of solid wastes. *ABNT - Associação Brasileira de Normas Técnicas*, Rio de Janeiro, RJ (in Portuguese).

DNIT. (2010). Pavimentação - Base de solo-cimento - Especificação de serviço DNIT 143. *DNIT -Departamento Nacional de Infraestrutura de Transportes*, Rio de Janeiro, RJ (in Portuguese).

USACE (1970). Engineering and Design: Stability of Earth and Rock-Fill Dams, Engineering Manual 1110-2-1902. Corps of Engineers, Washington, D.C.

#### Web Page

Soils and Rocks. (2020). *Guide for Authors*. Soils and Rocks. Retrieved in September 16, 2020, from <http://www.soilsandrocks.com/>

### 6.3 Artworks and illustrations

Each figure should be submitted as a high-resolution image, according to the following mandatory requirements:

- Figures must be created as a TIFF file format using LZW compression with minimum resolution of 500 dpi.
- Size the figures according to their final intended size. Single-column figures should have a width of up to 82 mm. Double-column figures should have a maximum width of 170 mm.
- Use Times New Roman for figure lettering. Use lettering sized 8-10 pt. for the final figure size.
- Lines should have 0.5 pt. minimum width in drawings.
- Titles or captions should not be included inside the figure itself.

Figures must be embedded in the text near the position where they are first cited. Cite figures in the manuscript in consecutive numerical order. Denote figure parts by lowercase letters (a, b, c, etc.). Please include a reference citation at the end of the figure caption for previously published material. Authorization from the copyright holder must be provided upon submission for any reproduced material.

Figure captions must be placed below the figure and start with the term "Figure" followed by the figure number and a period. Example:

Figure 1. Shear strength envelope.

Do not abbreviate "Figure" when making cross-references to figures.

All figures are published in color for the electronic version of the journal; however, the print version uses grayscale. Please format figures so that they are adequate even when printed in grayscale.

**Accessibility:** Please make sure that all figures have descriptive captions (text-to-speech software or a text-to-Braille hardware could be used by blind users). Prefer using patterns (e.g., different symbols for dispersion plot) rather than (or in addition to) colors for conveying information (then the visual elements can be distinguished by colorblind users). Any figure lettering should have a contrast ratio of at least 4.5:1

**Improving the color accessibility for the printed version and for colorblind readers:** Authors are encouraged to use color figures because they will be published in their original form in the online version. However, authors must consider the need to make their color figures accessible for reviewers and readers that are colorblind. As a general rule of thumb, authors should avoid using red and green simultaneously. Red should be replaced by magenta, vermillion, or orange. Green should be replaced by an off-green color, such as blue-green. Authors should prioritize the use of black, gray, and varying tones of blue and yellow.

These rules of thumb serve as general orientations, but authors must consider that there are multiple types of color blindness, affecting the perception of different colors. Ideally, authors should make use of the following resources: 1) for more information on how to prepare color figures, visit <https://jfly.uni-koeln.de/>; 2) a freeware software available at <http://www.vischeck.com/> is offered by Vischeck, to show how your figures would be perceived by the colorblind.

## 6.4 Tables

Tables should be presented as a MS Word table with data inserted consistently in separate cells. Place tables in the text near the position where they are first cited. Tables should be numbered consecutively using Arabic numerals and have a caption consisting of the table number and a brief title. Tables should always be cited in the text. Any previously published material should be identified by giving the original source as a reference at the end of the table caption. Additional comments can be placed as footnotes, indicated by superscript lower-case letters.

When applicable, the units should come right below the corresponding column heading. Horizontal lines should be used at the top and bottom of the table and to separate the headings row. Vertical lines should not be used.

Table captions must be placed above the table and start with the term “Table” followed by the table number and a period. Example:

Table 1. Soil properties.

Do not abbreviate “Table” when making cross-references to tables. Sample:

Table 1. Soil properties

Parameter	Symbol	Value
Specific gravity of the sand particles	$G_s$	2.64
Maximum dry density (Mg/m <sup>3</sup> )	$\rho_{d(max)}$	1.554
Minimum dry density (Mg/m <sup>3</sup> )	$\rho_{d(min)}$	1.186
Average grain-size (mm)	$d_{50}$	0.17
Coefficient of uniformity	$C_u$	1.97

## 6.5 Mathematical equations

Equations must be submitted as editable text, created using MathType or the built-in equation editor in MS Word. All variables must be presented in italics.

Equations must appear isolated in a single line of the text. Numbers identifying equations must be flushed with the right margin. International System (SI) units must be used. The definitions of the symbols used in the equations must appear in the List of Symbols.

Do not abbreviate “Equation” when making cross-references to an equation.